On-Chip Silicon Optomechanical Cavities at Low Temperatures

by

Bradley Hauer

A thesis submitted in partial fulfillment of the requirements for the degree of

Doctor of Philosophy

Department of Physics

University of Alberta

Abstract

Cryogenic optomechanical cavities fabricated from silicon are promising candidates for quantum information applications and platforms to study mesoscale quantum physics. However, the low temperature behaviour of these devices remains shrouded in mystery. To elucidate this, we have designed and built an optomechanical coupling apparatus inside of a dilution refrigerator, which we use to study on-chip silicon optical microdisks coupled to nanomechanical beams. Using an optomechanically mediated thermal ringdown technique, we measure the dissipation in a half-ring resonator between 10 mK to 10 K, and attribute it to two-level system defects embedded within the one-dimensional geometry of the device. Modifying the standard tunneling model to describe this damping mechanism, we determine the density of states and deformation potentials of these two-level system ensembles, postulating that they originate from surface defects. We also study a low temperature photothermal backaction force observed in our devices that acts to suppress conventional radiation-pressure effects. Using a photothermal optomechanical model, we find that this interaction can, in principle, be exploited to cool our resonator's motion into its ground state. Finally, we use a master equation approach to assess the feasibility of using our device geometry to perform nonlinear optomechanical measurements of quantized mechanical energy. In doing so, we set an upper limit on the allowable linear coupling strength of the system, which is significantly less stringent than the single-photon strong coupling regime required in previously studied optomechanical cavities.

Preface

Much of the work detailed in this thesis was a collaborative effort involving a number of members of the Davis group, including (but not limited to) Allison MacDonald (AM), Paul Kim (PK), Callum Doolin (CD), Tommy Clark (TC), Hugh Ramp (HR), Fabien Souris (FS), Xavier Rojas (XR), Greg Popowich (GP), and John Davis (JD). The general contributions from each are described below, with the specific contributions to each experiment detailed in the following paragraphs. The optomechanical device fabrication outlined in Section 5.2.2 was undertaken by PK. The low temperature imaging system detailed in Section 5.4.1 was designed and built by AM, GP, and JD. The cryogenic optomechanical coupling apparatus discussed in Section 5.4.2 was designed and built by AM, PK, XR, GP, JD, and myself. The dilution refrigerator was operated and maintained by PK, XR, FS, HR, GP, JD, and myself. The optical detection circuit described in Section 5.4.3 was designed and built by AM, PK, CD, TC, HR, JD, and myself. Data acquisition software was developed and maintained by CD and HR.

Section 5.3 of Chapter 5 is based on the publication B. D. Hauer, P. H. Kim, C. Doolin, A. J. R. MacDonald, H. Ramp, and J. P. Davis, "On-chip cavity optomechanical coupling," *EPJ Tech. Intrum.* **1**, 4 (2014). In this work, the tapered fiber puller was designed and built by myself, while the fiber tapering, dimpling, and mounting procedure was developed by PH, CD, and myself. All data collection and analysis was performed by PK and myself. All theoretical calculations were performed by myself.

Chapter 6, Appendix F, and Appendix G are based on the publication B. D. Hauer, P. H. Kim, C. Doolin, F. Souris, and J. P. Davis, "Two-level system damping in a quasi-one-dimensional optomechanical resonator," *Phys. Rev. B* **98**, 214303 (2018). In this work, all theoretical calculations, data taking, and analysis

was performed by myself. The pulsed homodyne detection scheme was developed by CD and myself. Signal processing (described in Section 6.4.2 of this thesis) was performed by CD.

Chapter 7 and Appendix H are based on the publication B. D. Hauer, T. J. Clark, P. H. Kim, C. Doolin, and J. P. Davis, "Dueling dynamical backaction in a cryogenic optomechanical cavity," *Phys. Rev. A* **99**, 053803 (2019). In this work, all simulations, data taking, and analysis was performed by myself. All theoretical calculations were performed by myself, with the exception of the calculations for the attractor diagrams, for which I had assistance from TC.

Finally, Chapter 8 and Appendix C are based on the theoretical work B. D. Hauer, A. Metelmann, and J. P. Davis, "Phonon quantum nondemolition measurements in nonlinearly coupled optomechanical cavities," *Phys. Rev. A* **98**, 043804 (2018) written in collaboration with Dr. Anja Metelmann from the Freie Universität Berlin. In this work, all theoretical calculations were carried out by myself, save for the master equation calculations in Section 8.4, which were performed by Dr. Metelmann.

We conclude this preface with a brief comment on notation. In this thesis, we have chosen to express vectors in bold and tensors with an overhead double arrow, with the components of each expressed with subscripted indices. Meanwhile, scalars are represented in standard or italicized font, with an overheard tilde to distinguish between similarly labelled quantities. Though there is some overlap between the components of tensors/vectors and scalars, the presence of subscripts on the components removes ambiguity in this case.

To my parents

For always believing in me.

And to Allison

For always being there for me.

Whatever doesn't kill you simply makes you...stranger.

– The Joker, *The Dark Knight*, 2008.

Acknowledgements

First and foremost, I would like to thank my supervisor, Prof. John Davis, for his mentorship throughout my last eight years at the University of Alberta. John's charismatic demeanor and self-described "cautious optimism" has been a driving force in helping me to stay motivated through the rough patches of my degree. No matter what the situation, John has always been there to give me advice and support my endeavours, and has truly always wanted what is best for me. I would also like to thank the two other members of my advisory committee, Prof. Mark Freeman and Prof. Frank Hegmann for their guidance and insightful comments on my work, as well making time in their schedules on short notice to attend "emergency" committee meetings.

I want to give a huge thank you to all of the members of the Davis Lab who helped me get through my degree in one way or another, whether by directly contributing to my experiments or simply just chatting over a lunch break. I also want to give a special thanks to the "original" members of the Davis Lab optomechanics crew. Thank you to Paul Kim for your stalwart determination and for your keen attention to detail in both your experiments and device fabrication. My PhD work would literally have been impossible without you. Thank you to Callum Doolin for always being so accommodating in helping develop software and measurement techniques in the lab. I was honestly terrified that you were going to graduate before I finished my experiments and the whole system would collapse without you. Thank you to Hugh Ramp who always seemed to have a MacGyver-like solution to any technical problems that I had and has done an amazing job at continuing the pulsed low temperature optomechanics work that I started on the fridge. Thank you to my two "Frenchmen" office mates (there must always be one), Xavier Rojas and Fabien Souris, who taught me the ropes of low

temperature physics and how to properly pronounce the word “marmot”. And also thank you to David Purschke (and Hugh Ramp) for making sure that I got out of the lab from time to time to play and watch basketball (Go Raptors!).

Outside of the lab, I want to thank all of my friends and family that supported me throughout my PhD. First of all thank you to my parents, Colleen and Gerald, who memorized the phrase “Low Temperature Optomechanics” so that they could tell their friends what it was that I worked on and put up with me always being “2-3 years” from graduating. Thank you to my two sisters, Amanda and Michelle, who also put an effort into understanding what exactly it was that I worked on and would always lend an ear if I needed to discuss difficult topics with them. Thank you to my cousin Adam, who has always been there for be and is always available to chat no matter what the topic or hour. Thank you to the MacDonald Clan, Anne, Gord, and Kim, who adopted me into their family during my PhD and continually show interest in my work. And a special thanks to Paul and Jo for letting me be their third wheel roommate so that I wasn’t homeless when I came back to Edmonton during the last two years of my degree.

And last, but most certainly not the least, I owe an enormous debt of gratitude to my motivational coach, personal caretaker, editor, and better half, Allison MacDonald, without whom I never would have completed my PhD. Allison, you are my rock and I will never take for granted the patience and support that I received from you throughout my graduate degree. I love you Allison, and I look forward to our many PhD-less years together in the future.

Contents

List of Tables

List of Figures

List of Abbreviations

ACF	autocorrelation function	258
ADC	analog-to-digital converter	126
AOM	acousto-optic modulator	148
BPD	balanced photodetector	93
BS	beamsplitter	89
DAQ	data acquisition	112
DOS	density of states	29
FEM	finite element method	21
FMF	free molecular flow	51
FPC	fiber polarization controller	125
FS	fiber stretcher	126
HF	hydrofluoric acid	104
IVC	inner vacuum can	127
LO	local oscillator	93
MIM	membrane-in-the-middle	199
NO	nuclear orientation	127
PD	photodetector	89
PID	proportional-integral-derivative	126
PM	power meter	125
PSD	power spectral density	84
QLE	quantum Langevin equation	79
QND	quantum nondemolition	198
SBR	sideband-resolved	82
SCA	strongly-confined approximation	65
SEM	scanning electron microscope	114
SNR	signal-to-noise ratio	185

SOI	silicon-on-insulator	103
SQL	standard quantum limit	95
STM	standard tunneling model	132
SW	optical switch	126
TED	thermoelastic damping	36
TE	transverse electric	63
TLS	two-level system	37
TM	transverse magnetic	63
VC	variable coupler	125
VOA	variable optical attenuator	112
WGA	weakly-guiding approximation	268
WGM	whispering-gallery mode	63
WKB	Wentzel-Kramers-Brillouin	133
WLM	wavelength meter	125

List of Symbols

$\mathcal{N}_{\rm th}$	number of thermally active TLS defects ($\sim \mathcal{P}_0 V_{\rm str} k_{\rm B} T$)	162
ν	photon-photon coupling rate in a two-mode cavity [Hz]	204
$\omega_{\rm c}$	resonant angular frequency of the optical cavity [Hz]	60
$\omega_{\rm d}$	optical cavity drive frequency [Hz]	77
$\omega_{\rm m}$	resonant angular frequency of the mechanical mode [Hz]	8
$\delta\omega_{\rm m}$	optomechanical shift in mechanical resonance frequency [Hz]	82
$p(t)$	momentum of the mechanical motion [kg·m/s]	12
$P_{\rm in}$	optical cavity input power [W]	78
$P_{\rm abs}$	optical power absorbed in the mechanical element [W]	88
$\mathcal{P}_0$	TLS density of states parameter [$\rm J^{-1}{\cdot}m^{-1}$]	44
$Q_{\rm c}$	optical quality factor	62
$Q_{\rm m}$	mechanical quality factor	11
R	optical microdisk radius [m]	63
$\rho(\mathbf{r})$	mass density of the optomechanical cavity [$\rm kg/m^3$]	9
$\hat{\rho}$	density matrix of the system	210
$S_{NN}(\omega)$	photon number PSD [$\rm Hz^{-1}$]	85
$S_{xx}(\omega)$	mechanical position PSD [$\rm m^2/Hz$]	84
$\overleftrightarrow{\sigma}(\mathbf{r},t)$	stress tensor of the mechanical resonator [$\rm N/m^2$]	14
T	temperature [K]	27
$T_{\rm m}$	mechanical mode temperature [K]	86
$T_{\rm b}$	thermal bath temperature [K]	86
$\tau_{\rm c}$	optical cavity photon lifetime [s]	62
$\tau_{\rm pt}$	photothermal time constant [s]	168
$\tau_{\rm TLS}$	TLS relaxation time [s]	43
$\mathcal{T}(\Delta)$	transmission through the optical cavity	90
$\mathbf{u}(\mathbf{r},t)$	displacement field of the mechanical resonator [m]	8
$V_{\rm opt}$	effective optical mode volume [$\rm m^3$]	61
$V_{\rm str}$	effective mechanical strain volume [$\rm m^3$]	26
$x(t)$	time-dependent amplitude of mechanical motion [m]	8
$x_{\rm zpf}$	mechanical zero-point fluctuation amplitude ($= \sqrt{\hbar/2m\omega_{\rm m}}$) [m]	12
$\chi_{\rm c}(\omega)$	optical susceptibility [s]	80
$\chi_{\rm m}(\omega)$	mechanical susceptibility [$\rm s^2/kg$]	80

Chapter 1

Introduction

In its most general form, optomechanics is the study of the interaction between the mechanical motion of an object and an electromagnetic field. In this situation, one finds that the electromagnetic field can manipulate the motion of the object by via a radiation pressure or photothermal force. Conversely, the mechanical object will imprint a phase on the interacting light, which when detected, can be used to read out the object's displacement. In this way, the motion of the mechanical object and the outgoing electromagnetic radiation are intimately related to each other.

The initial observation of optomechanical effects can be dated back to nearly 500 years ago, when Peter Apian discovered Halley's Comet in 1531 [1] and noted that its tail always pointed away from the sun (see Fig. 1.1). When Halley's Comet returned 76 years later in 1607, it was observed by Johannes Kepler [2] who theorized that solar radiation acted to push the comet's tail away from the sun, stating that [3]:

> "The direct rays of the sun strike upon it [the comet], penetrate its substance, draw away with them a portion of this matter, and issue thence to form the track of light we call the tail of the comet."
>
> (Johannes Kepler, 1607)

While this statement was essentially correct[1], it would be over 250 years before James Clerk Maxwell explained this phenomenon in 1873 [4] as being due to

[1] More precisely, a comet has two tails: a dust tail, which as theorized by Kepler is caused by solar radiation pressure, along with a gas or ion tail that is generated by charged particles emitted from the sun known as solar wind [3].

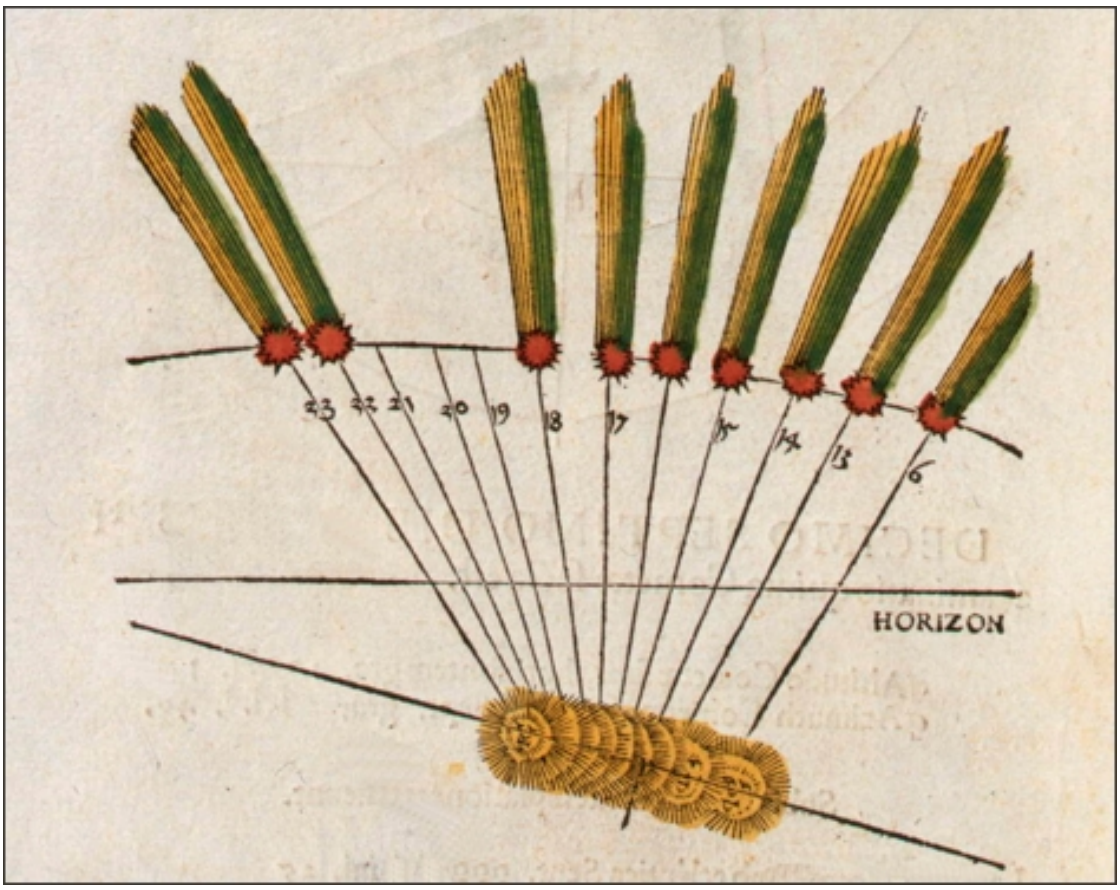

Figure 1.1: Diagram by Peter Apian from his book *Astronicum Caesareum* [1], indicating that when Halley's Comet entered the solar system in 1531, its tail always faced away from the sun. This effect is in part due to radiation pressure exerted on the comet's tail by photons originating from the sun.

radiation pressure, whereby an electromagnetic field imparts momentum to an object by being absorbed or reflected by its surface, thus applying a force to it. In fact, Maxwell went as far as to propose the first laboratory optomechanical experiment, commenting that

> "It is probable that a much greater energy of radiation might be obtained by means of the concentrated rays from an electric lamp. Such rays falling on a thin metallic disc, delicately suspended in a vacuum, might perhaps produce an observable mechanical effect."
>
> (James Clerk Maxwell, 1873)

The radiation pressure force would later be verified in the early 1900s through experiments performed independently by Lebedew [5] and Nichols and Hull [6–8].

With the advent of the laser in 1960 [9], Gertsenshtein and Pustovoit [10, 11] and Braginsky *et al*. [12–15] began to explore the idea of using an optical cavity to enhance the radiation pressure interaction between a confined electromagnetic field and a mechanical test mass in the context of gravitational wave observatories. These theoretical proposals were realized by Braginsky *et al*. in 1970 [16] for a microwave cavity coupled to an aluminium pendulum, though it would be another decade before the first cavity optomechanical experiment would be performed in the optical domain by Dorsel *et al*. in 1983 [17] using a suspended mirror Fabry-Perot cavity. These pioneering experiments set the groundwork for future generations of gravitational wave detectors, the most famous of which is the Laser Interferometer Gravitational-Wave Observatory (LIGO) collaboration [18], which won the 2017 Nobel Prize in Physics for its observation of gravitational waves from a binary black hole merger [19].

Owing to its extreme sensitivity, a trend emerged at the turn of the millennium geared towards using the cavity optomechanical interaction to measure and manipulate the motion of miniaturized mechanical objects. This began in 1999 when Tittonen *et al*. [20] used a Fabry-Perot etalon to observe the thermal motion of a cm-sized silicon torsional resonator at temperatures down to 4.5 K. As nanofabrication techniques continued to improve through the early 2000s, this seminal work was followed by a number of optomechanical geometries at visible and infrared wavelengths, including Fabry-Perot cavities integrated with metallized μm-scale cantilevers [21–25], suspended micromirrors [26–32], micropillars [33, 34], membranes [35–39], nanorods [40–42], micro/nanoparticles [43–45], and cold atom clouds [46–50], whispering gallery mode optical cavities comprised of toroidal [51–53], spherical [54–57], bottle [58, 59], and disk [60–63] geometries, and photonic crystal structures [64–71]. In addition to the experiments operating in the optical domain, a number of microwave optomechanical cavities consisting of electromagnetic LC circuits coupled to the displacement of thin mechanically compliant metallic plates [72–74] and beams [75–77], as well as the motion of confined superfluid helium [78, 79], have also been developed. In fact, new optomechanical geometries continue to emerge, resulting in novel implementations such as optomechanical cavities coupled to exotic superfluids [80–84], magnetic systems [85, 86], and THz radiation [87].

Using these state-of-the-art optomechanical geometries, a number of interesting experiments have been performed on mechanical systems over the past decade. On the more practical side, the precise detection scheme offered by cavity optomechanics has allowed for a drastic reduction in the size, and therefore increase in sensitivity, of nanomechanical sensors, providing exquisite measurements of displacement [88–90], acceleration [91], force [92–96], torque [70, 97–99], mass [100], temperature [101], electron spin [102], magnetic fields [85, 103, 104], and biomolecules [105]. Beyond these metrological applications, cavity optomechanics can also be used to manipulate and control the states of mesoscopic mechanical resonators at or near their quantum level, which has been exhibited by experiments demonstrating motional ground state cooling [106, 107], Raman sideband asymmetry [108, 109], preparation of the system into squeezed [110–112] and entangled [113] states, quantum nondemolition [114, 115] and back-action evading [116–118] measurements of a single mechanical quadrature and measurement-based quantum manipulation of the mechanical element [119–122]. This level of quantum control has generated significant interest for the use of optomechanical resonators for applications in the burgeoning quantum information sector, such as coherent interfacing between two nonclassical degrees of freedom [123–125] and storage of quantum information [126, 127]. Along with these quantum applications, optomechanical cavities have also demonstrated potential in providing experimental testbeds to help answer a number of fundamental questions in quantum mechanics [128–131] and gravity [19, 132–134].

In order to observe the abovementioned quantum effects in an optomechanical cavity, it is crucial that the mechanical resonator be cooled near to its ground state. One must also minimize the dissipation of the nanomechanical resonator at these temperatures, such that it can maintain its quantum coherence over the duration of the intended operation. Therefore, in order for these systems to be used as a viable quantum resource, we must understand their behaviour at low temperatures. This is especially true for silicon optomechanical cavities, whose long lifetimes [135] and ability to nonclassically interface between the photonic and phononic modes [136–138] have already allowed them to be used as quantum memories [139] and transducers [140], as well as perform Hanbury, Brown, and Twiss interferometry

[141], remote entanglement [142], and Bell tests [143] on mesoscopic mechanical systems. To this end, we have designed and built a cryogenic optomechanical coupling apparatus operating on the base plate of a dilution refrigerator [58]. Using a dimpled tapered fiber coupling technique, we perform measurements of on-chip single-crystal silicon nanobeam resonators side-coupled to whispering gallery mode optical microdisks, characterizing the low temperature dependence of their mechanical dissipation and revealing a counterintuitive photothermal effect that emerges in cryogenic environments. The information gleaned from these experiments will inform future generations of silicon quantum optomechanical devices by offering guidance on how to improve their quantum coherence, as well as providing further tools to manipulate the mechanical motion at low temperatures.

The rest of the thesis is structured as follows. In Chapter 2, we introduce our formalism for describing the classical and quantum motion of our nanomechanical resonators, detailing a number of different dissipation mechanisms that exist in these structures. In Chapter 3, we discuss the general theory of optical cavities, while applying this treatment to the specific cylindrical geometries associated with our microdisk resonators. In Chapter 4, we review the general theory of dispersively coupled, radiation-pressure-driven optomechanical cavities, as is applicable to the systems studied in this thesis. In Chapter 5, we provide details of the fabrication and material properties of our devices, as well as the experimental apparatus used to address them. In Chapter 6, we present measurements of the low-temperature damping in a nanomechanical silicon resonator using a novel optomechanically mediated thermal ringdown technique. Analyzing these data quantitatively, we identify the resonator's dissipation as being limited by interactions with two level system defects confined to its one-dimensional geometry. In Chapter 7, we analyze the seemingly anomalous photothermal behaviour observed in a similar geometry at low-temperatures. Quantifying this effect, we assess the device's ability to amplify the mechanical motion by nearly three orders of magnitude, as well as cool the system into its motional ground state. In Chapter 8, we theoretically evaluate a nonlinear quantum nondemolition measurement protocol for our WGM optomechanical architecture, providing clear limits on the requirements for this technique to be used to measure the quantized mechanical Fock states of the system.

Finally, in Chapter 9, we offer concluding thoughts and future directions for the optomechanical systems studied in this thesis.

Chapter 2

Mechanical Resonators

2.1 Introduction

Here we consider an isolated mechanical resonator, providing a theoretical framework to characterize its displacement, as well as its energy dissipation due to interactions with its surrounding environment. We begin in Section 2.2 by first establishing a mathematical formalism to describe the mechanical resonator's motion according to a classical damped harmonic oscillator model, which we use to define its effective mass and quality factor. We then demonstrate how this treatment can be extended into the quantum realm, providing a fully nonclassical description of the mechanical resonator's motion. In Section 2.3, we use the theory of linear elasticity to derive an equation of motion for the resonator's displacement, allowing us to determine its spatially varying modeshape, as well as characterize the distribution of its strain profile. Continuing in Section 2.4, we describe the properties of the mechanical resonator's environmental bath, where we use the Debye model to specify its energy, density of states, and thermal properties. Furthermore, we show how this reservoir acts to thermalize the mechanical resonator, effectively driving its motion according to the equipartition theorem. Finally, in Section 2.5, we discuss a number of specific mechanical dissipation mechanisms that are caused by interactions with this bath, focusing on those that are prevalent in nanomechanical systems.

2.2 Mechanical Motion

2.2.1 Displacement Function

In order to completely describe the motion of an extended mechanical structure, we must determine its total displacement $\mathbf{u}_{\mathrm{tot}}(\mathbf{r}, t)$ at each point in time and space[1], as denoted by the variable t and the position vector

$$\mathbf{r} = \tilde{x}_1\mathbf{i}_1 + \tilde{x}_2\mathbf{i}_2 + \tilde{x}_3\mathbf{i}_3. \tag{2.1}$$

Here $\tilde{x}_j$ are the position coordinates[2] associated with each of the arbitrary, but mutually perpendicular, unit vectors $\mathbf{i}_j$ that form the basis for our chosen coordinate system [144]. In its most general form, this displacement function can be expressed as[3] [145, 146]

$$\mathbf{u}_{\mathrm{tot}}(\mathbf{r}, t) = \sum_k \mathbf{u}_k(\mathbf{r}, t) = \sum_k x_k(t)\mathbf{u}_k(\mathbf{r}), \tag{2.2}$$

such that the resonator's total displacement is decomposed into a superposition of the individual contributions $\mathbf{u}_k(\mathbf{r}, t) = x_k(t)\mathbf{u}_k(\mathbf{r})$ from each of its k mechanical modes. In this way, $x_k(t)$ characterizes the amplitude of motion for the kth mechanical mode, with its spatial distribution specified by the modeshape function $\mathbf{u}_k(\mathbf{r})$. While this representation provides the full description of the resonator's total displacement, we generally wish to consider a single mechanical mode independently. Such a treatment, known as the quasi-mode approach [147], is appropriate when the separation between mechanical modes in frequency space is much larger than their linewidths, allowing one to individually access a given mode. Therefore, in what follows we drop the subscripts in Eq. (2.2), such that we consider a single mechanical mode with resonant angular frequency ω_{m} and displacement

$$\mathbf{u}(\mathbf{r}, t) = x(t)\mathbf{u}(\mathbf{r}). \tag{2.3}$$

[1] Note that while we have chosen to characterize the resonator's motion in terms of its displacement profile, we could have alternatively used its momentum.

[2] We have included a tilde over each of these coordinates to differentiate them from the time-dependent mechanical amplitude $x(t)$ introduced below.

[3] In this notation, we differentiate the temporally and spatially varying mechanical displacement $\mathbf{u}_k(\mathbf{r}, t)$ from the modeshape function $\mathbf{u}_k(\mathbf{r})$ by explicitly stating each vector's arguments. In the case that no arguments are provided, it is assumed that we are talking about the former quantity. We use this convention throughout the thesis for similarly defined vectors and tensors.

In this representation, we have expressed the total displacement of the resonator as a product of two independent functions, such that we have the freedom to choose the normalization and units of one function, which then constrains the other. Here we choose the normalization convention $\max|\mathbf{u}(\mathbf{r})| = 1$ (*i.e.* the maximum magnitude of the modeshape function is unity), such that $\mathbf{u}(\mathbf{r})$ is a unitless representation of the spatial distribution of the resonator's motion [145, 146]. Note that in practice, this normalization can be obtained simply by dividing any arbitrary mechanical modeshape by its maximal value. In this situation, $x(t)$ then carries units of m and represents the resonator's true physical displacement at its point of maximum deflection, while being appropriately scaled throughout the rest of the geometry by $\mathbf{u}(\mathbf{r})$.

2.2.2 Effective Motional Mass

In order to fully characterize the extended nature of a mechanical resonator's displacement, we introduce a quantity known as its effective motional mass, which accounts for the fact that not all mass participates equally in the oscillatory motion of each of its vibrational modes. We determine this effective mass by considering the potential energy of a differential element of the mechanical resonator, located at the position denoted by $\mathbf{r}$, with differential volume $dV = d\tilde{x}_1 d\tilde{x}_2 d\tilde{x}_3$ and mass $dm = \rho(\mathbf{r})dV$, where $\rho(\mathbf{r})$ is the mass density profile of the resonator. In this case, the time-dependent potential energy density $U_\mathrm{p}(\mathbf{r}, t)$ of the mechanical mode will be given by [145]

$$U_\mathrm{p}(\mathbf{r}, t) = \frac{1}{2}\rho(\mathbf{r})\omega_\mathrm{m}^2|\mathbf{u}(\mathbf{r}, t)|^2 = \frac{1}{2}\rho(\mathbf{r})\omega_\mathrm{m}^2 x^2(t)|\mathbf{u}(\mathbf{r})|^2. \tag{2.4}$$

The total potential energy of the mode is then found by integrating this quantity over the entire volume of the resonator, resulting in

$$E_\mathrm{p}(t) = \frac{1}{2}m\omega_\mathrm{m}^2 x^2(t), \tag{2.5}$$

where we define the effective motional mass of the mechanical mode as [145, 146, 148]

$$m = \int \rho(\mathbf{r})|\mathbf{u}(\mathbf{r})|^2 dV. \tag{2.6}$$

Therefore, the effective mass of a given mode is entirely determined by its modeshape function and the density profile of the resonator. Note that since the modeshape function varies from mode to mode, so does the effective mass. Furthermore, since $\max|\mathbf{u}(\mathbf{r})| = 1$, it follows that $m \leq m_0$, where $m_0 = \int \rho(\mathbf{r})dV$ is the geometric mass of the resonator.

2.2.3 Damped Harmonic Oscillator Model

With the spatial character of the mechanical displacement specified, we now look to determine its time dependence. This is done by modelling the resonator as a classical damped harmonic oscillator, such that $x(t)$ obeys the equation of motion [145, 149–151]

$$\ddot{x}(t) + \Gamma_\mathrm{m}\dot{x}(t) + \omega_\mathrm{m}^2 x(t) = \frac{F(t)}{m}, \tag{2.7}$$

where Γ_m is the mechanical (energy) damping rate and $F(t)$ represents the forces exerted on the system. For an undriven mechanical oscillator (*i.e.* $F(t) = 0$) in the underdamped regime ($\Gamma_\mathrm{m} < 2\omega_\mathrm{m}$), the solution to Eq. (2.7) has the form [151, 152]

$$x(t) = Ae^{-\Gamma_\mathrm{m}t/2}\cos\left(\omega_\mathrm{m}' t + \theta_0\right), \tag{2.8}$$

where A and θ_0 are the amplitude and phase offset of the resonator's motion set by its initial conditions. Here we have also introduced the new mechanical resonance frequency $\omega_\mathrm{m}' = \omega_\mathrm{m}\sqrt{1 - \Gamma_\mathrm{m}^2/4\omega_\mathrm{m}^2}$ which is shifted due to the system's damping. However, as the vast majority of mechanical resonators exist in the low-damping limit, where $\Gamma_\mathrm{m} \ll \omega_\mathrm{m}$, we ignore this damping-induced frequency shift and simply take $\omega_\mathrm{m}' \approx \omega_\mathrm{m}$.

2.2.4 Quality Factor

In the previous subsection, the dissipation of the mechanical mode's energy is characterized by its damping rate Γ_m. However, this parameter is intimately tied to the frequency at which the resonator oscillates, and must be compared to this resonant frequency in order to assess the damping of the system. We therefore look to define a dimensionless damping parameter that can be used to gauge the oscillator's damping strength without the knowledge of its resonant frequency.

While a number of such parameters exist [152], here we choose to use the quality factor of the system, which is defined for a general damped harmonic oscillator as [151, 153]

$$Q = 2\pi \frac{E}{\Delta E}, \tag{2.9}$$

where E is the energy stored within the resonator, while ΔE is the energy dissipated per oscillation cycle. Therefore, the quality factor gives a measure of the ability of a resonator to store energy.

Using Eq. (2.8), the total (time-dependent) energy of the mechanical resonator is determined as [151]

$$E_{\mathrm{m}}(t) = \frac{1}{2} m \left[\dot{x}^2(t) + \omega_{\mathrm{m}}^2 x^2(t)\right] = \frac{1}{2} m \omega_{\mathrm{m}}^2 A^2 e^{-\Gamma_{\mathrm{m}} t}, \tag{2.10}$$

where in the spirit of the low-damping limit, we have neglected a term proportional to Γ_{m} in the time-derivative of $x(t)$. As expected, the total mechanical energy of the system decays in time at a rate determined by Γ_{m}. The energy dissipated after one mechanical oscillation period τ_{m} is then given by [151]

$$\begin{aligned} \Delta E_{\mathrm{m}}(t) &= \frac{1}{2} m \omega_{\mathrm{m}}^2 A^2 e^{-\Gamma_{\mathrm{m}} t} - \frac{1}{2} m \omega_{\mathrm{m}}^2 A^2 e^{-\Gamma_{\mathrm{m}}(t+\tau_{\mathrm{m}})}, \\ &= \frac{1}{2} m \omega_{\mathrm{m}}^2 A^2 e^{-\Gamma_{\mathrm{m}} t} \left(1 - e^{-\Gamma_{\mathrm{m}} \tau_{\mathrm{m}}}\right). \end{aligned} \tag{2.11}$$

Inputting Eqs. (2.10) and (2.11) into Eq. (2.9), we find that the quality factor for our mechanical resonator can be expressed as [149–151]

$$Q_{\mathrm{m}} = 2\pi \frac{E_{\mathrm{m}}(t)}{\Delta E_{\mathrm{m}}(t)} = \frac{2\pi}{1 - e^{-\Gamma_{\mathrm{m}} \tau_{\mathrm{m}}}} \approx \frac{2\pi}{1 - (1 - \Gamma_{\mathrm{m}} \tau_{\mathrm{m}})} = \frac{\omega_{\mathrm{m}}}{\Gamma_{\mathrm{m}}}, \tag{2.12}$$

where we have again made use of the low-damping limit, as well as the fact that we can relate the mechanical period to the resonant mechanical frequency via $\tau_{\mathrm{m}} = 2\pi/\omega_{\mathrm{m}}$. Therefore, in the low-damping limit (which we now see is synonymous with the high-Q limit), the quality factor is simply given by the ratio of the oscillator's resonator frequency to its damping rate. Finally, we note that in this limit, the mechanical motion will be relatively unchanged on timescales $t \ll \Gamma_{\mathrm{m}}^{-1}$, such that we can approximate Eq. (2.7) as

$$\ddot{x}(t) + \omega_{\mathrm{m}}^2 x(t) = 0, \tag{2.13}$$

which has the undamped harmonic solution

$$x(t) = A \cos\left(\omega_{\mathrm{m}} t + \theta_0\right). \tag{2.14}$$

2.2.5 Quantization of Mechanical Motion

Up to this point, we have treated the displacement of the mechanical resonator completely classically. However, by introducing the (time-dependent) phonon creation and annihilation (ladder) operators[4], $\hat{b}^\dagger(t)$ and $\hat{b}(t)$, it is possible to quantize the classical field given in Eq. (2.3), resulting in the quantum mechanical displacement operator [154]

$$\hat{\mathbf{u}}(\mathbf{r},t) = x_{\mathrm{zpf}}\left[\hat{b}^\dagger(t)\mathbf{u}(\mathbf{r}) + \hat{b}(t)\mathbf{u}^*(\mathbf{r})\right]. \tag{2.15}$$

Here $x_{\mathrm{zpf}} = \sqrt{\hbar/2m\omega_{\mathrm{m}}}$ is the zero-point fluctuation amplitude of the mechanical mode's motional ground state, which is typically on the order of tens of fm for the mechanical resonances studied in this thesis. We note that the creation and annihilation operators introduced in Eq. (2.15) obey the standard commutation relation $[\hat{b}, \hat{b}^\dagger] = 1$. Choosing the phase of the mechanical modeshape to ensure that it is real (as it describes a physical displacement in space), we have that $\mathbf{u}(\mathbf{r}) = \mathbf{u}^*(\mathbf{r})$, allowing us to recast Eq. (2.15) into a form reminiscent of Eq. (2.3) as

$$\hat{\mathbf{u}}(\mathbf{r},t) = \hat{x}(t)\mathbf{u}(\mathbf{r}), \tag{2.16}$$

where we have introduced the quantized position operator

$$\hat{x}(t) = x_{\mathrm{zpf}}\left[\hat{b}^\dagger(t) + \hat{b}(t)\right]. \tag{2.17}$$

From this equation, we can also use the properties of the creation and annihilation operators to calculate the root-mean-square amplitude of the mechanical motion as [151]

$$x_{\mathrm{rms}} = \sqrt{\langle \hat{x}^2 \rangle} = x_{\mathrm{zpf}}\sqrt{2\langle n \rangle + 1}, \tag{2.18}$$

where $\langle n \rangle$ is the average phonon occupancy of the resonator, such that when the system is in its motional ground state ($\langle n \rangle = 0$), $x_{\mathrm{rms}} = x_{\mathrm{zpf}}$ as expected.

We also introduce the conjugate momentum of the mechanical position operator as

$$\hat{p}(t) = ip_{\mathrm{zpf}}\left[\hat{b}^\dagger(t) - \hat{b}(t)\right], \tag{2.19}$$

[4]For a freely evolving harmonic oscillator $\hat{b}(t) = \hat{b}e^{-i\omega_{\mathrm{m}}t}$, however, here we allow for a more general time dependence in order to include effects due to the interaction with the optical cavity, surrounding environmental bath, etc.

where $p_{\mathrm{zpf}} = \sqrt{\hbar m \omega_{\mathrm{m}}/2}$ represents the zero-point fluctuations of the resonator's momentum. Using the commutation relation for $\hat{b}$ and $\hat{b}^\dagger$, it is straightforward to show that these two operators obey the canonical commutation relation $[\hat{x}, \hat{p}] = i\hbar$. Furthermore, one finds that $x_{\mathrm{zpf}} p_{\mathrm{zpf}} = \hbar/2$, which asserts that when the resonator is in its quantum ground state, the Heisenberg uncertainty principle is minimized such that equality is reached.

2.3 Linear Elastic Theory

2.3.1 Stress and Strain

As a number of dissipation channels in nanomechanical systems are coupled to their strain, it is important that we carefully consider the stress and strain distributions generated within a resonator due to its motion. To do this, we turn to the theory of linear elasticity [144, 153, 155–157], which allows us to determine the stress and strain profiles of the system, along with an equation of motion for the displacement of each mechanical mode. Using a linear elastic approach[5], we assume that the motion of the resonator is caused by a deformation from its original shape (*i.e.* the resonator is anchored such that it cannot be entirely rotated or displaced as a rigid body) and that this deflection is small enough that the mechanical resonator does not yield to plastic deformation. Under these constraints, the strain induced by the motion of the considered mechanical mode will be characterized by the tensor $\overleftrightarrow{\varepsilon}(\mathbf{r}, t)$ whose components are given by[6] [144, 153, 155]

$$\varepsilon_{ab}(\mathbf{r}, t) = \frac{1}{2}\left(\frac{\partial u_a(\mathbf{r}, t)}{\partial \tilde{x}_b} + \frac{\partial u_b(\mathbf{r}, t)}{\partial \tilde{x}_a}\right). \tag{2.20}$$

Since the derivatives in Eq. (2.20) act only on the spatial component of $\mathbf{u}(\mathbf{r}, t)$, we can use Eq. (2.3) to write the strain in tensorial form as [162, 163]

$$\overleftrightarrow{\varepsilon}(\mathbf{r}, t) = x(t)\overleftrightarrow{\varepsilon}(\mathbf{r}), \tag{2.21}$$

[5] The more general, and more involved, theory of nonlinear elasticity (also known as finite strain theory or large deformation theory) will not be considered here, though we refer the interested reader to numerous texts on the subject [158–161].

[6] Some references use the so-called "engineering strains" γ_{ab}, which define the shear strains as $\gamma_{ab} = 2\varepsilon_{ab}$ for $a \neq b$. However, in this thesis we opt to use the tensorial strains given by Eq. (2.20).

where $\overleftrightarrow{\varepsilon}(\mathbf{r})$ is a spatially-varying profile tensor whose elements are given in terms of the mechanical modeshape function as

$$\varepsilon_{ab}(\mathbf{r}) = \frac{1}{2}\left(\frac{\partial u_a(\mathbf{r})}{\partial \tilde{x}_b} + \frac{\partial u_b(\mathbf{r})}{\partial \tilde{x}_a}\right), \tag{2.22}$$

with $u_j(\mathbf{r})$ being the components of $\mathbf{u}(\mathbf{r})$ aligned along $\mathbf{i}_j$. Note that we have chosen to normalize the time-varying amplitude of our strain tensor to match the definition of the mechanical displacement vector given in Eq. (2.3), such that $\overleftrightarrow{\varepsilon}(\mathbf{r})$ has units of m^{-1}, while $\overleftrightarrow{\varepsilon}(\mathbf{r},t)$ remains unitless as expected. Due to the symmetries found in Eqs. (2.20) and (2.22), it follows that $\varepsilon_{ab}(\mathbf{r},t) = \varepsilon_{ba}(\mathbf{r},t)$ and $\varepsilon_{ab}(\mathbf{r}) = \varepsilon_{ba}(\mathbf{r})$. Therefore, $\overleftrightarrow{\varepsilon}(\mathbf{r},t)$ is a symmetric, second-rank tensor that in general has 6 independent components [149, 153, 155]: ε_{11}, ε_{22}, ε_{33}, $\varepsilon_{12} = \varepsilon_{21}$, $\varepsilon_{13} = \varepsilon_{31}$, and $\varepsilon_{23} = \varepsilon_{32}$. If we consider a differential element of the mechanical resonator's material, located at the position denoted by $\mathbf{r}$ with volume $dV = d\tilde{x}_1 d\tilde{x}_2 d\tilde{x}_3$, the diagonal components of the strain tensor (ε_{11}, ε_{22}, and ε_{33}) represent the relative elongation of this element along each of its coordinate axes. To first order, the trace of the strain tensor (*i.e.* $\mathrm{Tr}\{\overleftrightarrow{\varepsilon}\} = \sum \varepsilon_{aa} = \varepsilon_{11} + \varepsilon_{22} + \varepsilon_{33}$) then characterizes the relative change in volume of this differential element such that this quantity is invariant under change of coordinate basis [144]. Meanwhile, the off-diagonal elements of the strain tensor (ε_{12}, ε_{13}, and ε_{23}) characterize the angular distortion of the differential element.

Along with these induced mechanical strains, the motion of the resonator will also create stresses within its material, as characterized by the stress tensor

$$\overleftrightarrow{\sigma}(\mathbf{r},t) = x(t)\overleftrightarrow{\sigma}(\mathbf{r}). \tag{2.23}$$

As was the case with the strain tensor, the stress tensor is also a symmetric, second-rank tensor obeying $\sigma_{ab}(\mathbf{r},t) = \sigma_{ba}(\mathbf{r},t)$ (and therefore, $\sigma_{ab}(\mathbf{r}) = \sigma_{ba}(\mathbf{r})$). Furthermore, we have also chosen to normalize $\overleftrightarrow{\sigma}(\mathbf{r},t)$ similar to $\overleftrightarrow{\varepsilon}(\mathbf{r},t)$, such that $\overleftrightarrow{\sigma}(\mathbf{r})$ has units of $\mathrm{N/m}^3$, while $\overleftrightarrow{\sigma}(\mathbf{r},t)$ has the standard units of $\mathrm{Pa} = \mathrm{N/m}^2$. The diagonal components of the stress tensor (σ_{11}, σ_{22}, and σ_{33}) indicate the normal force per unit area acting on a differential element of the resonators material, while the off-diagonal components (σ_{12}, σ_{13}, and σ_{23}) represent the shear forces per unit area. Therefore, the components $F_a(\mathbf{r},t)$ of the internal forces acting on this volume

element are given in terms of the stress tensor as [144, 155]

$$F_a(\mathbf{r},t) = \frac{\partial \sigma_{ab}(\mathbf{r},t)}{\partial \tilde{x}_b} dV. \tag{2.24}$$

where unless explicit sums are used, we have adopted the standard Einstein summation notation (*i.e.* sum over repeated indices).

2.3.2 Elastic Modulus Tensor

In the linear elastic model, the stresses within a deformed body can be written in terms of its strains via a generalized form of Hooke's law given by [144, 153, 155, 164]

$$\sigma_{ab}(\mathbf{r},t) = C_{abcd}\varepsilon_{cd}(\mathbf{r},t), \tag{2.25}$$

where C_{abcd} are the components of the fourth-rank elastic modulus tensor $\overleftrightarrow{C}$ of the resonator's material (also known as the elasticity tensor or the stiffness modulus tensor)[7]. By virtue of our choice of normalization for $\overleftrightarrow{\sigma}$ and $\overleftrightarrow{\varepsilon}$, their profile tensors also obey Hooke's law, such that

$$\sigma_{ab}(\mathbf{r}) = C_{abcd}\varepsilon_{cd}(\mathbf{r}). \tag{2.26}$$

The components C_{abcd} of the elastic modulus tensor are a unique property of the material being considered and, in the case of an anisotropic crystal, are specified along its crystallographic axes. Therefore, if one chooses a set of coordinates $\tilde{x}_i$ that does not match the crystallographic axes defined by the coordinate system $\tilde{x}'_i$ (as is the case for our devices, which are aligned along the [011] direction of silicon), the components of the elastic modulus tensor must be transformed according to

$$C_{abcd} = \frac{\partial \tilde{x}_a}{\partial \tilde{x}'_\alpha}\frac{\partial \tilde{x}_b}{\partial \tilde{x}'_\beta}\frac{\partial \tilde{x}_c}{\partial \tilde{x}'_\gamma}\frac{\partial \tilde{x}_d}{\partial \tilde{x}'_\delta} C'_{\alpha\beta\gamma\delta}. \tag{2.27}$$

Furthermore, as a result of the symmetries of the stress and strain tensors, we find that the elastic modulus tensor obeys the relations [144, 164]

$$C_{abcd} = C_{bacd} = C_{abdc} = C_{cdab}. \tag{2.28}$$

[7] Note that while we have chosen to write the stress in terms of the strain here, we could have alternatively related the strain to the stress via the compliance tensor, which is simply the inverse of the elastic modulus tensor [155].

With these symmetries, one can show that the maximum number of independent components for the elastic modulus tensor is 21, which occurs for a triclinic crystal structure [144, 155]. However, here we consider the much simpler isotropic and simple cubic systems, for which the elastic modulus tensor has two and three independent components, respectively [153, 155].

To gain a firm understanding of linear elasticity, it is easiest to first consider the simplest case of an isotropic system, where the nonzero components of the elastic modulus tensor are given by [149, 155]

$$C_{1111} = C_{2222} = C_{3333} = \frac{Y(1-\nu)}{(1+\nu)(1-2\nu)}, \tag{2.29}$$

$$C_{1122} = C_{1133} = C_{2211} = C_{2233} = C_{3311} = C_{3322} = \frac{Y\nu}{(1+\nu)(1-2\nu)}, \tag{2.30}$$

$$\begin{aligned} &C_{1212} = C_{1221} = C_{1313} = C_{1331} = C_{2112} = C_{2121} = C_{2323} = C_{2332} \\ &= C_{3113} = C_{3131} = C_{3223} = C_{3232} = \frac{Y}{2(1+\nu)} = \mu. \end{aligned} \tag{2.31}$$

Here, we have introduced the Young's modulus Y and Poisson ratio ν of the solid, defined respectively as the ratio of the longitudinal stress to the longitudinal strain and the negative ratio of the transverse compression to the longitudinal extension when the solid is under uniaxial (or simple) extension [144, 155]. We have also introduced the shear modulus (also known as the second Lamé constant) μ, which is defined as the ratio of the shear stress to the shear strain and, for an isotropic medium, is dependent on Y and ν according to $\mu = Y/2(1+\nu)$. It is therefore clear that for isotropic media, the elasticity tensor is completely determined by two parameters, which in this case we have chosen to be the Young's modulus and the Poisson ratio[8].

More important for our experiments, however, is the cubic crystal structure, which is the next step up in complexity from an isotropic material and represents the simplest anisotropic system. In this case, the elastic modulus tensor is specified

[8] We could have alternatively chosen to use any combination of two of the five elastic constants, *i.e.* the Young's modulus, the Poisson ratio, the bulk modulus, the shear modulus, and the second Lamé constant.

as

$$C_{1111} = C_{2222} = C_{3333} = C_{11}, \tag{2.32}$$

$$C_{1122} = C_{1133} = C_{2211} = C_{2233} = C_{3311} = C_{3322} = C_{12}, \tag{2.33}$$

$$\begin{aligned} C_{1212} &= C_{1221} = C_{1313} = C_{1331} = C_{2112} = C_{2121} = C_{2323} = C_{2332} \\ &= C_{3113} = C_{3131} = C_{3223} = C_{3232} = C_{44}, \end{aligned} \tag{2.34}$$

where C_{11}, C_{12}, and C_{44} are three independent elastic moduli that are specified for the considered material [153, 155, 164]. Note that each of these moduli obey the symmetries given in Eq. (2.28). By comparing these moduli to those in Eqs. (2.29)–(2.31), we can also define an effective Young's modulus $\tilde{Y}$, Poisson ratio $\tilde{\nu}$, and shear modulus $\tilde{\mu}$ for the cubic crystalline system as

$$\tilde{Y} = \frac{(C_{11} + 2C_{12})(C_{11} - C_{12})}{C_{11} + C_{12}}, \tag{2.35}$$

$$\tilde{\nu} = \frac{C_{12}}{C_{11} + C_{12}}, \tag{2.36}$$

$$\tilde{\mu} = C_{44}. \tag{2.37}$$

Unlike the isotropic case, these three effective elastic parameters are independent of each other, such that $\tilde{\mu}$ cannot be written in terms of $\tilde{Y}$ and $\tilde{\nu}$ (*i.e.* $\tilde{\mu} \neq \tilde{Y}/2(1+\tilde{\nu})$ in general). We reiterate that these parameters, as well as the elastic moduli given in Eqs. (2.32)–(2.34), are defined only for the coordinate system aligned with the crystallographic axes of the material and any deviation from this choice of coordinates will act to change these constants in accordance with Eq. (2.27)[9]. For instance, in a Cartesian coordinate system aligned with the [011] direction in silicon, as is relevant for our devices, the effective Young's modulus associated with in-plane flexural motion is $\tilde{Y} = 169$ GPa [166–168].

2.3.3 Elastic Equations of Motion

With Hooke's law allowing us to write the the stresses of the mechanical system in terms of its strains, we are now prepared to determine the equation of motion for the displacement of the resonator. This is done by using Newton's second law of motion to equate the internal forces acting on each differential element of

[9]For the effective Young's modulus, Poisson ratio, and shear modulus for arbitrary crystal directions, the curious reader is directed to Refs. [165–168].

the resonator given by Eq. (2.24)[10], to the mass $dm = \rho(\mathbf{r})dV$ of that element multiplied by the corresponding component of its acceleration vector $\ddot{u}_a$. The general equations of motion for an anisotropic elastic medium can then be written in component form as [144, 155, 164]

$$\rho(\mathbf{r})\ddot{u}_a(\mathbf{r},t) = \frac{\partial \sigma_{ab}(\mathbf{r},t)}{\partial \tilde{x}_b} = C_{abcd}\frac{\partial^2 u_d(\mathbf{r},t)}{\partial \tilde{x}_b \partial \tilde{x}_c}, \tag{2.38}$$

where we have used Eqs. (2.20) and (2.25) to write $\overleftrightarrow{\sigma}(\mathbf{r},t)$ in terms of the displacement vector $\mathbf{u}(\mathbf{r},t)$, as well as capitalized on the symmetries of $\overleftrightarrow{C}$ to equate $C_{abcd}\partial^2 u_c/\partial \tilde{x}_b \partial \tilde{x}_d$ and $C_{abcd}\partial^2 u_d/\partial \tilde{x}_b \partial \tilde{x}_c$.

In order to firmly establish the concept of breaking a displacement field into its longitudinal and transverse components, we first consider the simplest case of propagating waves in an infinite isotropic medium with uniform mass density $\rho(\mathbf{r}) = \rho$. We begin by using Eqs. (2.29)–(2.31) to rewrite the elastic equations of motion in component form as

$$\ddot{u}_a(\mathbf{r},t) = \frac{Y}{2\rho(1+\nu)}\frac{\partial^2 u_a}{\partial \tilde{x}_b^2} + \frac{Y}{2\rho(1+\nu)(1-2\nu)}\frac{\partial^2 u_b}{\partial \tilde{x}_a \partial \tilde{x}_b}, \tag{2.39}$$

or alternatively, in vector (or Navier-Cauchy) form as

$$\ddot{\mathbf{u}} = \frac{Y}{2\rho(1+\nu)}\nabla^2\mathbf{u} + \frac{Y}{2\rho(1+\nu)(1-2\nu)}\nabla(\nabla\cdot\mathbf{u}), \tag{2.40}$$

where $\nabla = \mathbf{i}_1\partial/\partial\tilde{x}_1 + \mathbf{i}_2\partial/\partial\tilde{x}_2 + \mathbf{i}_3\partial/\partial\tilde{x}_3$, allowing us to define the Laplacian operator $\nabla^2 = \nabla\cdot\nabla = \partial^2/\partial\tilde{x}_1^2 + \partial^2/\partial\tilde{x}_2^2 + \partial^2/\partial\tilde{x}_3^2$ [144, 164]. At this point, we rewrite the displacement vector $\mathbf{u}(\mathbf{r},t)$ in terms of its longitudinal or curl-free portion $\mathbf{u}_l(\mathbf{r},t)$ ($\nabla\times\mathbf{u}_l = 0$) and its transverse or divergence-free part $\mathbf{u}_t(\mathbf{r},t)$ ($\nabla\cdot\mathbf{u}_t = 0$) as[11]

$$\mathbf{u}(\mathbf{r},t) = \mathbf{u}_l(\mathbf{r},t) + \mathbf{u}_t(\mathbf{r},t). \tag{2.41}$$

By virtue of the fact that $\nabla\cdot\mathbf{u}_t = \mathrm{Tr}\{\overleftrightarrow{\varepsilon}\} = 0$, the transverse motion characterized by $\mathbf{u}_t(\mathbf{r},t)$ does not involve changes in the structure's volume, while the longitudinal

[10]Here we assume there are no external forces acting on the resonator and neglect any gravitational forces/accelerations due to the fact that the resonator is rigidly held in place by its supports.

[11]We can choose to write the displacement vector in this way because one can always express any arbitrary vector as the sum of the gradient of a scalar and the curl of a divergence-less vector (known as the Helmholtz decomposition) [144, 169].

motion described by $\mathbf{u}_l(\mathbf{r},t)$ allows for compression and extension of the solid. Inputting Eq. (2.41) into Eq. (2.40), we then find that the vector equation of motion becomes

$$\ddot{\mathbf{u}}_l + \ddot{\mathbf{u}}_t = \frac{Y}{2\rho(1+\nu)}\nabla^2(\mathbf{u}_l + \mathbf{u}_t) + \frac{Y}{2(1+\nu)(1-2\nu)}\nabla(\nabla\cdot\mathbf{u}_l). \tag{2.42}$$

Taking the divergence of Eq. (2.42), while using the fact that if the divergence and curl of a vector are both zero, then the vector is identically zero [144], we find the equation of motion for $\mathbf{u}_l(\mathbf{r},t)$ obeys the wave equation

$$\ddot{\mathbf{u}}_l = c_l^2\nabla^2\mathbf{u}_l, \tag{2.43}$$

where c_l is the longitudinal speed of sound given by

$$c_l = \sqrt{\frac{Y(1-\nu)}{\rho(1+\nu)(1-2\nu)}}. \tag{2.44}$$

Likewise, if we take the curl of Eq. (2.42), we instead find that $\mathbf{u}_t(\mathbf{r},t)$ is governed by the wave equation

$$\ddot{\mathbf{u}}_t = c_t^2\nabla^2\mathbf{u}_t, \tag{2.45}$$

where c_t is the transverse speed of sound

$$c_t = \sqrt{\frac{Y}{2\rho(1+\nu)}} = \sqrt{\frac{\mu}{\rho}}. \tag{2.46}$$

Hence, we have found that for an infinite isotropic material, the displacement of a propagating sound wave can be broken into two waves: a longitudinal wave and a transverse wave characterized by the displacement vectors $\mathbf{u}_l$ and $\mathbf{u}_t$, with each travelling at the speed of sound c_l and c_t, respectively.

While the situation becomes considerably more complicated in the case of an anisotropic material, one can always use Eq. (2.38) to find three orthogonal components of the displacement vector $\mathbf{u}$ corresponding to three independent speeds of sound [157, 170]. However, these displacement vector components are generally not purely longitudinal or purely transverse waves [144, 164]. Fortunately, for systems exhibiting cubic symmetry, there exist special propagation directions where the displacement can be broken into pure longitudinal and pure transverse motion

[155, 164]. One such direction, which is the most relevant for the mechanical modes studied in this thesis, is where the propagation of the elastic wave is parallel to the unit vector

$$\mathbf{n}_{110} = \frac{1}{\sqrt{2}}\mathbf{i}_1 + \frac{1}{\sqrt{2}}\mathbf{i}_2, \tag{2.47}$$

such that the longitudinal portion of the elastic wave is polarized in the [110] crystal direction, with two orthogonal transverse components polarized in the [001] and $[1\bar{1}0]$ crystal directions. In this case, we can write the displacement vector as [155, 164]

$$\mathbf{u}(\mathbf{r},t) = \mathbf{u}_{\mathrm{l}}(\mathbf{r},t) + \mathbf{u}_{\mathrm{t}_1}(\mathbf{r},t) + \mathbf{u}_{\mathrm{t}_2}(\mathbf{r},t), \tag{2.48}$$

where

$$\mathbf{u}_{\mathrm{l}}(\mathbf{r},t) = \bar{u}_{\mathrm{l}}(\mathbf{r},t)\left\{\frac{1}{\sqrt{2}}\mathbf{i}_1 + \frac{1}{\sqrt{2}}\mathbf{i}_2\right\}, \tag{2.49}$$

$$\mathbf{u}_{\mathrm{t}_1}(\mathbf{r},t) = \bar{u}_{\mathrm{t}_1}(\mathbf{r},t)\left\{\mathbf{i}_3\right\}, \tag{2.50}$$

$$\mathbf{u}_{\mathrm{t}_2}(\mathbf{r},t) = \bar{u}_{\mathrm{t}_1}(\mathbf{r},t)\left\{\frac{1}{\sqrt{2}}\mathbf{i}_1 - \frac{1}{\sqrt{2}}\mathbf{i}_2\right\}, \tag{2.51}$$

are the displacement vectors associated with the [110], [001], and $[1\bar{1}0]$ polarizations, respectively, with corresponding amplitudes $\bar{u}_i(\mathbf{r},t)$ and speeds of sound [155, 164, 171]

$$c_l = \sqrt{\frac{C_{11}+C_{12}+2C_{44}}{2\rho}} = \sqrt{\frac{1}{2\rho}\left(\frac{\tilde{Y}}{(1+\tilde{\nu})(1-2\tilde{\nu})} + \tilde{\mu}\right)}, \tag{2.52}$$

$$c_{t_1} = \sqrt{\frac{C_{11}-C_{12}}{2\rho}} = \sqrt{\frac{\tilde{Y}}{2\rho(1+\tilde{\nu})}}, \tag{2.53}$$

$$c_{t_2} = \sqrt{\frac{C_{44}}{\rho}} = \sqrt{\frac{\tilde{\mu}}{\rho}}. \tag{2.54}$$

When written in terms of the effective elastic moduli $\tilde{Y}$, $\tilde{\nu}$, and $\tilde{\mu}$ (defined with respect to the crystal axes), the transverse sounds speeds are similar to those for an isotropic medium, with c_{t_1} (c_{t_2}) resembling the middle (last) term in Eq. (2.46). However, we reiterate that since $\tilde{\mu} \neq \tilde{Y}/2(1+\tilde{\nu})$, $c_{t_1} \neq c_{t_2}$ in general. Indeed, we find that with this choice of propagation direction and polarization, $\mathbf{n}_{110} \times \mathbf{u}_l = 0$, such that $\mathbf{u}_l$ describes purely longitudinal displacements (parallel to the direction

of propagation), while $\mathbf{u}_{t_1}$ and $\mathbf{u}_{t_2}$ are purely transverse (perpendicular to the direction of propagation) in the sense that $\mathbf{n}_{110} \cdot \mathbf{u}_{t_1} = \mathbf{n}_{110} \cdot \mathbf{u}_{t_2} = 0$ [164].

Up to this point, we have largely focused on the propagation of elastic waves in infinite media. However, for the devices studied in this thesis, we are interested in the bound elastic modes of mechanical resonators. Therefore, we will spend the remainder of this section discussing how to adapt the linear elastic theory described above to these finite resonant structures. We begin by using Eq. (2.3) to rewrite the elastic equation of motion given by Eq. (2.38) in terms of $x(t)$ and the components of $\mathbf{u}(\mathbf{r})$ as

$$\rho(\mathbf{r})\ddot{x}(t)u_a(\mathbf{r}) = C_{abcd}x(t)\frac{\partial^2 u_d(\mathbf{r})}{\partial\tilde{x}_b\partial\tilde{x}_c}. \tag{2.55}$$

We then make a high-Q approximation, allowing us to input Eq. (2.13) into Eq. (2.55) to generate a self-contained equation of motion for the mechanical modeshape of our systems as

$$u_a(\mathbf{r}) + \frac{C_{abcd}}{\rho(\mathbf{r})\omega_{\mathrm{m}}^2}\frac{\partial^2 u_d(\mathbf{r})}{\partial\tilde{x}_b\partial\tilde{x}_c} = 0. \tag{2.56}$$

One noteworthy consequence of this equation of motion is that the resulting modeshape function solutions will be orthogonal in the sense that

$$\int \rho(\mathbf{r})\mathbf{u}_k(\mathbf{r}) \cdot \mathbf{u}_{k'}(\mathbf{r})dV = m_k\delta_{kk'}, \tag{2.57}$$

where $\mathbf{u}_k(\mathbf{r})$ and m_k are the modeshape vector and effective mass of the kth mechanical mode, while $\delta_{kk'}$ is the Kronecker delta function (see Appendix A), such that when $k = k'$ the orthogonality condition is simply the definition of the effective motional mass given by Eq. (2.6). Aside from a very small subset of simple systems [145] (see the next subsection on the flexural modes of narrow beams for example), it is very difficult to determine analytical mechanical modeshapes using Eq. (2.56), especially for complex geometries embedded in three dimensions. Fortunately, this equation can be solved numerically for nearly any arbitrary geometry using finite element method (FEM) solvers such as COMSOL MULTIPHYSICS® [172].

2.3.4 Flexural Modes of Narrow Beams

As the majority of the mechanical modes considered in this thesis are the flexural (bending) modes of curved nanomechanical beam resonators, we find it informative

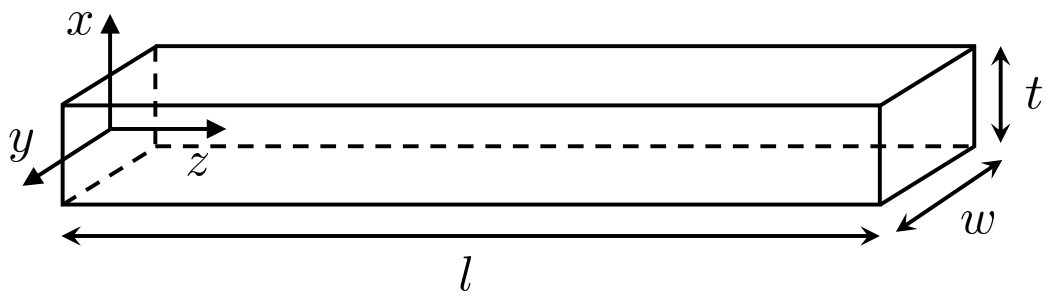

Figure 2.1: Schematic of the long, thin rectangular beam geometry considered in this section, indicating its length l, width w, and thickness t, as well as its Cartesian coordinate axes.

to briefly discuss an approximate analytical method, known as Euler-Bernoulli beam theory [149, 156], that can be used to calculate the resonant frequencies and modeshapes of this type of motion in one-dimensional beams. Here we consider the rectangular beam[12] shown in Fig. 2.1, with length l, width w, and thickness t, in both the doubly-clamped and clamped-free (cantilevered) situations. For the case of a long, narrow beam (*i.e.* $l \gg w, t$), an equation of motion for the modeshape function $u_n(z)$ of the beam's nth flexural mode, with a resonant angular frequency of ω_n, can be found by balancing its net forces and torques, resulting in [145, 149, 153]

$$\frac{\partial^4 u_n}{\partial z^4} + \frac{\rho \mathcal{A}}{\tilde{Y} I} \omega_n^2 u_n = 0. \tag{2.58}$$

Here ρ, $\mathcal{A} = wt$, and $I = tw^3/12$ ($I = wt^3/12$) are the uniform density, cross-sectional area, and bending moment of inertia for the in-plane (out-of-plane) motion of the beam, while $\tilde{Y}$ is the effective Young's modulus of the system. Note that while similar to Eq. (2.56), Eq. (2.58) contains derivatives to fourth order in the position z, such that the solution of the nth flexural mode of the beam is given by [145, 149, 153]

$$u_n(z) = \mathcal{U}_n \left[\cosh\left(\frac{q_n z}{l}\right) - \cos\left(\frac{q_n z}{l}\right) \right] - \mathcal{W}_n \left[\sinh\left(\frac{q_n z}{l}\right) - \sin\left(\frac{q_n z}{l}\right) \right]. \tag{2.59}$$

Here, $\mathcal{U}_n = \mathcal{O}_n \left[\sinh(q_n) \pm \sin(q_n)\right]$ and $\mathcal{W}_n = \mathcal{O}_n \left[\cosh(q_n) \pm \cos(q_n)\right]$, where $\mathcal{O}_n$ is a normalization constant defined on a per-mode basis to ensure $\max|u_n(z)| = 1$,

[12] We assume a rectangular cross-section for simplicity, though this formalism can be used for any arbitrary cross-section, provided it is uniform and the bending moment of inertia is known.

while the factor q_n is determined as the nth solution of[13]

$$\cos(q_n)\cosh(q_n) \pm 1 = 0, \tag{2.60}$$

with the positive (minus) sign corresponding to cantilevered (doubly-clamped) beams. The values of q_n and $\mathcal{U}_n/\mathcal{W}_n$ for both of these clamping conditions are given in Table 2.1, with the first six modeshapes calculated by inserting these values into Eq. (2.59) shown in Fig. 2.2.

Mode	Cantilever		Doubly Clamped Beam	
Number (n)	q_n	$\mathcal{U}_n/\mathcal{W}_n$	q_n	$\mathcal{U}_n/\mathcal{W}_n$
1	1.8751	1.3622	4.7300	1.0178
2	4.6941	0.9819	7.8532	0.9992
3	7.8548	1.0001	10.9955	1.0000
$n > 3$	$(n-1)\pi + \pi/2$	1	$n\pi + \pi/2$	1

Table 2.1: Values of q_n and the ratio $\mathcal{U}_n/\mathcal{W}_n$ for cantilevers and doubly clamped beams. The last row provides an approximation of these quantities for $n > 3$ [153], which can be obtained from the fact that for large n, $\cosh(q_n)$ and $\sinh(q_n)$ are so large that we require $\cos(q_n)$ to be very close to zero to satisfy Eq. (2.60) and $\mathcal{U}_n/\mathcal{W}_n \approx \sinh(q_n)/\cosh(q_n) \approx 1$.

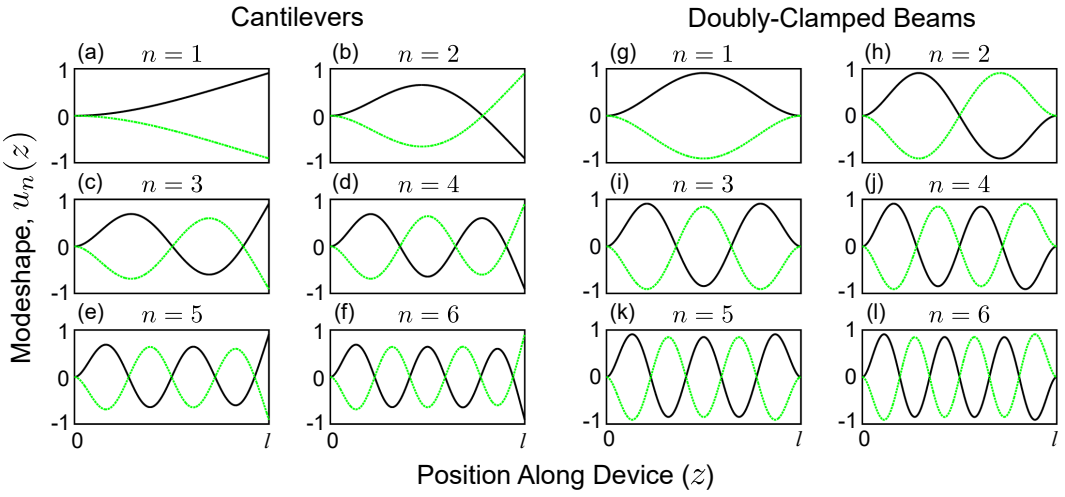

Figure 2.2: Modeshape functions for the first six flexural modes of (a)–(f) a cantilever and (g)–(l) a doubly-clamped beam. The solid black and dashed green lines represent the positive and negative maximum displacement (*i.e.* 180° out of phase in time with respect to each other), with each mode normalized such that its maximum displacement is equal to one.

[13]Since $n = 0$ results in the trivial solution $q_n = 0$, we are only concerned with $n \geq 1$ here.

By inputting the modeshape solution given by Eq. (2.59) into Eq. (2.58), we can determine a dispersion relation for the resonant frequency of the nth flexural mode in terms of the beam's properties and q_n as

$$\omega_n = \frac{q_n^2}{l^2}\sqrt{\frac{\tilde{Y}I}{\rho\mathcal{A}}}. \tag{2.61}$$

Finally, we can directly input the cross-sectional area and moment of inertia of a rectangular beam into Eq. (2.61) to determine the resonant frequency for in-plane flexural modes as

$$\omega_n = \frac{q_n^2 w}{l^2}\sqrt{\frac{\tilde{Y}}{12\rho}}. \tag{2.62}$$

While the results from this section do not directly apply to the in-plane flexural modes of the curved beam geometry studied in this thesis, they provide an intuition of their qualitative nature. Furthermore, we use this prismatic beam treatment when discussing the individual dissipation mechanisms of nanomechanical resonators in Section 2.5, as this simplified geometry can be used to calculate analytical results that provide order of magnitude estimates for the mechanical quality factors of our devices.

2.3.5 Strain Energy Fractions

Once the modeshape of the mechanical resonator is solved for, it is possible to ascertain the degree to which the mode behaves like a longitudinal elastic wave, and likewise for a transverse elastic wave. This distinction turns out to be very important when considering the damping due to two-level systems in nanobeam resonators, as is discussed in Section 2.5.4 and Chapter 6 below. To calculate these fractions, we begin with the total mechanical energy E_{m} for a given mode, which can be found in terms of its time-dependent kinetic energy density

$$U_{\mathrm{k}}(\mathbf{r},t) = \frac{1}{2}\rho(\mathbf{r})|\dot{\mathbf{u}}(\mathbf{r},t)|^2, \tag{2.63}$$

and its time-dependent elastic potential energy density (written in terms of a contraction over the stress and strain tensors)

$$U_{\mathrm{e}}(\mathbf{r},t) = \frac{1}{2}\varepsilon_{ab}(\mathbf{r},t)\sigma_{ab}(\mathbf{r},t) = \frac{1}{2}C_{abcd}\varepsilon_{ab}(\mathbf{r},t)\varepsilon_{cd}(\mathbf{r},t), \tag{2.64}$$

as[14] [162, 163]

$$\begin{aligned} E_{\mathrm{m}} &= \int \left[U_{\mathrm{k}}(\mathbf{r},t) + U_{\mathrm{e}}(\mathbf{r},t)\right] dV \\ &= \frac{1}{2}\int \left[\rho(\mathbf{r})|\dot{\mathbf{u}}(\mathbf{r},t)|^2 + C_{abcd}\varepsilon_{ab}(\mathbf{r},t)\varepsilon_{cd}(\mathbf{r},t)\right] dV. \end{aligned} \tag{2.65}$$

Note that in Eq. (2.64), we have used the generalized form of Hooke's law given by Eq. (2.25) to eliminate the stress tensor from the elastic potential energy density, allowing us to express the mechanical energy density of the mode solely in terms of its strain tensor and elastic modulus constants [173, 174].

For the case of a cubic crystal, we can integrate the potential energy by parts, while using Eqs. (2.21), (2.22), and (2.56) to express the total mechanical energy of the mode in terms of $x(t)$ and the components of $\overleftrightarrow{\varepsilon}(\mathbf{r})$ as[15] [163]

$$\begin{aligned} E_{\mathrm{m}} = \frac{1}{2}m\left[\dot{x}^2(t) + \omega_{\mathrm{m}}^2 x^2(t)\right] \Bigg\{ \frac{1}{m\omega_{\mathrm{m}}^2}\int \rho(\mathbf{r}) \Bigg[c_l^2 \sum_{a,b} \varepsilon_{aa}(\mathbf{r})\varepsilon_{bb}(\mathbf{r}) \\ + c_{t_1}^2 \left(\sum_a [\varepsilon_{aa}(\mathbf{r})]^2 - \sum_{a\neq b} \varepsilon_{aa}(\mathbf{r})\varepsilon_{bb}(\mathbf{r}) \right) \\ + c_{t_2}^2 \left(2\sum_{a\neq b} [\varepsilon_{ab}(\mathbf{r})]^2 - \sum_{a,b} \varepsilon_{aa}(\mathbf{r})\varepsilon_{bb}(\mathbf{r}) \right) \Bigg] dV \Bigg\}. \end{aligned} \tag{2.66}$$

Upon inspection of Eq. (2.66), we immediately find that the expression to the left of the curly brackets is identical to the total energy of the mechanical mode given in Eq. (2.10). Therefore, the term that follows must be equal to one. This allows us to interpret the mechanical energy of the system, and therefore the mode itself, as being partitioned into the fractions

$$e_l = \frac{c_l^2}{m\omega_{\mathrm{m}}^2}\int \rho(\mathbf{r}) \sum_{a,b} \varepsilon_{aa}(\mathbf{r})\varepsilon_{bb}(\mathbf{r}) dV, \tag{2.67}$$

$$e_{t_1} = \frac{c_{t_1}^2}{m\omega_{\mathrm{m}}^2}\int \rho(\mathbf{r}) \left(\sum_a [\varepsilon_{aa}(\mathbf{r})]^2 - \sum_{a\neq b} \varepsilon_{aa}(\mathbf{r})\varepsilon_{bb}(\mathbf{r}) \right) dV, \tag{2.68}$$

$$e_{t_2} = \frac{c_{t_2}^2}{m\omega_{\mathrm{m}}^2}\int \rho(\mathbf{r}) \left(2\sum_{a\neq b} [\varepsilon_{ab}(\mathbf{r})]^2 - \sum_{a,b} \varepsilon_{aa}(\mathbf{r})\varepsilon_{bb}(\mathbf{r}) \right) dV, \tag{2.69}$$

[14] The total mechanical energy of the system is time-independent due to the conservation of energy.

[15] Here we must also use the fact that the total kinetic and potential energy of the resonator (*i.e.* considering all mechanical modes) will each be equal to half of the total mechanical energy of the entire resonator [162].

corresponding to the longitudinal and transverse polarizations associated with the speeds of sound given in Eqs. (2.52)–(2.54). These fractions allow us to determine the extent to which we can consider a given mechanical mode as quasi-longitudinal or quasi-transverse. Note that since $\sum \varepsilon_{aa}(\mathbf{r})\varepsilon_{bb}(\mathbf{r}) = [\mathrm{Tr}\{\overleftrightarrow{\varepsilon}(\mathbf{r})\}]^2$, e_l is invariant with respect to changes of coordinates (*i.e.* crystal orientations) for a given mechanical mode, however, this is not the case for e_{t_1} and e_{t_2}. Finally, we point out that similar fractions can be determined for the case of an isotropic system [162].

2.3.6 Effective Strain Volume

Another useful parameter to characterize the strain energy distributions in our resonator is its effective strain volume, which quantifies the spatial extent of the strain profiles of a given mechanical mode similar to the way that the effective mass accounts for the the fraction of the resonator that participates in its motion. To calculate this quantity, we again use the elastic strain energy density given by Eq. (2.64), which can be integrated over the entire volume of the mechanical resonator to obtain the total (time-dependent) elastic potential energy of the mode as[16]

$$E_{\mathrm{p}}(t) = \int U_{\mathrm{e}}(\mathbf{r},t)dV. \tag{2.70}$$

Focusing on a system that exhibits cubic crystal symmetry, we write out the tensor product in Eq. (2.64) explicitly in terms of the elastic moduli and strain profile components as

$$\begin{aligned} C_{abcd}\varepsilon_{ab}(\mathbf{r})\varepsilon_{cd}(\mathbf{r}) = \frac{1}{4}\Big\{ & C_{11}\left[\varepsilon_{11}^2(\mathbf{r}) + \varepsilon_{22}^2(\mathbf{r}) + \varepsilon_{33}^2(\mathbf{r})\right] \\ & + 2C_{12}\left[\varepsilon_{11}(\mathbf{r})\varepsilon_{22}(\mathbf{r}) + \varepsilon_{11}(\mathbf{r})\varepsilon_{33}(\mathbf{r}) + \varepsilon_{22}(\mathbf{r})\varepsilon_{33}(\mathbf{r})\right] \\ & + 4C_{44}\left[\varepsilon_{12}^2(\mathbf{r}) + \varepsilon_{13}^2(\mathbf{r}) + \varepsilon_{23}^2(\mathbf{r})\right]\Big\}. \end{aligned} \tag{2.71}$$

The effective strain volume of the mode is then defined as [135, 163, 175]

$$V_{\mathrm{str}} = \int \frac{U_{\mathrm{e}}(\mathbf{r},t)}{\max[U_{\mathrm{e}}(\mathbf{r},t)]}dV = \int \frac{C_{abcd}\varepsilon_{ab}(\mathbf{r})\varepsilon_{cd}(\mathbf{r})}{\max[C_{abcd}\varepsilon_{ab}(\mathbf{r})\varepsilon_{cd}(\mathbf{r})]}dV, \tag{2.72}$$

where $\max[U_{\mathrm{e}}(\mathbf{r},t)] = \frac{x^2(t)}{2}\max[C_{abcd}\varepsilon_{ab}(\mathbf{r})\varepsilon_{cd}(\mathbf{r})]$ is the maximum value of the elastic potential energy density for the studied mechanical mode. Provided the

[16] This potential energy is identical to that given by Eq. (2.5).

strain profile of a mechanical mode is known (this is generally determined using FEM simulation), one can use Eq. (2.72) to calculate its effective strain volume, quantifying the extent through which mechanical strains permeate the resonator.

2.4 Thermal Phonon Bath

The dissipation introduced in Section 2.2.3 arises from the fact that any realistic mechanical resonator will be coupled to its surroundings, causing it to lose energy to its external bath at its mechanical damping rate. Therefore, before we begin to investigate specific mechanical damping mechanisms, it is imperative that we have a thorough understanding of this external bath. Here, we consider this bath for a semiconductor (or insulator) at low temperatures (as is appropriate for the silicon devices studied in this thesis), which is comprised of thermal excitations of low-lying vibrational modes in the material's lattice (*i.e.* phonons), characterizing its thermal properties, as well as its density of states.

2.4.1 Bath Occupancies and Energies

As was initially proposed by Feynman and Vernon [176] and later developed further by Caldiera and Leggett [177–179] (into the so-called Caldiera-Leggett model), in the linear dissipation regime a phononic bath can be modelled as an infinite set of harmonic oscillators. Due to the bosonic nature of phonons, each of these bath modes obey Bose-Einstein statistics, such that their average occupancy is given by

$$\bar{n}_{\mathrm{b}}(\omega_q) = \frac{1}{e^{\hbar\omega_q/k_{\mathrm{B}}T} - 1}, \tag{2.73}$$

where T is the temperature of the bath and ω_q is the angular frequency of the qth bath mode [149, 171]. The average energy of the entire bath is then given by

$$E_{\mathrm{b}} = \sum_q \left[\bar{n}_{\mathrm{b}}(\omega_q) + \frac{1}{2}\right] \hbar\omega_q, \tag{2.74}$$

where the addition of one-half is due to the ground state energy of each bath mode. Note that while this sum is formally performed over the infinite number of considered harmonic modes, for any realistic D-dimensional bath, this sum is limited to the system's $D\mathcal{N}_{\mathrm{b}}$ degrees of freedom, where $\mathcal{N}_{\mathrm{b}}$ is the number of atoms

in the bath. In practice, any realistic bath will contain a large number of atoms, such that the approximation of an infinite number of modes is a good one.

Here we consider the bath temperature T to be constant in time (see Appendix F for the treatment of a transient bath temperature), such that the $D\mathcal{N}_\mathrm{b}$ modes of the bath are not equally populated due to their varying frequencies. For high frequency modes ($k_\mathrm{B}T \ll \hbar\omega_q$) we find

$$\bar{n}_\mathrm{b}(\omega_q) \approx e^{-\hbar\omega_q/k_\mathrm{B}T} \approx 0, \tag{2.75}$$

such that bath modes with energy spacings larger than the available thermal energy are effectively frozen out and have no thermal occupation. For the extreme case of absolute zero ($T = 0$ K), all bath modes are completely frozen out, regardless of their frequency. In this situation, the total bath energy is expressed as a sum of the ground state energies of each mode as

$$E_\mathrm{b} = \frac{1}{2}\sum_q \hbar\omega_q. \tag{2.76}$$

Conversely, in the low frequency regime ($k_\mathrm{B}T \gg \hbar\omega_q$), the bath mode occupation becomes

$$\bar{n}_\mathrm{b}(\omega_q) \approx \frac{k_\mathrm{B}T}{\hbar\omega_q}. \tag{2.77}$$

This limit can be interpreted as the thermal energy budget of a given high temperature bath mode[17] being divided amongst $\bar{n}_\mathrm{b}$ phonons on average, each with an energy of $\hbar\omega_q$. For a bath at a high enough temperature (*i.e.* greater than the Debye temperature that will be introduced in the next subsection), all of its modes will be thermally populated according to Eq. (2.77) and the total energy of the bath will be given by [149]

$$E_\mathrm{b} = D\mathcal{N}_\mathrm{b}k_\mathrm{B}T. \tag{2.78}$$

This result is the classical law of Dulong and Petit [181], whereby the $D\mathcal{N}_\mathrm{b}$ modes of the bath are thermally populated such that they each contribute $k_\mathrm{B}T$ to the total energy of the bath.

[17] According to the equipartition theorem, the total thermal energy of each bath mode is given by $k_\mathrm{B}T$, half of which comes from its potential energy, with the other half from its kinetic energy [180].

2.4.2 Density of States

In the previous subsection, we discussed the thermal occupancies of a given mode at a frequency ω_q. However, in order to have a true understanding of the total number of phonons in this reservoir, we must determine its density of normal modes or density of states (DOS). In general, the D-dimensional DOS of a phononic system is given by [182]

$$\varrho_D(\omega) = \frac{1}{(2\pi)^D} \sum_{\eta} \int \delta\left(\omega - \omega_\eta(\mathbf{k})\right) d\mathbf{k}, \tag{2.79}$$

where the sum is performed over the D polarizations of the system labelled by η, with each having a dispersion relation $\omega_\eta(\mathbf{k})$, while the integral is performed over the first Brillouin zone. With this definition[18], $\varrho_D(\omega)d\omega$ gives the number of phonon modes (per unit volume) contained within the infinitesimal frequency interval from ω to $\omega + d\omega$. Assuming the continuum limit for a large number of states, one can also use the DOS of the system to replace any sum over the bath modes (see Eqs. (2.74) and (2.76) for instance) with an integral according to [162, 182]

$$\sum_q \to V_D \int \varrho_D(\omega) d\omega, \tag{2.80}$$

where V_D is the D-dimensional volume of the considered bath (*i.e.* V_1 is a length, V_2 is an area, and V_3 is a conventional volume). Finally, we note that the DOS obeys the relation

$$V_D \int \varrho_D(\omega) d\omega = D\mathcal{N}_\mathrm{b}, \tag{2.81}$$

that is to say, by integrating the DOS over all frequencies and multiplying by the system's D-dimensional volume, we retrieve the total number of bath modes as expected. As we will see below, the choice of DOS will have drastic effects on many of the bath's properties, such as its energy, heat capacity, and thermal conductivity, which in turn will affect the dissipation mechanisms of the nanomechanical resonator. We therefore spend considerable effort in this and the proceeding subsection detailing the DOS of the bath, as well as the effect they have on its properties.

[18] Here we have chosen to use the density of states per unit volume, from which we can find the true density of states by simply multiplying by the D-dimensional volume of the system [149, 182].

Typically, the dispersion relation $\omega_\eta(\mathbf{k})$ given in Eq. (2.79) is a complex function of the phononic wavevector $\mathbf{k}$ and varies from material to material, making the exact form of the DOS very difficult to determine [182]. However, Debye [183] introduced a very simple, yet effective, approximation that can be used in the situation where only long-wavelength, low-frequency phonon modes are considered [149, 171, 182]. In this case, only the low-lying portions of the acoustic phonon branches are excited, such that the dispersion relation of each polarization will be given by $\omega_\eta(\mathbf{k}) = c_\eta k$, where $k = |\mathbf{k}|$ is the phononic wavenumber. Furthermore, in the Debye approximation, we replace the k-space integral over the Brillouin zone in Eq. (2.79) with an integral over a sphere of radius[19] [149, 171]

$$k_D = \sqrt[D]{\frac{(2\pi)^D D}{\mathcal{S}_{D-1}} \frac{\mathcal{N}_\mathrm{b}}{V_D}}, \tag{2.82}$$

where $\mathcal{S}_D$ is the surface area of the D-dimensional unit hypersphere. From this wavevector radius, we can also define the D-dimensional Debye frequency as $\varpi_D = \bar{c}_D k_D$, where $\bar{c}_D$ is the average Debye speed of sound given by

$$\bar{c}_D = \left(\frac{1}{D} \sum_\eta \frac{1}{c_\eta^D} \right)^{-1/D}, \tag{2.83}$$

We note that is it often the case that even if a system is dimensionally reduced, it is embedded in three-dimensional space such that it still accesses all three phonon polarizations (*e.g.* a narrow beam with transverse and longitudinal modes). In this situation, we simply replace $\bar{c}_D$ with $\bar{c}_3 = \bar{c}$ [149, 171], where we have dropped the subscript 3 for brevity. Finally, we also define a Debye temperature $\Theta_D = \hbar\varpi_D/k_\mathrm{B}$, above which all phononic modes of the bath are classically occupied according to Eq. (2.77), and below which these modes begin to freeze out [149, 171, 182]. For the three dimensional case in silicon, the sum in Eq. (2.83) is taken over the single longitudinal (l) and two transverse (t_1, t_2) phonon polarizations, such that $\bar{c} = \left(\frac{1}{3}\sum \frac{1}{c_\eta^3}\right)^{-1/3} = 5718$ m/s [184, 185], where we have taken $c_l = 9148$ m/s, $c_{t_1} = 4679$ m/s, and $c_{t_2} = 5857$ m/s (see Table 5.1). Furthermore, we find that $\Theta = 645$

[19] Throughout this thesis, subscript D labels the dimensionality of the system. The same applies to a superscript D in parentheses, while a superscript D without parentheses indicates a parameter taken to the power of the system's dimensionality.

K [154, 186, 187], resulting in $\varpi/2\pi = 13.4$ THz, where we have again dropped the subscript for the 3D case.

Inputting the Debye dispersion relation into Eq. (2.79), and integrating over the k-sphere of radius k_D, we find the Debye density of states (for a D-dimensional system) to be [162]

$$\varrho_D(\omega) = \frac{1}{(2\pi)^D} \sum_\eta \mathcal{S}_{D-1} \frac{\omega^{D-1}}{c_\eta^D} = \frac{D\mathcal{S}_{D-1}}{(2\pi)^D} \frac{\omega^{D-1}}{\bar{c}_D^D}, \tag{2.84}$$

for $\omega < \varpi_D$ and $\varrho_D(\omega) = 0$ for $\omega > \varpi_D$. Note that $\mathcal{S}_0 = 2$, $\mathcal{S}_1 = 2\pi$, and $\mathcal{S}_2 = 4\pi$, such that each of the one-, two-, and three-dimensional Debye density of states (corresponding to $D = 1$, 2, and 3) are given by [171]

$$\varrho_1(\omega) = \frac{1}{\pi c_\eta} = \frac{1}{\pi \bar{c}_1}, \tag{2.85}$$

$$\varrho_2(\omega) = \frac{1}{2\pi} \sum_\eta \frac{\omega}{c_\eta^2} = \frac{1}{\pi} \frac{\omega}{\bar{c}_2^2}, \tag{2.86}$$

$$\varrho_3(\omega) = \frac{1}{2\pi^2} \sum_\eta \frac{\omega^2}{c_\eta^3} = \frac{3}{2\pi^2} \frac{\omega^2}{\bar{c}_3^3}. \tag{2.87}$$

Using these density of states, we can replace the sum over q in Eq. (2.74) with an integral according to Eq. (2.80) to find the total energy of the bath in the Debye model as

$$E_{\rm b}^{(D)} = \int_0^{\varpi_D} \left[\bar{n}_{\rm b}(\omega) + \frac{1}{2}\right] \hbar\omega = E_{\rm b}^{(D)}(T) + E_{\rm b}^{(D)}(T=0). \tag{2.88}$$

Here we have broken the bath energy into its temperature-dependent portion

$$E_{\rm b}^{(D)}(T) = D^2 \mathcal{N}_{\rm b} k_{\rm B} T \left(\frac{T}{\Theta_D}\right)^D \int_0^{z_D} \frac{z^D}{e^z - 1} dz, \tag{2.89}$$

due to thermal phonons in the bath, where we have introduced the variables $z = \hbar\omega/k_{\rm B}T$ and $z_D = \Theta_D/T$, as well as its temperature-independent component

$$E_{\rm b}^{(D)}(T=0) = \frac{D^2}{D+1} \mathcal{N}_{\rm b} \frac{\hbar\varpi_D}{2}, \tag{2.90}$$

resulting from the the ground state contributions of each mode that remain present at $T = 0$. Focussing on $E_{\rm b}^{(D)}(T)$, we find at high temperatures ($T \gg \Theta_D$), $z \ll 1$ and $e^z - 1 \approx z$, such that the integral in Eq. (2.89) can easily be solved, resulting

in the expected high-temperature limit given by Eq. (2.78). On the other hand, at low temperatures ($T \ll \Theta_D$), $z_D \gg 1$ such that we extend the upper limit of the integral in Eq. (2.89) to infinity, allowing us to calculate bath energy in this regime as

$$E_{\mathrm{b}}^{(D)}(T) = D^2 \mathcal{N}_{\mathrm{b}} k_{\mathrm{B}} T \left(\frac{T}{\Theta_D}\right)^D \zeta(D+1)\Gamma(D+1), \tag{2.91}$$

where $\Gamma(z)$ and $\zeta(z)$ are the Gamma and Riemann zeta functions, respectively [171]. We point out that in the three-dimensional case, $\zeta(4)\Gamma(4) = \pi^4/15$, such that the low temperature bath energy has the closed form solution [149, 171, 182, 188]

$$E_{\mathrm{b}}^{(3)}(T) = \frac{3\pi^4}{5} \mathcal{N}_{\mathrm{b}} k_{\mathrm{B}} T \left(\frac{T}{\Theta}\right)^3. \tag{2.92}$$

2.4.3 Thermal Properties of the Bath

We are also interested in calculating the specific heat capacity and thermal conductivity of the bath, as these two parameters are required in order to calculate the relevant thermal time scales associated with a number of temperature-dependent nanomechanical damping mechanisms, as well as the time constant of the photothermal force considered in Chapter 7. We begin by first determining the specific heat capacity (per unit volume), which gives a measure of the amount of energy that is required to increase the temperature of the bath. Here, we focus on the specific heat capacity at constant volume[20], defined for a conventional three-dimensional solid as [149, 171, 182, 189]

$$\mathcal{C}_V = \frac{1}{V}\frac{\partial E_{\mathrm{b}}}{\partial T}. \tag{2.93}$$

Inputting Eq. (2.88) into Eq. (2.93), we then find the D-dimensional heat capacity of the bath in the Debye model as

$$\mathcal{C}_V^{(D)} = \frac{1}{V}\frac{\partial E_{\mathrm{b}}^{(D)}}{\partial T} = \frac{D^2 \mathcal{N}_{\mathrm{b}} k_{\mathrm{B}}}{V}\left(\frac{T}{\Theta_D}\right)^D \int_0^{z_D} \frac{z^{D+1} e^z}{(e^z-1)^2} dz. \tag{2.94}$$

Taking the high-temperature limit of Eq. (2.94), we find

$$\mathcal{C}_V^{(D)} = \frac{D \mathcal{N}_{\mathrm{b}} k_{\mathrm{B}}}{V}, \tag{2.95}$$

[20] As opposed to the specific heat capacity at constant pressure, which is given in terms of $\mathcal{C}_V$ as $\mathcal{C}_P = \mathcal{C}_V + \tilde{\alpha}_V^2 BT$, where $\tilde{\alpha}_V$ and B are the volumetric thermal expansion coefficient and the bulk modulus of the considered solid [171]. Therefore, at low temperatures ($T \ll \mathcal{C}_V/\tilde{\beta}^2 B$) these two heat capacities are nearly identical and any distinction between them is unnecessary [188].

which matches with what one would expect from the Dulong-Petit law given in Eq. (2.78).

In the opposite limit, the low temperature specific heat capacity can be determined by taking the limit of the integral in Eq. (2.94) to infinity as we did for $E_{\mathrm{b}}^{(D)}(T)$ in the previous subsection (or by simply taking the derivative of Eq. (2.91) with respect to temperature and dividing by V) to obtain

$$\begin{aligned}\mathcal{C}_V^{(D)} &= \frac{D^2(D+1)\mathcal{N}_{\mathrm{b}}k_{\mathrm{B}}}{V}\zeta(D+1)\Gamma(D+1)\left(\frac{T}{\Theta_D}\right)^D \\ &= D(D+1)\mathcal{S}_{D-1}\zeta(D+1)\Gamma(D+1)\frac{V_D}{V}k_{\mathrm{B}}\left(\frac{k_{\mathrm{B}}T}{2\pi\hbar\bar{c}_D}\right)^D,\end{aligned} \tag{2.96}$$

where in the second line, we have input Θ_D in terms of V_D by rearranging Eq. (2.82). Note that the factor of V_D/V ensures that the D-dimensional heat capacity will have the proper units of J/kg·m^3. Therefore, we find that at temperatures far below the Debye temperature, the specific heat capacity obeys a ^{D} dependence that strongly depends on the dimensionality of the considered system. Focussing again on the $D = 3$ case, we determine the three-dimensional specific heat capacity to be[21]

$$\mathcal{C}_V = \frac{2\pi^2 k_{\mathrm{B}}^4}{5\hbar^3\bar{c}^3}T^3, \tag{2.97}$$

exhibiting the expected T^3 temperature dependence observed in bulk silicon at low temperatures [190, 191].

Treating the phonons in the bath as a diffuse, noninteracting gas, we can also determine its thermal conductivity as[22] [149, 188]

$$\mathcal{K} = \frac{1}{3}\mathcal{C}_V\Lambda\bar{c}. \tag{2.98}$$

where Λ is the phonon mean free path, which is in general temperature-dependent [192]. However, as pointed out by Peierls [193, 194] and Casimir [195], below a certain temperature this mean free path will become comparable to the dimensions

[21] Here we have dropped the superscript (3) for notational simplicity, as we use this expression frequently later in the thesis.

[22] In general, all three phonon polarizations carry heat, such that we use the three-dimensional average Debye speed of sound $\bar{c}$ in Eq. (2.98) regardless of the dimensionality of the system. However, if one knows exactly which polarizations are involved in heat transfer for a reduced dimensionality system, $\bar{c}$ can be replaced by the appropriate speed of sound according to Eq. (2.83).

of the system, such that it will be limited by the device's finite size[23]. This phenomenon is particularly important for the nanoscale devices studied in this thesis. Considering a beam with a rectangular cross section, this boundary-limited mean free path is given by

$$\Lambda_{\mathrm{C}} = \frac{\sqrt{wt}}{2}\left[3\ln\left(1+\sqrt{2}\right) - \sqrt{2} + 1\right] \approx 1.12\sqrt{wt}, \tag{2.99}$$

where w and t are the width and thickness of the beam [184, 185, 195–199]. Inputting Eq. (2.99), as well as Eq. (2.96), into Eq. (2.98), we determine the low-temperature Casimir-limited thermal conductivity of a rectangular beam in the Debye model as

$$\mathcal{K}^{(D)} = \frac{1}{3}D(D+1)\mathcal{S}_{D-1}\zeta(D+1)\Gamma(D+1)k_{\mathrm{B}}\Lambda_{\mathrm{C}}\bar{c}_D\left(\frac{k_{\mathrm{B}}T}{2\pi\hbar\bar{c}_D}\right)^D. \tag{2.100}$$

Here we see that in the Casimir regime associated with nanoscale systems at low temperatures, the thermal conductivity obeys the same T^D power law dependence observed for the specific heat capacity in Eq. (2.96). Therefore, in three dimensions we have

$$\mathcal{K} = \frac{2\pi^2\Lambda_{\mathrm{C}}k_{\mathrm{B}}^4}{15\hbar^3\bar{c}^2}T^3, \tag{2.101}$$

which again agrees with the cubic temperature dependence observed for the thermal conductivity of silicon nanobeams at low temperatures [197, 198].

Finally, we can calculate the thermal diffusivity $\mathcal{J}$ of the system, which is defined as the ratio of the bath's thermal conductivity to its heat capacity, such that it can be found from Eq. (2.98) as [149, 200]

$$\mathcal{J} = \frac{\mathcal{K}}{\mathcal{C}_V} = \frac{\Lambda_{\mathrm{C}}\bar{c}}{3}. \tag{2.102}$$

This quantity describes the rate at which heat is transferred across thermal gradients and is therefore useful for calculating the mechanical resonator's thermal time constants. Note that in the Casimir-limited Debye model considered here, the diffusivity given in Eq. (2.102) is independent of both the temperature and dimensionality of the system.

[23]For the typical dimensions of the silicon resonator studied in this work, this transition temperature is approximately 100 K [192].

2.4.4 Thermal Phonon Wavelength

In order to determine the bath dimensionality introduced in the previous subsection, we assign to each of its η-polarized modes an average thermal wavelength [162]

$$\lambda_{\mathrm{th}} = \frac{2\pi\hbar c_\eta}{k_{\mathrm{B}}T}, \tag{2.103}$$

where c_η is the speed of sound associated with the given mode. Generally, we are interested in the shortest thermal wavelength of the system, corresponding to the polarization with the slowest speed of sound. If this wavelength is longer than any of the device's characteristic dimensions, the system will be considered to be dimensionally-reduced in that direction [162, 201]. For silicon, the shortest thermal phonon wavelength is given by $\lambda_{\mathrm{th}} = 2\pi\hbar c_{t_1}/k_{\mathrm{B}}T \approx 225\ \mathrm{nm}\cdot\mathrm{K}/T$, where $c_{t_1} = 4679$ m/s is the slowest speed of sound in the system associated with the t_1 transverse polarization (see Table 5.1). Therefore, the resonators considered in this thesis, which have cross-sectional dimensions on the order of 200 nm, will behave one dimensionally for temperatures $T \lesssim 1$ K.

2.4.5 Thermalization of the Mechanical Mode

In the experiments considered in this thesis, we do not externally drive the motion of our nanomechanical resonators. Instead, we observe the thermomechanically driven motion of our resonators, whereby noise from the thermal bath will enter the device via its dissipation channels according to the fluctuation-dissipation theorem [202, 203], actively thermalizing the resonator to the bath's temperature. If the resonator is initially out of thermal equilibrium with the bath at time $t = t_0$, this thermalization process will occur according to the differential equation [150, 163, 204]

$$\dot{\langle n\rangle} = -\Gamma_{\mathrm{m}}\langle n\rangle + \Gamma_{\mathrm{m}}\bar{n}_{\mathrm{th}}, \tag{2.104}$$

which has the solution

$$\langle n\rangle(t) = \langle n\rangle(t_0)e^{-\Gamma_{\mathrm{m}}(t-t_0)} + \bar{n}_{\mathrm{th}}\left(1 - e^{-\Gamma_{\mathrm{m}}(t-t_0)}\right). \tag{2.105}$$

The resonator therefore thermalizes on a timescale set by the damping rate of the mechanical system, reaching a thermal equilibrium value of $\bar{n}_{\mathrm{th}} = \bar{n}_{\mathrm{b}}(\omega_{\mathrm{m}})$ for times

$t \gg \Gamma_{\mathrm{m}}^{-1}$. Note that if the resonator is initially in its ground state ($\langle n \rangle (t_0) = 0$), it will begin to heat towards thermal equilibrium at a rate given by $\Gamma_{\mathrm{th}}^{0} = \bar{n}_{\mathrm{th}} \Gamma_{\mathrm{m}}$. Once steady state has been achieved, thermal noise continues to be input from (and subsequently lost to) the external bath, which according to Eq. (2.18) actively drives the amplitude of the mechanical resonator's motion to a root-mean-square value of [151]

$$x_{\mathrm{th}} = x_{\mathrm{zpf}} \sqrt{2\bar{n}_{\mathrm{th}} + 1}. \tag{2.106}$$

Furthermore, if we assume that the mechanical oscillations are sinusoidal on short timescales ($t \ll \Gamma_{\mathrm{m}}^{-1}$), we can define an average thermal peak-to-peak amplitude of motion as

$$A_{\mathrm{th}} = \sqrt{2} x_{\mathrm{th}} = x_{\mathrm{zpf}} \sqrt{2(2\bar{n}_{\mathrm{th}} + 1)}. \tag{2.107}$$

In the classical high-temperature limit, where the thermal bath energy $k_{\mathrm{B}}T$ is much larger than the energy of a single mechanical phonon $\hbar\omega_{\mathrm{m}}$ (see Section 2.2.5 for the low-temperature limit of Eq. (2.106)), we then find that the thermal noise of the bath drives the resonator's motion to a root-mean-square position fluctuation of

$$x_{\mathrm{th}} = \sqrt{\frac{k_{\mathrm{B}}T}{m\omega_{\mathrm{m}}^2}}, \tag{2.108}$$

or equivalently, to an average peak-to-peak amplitude of

$$A_{\mathrm{th}} = \sqrt{\frac{2k_{\mathrm{B}}T}{m\omega_{\mathrm{m}}^2}}. \tag{2.109}$$

2.5 Mechanical Dissipation

Up until this point, we have treated the dissipation of energy from our mechanical resonator in a very secular manner, quantifying these losses with the phenomenological damping rate Γ_{m} and quality factor Q_{m}. However, as nanomechanical resonators encounter a number of temperature-dependent damping mechanisms at low temperatures, we spend considerable effort in this section providing estimates for specific dissipation sources that threaten to cause energy loss in our devices. Here we will study six different physical manifestations of mechanical dissipation: phonon-phonon interactions, thermoelastic damping (TED),

two-level system (TLS) damping, scattering from point defects, gas damping, and clamping losses. Assuming each of these dissipation processes are independent, we can sum the contributions Γ_i from each, allowing us to determine the total mechanical damping rate of the system as

$$\Gamma_{\mathrm{m}} = \sum_i \Gamma_i. \tag{2.110}$$

Generally, one or two specific mechanisms will dominate this total damping rate, such that only they need to be considered.

We further introduce the mechanical dissipation (also called the loss tangent or internal friction), which is defined as the inverse of the mechanical quality factor and characterizes the the fraction of energy lost per radian of oscillation in time [200]. This quantity sums similar to the damping rate, such that it is given by the expression

$$Q_{\mathrm{m}}^{-1} = \sum_i Q_i^{-1}, \tag{2.111}$$

where $Q_i^{-1} = \Gamma_i/\omega_{\mathrm{m}}$ is the inverse of the quality factor associated with each damping mechanism. In what follows, we will focus on this damping metric, as it provides a frequency-agnostic measure of the mechanical resonator's dissipation.

For the calculations performed in this section, we will consider the fundamental in-plane flexural mode of the rectangular doubly-clamped nanobeam detailed in Section 2.3.4, as this mode emulates the studied mechanical modes of our resonator. This beam is taken to be fabricated from single-crystal silicon and is aligned lengthwise along the [011] crystal direction, with an effective Young's modulus of $\tilde{Y} = 169$ GPa [166–168] and dimensions of length $l = 10$ μm, width $w = 200$ nm, and thickness $t = 250$ nm. Using the density of silicon ($\rho = 2330$ kg/m^3), we find the resonant frequency of this mode to be $\omega_{\mathrm{m}}/2\pi = 17.5$ MHz according to Eq. (2.62), with the corresponding modeshape given by inserting $n = 1$ into Eq. (2.59). All other material parameters are taken from Table 5.1. For each of the temperature-dependent damping mechanisms below (*i.e.* everything except clamping losses), we evaluate the dissipation at $T = 10$ K and $T = 10$ mK, as these are the limiting temperature values for our experiment, save for gas damping, as it is difficult to accurately determine the pressure of the system at 10 mK. Note at

10 K we evaluate the beam as a three-dimensional structure, while at 10 mK we use the one-dimensional treatment as necessary (see Section 2.4). This relatively simple prototypical device geometry, and its associated parameters, provides an excellent approximation of the flexural modes of the curved resonator geometries studied in this thesis, while simultaneously allowing us to analytically calculate estimates of the damping rates/quality factors for each of the mechanical dissipation mechanisms discussed above.

2.5.1 Generalized Relaxation Damping

A number of the damping mechanisms we consider in this section (specifically TLS damping, phonon-phonon interactions, and TED damping) are due to the mechanical resonator being perturbed by some process, which causes the system to radiate energy as it relaxes back to equilibrium. Therefore, we will briefly consider the general mathematical framework originally introduced by Zener [205–208] for dealing with this type of relaxation dissipation mechanism in an anelastic solid before continuing on to specific processes. To describe this general relaxation damping mechanism for the flexural modes of a thin beam, Zener modified Hooke's law given in Eq. (2.25) by allowing the perturbed stresses and strains of the beam to relax back to equilibrium via their first-order time derivatives according to [149, 200, 208]

$$\sigma + \tau_\sigma \dot{\sigma} = \tilde{Y}_{\mathrm{R}}(\varepsilon + \tau_\varepsilon \dot{\varepsilon}). \tag{2.112}$$

Here τ_σ (τ_ε) sets the timescale over which the the stress (stain) exponentially relaxes back to equilibrium at constant strain (stress) after it has been perturbed, while $\tilde{Y}_R = \tilde{Y}$ is the Young's modulus of the relaxed system. Assuming harmonic solutions for the stress and strain (*i.e.* $\sigma(\mathbf{r}, t) = e^{i\omega t}\sigma(\mathbf{r})$ and $\varepsilon(\mathbf{r}, t) = e^{i\omega t}\varepsilon(\mathbf{r})$, Eq. (2.112) becomes $\sigma(\mathbf{r}) = \tilde{Y}(\omega)\varepsilon(\mathbf{r})$, where we have introduced the frequency-dependent Young's modulus as [149, 200]

$$\tilde{Y}(\omega) = \left(\frac{1+\omega^2\tau^2}{1+\omega^2\tau_\sigma^2} + \frac{i\omega\tau}{1+\omega^2\tau_\sigma^2}\Delta\tilde{Y}\right)\tilde{Y}_{\mathrm{R}}. \tag{2.113}$$

Here $\Delta\tilde{Y} = (\tilde{Y}_{\mathrm{U}} - \tilde{Y}_{\mathrm{R}})/\tilde{Y}_{\mathrm{R}}$ is the relaxation strength of the Young's modulus, $\tilde{Y}_{\mathrm{U}} = (\tau_\varepsilon/\tau_\sigma)\tilde{Y}_{\mathrm{R}}$ is the unrelaxed Young's modulus, and $\tau = \sqrt{\tau_\sigma\tau_\varepsilon}$ is the mean

relaxation time of the system. With this definition of $\tilde{Y}(\omega)$, it is easy to see that for low frequencies ($\omega \ll 1/\tau_\varepsilon, 1/\tau_\sigma$), $\tilde{Y}(\omega) \approx \tilde{Y}_\mathrm{R}$ and the system behaves according to the standard, relaxed version of Hooke's law. Meanwhile, at high frequencies ($\omega \gg 1/\tau_\varepsilon, 1/\tau_\sigma$), the system still obeys Hooke's law, albeit with a new Young's modulus $\tilde{Y}(\omega) \approx \tilde{Y}_\mathrm{U}$.

For small $\Delta\tilde{Y}$ (and therefore small damping), the dissipation of such a system can be determined as the ratio of the imaginary portion of the frequency-dependent Young's modulus given in Eq. (2.112) to its real part, for which we find [149, 200, 209]

$$Q_\mathrm{rel}^{-1} = \Delta\tilde{Y}\frac{\omega\tau}{1+\omega^2\tau^2}. \tag{2.114}$$

In this Lorentzian form, we can classify the relaxation damping into one of three regimes, corresponding to $\omega\tau \ll 1$, $\omega\tau \gg 1$, and $\omega\tau \sim 1$. In the first regime, the frequency at which the mechanical resonator oscillates is much slower than the effective relaxation rate $1/\tau$ of the system, such that the motion evolves adiabatically and little energy is dissipation. In the opposite limit, the motion of the beam occurs so fast that the system is unable to properly equilibrate, and again, damping is minimal. However, when $\omega \sim 1/\tau$, the conditions for relaxation damping are optimal, resulting in a maximum dissipation of $Q_\mathrm{max}^{-1} = \Delta\tilde{Y}/2$ at $\omega\tau = 1$.

This general relaxation damping model is very useful for describing the damping resulting from TLS, phonon-phonon interactions, and TED discussed below, as we need only calculate the relaxation strength $\Delta\tilde{Y}$ and time constant τ associated with each process and put them into Eq. (2.114) to determine its corresponding dissipation.

2.5.2 Phonon-Phonon Interactions

As an initial example of relaxation damping, we consider the dissipation in our mechanical system due to scattering of its coherent phonons off of those present within its thermally excited bath. In a perfectly harmonic crystal, phonon-phonon interactions would not be able to occur, however, anharmonic deviations from this ideal situation allow such scattering to exist. This damping mechanism can broadly be categorized into two regimes by comparing the mechanical frequency of the

system to the timescale on which the thermal phonon distribution of the bath equilibrates, given by [149]

$$\tau_{\mathrm{ph}} = \frac{3\mathcal{J}}{\bar{c}^2} = \frac{1.12\sqrt{wt}}{\bar{c}}, \tag{2.115}$$

where we have used the thermal diffusivity in the Casimir-limited Debye model given by Eq. (2.102). Note that since $\mathcal{J}$ is independent of both the temperature and dimensionality of the system in this regime, so is τ_{ph}. For the case of $\omega_{\mathrm{m}}\tau_{\mathrm{ph}} \ll 1$, known as the Akhiezer limit [210–212], the thermal phonons are able to adiabatically follow the instantaneous strain profile of the mechanical mode, which periodically modulates local temperature variations in the resonator. Dissipation then occurs when heat flows across these gradients, increasing the entropy of the system. In the opposite limit of $\omega_{\mathrm{m}}\tau_{\mathrm{ph}} \gg 1$, known as the Landau-Rumer regime [213], a quantum mechanical approach must be used to determine the phonon scattering rate by employing higher-order perturbation theory [135, 149, 171, 214]. For the beam considered in this section, we calculate $\tau_{\mathrm{ph}} = 43$ ps, such that $\omega_{\mathrm{m}}\tau_{\mathrm{ph}} = 4.8\times10^{-3} \ll 1$ and we are deeply in the Akhiezer limit. Therefore, the thermodynamic relaxation description given in Section 2.5.1 suffices to describe the dissipation in our device due to phonon-phonon interactions with the thermal bath.

Mason [215] found that for the Akhiezer effect, the relaxation strength in Eq. (2.114) can be approximated as

$$\Delta\tilde{Y}_{\mathrm{Ak}} = \frac{\tilde{\gamma}^2\mathcal{C}_V T}{\tilde{Y}}, \tag{2.116}$$

where $\tilde{\gamma}$ is the Grüneisen parameter, which characterizes the effect that changing the volume of the crystal has on its vibrational properties and is defined as [216]

$$\tilde{\gamma} = \frac{3\tilde{\alpha}B}{\mathcal{C}_V}, \tag{2.117}$$

with $\tilde{\alpha}$ and B being the linear coefficient of thermal expansion[24] and the (isothermal) bulk modulus of the solid. Inputting Eqs. (2.115) and (2.116) into Eq. (2.114), we determine the dissipation in our nanobeam due to Akhiezer phonon-phonon

[24]This parameter characterizes changes in the length of the structure with respect to temperature, as opposed to volumetric thermal expansion coefficient $\tilde{\alpha}_V = 3\tilde{\alpha}$, which is associated with changes in its volume.

interactions as

$$Q_{\mathrm{Ak}}^{-1} = \frac{\tilde{\gamma}^2 \mathcal{C}_V T}{\tilde{Y}} \frac{\omega \tau_{\mathrm{ph}}}{1 + \omega^2 \tau_{\mathrm{ph}}^2}. \tag{2.118}$$

Note that as the Grüneisen parameter is relatively constant in silicon for temperatures below 10 K [216], we find that this dissipation mechanism scales with temperature as $Q_{\mathrm{Ak}}^{-1} \sim T^4$ ($Q_{\mathrm{Ak}}^{-1} \sim T^2$) due to the cubic (linear) dependence of $\mathcal{C}_V$ on temperature (see Eq. (2.96)) between 1 K and 10 K (below 1 K) where the beam behaves as a 3D (1D) system. Using the low temperature values of the Grüneisen parameter in silicon ($\tilde{\gamma} = 0.410$ at $T = 10$ K and $\tilde{\gamma} = 0.437$ at $T = 10$ mK [216]), along with the typical beam parameters given at the beginning of this section, we find that $Q_{\mathrm{Ak}} = 3.2 \times 10^{10}$ at $T = 10$ K, with an increase in quality factor to $Q_{\mathrm{Ak}} = 8.7 \times 10^{20}$ at $T = 10$ mK.

2.5.3 Thermoelastic Damping

Elastic modes that cause local changes in the resonator's volume[25], can also generate temperature gradients within the resonator due to its non-zero coefficient of thermal expansion. Similar to the Akhiezer effect[26], heat will then irreversibly flow across these gradients, causing energy to be lost as the system relaxes towards equilibrium. This process, known as thermoelastic damping, was first studied by Zener [205–208], who used the relaxation damping formalism introduced in Section 2.5.1 to calculate the TED dissipation for the flexural modes of a thin doubly-clamped beam. This was done by approximating the thermal relaxation of the resonator as occurring solely through its fundamental mode[27], resulting in a relaxation time constant set by the average time required for a thermal phonon to diffuse across the width of the beam given by [149, 200]

$$\tau_{\mathrm{z}} = \frac{w^2}{\pi^2 \mathcal{J}} = \frac{3}{1.12 \pi^2 \bar{c}} \sqrt{\frac{w^3}{t}}. \tag{2.119}$$

[25] Therefore, this process is important for longitudinal and flexural modes, while it is negligible in torsional modes [200].

[26] While there are many similarities between the Akhiezer effect and TED, their fundamental difference arises from the fact that in the former case, the resonator interacts with a pre-existing thermal bath, while in the latter, heat is generated by the mechanical motion itself [149].

[27] This approximation proves to be quite effective as 98.6 % of the beam's thermal relaxation occurs through this fundamental mode [205–208].

As was the case for the time constant τ_{ph} associated with Akhiezer damping, τ_{z} is independent of the temperature and dimensionality of the system. Furthermore, the relaxation strength in this model is given by[28]

$$\Delta\tilde{Y}_{\text{z}} = \tilde{Y}\tilde{\alpha}^2 T/\mathcal{C}_V. \tag{2.120}$$

Inputting the quantities given in Eqs. (2.119) and (2.120) into Eq. (2.114), we find the mechanical dissipation for Zener TED as [149, 200, 209]

$$Q_{\text{z}}^{-1} = \frac{\tilde{Y}\tilde{\alpha}^2 T}{\mathcal{C}_V}\frac{\omega_{\text{m}}\tau_{\text{z}}}{1+\omega_{\text{m}}^2\tau_{\text{z}}^2}. \tag{2.121}$$

In order to gain a better understanding of the temperature dependence of this damping mechanism, we also find it useful to express this dissipation in terms of the Grüneisen parameter given in Eq. (2.117), which results in

$$Q_{\text{z}}^{-1} = \frac{\tilde{Y}\tilde{\gamma}^2\mathcal{C}_V T}{9B^2}\frac{\omega_{\text{m}}\tau_{\text{z}}}{1+\omega_{\text{m}}^2\tau_{\text{z}}^2}. \tag{2.122}$$

In this form, the temperature dependence of Q_{z}^{-1} is given by the factor $\mathcal{C}_V T$ in its numerator, and such that similar to Q_{Ak}^{-1}, it has a quartic dependence on temperature for 1 K $< T <$ 10 K and a quadratic temperature dependence for $T <$ 1 K. For our considered prototypical beam resonator, we calculate $\tau_{\text{z}} = 8.5$ ps and $\omega_{\text{m}}\tau_{\text{z}} \approx 10^{-3}$, such that our system resides deeply within the adiabatic regime described in Section 2.5.1. Inputting this time constant, as well as the low temperature thermal expansion coefficient of silicon ($\tilde{\alpha} = 8.8\times10^{-10}$ K^{-1} at $T =$ 10 K and $\tilde{\alpha} = 9.4\times10^{-19}$ K^{-1} at $T = 10$ mK[29] [216]), into Eq. (2.121) we calculate estimates for the limiting TED quality factor of our beam's the fundamental mode. Here we find that at 10 K, $Q_{\text{z}} = 5.4\times10^{11}$, while at $T = 10$ mK, this value drastically increases to $Q_{\text{z}} = 1.5\times10^{25}$ due to the rapidly diminishing values of the thermal expansion coefficient [216–219] and heat capacity (see Eq. (2.96)) in silicon at low temperatures.

While the dissipation found using Zener's relaxation formalism given by the expression in Eq. (2.121) provides an excellent approximation for thin beams

[28] In its original form, Zener used $\mathcal{C}_P$ instead of $\mathcal{C}_V$, but at low temperatures we can use these two quantities interchangeably with minimal added error [200] (see also footnote 20).

[29] The value of $\tilde{\alpha}$ at $T = 10$ mK is calculated using Eqs. (2.97) and (2.117), as well as the fact that B is relatively temperature-independent below 40 K [216].

with large thermal diffusivity, Lifshitz and Roukes [200] showed that by using Euler-Bernoulli beam theory (see Section 2.3.4), an exact expression for the TED dissipation in flexural modes of doubly-clamped beams can be found as

$$Q_{\mathrm{TED}}^{-1} = \frac{\tilde{Y}\tilde{\alpha}^2 T}{\mathcal{C}_V}\frac{6}{\tilde{\xi}}\left(1 - \frac{1}{\tilde{\xi}}\frac{\sinh\tilde{\xi} + \sin\tilde{\xi}}{\cosh\tilde{\xi} + \cos\tilde{\xi}}\right), \tag{2.123}$$

where $\tilde{\xi}$ is the dimensionless parameter

$$\tilde{\xi} = w\sqrt{\frac{\omega_{\mathrm{m}}}{2\mathcal{J}}} = \pi\sqrt{\frac{\tau_{\mathrm{z}}\omega_{\mathrm{m}}}{2}}. \tag{2.124}$$

Using this exact equation, we calculate the TED-limited quality factor of our system to be $Q_{\mathrm{TED}} = 5.4 \times 10^{11}$ at $T = 10$ K and $Q_{\mathrm{TED}} = 1.5 \times 10^{25}$ at $T = 10$ mK. Therefore, for the thin beam geometry considered here, the relaxation method (Eq. (2.121)) very accurately describes the TED dissipation of the system, with only a few percent error relative to the exact expression given in Eq. (2.123).

2.5.4 Two-Level System Damping

The final relaxation damping process that we consider in this section is that due to interaction between the mechanical motion and TLS defects located within the resonator's material. In this situation, strain variations throughout the resonator perturb the local environment of the TLS, forcing them out of thermal equilibrium. Via their subsequent relaxation process, the TLS interact with the low frequency modes of the mechanical resonator, causing it to dissipate energy.

As our devices are expected to behave one-dimensionally for $T \lesssim 1$ K, here we consider TLS damping in a 1D system[30]. In this situation, TLS with an asymmetry energy E_Δ and a tunneling energy E_0 relax at a rate (see Eq. (6.40) in Section 6.2.5)

$$\tau_{\mathrm{TLS}}^{-1} = \frac{\gamma^2}{\mathcal{A}\rho c_{\mathrm{e}}^3\hbar^2}\frac{E_0^2}{E}\coth\left(\frac{E}{2k_{\mathrm{B}}T}\right), \tag{2.125}$$

where $E = \sqrt{E_\Delta^2 + E_0}$, $\mathcal{A} = wt$ is the cross-sectional area of the beam, γ is the TLS-phonon coupling constant (or deformation potential), and $c_{\mathrm{e}} = \bar{c}/\sqrt[3]{3}$ ($c_{\mathrm{e}} =$

[30] As mentioned in Section 6.2, this assumption is justified for $T \gtrsim 1$ K by the fact that at high temperatures the dissipation plateaus to a dimensionally-independent constant [162].

3965 m/s in silicon). Furthermore, we find in Section 6.2 that the relaxation strength for a given TLS can be determined as

$$\Delta\tilde{Y}_{\mathrm{TLS}} = \frac{\gamma^2}{\rho c_k^2 k_{\mathrm{B}} T}\left(\frac{E_\Delta}{E}\right)^2 \mathrm{sech}^2\left(\frac{E}{2k_{\mathrm{B}}T}\right), \tag{2.126}$$

where $c_k = \left(3\sum_\eta \frac{e_{k\eta}}{c_\eta^2}\right)^{-1/2}$ is a mode-dependent effective speed of sound. In order to determine the dissipation due to an entire ensemble of TLS, which will in general have varying E_Δ and E_0, we integrate over the TLS density of states $\mathcal{P}(E_\Delta, E_0)$ to find

$$Q_{\mathrm{TLS}}^{-1} = \frac{\gamma^2}{\rho c_k^2 k_{\mathrm{B}} T}\int_0^\infty\int_0^\infty \left(\frac{E_\Delta}{E}\right)^2 \mathrm{sech}^2\left(\frac{E}{2k_{\mathrm{B}}T}\right)\frac{\omega_{\mathrm{m}}\tau_{\mathrm{TLS}}}{1+\omega_{\mathrm{m}}^2\tau_{\mathrm{TLS}}^2}\mathcal{P}(E_\Delta, E_0)dE_\Delta dE_0. \tag{2.127}$$

Therefore, the TLS DOS $\mathcal{P}(E_\Delta, E_0)$ has a significant influence on the behaviour of the TLS damping. Here we focus on amorphous TLS ensembles[31], whereby the TLS DOS is modelled as $\mathcal{P}_{\mathrm{a}}(E_\Delta, E_0) = \mathcal{P}_0/E_0$, where $\mathcal{P}_0$ is a constant that characterizes the amorphous nature of the TLS ensemble [220–223]. To estimate the dissipation in our prototypical beam resonator resulting from coupling to an ensemble of amorphous TLS, we input this DOS into Eq. (2.127), while using the average values of $\mathcal{P}_0 = 3.8\times10^{44}$ J^{-1}m^{-3} and $\gamma = 1.25$ eV for the two middle frequency mechanical modes of our device found in Table 6.4. Furthermore, we use the strain energy fractions of $e_l = 0.397$, $e_{t_1} = 0.238$, and $e_{t_2} = 0.365$ calculated using Eqs. (2.67)–(2.69) to determine $c_k = 10689$ m/s for the fundamental in-plane flexural mode of the beam. In doing so we find that $Q_{\mathrm{TLS}} = 2.4\times10^4$ at 10 K, while $Q_{\mathrm{TLS}} = 1.7\times10^7$ at 10 mK, in good agreement with our findings in Chapter 6.

2.5.5 Scattering from Point Defects

Along with the TLS dissipation discussed in the previous subsection, resonant mechanical phonons can also scatter off of point defects located within the device's material. For a monatomic crystal, the leading candidates for point defects are generally caused by isotopic variation of the considered element, substitutional

[31] See Appendix G for treatment of TLS defects in a crystalline matrix.

impurity (or dopant) atoms, or vacancies (also known as Schottky defects [189]). Here we will use the theory of phonon scattering to determine the damping rate and quality factors associated with general point defects, and then apply this theory to our silicon beam for each of these three specific cases.

To treat phonon scattering from an ensemble of point defects, we use a perturbation approach similar to what was initially developed by Pomeranchuk [224] and Klemens [225, 226] to model the effect of mass fluctuations on the thermal conductivity of solids. Here, we consider the situation where the atoms at a number of lattice sites within the crystal are replaced by some substance (or vacancy) that will in general cause mass variations throughout the solid. Acoustic loss will then occur when phonons scatter elastically off these sites, transitioning from an initial momentum state coherent with the mechanical oscillations to an equal energy state located within the resonator's incoherent thermal phonon bath. Assuming that these phonons have wavelengths that are much larger than the atomic spacing, they will sample multiple lattice points within the solid, leading to an average mass of

$$\bar{M} = \sum_j \tilde{f}_j M_j, \tag{2.128}$$

where M_j are the masses of the atom (or lack thereof) at each lattice point, with the associated fractional abundances of $\tilde{f}_j$ [227, 228]. In most solids, this expression is dominated by isotopic variance, such that $\bar{M}$ is simply the average atomic mass of the considered element. We further assume that these mass variations are randomly distributed and affect only the kinetic energy of the crystal, leaving its potential energy unperturbed. These assumptions prove to be an excellent approximation for isotopic variation and vacancies in the crystal (provided we use a simple trick for the latter case which will be detailed below), however, they are less effective for substitutional impurities where chemical changes in the crystal's structure have a larger effect on its interaction potential [149]. Nonetheless, we proceed by applying these mass variations as a perturbation to the crystal Hamiltonian, using Fermi's Golden Rule to determine the phonon scattering rate, or equivalently, the mechanical damping rate as [149, 227, 228]

$$\Gamma_{\mathrm{pd}} = \frac{\pi V_{\mathrm{a}} \Omega}{6} \frac{\omega_{\mathrm{m}}^2 \varrho_D(\omega_{\mathrm{m}})}{1 - e^{-\hbar\omega_{\mathrm{m}}/k_{\mathrm{B}}T}}, \tag{2.129}$$

where V_{a} is the atomic volume of the solid (*i.e.* the reciprocal of its atomic density). Furthermore, we have introduced the mass fluctuation factor

$$\Omega = \sum_j \tilde{f}_j \left(\frac{\Delta M_j}{\bar{M}} \right)^2 , \tag{2.130}$$

which accounts for the concentrations and mass variations of the impurities, where $\Delta M_j = \bar{M} - M_j$ is the mass difference between each scatterer and the average mass of the solid $\bar{M}$ [227, 228]. Note that the temperature dependence of the damping rate given in Eq. (2.129) is due to the Bose-Einstein distribution of the phonon bath [149]. From this damping rate, we can also determine the mechanical dissipation as

$$Q_{\mathrm{pd}}^{-1} = \frac{\Gamma_{\mathrm{pd}}}{\omega_{\mathrm{m}}} = \frac{\pi V_{\mathrm{a}} \Omega}{6} \frac{\omega_{\mathrm{m}} \varrho_D(\omega_{\mathrm{m}})}{1 - e^{-\hbar\omega_{\mathrm{m}}/k_{\mathrm{B}}T}}. \tag{2.131}$$

Inputting the three-dimensional Debye density of states of the resonator's bath given by Eq. (2.87) into Eq. (2.131), we determine the three-dimensional mechanical dissipation due to point defect scattering as

$$Q_{\mathrm{pd},3}^{-1} = \frac{V_{\mathrm{a}} \Omega}{4\pi \bar{c}^3} \frac{\omega_{\mathrm{m}}^3}{1 - e^{-\hbar\omega_{\mathrm{m}}/k_{\mathrm{B}}T}}. \tag{2.132}$$

We also find it informative to calculate the low- and high-temperature limits of this dissipation, which are given by

$$Q_{\mathrm{pd},3}^{-1} = \frac{V_{\mathrm{a}} \Omega}{4\pi \bar{c}^3} \omega_{\mathrm{m}}^3 \qquad (k_{\mathrm{B}}T \ll \hbar\omega_{\mathrm{m}}), \tag{2.133}$$

$$Q_{\mathrm{pd},3}^{-1} = \frac{V_{\mathrm{a}} \Omega}{4\pi \bar{c}^3} \frac{k_{\mathrm{B}}T}{\hbar} \omega_{\mathrm{m}}^2 \qquad (k_{\mathrm{B}}T \gg \hbar\omega_{\mathrm{m}}). \tag{2.134}$$

Therefore, $Q_{\mathrm{pd},3}^{-1}$ ($\Gamma_{\mathrm{pd},3}$) exhibits a temperature-independent plateau at low temperatures that is cubic (quartic) in mechanical frequency, while at high-temperatures a linear temperature dependence and a quadratic (cubic) frequency dependence is observed in the mechanical dissipation (damping rate).

As we are considering narrow mechanical resonator beams at cryogenic temperatures, we are interested in how the behaviour of this damping mechanism changes once the average thermal wavelength of the phonon bath becomes large enough that we deem the system one-dimensional. In this case, we must instead use the one-dimensional Debye density of states given by Eq. (2.85) to determine the dissipation due to point defect scattering as

$$Q_{\mathrm{pd},1}^{-1} = \frac{l_{\mathrm{a}} \Omega}{6\bar{c}} \frac{\omega_{\mathrm{m}}}{1 - e^{-\hbar\omega_{\mathrm{m}}/k_{\mathrm{B}}T}}, \tag{2.135}$$

where we have replaced the atomic volume with the atomic length $l_\mathrm{a} = V_\mathrm{a}/\mathcal{A}$ (*i.e.* the inverse of the linear atomic density of the beam). As we did in the three-dimensional case, we also present the low- and high-temperature limits of Eq. (2.135) as

$$Q_{\mathrm{pd},1}^{-1} = \frac{l_\mathrm{a}\Omega}{6\bar{c}}\omega_\mathrm{m} \qquad (k_\mathrm{B}T \ll \hbar\omega_\mathrm{m}), \tag{2.136}$$

$$Q_{\mathrm{pd},1}^{-1} = \frac{l_\mathrm{a}\Omega}{6\bar{c}}\frac{k_\mathrm{B}T}{\hbar} \qquad (k_\mathrm{B}T \gg \hbar\omega_\mathrm{m}). \tag{2.137}$$

Similar to the three-dimensional case, $Q_{\mathrm{pd},1}^{-1}$ ($\Gamma_{\mathrm{pd,1D}}$) plateaus to a temperature-independent value at low temperature, while demonstrating a linear temperature dependence for high T. However, this one-dimensional mechanical dissipation (damping rate) exhibits a much weaker frequency dependence than its three-dimensional counterpart, being linear (quadratic) in frequency for low temperatures and completely frequency independent at high temperatures. Note that for the mechanical frequencies considered in this work ($\omega_\mathrm{m}/2\pi \sim 10$ MHz), the high-temperature limits given by Eqs. (2.134) and (2.137) are the relevant expressions for point defect scattering, as the low-temperature regime ($T \lesssim 1$ mK) is inaccessible with our current experimental setup.

It is also interesting to compare the ratio between the quality factors for point defect scattering in the three- and one-dimensional cases, for which we find

$$\frac{Q_{\mathrm{pd},3}}{Q_{\mathrm{pd},1}} = \frac{4\pi\bar{c}^2}{6\mathcal{A}\omega_\mathrm{m}^2}. \tag{2.138}$$

Here both the mass fluctuation factor and the Boltzmann factor cancel, such that this relation is independent of temperature and the specific point defect being considered. Inputting the values for our silicon beam, we find $Q_{\mathrm{pd},3}/Q_{\mathrm{pd},1} \sim 10^5$, indicating that at a given temperature, the quality factor for the 3D case will be approximately five orders magnitude larger than in the 1D case due to their differing density of states. As we shall see below, this will cause the counterintuitive result that point defect scattering losses will be weaker at 10 K compared to those at 10 mK, as we cross the boundary from a 3D system to a 1D system between these two temperatures, such that we must use Eq. (2.134) in the former case, while we use Eq. (2.137) in the latter.

With this general theory describing mechanical dissipation due to phonon scattering off of point defects, we can now investigate how this damping effect manifests in mechanical resonators for different species of defects. Note that aside from the cross-sectional area required to determine l_a in the one-dimensional case, the dissipation of this kind is not directly dependent on the geometry of the structure being considered. Therefore, Eqs. (2.129)–(2.138) hold for any geometry with a uniform cross-section, provided one knows the resonant frequency of the mechanical resonator and the speeds of sound in its material. However, in what follows, we continue to consider our prototypical silicon beam in order to allow for comparison with the other dissipation mechanisms considered in this section.

Isotopic Variations

We begin by considering phonon scattering from mass deviations due to the naturally occurring isotopes of silicon. Using the fractional abundances and the atomic masses of natural silicon given in Table 2.2, we calculate an average atomic mass of $\bar{M}_{\mathrm{Si}} = 28.086$ amu and a fluctuation factor of $\Omega_{\mathrm{nat}} = 2 \times 10^{-4}$ [229, 230] according to Eqs. (2.128) and (2.130), respectively. Using the lattice constant of silicon ($\tilde{a}_0 = 5.43$ Å [186]), we determine its atomic volume as $V_a = \tilde{a}_0^3/8 = 2.0 \times 10^{-29}$ m^3, where the division by a factor of 8 occurs because silicon has a diamond crystal structure, and therefore, 8 atoms per unit cell. Inputting these values, as well as $\bar{c} = 5718$ m/s (see Section 2.4.2) into Eqs. (2.132) and (2.135), we then find $Q_{\mathrm{nat}} = 4.0 \times 10^{16}$ at $T = 10$ K and $Q_{\mathrm{nat}} = 3.4 \times 10^{14}$ for $T = 10$ mK in naturally occurring silicon. While the quality factor at $T = 10$ mK is lower than that at 10 K, it will improve as we move to lower temperatures, until it reaches the temperature independent limit of $Q_{\mathrm{nat}} = 4.2 \times 10^{15} \sim 10^{15}$ at $T \ll 1$ mK for the beam considered here.

We note that the calculations performed here are for the isotopic abundances in naturally occurring silicon and could be improved by using isotopically purified silicon. Using the isotopic abundances for the state-of-the-art isotopically enriched silicon [231] from the Avogadro project [232, 233] (see Table 2.2), we find that the mass fluctuation parameter can be improved by nearly four orders of magnitude to $\Omega_{\mathrm{iso}} = 1 \times 10^{-8}$ [231], resulting in a commensurate increase in the quality factors

to $Q_{\text{iso}} = 7.2 \times 10^{20}$ at $T = 10$ K and $Q_{\text{iso}} = 6.1 \times 10^{18}$ at $T = 10$ mK.

Isotope	Natural $\tilde{f}_j$ (%)	Purified $\tilde{f}_j$ (%)	Isotopic Mass M_j (amu)
^{28}Si	92.223	99.9993	27.9769
^{29}Si	4.686	6.583×10^{-6}	28.9764
^{30}Si	3.092	0.378×10^{-6}	29.9738

Table 2.2: Fractional abundances $\tilde{f}_j$ and isotopic masses M_j of ^{28}Si, ^{29}Si, and ^{30}Si for both naturally occurring and state-of-the-art isotopically purified silicon. Values for naturally occurring silicon (first column) are from Ref. [186], while the isotopically purified values (second column) are from Ref. [231].

Substitutional Impurities

Point defects in solids can also manifest as substitutional impurities, whereby atoms in the crystal lattice are replaced by a completely different species. This is especially true for n- and p-doped silicon samples, as these dopant atoms enter the system as substitutional impurities. We would, however, like to point out a few caveats to treating substitutional impurities as point defects using this simple scattering model. First off, this model does not consider the effects that these impurities would have on the interaction potential of the crystal [149]. Nor does it include potential electron-phonon interactions resulting from the free charges introduced by these dopants [149, 234], though for insulators and semiconductors at low temperatures, this effect would be very small as very few electrons are promoted to the conduction band. Finally, this simple treatment does not consider the fact that these impurities may exist in multiple configurational states, allowing them to act as tunneling systems, resulting in damping mechanisms similar to the TLS damping outlined in Section 2.5.4 and Section 6.2[32]. Nonetheless, if we assume these other effects are small or accounted for elsewhere, the simple mass variation model used here can be used to provide an estimate of the mechanical damping caused by substitutional impurities [234].

Here, we focus on p-type, boron-doped silicon with a dopant density of $\sim 10^{21}$ m^{-3} as this is the material used to fabricate the devices studied in Chapters 6 and

[32]In fact, we cannot definitively rule out the possibility of boron dopants being the cause of the TLS damping observed in Chapter 6.

7. From this dopant density, we can find the fractional abundance of boron dopants in the silicon as $\tilde{f}_{\mathrm{B}} \sim 10^{21}\ \mathrm{m}^{-3} \times V_{\mathrm{a}} = 2 \times 10^{-8}$, which along with the average atomic mass of boron ($\bar{M}_{\mathrm{B}} = 10.81$ amu [186]), can be used to determine the mass deviation factor of these dopants as $\Omega_{\mathrm{B}} = 8 \times 10^{-9}$. Using these values we calculate $Q_{\mathrm{B}} = 9.8 \times 10^{20}$ at 10 K and $Q_{\mathrm{B}} = 8.3 \times 10^{18}$ at 10 mK for scattering off of boron dopants in our prototypical beam resonator. Therefore, phonon scattering from these dopants is approximately five orders of magnitude smaller than that from isotopic variations, and is negligible in comparison.

Vacancies

The last point defect that we consider in this subsection are vacancies (or Schottky defects) where an atom has been completely removed from the crystal lattice, leaving behind a hole in its absence. A naive treatment of this point defect might lead one to think that by removing the mass of the atom, we arrive at the incorrect assumption that $\Delta M_{\mathrm{vac}} = \bar{M}$. However, one must realize that in order to remove the atom completely, bonds with neighbouring atoms must also be broken, leading to perturbations in the potential energy portion of the Hamiltonian. Fortunately, using the virial theorem (which states that the total kinetic and potential energies of the crystal are equal), as well as the fact that every linkage is shared by two atoms, we find that the lost potential energy due to the creation of a vacancy is equivalent to a change in the mass of $\Delta M = 2\bar{M}$ [235]. Therefore, including the perturbations to both the kinetic (due to the lost mass) and potential energies, we take $\Delta M_{\mathrm{vac}}/\bar{M} = 3$ for vacancies.

As for the concentrations of vacancies in a solid, the fractional abundances are determined by the Arrhenius equation

$$\tilde{f}_{\mathrm{vac}} = e^{-E_{\mathrm{vac}}/k_{\mathrm{B}}T}, \tag{2.139}$$

where E_{vac} is the enthalpy of formation for a vacancy [236]. This Arrhenius law therefore adds additional temperature dependence to the mechanical dissipation. In silicon, however, $E_{\mathrm{vac}} = 3.15$ eV [236, 237], such that even at $T = 10$ K, $\tilde{f}_{\mathrm{vac}}$ is vanishingly small. However, a finite number of vacancies still exist at low temperatures due to the limited mobility of these defects. Therefore, we make

a very conservative estimate of the number of vacancies at low temperature by taking the highest possible concentration (*i.e.* the concentration at the melting point of silicon) of $\sim 10^{21}$ m^3 [238]. Using this value, along with $\Delta M_{\text{vac}}/\bar{M} = 3$, we calculate a mass fluctuation factor of $\Omega_{\text{vac}} = 2 \times 10^{-7}$, leading to quality factors of $Q_{\text{vac}} = 4.1 \times 10^{19}$ at $T = 10$ K and $Q_{\text{vac}} = 3.5 \times 10^{17}$ at 10 mK. Therefore, as with the boron dopants, we find that phonon scattering from vacancies produces limiting quality factors that are far larger than those for isotopic variation. This is especially true considering that our calculations use very conservative vacancy concentrations, which would likely result in actual limiting quality factors that are much higher at low temperatures where the vacancy concentration would be smaller.

2.5.6 Gas Damping

Another source of damping in mechanical resonators is energy loss to the surrounding medium, often a fluid or a rarefied gas, which becomes increasingly important for nanoscale devices with large surface area to volume ratios [153]. Such an interaction is characterized by the Knudsen number, which for in-plane flexural modes is given by [239–242]

$$\text{Kn} = \frac{\Lambda_{\text{g}}}{t}, \tag{2.140}$$

where Λ_{g} is the mean free path of the surrounding gas calculated using the kinetic theory as [239, 242]

$$\Lambda_{\text{g}} = \frac{k_{\text{B}} T}{\sqrt{2}\pi d_{\text{g}} P}, \tag{2.141}$$

with d_{g} being the effective hard sphere diameter (also known as the kinetic diameter) of the gas molecules that exert a pressure P on the system. The value of the Knudsen number demarcates three separate regimes of gas behaviour [239–243]. For Kn < 0.01 (known as the continuum flow regime), the interactions of the gas molecules amongst themselves are non-negligible, such that the gas must be considered as a viscous fluid. When Kn > 10, however, the characteristic dimensions of the mechanical resonator are much smaller than the mean free path of the gas molecules and we enter into the free molecular flow (FMF) or Knudsen regime where the gas molecules can be treated as non-interacting particles. For intermediate

values of Kn, the system exists in either the slip flow ($0.01 < \mathrm{Kn} < 0.1$) or transition flow ($0.1 < \mathrm{Kn} < 10$) regime, where neither the continuum nor FMF treatment provide an accurate description of the gas behaviour.

At liquid helium temperatures, any residual air molecules will be frozen to the surfaces of the fridge with a vanishingly small vapour pressure and will therefore not contribute to gas damping at low temperatures. However, we often introduce a small amount of helium exchange gas to help thermalize our devices to the liquid helium bath of the fridge. In Section 5.4.5 below, we estimate the pressure of this helium exchange gas added to the vacuum can of the fridge to be on the order of $P \sim 10^{-1}$ Pa at 10 K. Using this pressure, along with $d_\mathrm{g} = 0.26$ nm for helium [244], we calculate $\Lambda_\mathrm{g} = 3.0$ cm and $\mathrm{Kn} = 1.2 \times 10^4$ for the exchange gas molecules surrounding the device, indicating that this system resides deeply within the FMF regime. We can therefore safely ignored viscous gas damping [240, 245], in favour of energy loss to the surrounding gas due to collisions between individual molecules and the resonator. This leads to gas-damping dissipation given by [153, 240, 242, 245–247]

$$Q_\mathrm{fmf}^{-1} = \frac{4P}{\rho w \omega_\mathrm{m}} \sqrt{\frac{2M_\mathrm{g}}{\pi \mathcal{R} T}}, \tag{2.142}$$

where $\mathcal{R}$ is the ideal gas constant and M_g is the molar mas of the gas (taken to be $M_\mathrm{g} = 4.003$ g/mol for the helium molecules considered here [186]). From Eq. (2.142), we see that Q_fmf is inversely proportional to P, as decreasing the pressure of the gas results in a decrease in the its collision rate with the resonator, and hence, a reduction in mechanical energy loss. Note that it also seems like Q_fmf decreases with decreasing temperature, as this reduces the average speed of the gas molecules, and therefore, their collision rate with the resonator. However, in the regime where the ideal gas law still holds, $P \sim T$ such that $Q_\mathrm{fmf} \sim 1/\sqrt{T}$, although this trend cannot continue indefinitely, and will indeed break down once the temperature is low enough that the gas begin to condense into a liquid or solid. Using Eq. (2.142), we find that $Q_\mathrm{fmf} = 1.5 \times 10^7$ at 10 K and $Q_\mathrm{fmf} = 4.7 \times 10^8$ at 10 mK for the fundamental in-plane flexural mode of the prototypical silicon beam considered here.

It was pointed out by Bao *et al*. [153, 246], however, that Eq. (2.142) considers an

isolated mechanical resonator and does not include effects caused by the proximity of another object such as a substrate, or in our case, an optical disk resonator. Here an additional damping process known as squeeze-film damping [241, 243] emerges, which in the FMF regime manifests as gas molecules becoming trapped within the gap region, thus colliding with the resonator multiple times. Note that if the thickness of the device t is smaller than the gap separation d_{sq}, the Knudsen number is redefined as $\mathrm{Kn} = \Lambda_{\mathrm{g}}/d_{\mathrm{sq}}$ [153, 243, 246]. For the situation where the length of this "squeezed" region l_{sq} is much larger d_{sq}, Bao showed that the quality factor given by Eq. (2.142) is reduced by a factor of $16\pi(d_{\mathrm{sq}}/l_{\mathrm{sq}})$ leading to [153, 242, 246]

$$Q_{\mathrm{sq}}^{-1} = \frac{1}{16\pi}\left(\frac{l_{\mathrm{sq}}}{d_{\mathrm{sq}}}\right) Q_{\mathrm{fmf}}^{-1} = \frac{P}{(2\pi)^{3/2}\rho w \omega_{\mathrm{m}}}\left(\frac{l_{\mathrm{sq}}}{d_{\mathrm{sq}}}\right)\sqrt{\frac{2M_{\mathrm{g}}}{\pi\mathcal{R}T}}. \tag{2.143}$$

To match the experimental conditions of our system[33], we take $d_{\mathrm{sq}} = 80$ nm and $l_{\mathrm{sq}} = l = 10$ μm (*i.e.* the squeezed region is over the entire length of our prototypical beam resonator), resulting in gas-damping-limited quality factors that are approximately halved to $Q_{\mathrm{sq}} = 6.0 \times 10^6$ at 10 K and $Q_{\mathrm{sq}} = 1.9 \times 10^8$ at 10 mK.

2.5.7 Support Losses

The final mechanical dissipation mechanism that we consider in this section are losses that originate from the forces and torques exerted on the resonator's supports as it oscillates, which can act to excite phononic modes that radiate into the substrate, carrying energy away from the system. This dissipation mechanism, known as support or clamping losses, strongly depends on both the geometry of the considered device, as well as the dimensionality of the support structure. Here, we consider the support structures consisting of either a two-dimensional infinite thin plate or a three-dimensional infinite half-space, as both of these geometries are relevant to our devices.

For the case of a rectangular beam attached to a two-dimensional thin plate support, it was determined that the dissipation of the resonator's flexural modes scales as $(w/l)^3$ [248–250]. This dimensional scaling can be interpreted as follows:

[33]Here we d_{sq} is given by the gap distance between the optical microdisk and mechanical resonator described in Section 6.3.1.

as the beam's length increases, so does it's stored energy [250–252], while a decrease in the beams width causes a larger acoustic impedance mismatch between the beam and the substrate [249]. Therefore, the longer and narrower a beam is, the smaller (larger) its dissipation (limited quality factor) associated with clamping losses. Surprisingly, the prefactor to this scaling depends only on the Poisson ratio of the support structure (and weakly at that), and was calculated by Hao *et al.* [250] for silicon supports ($\nu = 0.28$), resulting in a clamping loss dissipation of the form

$$Q_{\mathrm{s,2D}}^{-1} = 1.57 \left(\frac{w}{l}\right)^3. \tag{2.144}$$

For the beam parameters considered in this section ($w = 200$ nm, $t = 250$ nm, $l = 10$ μm), we find that $Q_{\mathrm{s,2D}} = 8.0 \times 10^4$.

If we instead consider an support comprised of a three-dimensional half-space, the impedance mismatch between the beam and its surrounds becomes even larger, resulting in a dissipation that scales as tw^4/l^5 [251–253]. As with the 2D case, the prefactor depends weakly on the support's Poisson ratio, which Judge *et al.* [252] calculated for silicon-like supports ($\nu \approx 0.25 - 0.30$), allowing them to determine the dissipation due to three-dimensional support losses as

$$Q_{\mathrm{s,3D}}^{-1} = 0.3 \frac{t}{l} \left(\frac{w}{l}\right)^4. \tag{2.145}$$

Note that this scaling indicates that for a long, thin beam, support losses will always be smaller in 3D than in 2D, with the ratio between the quality factors in these two cases scaling as

$$\frac{Q_{\mathrm{s,3D}}}{Q_{\mathrm{s,2D}}} \sim \frac{l^2}{wt}, \tag{2.146}$$

where the proportionality of this ratio is on the order of unity. For our prototypical nanobeam parameters, we calculate $l^2/wt = 2000$, which is consistent with the calculated 3D support loss quality factor $Q_{\mathrm{s,3D}} = 8.3 \times 10^8$ being approximated four orders of magnitude larger than $Q_{\mathrm{s,2D}}$.

For the devices studied in this theses, we expect support losses to be somewhere in between these two limiting quality factors (likely closer to the 2D case), as their support structure consists of a suspended device layer connected to a monolithic oxide/silicon handle. We further point out that since the dissipation in each case

depends strongly on the dimensions of the considered resonator, this damping mechanism can vary substantially from device to device. Finally, we note that this damping mechanism can be mitigated by employing phononic crystal radiation shields [67, 135, 254, 255] or soft-clamping techniques [256, 257] to prevent phonon radiation from a mechanical resonator, though these structures prove to be prohibitively large for our considered mechanical resonators.

2.5.8 Summary

In this section, we have considered a number of different mechanical dissipation mechanism for the in-plane flexural mode of a rectangular nanobeam resonator. In Table 2.3, we summarize these results, indicating the limiting quality factors calculated for each of the considered processes. Upon inspection of this table, some trends immediately become obvious. First, the limiting quality factors increase as we go to lower temperature (or stay constant in the case of the temperature-independent support losses), except in the case of scattering from point defects, where there is a decrease in Q from 10 K to 10 mK. This is due to the enhancement of this dissipation mechanism for $T < 1$ K where the beam behaves one-dimensionally. Furthermore, by comparing each of these results with one another, we find that at the low temperatures and pressures associated with our cryogenic environment, mechanical dissipation due to TED, scattering from point defects, gas damping, and phonon-phonon interactions are all negligible. The damping in our resonators is therefore limited by TLS interactions at 10 K and clamping losses at 10 mK, which as we shall see below, is consistent with the conclusion reached in Chapter 6.

We conclude this section by noting that while our devices are currently limited by TLS interactions and clamping losses, if we could mitigate these sources of dissipation[34], it may be possible to approach the regime where scattering from point defects becomes a limiting factor. In fact, recent measurements of breathing modes in one-dimensional silicon nanobeams have reported quality factors as high as $Q_{\mathrm{m}} = 5 \times 10^{10}$ [135] and are therefore rapidly approaching this limit, especially considering these resonators operate at GHz frequencies where point

[34]See Chapter 9 below for a discussion of potential methods that could be used to reduce these damping mechanisms.

Damping Mechanism		$T = 10$ K	$T = 10$ mK
Phonon-Phonon Interactions	Q_{Ak}	10^{10}	10^{21}
Thermoelastic Damping	Q_{z}	10^{11}	10^{25}
	Q_{TED}	10^{11}	10^{25}
Two-Level System Damping	Q_{TLS}	10^{4}	10^{7}
Scattering from Point Defects	Q_{iso}	10^{16}	10^{14}
	Q_{B}	10^{21}	10^{19}
	Q_{vac}	10^{19}	10^{17}
Gas Damping	Q_{fmf}	10^{7}	10^{8}
	Q_{sq}	10^{6}	10^{7}
Support Losses	$Q_{\mathrm{s,2D}}$	10^{5}	10^{5}
	$Q_{\mathrm{s,3D}}$	10^{9}	10^{9}

Table 2.3: Summary of the order of magnitude estimates for the limits on the mechanical quality factors calculated throughout this section for the in-plane flexural mode of a nanomechanical silicon beam. The considered dissipation mechanisms and their associated quality factors are: Akhiezer phonon-phonon interactions Q_{Ak}, TED in the Zener approximation Q_{z} and the exact result Q_{TED}, TLS damping Q_{TLS}, scattering from point defects due to isotopic variations Q_{iso}, boron dopants Q_{B}, and lattice vacancies Q_{vac}, gas damping in the FMF Q_{fmf} and squeeze film Q_{sq} regimes, and losses to two-dimensional $Q_{\mathrm{s,2D}}$ and three-dimensional supports $Q_{\mathrm{s,3D}}$.

defect scattering is more pronounced. In this regime, one would then need to consider using isotopically purified and/or high-resistivity (low-dopant) silicon in order to reduce this emerging dissipation mechanism.

2.6 Conclusion

In this chapter, we have presented a thorough discussion of the behaviour of our mechanical resonator. Using a simple separation of variables approach, we described the motion of our mechanical in terms of a time-varying amplitude and spatially varying modeshape, allowing us to characterize the degree to which the resonator participates in the motion via its effective mass. Treating the time-dependence of the mechanical resonator as a damping harmonic oscillator, we then introduced the device's damping rate and quality factor, providing a metric that could be used to describe its dissipation. We then moved on from a classical description of our resonator's motion, demonstrating how the motion can be quantized into individual phonons. Continuing on, we introduced the theory of elasticity, which allowed us

to characterize the stress and strain profiles of the mechanical motion through the effective strain volume and strain energy fractions, while also determining a differential equation for the mechanical modeshape. We then described the properties of the thermal bath to which the mechanical resonator couples, showing how this interaction acts to thermalize the mechanical motion to a steady state amplitude by injecting incoherent noise into the system. With the description of our bath laid out, we tackled the various damping mechanism that occur in nanomechanical resonators at low temperatures. After providing a brief introduction to relaxation damping, we discussed damping due to phonon-phonon interactions, thermoelastic damping, two-level system damping, scattering from points defects, gas damping, and support losses. Reflecting back upon the estimates calculated for each of these damping mechanisms, we concluded that most were negligible for the considered cryogenic conditions, with dissipation being dominated by TLS damping at relatively high temperatures ($T \sim 10$ K), while at low temperatures ($T \sim 10$ mK) dissipation in our system should stem from losses into the resonators support structure, in agreement with our measurements in Chapter 6 below.

Chapter 3

Optical Cavities

3.1 Introduction

In this chapter, we introduce the general theoretical framework used to describe optical cavities and apply it to our own microdisk resonators. We begin in Section 3.2, where we use Maxwell's equations to determine a separable solution and wave equation for the electromagnetic modes of a source-free dielectric cavity, which we use to define the optical mode volume of the system. We then quantize these electromagnetic fields as we did for the mechanical motion in the previous chapter, expressing them in terms of the photon ladder operators of the optical cavity, whose classical time-evolution we model using a damped harmonic oscillator approach. In Section 3.3, we apply this formalism to the specific case of optical microdisk cavities, allowing us to calculate the effective index of refraction and resonant wavelengths for the electromagnetic modes of this system. Finally, in Section 3.4 we quantify the optical losses for a number of prevalent damping processes present in our microdisk cavities, identifying surface absorption as the limiting dissipation mechanism.

3.2 Cavity Electromagnetic Field

3.2.1 Electromagnetic Wave Equation

In order to fully understand how an optical cavity couples to the mechanical element of an optomechanical device, we must first characterize its electric $\mathbf{E}(\mathbf{r}, t)$ and magnetic $\mathbf{B}(\mathbf{r}, t)$ fields. This is done using Maxwell's equations for a source-free

dielectric (*i.e.* no free charges or currents), which are given by [258]

$$\nabla \cdot \mathbf{E} = 0, \tag{3.1}$$

$$\nabla \cdot \mathbf{B} = 0, \tag{3.2}$$

$$\nabla \times \mathbf{E} = -\frac{\partial \mathbf{B}}{\partial t}, \tag{3.3}$$

$$\nabla \times \mathbf{B} = \frac{\tilde{n}^2(\mathbf{r})}{c^2}\frac{\partial \mathbf{E}}{\partial t}, \tag{3.4}$$

where $\tilde{n}(\mathbf{r})$ is the spatially varying index of refraction[1] that defines the geometry of the cavity and $c = \sqrt{1/\mu_0\epsilon_0}$ is the speed of light in vacuum, with μ_0 and ϵ_0 being the permeability and permittivity of free space, respectively. Here we assume a non-magnetic system with permeability $\mu(\mathbf{r}) = \mu_0$, such that we can express the cavity's index of refraction in terms of its dielectric profile $\epsilon(\mathbf{r})$ as $\tilde{n}(\mathbf{r}) = \sqrt{\epsilon(\mathbf{r})/\epsilon_0}$. As the electric and magnetic fields of a the system are intimately related by Maxwell's equations, it suffices to determine one of these two fields to fully characterize the electromagnetic field of the optical cavity. Here, we choose to focus on the electric field, from which we can determine the magnetic field using Eqs. (3.3) and (3.4), subject to the condition given by Eq. (3.2).

We proceed in this venture by taking the curl of Eq. (3.3), while making use of the identity $\nabla \times (\nabla \times \mathbf{A}) = \nabla(\nabla \cdot \mathbf{A}) - \nabla^2\mathbf{A}$ (where $\mathbf{A}$ is an arbitrary vector quantity), along with Eq. (3.1), to arrive at the following wave equation for the cavity's electric field[2]

$$\nabla^2\mathbf{E}(\mathbf{r}, t) = \frac{\tilde{n}^2}{c^2}\frac{\partial^2\mathbf{E}(\mathbf{r}, t)}{\partial t^2}. \tag{3.5}$$

To solve this equation, we express the total electric field of the optical cavity in the separable form

$$\mathbf{E}_{\text{tot}}(\mathbf{r}, t) = \sum_j \mathbf{E}_j(\mathbf{r}, t) = \sum_j \mathcal{E}_j(t)\mathbf{E}_j(\mathbf{r}), \tag{3.6}$$

where we have performed a summation over the contributions of the electric fields $\mathbf{E}_j(\mathbf{r}, t) = \mathcal{E}_j(t)\mathbf{E}_j(\mathbf{r})$ from each of the cavity's j optical modes. Here we have broken each of these electric fields into their time-varying amplitudes $\mathcal{E}_j(t)$ and their

[1] We have included a tilde over the symbol for index of refraction to differentiate it from the phonon number symbol introduced in Chapter 2.

[2] An identical equation can be found for $\mathbf{B}(\mathbf{r}, t)$ by taking the curl of Eq. (3.4) while using Eq. (3.2).

spatially-varying modeshape functions $\mathbf{E}_j(\mathbf{r})$. Again, we are typically interested in a single electromagnetic mode of the cavity, such that we drop the subscripts and ignore the sum, resulting in an electric field profile given by

$$\mathbf{E}(\mathbf{r}, t) = \mathcal{E}(t)\mathbf{E}(\mathbf{r}). \tag{3.7}$$

Similar to the mechanical displacement, we choose to normalize the electric field's modeshape according to $\max|\mathbf{E}(\mathbf{r})| = 1$, such that $\mathcal{E}(t)$ traces out the true amplitude of the electric field at its spatial maximum and carries the appropriate units of N/C.

Continuing with this separation of variables approach, we assume the electric (and magnetic) fields to be harmonic in time such that[3]

$$\frac{d\mathcal{E}}{dt} = -i\omega_c\mathcal{E}(t), \tag{3.8}$$

where ω_c is the resonance frequency of the optical cavity mode. Inputting this relation for the time derivative of $\mathcal{E}(t)$ into the wave equation for $\mathbf{E}(\mathbf{r}, t)$ given by Eq. (3.5), we find

$$\nabla^2\mathbf{E}(\mathbf{r}) = -\frac{\tilde{n}^2(\mathbf{r})\omega_c^2}{c^2}\mathbf{E}(\mathbf{r}) = -\tilde{k}^2(\mathbf{r})\mathbf{E}(\mathbf{r}), \tag{3.9}$$

where we have introduced the spatially-varying wavenumber of the optical mode $\tilde{k}(\mathbf{r}) = \tilde{n}(\mathbf{r})\tilde{k}_0$, with $\tilde{k}_0 = \omega_c/c$ being its vacuum wavenumber. This equation, known as the Helmholtz equation, can be used to determine the modeshape of the electric field for a given cavity geometry specified by the spatial dependence of its refractive index. Though the Helmholtz equation has analytical solutions for a number of very simple, highly symmetric geometries (see Appendix B for the solutions in cylindrical geometries), for more complex systems one generally resorts to a numerical solver such as FEM simulation [172]. Finally, we note that while here we have focussed on a bound mode in an optical cavity, the Helmholtz equation given in Eq. (3.9) can be used to describe any monochromatic field contained within a non-magnetic dielectric.

[3]This relation is justified provided we are considering a high-Q optical cavity.

3.2.2 Optical Mode Volume

In order to quantify the spatial extent of each of the cavity's optical mode profiles, we define a quantity known as the effective optical mode volume. In direct analogy to the effective strain volume introduced in Section 2.3.6, we define this effective volume in terms of the electric field of the mode as [146, 259]

$$V_{\text{opt}} = \int \frac{U_{\text{em}}(\mathbf{r})}{\max[U_{\text{em}}(\mathbf{r})]} dV = \int \frac{\epsilon(\mathbf{r})|\mathbf{E}(\mathbf{r})|^2}{\max[\epsilon(\mathbf{r})|\mathbf{E}(\mathbf{r})|^2]} dV, \tag{3.10}$$

where

$$U_{\text{em}}(\mathbf{r}, t) = \epsilon(\mathbf{r})|\mathbf{E}(\mathbf{r}, t)|^2, \tag{3.11}$$

is the energy density of the mode's electromagnetic field [258]. Note that the integral in Eq. (3.10) is performed over the entire volume of the optical mode (including its surroundings). In practice, however, this optical mode volume is generally determined using FEM-simulated modeshapes of the electric field, with an integration volume large enough that the electric field of the mode is negligible at its boundaries. As we shall see in Section 4.2, this optical mode volume is a crucial parameter that effects the coupling between the optical and mechanical elements of our optomechanical system.

3.2.3 Quantization of the Electric Field

Up until this point, we have concerned ourselves with a classical electromagnetic description in the framework laid out by Maxwell's equations. However, in order to describe the quantum mechanical behaviour of an optomechanical system, we must quantize these fields as we did with the displacement of the mechanical resonator in Section 2.2.5. This quantization is performed by introducing the time-dependent photon creation and annihilation operators[4] $\hat{a}^\dagger(t)$ and $\hat{a}(t)$, such that the classical electric field given in Eq. (3.7) becomes [260–262]

$$\hat{\mathbf{E}}(\mathbf{r}, t) = \mathcal{E}_{\text{zpf}} \left[\hat{a}^\dagger(t)\mathbf{E}(\mathbf{r}) + \hat{a}(t)\mathbf{E}^*(\mathbf{r})\right], \tag{3.12}$$

where $\mathcal{E}_{\text{zpf}} = \sqrt{\hbar\omega_{\text{c}}/2V_{\text{opt}}\epsilon_{\max}}$ is the zero-point fluctuation amplitude of the optical cavity's vacuum field. Here $\epsilon_{\max}$ is the dielectric constant at the position where

[4] Similar to $\hat{b}$ and $\hat{b}^\dagger$, these photonic ladder operators obey the commutator $[\hat{a}, \hat{a}^\dagger] = 1$.

the energy density of the optical cavity is maximized, such that $\mathcal{E}_{\text{zpf}}$ represents the electric field at this maximal point corresponding to a single photon in the cavity [262]. Choosing the phase of the electric field such that its modeshape is real, we can rewrite Eq. (3.12) as

$$\hat{\mathbf{E}}(\mathbf{r}, t) = \hat{\mathcal{E}}(t)\mathbf{E}(\mathbf{r}), \tag{3.13}$$

where $\hat{\mathcal{E}}(t)$ is the quantized electric field operator represented in terms of the photonic ladder operators as

$$\hat{\mathcal{E}}(t) = \mathcal{E}_{\text{zpf}} \left[\hat{a}^\dagger(t) + \hat{a}(t)\right]. \tag{3.14}$$

For completeness, we also introduce the quantized magnetic field operator, which is given by

$$\hat{\mathcal{B}}(t) = \mathcal{B}_{\text{zpf}} \left[\hat{a}^\dagger(t) + \hat{a}(t)\right], \tag{3.15}$$

where $\mathcal{B}_{\text{zpf}} = \sqrt{\hbar/2\omega_{\text{c}} V_{\text{opt}} \epsilon_{\max}}$, such that $\mathcal{E}_{\text{zpf}}\mathcal{B}_{\text{zpf}} = \hbar/2V_{\text{opt}}\epsilon_{\max}$ and $\mathcal{E}(t) = \omega_{\text{c}}\mathcal{B}(t)$. With this definition, the modeshape of the magnetic field is found using Eq. (3.3) as $\mathbf{B}(\mathbf{r}) = -i\nabla \times \mathbf{E}(\mathbf{r})$. Note that unlike $\hat{x}$ and $\hat{p}$ for the mechanical mode, $\hat{\mathcal{E}}$ and $\hat{\mathcal{B}}$ are not conjugates of each other, and therefore do not satisfy a commutation relation, nor the Heisenberg uncertainty principle.

3.2.4 Optical Equation of Motion

In order to understand the dynamics of our cavity's electric field, we employ a damped harmonic oscillator model to describe the time evolution of its electric field. Here, we choose to parametrize the time-dependence of the electric field via its classical complex amplitude a, defined as the expectation value of the annihilation operator $\hat{a}$ (*i.e.* $a = \langle\hat{a}\rangle$), which for an undriven optical cavity obeys the equation of motion [150]

$$\dot{a}(t) = -\frac{\kappa}{2}a(t) - i\omega_{\text{c}}a(t). \tag{3.16}$$

Here κ is the total decay rate of the electric field amplitude, such that $\tau_{\text{c}} = 1/\kappa$ is the lifetime of the photons confined within the optical cavity. For an underdamped cavity, we can also introduce the optical quality factor, which is defined in the same way as the mechanical quality factor in Eq. (2.9) as

$$Q_{\text{c}} = \frac{\omega_{\text{c}}}{\kappa} = \omega_{\text{c}}\tau_{\text{c}}. \tag{3.17}$$

In Section 3.4, we will investigate the specific damping processes that act to limit this quality factor in our optical microdisk cavities.

3.3 Optical Microdisks

Before investigating the optical loss mechanisms of our system, we briefly discuss the resonant optical whispering gallery modes (WGMs) that form within our microdisk structures as a result of total internal reflection at their boundaries. Due to the complexity of our device geometry, we generally use an FEM solver such as COMSOL MULTIPHYSICS® [172] to determine the optical modes of these devices. However, as the wavelengths of the optical modes of interest ($\lambda_c = 2\pi c/\omega_c \sim 1500$–$1640$ nm) are much smaller than the disk diameter (10 μm), these calculations can be computationally intensive and time consuming. Therefore, we also use the approximate analytical form of the electromagnetic fields given in Appendix B to describe some basic properties of the WGMs of our isolated microdisk cavities, before describing how these modes couple to the mechanical motion of our resonator in Chapter 4.

Here we consider the thin disk geometry associated with our optical cavities, with radius R, thickness t ($t \ll R$), and index of refraction $\tilde{n}_d$, immersed in a surrounding medium with index of refraction $\tilde{n}_s$. Within such a geometry, two types of optical modes can exist: transverse electric (TE) modes where $E_z = 0$ and transverse magnetic (TM) modes where $B_z = 0$[5]. Example electromagnetic field profiles for each of these mode families, calculated using parameters from the optical disks studied in this thesis, are shown in Fig. 3.1. Here we see that the evanescent field of the TM mode primarily leaks out of the top and bottom the disk, while for the TE mode, the electric field extends outwards in the radial direction. This results in a larger overlap between the optical field of the disk and our sidecoupled mechanical resonators for TE modes. Therefore, in the remainder of the thesis, we primarily focus on the TE modes of the microdisk, as these are the modes that we use to address our devices in the experiment.

[5]In reality, there exists a small, non-zero electric (magnetic) field in the z-direction for the TE (TM) modes of the disk, however, we neglect this contribution in our approximation and retain the nomenclature of TE (TM) modes.

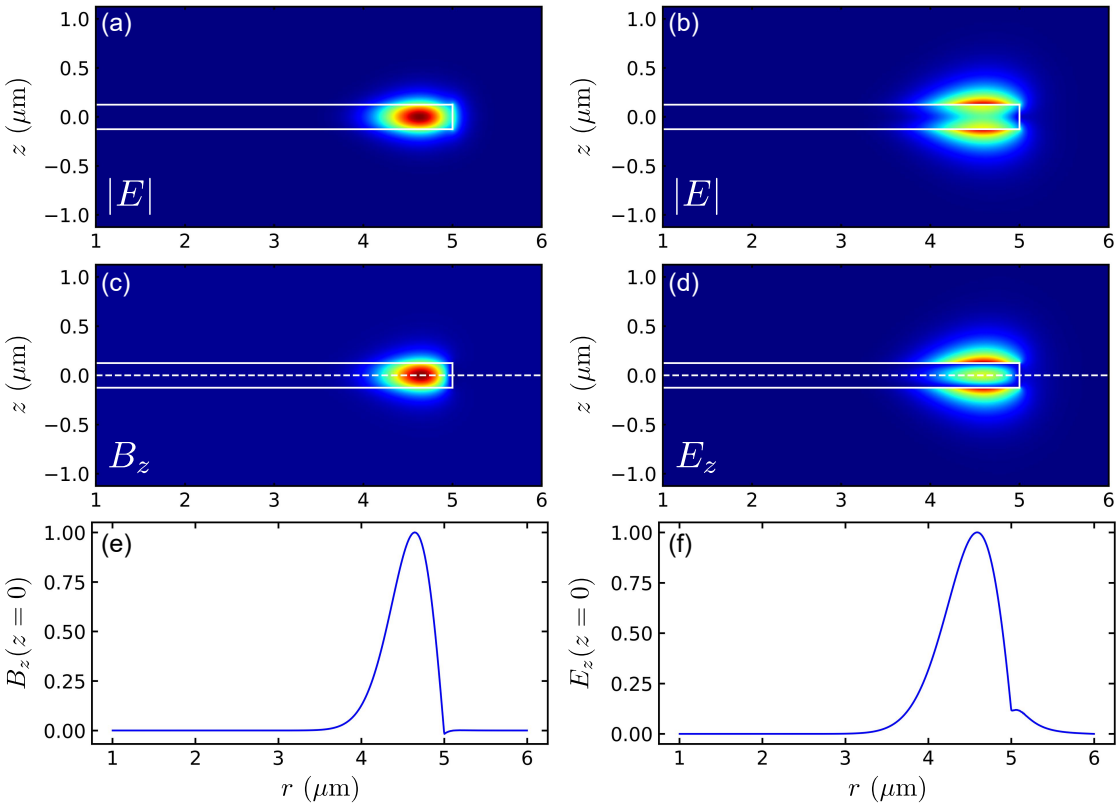

Figure 3.1: The FEM-simulated electromagnetic fields in the (r, z)-plane for the single-crystal silicon optical microdisks studied in this thesis ($R = 5$ μm, $t = 250$ nm). The index of refraction of the disk is taken from Fig. 3.2a. Here we display the magnitude of the electric field for the (a) the $n = 1$, $m = 1$ TE mode at $\lambda_c = 1555.821$ nm and (b) the $n = 1$, $m = 34$ TM mode at $\lambda_c = 1552.436$ nm. In the middle panel, we show the magnitude of (c) B_z for the TE mode and (d) E_z for the TM mode. Each field is normalized to its maximum value such that red (blue) indicates the field maximum (minimum), with the geometry of the disk highlighted via the white solid lines. Finally, in the bottom row we plot the field profiles along the dashed white lines in (c) and (d), displaying the r-dependence of the (e) B_z field of the TE mode and (f) E_z field of the TM mode along the center ($z = 0$) of the disk.

From the analytical approximations for the disk's electromagnetic fields given in Appendix B, we can determine the effective index of refraction and resonant wavelengths of these TE modes. This is done by using the two dispersion relations

for the mth-order azimuthal TE modes given by

$$\tan\left(\frac{\tilde{k}_0 t}{2}\sqrt{\tilde{n}_{\mathrm{d}}^2-\tilde{n}_{\mathrm{TE}}^2}\right)=\frac{\sqrt{\tilde{n}_{\mathrm{TE}}^2-\tilde{n}_{\mathrm{s}}^2}}{\sqrt{\tilde{n}_{\mathrm{d}}^2-\tilde{n}_{\mathrm{TE}}^2}}, \tag{3.18}$$

$$\frac{J_m'(q_{\mathrm{d}}R)}{\tilde{n}_{\mathrm{d}}^2 q_{\mathrm{d}} J_m(q_{\mathrm{d}}R)}+\frac{K_m'(q_{\mathrm{s}}R)}{\tilde{n}_{\mathrm{s}}^2 q_{\mathrm{s}} J_m(q_{\mathrm{s}}R)}=0, \tag{3.19}$$

where $J_m(x)$ ($K_m(x)$) is the mth-order (modified) Bessel function of the first (second) kind, with its derivative with respect to its argument x defined as $dJ_m/dx = J_m'(x)$ ($dK_m/dx = K_m'(x)$). Here, we have also introduced the quantities $q_{\mathrm{d}}^2 = k_{\mathrm{d}}^2 - \tilde{k}_z^2$ and $q_{\mathrm{s}}^2 = \tilde{k}_z^2 - k_{\mathrm{s}}^2$, expressed in terms of the wavenumbers $k_{\mathrm{d}} = \tilde{n}_{\mathrm{d}}\tilde{k}_0$ inside the disk and $k_{\mathrm{s}} = \tilde{n}_{\mathrm{s}}\tilde{k}_0$ in its surroundings, where $\tilde{k}_0 = 2\pi/\lambda_{mn}$ is the vacuum wavenumber for the nth-order radial, mth-order azimuthal TE mode with a resonant wavelength of λ_{mn}. Therefore, q_{d} describes the transverse component of the wavenumber inside the disk, while q_{s} represents an imaginary transverse wavenumber characterizing how the mode evanescently decays into its surroundings. Finally, $\tilde{n}_{\mathrm{TE}} = q_{\mathrm{d}}/\tilde{k}_0$ is the effective index of refraction for the TE mode, such that this quantity describes the index of refraction as viewed by the transverse wavevector with the disk. Note that $\tilde{n}_{\mathrm{TE}}$ depends on the considered wavelength, as well as the thickness and the refractive index of the disk, according to Eq. (3.18). In Fig. 3.2b, we display $\tilde{n}_{\mathrm{TE}}$ calculated for our silicon microdisks at low temperature using the procedure outlined in Section B.3 of Appendix B over the experimentally relevant wavelength range of 1500 – 1640 nm, for which we find $\tilde{n}_{\mathrm{TE}} \sim 2.82$ – 2.92. Furthermore, by inputting these effective indices into Eq. (3.19), we calculate the fundamental radial ($n = 1$) resonant wavelengths of the disk's TE modes within this range, which show good agreement with the FEM-simulated values as summarized in Table 3.1.

As the procedure used in Section B.3 to calculate the resonance wavelengths the TE disk modes is rather tedious, we look to determine an approximate analytical method to calculate these wavelengths (similar to the weakly guiding approximation used to determine the single-mode cut-off radii in infinite cylinders – see Appendix B). Here we use a method we name the strongly confined approximation (SCA) to estimate the resonance frequencies of the TE modes by requiring its B_z field to be radially confined to the disk (see Fig. 3.1e). This can be done by setting B_z equal

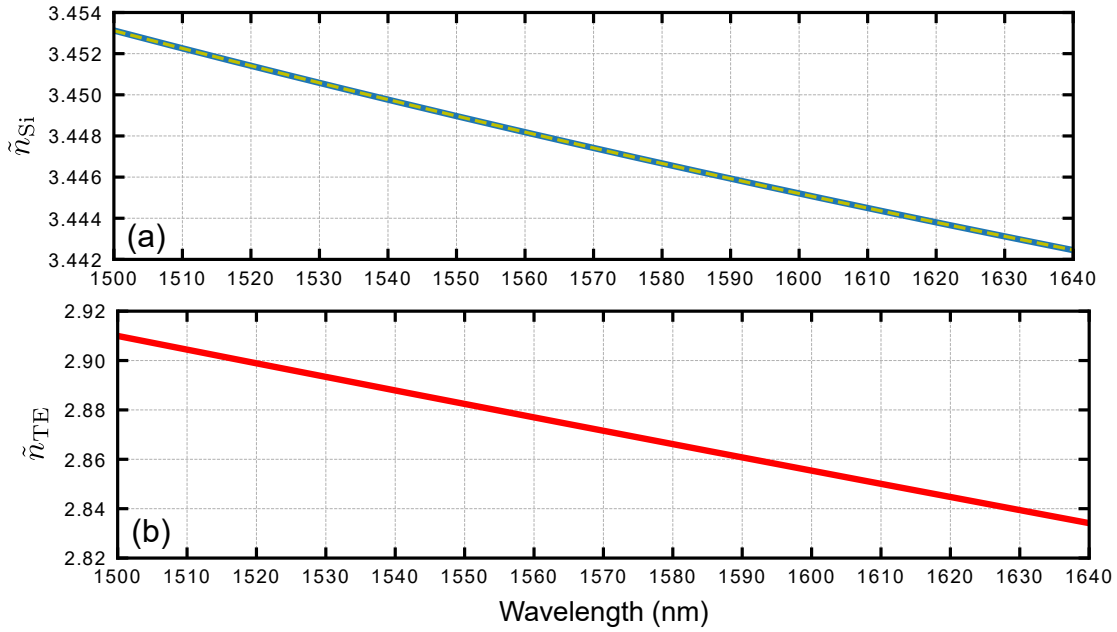

Figure 3.2: (a) The low temperature refractive index of single-crystal silicon $\tilde{n}_{\mathrm{Si}}$ (solid blue line) given over the wavelength range from 1500 to 1640 nm calculated for $T = 20$ K using the Sellmeier coefficients found in Ref. [263]. Due to the diminishing thermo-optic coefficients in silicon at low temperatures [264], these values can be used as a good approximation for the indices of refraction below 20 K, incurring an error of at most 10^{-4}. The dashed yellow line is a quadratic interpolation fit to $\tilde{n}_{\mathrm{Si}} = a\lambda^2 + b\lambda + c$, where $a = 7.566 \times 10^{-8}$ nm^{-2}, $b = -3.137 \times 10^{-4}$ nm^{-1}, and $c = 3.753$, with λ in units of nm. In (b), we use these values for $\tilde{n}_{\mathrm{Si}}$, to determine the low temperature effective refractive index for the TE modes of our 250-nm-thick silicon microdisks according to Eq. (3.18).

to zero at the $r = R$ boundary[6], which in order to be true for all z and ϕ requires $J_m(q_1 R) = 0$ (see Appendix B). Using this condition the resonant frequencies of the disk's TE modes can be found according to

$$\lambda_{mn} \approx \frac{2\pi \tilde{n}_{\mathrm{TE}} R}{Z_{mn}}, \tag{3.20}$$

where Z_{mn} is the nth zero of the mth-order Bessel function of the first kind. The values for λ_{mn} calculated using the SCA are given in Table 3.1, where we see that the resonant wavelengths using this approximate method more closely match the FEM-simulated values than those determined using Eq. (3.19).

Finally, we note that the effective index can also be used to define an effective

[6]Unfortunately, the SCA does not provide good estimates of the resonant wavelengths for TM modes, as $E_z \gg 0$ at the $r = R$ boundary (see Fig. 3.1f).

m	$\tilde{n}_{\mathrm{TE}}$	λ_{c} (nm)		
		Eq. (3.19)	SCA	FEM
48	2.843	1622.502	1623.123	1623.575
49	2.856	1599.254	1599.838	1600.287
50	2.868	1576.718	1577.271	1577.714
51	2.879	1554.861	1555.384	1555.821
52	2.891	1533.652	1534.147	1534.579
53	2.902	1513.060	1513.526	1513.957

Table 3.1: The resonant wavelengths of the $n = 1$ TE modes of a disk with radius $R = 5$ μm and thickness $t = 250$ nm, calculated using Eq. (3.19), the SCA given by Eq. (3.20), and FEM simulation. The wavelength dependence of the disk's refractive index is taken from Fig. 3.2. Here we see that the analytical results provide excellent estimates of the FEM-simulated resonant wavelengths, undershooting this value by approximately 1 nm and 0.5 nm for the approach using Eq. (3.19) and the SCA, respectively. Finally, we find that each of these methods predict the free spectral range of these fundamental radial TE modes to be approximately 20 nm.

radius of the mth-order azimuthal WGM as [265, 266]

$$m\lambda_{mn} = l_{\mathrm{opt}} = 2\pi\tilde{n}_{\mathrm{TE}}R_{\mathrm{opt}}, \tag{3.21}$$

which roughly states that m wavelengths fit inside the effective optical path length (*i.e.* circumference) of the disk $l_{\mathrm{opt}} = 2\pi\tilde{n}_j R_{\mathrm{opt}}$ with effective radius R_{opt}. Note that in the SCA, this effective radius will be given by

$$R_{\mathrm{opt}} = \frac{m}{Z_{mn}}R. \tag{3.22}$$

Therefore, R_{opt} will always be less than the physical radius of the disk R due to the fact that the maximum of the electromagnetic field intensity is confined within the disk as opposed to existing at its edge (see Fig. 3.1). Using the values in Table 3.1, we calculate the ratio between these two radii to be $R_{\mathrm{opt}}/R \approx 0.88$ for the fundamental radial TE modes of our microdisk.

3.4 Optical Losses

We conclude this section by investigating the mechanisms that contribute to the total loss rate κ of our microdisk cavities. We begin by first expressing this loss rate as

$$\kappa = \kappa_{\mathrm{e}} + \kappa_{\mathrm{i}}, \tag{3.23}$$

where κ_e is the rate at which the optical field within the disk couples to the external waveguide used to address it, while κ_i characterizes the internal loss mechanisms of the microdisk. In this sense, κ_e is associated with the "useful" losses that allow us to assess the optical cavity. Using coupled mode theory [267], one can show that for tapered fiber coupling, this external coupling rate is proportional to the overlap between the electric fields of the cavity $\mathbf{E}_c(\mathbf{r})$ and fiber $\mathbf{E}_f(\mathbf{r})$ modes according to [266, 268, 269]

$$\kappa_e \propto \frac{\omega_c \epsilon_0}{4} \int \left[\tilde{n}^2(\mathbf{r}) - \tilde{n}_2^2\right] \mathbf{E}_c^*(\mathbf{r}) \cdot \mathbf{E}_f(\mathbf{r}). \tag{3.24}$$

Therefore, in practice κ_e can be determined by varying the fiber-cavity separation, and thus the overlap of their fields, and observing the dependence κ has on this separation distance [58, 266, 270]. Meanwhile, κ_i corresponds to cavity dissipation mechanisms that act to reduce our optical signal and contaminate our measurement. We therefore wish to mitigate these losses as much as possible in our system.

Here we consider four separate loss mechanisms that contribute to κ_i in optical microdisks, namely bulk material absorption, radiation losses, Rayleigh surface scattering, and surface absorption. As with the mechanical dissipation mechanisms studied in Section 2.5, we assume that these processes are independent of one another, such that we can sum their corresponding loss rates κ_j as

$$\kappa_i = \sum_j \kappa_j. \tag{3.25}$$

The optical quality factors then add in parallel according to

$$Q_i^{-1} = \sum_j Q_j^{-1}, \tag{3.26}$$

where $Q_j^{-1} = \kappa_j/\omega_c$ is the inverse of the quality factor associated with the jth damping mechanism. In what follows, we estimate the optical dissipation in our microdisk cavities (with radius $R = 5$ μm and thickness $t = 250$ nm) by considering the losses associated with the prototypical TE mode shown in Fig. 3.1. That is, the $n = 1$, $m = 51$ TE mode at a simulated resonant wavelength of $\lambda_c = 1555.821$ nm, with corresponding effective index of refraction $\tilde{n}_{TE} = 2.88$ (see Table 3.1). We will use these representative limiting quality factors calculated for this mode to quantify the dissipation for all of the fundamental radial TE modes within our relatively narrow experimental wavelength range of 1500–1640 nm.

3.4.1 Bulk Material Absorption

The first loss mechanism we consider for our microdisks is that due to bulk material absorption, for which the limiting optical quality factor can be found as [271]

$$Q_{\mathrm{ba}} = \frac{2\pi\tilde{n}_j}{\alpha\lambda_{\mathrm{c}}}, \tag{3.27}$$

where α is the bulk optical absorption coefficient. In silicon, this parameter is relatively constant with respect to temperature [272], but depends strongly on its dopant concentration [273]. For the p-type single-crystal silicon used to fabricate our devices, with a resistivity of 13.5 Ω·cm (boron dopants with a density of $\sim 10^{21}$ m^3), we calculate[7] an optical absorption coefficient of $\alpha = 0.336\ \mathrm{m}^{-1}$. Inputting this value into Eq. (3.27), we calculate the bulk-absorption-limited quality factor for the considered TE mode to be $Q_{\mathrm{ba}} = 3.5 \times 10^7$.

3.4.2 Surface Absorption

Accompanying the optical absorption within the bulk of the resonator, there also exists the possibility of enhanced absorption at the surfaces due to imperfections such as surface adsorbates, improperly terminated silicon bonds, and lattice defects [266]. Borselli *et al*. [274] found that this effect can be accounted for by replacing α in Eq. (3.27) with the modified surface absorption coefficient

$$\alpha_{\mathrm{s}} = 2f'_{\mathrm{s}}\Xi, \tag{3.28}$$

where f'_{s} is the fraction of losses that occur in the surface, while Ξ is a parameter that quantifies the overlap of the mode's optical field with the surface region. Here the factor of two accounts for the fact that we consider both the top and bottom surfaces of the disk[8], where $\Xi = 3.5 \times 10^6\ \mathrm{m}^{-1}$ for TE modes [274]. For silicon disks with oxide-terminated surfaces, as is relevant for our devices[9], Borselli *et*

[7] Here we use the relation $\alpha = \frac{4.45}{\tilde{\rho}}\ \mathrm{m}^{-1}$, where $\tilde{\rho}$ is the resistivity of the silicon in units of Ω·cm [272].

[8] $\Xi = 2.3 \times 10^4\ \mathrm{m}^{-1}$ for the side of the disk [274], such that absorption at these surfaces is negligible.

[9] In our fabrication process, we perform a hydrofluoric acid etch of the silicon surfaces (see Section 5.2.2), however, as we do not immediately transport the device to an inert environment, this oxide layer likely reforms before we perform our measurements.

al. further found that $f_s' \sim 10^{-5}$ [274]. Inputting these values for Ξ and f_s' into Eq. (3.28), we find $\alpha_s = 24\ \mathrm{m}^{-1}$ for the considered TE mode, corresponding to a surface-absorption-limited quality factor of $Q_{sa} = 4.9 \times 10^5$.

3.4.3 Surface Scattering

Another mechanism by which optical losses can occur within our microdisks is Rayleigh scattering due to surface irregularities generated during their fabrication. Using the volume current method [275], Borselli *et al.* [276, 277] showed that the limiting quality factor due to this surface scattering process can be calculated as[10]

$$Q_{ss} = \frac{3\tilde{n}_1^2(\tilde{n}_{TE}^2 - \tilde{n}_2^2)\lambda_c^3}{8\pi^{7/2}\tilde{n}_2\tilde{n}_{TE}^2(\tilde{n}_1^2 - \tilde{n}_2^2)^2}\left(\frac{V_d}{V_s^2}\right). \tag{3.29}$$

Here, V_d is the geometric volume of the disk ($V_d = \pi R^2 t = 19.6\ \mu\mathrm{m}^3$ for our optical microdisks) and $V_s = \sqrt{Rl_c}t\delta R$ is the effective volume of the typical scatterer, with l_c and δR being the correlation length and standard deviation of the surface roughness. In Ref. [277], Borselli *et al.* found that $\sqrt{l_c}\delta R \approx 8.5 \times 10^{-14}\ \mathrm{m}^{3/2}$ for a fabrication procedure similar to what is used for our devices (see Section 5.2.2). Inputting this value into Eq. (3.29), we calculate a Rayleigh surface scattering quality factor of $Q_{ss} = 1.7 \times 10^7$ for our microdisk.

3.4.4 Radiation Losses

The final optical loss mechanism that we consider in this section is WGM radiative losses that occur due to imperfect total internal reflection that occurs at the curved boundaries of the microdisk. To describe this effect, Frateschi and Levi [278] used a ray optics model to calculate the radiation-limited quality factor for the mth azimuthal TE mode as [271]

$$Q_r = \frac{\pi\tilde{n}_{TE}l_m}{m\lambda_c}\exp\left(\frac{2}{3}Z_{m,1}\cos^3\theta_c\right). \tag{3.30}$$

Here, θ_c is the critical angle of incidence at the disk's surface, which is expressed in terms of the effective index as $\sin\theta_c = \tilde{n}_2/\tilde{n}_{TE}$, while $l_m = 2\pi R\,\mathrm{sinc}(\pi/2m)$ is the

[10] This equation was developed for TM modes, however, using this equation for TE modes incurs an error on the order of 50 % [277], such that it suffices for the order of magnitude estimates presented in this section.

polygon round trip of path of the WGM. For large m ($\gtrsim 20$), this polygon round trip path is essentially a circle, such that $\mathrm{sinc}(\pi/2m) \approx 1$ and $l_m = 2\pi R$ is the circumference of the disk [278]. Using Eq. (3.30), we find $Q_\mathrm{r} = 2.8 \times 10^{14}$ for the considered $m = 51$ TE mode of the microdisk.

3.4.5 Summary

In this section we have considered optical losses from our microdisk resonators due to absorption both within its bulk material and at its surfaces, Rayleigh scattering from surface irregularities and radiation loss for the $n = 1$ TE WGMs of our optical microdisks. The estimated order of magnitude for the limiting quality factor resulting from each of these process is summarized in Table 3.2. Here we see that optical losses are dominated in our devices by absorption at the surfaces of the microdisk, which limit our optical quality factors to $\sim 10^5$ in good agreement with what we measure in our experiments[11]. We conclude this section by noting that as the geometry and optical parameters of the microdisk are relatively independent with respect temperature, we expect the disk's optical loss mechanisms to be as well. This hypothesis has been confirmed by independent measurements of the optical quality factors at room and cryogenic temperatures between similar microdisks.

Loss Mechanism		TE Mode
Bulk Absorption	Q_ba	10^7
Surface Absorption	Q_sa	10^5
Surface Scattering	Q_ss	10^7
Radiation Losses	Q_r	10^{14}

Table 3.2: Summary of the order of magnitude estimates for the limits on the optical quality factors calculated throughout this section for the $n = 1$, $m = 51$ TE WGM shown in Fig. 3.1. The considered dissipation mechanisms are: bulk absorption Q_ba, surface absorption Q_sa, Rayleigh surface scattering Q_ss, and radiation losses Q_r.

[11] The exact measured quality factor varies slightly depending on the position of our tapered fiber (see Section 7.4), indicating that the fiber itself may induce a small amount of scattering as well.

3.5 Conclusion

In this chapter, we have discussed the optical WGMs of our microdisk resonators. Employing a similar separation of variables approach similar to that we used to describe the displacement of our mechanical resonator, we showed that the electric field of each mode can be expressed in terms of a time-varying amplitude and a spatially varying modeshape. Using Maxwell's equations, we determined the wave equation that governs this modeshape function, as well as utilized the electromagnetic energy density of the system to define an effective volume for each optical mode. We then proceeded to quantize the amplitude of the electric by expressing it in terms of photon annihilation and creation operators of the cavity, whose classical expectation values oscillate in time according to a damped harmonic oscillator description. With this general theoretical framework laid out, we applied it to our optical microdisk resonators, using a combination of FEM simulation and analytical approximations to determine the electromagnetic fields, effective indices, and resonant wavelengths in this geometry. Finally, we provided an estimate of the different electromagnetic dissipation mechanisms present in our microdisks, ascertaining that optical losses are dominated by absorption at their surfaces.

Chapter 4

Cavity Optomechanics

4.1 Introduction

In the previous two chapters, we studied how the mechanical resonator and optical cavity of an optomechanical system behave when kept in isolation from one another. We now look at a number of interesting quantum and classical phenomena that emerge when we couple these two elements together. We begin in Section 4.2, where we introduce the dispersive optomechanical coupling mechanism realized in our devices, providing an equation that can be used to quantify the strength of this coupling. In Section 4.3, we use a Hamiltonian approach to develop a linearized quantum mechanical description of our optomechanical system, which we use to model the backaction-mediated phenomena of optomechanical damping, spring effect, and cooling observed in our devices. Continuing in Section 4.4, we use this linearized treatment to theoretically describe the optical measurement techniques of direct and homodyne detection that we employ in later chapters to address our optomechanical devices. Here we unveil the standard quantum limit of continuous optomechanical detection, which can be overcome using the quantum nondemolition measurement protocol detailed in Chapter 8. Finally, in Section 4.5, we discuss the model used to describe the classical dynamics of optomechanical cavities in the nonlinear regime, which lays the framework for the photothermal nonlinearities discussed in Chapter 7.

4.2 Optomechanical Coupling

The interaction between the optical and mechanical modes of an optomechanical system can occur in a number of different ways, including dispersive coupling due to moving boundary conditions [53, 146, 279] or the photoelastic effect [67, 280–282], as well as dissipative coupling [70, 283–286]. In our optomechanical cavities, we realize the first of these coupling mechanisms, whereby the motion of a nanomechanical resonator perturbs the boundaries of an optical microdisk cavity. In this configuration, introducing the mechanical resonator into the evanescent field of the microdisk cavity acts to shift the optical resonance frequencies of its WGMs to longer wavelengths (lower frequencies). This is due to the fact that the presence of the resonator will displace low refractive index air/vacuum ($\tilde{n}_0 = 1$) in favour of the relatively high refractive index silicon ($\tilde{n}_{\mathrm{Si}} \approx 3.45$ at 1550 nm – see Fig. 3.2a), increasing each optical mode's effective index of refraction, and therefore, its optical path length and resonant wavelength according to Eq. (3.21). For this reason, it is difficult to analytically determine the exact modeshape and resonance frequency of the optical mode in the presence of the mechanical resonator, such that we resort to numerical FEM simulations.

In addition to this static shift, the motion of the resonator about its equilibrium position will modulate the WGM mode's effective index of refraction (and hence its optical path length and resonance frequency) in time according to

$$\delta\omega_{\mathrm{c}}(t) = -\frac{2\pi c}{\tilde{n}_{\mathrm{TE}}^2 \lambda_{\mathrm{c}}}\delta\tilde{n}_{\mathrm{TE}}(t) = -\frac{c}{\tilde{n}_{\mathrm{TE}}^2 \lambda_{\mathrm{c}} R_{\mathrm{opt}}}\delta l_{\mathrm{opt}}(t) = -G\hat{x}(t), \tag{4.1}$$

where we have introduced $G = -d\omega_{\mathrm{c}}/d\hat{x}$ as the first-order dispersive optomechanical coupling coefficient[1]. It is this mechanically induced shift in the optical cavity frequency that produces a dispersive optomechanical coupling in this geometry, perturbing the resonance frequency of the microdisk cavity to first order in position as[2]

$$\omega_{\mathrm{c}}(x) \approx \omega_{\mathrm{c}} - G\hat{x}. \tag{4.2}$$

[1] In general, the optomechanical coupling is described by a matrix, with components G_{jk} relating the first order shift in the jth optical cavity frequency ω_j to the displacement of the kth mechanical mode x_k. However, here we focus on the interaction between a single optical and mechanical mode, such that we only consider one component of this matrix.

[2] For second order expansion, see Appendix C.

We note that the exact quantitative shift of the effective index of refraction, and therefore the optomechanical coupling strength, will vary for different mechanical modes, though the qualitative nature of this coupling principle is valid for both of the resonator geometries studied in this thesis. We can, however, use a perturbative approach (see Appendix C) to determine this optomechanical coupling coefficient in terms of the mechanical and optical modeshapes of the system as [146]

$$G = -\frac{\omega_c}{2V_{opt}} \int_S \mathbf{u}(\mathbf{r}) \cdot \mathbf{n}(\mathbf{r}) \Big[\Delta\epsilon |\mathbf{E}^{\parallel}(\mathbf{r})|^2 - \Delta\epsilon^{-1} \epsilon^2(\mathbf{r}) |\mathbf{E}^{\perp}(\mathbf{r})|^2 \Big] dA. \tag{4.3}$$

Here the integral is performed over the cavity's surface, as defined by the position-dependent unit normal vector $\mathbf{n}(\mathbf{r})$, with $\mathbf{E}^{\parallel}(\mathbf{r})$ and $\mathbf{E}^{\perp}(\mathbf{r})$ being the components of the optical mode's electric field parallel and perpendicular to this surface. Furthermore, we have $\Delta\epsilon = \epsilon_d - \epsilon_s$ and $\Delta\epsilon^{-1} = \epsilon_d^{-1} - \epsilon_s^{-1}$, where ϵ_d and ϵ_s are the relative permittivities of the optomechanical device's material and the surrounding medium, respectively. Therefore, we see from Eq. (4.3) that the greater the overlap between the optical and mechanical modes of the system, and the smaller the cavity mode volume V_{opt}, the larger their optomechanical coupling will be. Throughout the rest of this chapter, we assume an optomechanical coupling of this form, as this matches what we expect for our experimental devices.

4.3 Quantum Optomechanics

4.3.1 Optomechanical Hamiltonian

In order to develop a fully quantum mechanical model of the optomechanical system, we begin by treating each of the optical cavity and mechanical resonator as independent quantum harmonic oscillators. In this case, we can write the Hamiltonian of the system as

$$\hat{H} = \hbar\omega_c \hat{a}^\dagger \hat{a} + \hbar\omega_m \hat{b}^\dagger \hat{b}, \tag{4.4}$$

where the first term ($\hat{H}_c = \hbar\omega_c \hat{a}^\dagger \hat{a}$) describes the free energy of the optical cavity mode, while the second term ($\hat{H}_m = \hbar\omega_m \hat{b}^\dagger \hat{b}$) accounts for the free energy of the mechanical resonance[3].

[3]Here we have neglected to include the ground state energies of each oscillator, as this simply introduces an inconsequential phase into the equations of motion for the ladder operators.

To introduce a dispersive optomechanical coupling between these two modes, we replace the static optical cavity frequency with the position-dependent one given in Eq. (4.2) (*i.e.* take $\omega_c \to \omega_c(\hat{x})$). Using this expansion, along with Eq. (2.17), we can then write the optomechanical Hamiltonian as

$$\hat{H} = \hbar\omega_c \hat{a}^\dagger \hat{a} + \hbar\omega_m \hat{b}^\dagger \hat{b} - \hbar g_0 \left(\hat{b}^\dagger + \hat{b}\right) \hat{a}^\dagger \hat{a}, \tag{4.5}$$

where we have introduced the single-photon, single-phonon optomechanical coupling rate $g_0 = G x_{\mathrm{zpf}}$. The last term in Eq. (4.5) is the optomechanical interaction Hamiltonian $\hat{H}_{\mathrm{om}} = -\hbar G \hat{x} \hat{a}^\dagger \hat{a} = -\hbar g_0 (\hat{b}^\dagger + \hat{b}) \hat{a}^\dagger \hat{a}$, which can be used to determine the radiation pressure force exerted by the photons within the optical cavity onto the mechanical resonator as

$$\hat{F}_{\mathrm{rp}} = -\frac{d\hat{H}_{\mathrm{om}}}{d\hat{x}} = \hbar G \hat{a}^\dagger \hat{a}. \tag{4.6}$$

Up to this point, we have only considered the interaction between the optical and mechanical modes of interest. However, in practice we deal with open quantum systems, such that each mode also interacts with its surrounding environment. To model this behaviour, we assume that the mechanical resonator is coupled to an environmental bath comprised of bosonic phonon modes, and is described by the Hamiltonian

$$\hat{H}_\Gamma = \sum_q \hbar\omega_q \hat{b}_q^\dagger \hat{b}_q + i\hbar \sum_q \left(f_q \hat{b}^\dagger \hat{b}_q - f_q^* \hat{b}_q^\dagger \hat{b}\right). \tag{4.7}$$

Here $\hat{b}_q$ ($\hat{b}_q^\dagger$) is the annihilation (creation) operator for each of the q phononic bath modes coupled to the mechanical resonator, with the ladder operators for a given mode obeying the standard commutation relation for the harmonic oscillator such that $[\hat{b}_q, \hat{b}_{q'}] = \delta_{qq'}$, where $\delta_{qq'}$ is the Kronecker delta symbol. The first term in Eq. (4.7) gives the free energy for each of the q bath modes, while the second term describes the linear interaction between the mechanical resonator and these bath modes, as characterized by the mode-dependent coupling coefficient f_q. This interaction, which amounts to a phonon in the mechanical resonator being annihilated and recreated within the bath for the $f_q^* \hat{b}_q^\dagger \hat{b}$ term (and vice versa for the $f_q \hat{b}^\dagger \hat{b}_q$ term), accounts for energy lost from the mechanical mode to its environment, as well as an intrinsic drive that results from noise (both quantum

and thermal) creeping into the system via these input/output channels. Due to the large density of states generated by the resonant structure of the mechanical mode, even frequency-independent white noise that enters the mode in this way can act to effectively drive the mechanical mode to significant amplitudes.

An analogous process occurs for the optical cavity as described by the Hamiltonian

$$\hat{H}_\kappa = \sum_p \hbar\omega_p \hat{a}_p^\dagger \hat{a}_p + i\hbar \sum_p \left(f_p\, \hat{a}^\dagger \hat{a}_p - f_p^* \hat{a}_p^\dagger \hat{a} \right), \tag{4.8}$$

where $\hat{a}_p$ ($\hat{a}_p^\dagger$) are the annihilation (creation) operators for each of the p photonic bath modes, which obey the commutator $[\hat{a}_p, \hat{a}_{p'}] = \delta_{pp'}$. As was the case for the mechanical bath, the first term in Eq. (4.8) accounts for the free energy of the p optical bath modes, while the second describes their interaction with the resonant optical cavity mode, annihilating (creating) photons in the cavity, with the accompanying creation (annihilation) of a photon in the bath at a rate determined by the coupling coefficient f_p (f_p^*).

For the experiments considered in this thesis, the optical bath differs from its phononic counterpart in that the optical cavity is excited by an external drive at frequency ω_d (such as a laser) to introduce a population of coherent photons into the cavity. It is this drive that breaks the symmetry between the optical cavity and mechanical resonator, as the optical mode is externally driven by a coherent source, while the mechanical mode is simply driven by input noise. Therefore, we single out a given bath mode as this input drive[4], with the annihilation (creation) operator $\hat{a}_\mathrm{dr}$ ($\hat{a}_\mathrm{dr}^\dagger$) corresponding to the cavity photon, drive photon coupling coefficient f_dr (f_dr^*), allowing us to introduce the Hamiltonian for this drive as

$$\hat{H}_\mathrm{dr} = \hbar\omega_\mathrm{d} \hat{a}_\mathrm{dr}^\dagger \hat{a}_\mathrm{dr} + i\hbar \left(f_\mathrm{dr} \hat{a}^\dagger \hat{a}_\mathrm{dr} - f_\mathrm{dr}^* \hat{a}_\mathrm{dr}^\dagger \hat{a} \right). \tag{4.9}$$

The total Hamiltonian for the driven, damped optomechanical system is then given

[4]Note that we redefine the sum over $\hat{a}_p$ in Eq. (4.8) to exclude this drive mode.

by the sum of these individual Hamiltonians as

$$\begin{aligned}\hat{H} &= \hat{H}_{\rm c} + \hat{H}_{\rm m} + \hat{H}_{\rm om} + \hat{H}_{\rm dr} + \hat{H}_{\kappa} + \hat{H}_{\Gamma} \\ &= \hbar\omega_{\rm c}\hat{a}^{\dagger}\hat{a} + \hbar\omega_{\rm m}\hat{b}^{\dagger}\hat{b} - \hbar g_0\left(\hat{b}^{\dagger}+\hat{b}\right)\hat{a}^{\dagger}\hat{a} + \hbar\omega_{\rm d}\hat{a}_{\rm dr}^{\dagger}\hat{a}_{\rm dr} \\ &+ i\hbar\left(f_{\rm dr}\hat{a}^{\dagger}\hat{a}_{\rm dr} - f_{\rm dr}^{*}\hat{a}_{\rm dr}^{\dagger}\hat{a}\right) + \sum_p \hbar\omega_p\hat{a}_p^{\dagger}\hat{a}_p + i\hbar\sum_p\left(f_p\,\hat{a}^{\dagger}\hat{a}_p - f_p^{*}\hat{a}_p^{\dagger}\hat{a}\right) \\ &+ \sum_q \hbar\omega_q\hat{b}_q^{\dagger}\hat{b}_q + i\hbar\sum_q\left(f_q\,\hat{b}^{\dagger}\hat{b}_q - f_q^{*}\hat{b}_q^{\dagger}\hat{b}\right).\end{aligned} \tag{4.10}$$

4.3.2 Quantum Langevin Equations

Using the Hamiltonian given in Eq. (4.10), we can determine differential equations describing the optomechanical cavity by transforming the system into the Heisenberg picture. In this case, the equation of motion for an arbitrary quantum mechanical operator $\hat{o}$ will be given by the Heisenberg equation [287, 288]

$$\dot{\hat{o}} = \frac{i}{\hbar}[\hat{H},\hat{o}]. \tag{4.11}$$

In Appendix D, we use this formalism to determine the equations of motion for the photonic and phononic annihilation operators of the optomechanical cavity in the frame that rotates at the optical drive frequency $\omega_{\rm d}$ as

$$\dot{\hat{a}} = -\frac{\kappa}{2}\hat{a} + i\Delta_0\hat{a} + ig_0\left(\hat{b}^{\dagger}+\hat{b}\right)\hat{a} + \sqrt{\kappa_{\rm e}}\hat{a}_{\rm in} + \sqrt{\kappa_{\rm i}}\hat{a}_{\rm i}\,, \tag{4.12}$$

$$\dot{\hat{b}} = -\frac{\Gamma_{\rm m}}{2}\hat{b} - i\omega_{\rm m}\hat{b} + ig_0\hat{a}^{\dagger}\hat{a} + \sqrt{\Gamma_{\rm m}}\hat{b}_{\rm i}\,, \tag{4.13}$$

where $\hat{a}_{\rm i}$ and $\hat{b}_{\rm i}$ are the operators associated with the noise, both quantum and thermal, that enters into the optical and mechanical modes of our system (see Eqs. (D.18) and (D.19)). We have also introduced the detuning of the cavity drive frequency from resonance as $\Delta_0 = \omega_{\rm d} - \omega_{\rm c}$, with $\hat{a}_{\rm in}$ being the electric field amplitude that characterizes the number of photons arriving to the cavity per second due to this optical drive as $\hat{a}_{\rm in}^{\dagger}\hat{a}_{\rm in}$ (*i.e.* $\hat{a}_{\rm in}$ has units of $1/\sqrt{\rm s}$), such that the average optical power input by the external coupler is given by [150]

$$P_{\rm in} = \hbar\omega_{\rm d}\left\langle\hat{a}_{\rm in}^{\dagger}\hat{a}_{\rm in}\right\rangle. \tag{4.14}$$

As the optical microcavity in our system couples directly to the position of our mechanical resonator, we also find it convenient to use Eq. (2.17) to rewrite

Eqs. (4.12) and (4.13) in terms of $\hat{x}(t)$. We do this in Appendix D, where we find

$$\dot{\hat{a}} = -\frac{\kappa}{2}\hat{a} + i\Delta_0\hat{a} + iG\hat{x}\hat{a} + \sqrt{\kappa_\mathrm{e}}\hat{a}_\mathrm{in} + \sqrt{\kappa_\mathrm{i}}\hat{a}_\mathrm{i}\,, \tag{4.15}$$

$$\ddot{\hat{x}} + \Gamma_\mathrm{m}\dot{\hat{x}} + \omega_\mathrm{m}^2\hat{x} = \frac{1}{m}\left[\hat{F}_\mathrm{th} + \hat{F}_\mathrm{rp}\right], \tag{4.16}$$

with $\hat{F}_\mathrm{th}$ being the thermal Langevin force acting upon the mechanical resonator given by Eq. (D.39). Upon inspection of Eq. (4.16), we find that we have arrived at a quantized version of the equation of motion for the classical damped harmonic oscillator (see Eq. (2.7)), with the forcing function identified as $\hat{F}(t) = \hat{F}_\mathrm{th}(t) + \hat{F}_\mathrm{rp}(t)$. That is to say, the mechanical motion is driven by an intrinsic thermal force due to its environment, as well as a radiation pressure force exerted by photons in the cavity. Meanwhile, Eq. (4.15) represents the quantization of Eq. (3.16), including the external optical drives given by $\sqrt{\kappa_\mathrm{e}}\hat{a}_\mathrm{in}$ and $\sqrt{\kappa_\mathrm{i}}\hat{a}_\mathrm{i}$, as well as the optomechanical interaction term $iG\hat{x}\hat{a}$. Equations (4.12), (4.13), (4.15), and (4.16) are known collectively as the quantum Langevin equations (QLEs) of the optomechanical system and provide the basis for the quantum mechanical description given below.

4.3.3 Linearized Optomechanical Equations of Motion

Though Eqs. (4.15) and (4.16) give a full quantum description of a dispersively coupled optomechanical system, the nonlinear nature of these equations makes them difficult to solve analytically[5]. Fortunately, the optomechanical systems studied in this thesis can be treated by linearizing these equations of motion. This is performed by expressing each quantity of the system as a combination of a classical, steady state amplitude (denoted by an overhead bar) and its temporal fluctuations about this mean value (denoted by a δ in front of the quantity). Mathematically, this amounts to $\hat{a}(t) = \bar{a} + \delta\hat{a}(t)$, $\hat{a}_\mathrm{in}(t) = \bar{a}_\mathrm{in} + \delta\hat{a}_\mathrm{in}(t)$, $\hat{a}_\mathrm{i}(t) = \delta\hat{a}_\mathrm{i}(t)$, $\hat{x}(t) = \bar{x} + \delta\hat{x}(t)$, and $\hat{F}_\mathrm{th}(t) = \delta\hat{F}_\mathrm{th}(t)$. In the case of the optical fields, breaking down the operators in this way amounts to accounting for the quantum fluctuations $\delta\hat{a}_\mathrm{in}(t)$ about a strong classical input drive amplitude $\bar{a}_\mathrm{in}$, leading to a steady state cavity amplitude[6] $\bar{a}$ with fluctuations $\delta\hat{a}(t)$. Meanwhile, the radiation pressure force of this steady state

[5] See Section 4.5 for the treatment of a nonlinear *classical* optomechanical system.

[6] Note that while these steady state optical amplitudes are time-independent in our chosen rotating frame, they oscillate at the optical drive frequency in the lab frame.

cavity occupation acts to displace the mechanical resonator to a new equilibrium position $\bar{x}$, with $\delta\hat{x}(t)$ being the mechanical fluctuations about this point. Finally, we note that each of the noise quantities (*i.e.* $\hat{a}_{\rm i}(t)$ and $\hat{F}_{\rm th}(t)$) are comprised solely of a fluctuating term, which in general includes both thermal and quantum noise.

Inputting each of these relations into Eqs. (4.15) and (4.16), while keeping only terms to first order in the fluctuations, we linearize these equations of motion, resulting in

$$\delta\dot{\hat{a}} = -\frac{\kappa}{2}\delta\hat{a} + i\Delta\delta\hat{a} + iG\bar{a}\delta\hat{x} + \sqrt{\kappa_{\rm e}}\delta\hat{a}_{\rm in} + \sqrt{\kappa_{\rm i}}\delta\hat{a}_{\rm i}\,, \tag{4.17}$$

$$\delta\ddot{\hat{x}} + \Gamma_{\rm m}\delta\dot{\hat{x}} + \omega_{\rm m}^2\delta\hat{x} = \frac{\hbar G}{m}\left[\bar{a}^*\delta\hat{a} + \bar{a}\delta\hat{a}^\dagger\right] + \frac{\delta\hat{F}_{\rm th}}{m}, \tag{4.18}$$

with the steady-state values of $\hat{a}(t)$ and $\hat{x}(t)$ being

$$\bar{a} = \frac{\sqrt{\kappa_{\rm e}}\bar{a}_{\rm in}}{\kappa/2 - i\Delta}, \tag{4.19}$$

$$\bar{x} = \frac{\hbar G|\bar{a}|^2}{m\omega_{\rm m}^2}. \tag{4.20}$$

Note that we have also introduced a new optical drive detuning $\Delta = \Delta_0 + G\bar{x}$ to account for the static shift in cavity frequency due to the steady-state displacement of the mechanical equilibrium position.

In this linearized form, Eqs. (4.17) and (4.18) can now be Fourier transformed, resulting in the frequency representation of the cavity field and mechanical displacement fluctuations as

$$\delta\hat{a}(\omega) = \chi_{\rm c}(\omega)\left[iG\bar{a}\delta\hat{x}(\omega) + \sqrt{\kappa_{\rm e}}\delta\hat{a}_{\rm in}(\omega) + \sqrt{\kappa_{\rm i}}\delta\hat{a}_{\rm i}(\omega)\right], \tag{4.21}$$

$$\delta\hat{x}(\omega) = \chi_{\rm m}(\omega)\left[\hbar G\left\{\bar{a}^*\delta\hat{a}(\omega) + \bar{a}\delta\hat{a}^\dagger(\omega)\right\} + \delta\hat{F}_{\rm th}(\omega)\right]. \tag{4.22}$$

Here we have implicitly used the fact that for a given operator $\hat{o}$, we have $\hat{o}^\dagger(\omega) = [\hat{o}(-\omega)]^\dagger$ [150], as well as introduced the frequency-dependent susceptibilities of the optical cavity $\chi_{\rm c}(\omega)$ and mechanical resonator $\chi_{\rm m}(\omega)$ as

$$\chi_{\rm c}(\omega) = \frac{1}{\kappa/2 - i(\Delta + \omega)}, \tag{4.23}$$

$$\chi_{\rm m}(\omega) = \frac{1}{m\left(\omega_{\rm m}^2 - \omega^2 - i\omega\Gamma_{\rm m}\right)}. \tag{4.24}$$

Furthermore, we determine the frequency representation of the fluctuations in the cavity photon creation operator as

$$\delta\hat{a}^{\dagger}(\omega) = [\delta\hat{a}(-\omega)]^{\dagger} = \chi_{\mathrm{c}}^{*}(-\omega)\left[-iG\bar{a}^{*}\delta\hat{x}(\omega) + \sqrt{\kappa_{\mathrm{e}}}\delta\hat{a}_{\mathrm{in}}^{\dagger}(\omega) + \sqrt{\kappa_{\mathrm{i}}}\delta\hat{a}_{\mathrm{in}}^{\dagger}(\omega)\right]. \quad (4.25)$$

Note that $[\delta\hat{x}(-\omega)]^{\dagger} = \delta\hat{x}(\omega)$ due to the fact that $\bar{x}$ is real and $\hat{x}$ is a Hermitian operator.

By investigating these frequency-domain representations of $\delta\hat{a}(\omega)$ and $\delta\hat{x}(\omega)$, we can immediately recognize a number of optomechanical hallmarks. First, from Eq. (4.21), we see that the fluctuations in the cavity field are driven by the mechanical fluctuations (first term on the right-hand side), as well as the vacuum noise inputs $\sqrt{\kappa_{\mathrm{e}}}\delta\hat{a}_{\mathrm{in}}(\omega)$ and $\sqrt{\kappa_{\mathrm{i}}}\delta\hat{a}_{\mathrm{i}}(\omega)$. On the other hand, the mechanical fluctuations are driven by the thermal noise force $\delta\hat{F}_{\mathrm{th}}(\omega)$, while being manipulated by the fluctuations in the cavity amplitude due to their exerted radiation-pressure force. This latter phenomenon, known as dynamical optomechanical backaction, leads to the optomechanical damping and spring effects, whereby the delayed nature of the radiation pressure force exerted on the mechanical element (due to the finite lifetime of photons in the cavity) can manipulate both its damping rate and resonance frequency. Furthermore, this radiation-pressure-driven backaction effect can also act to actively cool (or amplify) the device's mechanical motion. These optomechanical effects will be the subject of the following two subsections.

4.3.4 Optomechanical Damping and Spring Effect

Using the linearized mathematical framework introduced in the previous subsection, we first look to characterize the optomechanical damping and spring effect of the system. This is done by inputting Eq. (4.21) into Eq. (4.22), resulting in

$$\begin{aligned}\delta\hat{x}(\omega) = \chi_{\mathrm{eff}}(\omega)\Bigg[\delta\hat{F}_{\mathrm{th}}(\omega) + \hbar G\Big\{&\bar{a}^{*}\chi_{\mathrm{c}}(\omega)\left[\sqrt{\kappa_{\mathrm{e}}}\delta\hat{a}_{\mathrm{in}}(\omega) + \sqrt{\kappa_{\mathrm{i}}}\delta\hat{a}_{\mathrm{i}}(\omega)\right] \\ &+ \chi_{\mathrm{c}}^{*}(-\omega)\bar{a}\left[\sqrt{\kappa_{\mathrm{e}}}\delta\hat{a}_{\mathrm{in}}^{\dagger}(\omega) + \sqrt{\kappa_{\mathrm{i}}}\delta\hat{a}_{\mathrm{i}}^{\dagger}(\omega)\right]\Big\}\Bigg],\end{aligned} \quad (4.26)$$

with $\chi_{\rm eff}(\omega)$ being the effective mechanical susceptibility defined as [80, 150, 289–291]

$$\begin{aligned}\chi_{\rm eff}^{-1}(\omega) &= \chi_{\rm m}^{-1}(\omega) - i\hbar G^2|\bar{a}|^2\left[\chi_{\rm c}(\omega) - \chi_{\rm c}^*(-\omega)\right] \\ &\equiv m\left[(\omega_{\rm m}+\delta\omega_{\rm m})^2 - \omega - i\omega\left(\Gamma_{\rm m}+\delta\Gamma_{\rm m}\right)\right] \\ &\approx m\left[\omega_{\rm m}^2 + 2\omega_{\rm m}\delta\omega_{\rm m} - \omega^2 - i\omega\Gamma_{\rm m} - i\omega\delta\Gamma_{\rm m}\right],\end{aligned} \tag{4.27}$$

where in the last line we have assumed that $\delta\omega_{\rm m} \ll \omega_{\rm m}$. From this effective susceptibility, we can then extract the optomechanically induced shift in the mechanical resonance frequency, or optomechanical spring effect, as

$$\begin{aligned}\delta\omega_{\rm m} &= -\frac{\hbar G^2|\bar{a}|^2}{2m\omega_{\rm m}}{\rm Re}\left\{i\left[\chi_{\rm c}(\omega_{\rm m}) - \chi_{\rm c}^*(-\omega_{\rm m})\right]\right\} \\ &= 2\bar{g}^2\Delta\left(\frac{\kappa^2}{4}+\Delta^2-\omega_{\rm m}^2\right)|\chi_{\rm c}(\omega_{\rm m})|^2|\chi_{\rm c}(-\omega_{\rm m})|^2 \\ &= \bar{g}^2\left[\frac{\Delta+\omega_{\rm m}}{(\Delta+\omega_{\rm m})^2+\kappa^2/4} + \frac{\Delta-\omega_{\rm m}}{(\Delta-\omega_{\rm m})^2+\kappa^2/4}\right],\end{aligned} \tag{4.28}$$

as well as the shift in the mechanical damping rate, or optomechanical damping, as

$$\begin{aligned}\delta\Gamma_{\rm m} &= \frac{\hbar G^2|\bar{a}|^2}{m\omega_{\rm m}}{\rm Im}\left\{i\left[\chi_{\rm c}(\omega_{\rm m}) - \chi_{\rm c}^*(-\omega_{\rm m})\right]\right\} \\ &= -4\bar{g}^2\Delta\omega_{\rm m}\kappa|\chi_{\rm c}(\omega_{\rm m})|^2|\chi_{\rm c}(-\omega_{\rm m})|^2 \\ &= \bar{g}^2\left[\frac{\kappa}{(\Delta+\omega_{\rm m})^2+\kappa^2/4} - \frac{\kappa}{(\Delta-\omega_{\rm m})^2+\kappa^2/4}\right].\end{aligned} \tag{4.29}$$

Here we have introduced $\bar{g} = g_0\sqrt{\bar{N}}$ as the cavity-enhanced optomechanical coupling rate, with $\bar{N} = |\bar{a}|^2$ being the average number of coherent photons (originating from the drive field) that are confined to the optical cavity. Note that we have also taken $\omega \approx \omega_{\rm m}$ in Eqs. (4.28) and (4.29), as we are only concerned with effects near mechanical resonance.

As the devices we study in this thesis exist in the non-sideband-resolved (non-SBR) regime, where the linewidth of the optical cavity is much larger than the mechanical frequency of the system, we are interested in determining how the optomechanical spring effect and damping are simplified in this limit. Inputting the condition $\kappa \gg \omega_{\rm m}$ into Eqs. (4.28) and (4.29), we find the optomechanical spring

effect and damping of a non-SBR cavity as [150]

$$\delta\omega_{\mathrm{m}} = \frac{2\bar{g}^2\Delta}{\Delta^2 + \kappa^2/4}, \tag{4.30}$$

$$\delta\Gamma_{\mathrm{m}} = -\frac{4\bar{g}^2\Delta\omega_{\mathrm{m}}\kappa}{(\Delta^2 + \kappa^2/4)^2}. \tag{4.31}$$

Note the implicit detuning dependence of $\bar{g} = g_0\sqrt{\bar{N}}$ due to the fact that $\bar{N}$ is a function of detuning. From Eqs. (4.30) and (4.31), we can also determine the extrema for the optomechanical spring effect (damping) in the non-SBR regime, which are located at $\Delta_{\mathrm{ex}} = \pm\kappa/2\sqrt{3}$ ($\Delta_{\mathrm{ex}} = \pm\kappa/2\sqrt{5}$), with the extremal values corresponding to these detunings given by $\delta\omega_{\mathrm{m}}^{\mathrm{ex}} = \pm\sqrt{3}\bar{g}^2/\kappa$ ($\delta\Gamma_{\mathrm{m}}^{\mathrm{ex}} = \mp 200\omega_{\mathrm{m}}\bar{g}^2/9\sqrt{5}\kappa^2$).

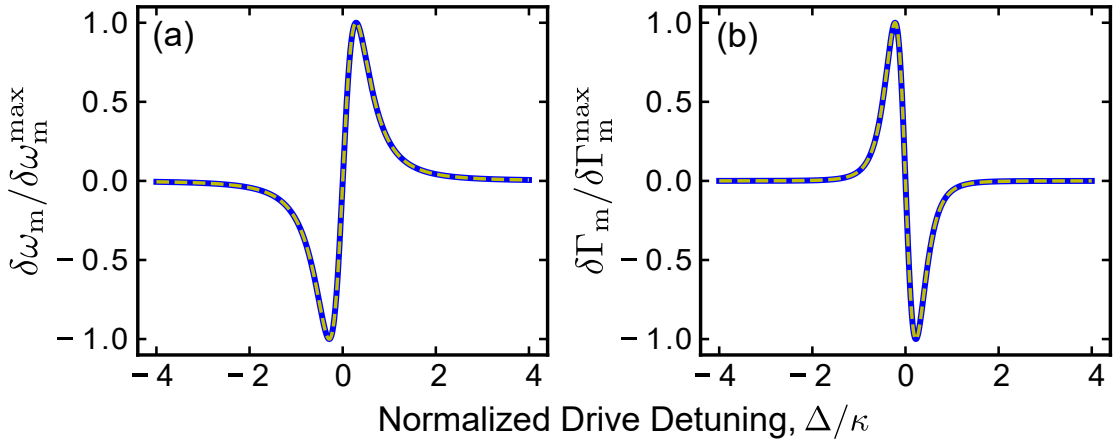

Figure 4.1: Plot of the optomechanical (a) spring effect and (b) damping as a function of normalized cavity drive detuning Δ/κ for $\kappa/\omega_{\mathrm{m}} = 100$, which is on the order of the SBR ratio found in our devices. The solid blue line indicates each quantity calculated using the exact representations given in Eqs. (4.28) and (4.29), while the dashed yellow lines show the approximations in the non-SBR regime according to Eqs. (4.30) and (4.31). Here we have normalized these effects by their maximal values, $\delta\omega_{\mathrm{m}}^{\mathrm{max}}$ and $\delta\Gamma_{\mathrm{m}}^{\mathrm{max}}$, which are taken as the positive values of $\delta\omega_{\mathrm{m}}^{\mathrm{ex}}$ and $\delta\Gamma_{\mathrm{m}}^{\mathrm{ex}}$, respectively.

In Fig. 4.1, we plot the optomechanical spring effect and damping versus detuning in the non-SBR regime using both the exact expression given by Eqs. (4.28) and (4.29), as well as the approximate ones given in Eqs. (4.30) and (4.31), demonstrating excellent agreement between these two cases for $\kappa/\omega_{\mathrm{m}} = 100$. Here we see that there is an increase in the mechanical damping rate for a red-detuned optical

pump, while for a blue-detuned pump, the damping rate decreases. This damping process is mirrored by the optomechanical spring effect, which results in a decrease (increase) in the resonance frequency of the mechanical oscillator for a red (blue) detuned pump, such that these two dynamical backaction effects obey the Kramers-Kronig relations [292]. Finally, for a resonantly driven optical cavity, each of these dynamical backaction effects vanish (as can be seen mathematically by setting $\Delta = 0$ in Eqs. (4.28) and (4.29)).

4.3.5 Optomechanical Cooling

As one can see from Fig. 4.1, by detuning an optical pump to the lower frequency (red) side of the optical cavity, the radiation-pressure force of the optomechanical interaction can be used to increase the damping rate of the mechanical resonator. In a quantum mechanical picture, this effect can be viewed as energy being extracted from the resonator via anti-Stokes scattering, whereby mechanical phonons are annihilated in order to promote detuned drive photons into the higher energy states of the optical cavity. This process can therefore be used to effectively cool the motion of the mechanical resonator.

To investigate this optomechanical cooling mechanism, we begin by determining the symmetrized two-sided power spectral density or PSD (see Appendix A) of the mechanical displacement $S_{xx}(\omega)$ in the presence of optomechanical effects, which quantifies the mechanical fluctuations of the system and can be found using the relation [151]

$$S_{xx}(\omega) = \frac{1}{2\pi}\int_{-\infty}^{\infty} \langle \delta\hat{x}(\omega)\delta\hat{x}(\omega')\rangle \, d\omega'. \tag{4.32}$$

This PSD is determined by first solving for the position fluctuation correlator under the integral in Eq. (4.32), which is found using Eq. (4.26) as

$$\begin{aligned}
&\langle \delta\hat{x}(\omega)\delta\hat{x}(\omega')\rangle = \chi_{\rm eff}(\omega)\chi_{\rm eff}(\omega')\Big[\langle \delta\hat{F}_{\rm th}(\omega)\delta\hat{F}_{\rm th}(\omega')\rangle \\
&+ \hbar^2 G^2 \bar{N}\chi_{\rm c}(\omega)\chi_{\rm c}^*(-\omega')\left\{\kappa_{\rm e}\left\langle \delta\hat{a}_{\rm in}(\omega)\delta\hat{a}_{\rm in}^\dagger(\omega')\right\rangle + \kappa_{\rm i}\left\langle \delta\hat{a}_{\rm i}(\omega)\delta\hat{a}_{\rm i}^\dagger(\omega')\right\rangle\right\}\Big] \\
&= \chi_{\rm eff}(\omega)\chi_{\rm eff}(\omega')2\pi\left[\hbar\omega m\Gamma_{\rm m}\coth\left(\frac{\hbar\omega}{2k_{\rm B}T}\right) + \hbar^2 G^2\bar{N}\kappa\chi_{\rm c}(\omega)\chi_{\rm c}^*(-\omega')\right]\delta(\omega+\omega'),
\end{aligned} \tag{4.33}$$

where we have input the Markovian noise correlators given by Eqs. (E.13) and (E.16) of Appendix E. Putting Eq. (4.33) into Eq. (4.32), while using the fact that

$\chi_{\rm eff}(-\omega) = \chi^*_{\rm eff}(\omega)$, we then find

$$S_{xx}(\omega) = |\chi_{\rm eff}(\omega)|^2 \left[S^{\rm th}_{FF}(\omega) + S^{\rm rp}_{FF}(\omega)\right], \tag{4.34}$$

where

$$S^{\rm th}_{FF}(\omega) = \hbar\omega m\Gamma_{\rm m} \coth\left(\frac{\hbar\omega}{2k_{\rm B}T}\right), \tag{4.35}$$

is the spectral density of the thermal force given in Eq. (4.35) (see Appendix E) and $S^{\rm rp}_{FF}(\omega) = \hbar^2 G^2 S_{NN}(\omega)$ is the radiation-pressure force spectral density, expressed in terms of the cavity photon number PSD [203, 293]

$$S_{NN}(\omega) = \bar{N}\kappa|\chi_{\rm c}(\omega)|^2 = \frac{\bar{N}\kappa}{(\Delta+\omega)^2 + \kappa^2/4}. \tag{4.36}$$

Using the spectral density function given in Eq. (4.34), we can determine the mean-squared value of the mechanical displacement fluctuations from the relation [151]

$$\langle \delta\hat{x}^2 \rangle = \frac{1}{2\pi}\int_{-\infty}^{\infty} S_{xx}(\omega) d\omega. \tag{4.37}$$

To perform this integral, we use the approximation

$$|\chi_{\rm eff}(\omega)|^2 \approx \frac{\pi}{2m^2\omega_{\rm m}^2\Gamma_{\rm tot}}\left[\delta(\omega-\omega_{\rm m}) + \delta(\omega+\omega_{\rm m})\right], \tag{4.38}$$

where $\Gamma_{\rm tot} = \Gamma_{\rm m} + \delta\Gamma_{\rm m}$ is the total mechanical damping rate, including both the intrinsic mechanical damping and optomechanical effects, and we have again assumed $\delta\omega_{\rm m} \ll \omega_{\rm m}$. The approximation given by Eq. (4.38) is valid for a high-Q mechanical resonator (*i.e.* $Q_{\rm m} = \omega_{\rm m}/\Gamma_{\rm m} \gg 1$), since the majority of the mechanical displacement spectrum is located near $\omega \approx \pm\omega_{\rm m}$. Inputting this approximation into Eq. (4.37) and evaluating the integral we find

$$\langle \delta\hat{x}^2 \rangle = \frac{x_{\rm zpf}^2}{\Gamma_{\rm tot}}\left\{(2\bar{n}_{\rm th}+1)\Gamma_{\rm m} + g_0^2\left[S_{NN}(\omega_{\rm m}) + S_{NN}(-\omega_{\rm m})\right]\right\}, \tag{4.39}$$

where we have used the relation $\coth(\hbar\omega_{\rm m}/2k_{\rm B}T) = 2\bar{n}_{\rm th}+1$. Comparing Eq. (4.39) to the expected expression for the mean-squared displacement obtained by taking the square of Eq. (2.106), we determine the average phonon occupancy $\langle n \rangle$ of a mechanical resonator subject to a radiation-pressure optomechanical force to be

$$\langle n \rangle = \frac{(2\bar{n}_{\rm th}+1)\Gamma_{\rm m} + g_0^2\left[S_{NN}(\omega_{\rm m}) + S_{NN}(-\omega_{\rm m})\right]}{2\Gamma_{\rm tot}} - \frac{1}{2}. \tag{4.40}$$

We note that using the identity [203, 290, 293]

$$\begin{aligned}\delta\Gamma_{\mathrm{m}} &= \frac{x_{\mathrm{zpf}}^2}{\hbar^2}\left[S_{FF}^{\mathrm{rp}}(\omega_{\mathrm{m}}) - S_{FF}^{\mathrm{rp}}(-\omega_{\mathrm{m}})\right] \\ &= g_0^2\left[S_{NN}(\omega_{\mathrm{m}}) - S_{NN}(-\omega_{\mathrm{m}})\right],\end{aligned} \tag{4.41}$$

we can recast Eq. (4.40) into the familiar rate equation form [150, 293, 294]

$$\langle n\rangle = \frac{\bar{n}_{\mathrm{th}}\Gamma_{\mathrm{m}} + \bar{n}_{\mathrm{min}}^{\mathrm{rp}}\delta\Gamma_{\mathrm{m}}}{\Gamma_{\mathrm{tot}}}. \tag{4.42}$$

This allows us to identify the minimum attainable average phonon occupancy set by the shot noise generated via photons impinging upon the mechanical resonator as [150, 290, 293]

$$\begin{aligned}\bar{n}_{\mathrm{min}}^{\mathrm{rp}} &= \left[S_{FF}^{\mathrm{rp}}(\omega_{\mathrm{m}})/S_{FF}^{\mathrm{rp}}(-\omega_{\mathrm{m}}) - 1\right]^{-1} \\ &= \left[S_{NN}(\omega_{\mathrm{m}})/S_{NN}(-\omega_{\mathrm{m}}) - 1\right]^{-1} \\ &= -\frac{\kappa^2/4 + (\Delta+\omega_{\mathrm{m}})^2}{4\Delta\omega_{\mathrm{m}}}.\end{aligned} \tag{4.43}$$

As expected, if we sever the connection to the optomechanical bath (*i.e.*, set $G = g_0 = 0$, which results in $\delta\Gamma_{\mathrm{m}} = 0$ in Eq. (4.42)), the mechanical resonator thermalizes to its environmental bath such that $\langle n\rangle = \bar{n}_{\mathrm{th}}$. Finally, we note that in the high-temperature (classical) limit, we can approximate $\langle n\rangle$ and $\bar{n}_{\mathrm{th}}$ according to Eq. (2.77), allowing us to determine the effective mechanical mode temperature in this regime as [150]

$$T_{\mathrm{m}} = T_{\mathrm{b}}\frac{\Gamma_{\mathrm{m}}}{\Gamma_{\mathrm{tot}}}, \tag{4.44}$$

where we have assumed a bath temperature $T_{\mathrm{b}} \gg \hbar\omega_{\mathrm{m}}\bar{n}_{\mathrm{min}}^{\mathrm{rp}}\delta\Gamma_{\mathrm{m}}/k_{\mathrm{B}}\Gamma_{\mathrm{m}}$.

The quantity in Eq. (4.43) describes the minimum attainable phonon occupation of the mechanical resonator using this optomechanical cooling mechanism, which can be reached if $\delta\Gamma_{\mathrm{m}}$ is large enough that $\Gamma_{\mathrm{tot}} \approx \delta\Gamma_{\mathrm{m}}$ and $\bar{n}_{\mathrm{th}}\Gamma_{\mathrm{m}} \ll \bar{n}_{\mathrm{min}}^{\mathrm{rp}}\delta\Gamma_{\mathrm{m}}$ for a given drive detuning Δ. In this sense, Eqs. (4.40) and (4.42) do not include effects that would arise when experimentally performing optomechanical cooling of the mechanical resonator, such as the inevitable heating due to photon absorption [290, 294]. We further point out that since Eq. (4.43) is a function of Δ, it will be minimized for the optimal drive detuning $\Delta_{\mathrm{min}} = -\sqrt{\kappa^2/4 + \omega_{\mathrm{m}}^2}$ that minimizes Eq. (7.28). In the non-SBR regime ($\kappa \gg \omega_{\mathrm{m}}$), we find $\Delta_{\mathrm{min}} \approx -\kappa/2$, leading to

$\bar{n}_{\mathrm{min}}^{\mathrm{rp}} \approx \kappa/4\omega_{\mathrm{m}} \gg 1$. Therefore, it is not possible to cool the mechanical resonator into its ground state (*i.e.* to an average occupancy of less than a single phonon) in this case [150]. It is important to note that this result only holds true for standard, dispersively coupled cavities, as it has been shown that ground state cooling can in theory be achieved using non-SBR, dissipatively coupled optomechanical systems [283–285]. Furthermore, in the opposite limit of a SBR cavity ($\kappa \ll \omega_{\mathrm{m}}$), we find that $\bar{n}_{\mathrm{min}}^{\mathrm{rp}} \approx (\kappa/4\omega_{\mathrm{m}})^2 < 1$ at $\Delta_{\mathrm{min}} \approx -\omega_{\mathrm{m}}$, such that dispersive ground state cooling is possible in this regime [150, 293].

4.4 Optomechanical Detection

In this section, we consider the optical detection protocols that we use to measure the optical signal recollected by the tapered fiber of our measurement system. Specifically, we consider the direct detection and homodyne measurement schemes whose experimental implementations are discussed in Section 5.4.3, including all inefficiencies and amplifications associated with each technique.

4.4.1 Detection Inefficiencies

In any realistic detection scheme, inefficiencies will arise due to the imperfect implementation of the intended setup, acting to contaminate the performed measurement. To determine how such inefficiencies propagate through our optical detection system, we begin by considering the optical field output directly from the cavity into an external coupler. Using the input-output relation determined in Appendix D, we find this output field amplitude in terms of the input field as

$$\hat{a}_{\mathrm{out}}(t) = \hat{a}_{\mathrm{in}}(t) - \sqrt{\kappa_{\mathrm{e}}}\hat{a}(t). \tag{4.45}$$

Continuing with our treatment of a linearized optomechanical system, we break this output optical field into its steady state amplitude and fluctuating parts as $\hat{a}_{\mathrm{out}}(t) = \bar{a}_{\mathrm{out}} + \delta\hat{a}_{\mathrm{out}}(t)$. This relation can easily be Fourier transformed to $\hat{a}_{\mathrm{out}}(\omega) = \bar{a}_{\mathrm{out}} + \delta\hat{a}_{\mathrm{out}}(\omega)$ where we find

$$\bar{a}_{\mathrm{out}} = \bar{a}_{\mathrm{in}} - \sqrt{\kappa_{\mathrm{e}}}\bar{a} = \bar{a}_{\mathrm{in}}\left(1 - \frac{\kappa_{\mathrm{e}}}{\kappa/2 - i\Delta}\right), \tag{4.46}$$

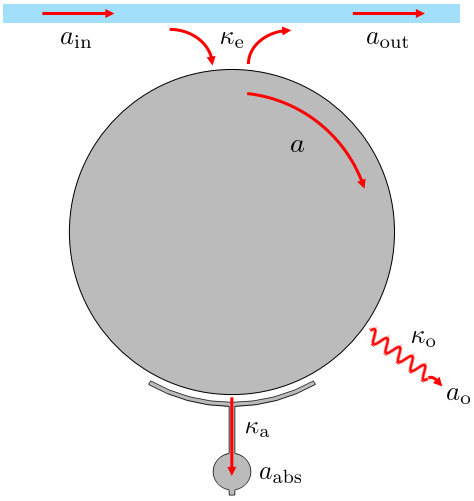

Figure 4.2: Schematic illustrating the flow of the optical field through an optomechanical cavity. Figure reproduced from Ref. [295]. © 2019 American Physical Society.

and

$$\begin{aligned}\delta\hat{a}_{\mathrm{out}}(\omega) &= \delta\hat{a}_{\mathrm{in}}(\omega) - \sqrt{\kappa_{\mathrm{e}}}\delta\hat{a}(\omega) \\ &= \left[1 - \kappa_{\mathrm{e}}\chi_{\mathrm{c}}(\omega)\right]\delta\hat{a}_{\mathrm{i}}(\omega) - \sqrt{\kappa_{\mathrm{e}}\kappa_{\mathrm{i}}}\delta\hat{a}_{\mathrm{in}}(\omega) - i\sqrt{\kappa_{\mathrm{e}}}\chi_{\mathrm{c}}(\omega)G\bar{a}\delta\hat{x}(\omega),\end{aligned} \tag{4.47}$$

using the input-output relation given in Eq. (4.45). Here we encounter the first inefficiency associated with the detection system as optical losses occurring within the cavity at a rate $\kappa_{\mathrm{i}} = \kappa_{\mathrm{a}} + \kappa_{\mathrm{o}}$, where κ_{a} and κ_{o} are the optical damping rates associated with photon absorption in the mechanical resonator and all other loss mechanisms.

To trace these optical losses, we consider the classical flow of electromagnetic power through the cavity as illustrated in Fig. 4.2. Using Eq. (4.45), we first determine the power recollected by the external waveguide (and subsequently sent to the detection apparatus) in terms of the power P_{in} input to the system (see Eq. (4.14)) as

$$P_{\mathrm{out}} = \hbar\omega_{\mathrm{d}}|\bar{a}_{\mathrm{out}}|^2 = P_{\mathrm{in}}\left[1 - \frac{\kappa_{\mathrm{e}}\kappa_{\mathrm{i}}}{\Delta^2 + (\kappa/2)^2}\right]. \tag{4.48}$$

Here we immediately see that a fraction of the power input to the cavity is dissipated as either power absorbed by the mechanical resonator according to

$$P_{\mathrm{abs}} = \hbar\omega_{\mathrm{d}}|\bar{a}_{\mathrm{abs}}|^2 = P_{\mathrm{in}}\frac{\kappa_{\mathrm{e}}\kappa_{\mathrm{a}}}{\Delta^2 + (\kappa/2)^2}, \tag{4.49}$$

or lost via other cavity dissipation channels (see Section 3.4) as

$$P_{\mathrm{o}} = \hbar\omega_{\mathrm{d}}|\bar{a}_{\mathrm{o}}|^2 = P_{\mathrm{in}}\frac{\kappa_{\mathrm{e}}\kappa_{\mathrm{o}}}{\Delta^2 + (\kappa/2)^2}, \tag{4.50}$$

where $\bar{a}_{\mathrm{abs}} = \sqrt{\kappa_{\mathrm{a}}}\bar{a}$ and $\bar{a}_{\mathrm{o}} = \sqrt{\kappa_{\mathrm{o}}}\bar{a}$ are the steady-state field amplitudes corresponding to these loss mechanisms. Note that Eqs. (4.48)–(4.50) obey the conservation of energy in the sense that $P_{\mathrm{in}} = P_{\mathrm{out}} + P_{\mathrm{abs}} + P_{\mathrm{o}}$.

As per the fluctuation dissipation theorem [202, 203], we also find that this loss of classical signal amplitude will be accompanied by an influx of vacuum noise in the quantum fluctuations of the signal (*i.e.* the first and second terms in the second line of Eq. (4.47)), which acts to contaminate the measurement. In fact, all of the inefficiencies of the optical detection system will behave this way, simultaneously reducing the classical amplitude of the transmitted signal, while adding quantum vacuum noise at each junction. For the detection schemes considered here, these signal losses will accumulate in such a way that we can treat all inefficiencies as a single effective beamsplitter (BS) with amplitude transmissivity $\sqrt{\eta}$ and an effective input vacuum noise of $\delta\hat{a}_{\mathrm{vac}}$ that obeys the correlators given by Eqs. (E.7), (E.8) and (E.13) of Appendix E [110]. Here η is the power transmission efficiency of the entire detection system (see Section 5.4.4) including all inefficiencies due to losses in the optical cavity and throughout the detection circuit, as well as the quantum efficiency of the photodetector (PD). With this approach, the signal transmitted through the detection circuit will then be given by

$$\hat{a}_{\mathrm{t}}(t) = \sqrt{\eta}\hat{a}_{\mathrm{out}}(t) + \sqrt{1-\eta}\delta\hat{a}_{\mathrm{vac}}(t), \tag{4.51}$$

with the classical power fluence through the circuit given by

$$P_{\mathrm{t}} = \hbar\omega_{\mathrm{d}}\langle\hat{a}_{\mathrm{t}}^{\dagger}\hat{a}_{\mathrm{t}}\rangle = \eta\hbar\omega_{\mathrm{d}}\langle\hat{a}_{\mathrm{out}}^{\dagger}\hat{a}_{\mathrm{out}}\rangle = \eta P_{\mathrm{out}}. \tag{4.52}$$

4.4.2 Direct Detection

Direct detection is the simplest technique that can be used to measure the output field from an optomechanical cavity. For this scheme, one simply directs the output field to a PD, which will in turn convert the optical field into a measurable

voltage[7] given by

$$v_{\mathrm{d}}(t) = H_{\mathrm{d}}\hat{a}_{\mathrm{d}}^{\dagger}(t)\hat{a}_{\mathrm{d}}(t), \tag{4.53}$$

where $\hat{a}_{\mathrm{d}}(t) = \sqrt{\eta_{\mathrm{d}}}\hat{a}_{\mathrm{out}}(t) + \sqrt{1-\eta_{\mathrm{d}}}\delta\hat{a}_{\mathrm{vac}}(t)$ is the optical field detected by the photodiode according to Eq. (4.51), including all inefficiencies throughout the detection system via the total power transmission coefficient η_{d}, while H_{d} is the gain of the direct detection system (which includes the internal gain of the PD, as well as any subsequent electronic gain). Continuing with our linearized approach, we break down the detected optical field into $\hat{a}_{\mathrm{d}}(t) = \bar{a}_{\mathrm{d}} + \delta\hat{a}_{\mathrm{d}}(t)$, where

$$\bar{a}_{\mathrm{d}} = \sqrt{\eta_{\mathrm{d}}}\bar{a}_{\mathrm{out}}, \tag{4.54}$$

$$\delta\hat{a}_{\mathrm{d}}(t) = \sqrt{\eta_{\mathrm{d}}}\delta\hat{a}_{\mathrm{out}}(t) + \sqrt{1-\eta_{\mathrm{d}}}\delta\hat{a}_{\mathrm{vac}}(t). \tag{4.55}$$

Using this notation, we can similarly express the measured direct detection voltage as a combination of its steady state and time varying parts as $v_{\mathrm{d}}(t) = \bar{v}_{\mathrm{d}} + \delta\hat{v}_{\mathrm{d}}(t)$, which can in practice be separated using a bias tee with a cutoff frequency $\omega_{\mathrm{co}} \ll \omega_{\mathrm{m}}$.

We first look at the steady state portion of this detected voltage, which is given by

$$\bar{v}_{\mathrm{d}} = H_{\mathrm{d}}^{\mathrm{DC}}\eta_{\mathrm{d}}|\bar{a}_{\mathrm{out}}|^2 = H_{\mathrm{d}}^{\mathrm{DC}}\eta_{\mathrm{d}}|\bar{a}_{\mathrm{in}}|^2\mathcal{T}(\Delta), \tag{4.56}$$

where

$$\mathcal{T}(\Delta) = 1 - \kappa_{\mathrm{e}}\kappa_{\mathrm{i}}|\chi_{\mathrm{c}}(0)| = 1 - \frac{\kappa_{\mathrm{e}}\kappa_{\mathrm{i}}}{\Delta^2 + \kappa^2/4} \tag{4.57}$$

is the transmission coefficient of the optical cavity. Therefore, we can extract information about the properties of the optical cavity by observing the low frequency portion of the measured voltage. Note that we have introduced the new gain factor $H_{\mathrm{d}}^{\mathrm{DC}}$ to account for the fact that once split, the low frequency and high frequency portions of the voltage signal may be subject to different amplification chains, though generally the ratio $H_{\mathrm{d}}^{\mathrm{DC}}/H_{\mathrm{d}}$ is known. Furthermore, we note that the measurement-dependent prefactor $H_{\mathrm{d}}^{\mathrm{DC}}\eta_{\mathrm{d}}|\bar{a}_{\mathrm{in}}|^2$ in Eq. (4.56) can be removed by normalizing the measured voltage by a far off-resonant value, where $\Delta \gg \kappa$ such that $\mathcal{T}(\Delta \gg \kappa) \approx 1$ and $\bar{v}_{\mathrm{d}} \approx H_{\mathrm{d}}^{\mathrm{DC}}\eta_{\mathrm{d}}|\bar{a}_{\mathrm{in}}|^2$.

[7] The measurable could also be an electrical current depending on the PD, but this could be converted to a voltage by introducing a resistor.

The high-frequency portion of the detected signal is then given by

$$\delta\hat{v}_{\mathrm{d}}(t) = H_{\mathrm{d}}\left[\bar{a}_{\mathrm{d}}^{*}\delta\hat{a}_{\mathrm{d}}(t) + \bar{a}_{\mathrm{d}}\delta\hat{a}_{\mathrm{d}}^{\dagger}(t)\right], \tag{4.58}$$

where we have neglected the small $\delta\hat{a}_{\mathrm{d}}^{\dagger}(t)\delta\hat{a}_{\mathrm{d}}(t)$ term. This fluctuating portion of the direct detection voltage measures the amplitude quadrature of the fluctuations in the field $\hat{a}_{\mathrm{d}}(t)$ reaching the PD, and therefore, $\delta\hat{a}_{\mathrm{out}}(t)$ via Eq. (4.55). In this linearized form, we can Fourier transform the signal, resulting in

$$\delta\hat{v}_{\mathrm{d}}(\omega) = H_{\mathrm{d}}\left[\bar{a}_{\mathrm{d}}^{*}\delta\hat{a}_{\mathrm{d}}(\omega) + \bar{a}_{\mathrm{d}}\delta\hat{a}_{\mathrm{d}}^{\dagger}(\omega)\right]. \tag{4.59}$$

In order to quantify the fluctuations of this Fourier-transformed voltage signal, we look to calculate its PSD (see Appendix A) using

$$S_{vv}^{\mathrm{d}}(\omega) = \frac{1}{2\pi}\int_{-\infty}^{\infty}\langle\delta\hat{v}_{\mathrm{d}}(\omega)\delta\hat{v}_{\mathrm{d}}(\omega')\rangle\, d\omega'. \tag{4.60}$$

Inputting Eq. (4.59) into Eq. (4.60), one finds [145]

$$S_{vv}^{\mathrm{d}}(\omega) = \alpha_{\mathrm{d}}(\omega)S_{xx}^{\mathrm{tot}}(\omega) + S_{vv}^{\mathrm{d,imp}}(\omega), \tag{4.61}$$

where $S_{vv}^{\mathrm{d,imp}}(\omega)$ is the technical noise floor associated with our detection electronics (detector dark noise, electronic noise, etc.), while $\alpha_{\mathrm{d}}(\omega)$ is the transduction coefficient that relates the total optically measured displacement PSD

$$S_{xx}^{\mathrm{tot}}(\omega) = S_{xx}^{\mathrm{int}}(\omega) + S_{xx}^{\mathrm{add}}(\omega) \tag{4.62}$$

to the direct detection voltage PSD. As the transduction coefficient $\alpha_{\mathrm{d}}(\omega)$ contains contributions from the optical cavity, the detection circuit, and the measurement electronics, it is a complicated function of frequency and cavity detuning[8], such that it is difficult to determine *a priori*. Therefore, this parameter is generally determined for a given set of experimental conditions using a calibration technique, such as thermomechanical calibration [145] (see Section 6.4.3) or phase calibration [59, 296].

In Eq. (4.62), we have expressed the total measured displacement $S_{xx}^{\mathrm{tot}}(\omega)$ as a combination of its contributions due to the intrinsic motion of the mechanical

[8]For direct detection, α_{d} is maximized versus cavity detuning for $\Delta \sim \kappa/2$, where the slope in the cavity resonance is largest [63].

resonator $S_{xx}^{\mathrm{int}}(x) = |\chi_{\mathrm{eff}}(\omega)|^2 S_{FF}^{\mathrm{th}}(\omega)$, which is driven by the thermal and quantum noise of the bath, and the added noise PSD due to the optical measurement $S_{xx}^{\mathrm{add}}(\omega)$ [150, 203]. This added noise is further broken into two parts: a broadband imprecision noise floor $S_{xx}^{\mathrm{imp}}(\omega)$ and a back-action force spectrum $S_{FF}^{\mathrm{ba}}(\omega)$, which is transduced into excess mechanical motion via $S_{xx}^{\mathrm{ba}}(\omega) = |\chi_{\mathrm{eff}}(\omega)|^2 S_{FF}^{\mathrm{ba}}(\omega)$ [150, 203]. We note here that while $S_{xx}^{\mathrm{ba}}(\omega)$ corresponds to noise due to a true physical displacement of the resonator, $S_{xx}^{\mathrm{imp}}(\omega)$ enters the system as an apparent displacement arising from an increase to the noise floor of the measurement. These added noise terms are caused by a variety of sources, including photon shot noise, laser noise, optical heating of the mechanics, etc., and obey the modified Heisenberg uncertainty relation

$$S_{xx}^{\mathrm{imp}}(\omega) S_{FF}^{\mathrm{ba}}(\omega) \geq \hbar^2/4, \tag{4.63}$$

with equality corresponding to the limit set by the fundamental quantum noise associated with photon number fluctuations in the measurement signal [150, 202, 203]. Considering only these quantum noise processes, the imprecision and back-action noise spectra are given by [297]

$$S_{xx}^{\mathrm{imp}}(\omega) = \frac{\hbar\omega_{\mathrm{d}}}{8\eta_{\mathrm{d}} G^2 P_{\mathrm{in}}} \left(\frac{\Delta^2 + \kappa^2/4}{\kappa}\right)^2 \left[1 + \omega^2 \frac{\omega^2 + \kappa^2/4 - 2\Delta^2}{(\Delta^2 + \kappa^2/4)^2 + \omega^2\kappa^2/4}\right], \tag{4.64}$$

$$S_{FF}^{\mathrm{ba}}(\omega) = \frac{\hbar G^2 P_{\mathrm{in}}}{2\omega_{\mathrm{d}}} \left(\frac{\kappa^2}{\kappa^2/4 + \Delta^2}\right) \left[\frac{1}{\kappa^2/4 + (\Delta - \omega)^2} + \frac{1}{\kappa^2/4 + (\Delta + \omega)^2}\right]. \tag{4.65}$$

Here we see that the fundamental imprecision noise (associated with photon shot noise) scales inversely with power input to the cavity, as well as the detection efficiency η_{d}. Unfortunately, any attempt to reduce this imprecision shot noise by increasing the optical power input to the cavity is met with a commensurate increase in the backaction noise as the number of photons in the cavity grows. Hence, there is an optimal power where the total added optical measurement noise $S_{xx}^{\mathrm{add}}(\omega)$ is minimized, which we will we discuss in more detail in Section 4.4.4.

4.4.3 Balanced Homodyne Detection

A slightly more complicated, yet more versatile optical detection method is optical homodyne detection. Here we consider the balanced homodyne detection scheme discussed in Section 5.4.3, where the output signal from the optical cavity

is mixed with a local oscillator (LO) on a 50/50 BS before being sent to a balanced photodetector (BPD). In this situation, the voltage measurement by the BPD will be given by

$$v_{\mathrm{h}}(t) = H_{\mathrm{h}}\left[\hat{a}_1^\dagger(t)\hat{a}_1(t) - \hat{a}_2^\dagger(t)\hat{a}_2(t)\right], \tag{4.66}$$

where H_{h} is the electronic gain factor of the homodyne detection system. Here we have also introduced the field operators $\hat{a}_1(t)$ and $\hat{a}_2(t)$ impinging upon each of the two PDs of the BPD, which can be written in terms of the field operators arriving at the BS from the LO $\hat{a}_{\mathrm{LO}}(t)$ and signal $\hat{a}_{\mathrm{s}}(t)$ arms as

$$\hat{a}_1(t) = \frac{\eta_{\mathrm{h}}}{\sqrt{2}}\left(\hat{a}_{\mathrm{LO}}(t) + i\hat{a}_{\mathrm{s}}(t)\right) + \sqrt{1-\eta_{\mathrm{h}}}\delta\hat{a}_{\mathrm{vac}}(t), \tag{4.67}$$

$$\hat{a}_2(t) = \frac{\eta_{\mathrm{h}}}{\sqrt{2}}\left(i\hat{a}_{\mathrm{LO}}(t) + \hat{a}_{\mathrm{s}}(t)\right) + \sqrt{1-\eta_{\mathrm{h}}}\delta\hat{a}_{\mathrm{vac}}(t), \tag{4.68}$$

where η_{h} is the detection efficiency of the entire homodyne setup. Here we have assumed that the efficiency of the two paths after the BS, leading the the each of the BPD's photodiodes have identical efficiencies (*i.e.* $\eta_1 = \eta_2$). The field $\hat{a}_{\mathrm{s}}(t)$ exiting the signal arm can be expressed in a form similar to $\hat{a}_{\mathrm{d}}(t)$ given in Eq. (4.55) as

$$\bar{a}_{\mathrm{s}} = \sqrt{\eta_{\mathrm{s}}}\bar{a}_{\mathrm{out}}, \tag{4.69}$$

$$\delta\hat{a}_{\mathrm{s}}(t) = \sqrt{\eta_{\mathrm{s}}}\delta\hat{a}_{\mathrm{out}}(t) + \sqrt{1-\eta_{\mathrm{s}}}\delta\hat{a}_{\mathrm{vac}}(t), \tag{4.70}$$

where we have replaced η_{d} with the efficiency η_{s} of the signal arm between the optical cavity and the BS.

At this point, we assume that the high power optical field in the LO behaves classically, such that we can replace its field operator with a classical amplitude[9] as $\hat{a}_{\mathrm{LO}}(t) = \bar{a}_{\mathrm{LO}}$, which is related to the power in the LO as $P_{\mathrm{LO}} = \hbar\omega_{\mathrm{d}}|\bar{a}_{\mathrm{LO}}|^2$. Inputting this relation, as well as Eqs. (4.67)–(4.70) into Eq. (4.66), we find that the low frequency homodyne voltage is given by

$$\bar{v}_{\mathrm{h}} = \frac{2H_{\mathrm{h}}^{\mathrm{DC}}\eta_1\sqrt{\eta_{\mathrm{s}}}}{\hbar\omega_{\mathrm{d}}}\sqrt{P_{\mathrm{LO}}P_{\mathrm{in}}\left(1 - \frac{\kappa_{\mathrm{e}}\kappa_{\mathrm{i}}}{\Delta^2 + \kappa^2/4}\right)}\sin(\Delta\theta), \tag{4.71}$$

where $\Delta\theta$ is the difference in phase between the LO and signal arms and $H_{\mathrm{h}}^{\mathrm{DC}}$ is defined similar to $H_{\mathrm{d}}^{\mathrm{DC}}$ in the direct detection case. Therefore, we can set the phase

[9] With this assumption $\hat{a}_{\mathrm{LO}}(t)$ is time-independent, as we are working in the frame rotating at the optical drive frequency.

difference between these two paths by using $\bar{v}_{\rm h}$ as an error signal. In what follows, we assume that $\Delta\theta = 0$ (corresponding to $\bar{v}_{\rm h} = 0$), as this is the condition that is generally used in our experiments. In this case, the high frequency fluctuating portion of the homodyne voltage signal is given by

$$\delta\hat{v}_{\rm h}(t) = iH_{\rm h}\left[\bar{a}^{*}_{\rm LO}\delta\hat{a}_{\rm s}(t) - \bar{a}_{\rm LO}\delta\hat{a}^{\dagger}_{\rm s}(t)\right], \tag{4.72}$$

which can be Fourier-transformed to produce

$$\delta\hat{v}_{\rm h}(\omega) = iH_{\rm h}\left[\bar{a}^{*}_{\rm LO}\delta\hat{a}_{\rm s}(\omega) - \bar{a}_{\rm LO}\delta\hat{a}^{\dagger}_{\rm s}(\omega)\right]. \tag{4.73}$$

Here we can see that a homodyne measurement at $\Delta\theta = 0$ probes the phase quadrature of the signal arm field fluctuations[10]. This fluctuating voltage can also be used to determine the homodyne detection PSD according to

$$S^{\rm h}_{vv}(\omega) = \frac{1}{2\pi}\int_{-\infty}^{\infty}\langle\delta\hat{v}_{\rm h}(\omega)\delta\hat{v}_{\rm h}(\omega')\rangle\, d\omega'. \tag{4.74}$$

Inputting $\delta\hat{v}_{\rm h}(\omega)$ into this equation, we find that the homodyne voltage PSD takes on a form similar to $S^{\rm d}_{vv}(\omega)$ as

$$S^{\rm h}_{vv}(\omega) = \alpha_{\rm h}(\omega)S^{\rm tot}_{xx}(\omega) + S^{\rm h,imp}_{vv}(\omega), \tag{4.75}$$

where $\alpha_{\rm h}(\omega)$ and $S^{\rm h,imp}_{vv}(\omega)$ are the homodyne transduction coefficient and electronic noise floor defined similar to $\alpha_{\rm d}(\omega)$ and $S^{\rm d,imp}_{vv}(\omega)$ in Eq. (4.61). Note that while Eq. (4.61) and (4.75) look nearly identical, they differ significantly due to the varying functional forms of $\alpha_{\rm d}(\omega)$ and $\alpha_{\rm h}(\omega)$. For instance, in the $\Delta\theta = 0$ case considered here, $\alpha_{\rm h}(\omega)$ is maximized for a resonantly probed cavity ($\Delta = 0$), such the the homodyne signal is largest at this detuning.

4.4.4 The Standard Quantum Limit

For the $\Delta = 0$ case mentioned above, we find that the expressions for the optical imprecision and backaction noise given in Eqs. (4.64) and (4.65) are simplified

[10] Homodyne detection can also be used to detect the amplitude quadrature of $\delta\hat{a}_{\rm s}(\omega)$ if we instead choose to set $\Delta\theta = \pm\pi/2$.

considerably to

$$S_{xx}^{\mathrm{imp}}(\omega) = \frac{\hbar\omega_{\mathrm{c}}\kappa^2}{64\eta G^2 P_{\mathrm{in}}}\left(1+4\frac{\omega^2}{\kappa^2}\right) = \frac{\kappa}{16\eta\bar{N}G^2}\left(1+4\frac{\omega^2}{\kappa^2}\right), \tag{4.76}$$

$$S_{FF}^{\mathrm{ba}}(\omega) = \frac{16\hbar G^2 P_{\mathrm{in}}}{\omega_{\mathrm{c}}\kappa^2}\left(1+4\frac{\omega^2}{\kappa^2}\right)^{-1} = \frac{4\hbar^2\bar{N}G^2}{\kappa}\left(1+4\frac{\omega^2}{\kappa^2}\right)^{-1}, \tag{4.77}$$

where we have used that fact that $\omega_{\mathrm{d}} = \omega_{\mathrm{c}}$ and $\bar{N} = 4P_{\mathrm{in}}/\kappa\hbar\omega_{\mathrm{c}}$ for a resonantly probed cavity. In this form, we immediately see that $S_{xx}^{\mathrm{imp}}(\omega)$ and $S_{FF}^{\mathrm{ba}}(\omega)$ achieve equality in Eq. (4.63) for the case of an ideal, lossless detection system (*i.e.* $\eta = 1$). In Fig. 4.3, we plot $S_{xx}^{\mathrm{tot}}(\omega)$ found by inputting the noise PSDs given by Eqs. (4.35), (4.76), and (4.77) into Eq. (4.62) versus both optical power input to the cavity and measured frequency. Note that since $\omega \approx \omega_{\mathrm{m}}$ over the narrow band of interest surrounding our mechanical resonance, $S_{xx}^{\mathrm{imp}}(\omega)$ and $S_{FF}^{\mathrm{ba}}(\omega)$ are relatively flat over this frequency range, such the $S_{xx}^{\mathrm{imp}}(\omega)$ appears as an increase in the measurement noise floor, while $S_{FF}^{\mathrm{ba}}(\omega)$ acts as an additional white-noise force acting on the resonator. Furthermore, we see that the total noise added to the system on mechanical resonance will be minimized to $S_{xx}^{\mathrm{add}}(\omega_{\mathrm{m}}) = S_{xx}^{\mathrm{zpf}}(\omega_{\mathrm{m}}) = 2x_{\mathrm{zpf}}^2/\Gamma_{\mathrm{m}}$ at an input optical power of

$$P_{\mathrm{SQL}} = \frac{\hbar\omega_{\mathrm{c}}\kappa}{16\eta C}\left(1+4\frac{\omega^2}{\kappa^2}\right), \tag{4.78}$$

where $C = 4g_0^2/\kappa\Gamma_{\mathrm{m}}$ is the single-photon cooperativity of the optomechanical system and $S_{xx}^{\mathrm{zpf}}(\omega)$ is the zero-point fluctuation PSD of the mechanical displacement. This point is known as the standard quantum limit (SQL) of the system, and corresponds to the smallest amount of noise that can possibly be introduced into our mechanical system using this linearized homodyne detection scheme. From Eq. (4.78), one can see that the larger the single photon cooperativity and detection efficiency of a given system, the smaller P_{SQL} will be, making the SQL more accessible.

We conclude this section by noting that it is often the case in the literature that the noise in an optomechanical system is expressed in terms of effective quanta that are added to the measurement of the mechanical motion [106, 119, 298]. To find these effective quanta, we divide Eq. (4.62) on resonance by $2S_{xx}^{\mathrm{zpf}}(\omega_{\mathrm{m}})$ to determine the total inferred quanta in the system from the measurement as

$$\bar{n}_{\mathrm{meas}} = \frac{S_{xx}^{\mathrm{tot}}(\omega_{\mathrm{m}})}{2S_{xx}^{\mathrm{zpf}}(\omega_{\mathrm{m}})} = \bar{n}_{\mathrm{th}} + \bar{n}_{\mathrm{imp}} + \bar{n}_{\mathrm{ba}} + \frac{1}{2}, \tag{4.79}$$

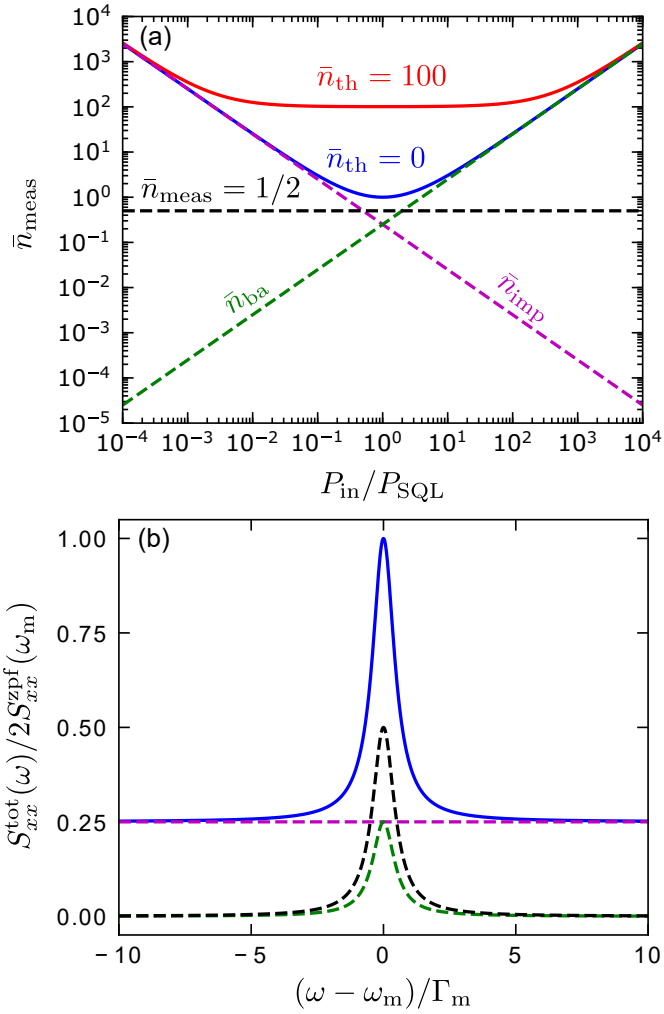

Figure 4.3: (a) The total mechanical mode occupancy, including thermal and ground state (dashed black) contributions, as well as those added by imprecision (Eq. (4.80) – purple dashed) and back-action (Eq. (4.81) – green dashed) noise due to a quantum-limited optomechanical homodyne measurement (*i.e.* $\eta = 1$ in Eq. (4.79)) versus input optical power normalized by $P_{\rm SQL}$. Both the zero temperature ($\bar{n}_{\rm th} = 0$ – blue solid) and finite temperature ($\bar{n}_{\rm th} = 100$ – red solid) traces exhibit a minimum at the SQL. (b) Total spectral density for a quantum-limited optomechanical homodyne measurement at the SQL for zero temperature (solid blue), comprised of the ground state motion (black dashed) as well as the associated imprecision (purple dashed) and back-action (green dashed) measurement noises. The spectrum is normalized such that on resonance, the peak values correspond to the effective quanta associated with each contribution.

with the effective noise quanta of the system defined as

$$\bar{n}_{\rm imp} = \frac{S_{xx}^{\rm imp}(\omega_{\rm m})}{2S_{xx}^{\rm zpf}(\omega_{\rm m})} = \frac{1}{16\eta\bar{C}}\left(1 + 4\frac{\omega_{\rm m}^2}{\kappa^2}\right), \tag{4.80}$$

$$\bar{n}_{\rm ba} = \frac{S_{xx}^{\rm ba}(\omega_{\rm m})}{2S_{xx}^{\rm zpf}(\omega_{\rm m})} = \bar{C}\left(1 + 4\frac{\omega_{\rm m}^2}{\kappa^2}\right)^{-1}, \tag{4.81}$$

where $\bar{C} = \bar{N}C$ is the cavity-enhanced cooperativity. In Fig. 4.3, we have scaled the y-axis in both plots according to this convention. Here the noise processes are reinterpreted as additional quanta $\bar{n}_{\mathrm{add}} = \bar{n}_{\mathrm{imp}} + \bar{n}_{\mathrm{ba}}$ on top of the thermal occupancy of the resonator, with $\bar{n}_{\mathrm{imp}}$ representing an apparent added phonon occupancy to the measurement and $\bar{n}_{\mathrm{ba}}$ producing an actual addition to the mechanical oscillator's occupation via the associated radiation back-action force (see Fig. 4.3b). Note that in order to experimentally observe the radiation-pressure backaction noise, one requires that $\bar{n}_{\mathrm{ba}} \gtrsim \bar{n}_{\mathrm{th}}$, which occurs for $\tilde{C} \gtrsim 1$, where $\tilde{C} = \bar{C}/\bar{n}_{\mathrm{th}}$ is the cavity-enhanced quantum cooperativity of the system [150, 299]. Once again, in the limit of perfect detection, the Heisenberg uncertainty principle restricts the product of these added noise quanta to $\bar{n}_{\mathrm{imp}}\bar{n}_{\mathrm{ba}} = 1/16$. Therefore, at the SQL where $\bar{n}_{\mathrm{imp}} = \bar{n}_{\mathrm{ba}} = 1/4$, the total added quanta due to measurement noise is $\bar{n}_{\mathrm{add}} = \bar{n}_{\mathrm{imp}} + \bar{n}_{\mathrm{ba}} = 1/2$, equal to the effective occupancy associated with the ground state motion, in direct agreement with what was found earlier for the unnormalized spectra. Though the SQL enforces a limit on the precision at which one can probe the motion of a mechanical resonator using the linear detection schemes described in the previous two subsections, as we shall see in Chapter 8, this limit can be overcome for specifically tailored nonlinear measurements.

4.5 Classical Nonlinear Optomechanics

In the previous section, we implicitly assumed an optomechanical system whose mechanical fluctuations are small enough to allow for a linearized treatment of the equations of motion. However, when the amplitude of oscillation A of the mechanical resonator becomes large enough ($GA \gg \omega_{\mathrm{m}}$), it is possible to enter a regime where keeping terms to first order in their fluctuations no longer suffices. One such situation where this occurs is optomechanical self-amplification [300–308], which onsets when $\delta\Gamma_{\mathrm{m}} = -\Gamma_{\mathrm{m}}$, such that Γ_{tot} drops to zero and a parametric instability emerges, driving the mechanical motion into large amplitude oscillations in order to counteract the optical drive forces. In this situation, the large amplitude mechanical oscillations associated with this nonlinear regime act to overwhelm any quantum noise (*i.e.* terms containing $\delta\hat{a}_{\mathrm{in}}(t)$ or $\delta\hat{a}_{\mathrm{i}}(t)$). We therefore restrict

ourselves to a classical treatment of the optomechanical system, which can by done by taking the expectation values of Eqs. (4.15) and (4.16) such that they become

$$\dot{a} = -\frac{\kappa}{2}a + i\Delta_0 a + iGxa + \sqrt{\kappa_e}\bar{a}_{in}, \tag{4.82}$$

$$\ddot{x} + \Gamma_m \dot{x} + \omega_m^2 x = \frac{1}{m}\left[F_{th} + F_{rp}\right]. \tag{4.83}$$

Here we have introduced $a(t) = \langle \hat{a}(t) \rangle$ and $x(t) = \langle \hat{x}(t) \rangle$ as the classical expectation values of the optical field amplitude and mechanical resonator displacement, along with the classical radiation-pressure force $F_{rp}(t) = \hbar G|a(t)|^2$ and thermal force $F_{th}(t) = \langle \hat{F}_{th}(t) \rangle$.

We continue by assuming a high-Q mechanical system, such that we can use the ansatz [150, 301, 302]

$$x(t) = \bar{x} + A\cos(\omega_m t), \tag{4.84}$$

as the solution to Eq. (4.83) for the resonator's displacement, where again $\bar{x}$ is the resonator's static displacement from equilibrium. Inputting this expression into Eq. (4.82), we solve for the optical field amplitude as [150, 309]

$$a(t) = \sqrt{\kappa_e}\bar{a}_{in} e^{i\theta(t)} \sum_{l=-\infty}^{\infty} \tilde{a}_l e^{il\omega_m t}, \tag{4.85}$$

where $\theta(t) = \xi \sin(\omega_m t)$ is the time-dependent global phase of the optical field and

$$\tilde{a}_l = \frac{J_l(-\xi)}{\kappa/2 - i\left(\Delta_0 + G\bar{x} - l\omega_m\right)}, \tag{4.86}$$

with $J_l(z)$ being the lth Bessel function of the first kind and $\xi = GA/\omega_m$ is the dimensionless mechanical modulation strength [150, 301, 302, 304, 310]. We point out that in this expression for $\tilde{a}_l$, we have explicitly written out the optical drive detuning $\Delta = \Delta_0 + G\bar{x}$, as we wish to be more transparent with the $\bar{x}$ term throughout this section for completeness. Note, however, that it is often the case that the effect of adding this $G\bar{x}$ term to the bare drive detuning is negligible, such that $\Delta \approx \Delta_0$. In this form, we interpret the optical field amplitude as being comprised of infinitely many sidebands at integer multiples of the mechanical frequency generated by multiphonon optomechanical interactions, with each having a strength set by the coefficient $\tilde{a}_l$. The linearized regime is then simply the case

where $\xi \ll 1$, such that only the first order sidebands at $l = \pm 1$ due to single-phonon optomechanical interactions are considered.

Here, we are interested in determining the optomechanical quantities $\bar{x}$, $\delta\omega_{\mathrm{m}}$, and $\delta\Gamma_{\mathrm{m}}$, as well as the steady state transmission through the optical cavity $\mathcal{T}$, in terms of the mechanical amplitude A using this nonlinear optomechanical treatment. In doing so, we neglect the thermal forces acting upon the resonator, as they will be dwarfed by the optically induced radiation-pressure force. Starting by taking the time average of Eq. (4.83) (*i.e.* balancing the time-averaged forces of the system) we find [150, 301–303]

$$\bar{x}(A) = \frac{\hbar G \kappa_{\mathrm{e}} |\bar{a}_{\mathrm{in}}|^2}{m\omega_{\mathrm{m}}^2} \sum_{l=-\infty}^{\infty} |\tilde{a}_l|^2, \tag{4.87}$$

where we have used the fact that $\langle \ddot{x}(t) \rangle = \langle \dot{x}(t) \rangle = 0$ and $\langle x(t) \rangle = \bar{x}$, as well as

$$\langle |a(t)|^2 \rangle = \kappa_{\mathrm{e}} |\bar{a}_{\mathrm{in}}|^2 \sum_{l=-\infty}^{\infty} |\tilde{a}_l|^2. \tag{4.88}$$

Note that since $\tilde{a}_l$ is implicitly dependent on $\bar{x}$, Eq. (4.87) represents a transcendental equation for $\bar{x}$ in terms of A and Δ_0, which in general must be solved numerically.

Next, we multiply Eq. (4.83) by $\dot{x}(t)$ and again take the time average, balancing the time-averaged power of the system. This leads to the condition that $\Gamma_{\mathrm{tot}} = \Gamma_{\mathrm{m}} + \delta\Gamma_{\mathrm{m}}(A) = 0$ [150, 301–303], where we identify the amplitude-dependent optomechanical damping of the system as

$$\delta\Gamma_{\mathrm{m}}(A) = \frac{2\hbar G \kappa_{\mathrm{e}} |\bar{a}_{\mathrm{in}}|^2}{A m \omega_{\mathrm{m}}} \sum_{l=-\infty}^{\infty} \mathrm{Im}\left\{ \tilde{a}_l \tilde{a}_{l+1}^* \right\}. \tag{4.89}$$

In order to obtain this result, we have used the relations $\langle \ddot{x}(t)\dot{x}(t) \rangle = \langle x(t)\dot{x}(t) \rangle = 0$ and $\langle \dot{x}^2(t) \rangle = \omega_{\mathrm{m}}^2 A^2/2$, along with

$$\langle |a(t)|^2 \dot{x}(t) \rangle = -A\omega_{\mathrm{m}} \kappa_{\mathrm{e}} |\bar{a}_{\mathrm{in}}|^2 \sum_{l=-\infty}^{\infty} \mathrm{Im}\left\{ \tilde{a}_l \tilde{a}_{l+1}^* \right\}. \tag{4.90}$$

Finally, it can be shown (see Ref. [311] for example) that the spring effect in the nonlinear optomechanical regime will be given by

$$\delta\omega_{\mathrm{m}}(A) = -\frac{\hbar G \kappa_{\mathrm{e}} |\bar{a}_{\mathrm{in}}|^2}{A m \omega_{\mathrm{m}}} \sum_{l=-\infty}^{\infty} \mathrm{Re}\left\{ \tilde{a}_l \tilde{a}_{l+1}^* \right\}. \tag{4.91}$$

Interestingly, one can use the time-averaged energy balance equation (by multiplying Eq. (4.83) by $x(t)$ and time-averaging), along with the relations $\langle \dot{x}(t)x(t)\rangle = 0$, $\langle \ddot{x}(t)x(t)\rangle = -\omega_{\rm m}^2 A^2/2$, and $\langle x^2(t)\rangle = \bar{x}^2 + A^2/2$, to show that $\delta\omega_{\rm m}(A) = 0$ while A is large enough that the system remains in the nonlinear regime. This frequency locking effect, coupled with the reduction of the resonance linewidth, is indicative of phonon lasing in the mechanical resonator [150].

We are also interested in determining how mechanical self-oscillations affect the optical transmission through the cavity. To do this, we consider the optical field output from the cavity, which can be found using

$$a_{\rm out}(t) = a_{\rm in}(t) - \sqrt{\kappa_{\rm e}}a(t), \tag{4.92}$$

which is simply the classical version of the input-output relation given in Eq. (4.45), where $a_{\rm out}(t) = \langle \hat{a}_{\rm out}(t)\rangle$ and $a_{\rm in}(t) = \langle \hat{a}_{\rm in}(t)\rangle$ are the expectation values of the field output from and input to the cavity [150]. Inserting Eq. (4.85) into this expression, while only considering the time-independent terms, we find the amplitude-dependent steady state transmission through the cavity as [150, 310]

$$\mathcal{T}(A) = \frac{|\bar{a}_{\rm out}|^2}{|\bar{a}_{\rm in}|^2} = 1 - 2\kappa_{\rm e}{\rm Re}\left\{\sum_{l=-\infty}^{\infty} J_{-l}(\xi)\tilde{a}_l\right\} + \kappa_{\rm e}^2\sum_{l=-\infty}^{\infty}|\tilde{a}_l|^2, \tag{4.93}$$

where we have made use of the Jacobi-Anger expansion [81]

$$e^{\pm i\phi(t)} = \sum_{l=-\infty}^{\infty} J_{-l}(\xi)e^{\pm il\omega_{\rm m}t}. \tag{4.94}$$

Finally we note that in the regime of small mechanical oscillations (*i.e.* $\xi \ll 1$), each of the amplitude-dependent quantities given above approach their linearized counterpart. That is, Eq. (4.87) $\rightarrow$ Eq. (4.20), Eq. (4.89) $\rightarrow$ Eq. (4.29), Eq. (4.91) $\rightarrow$ Eq. (4.28), and Eq. (4.93) $\rightarrow$ Eq. (4.57).

4.6 Conclusion

In this chapter, we introduced the theoretical framework used to describe the coupling between the optical cavity and mechanical resonator of our system, in both the linearized quantum and nonlinear classical regimes. First, we described

the physical basis of our coupling technique, whereby the motion of the mechanical resonator shifts the boundary conditions, and thus the resonant frequency, of our WGM cavity. Using this description, we were then able to determine the full Hamiltonian of our system, including the optomechanical interaction between these elements, as well as the coupling with their baths and an external optical drive. From this Hamiltonian, we derived the QLEs of the system, which we then linearized and used to study the backaction phenomena of optomechanical damping, spring effect, and cooling. Furthermore, we used this linearized treatment to investigate how direct and homodyne detection methods could be used to address our optomechanical cavities, where we determined the SQL associated with the minimum possible noise that can be introduced into the system using such measurement techniques. Finally, we took the expectation values of the QLEs to determine the nonlinear behaviour of our system in the classical regime, where we explored the concepts of optomechanical parametric amplification and phonon lasing, as well as the effects each of these phenomena have on the optomechanical properties of the system.

Chapter 5

Experimental Methods

Large portions of this chapter, specifically Section 5.3 discussing the tapered optical fibers used to couple light into our optical cavities, are based on the publication B. D. Hauer, P. H. Kim, C. Doolin, A. J. R. MacDonald, H. Ramp, and J. P. Davis, "On-chip cavity optomechanical coupling," *EPJ Tech. Intrum.* **1**, 4 (2014) (Ref. [312]) and draws heavily on the content therein. Note that in order to be consistent with the rest of the thesis, a number of minor notational changes have been made with respect to the original publication.

5.1 Introduction

In this chapter, we discuss the optomechanical cavities studied in this thesis, along with the experimental methods used to address them. We begin in Section 5.2 by introducing our optomechanical device architecture and providing details of their fabrication. Next, we discuss the dimpled tapered optical fibers used to address these on-chip optomechanical cavities in Section 5.3, providing both a theoretical background and fabrication methodology, as well as details on how to adapt this technology to cryogenic environments. Finally, in Section 5.4, we describe the cryogenic optomechanical detection system used to house and measure our devices during our low temperature experiments.

5.2 Optomechanical Devices

5.2.1 Whispering-Gallery-Mode Optomechanical Cavities

The optomechanical architecture studied in this work consists of a mechanical element – in the form of either a half-ring (see Fig. 6.2 in Section 6.3) or claw-like (see Fig. 7.2 in Section 7.3) resonator – sidecoupled to an optical microdisk, with both elements fabricated from the same single-crystal-silicon device layer of a silicon-on-insulator (SOI) chip. In this geometry, the microdisk cavity supports numerous optical WGMs (see Section 3.3) in the near-infrared frequency band, which are dispersively coupled to the motion of each mechanical resonator as described in Section 4.2. More details on the individual geometries studied in this thesis can be found in Sections 6.3 and 7.3.

5.2.2 Device Fabrication[1]

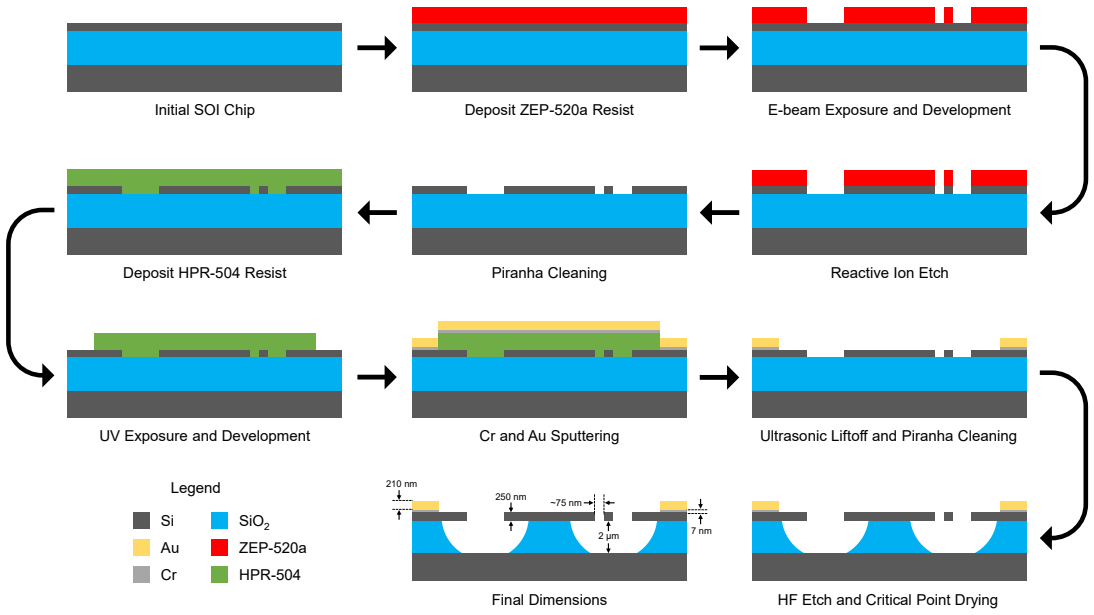

Figure 5.1: Schematic of the device fabrication procedure outlined in Section 5.2.2. The final thicknesses of the gold, chromium, silicon, and oxide layers are 210 nm, 10 nm, 250 nm, and 2 μm, respectively, while the separation gap between the optical microdisk and mechanical resonator is on the order of 80 nm.

[1]The process used to fabricate the optomechanical devices described in this section was developed and performed by Paul Kim. Here we provide a brief overview of this process, with further details found in Ref. [313].

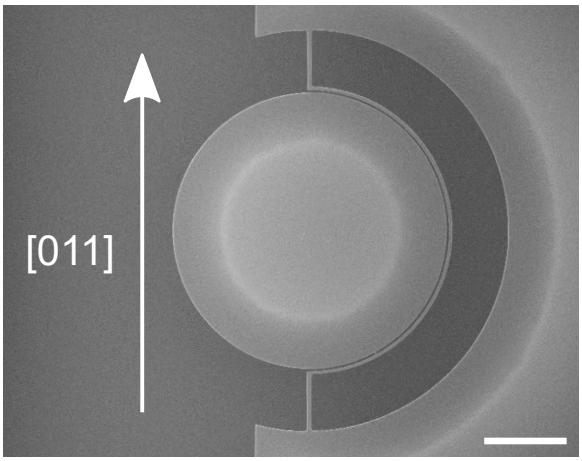

Figure 5.2: Scanning electron microscope image indicating the orientation of our optomechanical devices with respect to the [011] crystal direction in the silicon device layer. Scale bar is 3 μm. Figure reproduced from Ref. [163]. © 2018 American Physical Society.

To fabricate the optomechanical geometries described in the previous subsection, we start with a $\langle 100 \rangle$ p-doped (boron, 22.5 Ω·cm) SOI wafer, consisting of a 250-nm-thick device layer of monocrystalline silicon (see Table 5.1 for the properties of our single-crystal silicon devices) on top of a 3-μm-thick sacrificial layer of silicon dioxide supported by a 0.5-mm-thick silicon handle. The wafer is initially diced into 10 mm $\times$ 5 mm chips and cleaned using a hot piranha solution (75% H_2SO_4, 25% H_2O_2) for 20 min. A masking layer (positive resist, ZEP-520a) is deposited onto the clean silicon device layer to pattern the mechanical resonator/optical disk structure (oriented along the [011] crystal direction as indicated in Fig. 5.2) using a 30 kV e-beam lithography system (RAITH150 Two), followed by a cold development at –15 °C (ZED-N50). The chip is then reactive-ion etched (C_4F_8 and SF_6) to transfer the pattern to the silicon, and subsequently cleaned with piranha so that it can be spun with a new mask (positive photoresist, HPR-504). After optical lithography, Cr and Au layers (7 nm and 210 nm, respectively) are sputtered on both sides of the chip with equal thickness, surrounding the devices with a gold thermalization layer. Ultrasonic lift-off in acetone and room-temperature piranha cleaning are then used to ensure the cleanliness of the processed chips. Finally, the chips are immersed in a hydrofluoric acid (HF) solution (49% HF) for 1 minute to etch the sacrificial oxide layer, as well as attempt to passivate the exposed silicon surfaces

of our devices [274, 314–316], which is followed by critical point drying to avoid stiction.

5.2.3 Device Properties

In Table 5.1, we provide a table detailing the crystalline, mechanical, thermal, and optical properties of our optomechanical devices. Unless otherwise specified, we assume a temperature of 10 K and an optical wavelength of 1550 nm.

Property	Symbol	Value	Source
Crystalline			
Atomic mass	$\bar{M}$	28.086 amu	[186]
Mass density	ρ	2330 kg/m^3	[186]
Lattice spacing	$\tilde{a}_0$	5.43 Å	[186]
Atomic volume	V_a	20 Å^3	$\tilde{a}_0^3/8$
Mechanical			
Elastic coefficients	C_{11}	165.6 GPa	[155]
	C_{12}	63.9 GPa	[155]
	C_{44}	79.5 GPa	[155]
Speeds of sound	c_l	9148 m/s	Eq. (2.52)
	c_{t_1}	4679 m/s	Eq. (2.53)
	c_{t_2}	5857 m/s	Eq. (2.54)
Young's modulus	$\tilde{Y}'$	169 GPa	[167]
Bulk modulus	B	101.5 GPa	Eq. (2.117)
Thermal			
Debye temperature	Θ	645 K	[154]
Debye frequency	$\varpi/2\pi$	13.4 THz	$k_\mathrm{B}\Theta_D/\hbar$
Debye sound speed	$\bar{c}$	5718 m/s	Eq. (2.83)
Phonon mean free path	Λ_C	250 nm	Eq. (2.99)
Heat capacity	$\mathcal{C}_V$	654 J/kg·K	Eq. (2.97)
Thermal conductivity	$\mathcal{K}$	0.312 W/m·K	Eq. (2.101)
Thermal diffusivity	$\mathcal{J}$	4.77×10^{-4} m^2/s	Eq. (2.102)
Thermal expansion coefficient	$\tilde{\alpha}$	8.8×10^{-8} K^{-1}	[216]
Grüneisen parameter	$\tilde{\gamma}$	0.410	[216]
Optical			
Refractive index	$\tilde{n}$	3.45	[263]
Absorption coefficient	α	0.336 m^{-1}	[272]

Table 5.1: Summary of the crystalline, mechanical, thermal, and optical properties of our single-crystal silicon devices, with their sources given. Here we assume T = 10 K for the thermal properties and λ = 1550 nm for the optical properties. Where necessary, the beam cross-sectional dimensions are taken to be w = 200 nm and t = 250 nm.

5.3 Tapered Optical Fibers

A crucial element in any optomechanical device is the method by which light is injected into, and subsequently collected from, the optical cavity of the system. While a number of different options exist, including free space optical coupling [55, 57, 317], grating couplers [318–320] and fiber-to-waveguide coupling [321–323], we have chosen to use direct coupling from tapered optical fibers [270, 324–326]. Tapered fibers are more efficient, and require less on-chip space, than grating couplers, while free-space coupling is inconsistent with on-chip devices. It may prove that fiber-to-waveguide coupling [321–323] is more efficient and stable than tapered fibers, but the versatility and maneuverability of tapered fibers remains a significant advantage. Here we introduce the basic theory of tapered optical fibers, allowing us to described their shape and supported optical modes, as well as discuss the fiber pulling and dimpling procedure used to produce the cryogenic dimpled tapered fibers detailed in this thesis.

5.3.1 Tapered Fiber Shape

A tapered fiber is a standard optical fiber (high index core surrounded by a lower index cladding) that has had its diameter adiabatically reduced over a small length known as the tapered region. This can be performed either through hydrofluoric acid etching of an optical fiber [327, 328], or by a heat-and-pull procedure [329–334]. For our purposes, we chose to use the latter method, as the associated reflow of the waveguide material during this process provides a much smoother surface, and therefore lower losses, compared to tapered fibers produced through etching [327, 328].

In the heat-and-pull method, a small region of the initial optical fiber, known as the hot-zone, is heated using a flame [324, 329, 330] or a CO_2 laser [331–333]. We assume this hot-zone to be uniform across the diameter of the fiber, such that it is contained within a cylinder of length l_h (as will be the case for a stationary flame[2]). Therefore, any fiber material within the hot-zone is melted and can be stretched, while outside the hot-zone, material is frozen and immobile. To begin

[2]See Ref. [335] for the treatment of an arbitrary hot-zone.

the stretching process, we pull on both sides of the fiber at a constant speed of v_p, causing its total length to increase by an amount $l_\mathrm{p} = 2v_\mathrm{p}t$, where t is the amount of time the fiber has been pulled for and the factor of 2 arises because we are pulling on *both* sides of the fiber. The final tapered fiber will then consist of three regions, the initial unstreched fiber, the taper transition, and the taper waist, all of which are detailed in Fig. 5.3. Note that as a result of our assumptions, the fiber in this melted region is comprised of a cylinder of constantly reducing diameter as material is pulled out into the frozen taper transition, such that the length of the taper waist is always equal to the length of the hot-zone throughout the entire pulling process.

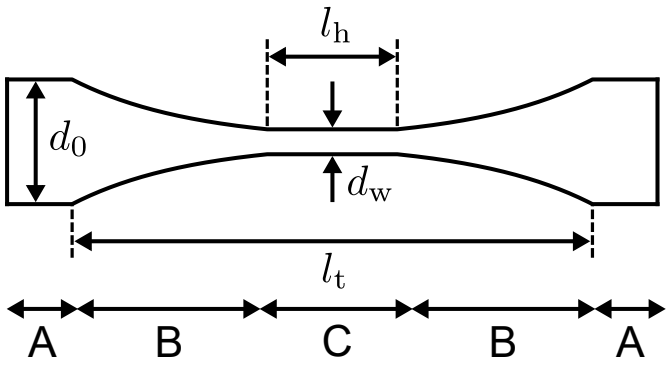

Figure 5.3: Diagram illustrating the shape of a tapered fiber. Region A is the unstreched fiber, where the fiber remains the original unperturbed diameter d_0. Region B is the taper transition over which the unstreched diameter is adiabatically reduced to the waist diameter d_w maintained over the length of the hot-zone l_h throughout Region C, which known as the taper waist. The total taper length $l_\mathrm{t} = l_\mathrm{h} + l_\mathrm{p}$ then spans the taper waist (Region C) and both taper transitions (Region B). A constant hot-zone length l_h is assumed such that the taper transition has an exponential profile. Figure adapted from Ref. [312] under the Creative Commons Attribution License.

In order to determine the diameter of the taper waist d_w as a function of pull time, and therefore, as a function of the pull length, we use a simple conservation of volume argument. That is, at a time t, the instantaneous volume of the taper waist (which is completely contained within the hot-zone) will be given by [335]

$$V_\mathrm{f} = \frac{\pi}{4} d_\mathrm{w}^2 l_\mathrm{h}. \tag{5.1}$$

At a moment $t + \delta t$ later, however, the fiber residing in the hot-zone will be stretched by an amount $\delta l_\mathrm{p} = 2v_\mathrm{p}\delta t$, resulting in a commensurate decrease in the

waist diameter δd_{w} to conserve the volume of the fiber according to [335]

$$V_{\mathrm{f}} = \frac{\pi}{4}(d_{\mathrm{w}} + \delta d_{\mathrm{w}})^2(l_{\mathrm{h}} + 2v_{\mathrm{p}}\delta t) \approx \frac{\pi}{4}(d_{\mathrm{w}}^2 l_{\mathrm{h}} + 2d_{\mathrm{w}} l_{\mathrm{h}}\delta d_{\mathrm{w}} + 2d_{\mathrm{w}}^2 v_{\mathrm{p}}\delta t), \tag{5.2}$$

where we have only kept terms to first order in the small quantities δl_{h} and δd_{w}. Equating Eqs. (5.1) and (5.2), we arrive at a differential equation for the taper waist diameter as [335]

$$\dot{d}_{\mathrm{w}} = -\frac{v_{\mathrm{p}}}{l_{\mathrm{h}}} d_{\mathrm{w}}. \tag{5.3}$$

The solution to this differential equation is a simple exponential decay, which when subject to the initial condition $d_{\mathrm{w}}(0) = d_0$ results in [335]

$$d_{\mathrm{w}}(t) = d_0 e^{-v_{\mathrm{p}} t/l_{\mathrm{h}}}. \tag{5.4}$$

Therefore, the diameter of the taper waist is set by three parameters: the pull speed v_{p}, the pull time t, and the size of the hot-zone characterized by its length l_{h}.

This exponential time dependence of $d_{\mathrm{w}}(t)$ given in Eq. (5.4) can also be used to determine the shape of the tapered fiber along its axial coordinate z. This is because as the fiber is lengthened, the material that is pulled out of the hot-zone freezes in place at the instantaneous waist diameter $d_{\mathrm{w}}(t)$, resulting in an exponential profile in the taper transition. The resulting shape of the entire tapered fiber (including the unstretched, taper transition, and waist regions) can then be found as [335]

$$d_{\mathrm{f}}(z) = \begin{cases} d_0, & z \leq -\frac{l_{\mathrm{h}}+l_{\mathrm{p}}}{2} \\ d_0 e^{-\left(z+\frac{l_{\mathrm{h}}+l_{\mathrm{p}}}{2}\right)/l_{\mathrm{h}}}, & -\frac{l_{\mathrm{h}}+l_{\mathrm{p}}}{2} \leq z \leq -\frac{l_{\mathrm{h}}}{2} \\ d_0 e^{-l_{\mathrm{p}}/2l_{\mathrm{h}}}, & -\frac{l_{\mathrm{h}}}{2} \leq z \leq \frac{l_{\mathrm{h}}}{2} \\ d_0 e^{\left(z-\frac{l_{\mathrm{h}}+l_{\mathrm{p}}}{2}\right)/l_{\mathrm{h}}}, & \frac{l_{\mathrm{h}}}{2} \leq z \leq \frac{l_{\mathrm{h}}+l_{\mathrm{p}}}{2} \\ d_0, & \frac{l_{\mathrm{h}}+l_{\mathrm{p}}}{2} \leq z \end{cases}, \tag{5.5}$$

with the total length of the tapered region given by

$$l_{\mathrm{t}} = l_{\mathrm{h}} + l_{\mathrm{p}} = l_{\mathrm{h}} + 2v_{\mathrm{p}} t. \tag{5.6}$$

This taper profile is shown schematically in Fig. 5.3. Finally, we can confirm that the taper profile given in Eq. (5.5) satisfies the conservation of volume by integrating the volume element $dV = \frac{\pi}{4} d_{\mathrm{f}}^2(z) dz$ over the tapered region to find its volume as

$$V_{\mathrm{t}} = \frac{\pi}{4} \int_{-\frac{l_{\mathrm{h}}+l_{\mathrm{p}}}{2}}^{\frac{l_{\mathrm{h}}+l_{\mathrm{p}}}{2}} d_{\mathrm{f}}^2(z) dz = \frac{\pi}{4} d_0^2 l_{\mathrm{h}}, \tag{5.7}$$

which is simply the initial unstretched volume of the hot-zone as expected.

Upon inspection of the taper profile given in Eq. (5.5), we can immediately make the observation that for a given hot-zone length l_h and taper waist diameter (set by the total pull length l_p and the initial fiber diameter d_0), the final taper shape is independent of the pulling speed v_p and pull time t. Therefore, for a given desired taper waist diameter, the steepness of the taper transition, and hence the fiber transmission efficiency, is entirely set by the length of the hot-zone l_h. Any change in pull speed therefore simply amounts to reaching this desired taper waist in a shorter amount of time and does not affect the taper profile[3]. This means that a larger hot-zone generates a more adiabatic transition from the unstretched diameter to the taper waist, and therefore a more efficient fiber.

5.3.2 Single-Mode Tapered Optical Fibers

Following the heat-and-pull process, a new air-clad core exists in the taper waist, comprised of a composite material with an effective index determined by the indices and relative sizes of the initial core and cladding. As it is this tapered waist region that we use to couple light into and out of our optomechanical devices, we are mainly concerned with the electromagnetic profile in this portion of the fiber. For the tapered fibers considered in this work, we have $l_\mathrm{h} \sim 1$ mm and $d_\mathrm{w} \sim 1$ μm, such that the taper waist has an aspect ratio of $l_\mathrm{h}/d_\mathrm{w} \sim 1000$, and can be modelled as a long, dielectric cylinder. As discussed in Appendix B, such a structure will in general support many modes, with their optical fields described by Eqs. (B.23)–(B.34) (inputting $\tilde{n}_1 = \tilde{n}_\mathrm{f}$ and $r_\mathrm{c} = d_\mathrm{w}/2$ as appropriate), and will therefore act as a multimode waveguide. However, once the fiber's diameter drops below the single mode cut-off diameter d_* given by Eq. (B.50), only the HE_{11} mode remains [336], as all other spatial modes decay evanescently. For the index of refraction of our optical fiber ($\tilde{n}_1 = \tilde{n}_\mathrm{f} = 1.47$) clad in air/vacuum ($\tilde{n}_2 = 1$), we find $d_* = 1.1$ μm at $\lambda_0 = 1550$ nm (see Table B.1). Extending this treatment to determine the critical diameter over the entire optical bandwidth of interest for our experiment (1500 - 1630 nm) by assuming that the index of the fiber remains

[3]This is assumes a reasonably slow pulling speed such that the fiber is drawn out smoothly.

relatively constant over this wavelength range [337], we find

$$d_* \approx 0.71\lambda_0 \approx \lambda_\mathrm{f}, \tag{5.8}$$

where $\lambda_\mathrm{f} = \lambda_0/\tilde{n}_\mathrm{f}$ is the wavelength of the guided light within the fiber. Therefore, for the fiber used in our experiment, the critical diameter is approximately equal to the wavelength of the guided light. Any fiber diameter on the order of or smaller than, this critical diameter will then result in a large portion of the guided optical field existing as an evanescent wave surrounding the core in the air/vacuum cladding of the fiber. This condition allows for substantial overlap between the microdisk's optical WGMs and the single guided HE_{11} mode of the fiber when it is approached to the cavity, providing efficient and stable coupling between these two optical components.

5.3.3 Tapered Fiber Puller

To fabricate the tapered fibers used in our experiment, we adopt the heat-and-pull procedure described theoretically in Section 5.3.1. In our pulling apparatus, the hot-zone is produced using a flame from a custom-built mountable hydrogen torch (see Fig. 5.4a), which is fed by a needle-valve-controlled line to allow for a very small and stable flame. The torch itself is threaded using a 7/16"-24 die to produce standard threads that allow for interchangeability of a number of different torch tips. The tips that we use are shown in Fig. 5.4b, which provide a wide variety of flames that are able to generate varying hot-zone sizes, and therefore, different tapered fiber shapes (see Eq. (5.5)).

The hydrogen torch is mounted on a three-axis positioning system, consisting of an automated xy-translation gantry system in the plane of the optical table on which the apparatus is mounted, along with perpendicularly oriented manual z-adjustment. Each orthogonal in-plane axis in the gantry system is driven by a linear motorized stage, allowing for a total travel range of 200 mm in either dimension with a minimum step size of 50 nm. Manual z-adjustment is provided by a "gothic-arch" translation stage mounted using an angle bracket. The stage is manipulated by a micrometer, providing a 25 mm travel range with 10 μm resolution. This system is used for precise and reproducible placement of the

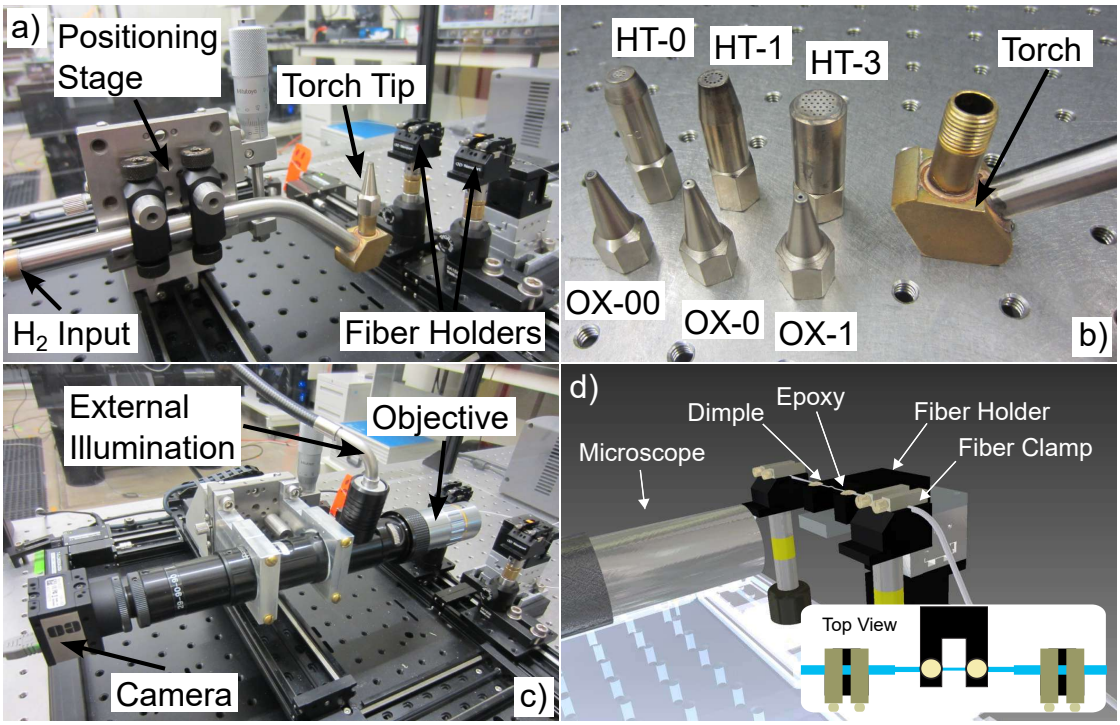

Figure 5.4: (a) Picture of the tapered fiber pulling apparatus with the hydrogen torch attached. (b) Close-up view of the hydrogen torch along with the HT and OX series torch tips. (c) Picture of the microscope imaging system mounted on the positioning gantry. (d) Labelled schematic detailing the fiber gluing process. Once the tapering/dimpling process is complete, two droplets of epoxy located on the fiber holder are approached to the newly created dimpled fiber using the manually adjustable stage behind the fiber mounts, the end result of which can be seen in Fig. 5.7e. This entire process is observed in real time to ensure proper gluing using the microscope imaging system shown in (c). Inset is a top-down view of this schematic, depicting the fiber, fiber holder and fiber clamps. Figure adapted from Ref. [312] under the Creative Commons Attribution License.

hydrogen torch flame as it heats the fiber, which is an important element required to consistently produce high quality tapered fibers. The fiber itself is held using two dual-arm V-groove fiber holders, each of which is connected to an adjustable optical post mounted on a linear motorized stage. Each stage has a travel range of 100 mm with a resolution of 50 nm and can pull the melted fiber at speeds up to 7 mm/s. All of the motorized stages are automated in software, allowing for precise, reproducible xy-positioning of the torch gantry, as well as the ability to set a consistent pull speed. The adjustable optical posts help to ensure that the fiber is level, as proper alignment is crucial for producing a low-loss taper. This entire

setup is surrounded by a protective box, built from optical rails and acrylic sheets, which helps reduce flame instability due to air currents, and prevents contaminants from entering the system.

It is also possible to attach a microscope imaging system directly to our torch positioning gantry, as shown in Fig. 5.4c. The microscope is comprised of a 10× long-working-distance infinity-corrected objective attached to a zoom lens system, allowing for up to 70× magnification of the setup. This image is recorded using a USB webcam, providing a video feed to a nearby computer. To ensure proper lighting and image quality, light from an external microscope LED illuminator is coupled into the lens system's coaxial illumination port using a fiber optic waveguide. This system is very useful, as it allows for real time imaging of our completed tapered fibers when dimpling or gluing it to its holder, with full three-axis control.

As tapered fibers are quite fragile, it is difficult to move them without breaking. For this reason, we first attach the tapered fiber to a holder (see Fig. 5.4d), creating a more robust system which can easily be relocated. To this end, we have included a manually adjustable three-dimensional linear positioning stage into our system, which is located opposite the positioning gantry and allows for 1 μm sensitivity over a travel range of 14 mm in each of x and y and 5 mm in z. This stage permits us to properly position and align the fiber holder, as well as gradually approach it to the fiber for gluing. In addition, it is used to position the fiber mold used in the dimpling process, which must be approached and raised precisely at the thinnest point of the tapered fiber (see Section 5.3.6).

5.3.4 Transmission Monitoring

Another important aspect of the tapered fiber puller is the fiber transmission monitoring system, which allows us to determine the point at which the taper becomes single mode (and therefore an upper bound of d_* on its diameter), as well as assess fiber losses both during and after tapering. To perform this measurement 1550 nm laser light from a tunable diode laser is injected into the fiber, with its input power controlled via a variable optical attenuator (VOA) and its output power measured using a PD. The low frequency electrical signal from this PD is then recorded for the duration of the fiber pull using a data acquisition (DAQ)

card, providing a record of transmission versus pull time, an example of which can be seen in Fig. 5.5.

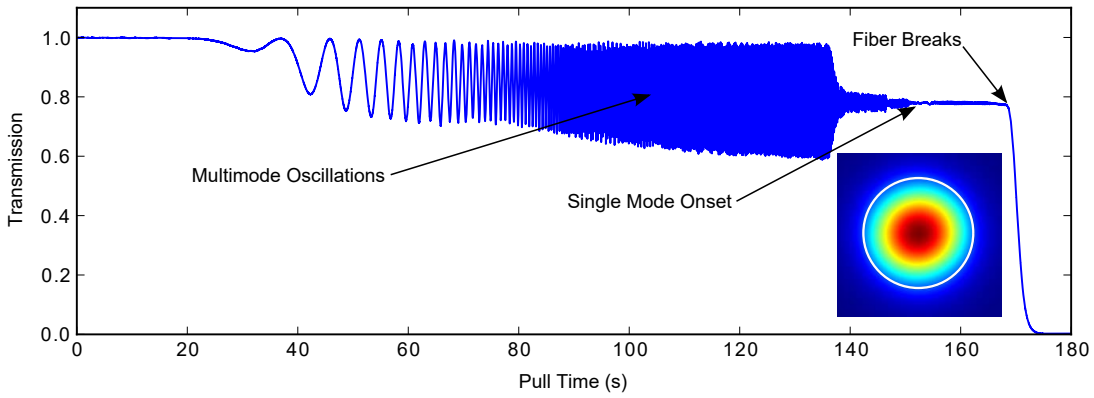

Figure 5.5: Plot of transmission (normalized to the maximum transmission through the fiber before the pull) versus pull time for a tapered fiber pull. This pull was performed using a hydrogen flame generated by the OX-00 torch tip seen in Fig. 5.4b (producing a hot-zone of ∼1.3 mm) at a pull speed of 40 μm/s, which resulted in a final transmission efficiency of 78%. The important regions of the transmission profile are labelled accordingly. Inset is a finite element method simulation of the time averaged energy density for the fundamental HE_{11} mode at 1550 nm of an air-clad tapered fiber with a diameter of 1 μm and index of refraction 1.4677. The white circle indicates the limits of the fiber geometry, separating the internal guided mode from the evanescent field located outside the fiber. Figure reproduced from Ref. [312] under the Creative Commons Attribution License.

5.3.5 Tapering Procedure

To create tapered fibers, we begin with a standard optical fiber (Corning SMF-28e) that has silica core and cladding diameters of 8.2 μm and 125 μm, respectively, all of which is protected by an acrylate coating that extends out to a diameter of 245 μm. The indices of refraction and dimensions of the core and cladding are chosen such that this original fiber is single mode for wavelengths exceeding 1260 nm, which includes both the dispersionless and minimum loss wavelengths in silica of 1310 nm and 1550 nm.

To begin the tapering process, the acrylate coating is removed using a stripping tool over a region approximately 1 cm long in the center of an SMF-28e fiber around one meter in total length. This section of stripped fiber is subsequently

cleaned using acetone to remove any remaining acrylate. The tapering occurs in this stripped region, where the flammable acrylate has been removed. In addition, the two ends of the fiber are stripped of acrylate, cleaved flat using a fiber cleaver, and fusion-spliced onto the ends of two severed FC/APC patch cables, one of which leads to the photodiode, the other to the diode laser. Optical losses through the fiber vary depending on the quality of the splices, but we are only concerned with providing enough power to observe variations in fiber transmission. Once we have ensured that the splices provide sufficient power to the photodiode, the fiber is placed in the V-groove fiber holders, with the stripped region centered between them.

At this point, the hydrogen torch is lit using a butane lighter and gas flow is adjusted to ensure a steady flame about 1 cm high. After it has been lit, the flame is approached towards the fiber until a small portion of the stripped region (a few mm in length) begins to glow, indicating that the fiber is in a molten state. The position of the flame is then adjusted to maximize the size of this molten region (*i.e.* the hot-zone), thus maximizing the completed tapered fiber's transmission efficiency. Once this point has been reached, the two pulling stages move in opposite directions, each at a constant speed generally chosen to be 40 μm/s.

During each pull, the transmission of 1550 nm light through the fiber versus pull time is measured as described in Section 5.3.4. By monitoring fiber transmission, we are able to simultaneously assess fiber losses induced by the tapering procedure, as well as determine the point at which the fiber waist has become single mode. The emergence of this single guided fundamental mode is indicated as a stabilization of the fiber transmission (which is evident in Fig. 5.5) due to the fact that the diameter-dependent higher-order modes of the fiber have all died out. Using scanning electron microscope (SEM) images of complete tapered fibers from our pulling apparatus (see inset of Fig. 5.6), we have experimentally measured the diameters of our fibers at the single mode transition to be $\sim$1.1 μm, consistent with the theoretically predicted diameter for an air-clad fiber with an index of 1.47 at 1550 nm. By measuring the time required to reach this transition from a single pull, it is possible to determine a value for the hot-zone length l_{h} by inverting Eq. (5.4), provided that the pull speed and initial fiber diameter are known *a priori*. Once

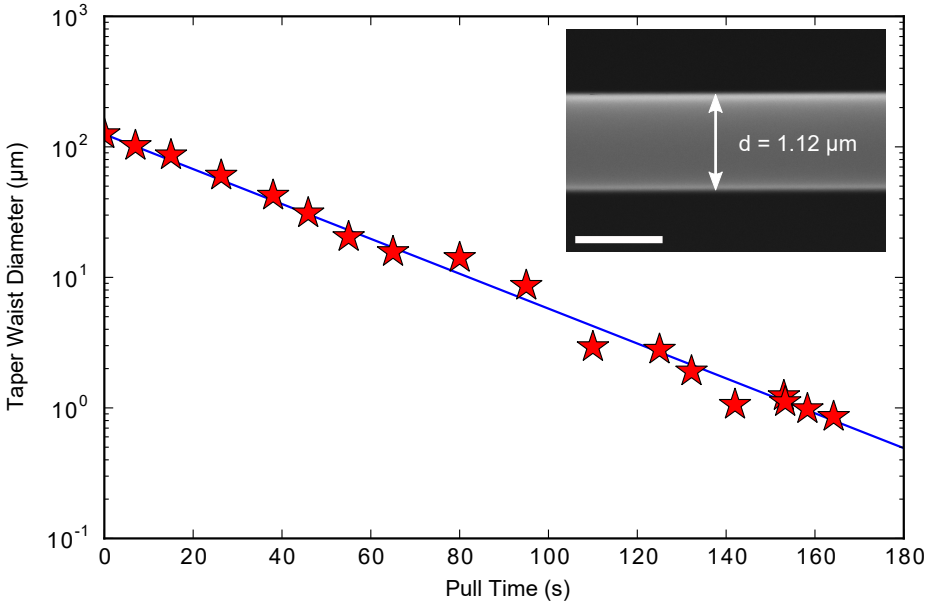

Figure 5.6: Plot of fiber waist diameter versus pull time for fibers pulled using the same parameters as described in Fig. 5.5. The red stars represent experimentally measured fiber waist diameters using an SEM, while the blue line is a fit to Eq. (5.4) with l_{h} as the only free parameter. This fit produces a value of $l_{\mathrm{h}} = 1.29$ mm, in excellent agreement with the predetermined value of 1.30 mm using the single mode cut-off point. Inset is an SEM image of the tapered fiber waist at the single mode transition. The waist diameter is measured to be 1.12 μm. Scale bar is 1 μm. Figure reproduced from Ref. [312] under the Creative Commons Attribution License.

we have determine this hot-zone length for a given set of pulling conditions, we are then able to predict the fiber waist diameter for a given pull time. Note that in order for this prediction to be accurate, care must be taken to ensure that all subsequent pulls have conditions matching the original one to provide a consistent hot-zone length, which is readily accomplished by the repeatability of our system. A plot of fiber waist diameter (measured using SEM images) versus pull time using the apparatus described in this section is presented in Fig. 5.6, indicating excellent agreement between the hot-zone length of 1.30 mm determined using the single mode cutoff point and the fit value of 1.29 mm. The ability to predict the fiber waist diameter is useful, as it allows for fabrication of fibers with varying diameters. This process could then, for instance, be used to engineer tapered fibers supporting a fundamental propagating mode that is phase-matched with a given

optical resonance of interest, enhancing coupling of light from the tapered fiber to the cavity mode [324].

At the point of single mode transition, the fiber waist diameter is small enough to produce the evanescent field required for coupling to an optical cavity, which can be seen in the inset of Fig. 5.5. However, it is often advantageous to continue pulling fibers to smaller diameters, further increasing the extent of the evanescent field outside the fiber geometry, allowing for a larger range of coupling before the fiber contacts the optical resonator. It is possible to create these sub-μm diameter fibers by continuing to pull for a small amount of time ($\sim$10 s) after the single mode transition has been reached. Using the OX-00 torch tip (see Fig. 5.4b), we have produced fibers with diameters as small as 850 nm before they break due to the pressure of the flowing hydrogen gas from the torch. By using the HT-3, our largest torch tip, the flame size increases, nearly doubling the hot-zone to 2.4 mm, allowing for the fabrication of tapered fibers with diameters down to 500 nm and slowly varying taper transitions, leading to transmission efficiencies in excess of 99%, which is on par with state-of-the-art, ultralow loss fiber pullers [334]. However, these narrow tapered fibers are extremely delicate, as well as very long ($l_\mathrm{t} \approx 30$ mm), making them difficult to mount within the limited space of our experimental apparatus. For this reason, we use the OX-1 torch tip to fabricate our cryogenic tapered fibers, as this tip creates a hot-zone with length $l_\mathrm{h} \approx 1.5$ mm (corresponding to a single-mode cutoff time of $\sim$180 s), resulting in the ideal tradeoff of compact ($l_\mathrm{t} = 16$ mm), yet highly efficient (transmission efficiency $>$ 90%) tapered fibers.

5.3.6 Dimpling Procedure

While this straight tapered fiber is useful for coupling to a single off-chip device, such as a microsphere [55, 57, 317, 324] or a bottle resonator [58, 59, 338], it is difficult to use as a probe of on-chip devices, although it can be done if the device is cleaved to hang over the edge of the chip [53] or isolated using a mesa [339]. Instead, we find it useful to introduce a small dimple into the tapered region of the fiber, which when approached towards the sample chip produces a portion of the taper waist that can be used as a probe of an individual on-chip optomechanical device

[312, 326]. By combining this probe with a precise positioning system, numerous devices can be sampled using the localized coupling region at the tip of the same dimple of the tapered fiber.

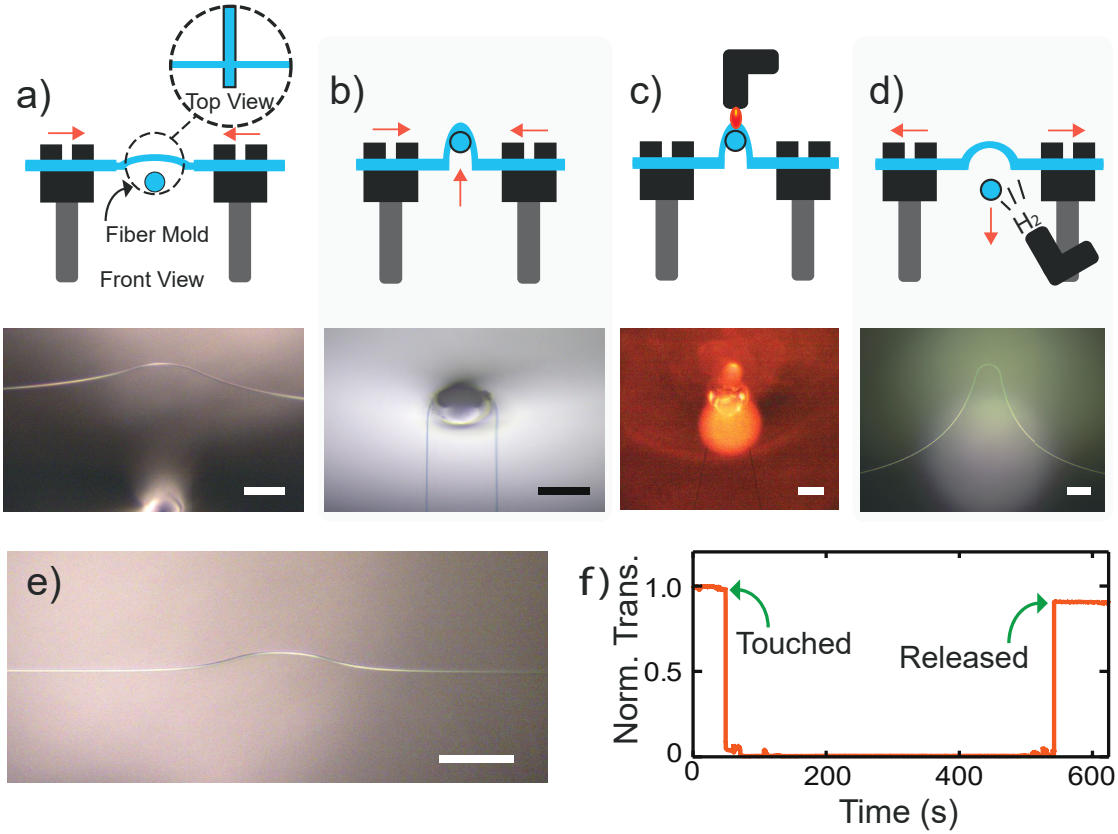

Figure 5.7: Schematics and microscope images illustrating the tapered fiber dimpling procedure. All scale bars are 125 μm. (a) The fiber is detensioned slightly (by about 10 μm) by moving the fiber mounts inward, producing a small protrusion at the fiber's thinnest point. The fiber mold is then adjusted such that it is aligned with this section of the fiber. (b) The fiber mold is raised upwards approximately 5 mm allowing the tapered fiber to wrap around it. During this process, the fiber mounts are gradually moved inwards to prevent the fiber from breaking, while still maintaining tension on the fiber mold. (c) An inverted hydrogen torch with a large flame (using an HT series torch tip) is approached by hand, annealing the tapered fiber into a dimpled shape. (d) The fiber mold is lowered while the fiber mounts are moved outwards to restore tension to the newly formed dimple. The dimple is gently removed from the fiber mold by flowing low pressure hydrogen gas from below. (e) Optical microscope image of the resulting dimpled tapered fiber using this procedure. (f) Plot indicating transmission (normalized to the pre-dimpled value) through the tapered fiber before and after dimpling. Losses induced by introducing the dimple to the fiber are ~8%. Figure reproduced from Ref. [312] under the Creative Commons Attribution License.

Once a tapered fiber has been pulled, we proceed with the dimpling procedure. To begin this process, we tape an optical fiber to the xyz-positioning stage located opposite the hydrogen torch, mounting it perpendicular to the tapered fiber so that it can be used as a mold in the dimpling process (see Fig. 5.7). The fiber mold is prepared by stripping off its acrylic coating and cleaning it with acetone, producing a mold of 125 μm in diameter. Alternatively, this fiber can be pre-tapered to a smaller diameter using the process described in Section 5.3.5, allowing for dimples with a smaller radius of curvature, which are generally more stable and maneuverable. A small amount of graphite powder is also applied to this fiber mold to prevent it from sticking to the tapered fiber, with excess removed using a fiber wipe or compressed air to avoid contaminating the dimple.

Continuing with the dimpling procedure, the torch is replaced by the microscope imaging system on the positioning gantry to allow the dimpling process to be observed in real time. We also monitor the transmission through the tapered fiber to quantify any losses induced by the dimpling procedure (see Fig. 5.7f). While watching with the microscope, the tapered fiber is detensioned by approximately 10 μm to reveal its thinnest point, which appears as a small bend upwards in the fiber (see Fig. 5.7a). The fiber mold is centered on this point and manually raised to touch the tapered fiber using the z-positioning stage. Once the mold fiber touches the waist of the tapered fiber, it's transmission immediately drops to zero due to scattering of the guided light off of the mold fiber. The mold fiber is then raised approximately 5 mm, while simultaneously detensioning the tapered fiber, allowing the fiber to wrap itself around the mold producing the desired dimpled shape, as shown in Fig. 5.7b. During this process, the tapered fiber remains tensioned tightly around the mold at all times to prevent it from twisting. A hydrogen flame produced by the tapering torch is then introduced to anneal the fiber into a dimpled shape. For this process, one of the HT series torch tips is used, producing a wide flame that allows for the increase in heat distribution required for annealing. This flame is approached to the dimple by hand, touching the mold and tapered fiber lightly (for about one second) until it glows red (see Fig. 5.7c). At this point, any graphite remaining on the mold will be burned away. The mold fiber is then slowly lowered in the same manner it was raised, this time tensioning the tapered fiber,

until the mold is returned to its initial position. The dimple is then extracted from the mold by using the unlit torch to flow hydrogen from below, applying a gentle pressure that releases the dimpled fiber. Typically, this process returns a dimple with minimal losses (we observed ∼8% losses in Fig. 5.7f). A microscope image of a dimpled fiber produced using this procedure is shown in Fig. 5.7e.

5.3.7 Gluing Procedure

Once a dimpled tapered fiber is produced, we carefully attach it to the custom-built fiber holder seen in Fig 5.8 using the gluing apparatus, while monitoring the entire process in real time with the microscope imaging system mounted on the positioning gantry. By imaging the tapered region, as well as monitoring transmission down the fiber, we can determine whether or not the tapered fiber has survived the gluing process.

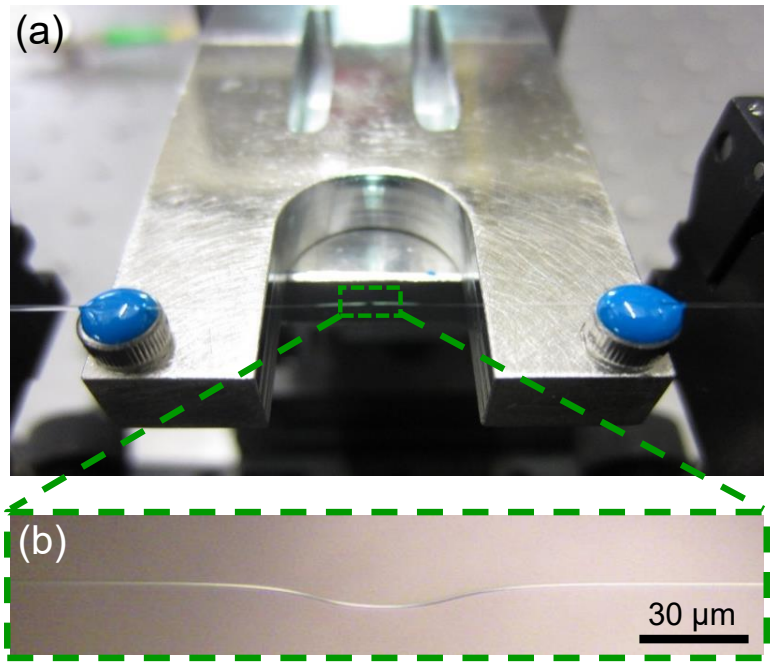

Figure 5.8: (a) A photograph of a dimpled tapered fiber glued onto its fiber holder using the procedure outlined in Section 5.3.7. (b) An optical microscope image of this fiber showing its dimpled region. This image is produced using the optical imaging system shown in Fig. 5.4c.

To begin this process, a low-temperature-compatible epoxy (Trabond 2151) is deposited into the heads of two 4-40 screws inserted into either side of the fiber

holder, as can be seen in Fig. 5.8a. Inserting the glue into the screws helps to ensure that both droplets of epoxy are approximately the same height, such that they will contact the unstretched portion of the fiber on both sides of the tapered region at the same time. Furthermore, with this modular design we can dispose of the screws once we are finished with the fiber, allowing us to reuse the fiber holder in the future. Once the epoxy is applied to the fiber holder, it is placed on its holding plate located on the gluing apparatus. The fiber holder is then carefully aligned beneath the fiber, ensuring that the dimple is centered between the two gluing points. Next, the fiber holder is slowly raised using the z-axis of the positioning stages until the fiber has been enveloped in epoxy on both sides of the taper. The initial epoxy is then left to dry (for about 30 minutes) allowing the fiber to be held rigidly in place, drastically increasing its durability. Once the initial epoxy dries, a second round of gluing is typically applied to the fiber, ensuring that the epoxy overlaps with the unstretched region of the fiber still coated in acrylate, which allows for the flexibility required to mount the dimpled fiber inside of the cryostat. The system is then left for at least 12 hours to permit the epoxy to properly set. After this curing process is complete, the fiber holder is removed from the tapering setup and is transferred directly to the optomechanical coupling system located inside the fridge (see Section 5.4.2) where it is fusion spliced into the existing optical circuit.

5.4 Cryogenic Optomechanical Coupling System

All measurements of our optomechanical cavities are performed using a low-temperature optical coupling apparatus located within the cryogenic environment of a dilution refrigerator. In this section, we describe this coupling apparatus, including its low-temperature imaging system, optical detection circuit, and temperature/thermometry control.

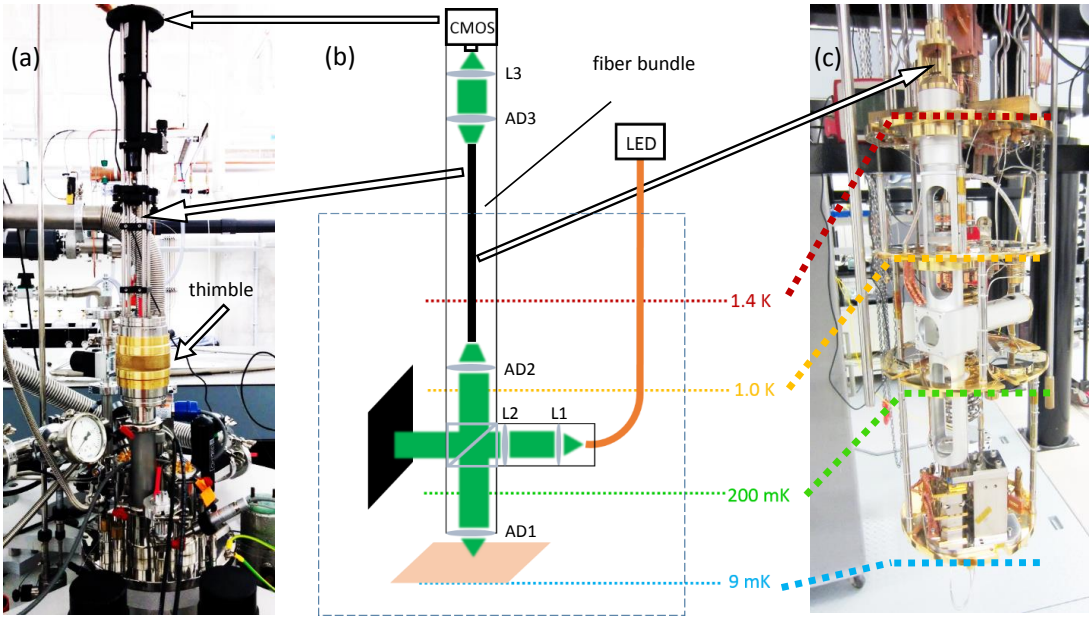

Figure 5.9: (a) Photograph of the of the optical imaging components located at room temperature on top of the fridge, highlighting the CMOS camera chip, adjustment thimble, and fiber bundle. (b) A schematic of the optical imaging system. Included are the illumination source (LED) and camera chip (CMOS), as well as the strong condenser lens (L1), plano-convex lenses (L2, L3), and achromatic doublets (AD1, AD2, AD3) used to collimate and focus the imaging beam. (c) Photograph of the cage-mount system housed within the dilution refrigerator used to ensure consistent alignment of all the optical components of the imaging system. Figure reproduced from Ref. [58]. Copyright 2015, AIP Publishing LLC.

5.4.1 Low Temperature Imaging System[4]

In order to ensure proper alignment between our dimpled tapered fiber and optomechanical cavities, we require the ability to view both components in real time. This is accomplished using a custom-built low temperature optical imaging system [58], as can be seen in Fig. 5.9, which allows for 1 μm resolution over a $\sim$250 μm diameter field of view. To observe our chip and tapered fiber at low temperatures, we illuminate them with low power light from a green LED (530 nm). This green light is coupled into our imaging system via a multimode fiber, where it is emitted into free space and collimated using a combination of a strong condenser (L1) and weak plano-convex (L2) lenses. The light is then sent to a 90/10

[4]The low temperature imaging system discussed in this section was designed and built by Allison MacDonald, and is described in further detail in Refs. [58, 309].

beam splitter, such that 90% of the initial beam's power is dumped onto a black metal velvet sheet located on the interior of the fridge's radiation shield, while the remaining 10% is sent to an achromatic doublet to focus light onto our device chip. Achromatic doublets are then used to focus light onto the sample (AD1), as well as recollect this light and inject it into bundle of 37,000 coherent optical fibers (AD2). The collected light is subsequently guided to room temperature through this bundle, where it is collimated by a third achromatic doublet (AD3) and focused onto a CMOS camera chip from a commercially available webcam using a plano-convex lens (L3). All lenses are housed in one-inch diameter aluminum lens tubes and are connected through a cage-mount alignment system that can be translated along the optical imaging axis via a thimble (50 μm positioning resolution over a full range of 50 mm) operated at room temperature, allowing for precise focus of the illumination beam on its intended target.

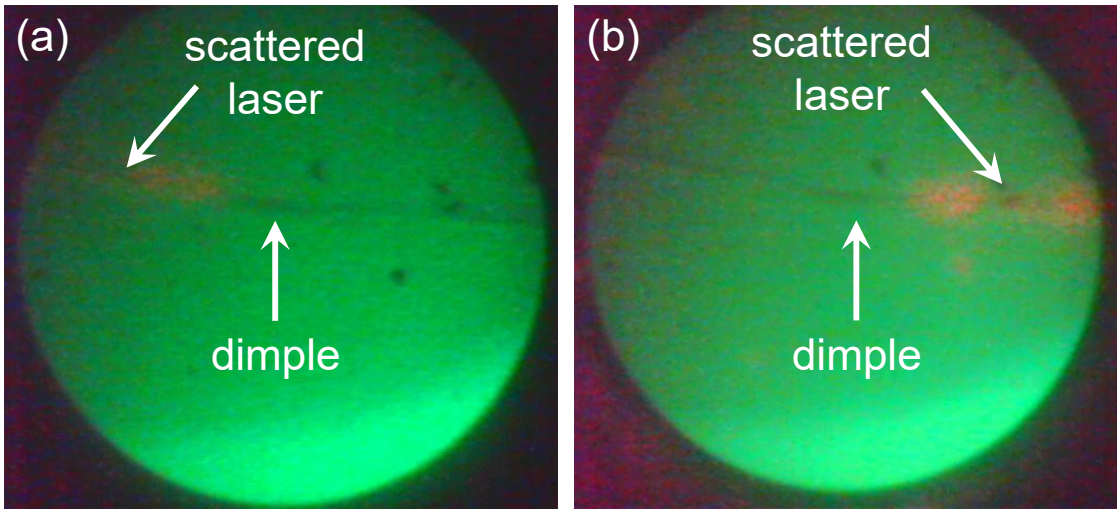

Figure 5.10: Images taken using the low temperature imaging system described in Section 5.4.1 highlighting red laser light from the handheld laser source scattering from the dimpled region of the fiber. In (a), the laser is sent in from the left side of the image, while in (b) light enters from the right. Scattering always occurs before the dimple, such that it is located in between the two bright spots in (a) and (b), as labelled in the figure.

Unfortunately, due to its 1 μm resolution, it is difficult to find the $\sim$1 μm diameter tapered fiber using this optical imaging system. However, by coupling red light (635 nm) from a handheld laser source into our optical circuit, we can ascertain the location of the fiber by observing enhanced scattering near the dimpled region.

Images demonstrating this fiber location techniques can be seen in Fig. 5.10.

5.4.2 Tapered Fiber Coupling System

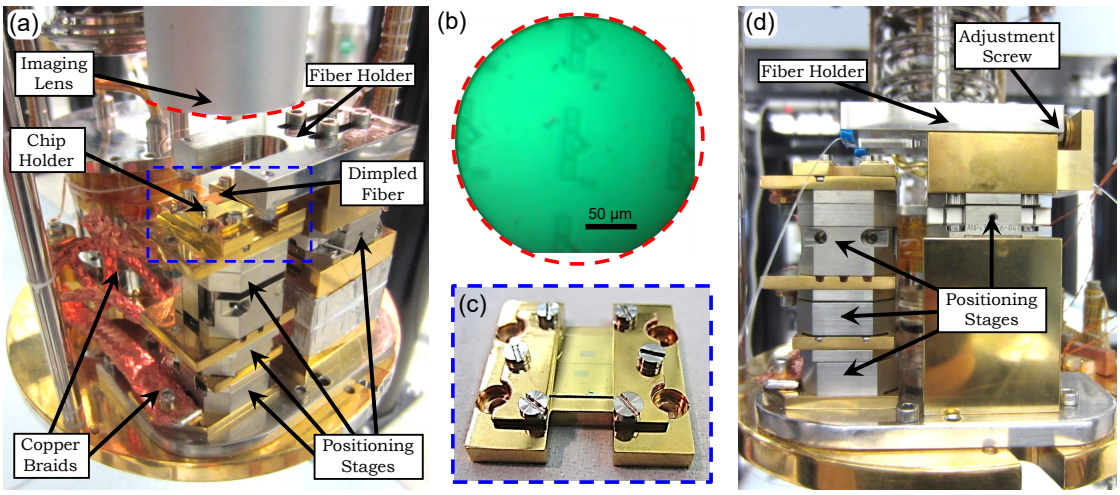

Figure 5.11: (a) The low-temperature coupling apparatus located on the mixing chamber plate of the dilution refrigerator. Red dashed line shows the optical imaging system lens tube used to produce the photograph in (b) of an array of on-chip optomechanical devices housed within the fridge at low temperature. Scale bar in (b) is 50 μm. The blue dashed line highlights the gold-plated copper chip holder shown in (c). Here the chip holder contains two silicon chips, where we can see the gold layer deposited on the chips to improve their thermal conductivity at low temperatures. The optomechanical device arrays are located in the small patch on each chip where the gold appears to be missing. (d) A profile view of the optical coupling system, allowing one to see the manual adjustment screw used to slide the fiber holder into position before cooldown.

All experiments presented in this thesis are performed using a cryogenic optomechanical coupling system located on the base plate of a dilution refrigerator as shown in Fig. 5.11. In this system, a gold-plated chip holder (see Fig. 5.11c) is placed on top of a stack of three low-temperature xyz linear position stages, each of which are anchored on a gold-plated copper mount (with dimensions of 31.6 mm x 24 mm $\times$ 3 mm). These stages are driven by a slip-stick piezo positioner allowing for coarse positioning with a step size of 50 nm over a full travel range of 5 mm, as well as fine positioning over 0.8 μm (at 4.2 K) with sub-nm resolution. The fiber holder is fastened to a separate positioning stack, consisting of another linear translation stage (same step sizes as the chip positioning stages, except with a full range of

motion of 6 mm and 1.2 μm for coarse and fine tuning, respectively) sandwiched between two gold-plated Invar blocks. Once mounted, the fiber is translated at room temperature using a manually adjusted 4-40 screw inserted into the back of its holder (see Fig. 5.11d). To account for thermal contractions of the coupling system as the fridge cools down, we translate the fiber to a known position (3/8 of a turn of the adjustment screw, corresponding to approximately 240 μm, outside of the optical imaging region) before tightening it down to ensure that the fiber will come back into view at low temperatures. The fiber can then be translated along its long axis using the linear positioning stage within its mount to locate its dimpled region while the fridge is operating. Finally, both the chip and fiber positioning apparatuses are fastened to an Invar plate, which is in turn attached to the base plate of the fridge, in order to minimize any relative displacement between these two stacks.

When operating the chip positioning stack, the motion of its translation stages leads to a heat load generated by their piezos calculated to be $\dot{\mathcal{Q}}_{\mathrm{p}} = 2.3$ mW for standard operating parameters[5]. We experimentally observe this positioner-induced heating as an increase in the base temperature of our fridge of up to 200 mK. It is therefore very important that we establish good thermal contact between these stages and the mixing chamber of the fridge to ensure that they quickly thermalize back to the base temperature of the fridge after operation. This thermal link is provided by a copper braid affixed to each stage's gold-plated copper mount, as seen in Fig. 5.11a.

5.4.3 Optical Detection Circuit

In order to address the optomechanical devices studied in this work, we have implemented a cryogenic optical detection system, shown schematically in Fig. 5.12, that allows for both direct detection and homodyne measurements of the collected optical signal. Light from a tunable external cavity diode laser (1550–1630 nm) is fiber coupled into the optical circuit, where its wavelength is monitored by

[5]This heat load is calculated using the equation $\dot{\mathcal{Q}}_{\mathrm{p}} = 2\pi f C V^2 \tan(\delta)$, where $f = 50$ Hz and $V = 50$ V are the standard frequency and voltage of the positioner drive signal, while $C \approx 170$ nF and $\delta = 1^\circ$ are the capacitance and loss angle of the piezo at low temperatures [340].

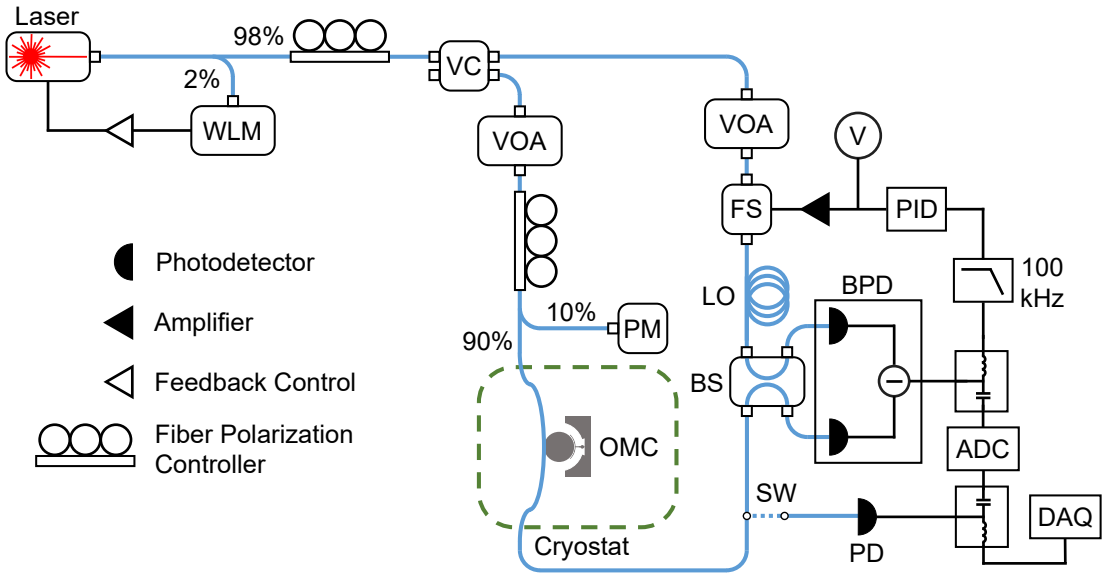

Figure 5.12: Schematic of the optical detection system used to probe the optical and mechanical properties of the device under study. WLM = wavelength meter, VC = variable coupler, VOA = variable optical attenuator, PM = power meter, OMC = optomechanical cavity, FS = fiber stretcher, PID = proportional-integral-derivative controller, V = voltmeter, LO = local oscillator, SW = optical switch, BS = beam splitter, BPD = balanced photodetector, PD = photodetector, ADC = analog-to-digital converter, DAQ = data acquisition. Figure reproduced from Ref. [295]. © 2019 American Physical Society.

sending 2% of its power to a wavelength meter (WLM), with this reading fed back into the laser controller to ensure long-term (several hour) frequency stability. The remainder of this signal is then sent through a variable coupler (VC), where it is split into two separate paths: the signal and the LO, with the power in each arm set by a VOA. For the measurements detailed in this work, the LO is kept at a constant power of ∼2.6 mW. The power in the signal arm, however, is varied depending on the experiment, all while being monitored by a 10% pickoff to a power meter (PM). Following the VOA, the signal arm continues through a fiber polarization controller (FPC), ensuring that the laser light headed towards the optical cavity is polarization-matched to the optical mode of interest. This polarization-controlled light is then coupled into (and subsequently out of) the dilution unit using vacuum-compatible optical fiber feedthroughs. Once inside the fridge, a dimpled tapered fiber [163, 312, 326] residing within the cryogenic optical coupling apparatus (see Fig. 5.11a) is used to inject light into the optomechanical

device, while also collecting the optical signal exiting the cavity. After coupling out of the fridge, the collected optical signal is sent to an optical switch (SW) that toggles between a standard, single-channel PD for direct detection and a BPD for homodyne measurements. In the latter case, light from the signal arm is recombined with the LO via a 50/50 fiber BS, with both outputs sent to the BPD. To ensure phase coherence between the two beams incident on the BS, the optical path length between the LO and signal arm are balanced to within a few mm using the procedure outlined in [309]. The remaining path length difference between these two arms of the circuit is maintained by feeding the low-frequency (< 15 kHz) voltage difference signal of the BPD (see Eq. (4.71)), which is monitored in real time using a voltmeter, through a proportional-integral-derivative (PID) controller and into a fiber stretcher (FS) located in the LO arm, such that deviations from the optical path length setpoint are compensated for. This process locks the phase of the homodyne measurement and allows for phase-sensitive probing of a specific quadrature of the optical field, with the mechanical motion extracted as fluctuations in the high-frequency portion (> 40 kHz) of the BPD's voltage difference signal, which is recorded in the time domain using a 500 MS/s analog-to-digital converter (ADC). The two low-frequency voltage readouts from each of the BPD's individual photodetectors are also collected, with one output sent to a low-frequency DAQ card to monitor slow drifts, while the other is sent to the ADC to observe rapid transients in this signal. Finally, the transmission through the optical cavity is obtained by monitoring the low frequency ($<$25 kHz) channel of the direct detection PD using the DAQ card.

5.4.4 Optical Detection Efficiency

To determine the overall efficiency of our optomechanical detection, we analyze the losses at each junction of our optical circuit. While coupling to the device, light from the tapered optical fiber is scattered off the substrate, as well as lost as photons travel through the fiber and out of the fridge, with corresponding transmission efficiencies of $\eta_{\mathrm{s}} = 62.6\%$ and $\eta_{\mathrm{f}} = 72.0\%$, respectively. Further losses in the fiber at room temperature result in a fraction $\eta_{\mathrm{RT}} = 81.6\%$ of the light that exits the fridge reaching the BPD. Including the quantum efficiency of the BPD itself, η_{BPD}

= 78.1%, the total efficiency of the optical detection circuit (*i.e.* the fraction of photons coupled out of the device that are converted into measured photoelectrons) is given by $\eta_{\mathrm{det}} = \eta_{\mathrm{s}}\eta_{\mathrm{f}}\eta_{\mathrm{RT}}\eta_{\mathrm{BPD}} = 28.7\%$. Note that in order to determine the total optomechanical detection efficiency η introduced in Section 4.4.1, which includes cavity losses, we need to multiply η_{det} by the cavity coupling efficiency $\eta_{\mathrm{c}} = \kappa_{\mathrm{e}}/\kappa$ associated with the considered experiment.

5.4.5 Thermometry and Temperature Control

To measure the temperature of the base plate of the dilution refrigerator, two complementary thermometers are used. The counts of gamma ray emission from a ^{60}Co nuclear orientation (NO) thermometer over a 570 s time window, referenced to a high temperature count rate at 4.2 K, provides accurate temperature readings below 50 mK, while the resistance curve of a RuO thermometer is used for $T \geq 50$ mK. Uncertainty in the temperature readings of the NO thermometer are obtained as the standard deviation in the spread of reported temperatures over the course of a measurement, while the RuO error is taken as the uncertainty in the accuracy of the sensor as specified by the supplier. Using measurements from the NO thermometer displayed in Fig. 5.13, we determine the base temperature of the fridge to be $T_{\mathrm{b}} = 9.3 \pm 0.2$ mK.

In order to heat the mixing chamber plate above its base temperature while the fridge is operating, current is applied to a resistive heater mounted on the mixing chamber plate, with temperature stability for the duration of a given measurement ensured by a PID-controlled feedback loop referenced to the RuO thermometer. In the range of 10 mK to 800 mK, the cooling power is provided by operating the dilution unit, while for temperatures up to 4.2 K, fridge circulation is ceased and cooling is supplied by the 1K pot. Above 4.2 K, the 1K pot is stopped, such that connection to the liquid helium bath surrounding the fridge is the source of cooling for the base plate.

We also perform experiments where exchange gas is added to the inner vacuum can (IVC) of the fridge while the dilution unit is not in operation to enhance the thermalization the system to the helium bath temperature of 4.2 K. This is done by adding $\sim$1 cm^3 of helium gas (at room temperature and atmospheric

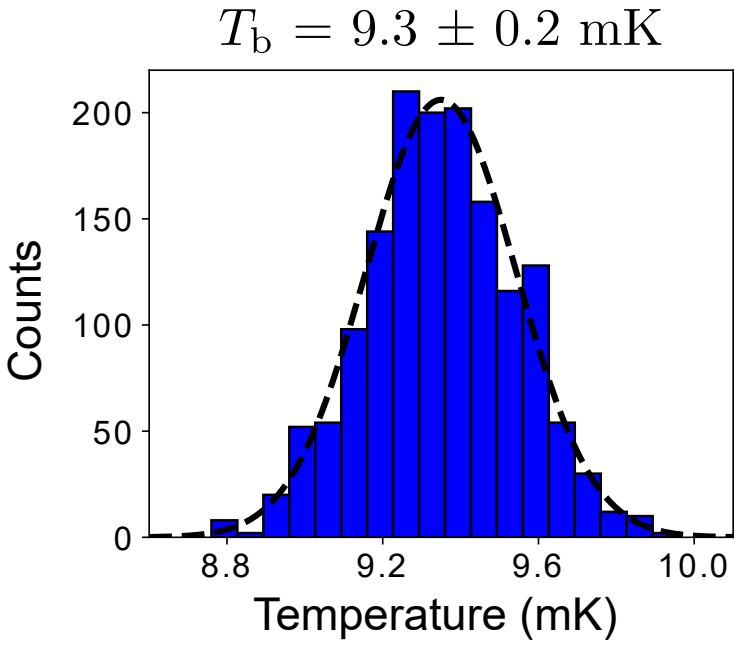

Figure 5.13: Histogram of the base temperatures of the fridge obtained using the NO thermometer for 1500 individual measurements taken over 13 days between May 3, 2017 and May 16, 2017. The black dashed line is a fit of the data to a normal distribution, from which we extract an average base temperature of $T_b = 9.3 \pm 0.2$ mK, where the uncertainty is the standard deviation of the distribution.

pressure) to the volume of the IVC ($V_{IVC} = 2.2 \times 10^{-2}$ m^3). Using the ideal gas law, this results in an exchange gas pressure within the IVC of $P_{IVC} = 6.5 \times 10^{-2}$ Pa $\sim 10^{-1}$ Pa at 4.2 K. Note that at our highest operating temperature of 10 K, this pressure rises slightly to $P_{IVC} = 1.6 \times 10^{-1}$ Pa, while dropping by a factor of 1000 to $P_{IVC} = 1.6 \times 10^{-4}$ Pa at 10 mK. In reality, these pressures will certainly be lower due to condensation of helium on the fridge's surfaces, as well as residual volumes from pumping lines, inputs, etc., however, we use these values as an upper bound when calculating the effects of gas-induced damping on our mechanical resonator in Section 2.5.6.

5.5 Conclusion

In this chapter, we detailed the optomechanical devices considered in this thesis and the methods used to study them. We began by providing a brief overview of these devices and their material properties, as well as the procedure used to

fabricated them. We then gave a theoretical introduction to the tapered fiber optical waveguides used to couple light into our devices, modelling their shape, electromagnetic fields, and single-mode cut-off diameter. With this description in place, we detailed the heat-and-pull rig used to create and mount our cryogenic dimpled tapered fibers. Finally, we discussed the low temperature coupling apparatus that uses this fiber to address our optomechanical devices.

Chapter 6

Two-Level System Damping in a Quasi-One-Dimensional Optomechanical Resonator

This chapter is based on the publication B. D. Hauer, P. H. Kim, C. Doolin, F. Souris, and J. P. Davis, "Two-level system damping in a quasi-one-dimensional optomechanical resonator," *Phys. Rev. B* **98**, 214303 (2018) (Ref. [163]) and draws heavily on the content therein. Note that in order to be consistent with the rest of the thesis, a number of minor notational changes have been made with respect to the original publication.

6.1 Introduction

The TLS relaxation damping model introduced in Section 6.2 has been very successful in describing the absorption of sound waves in bulk amorphous solids, where a T^3-dependence in acoustic attenuation has been observed at low temperatures for a number of glassy materials in accordance with their three-dimensional nature [341]. However, the situation becomes significantly more complicated when considering the reduced geometries associated with nano/micromechanical resonators. Although a linear temperature dependence in mechanical dissipation was first observed for early cryogenic measurements of cm-scale single-crystal silicon torsional oscillators [342, 343], this behaviour was rationalized as being due to the crystalline nature of the resonator material [344] or electronic defects [345], as opposed to reduced dimensionality effects. While

a similar linear trend was later reported in polycrystalline aluminum nanobeams [346], the vast majority of cryogenic dissipation measurements performed on driven micro/nanomechanical resonators have demonstrated a considerably weaker temperature dependence of $\Gamma \sim T^{1/3}$ [347–350]. Attempts to explain this sublinear temperature dependence have associated it with the large strain induced by the external drive fields applied to these resonators [351] or possibly their beamlike geometries [201, 352], however, a full quantitative description has yet to be found. In light of this disconnect between theory and experiment, a clear and careful analysis of TLS damping in reduced-dimensionality nanomechanical resonators is required in order to comprehend this dissipation mechanism [162].

In this chapter, we present measurements of the low temperature dissipation in a silicon nanobeam due to coupling with TLS defects confined within its one-dimensional geometry. In Section 6.2, we begin by modifying the standard tunneling model, which has been used to successfully describe acoustic attenuation due to TLS defects in bulk amorphous materials, to properly account for the one-dimensional geometry of our crystalline nanobeam. We continue in Section 6.3 by briefly discussing the geometry of our half-ring resonator, providing FEM simulations of its optical and mechanical modes, which allow us to calculate its optomechanical properties and strain distributions. We follow in Section 6.4 by detailing the optomechanically-mediated ringdown technique used to measure the nanomechanical resonator's damping rate. Here we describe the pulsed homodyne detection system and the mechanical mode temperature calibration technique used to characterize our optomechanical system, as well as assess the possibility of measurement-induced heating of the device chip. Using this measurement scheme, we determine the mechanical damping rate for four of the device's mechanical modes over three orders of magnitude in fridge temperature ranging from 10 mK to 10 K. In Section 6.5, we fit these data, demonstrating quantitative agreement with the tunneling model for relaxation damping due to TLS defects embedded in a one-dimensional geometry. Extracting information about the density of states and deformation potentials of the TLS ensembles that couple to the resonator's motion, we speculate that they are caused by glassy surface defects created during fabrication of the device. Finally, we show that at 10 mK each mechanical mode

couples on average to less than a single thermally-active defect, entering the regime where quantum-coherent interactions between phonons and an individual defect may be possible.

6.2 Two-Level System Damping

At cryogenic temperatures phononic energy loss is often caused by coupling between the motion of the resonator and defects within its material [353]. This was first discovered in the early 1970s by Zeller and Pohl [354] who noticed that the cryogenic thermal properties of a number of glassy solids deviated significantly from what was expected according to the Debye model (see Section 2.4.3). To account for this anomalous behaviour, Anderson *et al.* [220] and Phillips [221] simultaneously developed what is now known as the standard tunneling model (STM), whereby phonons in a solid exchange energy with the medium by driving configurational changes of intrinsic defect states. Further extensions to this model were made by Jäckle *et al.* [355, 356], who used it to correctly describe the anomalous acoustic absorption observed in fused quartz [357].

While early incarnations of the STM were used with great success to describe the cryogenic properties of bulk amorphous solids, modifications to this model are necessary in order to account for the behaviour of defect-phonon coupling in reduced dimensionality systems fabricated from crystalline solids [162]. Here, we introduce the standard tunneling model in the original form used to model defects in amorphous solids and extend it to describe the mechanical dissipation in crystalline nanomechanical resonators.

6.2.1 Double-Well Potential Model for Tunneling Systems

In the STM, the configurational states of each defect in the solid are modelled as a particle of mass m_0 confined to an asymmetric double-well potential [220, 221], as seen in Fig. 6.1. We assume this potential to be comprised of two identical harmonic wells, each with a ground state energy $E_\mathrm{g} = \hbar\omega_\mathrm{g}/2$, offset by an asymmetry energy E_Δ, and separated by a barrier of height E_B and the configurational coordinate q. We consider the system to be at low enough temperatures ($k_\mathrm{B}T \ll \hbar\omega_\mathrm{g}$) such that

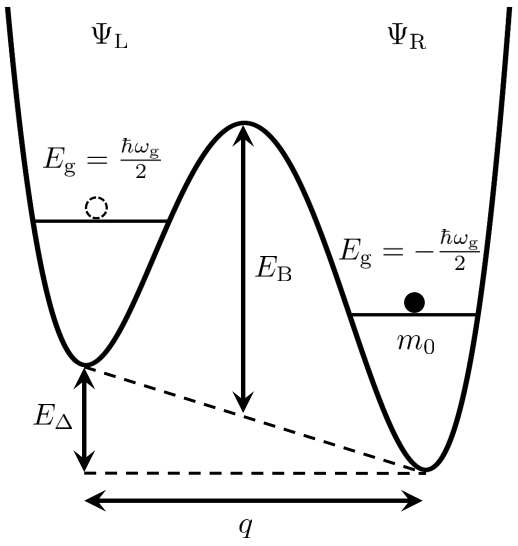

Figure 6.1: Schematic of a particle of mass m_0 tunneling between the two ground states of a double-well potential, separated by a barrier of height E_{B} and a generalized configurational coordinate q, with an asymmetry E_Δ between their two minima. The particle can tunnel through the barrier, allowing it to be localized in the ground state of either the left or right well (each with a ground state energy of $E_{\mathrm{g}} = \hbar\omega_{\mathrm{g}}/2$), as described by the wavefunctions Ψ_{L} and Ψ_{R}, respectively. Figure adapted from Ref. [163]. © 2018 American Physical Society.

only the ground state of each well will be populated with any significant probability. This allows for a TLS description of these two lowest lying configurational states, with wavefunctions $\Psi_{\mathrm{L}}(\vec{r})$ ($\Psi_{\mathrm{R}}(\vec{r})$) corresponding to the particle occupying the higher (lower) energy state in the left (right) well. In this set of localized basis states, the Hamiltonian will be given by [222, 223]

$$\hat{\mathcal{H}}_{\mathrm{TLS}} = \frac{1}{2}E_\Delta\hat{\sigma}_z - \frac{1}{2}E_0\hat{\sigma}_x, \tag{6.1}$$

where we have chosen zero energy to be the midway point between the minimum of each well and $\hat{\sigma}_x$ ($\hat{\sigma}_z$) is the x (z) Pauli spin matrix. In this Hamiltonian, quantum tunneling between the two states of the TLS is characterized by the tunnel splitting or tunneling energy E_0, which can be determined using the Wentzel-Kramers-Brillouin (WKB) approximation to be $E_0 \approx \hbar\omega_{\mathrm{g}}e^{-\zeta}$, where $\zeta = \sqrt{2m_0E_{\mathrm{B}}q^2/\hbar^2}$ is known as the tunneling or Gamow parameter and characterizes the penetration of the wavefunctions into the barrier [222].

The Hamiltonian in Eq. (6.1) can be diagonalized by rotating the basis by an

angle φ defined by $\tan(2\varphi) = E_0/E_\Delta$, resulting in the new Hamiltonian [222, 223]

$$\hat{H}_{\mathrm{TLS}} = \frac{1}{2} E \hat{\sigma}_z, \tag{6.2}$$

in the energy eigenstate basis

$$\Psi_+(\vec{r}) = \Psi_{\mathrm{L}}(\vec{r})\cos(\varphi) - \Psi_{\mathrm{R}}(\vec{r})\sin(\varphi), \tag{6.3}$$

$$\Psi_-(\vec{r}) = \Psi_{\mathrm{L}}(\vec{r})\sin(\varphi) + \Psi_{\mathrm{R}}(\vec{r})\cos(\varphi). \tag{6.4}$$

Here, $E = \sqrt{E_\Delta^2 + E_0^2}$ is the energy separation between the two states of the TLS, with the wavefunctions $\Psi_\pm(\vec{r})$ corresponding to the $\pm E/2$ eigenvalues. If the TLS is in thermal equilibrium with a bath at temperature T, we can use the diagonalized Hamiltonian of Eq. (6.2) to determine the probability that the TLS is in either of its two states as

$$p_\pm^0 = \frac{e^{\mp E/2k_{\mathrm{B}}T}}{e^{E/2k_{\mathrm{B}}T} + e^{-E/2k_{\mathrm{B}}T}} = \frac{1}{e^{\pm E/k_{\mathrm{B}}T} + 1}, \tag{6.5}$$

with p_+^0 (p_-^0) corresponding to the excited (ground) state. From these probabilities, we also define a population inversion probability as

$$s^0 = p_+^0 - p_-^0 = -\tanh\left(\frac{E}{2k_{\mathrm{B}}T}\right). \tag{6.6}$$

6.2.2 Resonant Interaction

Tunneling systems that are embedded in a solid are able to exchange energy with the various excitations of the surrounding medium. Here, we focus on insulating solids, such that the dominant excitation at low temperatures will be phonons. If the interacting phonon has energy on the order of, or greater than, the TLS separation energy, it can be directly absorbed, promoting a TLS in its ground state to its excited state. Therefore, the mechanical dissipation rate Γ_{res} due to this resonant interaction is proportional to the population inversion probabilities of the interacting TLSs, such that [162, 187, 222, 223]

$$\Gamma_{\mathrm{res}} \propto \tanh\left(\frac{E}{2k_{\mathrm{B}}T}\right). \tag{6.7}$$

However, for the temperatures (10 mK to 10 K) and frequencies ($<$ 20 MHz) considered in this thesis, TLS with energies relevant for this resonant interaction

will be thermally saturated ($E \sim \hbar\omega_{\mathrm{m}} << k_{\mathrm{B}}T$), such that absorption or emission of a phonon is equally likely [162]. Therefore, this dissipation mechanism does not need to be considered.

6.2.3 Relaxation Interaction

For non-resonant defect-phonon interactions at low frequencies (*i.e.* where the phonon energy is less than the separation between these two defect states), we instead focus on the relaxation interaction [187, 222, 223]. In this situation, local strain variations due to the motion of the resonator distort the environment of the TLS defects, driving the system out of thermal equilibrium by shifting the energy separation between their two levels. This allows the TLS to interact with the lower frequency vibrational modes of the solid, absorbing and emitting phonons until it can relax to this new thermal equilibrium.

To model this relaxation effect, we consider the full Hamiltonian for the interaction between the modes of a mechanical resonator and an ensemble of TLS defects, given by the so-called "spin-boson" Hamiltonian [162, 201, 358]

$$\hat{H} = \sum_k \hbar\omega_k \hat{b}_k^\dagger \hat{b}_k + \frac{1}{2}\sum_j E_j \hat{\sigma}_z + \sum_j \left(\frac{E_{\Delta j}}{E_j}\hat{\sigma}_x + \frac{E_{0j}}{E_j}\hat{\sigma}_z\right) \overleftrightarrow{\gamma}_j : \overleftrightarrow{\varepsilon} + \hat{H}_{\Gamma_{\mathrm{i}}}. \tag{6.8}$$

In this Hamiltonian, the first two terms correspond to the energies of the resonator's mechanical modes, each with angular frequency ω_k and annihilation (creation) operator $\hat{b}_k$ ($\hat{b}_k^\dagger$), and the TLS ensemble, with asymmetry, tunneling, and separation energies of $E_{\Delta j}$, E_{0j}, and $E_j = \sqrt{E_{\Delta j}^2 + E_{0j}^2}$ for each TLS. The third term then describes the coupling between the TLS ensemble and the mechanical motion of the resonator, characterized by the dyadic (tensor) product $\overleftrightarrow{\gamma}_j : \overleftrightarrow{\varepsilon} = \gamma_{j,ab}\varepsilon_{ab}$ between the deformation potential tensor (*i.e.* the strain-TLS coupling tensor) $\overleftrightarrow{\gamma}_j$ of the jth TLS and the total strain tensor $\overleftrightarrow{\varepsilon}$ induced by the resonator motion [162, 223, 359]. Using Eq. (2.21), along with the fact that the (quantized) displacement amplitude of each mechanical mode can be expressed as $\hat{x}_k = x_{\mathrm{zpf}}(\hat{b}_k^\dagger + \hat{b}_k)$ (see Eq. (2.17)), we can write the system Hamiltonian in the more succinct form

$$\hat{H} = \sum_k \hbar\omega_k \hat{b}_k^\dagger \hat{b}_k + \frac{1}{2}\sum_j E_j \hat{\sigma}_z + \sum_j \sum_k \left(\mu_{kj}\hat{\sigma}_x + \nu_{kj}\hat{\sigma}_z\right)\left(\hat{b}_k^\dagger + \hat{b}_k\right) + \hat{H}_{\Gamma_{\mathrm{i}}}, \tag{6.9}$$

where we have introduced the TLS-phonon coupling coefficients

$$\mu_{kj} = \frac{E_{0j}}{E_j}\sqrt{\frac{\hbar}{2\omega_k}}\overleftrightarrow{\gamma}_j : \overleftrightarrow{\varepsilon}_k(\mathbf{r}_j), \tag{6.10}$$

$$\nu_{kj} = \frac{E_{\Delta j}}{E_j}\sqrt{\frac{\hbar}{2\omega_k}}\overleftrightarrow{\gamma}_j : \overleftrightarrow{\varepsilon}_k(\mathbf{r}_j), \tag{6.11}$$

with $\overleftrightarrow{\varepsilon}_k(\mathbf{r}_j)$ being the strain profile of the kth mechanical mode evaluated at the position of the jth TLS denoted by the vector $\mathbf{r}_j$. Finally, similar to Eq. (4.7), $\hat{H}_{\Gamma_\mathrm{i}}$ is given by

$$\hat{H}_{\Gamma_\mathrm{i}} = \sum_q \hbar\omega_q \hat{b}_q^\dagger \hat{b}_q + i\hbar \sum_q \sum_k \left(f_{qk}\hat{b}_k^\dagger \hat{b}_q - f_{qk}^* \hat{b}_q^\dagger \hat{b}_k \right), \tag{6.12}$$

such that this Hamiltonian describes the interaction of the resonator with its environmental bath, accounting for dissipation mechanisms aside from those due to TLS-phonon interactions, as well as the thermal drive of the mechanical motion.

Coupling between the mechanical modes of the resonator and the TLS ensemble as described by the the Hamiltonian in Eq. (6.9) will act to shift the energy separation of each TLS in time according to

$$E_j'(t) = E_j + \delta E_j(t), \tag{6.13}$$

with

$$\delta E_j(t) = 2\sum_q \nu_{qj}\left[b_k(t) + b_k^*(t)\right], \tag{6.14}$$

where we have introduced the expectation value of the kth mechanical mode's annihilation operator as $b_k(t) = \langle \hat{b}_k(t) \rangle$. This shift in the separation energy will additionally act to perturb the difference in population between the excited and ground state of each TLS away from equilibrium, leading to a time-dependent inversion probability

$$s_j(t) = \langle \sigma_z \rangle = p_{j,+}(t) - p_{j,-}(t) = s_j^0 + \delta s_j(t), \tag{6.15}$$

where $\delta s_j(t)$ is the instantaneous deviation of the inversion probability away from its equilibrium value s_j^0 in the absence of the phonon-induced strain, while $p_{j,+}(t)$ and $p_{j,-}(t)$ are the instantaneous probabilities of the jth TLS being in its excited and ground state, respectively.

In order to determine $\delta s_j(t)$, we must first realize that the perturbed system will strive towards a new, time-dependent equilibrium inversion probability $\bar{s}_j(t) = \bar{p}_{j,+}(t) - \bar{p}_{j,-}(t)$, which can be found by inputting Eq. (6.13) into the expression for s_j^0 in Eq. (6.6) and expanding to first order to obtain

$$\bar{s}_j(t) = s_j^0 + \frac{ds_j^0}{dE_j}\delta E_j(t) = s_j^0 - \operatorname{sech}^2\left(\frac{E_j}{2k_\mathrm{B}T}\right)\frac{\delta E_j(t)}{2k_\mathrm{B}T}. \tag{6.16}$$

This "instantaneous" equilibrium probability can be interpreted as the inversion probability that the system would reach if the TLS energy separation stayed at $E_j'(t)$ for a sufficiently long time. However, a given TLS cannot immediately achieve this new equilibrium, as it must do so by exchanging energy with the surrounding phonon bath, such that the probabilities of the excited and ground states evolve according to [222]

$$\dot{p}_{j,+} = -p_{j,+}\upsilon_{j,-} + p_{j,-}\upsilon_{j,+}, \tag{6.17}$$

$$\dot{p}_{j,-} = p_{j,+}\upsilon_{j,-} - p_{j,-}\upsilon_{j,+}, \tag{6.18}$$

where $\upsilon_{j,-}$ ($\upsilon_{j,+}$) is the phonon-induced transition rate associated with the excitation (de-excitation) of the TLS. By examining the steady state of Eqs. (6.17) and (6.18), we can see that these transition rates obey the condition of detailed balance, such that $\upsilon_{j,+}/\upsilon_{j,-} = p_{j,+}^0/p_{j,-}^0 = \bar{p}_{j,+}(t)/\bar{p}_{j,-}(t) = e^{-E_j/k_\mathrm{B}T}$ [223, 356]. Using this relation, along with the conservation of probability, $p_{j,+}(t) + p_{j,-}(t) = 1$, we find

$$\dot{s}_j = -(p_{j,+} - p_{j,-})(\upsilon_{j,+} + \upsilon_{j,-}) + \upsilon_{j,+} - \upsilon_{j,-} = -\frac{s_j - \bar{s}_j}{\tau_j}, \tag{6.19}$$

where we have introduced the relaxation rate of the TLS populations as

$$\tau_j^{-1} = \upsilon_{j,+} + \upsilon_{j,-} = \upsilon_{j,-}(e^{-E_j/k_\mathrm{B}T} + 1). \tag{6.20}$$

This rate can be interpreted as the inverse of the relaxation time τ_j required for the inversion probability of a given TLS to relax back to its steady-state value after it has been perturbed away from equilibrium. By inputting Eq. (6.16) into Eq. (6.19), while using the fact that $\dot{s}_j(t) = \delta\dot{s}_j(t)$, we then find

$$\tau_j\delta\dot{s}_j = -\delta s_j - \frac{1}{2k_\mathrm{B}T}\operatorname{sech}^2\left(\frac{E_j}{2k_\mathrm{B}T}\right)\delta E_j(t), \tag{6.21}$$

which can be Fourier transformed to obtain

$$\delta s_j(\omega) = -\frac{1}{2k_{\mathrm{B}}T}\mathrm{sech}^2\left(\frac{E_j}{2k_{\mathrm{B}}T}\right)\frac{\delta E_j(\omega)}{1-i\omega\tau_j}, \tag{6.22}$$

resulting in the frequency domain solution for the deviation of the inversion probability from equilibrium.

We now look to determine an expression for the TLS relaxation rate given by Eq. (6.20). This can be done by applying a Fermi's Golden Rule calculation using the interaction Hamiltonian (*i.e.* the third term in Eq. (6.9)) to determine the transition rate from the initial state $|\Psi_i\rangle = |\Psi_{j,+}, n_i\rangle$ to the final state $|\Psi_f\rangle = |\Psi_{j,-}, n_f\rangle$, where n_i (n_f) is the initial (final) occupancy of the phonon state and $\Psi_{j,+}$ ($\Psi_{j,-}$) is the wavefunction corresponding to the TLS in its excited (ground) state. Enforcing $n_f = n_i + 1$, as well as $E_j = \hbar\omega_k$ (when the TLS de-excites, it creates a single phonon of frequency ω_k), while averaging over the initial phonon states and summing over the final phonon states, gives the total TLS de-excitation rate [187, 222]

$$\upsilon_{j,-} = \left(\frac{E_{0j}}{E_j}\right)^2 \sum_k \frac{\pi}{\omega_k}\left(\langle n_k\rangle + 1\right)|\overleftrightarrow{\gamma}_j : \overleftrightarrow{\varepsilon}_k(\mathbf{r}_j)|^2\delta(E_j - \hbar\omega_k), \tag{6.23}$$

where $\langle n_k\rangle = (e^{\hbar\omega_k/k_{\mathrm{B}}T}-1)^{-1}$ is the average phonon occupation of the kth mechanical mode according to Bose-Einstein statistics. Inputting this expression into Eq. (6.20), the TLS relaxation rate is then be found to be [162]

$$\tau_j^{-1} = \left(\frac{E_{0j}}{E_j}\right)^2 \sum_k \frac{\pi}{\omega_k}\coth\left(\frac{E_j}{2k_{\mathrm{B}}T}\right)|\overleftrightarrow{\gamma}_j : \overleftrightarrow{\varepsilon}_k(\mathbf{r}_j)|^2\delta(E_j - \hbar\omega_k). \tag{6.24}$$

To analyze how the delay in equilibration due this finite relaxation rate affects the dissipation of acoustic energy in each of the mechanical modes, we again look to the Hamiltonian in Eq. (6.9) to determine the Heisenberg equation of motion for $\hat{b}_k$ as

$$\dot{\hat{b}}_k = \frac{i}{\hbar}[\hat{H}, \hat{b}_k] = -\left(i\omega_k + \frac{\Gamma_{k,\mathrm{i}}}{2}\right)\hat{b}_q - \frac{i}{\hbar}\sum_j\left(\mu_{qj}\hat{\sigma}_x + \nu_{qj}\hat{\sigma}_z\right) - \sqrt{\Gamma_{k,\mathrm{i}}}\hat{b}_{k,\mathrm{i}}, \tag{6.25}$$

where we have used the fact that (see Section 4.3.2)

$$\frac{i}{\hbar}[\hat{H}_{\Gamma_\mathrm{i}}, \hat{b}_k] = -\frac{\Gamma_{k,\mathrm{i}}}{2}\hat{b}_k - \sqrt{\Gamma_{k,\mathrm{i}}}\hat{b}_{k,\mathrm{i}}. \tag{6.26}$$

Here we have introduced $\Gamma_{k,\mathrm{i}}$ as the damping rate for the kth mechanical mode due to sources other than the TLS ensemble, while $\hat{b}_{k,\mathrm{i}}$ is a drive term due to noise (both thermal and quantum) leaking in from the environment [151, 203]. Taking the expectation value of Eq. (6.25), we find an analogous equation of motion for b_k as

$$\dot{b}_k = -\left(i\omega_k + \frac{\Gamma_{k,\mathrm{i}}}{2}\right) b_k - \frac{i}{\hbar}\sum_j \nu_{kj} s_j - \sqrt{\Gamma_{k,\mathrm{i}}} b_{k,\mathrm{i}}, \tag{6.27}$$

where we have neglected the term proportional to μ_{kj}. Fourier transforming Eq. (6.27) and grouping terms proportional to b_k, while using the fact that only the dynamical part of s_j (*i.e.* $\delta s_j(\omega)$ given by Eq. (6.22)) will contribute to the mechanical damping, we find the expression for the total dissipation rate of the kth mechanical mode as

$$\Gamma_k = \Gamma_{k,\mathrm{i}} + \Gamma_{k,\mathrm{TLS}}, \tag{6.28}$$

where

$$\Gamma_{k,\mathrm{TLS}} = \sum_j \left(\frac{E_{\Delta j}}{E_j}\right)^2 \frac{|\overleftrightarrow{\gamma}_j : \overleftrightarrow{\varepsilon}_k(\mathbf{r}_j)|^2}{k_\mathrm{B}T} \mathrm{sech}^2\left(\frac{E_j}{2k_\mathrm{B}T}\right) \frac{\tau_j}{1+\omega_k^2\tau_j^2}, \tag{6.29}$$

is the mechanical damping rate due to the TLS-phonon relaxation interaction. We note that in the situation where TLS damping dominates (*i.e.* $\Gamma_{k,\mathrm{TLS}} \gg \Gamma_{k,\mathrm{i}}$) for a given mode, we can take $\Gamma_k \approx \Gamma_{k,\mathrm{TLS}}$, as is done for the fits in Section 6.5 below.

6.2.4 Determination of $\gamma_j : \varepsilon_q(\mathbf{r}_j)$

In general, the product $\overleftrightarrow{\gamma}_j : \overleftrightarrow{\varepsilon}_k(\mathbf{r}_j)$ found in Eq. (6.29) is a complicated, spatially varying sum over a number of tensor components. However, by using the local symmetries of the simple cubic lattice of crystalline silicon, as well as making some assumptions about our TLS ensemble, we can simplify this quantity considerably. We begin by expressing the deformation potential tensor of the jth TLS as $\overleftrightarrow{\gamma}_j = \overleftrightarrow{R} : \overleftrightarrow{W}_j = R_{abcd} W_{j,ab}$ [359], where $\overleftrightarrow{R}$ is a fourth rank tensor that describes the TLS environment and

$$\overleftrightarrow{W}_j = \begin{bmatrix} W_{j,x}^2 & W_{j,x}W_{j,y} & W_{j,x}W_{j,z} \\ W_{j,x}W_{j,y} & W_{j,y}^2 & W_{j,y}W_{j,z} \\ W_{j,x}W_{j,z} & W_{j,y}W_{j,z} & W_{j,z}^2 \end{bmatrix} \tag{6.30}$$

is a second rank tensor that characterizes the orientation of each TLS. Here, $W_{j,x} = \sin(\theta_j)\cos(\phi_j)$, $W_{j,y} = \sin(\theta_j)\sin(\phi_j)$ and $W_{j,z} = \cos(\theta_j)$ are the components

of the unit vector parallel to the defect's elastic dipole moment, with θ_j and ϕ_j specifying its orientation [162, 359]. Using this formalism, the tensor product found in μ_{kj}, ν_{kj}, and $\Gamma_{k,\mathrm{TLS}}$ can then be written as $\overleftrightarrow{\gamma}_j : \overleftrightarrow{\varepsilon}_k(\mathbf{r}_j) = R_{abcd} W_{j,ab} \varepsilon_{k,cd}(\vec{r}_j)$.

Due to the simple cubic symmetry of the silicon lattice, $\overleftrightarrow{R}$ will have only three independent parameters [359], namely

$$R_{xxxx} = R_{yyyy} = R_{zzzz} = R_{11}, \tag{6.31}$$

$$R_{xxyy} = R_{xxzz} = R_{yyxx} = R_{yyzz} = R_{zzxx} = R_{zzyy} = R_{12}, \tag{6.32}$$

$$\begin{aligned} &R_{xyxy} = R_{xyyx} = R_{xzxz} = R_{xzzx} = R_{yxxy} = R_{yxyx} = R_{yzyz} = R_{yzzy} \\ &= R_{zxxz} = R_{zxzx} = R_{zyyz} = R_{zyzy} = R_{44}, \end{aligned} \tag{6.33}$$

directly analogous to the elasticity tensor of the system given in Eqs. (2.32)–(2.34). Furthermore, assuming the TLS ensemble is uniformly distributed (both in spatial density and orientation), we can average $|\overleftrightarrow{\gamma}_j : \overleftrightarrow{\varepsilon}_k(\mathbf{r}_j)|^2$ over the total volume V of the resonator and the solid angle of TLS orientations, resulting in [162]

$$\langle |\overleftrightarrow{\gamma}_j : \overleftrightarrow{\varepsilon}_k(\mathbf{r}_j)|^2 \rangle_V = \frac{3\omega_k^2}{V\rho} \sum_\eta \frac{\gamma_\eta^2}{c_\eta^2} e_{k\eta}. \tag{6.34}$$

Here, the sum is over the three different phonon polarizations (one longitudinal and two transverse), where γ_η, c_η, and $e_{k\eta}$ are the deformation potential, speed of sound, and fraction of the resonance mode's energy associated with each polarization. In terms of the components of $\overleftrightarrow{R}$, the deformation potentials for each phonon polarization are given by

$$\gamma_l = \sqrt{\frac{2R_{11}^2 + 7R_{12}^2 + 6R_{11}R_{12} + 4R_{44}^2}{45}}, \tag{6.35}$$

$$\gamma_{t_1} = \sqrt{\frac{(R_{11} - R_{12})^2}{45}}, \tag{6.36}$$

$$\gamma_{t_2} = \frac{2R_{44}}{\sqrt{45}}, \tag{6.37}$$

while explicit forms of c_η and $e_{k\eta}$ are given by Eqs. (2.52)–(2.54) and Eqs. (2.67)–(2.69) in Section 2.3, respectively.

6.2.5 Coupling to Ensembles of Amorphous TLS Defects

Using the previous results of this section, we are now equipped to determine the mechanical dissipation due to coupling to a given ensemble of TLS defects. Starting

with the relaxation rate, we input the result for $\langle|\overleftrightarrow{\gamma}_j : \overleftrightarrow{\varepsilon}_k(\mathbf{r}_j)|^2\rangle_V$ from Eq. (6.34) into Eq. (6.24) to obtain

$$\tau_j^{-1} = \frac{3\pi}{V\rho\hbar}\sum_{k,\eta}\frac{E_{0j}^2}{E_j}\frac{\gamma_\eta^2}{c_\eta^2}e_{k\eta}\coth\left(\frac{E_j}{2k_\mathrm{B}T}\right)\delta(E_j-\hbar\omega_k). \tag{6.38}$$

To evaluate the sum over k, we must carefully consider the density of states $\varrho_\eta(\omega)$ associated with η-polarized phonons. For the system at hand, a discrete density of states associated with the mechanical modes of the resonator would seem to be an obvious choice. However, because a large number of these modes are thermally populated for the temperature range considered (at $T = 10$ mK, modes with frequencies up to $\omega_k/2\pi = 144$ MHz are occupied by at least one thermal phonon on average), we can instead use the simpler continuum (Debye) density of states given by Eq. (2.84) [162]. That said, we still need to determine the dimensionality of this density of states. This was done in Section 2.4.4, where we compared the characteristic dimensions of the device to its shortest thermal phonon wavelength and found that the devices considered in this thesis can be treated as one-dimensional for $T \lesssim 1$ K. In the temperature range $T > 1$ K, we assume the resonator to be quasi-one-dimensional, such that for all relevant temperatures we can use the one-dimensional phononic density of states given by Eq. (2.85). With this choice of density of states, we can replace the sum in Eq. (6.38) using Eq. (2.80), which upon performing the integral, results in

$$\tau_j^{-1} = \frac{1}{\mathcal{A}\rho\hbar^2}\sum_{\eta}\frac{E_{0j}^2}{E_j}\frac{\gamma_\eta^2}{c_\eta^3}\coth\left(\frac{E_j}{2k_\mathrm{B}T}\right). \tag{6.39}$$

Here, $\mathcal{A} = wt$ is the cross-sectional area of the device ($\mathcal{A} = 5.0\times10^{-14}$ m^2 for our half-ring resonator) and we have assumed $e_{kl} = e_{kt_1} = e_{kt_2} \approx 1/3$, as this is the average value for each fraction when a large number of mechanical modes are considered. We further note that each phonon polarization will in general have a unique deformation potential γ_η, however, determining exact values for these parameters is beyond the scope of this work. Therefore, we further simplify this expression for the relaxation rate by assuming $\gamma_l = \gamma_{t_1} = \gamma_{t_2} = \gamma$, allowing us to

introduce an effective speed of sound $c_{\mathrm{e}} = \sqrt[3]{\sum_{\eta} \frac{1}{c_\eta^3}} = \bar{c}/\sqrt[3]{3} = 3965$ m/s, such that

$$\tau_{\mathrm{TLS}}^{-1} = \frac{\gamma^2}{\mathcal{A}\rho c_{\mathrm{e}}^3 \hbar^2} \frac{E_0^2}{E} \coth\left(\frac{E}{2k_{\mathrm{B}}T}\right). \tag{6.40}$$

Finally, inputting this relaxation rate, as well as the spatially averaged value of $|\overleftrightarrow{\gamma}_j : \overleftrightarrow{\varepsilon}_k(\mathbf{r}_j)|^2$ from Eq. (6.34) into Eq. (6.29), while replacing the sum over the TLS ensemble with an integral over the TLS density of states $\sum_j \rightarrow \int_0^\infty \int_0^\infty V\mathcal{P}(E_\Delta, E_0) dE_\Delta dE_0$ [360], we get the ensemble-averaged TLS-induced damping rate

$$\Gamma_{\mathrm{TLS}} = \frac{\gamma^2}{\rho c_k^2 k_{\mathrm{B}} T} \int_0^\infty \int_0^\infty \left(\frac{E_\Delta}{E}\right)^2 \mathrm{sech}^2\left(\frac{E}{2k_{\mathrm{B}}T}\right) \frac{\omega_{\mathrm{m}}^2 \tau_{\mathrm{TLS}}}{1+\omega_{\mathrm{m}}^2 \tau_{\mathrm{TLS}}^2} \mathcal{P}(E_\Delta, E_0) dE_\Delta dE_0, \tag{6.41}$$

where we have introduced a mode-dependent effective speed of sound $c_k = \sqrt{3\sum_\eta \frac{e_{k\eta}}{c_\eta^2}}$. Note that in Eqs. (6.40) and (6.41) we have taken $\omega_k \rightarrow \omega_{\mathrm{m}}$, as well as dropped the explicit subscripts j and k, with the assumption that we are considering the coupling between a TLS ensemble and a single mechanical mode.

The functional form of $\mathcal{P}(E_\Delta, E_0)$ is chosen to reflect the energy distribution of the TLS ensemble in question and, depending on the dimensionality of the system, can have a drastic effect on the temperature dependence of the TLS-induced mechanical damping rate [162, 222]. In the STM, this energy density function has the form

$$\mathcal{P}_{\mathrm{a}}(E_\Delta, E_0) = \frac{\mathcal{P}_0}{E_0}, \tag{6.42}$$

where $\mathcal{P}_0$ is a constant that characterizes the density of states of the TLS ensemble [220–223], and is typically on the order of 10^{44} J^{-1} m^{-3} for glassy solids [162, 201]. An energy density function of this form reflects the broad distribution in E_Δ and E_0 exhibited for amorphous TLS distributions[1], and for the one-dimensional resonator geometry considered here, results in the damping rate

$$\Gamma_{\mathrm{TLS}} = \frac{\gamma^2 \mathcal{P}_0}{\rho c_k^2 k_{\mathrm{B}} T} \int_0^\infty \int_0^\infty \frac{E_\Delta^2}{E_0 E^2} \mathrm{sech}^2\left(\frac{E}{2k_{\mathrm{B}}T}\right) \frac{\omega_{\mathrm{m}}^2 \tau_{\mathrm{TLS}}}{1+\omega_{\mathrm{m}}^2 \tau_{\mathrm{TLS}}^2} dE_\Delta dE_0. \tag{6.43}$$

[1] See Appendix G for treatment of crystalline TLS distributions.

At low temperatures ($\omega_{\mathrm{m}}\tau_{\mathrm{min}} \gg 1$, where $\tau_{\mathrm{min}} = \tau_{\mathrm{TLS}}(E = E_0)$), this mechanical damping rate can be approximated as

$$\Gamma_{\mathrm{TLS}} \approx \frac{\pi^2\gamma^4\mathcal{P}_0 k_{\mathrm{B}} T}{6\mathcal{A}\rho^2\hbar^2 c_k^2 c_{\mathrm{e}}^3}, \tag{6.44}$$

which is linear in T as expected [162]. Meanwhile, at high-temperatures ($\omega_{\mathrm{m}}\tau_{\mathrm{min}} \ll 1$) we find

$$\Gamma_{\mathrm{TLS}} \approx \frac{\pi\gamma^2\mathcal{P}_0\omega_{\mathrm{m}}}{2\rho c_k^2}. \tag{6.45}$$

We note that while the temperature-dependence of Γ_{TLS} in Eq. (6.44) differs significantly from the T^3-dependence observed in bulk amorphous solids [341], at high temperatures the mechanical damping rate approaches the same constant value regardless of the dimensionality of the system [162], minimizing the effect of our choice of a one-dimensional phonon density of states for $T > 1$ K.

6.3 Half-Ring Optomechanical Resonator

6.3.1 Device Description

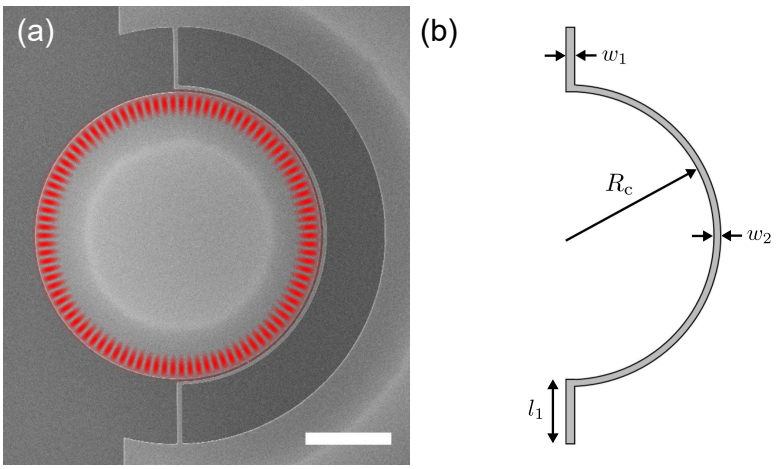

Figure 6.2: (a) A SEM image of the optomechanical half-ring resonator studied in this chapter. Overlaid in red is a FEM simulation showing the magnitude of the electric field for the $n = 1$, $m = 49$ TE WGM of the disk with a measured resonance frequency of $\omega_{\mathrm{c}}/2\pi = 188.8$ THz ($\lambda_{\mathrm{c}} = 1587.9$ nm). Scale bar is 3 μm. (b) Schematic of the half-ring resonator indicating its critical dimensions. The numerical values for the device studied in this chapter are: $l_1 = 2.20$ μm, $w_1 = 200$ nm, $w_2 = 150$ nm, and $R_{\mathrm{c}} = 5.08$ μm. Device thickness was taken to be $t = 250$ nm as specified by the manufacturer.

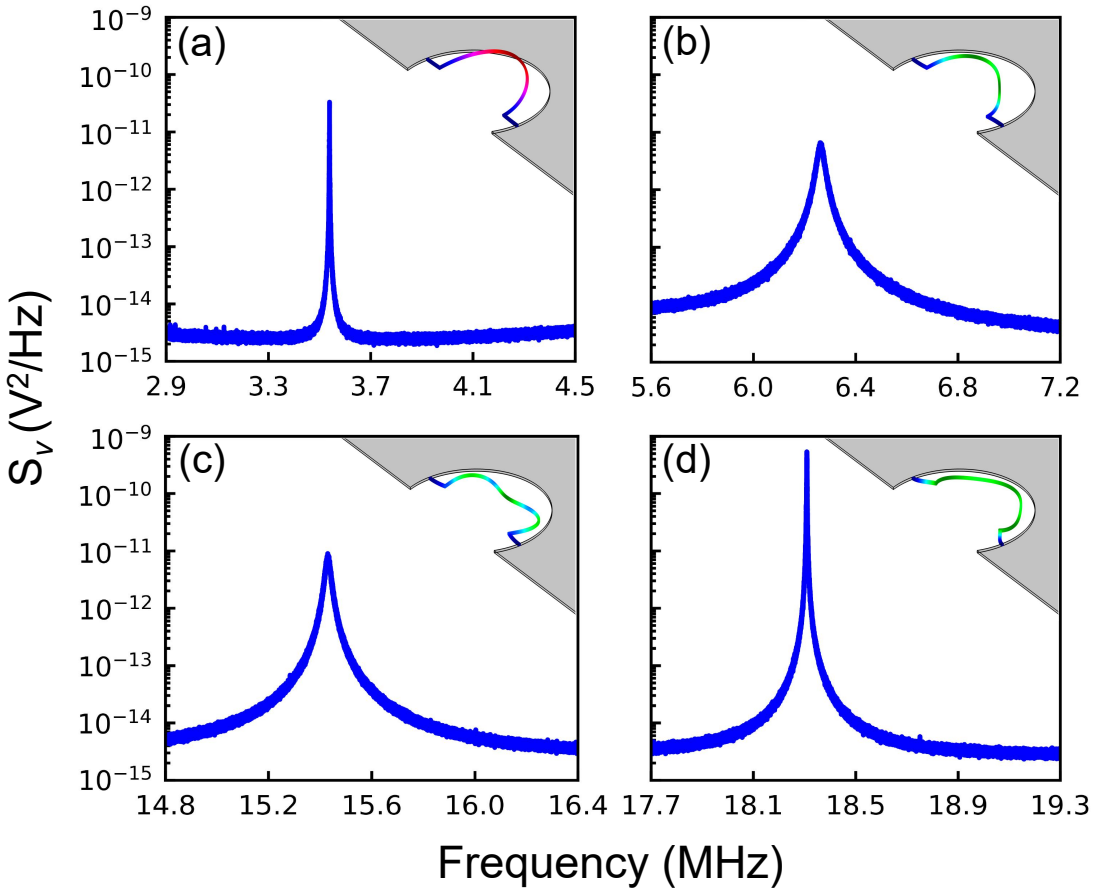

Figure 6.3: The voltage spectral density $S_{vv}(\omega)$ obtained by continuously monitoring the resonator's mechanical motion in exchange gas at 4.2 K. Measurements were performed with 10 μW of optical power input to the fridge (corresponding to an input power of $P_{\rm in} = 7.5$ μW at the microdisk) and 2.6 mW in the LO. Inset are FEM simulations of the displacement profiles for (a) the fundamental out-of-plane torsional mode ($\omega_{\rm m}/2\pi = 3.53$ MHz), along with the (b) "side-to-side" ($\omega_{\rm m}/2\pi = 6.28$ MHz), (c) antisymmetric "breathing-like" ($\omega_{\rm m}/2\pi = 15.44$ MHz), and (d) symmetric "breathing-like" ($\omega_{\rm m}/2\pi = 18.31$ MHz) in-plane flexural modes. Red (green) indicates out-of-plane (in-plane) motion, while blue denotes zero displacement. Figure adapted from Ref. [163]. © 2018 American Physical Society.

The optomechanical device studied in this chapter is that of a "half-ring" resonator (see Fig. 6.2) consisting of a doubly supported narrow ring that surrounds half of a 10 μm diameter optical microdisk cavity, both of which are fabricated from the same 250-nm-thick single-crystal-silicon device layer of a standard SOI chip (see Section 5.2.2 for details). The idea behind this device geometry is simple; the large coverage of the optical cavity by the mechanical resonator, in combination with the small vacuum gap (∼80 nm) between these two elements, maximizes the

device's optomechanical coupling (see Eq. (4.3)), while simultaneously leaving half of the microdisk easily accessible for dimpled fiber optical coupling. A schematic of the mechanical resonator geometry can be seen in Fig. 6.2b, with each of its critical dimensions labelled and the numerical values given in the caption.

The optical modes of this microcavity are the disk WGMs discussed in Section 3.3, albeit slightly perturbed by the presence of the mechanical resonator. Here we concern ourselves with the first-order radial TE mode shown in the overlay of Fig. 6.2a (radial and azimuthal mode numbers of $n = 1$ and $m = 49$), which has a measured resonant frequency $\omega_c/2\pi = 188.8$ THz ($\lambda_c = 1587.9$ nm) and linewidth $\kappa/2\pi = 1.0$ GHz ($Q_c = 1.9{\times}10^5$), as this is the optical mode used to transduce the motion of the half-ring resonator. The mechanical modes of the resonator on the other hand, are significantly more complicated, requiring us to turn to FEM simulation to determine their displacement profiles. Fig. 6.3 shows these simulated modeshape functions for the four lowest lying mechanical modes of the half-ring resonator, along with their optomechanically measured spectra.

$\omega_m/2\pi$ (MHz)	m (fg)	x_{zpf} (fm)	$G/2\pi$ (GHz/nm)	$g_0/2\pi$ (kHz)
3.53	610	62.4	–	–
6.28	836	40.0	–	–
15.44	743	27.0	2.34	63.4
18.31	772	24.4	5.13	125

Table 6.1: Summary of the optomechanical properties for the four lowest frequency mechanical modes of the half-ring resonator coupled to the $n = 1$, $m = 49$ TE optical WGM shown in Fig. 6.2a. The effective mass m and optomechanical coupling coefficient G are determined by inputting the simulated electric fields and displacement profiles of the optomechanical device into Eqs. (2.6) and (4.3), respectively. From these values, the zero-point fluctuation amplitude $x_{zpf} = \sqrt{\hbar/2m\omega_m}$ and the single-photon optomechanical coupling rate $g_0 = Gx_{zpf}$ are also calculated. Note that due to the symmetry of the simulated system, the values of G given here represent a lower bound for the considered geometry and are only nonzero for the two higher frequency mechanical modes.

Due to optical heating of the mechanical modes, it is difficult to obtain an experimentally-determined value of their optomechanical coupling coefficient G. However, by using the aforementioned FEM simulations of the optical cavity's electric field and the resonator's displacement, we calculate G for each mechanical

mode according to Eq. (4.3). Furthermore, we use these simulated mechanical modeshapes to determine the effective mass m for each mechanical mode, from which we also find x_{zpf}, and subsequently, g_0. The results of these calculations are summarized in Table 6.1. We note that due to the symmetry of the displacement with respect to the optical field, we simulate $G \approx 0$ for the two lower frequency mechanical modes, even though this symmetry is broken in the experiment, such that significant optomechanical coupling exists.

6.3.2 Mechanical Strain Distributions

We can also use the FEM simulations presented in the previous subsection to determine the spatially varying strain profiles induced within the resonator by the displacement of each mechanical mode (see the insets of Fig. 6.11 below), allowing us to calculate their strain energy fractions and effective strain volumes using Eqs. (2.67)–(2.69) and (2.72), respectively. The numerical values for each of these parameters are given in Table 6.2. Here we see that the longitudinal energy fraction e_l for the lowest frequency torsional mode is much smaller than the other three flexural modes, which is unsurprising as one would expect a torsional mode to exhibit much more of a transverse nature than the in-plane flexural modes. Moreover, we see that this torsional mode and the highest frequency flexural mode have considerably smaller effective strain volumes than the two middle frequency modes.

$\omega_{\mathrm{m}}/2\pi$	e_l	e_{t_1}	e_{t_2}	V_{str} ($\times 10^{-21}$ m^3)
3.53 MHz	0.15	0.42	0.43	3.6 (0.44%)
6.28 MHz	0.34	0.54	0.12	6.3 (0.77%)
15.44 MHz	0.34	0.52	0.14	11 (1.4%)
18.31 MHz	0.39	0.32	0.29	1.7 (0.21%)

Table 6.2: Mechanical energy fractions and effective strain volumes calculated for each of the four modes studied in this work using the smallest mesh allowable (set by computing constraints). The values are determined using FEM simulations of the strain energy density profile for each mode (see insets of Fig. 6.11), with the orientation of the silicon crystal axes chosen to match the device used in the experiment (see Fig. 5.2). The percentage of the total geometric volume $V_0 = 8.1 \times 10^{-19}$ m^3 occupied by each effective strain volume is given in parentheses.

We are further interested in determining the fraction of the strain energy that

is localized to the surface of the resonator. To do this, we use FEM simulations to compare the strain energy (calculated using Eq. (2.64)) located within the first 5, 10, 20, and 40 nm of each of the resonator's four surfaces[2] to the strain energy of the entire structure for each mechanical mode. The results of these calculations are given in Table 6.3. Here we see that over half of the strain energy is localized to the small volume contained within the first 20 nm of the resonator's surfaces (corresponding to roughly 37% of the resonator's geometric volume) for each mechanical mode, with nearly all of the strain energy residing within 40 nm of these surfaces. We also point out that there is slightly less strain at the surface for the two lower effective strain volume modes (3.53 MHz, 18.31 MHz) than there is for the two high effective strain volume modes (6.28 MHz, 15.44 MHz).

$\omega_m/2\pi$	5 nm	10 nm	20 nm	40 nm
3.53 MHz	0.17	0.31	0.55	0.83
6.28 MHz	0.21	0.38	0.64	0.91
15.44 MHz	0.21	0.39	0.65	0.92
18.31 MHz	0.19	0.35	0.60	0.87

Table 6.3: Fraction of the strain energy localized to within 5, 10, 20, and 40 nm of each of the resonator's surfaces for the four studied mechanical modes.

6.4 Cryogenic Optomechanical Ringdown Measurements

6.4.1 Pulsed Optical Detection

In this section, we detail the pump-probe measurement scheme used to determine the dissipation of the thermally-driven silicon half-ring resonator described in the previous section. Our method – which is itself a modified version of the optomechanically-mediated thermal ringdown technique developed by Meenehan *et al.* [204] – is capable of simultaneously transducing the motion of several mechanical modes of the half-ring resonator with sub-microsecond resolution in the time domain, while circumventing the need for single photon detectors, as well as the requirement that the device exist in the SBR regime. Furthermore, by measuring the Brownian

[2]This corresponds to roughly the first 10, 20, 40, and 80 atomic monolayers at each surface, as silicon has a lattice constant of 5.43 Å [186].

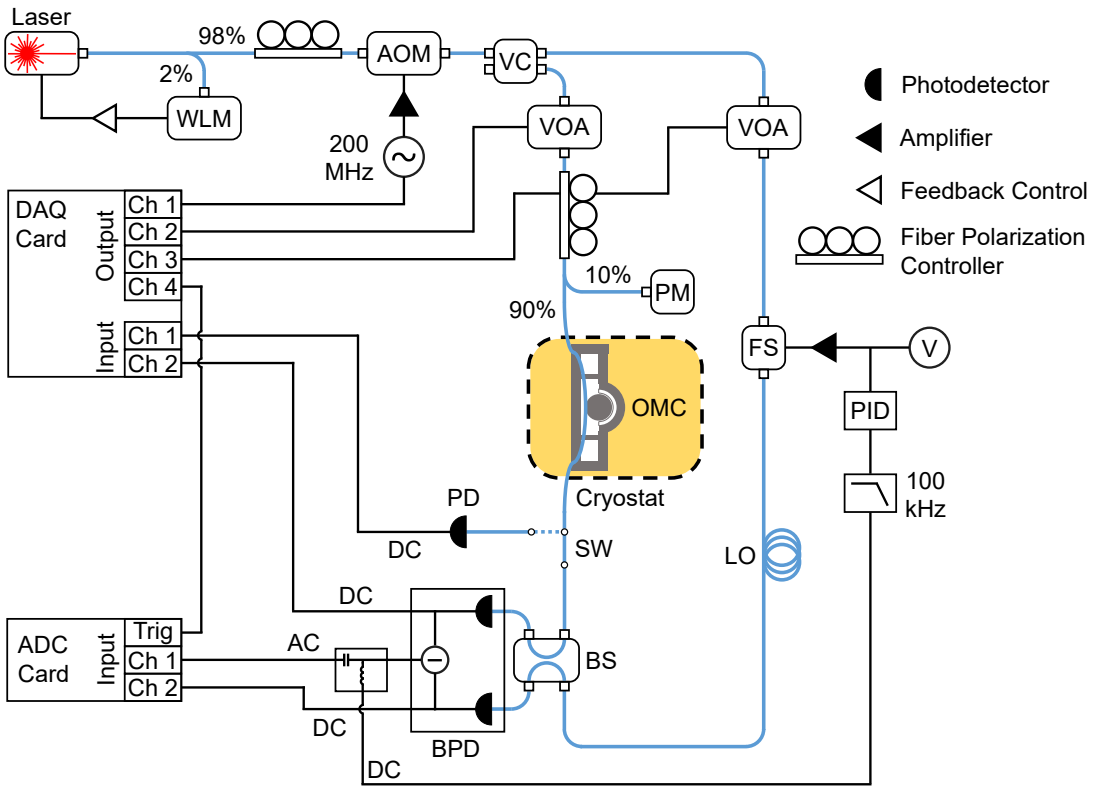

Figure 6.4: Detailed schematic of the gated optical detection system used to perform the pulsed homodyne measurements of the cryogenic optomechanical device studied in this chapter. This detection scheme differs from the one shown in Fig. 5.12 in that we have inserted an AOM into the system before the VC, allowing us to toggle the input optical signal on and off with a switching time of $\sim$5 ns. WLM = wavelength meter, AOM = acousto-optic modulator, VC = variable coupler, VOA = variable optical attenuator, PM = power meter, OMC = optomechanical cavity, FS = fiber stretcher, PID = proportional-integral-derivative controller, V = voltmeter, LO = local oscillator, SW = optical switch, BS = beam splitter, BPD = balanced photodetector, PD = photodetector, ADC = analog-to-digital converter, DAQ = data acquisition. Figure reproduced from Ref. [163]. © 2018 American Physical Society.

motion of the device, our detection scheme avoids any effects that may arise from large strains due to an external drive [351].

In order to generate the pulses required to implement our optomechanical ringdown technique, we modify the detection circuit detailed in Section 5.4.3 to allow for gated optical homodyne measurements (see Fig. 6.4). This is done by inserting an acousto-optic modulator (AOM) into the optical circuit before the VC, as well as introducing the appropriate triggering electronics, allowing for gating of

the optical signal with a rise/fall time of ∼5 ns. In this gated measurement setup, the low frequency voltage readouts from each of the BPD's individual photodetectors are also collected, with one output sent to a DAQ card to monitor slow drifts, while the other is sent to an ADC to observe rapid transients in this signal.

To perform pulsed homodyne measurements with this gated optical circuit, the optomechanical detection system is initially set up by sending a continuous-wave laser signal through the optical circuit. The dimpled tapered fiber is then carefully aligned to couple with the microdisk, after which the laser wavelength is tuned onto resonance with the optical WGM discussed in Section 6.3.1 and the transduction of the mechanical signal is optimized. We note that due to the relatively high optical powers (10 – 100 μW) continuously input to the fridge during this initial set up, the base plate, along with the optomechanical device, heats up significantly. Therefore, once we have ensured that the fiber is in place, the optical circuit is toggled into the "off" state by closing the AOM (extinction ratio of 50 dB), preventing optical power from reaching the dimple. After approximately 1 – 2 hours in this state, the fridge returns to its set-point temperature and is ready for pulsing measurements.

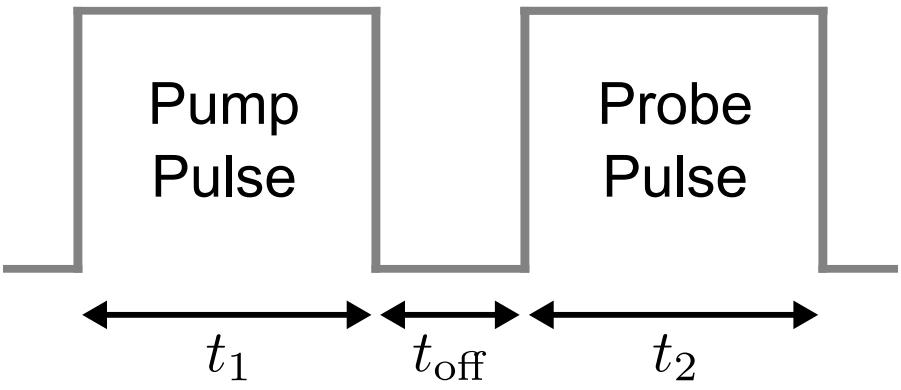

Figure 6.5: Schematic of the double pulse sequence used to perform pump-probe measurements. The grey line indicates the state of the laser (high = on, low = off), with t_1 and t_2 being the durations of the pump and probe pulses, respectively, while t_{off} is the delay between these two pulses.

Once the fridge temperature stabilizes, we implement the double pulse pump-probe measurement scheme outlined in Fig. 6.5. We begin by sending a trigger signal from the DAQ card to a 200 MHz frequency source, activating voltage output

that is amplified to 10 V_{RMS} and sent to the AOM. This electrical signal opens the AOM, generating the initial pump pulse that is used to thermally excite the motion of the mechanical resonator. The AOM is left open until the predetermined pulse time t_1 has passed, at which point it is closed by turning the frequency source off with a second signal from the DAQ card. The mechanical resonator is then left in the dark to decay towards thermal equilibrium for a set wait time t_{off}, after which a probe pulse, created in an identical manner to the pump pulse, is sent to access the device. To ensure the data from the probe pulse is recorded, the ADC is activated using another trigger signal generated by the DAQ card at a time chosen to be 10 or 100 μs before the probe pulse is created (depending on the length of t_{off}, which varies from 100 μs to 1 s). Finally, the AOM is closed after a time t_2 has elapsed following the generation of the probe pulse, returning the optical circuit back to its "off" state. Note that for the double pulse measurements detailed in this chapter, we always take $t_1 = t_2 = 2$ ms, such that the phonon occupation of the mechanical mode at the end of the pump pulse can be inferred from observation of the probe pulse (see Section 6.4.5 below), minimizing the amount of data that needs to be collected. After a 200 ms wait to reinitialize the ADC, this procedure is repeated until the desired number of pulses is acquired. Single pulse measurements can also be performed identically to the double pulse measurements, with the omission of the pump pulse. We note that the gating of the optical circuit is completely controlled by outputs from the DAQ card, ensuring consistent timing referenced to its 1 MHz internal clock.

6.4.2 Data Collection and Signal Processing[3]

The displacement of the half-ring resonator is dispersively coupled to the monitored optical mode, such that the mechanical motion is transduced into the fluctuating phase of the optical signal that is transmitted through the cavity. Therefore, once this signal beam is recombined with the LO and sent to the BPD, the mechanical motion is encoded into a time-varying voltage signal $v(t)$ acquired using the ADC. To reduce the noise of this collected signal, we average each 50

[3]The signal processing and Fourier transform discussed in this subsection was performed by Callum Doolin and is described in greater detail in Ref. [361].

point interval of data into a single datum, leading to an effective data sampling rate of 10 MS/s (effective sampling time of 100 ns). Following this averaging process, the data is digitally demodulated, as well as band-pass filtered (–3 dB bandwidth of ∼1.2 MHz, time constant $\tau_{\mathrm{f}} \approx 0.8$ μs) around the frequency of interest ω via convolution with a Blackman window $\Pi(t)$ [362]. Mathematically, this is interpreted as the "band-passed" Fourier transform of the signal voltage

$$\mathcal{V}(\omega, t) = \int_{-\infty}^{\infty} v(t - t') e^{-i\omega(t-t')} \Pi(t') dt', \tag{6.46}$$

performed at each time step t of the ADC signal. Note that the ∼1.2 MHz bandwidth of the filter function is much larger than the linewidth of any of the studied mechanical modes, ensuring that the entire area of each considered resonance peak will be encapsulated. Furthermore, while the data is taken with an effective time step of 100 ns, this filter will smooth over any features that evolve faster than its 0.8 μs time constant. We note that this relatively large integration bandwidth prevents us from monitoring frequency shifts in our mechanical resonances, as have previously been observed due to TLS in other mechanical systems [342, 343, 347–350], as well as superconducting microwave circuits [363–365]. However, if we were to reduce this bandwidth, at the expense of time resolution, it may be possible to track the mechanical resonance frequency of the device throughout the duration of the pulse.

From the Fourier transform in Eq. (6.46), we can determine the time-resolved, band-passed PSD of $v(t)$ as

$$\mathcal{S}_{vv}(\omega, t) = \frac{|\mathcal{V}(\omega, t)|^2}{\tau_0} = \sum_k \alpha_k(\omega, t) \mathcal{S}_{xx}^k(\omega, t) + \mathcal{S}_{vv}^{\mathrm{imp}}(\omega), \tag{6.47}$$

where $\alpha_k(\omega, t)$ is the transduction coefficient for the band-passed displacement spectral density $\mathcal{S}_{xx}^k(\omega, t)$ corresponding to the kth mechanical mode of the resonator and $\mathcal{S}_{vv}^{\mathrm{imp}}(\omega)$ is the band-passed frequency-dependent imprecision noise floor of the measurement. If we consider a finite frequency band $\Delta\omega$ surrounding the resonance frequency of a single mechanical mode, the sum in Eq. (6.47) collapses and we can approximate the transduction coefficient and noise floor as constant over this frequency range. Furthermore, the time-dependence in $\alpha_k(\omega, t)$ is due to the ring-up of the optical cavity, which occurs on a timescale of $1/\kappa \approx 1$ ns, much faster than

any other component in our detection system. We can therefore treat $\alpha_k(\omega, t)$ as a step function in time, such that it takes on a constant value once the laser populates the optical cavity. We then have $\sum_k \alpha_k(\omega,t)\mathcal{S}^k_{xx}(\omega,t) \approx \alpha\mathcal{S}_{xx}(\omega,t)$ and $\mathcal{S}^{\rm imp}_{vv}(\omega) \approx \mathcal{S}^{\rm imp}_{vv}$ resulting in

$$\mathcal{S}_{vv}(\omega,t) \approx \alpha\mathcal{S}_{xx}(\omega,t) + \mathcal{S}^{\rm imp}_{vv}, \tag{6.48}$$

where $\mathcal{S}_{xx}(\omega,t)$ is the displacement spectral density of the mechanical mode of interest, with resonant frequency $\omega_k = \omega_{\rm m}$.

6.4.3 Mechanical Mode Temperature Calibration

In general, the coefficient α in Eq. (6.48) is a combination of experimental device parameters and specifications from the measurement instrumentation (see Eq. (4.75)), such that it is difficult to determine *a priori*. We therefore look for a simple way to relate the spectral density of our measurement to the temperature of the mode in question. This is done by integrating the spectrum of the mechanical mode to obtain its time-dependent temperature $T_{\rm m}(t)$ using the expression [151]

$$\int \mathcal{S}_{xx}(\omega,t)d\omega \approx \frac{4\pi x^2_{\rm zpf} k_{\rm B}}{\hbar\omega_{\rm m}} T_{\rm m}(t), \tag{6.49}$$

where the integration is performed over the frequency band $\Delta\omega \gg \Gamma_{\rm m}$ centered on $\omega_{\rm m}$ and we have assumed the experimentally-relevant high-temperature regime (*i.e.* $k_{\rm B}T_{\rm m}(t) \gg \hbar\omega_{\rm m}$)[4] for all t. Combining Eq. (6.49) with Eq. (6.48), we find that

$$\int \mathcal{S}_{vv}(\omega,t)d\omega = \mathcal{F}T_{\rm m}(t) + \mathcal{I}, \tag{6.50}$$

indicating that the area under the curve of the measured voltage spectral density is linearly related to the mechanical mode temperature, with proportionality $\mathcal{F} = 4\pi x^2_{\rm zpf} k_{\rm B}\alpha/\hbar\omega_{\rm m}$ and a constant offset $\mathcal{I} = S^{\rm imp}_{vv}\Delta\omega$ set by the noise floor and frequency band of the measurement. Fitting Eq. (6.50) to the area under the voltage spectral density at the beginning of the pulse, when the mechanical mode is thermalized to the fridge temperature $T_{\rm fr}$ at $t = t_0$, allows us to infer the

[4] At the largest considered mechanical frequency of $\omega_{\rm m}/2\pi = 18.31$ MHz, this corresponds to temperatures of $T \gtrsim 1$ mK, such that even at the base temperature of our fridge ($T_{\rm fr} \approx 10$ mK) our device is still in the high-temperature regime.

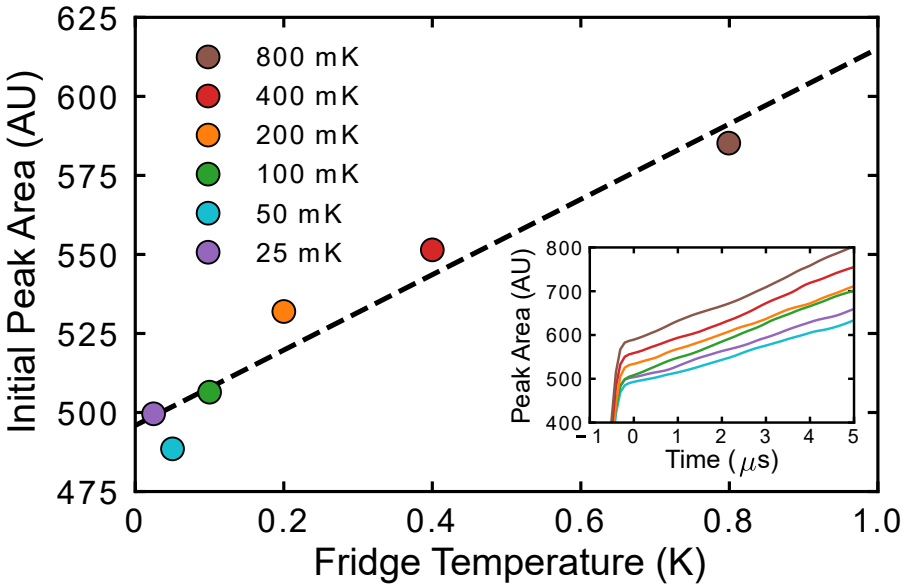

Figure 6.6: Area under the peak (including contributions from both the mechanical signal and imprecision noise) at the beginning of the measurement pulse for the 18.31 MHz mode plotted versus fridge temperature. The uncertainty in each point is smaller than the marker size. For the high input power used here ($P_{\rm in} = 75$ μW), the shot-noise of the optomechanical measurement is sufficiently suppressed to resolve the mode's initial phonon occupation. Fitting this linear trend (dashed line), we calibrate the peak area in terms of the mechanical mode temperature, with the y-intercept indicating an imprecision noise floor equivalent to 29.5 fm^2/Hz (see Eq.(6.50)). The inset highlights the rapid increase in the peak area during the first 5 μs of the measurement for each temperature (color-coded to match the main figure), taken by averaging data from 5000 individual optical pulses 4 ms in length and scaled by discarding the initial 20 μs of transient signal due to the applied numerical bandpass filter. Each data point in the main figure is extracted from a fit of Eq. (6.52) over the full pulse duration of this data. The rapid settling of the signal for $t < 0$ is set by the 10 MS/s effective sampling rate of our data acquisition. Figure adapted from Ref. [163]. © 2018 American Physical Society.

initial mode temperature as $T_{\rm m}(t_0) = T_{\rm fr}$ and extract values for $\mathcal{F}$ and $\mathcal{I}$. Provided the conditions stay the same throughout a single set of pulsing measurements (performed on the time-scale of hours), we can use these parameters to determine the mechanical mode temperatures at all times during the pulse as the device rapidly heats due to interaction with the photon-induced bath. Finally, as this experiment operates in the high temperature limit, we can then use this calibrated mode temperature to infer the time-dependent phonon occupation of the mechanical mode through the relation $\langle n \rangle (t) \approx k_{\rm B} T_{\rm m}(t)/\hbar\omega_{\rm m}$ (see Eq. (2.77)). An example of

this type of calibration is seen in Fig. 6.6.

6.4.4 Chip Heating Effects

In the previous subsection, we assumed that the device and its surrounding bath are initially thermalized to the base plate of the dilution unit such that at $t = t_0$ their temperatures are identical to that of the fridge. However, due to diminishing thermal conductivities at low temperatures, this may not be the case. To investigate this, we use a simple model to estimate the chip temperature in the vicinity of the device for varying average input powers to the chip.

The chip containing the half-ring optomechanical resonator is housed within our custom-built cryogenic optical coupling system, with a thermal link between it and the the mixing chamber established via a copper braid that connects to its gold-plated copper chip holder (see Fig. 5.11). We therefore assume that the chip holder is well thermalized to the fridge such that its temperature is equal to that of the base plate. Furthermore, we assume that the cooling power of the mixing chamber is large enough that this temperature remains constant over the course of the measurement (as we observe that the temperature of the base plate remains unchanged for the duration of the experiment). The temperature T_b of the thermal bath surrounding our device is then limited by the thermal conductivity of the 210-nm-thick gold layer applied to the top of our silicon device layer. Taking the thermal conductivity of the gold layer to vary linearly at low temperatures as $\mathcal{K}_\mathrm{g} = \mathcal{K}_0 T$, where $\mathcal{K}_0 \approx 30$ W/m·K^2 [366], the temperature of the thermal bath surrounding the device will be given by [188]

$$T_\mathrm{b} = \sqrt{\frac{2 l_\mathrm{g} \dot{\mathcal{Q}}_\mathrm{d}}{\mathcal{A}_\mathrm{g} \mathcal{K}_0} + T_\mathrm{fr}^2}. \tag{6.51}$$

Here, $\dot{\mathcal{Q}}_\mathrm{d}$ is the heat load applied to the device, with l_g and $\mathcal{A}_\mathrm{g}$ being the length and cross-sectional area of the thermalizing gold layer.

For a double pulse measurement at a power of $P_\mathrm{f} = 10$ μW input to the fridge, as is done during the measurement, the fraction of power absorbed at the chip can be approximated as $P_\mathrm{abs} \approx \eta_f (1 - \eta_s) P_\mathrm{f} = 2.7$ μW, where η_f and η_s are the efficiencies associated with losses in the fiber and scattering off of the substrate

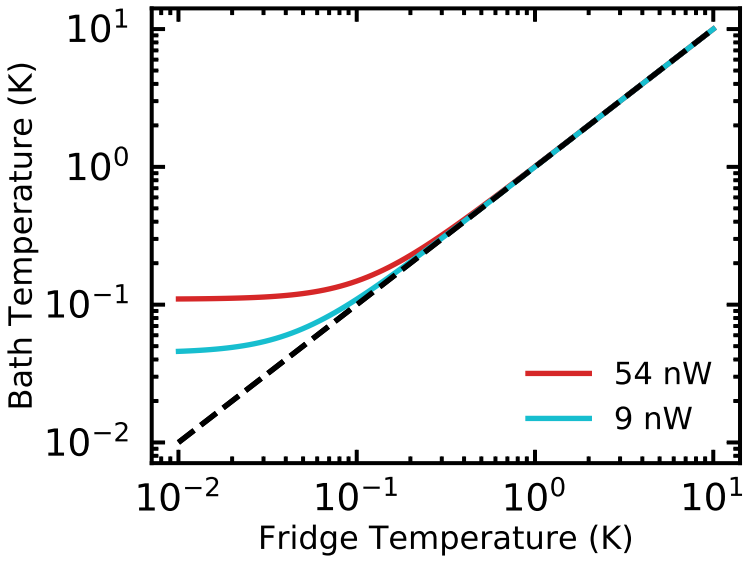

Figure 6.7: Plot of the thermal bath temperature T_b versus fridge/chip-holder temperature T_fr according to Eq. (6.51) for the largest (54 nW) and smallest (9 nW) estimated average heat loads $\dot{\mathcal{Q}}_\mathrm{d}$ applied to the device during pulsed measurements. The black dashed line is that of a perfectly thermalized device, *i.e.* $T_\mathrm{b} = T_\mathrm{fr}$. Figure reproduced from Ref. [163]. © 2018 American Physical Society.

introduced in Section 5.4.4. Including the duty cycle of the measurement, which for pulse delay times much less than the 200 ms wait time per measurement can be approximated as 2×2 ms/200 ms ≈ 0.02, we get an average power applied to the device during measurement of $\dot{\mathcal{Q}}_\mathrm{d} \approx 54$ nW. Conversely, for our longest wait time of 1 s, the duty cycle decreases to 2×2 ms/1200 ms ≈ 0.003, leading a lower average measurement power of $\dot{\mathcal{Q}}_\mathrm{d} \approx 9$ nW.

Fig. 6.7 shows the values of T_b according to Eq. (6.51) versus fridge/chip holder temperature T_fr for both of these heat loads input to the device, where we have taken $l_\mathrm{g} = 3.5$ mm and $\mathcal{A}_g = 5$ mm $\times$ 210 nm $= 1.05{\times}10^{-9}$ m^2 according to the experiment. Here we can see that for these applied heat loads, the device is no longer thermalized to the fridge at temperatures $T \lesssim 100$ mK. We note that this treatment neglects a number of effects, such as a Kapitza boundary resistance [188] between each interface of the apparatus, as well as the relevant time scales associated with the measurements and heating/cooling processes. Nonetheless, this simple model provides evidence that for low fridge temperatures ($T \lesssim 100$ mK), the thermal bath of the chip may be elevated due to the absorbed power of the

optical measurement.

6.4.5 Thermal Ringdown Measurement

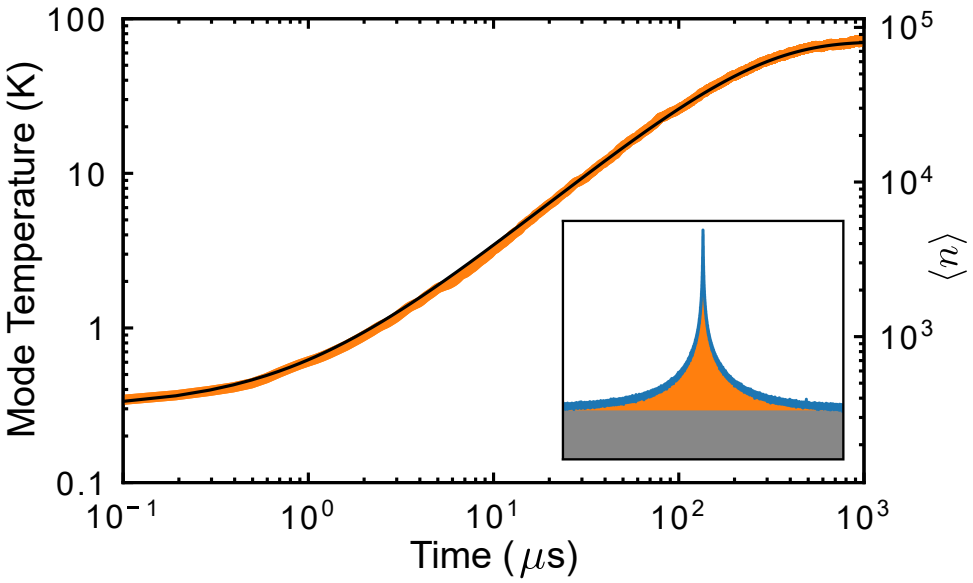

Figure 6.8: A typical heating curve corresponding to the orange point in Fig. 6.6 with a fridge temperature of 200 mK. The data (orange) is calibrated in terms of both temperature and average phonon occupancy, showing that the mechanical mode heats to $T \approx 80$ K ($\langle n \rangle \approx 10^5$) within the first millisecond of the measurement pulse. The solid black line is a fit to Eq. (6.52), and is used to extract the initial and final phonon occupancy of the mode. Inset shows the continuously-monitored spectral density of the mechanical resonance over the ∼1.2 MHz window used for these measurements. Orange illustrates the area under the peak due to mechanical motion, while grey indicates the imprecision noise floor. Figure adapted from Ref. [163]. © 2018 American Physical Society.

Due to the large disparity between the energy of the optical mode of the cavity (hundreds of THz) and the probed mechanical modes (tens of MHz), coupled with the diminishing thermal conductivity of silicon at low temperatures [192, 197, 198, 367] (see also Section 2.4.3), we find that even small input powers to the optical cavity act to rapidly heat the mechanical element as well. This heating effect can be modelled by considering a mechanical mode simultaneously coupled at its intrinsic damping rate Γ_m to the thermal phonon bath surrounding the device, and at a rate Γ_p to an additional hot phonon bath generated by either the absorption of cavity photons or radiation pressure backaction (or a combination of the two), with the

total (hot) mechanical damping rate of the system given by $\Gamma_\mathrm{h} = \Gamma_\mathrm{m} + \Gamma_\mathrm{p}$. If light is coupled into the optical cavity at time $t = t_0$, the average phonon occupancy of the mechanical mode as a function of time is then given by [163, 204]

$$\langle n \rangle (t) = \langle n \rangle (t_0) e^{-\Gamma_\mathrm{h}(t-t_0)} + \bar{n}_\mathrm{eq} \left(1 - e^{-\Gamma_\mathrm{h}(t-t_0)}\right). \tag{6.52}$$

Here, $\bar{n}_\mathrm{eq} = \left(\bar{n}_\mathrm{th}\Gamma_\mathrm{m} + \bar{n}_\mathrm{p}\Gamma_\mathrm{p}\right)/\Gamma_\mathrm{h}$ is the equilibrium phonon occupation of the mode, with $\bar{n}_\mathrm{p}$ being the average phonon occupancy of the hot photon-induced bath (see Appendix F). We note that for the temperatures considered here, $\bar{n}_\mathrm{p} \gg \bar{n}_\mathrm{th}$ and $\Gamma_\mathrm{h} \approx \Gamma_\mathrm{p}$, such that $\bar{n}_\mathrm{eq} \approx \bar{n}_\mathrm{p}$.

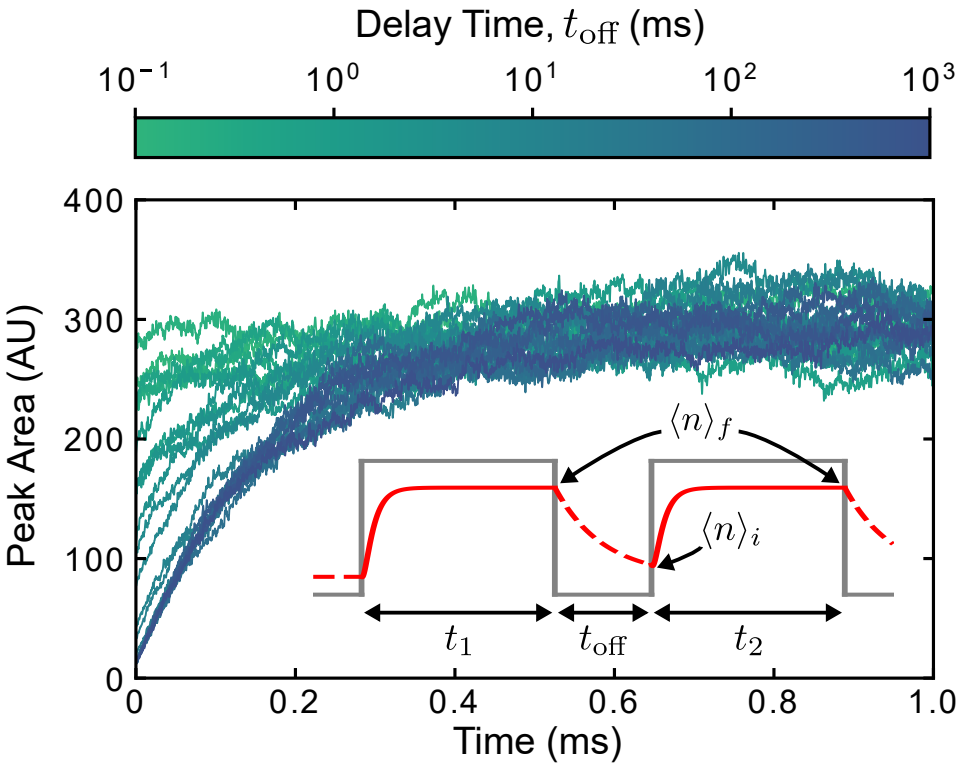

Figure 6.9: The first millisecond of pulsed data for the 18.31 MHz mechanical mode, obtained by averaging 500 individual probe pulses with the fridge at its base temperature of 10 mK. Measurements are performed by varying the delay time between pump and probe pulses (each with $P_\mathrm{in} = 7.5$ μW and a full duration of 2 ms) as indicated by the color bar. These traces are fit with Eq. (6.52) to extract their initial and final occupations. Inset is a schematic of the pump-probe sequence. The grey line indicates the state of the laser (high = on, low = off), with the solid (dashed) red line being the average occupancy of the mechanical mode with the laser on (off). Figure adapted from Ref. [163]. © 2018 American Physical Society.

This rapid heating prevents one from continuously monitoring the device's

motion at low temperatures. However, by performing time-resolved measurements of the mechanical resonator's motion as described in Section 6.4.1 and looking at its phonon occupancy within the first μs of the pulse, we show that the device is initially thermalized to the fridge, allowing for complete calibration of the device temperature at all times during the measurement (see Fig. 6.8). We note that for our highest mechanical frequency mode ($\omega_{\rm m}/2\pi = 18.31$ MHz) at our lowest calibrated fridge temperature ($T = 25$ mK – see Fig. 6.6), this results in an average initial phonon occupancy of $\langle n \rangle \approx 28$.

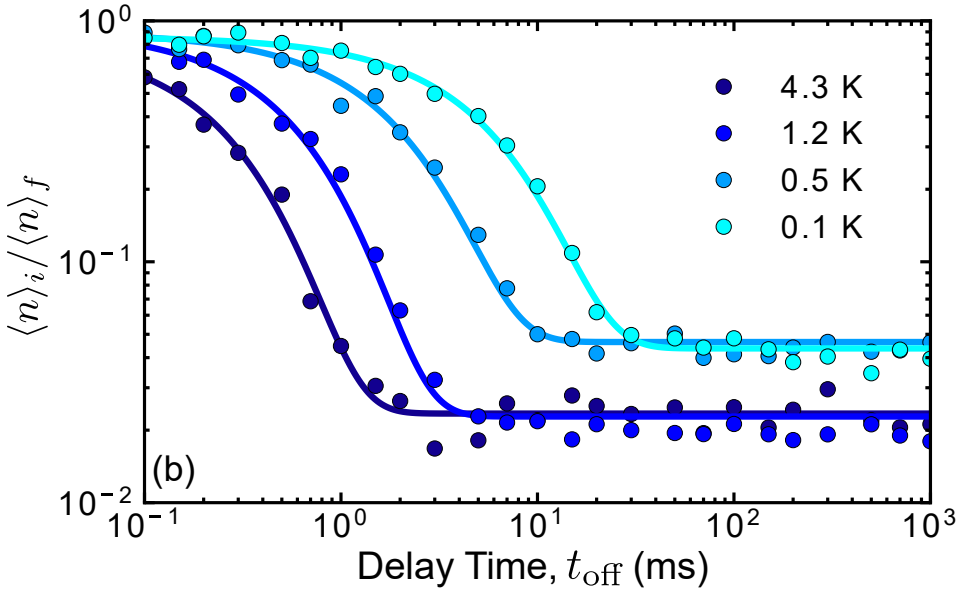

Figure 6.10: Thermally excited ringdown measurements at a number of fridge temperatures. The solid lines are fits to the data using Eq. (6.53), allowing for extraction of the intrinsic damping rate $\Gamma_{\rm m}$ at each temperature. The disparity in the noise floor between the low temperature (0.1 K, 0.5 K) and high temperature (1.2 K, 4.3 K) data results from varying levels of optomechanical transduction (*i.e.* small variations in input power, optical coupling to the device, etc.) between data runs and does not have an effect on the extracted intrinsic mechanical damping rate. Figure adapted from Ref. [163]. © 2018 American Physical Society.

We capitalize on this optically-induced heating to implement a pump-probe measurement technique [135, 163, 204], as illustrated in the inset of Fig. 6.9. This detection scheme allows us to observe the thermalization of the laser-heated mechanical mode back to the fridge temperature at its intrinsic damping rate

according to

$$\frac{\langle n\rangle_i}{\langle n\rangle_f} = \frac{(\bar{n}_{\rm eq} - \bar{n}_{\rm th})\, e^{-\Gamma_{\rm m} t_{\rm off}} + \bar{n}_{\rm th} + \bar{n}_{\rm imp}}{\bar{n}_{\rm eq} + \bar{n}_{\rm imp}}. \tag{6.53}$$

Here, $\langle n\rangle_i$ and $\langle n\rangle_f$ are the measured phonon occupancies of the mechanical mode (including the apparent contribution $\bar{n}_{\rm imp}$ due to imprecision noise) at the beginning of the probe pulse and at the end of the pump pulse, respectively, while $t_{\rm off}$ is the time delay between turning off the pump pulse and turning on the probe pulse (see Appendix F). In Eq. (6.53), as well as the experiment, we have chosen the lengths of the pump pulse t_1 and probe pulse t_2 to be equal, as well as satisfy $t_1 = t_2 \gg \Gamma_{\rm h}^{-1}$ such that $\langle n\rangle_f = \bar{n}_{\rm eq} + \bar{n}_{\rm imp}$ at the end of each pulse. By varying the delay between pulses and fitting the data to Eq. (6.53), as seen in Fig. 6.10, we can extract the intrinsic mechanical damping rate of the device, allowing us to map out its low-temperature dependence.

6.5 Quantitative Agreement with the One-Dimensional Standard Tunneling Model

Measurements of the damping rate for each of the four studied mechanical modes are performed with fridge temperatures varying from 10 mK to 10 K. In Fig. 6.11, we see that each mode exhibits qualitatively similar behaviour, with a plateau at low temperature ($T \lesssim 100$ mK), a linear temperature dependence for intermediate temperatures (100 mK $\lesssim T \lesssim$ 10 K), and finally, a high-temperature shoulder that begins to emerge around 10 K. We note that while a linear temperature dependence arises in a number of possible mechanical dissipation mechanisms, such as TLS relaxation damping and point defect scattering (see Section 2.5 for details), the roll-off to a constant at high temperature is distinctly unique to TLS damping. Moreover, in Section 2.5 we show that these other sources of mechanical loss (*i.e.* point defect scattering) are negligible for the silicon beams considered in this work. Therefore, for $T > 100$ mK, we attribute the mechanical losses in these beams to be due to relaxation damping caused by interactions with TLSs.

In order to quantitatively analyze the data in the context of this TLS damping model, we must first determine the dimensionality of the resonator. As detailed in Section 2.4.4, this is done by comparing the transverse dimensions of our device

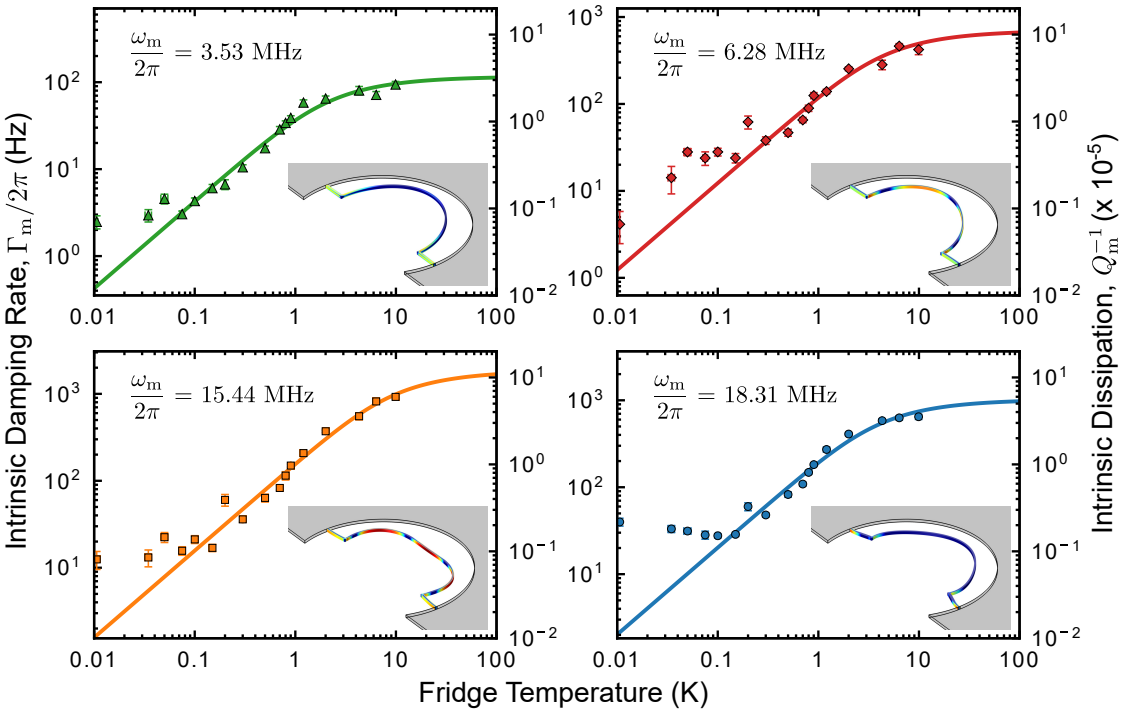

Figure 6.11: The intrinsic damping rate Γ_m measured for each of the four studied mechanical modes plotted versus fridge temperature, with the right axis displaying their intrinsic dissipation $Q_m^{-1} = \Gamma_m/\omega_m$. Markers in each plot represent the experimentally-determined damping rate extracted from fits of Eq. (6.53) to data similar to that seen in Fig. 6.10, with error bars representing a single standard deviation in the uncertainty of the fit. Solid lines are fits to Eq. (6.43), demonstrating the temperature dependence of the mechanical damping rate according to a one-dimensional TLS relaxation interaction model. From these fits, we obtain the parameters $\mathcal{P}_0$ and γ for the TLS ensemble coupled to each mechanical mode, which are given in Table 6.4. For $T \lesssim 100$ mK, the damping rate plateaus to a relatively constant value, which could be due to a number of effects, including temperature independent radiation of acoustic energy into the substrate [249, 253] or heating of the chip due to measurement (see Section 6.4.4). Inset are the logarithm of the normalized strain energy density simulated using FEM analysis for each mechanical mode. These simulations highlight the fact that the 3.53 MHz and 18.31 MHz modes have smaller spatial strain profiles that are localized to the supports of the half-ring (as characterized by their effective strain volumes – see Table 6.4), whereas the strain energy density profiles of the 6.28 MHz and 15.44 MHz modes extend into the rounded portion of the resonator. Figure reproduced from Ref. [163]. © 2018 American Physical Society.

($w = 200$ nm, $t = 250$ nm) to the shortest thermal phonon wavelength present in the system, which according to Eq. (2.103) is given by $\lambda_{th} = 2\pi\hbar c_{t_1}/k_B T \approx 225\ \text{nm}\cdot\text{K}/T$, where $c_{t_1} = 4679$ m/s is the slowest speed of sound in single-crystal silicon (see Table

5.1). Our resonator therefore behaves one-dimensionally for $T \lesssim 1$ K, however, to simplify the analysis we consider our device to be quasi-one-dimensional for all temperatures considered here. This approximation is justified by the fact that at high temperatures, the TLS-induced damping rate plateaus to a constant value that is independent of the dimensionality of the system [162]. With this approximation, we fit the data in Fig. 6.11 using the one-dimensional TLS relaxation damping model found by numerically integrating Eq. (6.43). Parameters extracted from these fits are summarized in Table 6.4.

$\omega_m/2\pi$ (MHz)	V_{str} ($\times 10^{-21}$ m^3)	$\mathcal{P}_0$ (J^{-1} m^{-3})	γ (eV)	$\mathcal{N}_{th}$ at 10 mK
3.53	3.6	$(9.7 \pm 3.4)\times 10^{43}$	1.3 ± 0.1	0.05
6.28	6.3	$(4.0 \pm 2.7)\times 10^{44}$	1.2 ± 0.2	0.35
15.44	11	$(3.6 \pm 1.9)\times 10^{44}$	1.3 ± 0.2	0.55
18.31	1.7	$(7.0 \pm 4.3)\times 10^{43}$	2.2 ± 0.4	0.02

Table 6.4: Summary of the density of states parameter $\mathcal{P}_0$ and deformation potential γ extracted from fits of the data in Fig. 6.11 to the one-dimensional TLS relaxation damping model given by Eq. (6.43). Also included is the number of thermally-active defects $\mathcal{N}_{th} \sim \mathcal{P}_0 V_{str} k_B T$, calculated using the fridge base temperature of 10 mK for the TLS ensembles contained within the effective strain volume V_{str} of a given mechanical mode. As one can see, the two modes with a larger effective strain volume (6.28 MHz, 15.44 MHz) couple to TLS ensembles with a defect density of states approximately four times larger than that observed for the two modes with a smaller effective strain volume (3.53 MHz, 18.31 MHz).

Upon inspection of these fit parameters, one can immediately see that the 6.28 MHz and 15.44 MHz mechanical modes couple to a defect density ($\mathcal{P}_0 \sim 4 \times 10^{44}$ J^{-1} m^{-3}) that is approximately four times larger than that sampled by the 3.53 MHz and 18.31 MHz modes ($\mathcal{P}_0 \sim 1 \times 10^{44}$ J^{-1} m^{-3}). We attribute this disparity in TLS ensemble densities to the fact that the two modes at 6.28 MHz and 15.44 MHz have a larger extent to their strain energy distribution than the other two modes – as quantified by their effective strain volumes V_{str} (see Table 6.2) – along with a significant portion of their strain energy density localized to the rounded portion of the ring (see Fig. 6.11 inset), where multiple crystal axis orientations are sampled. We also point out that the extracted TLS density parameters are on the order of those observed in bulk amorphous silica [368–370], much larger than

what would be expected for crystalline silicon resonators, where the TLS density of states has been found to be at least an order of magnitude smaller [342, 344]. This is likely due to the significantly larger surface-to-volume ratio of our nanoscale devices, which results in defects at the surface of the resonator [201, 274, 363, 371] providing a larger contribution to the overall defect density, as has been previously reported in optomechanically-measured gallium arsenide microdisks [372]. We note that this hypothesis is further supported by the fact that over half of the strain energy for each mechanical mode exists within the first 20 nm of the resonator's surface (see Table 6.3).

From $\mathcal{P}_0$, we can also infer the total number of thermally-active defects located within the effective strain volume of the resonator as $\mathcal{N}_{\text{th}} \sim \mathcal{P}_0 V_{\text{str}} k_{\text{B}} T$ [162, 201]. As can be seen from Table 6.4, at the lowest achievable temperature of our fridge (10 mK), the resonator is already at the point of coupling to less than a single defect on average. In this situation, known as the small mode volume limit, the TLS no longer act as a bath and a fully quantum mechanical description must be applied, resulting in the defect-phonon system undergoing Rabi oscillation [162]. It is possible that this is the cause of the mechanical damping rate flattening out to a constant value for $T \lesssim 100$ mK, as in this regime other temperature-independent loss mechanisms, such as radiation of acoustic energy at the resonator's clamping points [249, 253], would begin to dominate. An alternative explanation is that this plateau is due to measurement-induced heating of the chip at low temperatures (see Section 6.4.4).

Finally, the extracted deformation potentials are on the order of $\gamma \sim 1{-}2$ eV, comparable to the those found in bulk amorphous silica [368, 369, 373]. We point out that these values are notably less than the 3 eV that has been previously reported for TLS defects caused by boron dopants in crystalline silicon [374], further supporting the hypothesis that these TLS are instead caused by glassy defects at the surface of the resonator [201].

6.6 Conclusion

In this chapter, we have detailed an optomechanical ringdown technique that can be used to simultaneously measure the thermally-driven motion of four mechanical modes (with resonant frequencies ranging from 3 to 19 MHz) in a single-crystal silicon nanomechanical resonator. From these low-strain measurements, we extract the damping rate for each mechanical mode over a fridge temperatures ranging from 10 mK to 10 K. Fitting these data to a one-dimensional TLS damping model, we demonstrate that dimensionality has a strong effect on the defect-phonon interaction, which is especially important for the reduced geometries associated with nanoscale resonators. Extracting information about the density of states and deformation potentials of the TLS ensembles, we find that they are consistent with glassy surface defects created during fabrication of the nanoresonator, with a concentration similar to that observed in bulk amorphous silica. Comparing the density of states for the TLS ensembles coupled to each mechanical mode, we find that the two modes exhibiting a larger spatial extent to their strain profiles couple to TLS ensembles roughly four times more dense than those coupling to modes with smaller effective strain volumes. Finally, at the fridge base temperature of 10 mK we find that the small effective mode volumes of our device should allow us to achieve coupling to less than one thermally-active defect on average for each of the four studied mechanical modes.

Chapter 7

Dueling Dynamical Backaction in a Cryogenic Optomechanical Cavity

This chapter is based on the publication B. D. Hauer, T. J. Clark, P. H. Kim, C. Doolin, and J. P. Davis, "Dueling dynamical backaction in a cryogenic optomechanical cavity," *Phys. Rev. A* **99**, 053803 (2019) (Ref. [295]) and draws heavily on the content therein. Note that in order to be consistent with the rest of the thesis, a number of minor notational changes have been made with respect to the original publication.

7.1 Introduction

In Chapter 4, we showed that the radiation-pressure force of photons confined within the optical cavity of an optomechanical system can act back upon the mechanical element by actively driving or damping its motion. This ability to manipulate the mechanical resonator's motion via the radiation-pressure force has proven to be one of the most powerful phenomena observed in optomechanical systems to date. In fact, by employing these radiation-pressure-driven effects, a number of groundbreaking experiments have been performed using optomechanical cavities, including motional ground state cooling of micro/nanomechanical resonators [106, 107], entanglement of photonic and phononic modes [113, 142, 375] and preparation of other nonclassical states of mechanical motion [111, 112, 137].

Though efforts have largely focussed on this radiation-pressure-driven interaction,

optomechanical coupling can also be mediated by other means, such as the photothermal (or bolometric) force, whereby photon absorption in the mechanical element introduces a temperature gradient across the device, causing it to deflect due to differential thermal contractions [289–291, 294, 376]. Photothermal effects have historically been studied in optical cavities comprised of metal-coated cantilevers [21–25, 303, 377, 378], but have also been observed in buckled microcavities [379, 380], multilayered Bragg-mirror beams [26, 381], membranes [382–384], thin metallic mirrors [385], nanowires [379, 386, 387], split-ring resonators [87], and superfluid helium [80–82]. As in the case of radiation-pressure-driven optomechanics, photothermal forces can also be used to manipulate the motion of mechanical resonators. In fact, in a somewhat paradoxical sense, photothermal coupling can in principle be used to cool a resonator's motion to occupancies of less than a single phonon on average [289–291, 294, 376]. Furthermore, photothermal dynamical backaction is peculiar in that it is able to invert the detuning dependence of the optomechanical damping (and spring effect) with respect to that found in conventional radiation-pressure-driven systems, where such a reversal is only possible for cavities that are externally-driven to large mechanical amplitudes in the SBR regime [301, 302, 304, 305]. In the non-SBR regime, however, this inversion effect results in amplification of the resonator's motion (accompanied by an increase in the mechanical resonance frequency) for red-detuned pumps, while cooling (along with a decrease in the mechanical resonance frequency) occurs for blue-detuned pumps [22, 25, 303, 378, 380–382], seemingly violating the conservation of energy. While there have been brief mentions of a radiation-pressure-dominated spring effect observed in photothermally-driven optomechanical devices [22, 25, 378, 381], to date there has not been a thorough experimental investigation of how the photothermal and radiation-pressure forces interact with each other. Therefore, a comprehensive study of this interaction is warranted, especially in the case of cryogenic silicon optomechanical cavities, as these devices are integral to a number of recent quantum optomechanical experiments [135–139, 141–143].

In this chapter, we present and quantitatively analyze measurements of a silicon WGM optomechanical cavity that exists in a parameter regime where both radiation-pressure and photothermal effects are relevant. We begin in

Section 7.2 by demonstrating how the introduction of the photothermal force into the standard optomechanical model modifies the radiation-pressure interaction described in Chapter 4. In Section 7.3, we then introduce the studied optomechanical claw resonator, as well as calculate the thermal relaxation time associated with this geometry. Continuing in Section 7.4, we briefly detail our optomechanical measurement setup, as well as apply the theory developed in Section 7.2 to measurements taken with this system, observing that radiation pressure dominates the optical spring effect, while the photothermal force governs the system's optomechanical damping. Moreover, the photothermal force acts to oppose its radiation-pressure counterpart, such that the optomechanical damping has the opposite detuning-dependence from what one would expect for a conventional radiation-pressure-driven system, resulting in an oddly similar detuning-dependence between the optomechanical damping and spring effect. With this photothermal enhancement to the optomechanical damping, we find that for high enough optical input powers we are able to drive the mechanical resonator into self-oscillations using a red-detuned pump. We show that in this self-oscillating regime, the transmission through the optical cavity, as well as the optomechanical damping and spring effect, become highly nonlinear, while demonstrating hysteretic behaviour depending on the sweep direction of the optical drive. Using our fully nonlinear treatment of the system, we fit these data, extracting the optomechanical properties of this photothermally driven system. Finally, in Section 7.5, we use these experimentally-determined system parameters to assess the optical cavity's ability to cool the motion of the resonator using the photothermal effect for a blue-detuned optical pump. In doing so, we find that the mechanical occupancy can in principle be reduced to less than a single phonon on average, despite the fact that the optomechanical cavity resides deeply in the non-SBR regime.

7.2 Cavity Optomechanics with both Radiation-Pressure and Photothermal Interactions

In this section, we look to theoretically model the behaviour of an optomechanical cavity that is subject to both radiation-pressure and photothermal effects.

Specifically, we determine in which parameter regimes these individual forces will dominate each of the optomechanical damping and spring effect, as well as investigate how the inclusion of the photothermal force modifies the radiation-pressure-driven optomechanical phenomena of cooling and nonlinear parametric amplification.

7.2.1 Inclusion of Photothermal Interactions

In order to include photothermal interactions into our optomechanical model, we make two simple modifications to the equations of motion for a purely radiation-pressure-driven optomechanical system given by Eqs. (4.15) and (4.16). First, we separate cavity loss due to absorption in the mechanical resonator, quantified by the loss rate κ_{a} and the vacuum noise input operator $\hat{a}_{\mathrm{a}}$, from internal losses due to all other sources, which occur at a rate κ_{o} with an associated vacuum noise input operator $\hat{a}_{\mathrm{o}}$. Note that both κ_{a} and κ_{o} contribute to the total intrinsic damping rate of the optical cavity, such that $\kappa_{\mathrm{i}} = \kappa_{\mathrm{a}} + \kappa_{\mathrm{o}}$. Mathematically, this amounts to replacing the internal vacuum noise input term $\sqrt{\kappa_{\mathrm{i}}}\hat{a}_{\mathrm{i}}(t)$ on the right side of Eq. (4.15) with $\sqrt{\kappa_{\mathrm{a}}}\hat{a}_{\mathrm{a}}(t) + \sqrt{\kappa_{\mathrm{o}}}\hat{a}_{\mathrm{o}}(t)$, producing a new equation of motion for the cavity photon annihilation operator as

$$\dot{\hat{a}} = -\frac{\kappa}{2}\hat{a} + i\Delta_0\hat{a} + iG\hat{x}\hat{a} + \sqrt{\kappa_{\mathrm{e}}}\hat{a}_{\mathrm{in}} + \sqrt{\kappa_{\mathrm{a}}}\hat{a}_{\mathrm{a}} + \sqrt{\kappa_{\mathrm{o}}}\hat{a}_{\mathrm{o}}. \tag{7.1}$$

This modification allows us to track the proportion of internal cavity losses that are caused by photon absorption in the mechanical element, which as we shall see below is an important consideration when determining the efficacy of the photothermal force in cooling the mechanical resonator.

The second modification we make to our optomechanical model is the inclusion of an optically mediated photothermal force $\hat{F}_{\mathrm{pt}}$ acting upon the mechanical resonator, which we add to the right-hand side of Eq. (4.16), resulting in

$$\ddot{\hat{x}} + \Gamma_{\mathrm{m}}\dot{\hat{x}} + \omega_{\mathrm{m}}\hat{x} = \frac{1}{m}\left[\hat{F}_{\mathrm{th}} + \hat{F}_{\mathrm{rp}} + \hat{F}_{\mathrm{pt}}\right]. \tag{7.2}$$

As mentioned in the introduction, this photothermal force arises as a result of photon-absorption-induced heating in the mechanical resonator which causes it to deform due to differential thermal contractions. Mathematically, this photothermal

force is given in terms of the field operator characterizing these absorbed photons $\hat{a}_{\mathrm{abs}}(t) = \sqrt{\kappa_{\mathrm{a}}}\hat{a}(t) - \hat{a}_{\mathrm{a}}(t)$ as [80, 289–291, 294, 376]

$$\hat{F}_{\mathrm{pt}}(t) = \frac{\hbar G \beta}{\kappa_{\mathrm{a}} \tau_{\mathrm{pt}}} \int_{-\infty}^{t} e^{-\frac{t-t'}{\tau_{\mathrm{pt}}}} \hat{a}_{\mathrm{abs}}^{\dagger}(t') \hat{a}_{\mathrm{abs}}(t') dt'. \tag{7.3}$$

Here we see that adiabatic elimination of the phononic bath [383] gives rise to an integral of an exponential that decays on a time scale set by the thermal relaxation time of the mechanical resonator τ_{pt} (see Section 7.3.2 for an indepth discussion of this time constant). Also included in Eq. (7.3) is the dimensionless parameter β that determines the relative strength and direction of the photothermal force with respect to the radiation-pressure force. This parameter is heavily dependent on the optical and mechanical modeshapes being considered [25, 80], as well as the thermal properties of the resonator [291, 376]. It is important to note that it is possible for β to be negative [22, 25, 303, 378, 380–382], such that the photothermal force acts to directly oppose radiation-pressure effects, which has significant consequences for the detuning-dependence of the optomechanical damping and spring effects. Furthermore, setting $\beta = 0$ eliminates this photothermal interaction, reverting our treatment back to that of a purely radiation-pressure-driven system. Finally, while we have chosen to explicitly identify the force in Eq. (7.3) as photothermal in nature, with the appropriate choice of τ_{pt}, β, and κ_{a}, the analysis that follows is valid for any optomechanical force that has a delayed response with respect to the occupation of the optical cavity.

7.2.2 Linearized Photothermal Equations of Motion

To determine how the inclusion of a photothermal force modifies the properties of the optomechanical system, we linearize the equations of motion given in Eqs. (7.1) and (7.2), as we did with their radiation-pressure counterparts in Section 4.3.3,

while taking $\hat{a}_{\rm a}(t) = \delta\hat{a}_{\rm a}(t)$ and $\hat{a}_{\rm o}(t) = \delta\hat{a}_{\rm o}(t)$ to arrive at

$$\delta\dot{\hat{a}} = -\frac{\kappa}{2}\delta\hat{a} + i\Delta\delta\hat{a} + iG\bar{a}\delta\hat{x} + \sqrt{\kappa_{\rm e}}\delta\hat{a}_{\rm in} + \sqrt{\kappa_{\rm a}}\delta\hat{a}_{\rm a} + \sqrt{\kappa_{\rm o}}\delta\hat{a}_{\rm o}, \tag{7.4}$$

$$\begin{aligned}\delta\ddot{\hat{x}} + \Gamma_{\rm m}\delta\dot{\hat{x}} + \omega_{\rm m}^2\delta\hat{x} = \frac{1}{m}\Bigg[&\hat{F}_{\rm th} + \hbar G\left[\bar{a}^*\delta\hat{a} + \bar{a}\delta\hat{a}^\dagger\right] \\ &+\frac{\hbar G\beta}{\tau_{\rm pt}}\int_{-\infty}^{t} e^{-\frac{t-t'}{\tau_{\rm pt}}}\Bigg(\left[\bar{a}^*\delta\hat{a}(t') + \bar{a}\delta\hat{a}^\dagger(t')\right] \\ &-\frac{1}{\sqrt{\kappa_{\rm a}}}\left[\bar{a}^*\delta\hat{a}_{\rm a}(t') + \bar{a}\delta\hat{a}_{\rm a}^\dagger(t')\right]\Bigg)dt'\Bigg],\end{aligned} \tag{7.5}$$

with the associated steady-state values of $\hat{a}$ and $\hat{x}$ given by Eq. (4.19) and

$$\bar{x} = \frac{\hbar G|\bar{a}|^2(1+\beta)}{m\omega_{\rm m}^2}, \tag{7.6}$$

respectively. Note the additional photothermal terms proportional to β in Eqs. (7.5) and (7.6) with respect to Eqs. (4.18) and (4.20).

Fourier transforming Eqs. (7.4) and (7.5), we find the frequency representations of the fluctuations in $\hat{a}$ and $\hat{x}$ as

$$\delta\hat{a}(\omega) = \chi_{\rm c}(\omega)\left[iG\bar{a}\delta\hat{x}(\omega) + \sqrt{\kappa_{\rm e}}\delta\hat{a}_{\rm in}(\omega) + \sqrt{\kappa_{\rm a}}\delta\hat{a}_{\rm a}(\omega) + \sqrt{\kappa_{\rm o}}\delta\hat{a}_{\rm o}(\omega)\right], \tag{7.7}$$

$$\begin{aligned}\delta\hat{x}(\omega) = \chi_{\rm m}(\omega)\Bigg[&\delta\hat{F}_{\rm th}(\omega) + \hbar G\Bigg\{\left(1 + \frac{\beta}{1-i\omega\tau_{\rm pt}}\right)\left[\bar{a}^*\delta\hat{a}(\omega) + \bar{a}\delta\hat{a}^\dagger(\omega)\right] \\ &-\frac{\beta}{\sqrt{\kappa_{\rm a}}(1-i\omega\tau_{\rm pt})}\left[\bar{a}^*\delta\hat{a}_{\rm a}(\omega) + \bar{a}\delta\hat{a}_{\rm a}^\dagger(\omega)\right]\Bigg\}\Bigg].\end{aligned} \tag{7.8}$$

where again $\chi_{\rm c}(\omega)$ and $\chi_{\rm m}(\omega)$ are the optical and mechanical susceptibilities of the optomechanical system given by Eqs. (4.23) and (4.24) in Section 4.3.3.

7.2.3 Photothermal Damping and Spring Effect

Proceeding as we did in Section 4.3.4, we determine the optomechanical damping and spring effect in the presence of a photothermal force by inputting Eq. (7.7) into Eq. (7.8), resulting in

$$\begin{aligned}\delta\hat{x}(\omega) = \chi_{\rm eff}(\omega)\Bigg[&\hat{F}_{\rm th}(\omega) + \hbar G\Bigg\{\left(1 + \frac{\beta}{1-i\omega\tau_{\rm pt}}\right) \\ &\times\Bigg(\chi_{\rm c}(\omega)\bar{a}^*\left[\sqrt{\kappa_{\rm e}}\delta\hat{a}_{\rm in}(\omega) + \sqrt{\kappa_{\rm a}}\delta\hat{a}_{\rm a}(\omega) + \sqrt{\kappa_{\rm o}}\delta\hat{a}_{\rm o}(\omega)\right] \\ &+\chi_{\rm c}^*(-\omega)\bar{a}\left[\sqrt{\kappa_{\rm e}}\delta\hat{a}_{\rm in}^\dagger(\omega) + \sqrt{\kappa_{\rm a}}\delta\hat{a}_{\rm a}^\dagger(\omega) + \sqrt{\kappa_{\rm o}}\delta\hat{a}_{\rm o}^\dagger(\omega)\right]\Bigg) \\ &-\frac{\beta}{\sqrt{\kappa_{\rm a}}(1-i\omega\tau_{\rm pt})}\left[\bar{a}^*\delta\hat{a}_{\rm a}(\omega) + \bar{a}\delta\hat{a}_{\rm a}^\dagger(\omega)\right]\Bigg\}\Bigg].\end{aligned} \tag{7.9}$$

Here we have introduced the photothermal effective mechanical susceptibility given by [80, 150, 289–291]

$$\chi_{\rm eff}^{-1}(\omega) = \chi_{\rm m}^{-1}(\omega) - i\hbar G^2|\bar{a}|^2\left(1+\frac{\beta}{1-i\omega\tau_{\rm pt}}\right)\Big[\chi_{\rm c}(\omega)-\chi_{\rm c}^{*}(-\omega)\Big], \tag{7.10}$$

where we have again assumed that $\delta\omega_{\rm m} \ll \omega_{\rm m}$. From this effective susceptibility, we can extract the optomechanical spring effect in a photothermally driven cavity as

$$\begin{aligned}\delta\omega_{\rm m} &= -\frac{\hbar G^2|\bar{a}|^2}{2m\omega_{\rm m}}{\rm Re}\left\{i\left(1+\frac{\beta}{1-i\omega_{\rm m}\tau_{\rm pt}}\right)\Big[\chi_{\rm c}(\omega_{\rm m})-\chi_{\rm c}^{*}(-\omega_{\rm m})\Big]\right\}\\ &= 2\bar{g}^2\Delta|\chi_{\rm c}(\omega_{\rm m})|^2|\chi_{\rm c}(-\omega_{\rm m})|^2\\ &\times\left[\frac{\kappa^2}{4}+\Delta^2-\omega_{\rm m}^2+\frac{\beta}{1+\omega_{\rm m}^2\tau_{\rm pt}^2}\left(\frac{\kappa^2}{4}+\Delta^2-\omega_{\rm m}^2-\omega_{\rm m}^2\kappa\tau_{\rm pt}\right)\right],\end{aligned} \tag{7.11}$$

while the photothermal optomechanical damping is given by

$$\begin{aligned}\delta\Gamma_{\rm m} &= \frac{\hbar G^2|\bar{a}|^2}{m\omega_{\rm m}}{\rm Im}\left\{i\left(1+\frac{\beta}{1-i\omega_{\rm m}\tau_{\rm pt}}\right)\Big[\chi_{\rm c}(\omega_{\rm m})-\chi_{\rm c}^{*}(-\omega_{\rm m})\Big]\right\}\\ &= -4\bar{g}^2\Delta\omega_{\rm m}|\chi_{\rm c}(\omega_{\rm m})|^2|\chi_{\rm c}(-\omega_{\rm m})|^2\\ &\times\left\{\kappa+\frac{\beta}{1+\omega_{\rm m}^2\tau_{\rm pt}^2}\left[\kappa+\tau_{\rm pt}\left(\frac{\kappa^2}{4}+\Delta^2-\omega_{\rm m}^2\right)\right]\right\}.\end{aligned} \tag{7.12}$$

The two expressions given in Eqs. (7.11) and (7.12) resemble what we found for the optomechanical spring effect and damping for a radiation-pressure-driven optomechanical system in Eqs. (4.28) and (4.29), with the addition of the terms proportional to β to account for photothermal effects [301]. Photothermal forces will therefore govern these dynamical backaction effects when these additional terms overwhelm their radiation-pressure counterparts. By inspection of Eqs. (7.11) and (7.12), we find that this will occur for the spring effect when

$$\left|\frac{\kappa^2}{4}+\Delta^2-\omega_{\rm m}^2\right| < \left|\frac{\beta}{1+\omega_{\rm m}^2\tau_{\rm pt}^2}\left(\frac{\kappa^2}{4}+\Delta^2-\omega_{\rm m}^2-\omega_{\rm m}^2\kappa\tau_{\rm pt}\right)\right|, \tag{7.13}$$

while the photothermal force will dominate the optomechanical damping if

$$\kappa < \left|\frac{\beta}{1+\omega_{\rm m}^2\tau_{\rm pt}^2}\left[\kappa+\tau_{\rm pt}\left(\frac{\kappa^2}{4}+\Delta^2-\omega_{\rm m}^2\right)\right]\right|. \tag{7.14}$$

These inequalities are simplified considerably if we restrict ourselves to the experimentally relevant parameter space of $\kappa \gg \omega_{\rm m}$ (*i.e.* the non-SBR regime) and

$\omega_{\mathrm{m}}\tau_{\mathrm{pt}} \sim 1$, which together imply $\kappa\tau_{\mathrm{pt}} \gg 1$. Using these conditions, Eq. (7.13) will be satisfied if

$$1 + \omega_{\mathrm{m}}^2\tau_{\mathrm{pt}}^2 \lesssim |\beta|, \tag{7.15}$$

while Eq. (7.14) becomes

$$\kappa < \frac{|\beta|\,\tau_{\mathrm{pt}}}{1 + \omega_{\mathrm{m}}^2\tau_{\mathrm{pt}}^2}\left(\frac{\kappa^2}{4} + \Delta^2\right). \tag{7.16}$$

Finally, Eq. (7.16) can be further simplified if we assume $\Delta \sim \pm\kappa/2$ (*i.e.* only consider the region where optomechanical damping is maximized) which results in

$$1 + \omega_{\mathrm{m}}^2\tau_{\mathrm{pt}}^2 \lesssim \frac{|\beta|\,\kappa\tau_{\mathrm{pt}}}{2}. \tag{7.17}$$

Note that for the above inequalities we have taken the absolute value of β as it can be positive or negative depending on the orientation of the photothermal force with respect to the radiation-pressure force. We further point out the difference of $\kappa\tau_{\mathrm{pt}}/2$ between Eqs. (7.15) and (7.17), as this factor quantifies the ratio of the photothermal time constant τ_{pt} to the cavity photon lifetime $\tau_{\mathrm{c}} = 1/\kappa$ (*i.e.* the relevant time scales associated with each optical force) and is significant in determining which force dominates each of these dynamical back-action effects [378, 381]. This is especially true for non-SBR optomechanical cavities, where $\kappa\tau_{\mathrm{pt}}$ tends to be large and photothermal damping effects are generally stronger than those found in SBR systems [289–291, 376].

In Fig. 7.1, we investigate three different optomechanical regimes according to Eqs. (7.15) and (7.17). Interestingly, we find that there exists a parameter space where $|\beta| < 1 + \omega_{\mathrm{m}}^2\tau_{\mathrm{pt}}^2$, such that the spring effect is dominated by the radiation-pressure force, but $\kappa\tau_{\mathrm{pt}}$ is large enough that Eq. (7.17) is satisfied and optomechanical damping is governed by the photothermal force. This regime is particularly intriguing in the case where β is negative, resulting in the bizarre effect of a qualitatively similar detuning dependencies between the optomechanical damping and spring effect, as seen in Figs. 7.1c/f. It is this regime, which we refer to as the "dueling regime," that we investigate experimentally in this chapter.

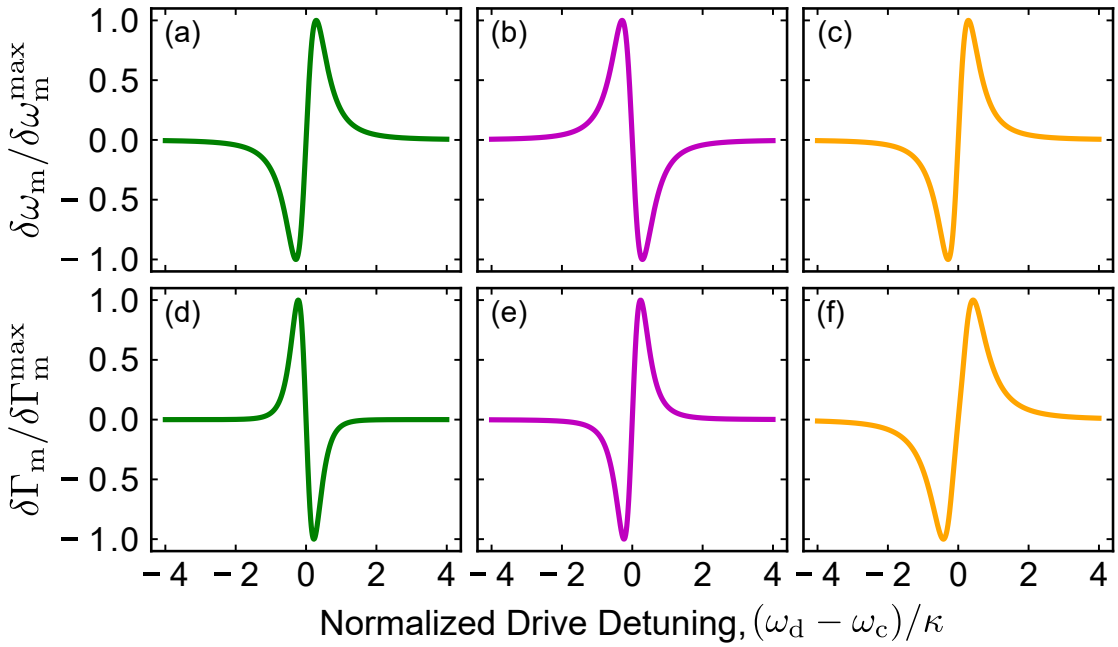

Figure 7.1: Plots of the optomechanical (a)–(c) spring effect and (d)–(f) damping, normalized to their respective maximum values, $\delta\omega_{\rm m}^{\rm max}$ and $\delta\Gamma_{\rm m}^{\rm max}$. Here we consider the small mechanical amplitude regime, with both radiation-pressure and photothermal effects included (*i.e.* Eqs. (7.11) and (7.12)), where we have taken (a)/(d) $\beta = -0.1$, $\omega_{\rm m}\tau_{\rm pt} = 0.01$, (b)/(e) $\beta = -10$, $\omega_{\rm m}\tau_{\rm pt} = 0.01$, and (c)/(f) $\beta = -0.1$, $\omega_{\rm m}\tau_{\rm pt} = 1$; with $\kappa/\omega_{\rm m} = 100$ in all plots. Therefore, according to Eqs. (7.15) and (7.17), in (a)/(d) radiation pressure dominates both the spring effect and damping, while in (b)/(e) dynamical backaction is driven by photothermal forces. Finally, in (c)/(f) we enter into the dueling regime studied in this chapter, where the spring effect is dominated by the radiation-pressure force, while the optomechanical damping is governed by photothermal effects. Figure reproduced from Ref. [295]. © 2019 American Physical Society.

7.2.4 Nonlinear Photothermal Optomechanics

We are also interested in determining how the inclusion of the photothermal interaction affects the properties of an optomechanical cavity in the nonlinear regime that coincides with the mechanical resonator being driven to a large amplitude of oscillation. Following the same procedure we used in Section 4.5 for a radiation-pressure-driven system, we begin with the classical photothermal equations of motion. These can be found by taking the expectation values of Eqs. (7.1) and

(7.2), resulting in

$$\dot{a} = -\frac{\kappa}{2}a + i\Delta_0 a + iGxa + \sqrt{\kappa_e}\bar{a}_{in}, \tag{7.18}$$

$$\ddot{x} + \Gamma_m\dot{x} + \omega_m^2 x = \frac{1}{m}\left[F_{th} + F_{rp} + F_{pt}\right], \tag{7.19}$$

where we have introduced the classical photothermal force by taking the expectation value of Eq. (7.3) to obtain

$$F_{pt}(t) = \frac{\hbar G\beta}{\tau_{pt}}\int_{-\infty}^{t} e^{-\frac{t-t'}{\tau_{pt}}}|a(t')|^2 dt'. \tag{7.20}$$

Note that since the photothermal force is only introduced into the mechanical equation of motion[1], the optical amplitude is not directly perturbed by the introduction of the photothermal interaction. Therefore, the mathematical form of the transmission through the cavity remains the same as it was for the case of a radiation-pressure-driven system (*i.e.* Eq. (4.93)), provided any photothermal effects that modify the mechanical amplitude A are accounted for.

Continuing as we did in Section 4.5, we assume solutions for $x(t)$ and $a(t)$ of the form given by Eqs. (4.84) and (4.85). We then balance the cavity's time-averaged forces, energy, and power[2] to determine the steady-state mechanical amplitude, along with the optomechanical spring effect and damping of the photothermal system, as a function of mechanical amplitude A according to [150, 301–303, 311]

$$\bar{x}(A) = \frac{\hbar G\kappa_e|\bar{a}_{in}|^2}{m\omega_m^2}(1+\beta)\sum_{l=-\infty}^{\infty}|\tilde{a}_l|^2, \tag{7.21}$$

$$\delta\omega_m(A) = -\frac{\hbar G\kappa_e|\bar{a}_{in}|^2}{Am\omega_m}\sum_{l=-\infty}^{\infty}\mathrm{Re}\left\{\tilde{a}_l\,\tilde{a}_{l+1}^*\left(1+\frac{\beta}{1-i\omega_m\tau_{pt}}\right)\right\}, \tag{7.22}$$

$$\delta\Gamma_m(A) = \frac{2\hbar G\kappa_e|\bar{a}_{in}|^2}{Am\omega_m}\sum_{l=-\infty}^{\infty}\mathrm{Im}\left\{\tilde{a}_l\,\tilde{a}_{l+1}^*\left(1+\frac{\beta}{1-i\omega_m\tau_{pt}}\right)\right\}, \tag{7.23}$$

where $\tilde{a}_l$ is given by Eq. (4.86). Note that in order to obtain the optomechanical quantities given in Eqs. (7.21)–(7.23), we have used the time-average identities

[1] In modifying the optical equation of motion from Eq. (4.82) to Eq. (7.18), we have simply broken up the internal cavity losses to account for optical absorption in the mechanical element, such that both of these equations describe identical physical systems.

[2] We determine the time-averaged forces by simply taking the time-average of Eq. (7.19), while for the time-averaged energy and power, we first multiply Eq. (7.19) by $x(t)$ and $\dot{x}(t)$, respectively, before time-averaging.

interspersed throughout Section 4.5, as well as

$$\langle \frac{\beta}{\tau_{\rm pt}} \int_{-\infty}^{t} e^{-\frac{t-t'}{\tau_{\rm pt}}} |a(t')|^2 dt' \rangle = \beta \kappa_{\rm e} |\bar{a}_{\rm in}|^2 \sum_{l=-\infty}^{\infty} |\tilde{a}_l|^2, \tag{7.24}$$

$$\langle \frac{\beta}{\tau_{\rm pt}} \int_{-\infty}^{t} e^{-\frac{t-t'}{\tau_{\rm pt}}} |a(t')|^2 \dot{x}(t) dt' \rangle = -A\omega_{\rm m} \kappa_{\rm e} |\bar{a}_{\rm in}|^2 \sum_{l=-\infty}^{\infty} {\rm Im} \left\{ \frac{\beta \tilde{a}_l \, \tilde{a}_{l+1}^*}{1 - i\omega_{\rm m} \tau_{\rm pt}} \right\}. \tag{7.25}$$

Upon inspection of Eqs. (7.21)–(7.23), we therefore find that the addition of photothermal effects into the system amounts to multiplying the steady-state mechanical amplitude of a purely radiation-pressure-driven system given in Eq. (4.87) by a factor of $(1 + \beta)$ (as was also the case in the linearized regime – see Eq. (4.20) and (7.6)). Meanwhile the optomechanical damping and spring effect are each modified by multiplying the $\tilde{a}_l \, \tilde{a}_{l+1}^*$ term located within the curly brackets of Eq. (4.89) and (4.91) by $1 + \beta/(1 - i\omega_{\rm m}\tau_{\rm pt})$. Finally, as was the case for the radiation-pressure-driven system, the mechanical-amplitude-dependent optomechanical quantities determined in this section, *i.e.* Eqs. (7.21), (7.22), and (7.23), are restored to their linearized forms given by Eqs. (7.6), (7.11), and (7.12) in the small mechanical amplitude regime of $\xi = GA/\omega_{\rm m} \ll 1$.

7.2.5 Photothermal Cooling

The inclusion of the photothermal interaction also significantly modifies the conventional radiation-pressure-driven backaction cooling process. To quantify the extent of this effect, we calculate the two-sided PSD of the mechanical displacement $S_{xx}(\omega)$ in the presence of a photothermal force, which can be found by inserting Eq. (7.9) into Eq. (4.32) to find

$$S_{xx}(\omega) = |\chi_{\rm eff}(\omega)|^2 \left[S_{FF}^{\rm th}(\omega) + S_{FF}^{\rm opt}(\omega) \right], \tag{7.26}$$

where we have used the fact that the correlators for the vacuum noise inputs $\delta\hat{a}_{\rm a}(\omega)$ and $\delta\hat{a}_{\rm o}(\omega)$ obey Eq. (E.13) in Appendix E. Here we have introduced $S_{FF}^{\rm opt}(\omega) = S_{FF}^{\rm rp}(\omega) + S_{FF}^{\rm pt}(\omega)$ as the optical force spectral density, which in addition to the radiation-pressure force spectral density $S_{FF}^{\rm rp}(\omega)$, includes the spectral density

of the photothermal force $S_{FF}^{\mathrm{pt}}(\omega) = \hbar^2 G^2 S_{NN}^{\mathrm{pt}}(\omega)$ where

$$S_{NN}^{\mathrm{pt}}(\omega) = \frac{\bar{N}}{(\Delta+\omega)^2 + (\kappa/2)^2} \frac{\beta}{1+\omega^2\tau_{\mathrm{pt}}^2} \times \left[\kappa\left(\frac{\beta\kappa}{4\kappa_{\mathrm{a}}}+1\right) + (\Delta+\omega)\left(\frac{\beta(\Delta+\omega)}{\kappa_{\mathrm{a}}} - 2\omega\tau_{\mathrm{pt}}\right)\right], \tag{7.27}$$

is the effective cavity photon number spectral density associated with the photothermal force [203, 293].

Inputting the PSD given in Eq. (7.26) into Eq. (4.37) to determine the phonon occupancy of the mechanical mode, we find an expression for $\langle n \rangle$ similar to Eq. (4.40), where we replace $\delta\Gamma_{\mathrm{m}}$ with the result found in Eq. (7.12) and have a new minimum achievable phonon average phonon occupancy of

$$\begin{aligned}\bar{n}_{\mathrm{min}} &= \left[S_{FF}^{\mathrm{opt}}(\omega_{\mathrm{m}})/S_{FF}^{\mathrm{opt}}(-\omega_{\mathrm{m}}) - 1\right]^{-1} = \left[S_{NN}^{\mathrm{opt}}(\omega_{\mathrm{m}})/S_{NN}^{\mathrm{opt}}(-\omega_{\mathrm{m}}) - 1\right]^{-1} \\ &= -\frac{\frac{\kappa^2}{4} + (\Delta+\omega_{\mathrm{m}})^2}{4\Delta\omega_{\mathrm{m}}\left\{\kappa + \frac{\beta}{1+\omega_{\mathrm{m}}^2\tau_{\mathrm{pt}}^2}\left[\kappa + \tau_{\mathrm{pt}}\left(\frac{\kappa^2}{4}+\Delta^2-\omega_{\mathrm{m}}^2\right)\right]\right\}} \\ &\times \left\{\kappa + \frac{\beta}{1+\omega_{\mathrm{m}}^2\tau_{\mathrm{pt}}^2}\left[\kappa\left(\frac{\beta\kappa}{4\kappa_{\mathrm{a}}}+1\right) + (\Delta-\omega_{\mathrm{m}})\left(\frac{\beta(\Delta-\omega_{\mathrm{m}})}{\kappa_{\mathrm{a}}} + 2\omega_{\mathrm{m}}\tau_{\mathrm{pt}}\right)\right]\right\}.\end{aligned} \tag{7.28}$$

Therefore, the inclusion of the photothermal interaction has a substantial influence on this minimal phonon occupation when compared to the result determined using solely radiation pressure given by Eq. (4.43)[3], especially in the non-SBR regime [289–291, 294, 376]. In fact, due to interference between the radiation-pressure and photothermal forces [290], it is possible to cool the mechanical resonator to an average phonon occupancy below one while operating in the non-SBR regime [289–291, 294, 376], a feat which is not possible for a dispersively coupled optomechanical cavity driven solely by radiation pressure [150, 293].

In order to determine the absolute minimum phonon occupancy that can be reached for a given optomechanical cavity, the expression given in Eq. (7.28) must be optimized with respect to the optical drive detuning Δ. Unfortunately, we are unable to determine a closed-form solution for the detuning Δ_{min} due to the added complexity introduced by photothermal effects. However, Δ_{min} can be determined numerically for a given set of conditions (see Section 7.5 below).

[3]This result can be obtained by simply setting $\beta = 0$ to remove the photothermal effects from Eq. (7.28).

7.3 Optomechanical Claw Resonator

7.3.1 Device Description

The optomechanical device studied in this work is comprised of a "claw-like" mechanical resonator that surrounds roughly one quarter of the circumference of a 10-μm-diameter microdisk as seen in Fig. 7.2. Both elements are fabricated from the same 250-nm-thick single-crystal-silicon device layer of a standard SOI chip (see Section 5.2.2 for details). A schematic of the mechanical resonator, along with critical dimensions can be seen in Fig. 7.3, with the numerical values used in the experiment summarized in Table 7.1.

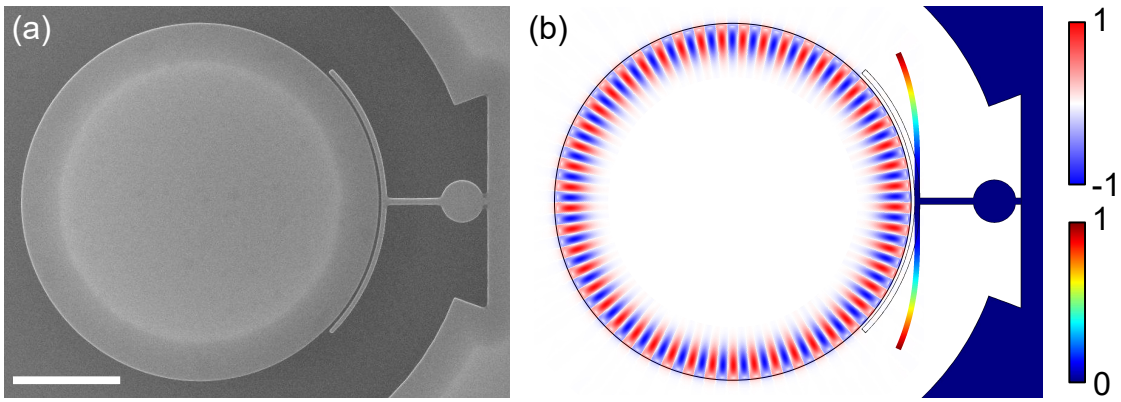

Figure 7.2: (a) A scanning electron microscope image of the device studied in this work. Scale bar is 3 μm (see Table 7.1 for detailed device dimensions). (b) FEM simulations of the normalized electric field magnitude for the optical WGM of the disk with radial mode number $n = 1$ and azimuthal mode number $m = 49$. Colours indicate the direction of the normalized in-plane electric field, with blue/negative (red/positive) corresponding to an inward (outward) facing field with respect to the center of the disk. Also included is a finite element method simulation of the in-plane flexural crab mode of the mechanical resonator with the normalized displacement expressed in rainbow scale. Both mechanical and optical simulations are for the device in (a). Figure reproduced from Ref. [295]. © 2019 American Physical Society.

The optical microdisk supports WGM resonances in the telecom band (see Section 3.3), while the mechanical element exhibits a number of MHz-frequency flexural and torsional modes[4] . In this work, we focus on the in-plane flexural "crab"

[4]In fact, this resonator design was initially conceptualized as a low moment of inertia optomechanical torque sensor [98, 104, 388].

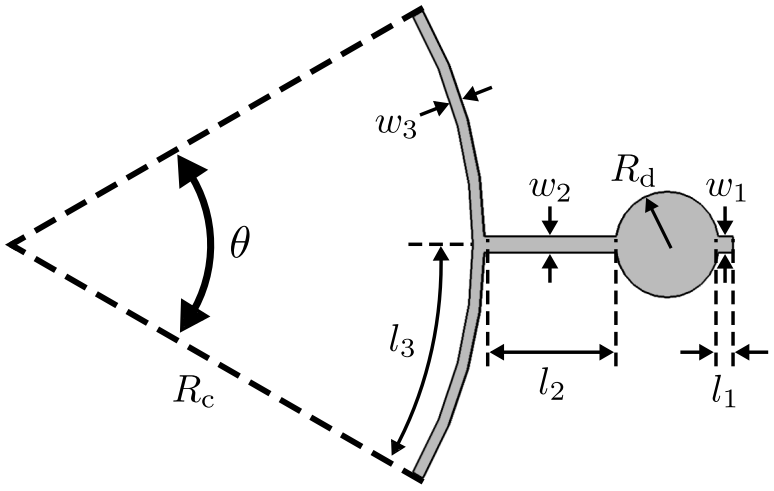

Figure 7.3: Schematic of the studied mechanical claw resonator, indicating each of its critical dimensions. Numerical values for each dimension are given in Table 7.1. Figure reproduced from Ref. [295]. © 2019 American Physical Society.

Measured Dimensions		
$l_1 = 143$ nm	$w_1 = 177$ nm	$R_\mathrm{d} = 595$ nm
$l_2 = 1.53$ μm	$w_2 = 177$ nm	$R_\mathrm{c} = 5.26$ μm
$l_3 = 4.20$ μm	$w_3 = 151$ nm	$\theta = 92.7$ deg

Table 7.1: Numerical values for the dimensions of the device studied in this chapter (see Fig. 7.3). Measurements were performed using the scanning electron microscope image shown in Fig. 7.2a. Device thickness was taken to be $t = 250$ nm as specified by the manufacturer.

mode of the mechanical resonator depicted in Fig. 7.2b, with a measured resonant frequency of $\omega_\mathrm{m}/2\pi = 11.2$ MHz, as this mode traverses the steepest gradient of the optical field profile, resulting in a large optomechanical coupling of $G/2\pi = 0.817$ GHz/nm. Using the measured dimensions of the mechanical resonator (see Table 7.1), along with its simulated modeshape, we find the effective motional mass of this mode to be $m = 183$ fg, allowing us to determine its zero-point fluctuation amplitude as $x_\mathrm{zpf} = \sqrt{\hbar/2m\omega_\mathrm{m}} = 64$ fm.

7.3.2 Thermal Relaxation Time

The thermal relaxation time τ_pt introduced in Eq. (7.3) is a very important quantity that sets the time scale, and in some instances the strength, of

photothermally driven optomechanical effects. For a thin beam of rectangular cross section, Zener showed that this time constant is dominated by thermal relaxation of the fundamental mode of the beam, resulting in

$$\tau_{\mathrm{pt}} = \frac{l^2 \mathcal{C}_V}{\pi^2 \mathcal{K}}, \tag{7.29}$$

where l, $\mathcal{C}_V$, and $\mathcal{K}$ are the length, volumetric specific heat capacity at constant volume (with units of J/m^3·K), and thermal conductivity of the beam, respectively [200, 208, 389]. For the claw resonator studied in this chapter ($w \sim t \sim 100$ nm), we are deep within the Casimir regime (*i.e.* the regime where the phonon mean free path in the beam is limited by its cross-sectional dimensions) for the experimental operating temperature of $T = 4.2$ K [192]. Therefore, we can input the Debye heat capacity and thermal conductivity found in Section 2.4.2 (*i.e.* Eqs. (2.97) and (2.101)), as well as the Casimir-limited phonon mean free path given by Eq. (2.99), into Eq. (7.29) to find an expression for the thermal relaxation time of the beam as

$$\tau_{\mathrm{pt}} = \frac{3l^2}{1.12\pi^2 \bar{c}\sqrt{wt}}, \tag{7.30}$$

where $\bar{c} = 5718$ m/s [184] is the average Debye speed of sound given by Eq. (2.83). Note that in this regime ($T \lesssim 100$ K for dimensions on the order of 100 nm [192]), the thermal relaxation time in silicon depends only on the geometry and speed of sound of the system, which are to first order temperature-independent. Furthermore, due to the factor $\mathcal{C}_V$ /$\mathcal{K}$ in Eq. (7.29), the dimensional dependences of the specific heat capacity and thermal conductivity cancel, such that the result given by Eq. (7.30) is independent of the dimensionality of the system.

While the above description works well for determining the thermal time constant for the geometry of a simple beam with a uniform rectangular cross section, it is unclear if such an analysis applies to the complex device structure studied in this chapter. We have therefore performed FEM simulations to accurately determine the thermal relaxation time for this device [381]. Here, the phonon mean free path is limited by the smallest dimension of our resonator (*i.e.* $w_3 = 151$ nm in Fig. 7.3), leading to a Casimir-limited mean free path of $\Lambda_{\mathrm{C}} \approx 1.12\sqrt{w_3 t} = 218$ nm (see Eq. (2.99)), where we have taken $t = 250$ nm as the thickness of the silicon device. Using this value for the mean free path, along with the temperature-dependent expressions for the specific heat capacity and thermal conductivity

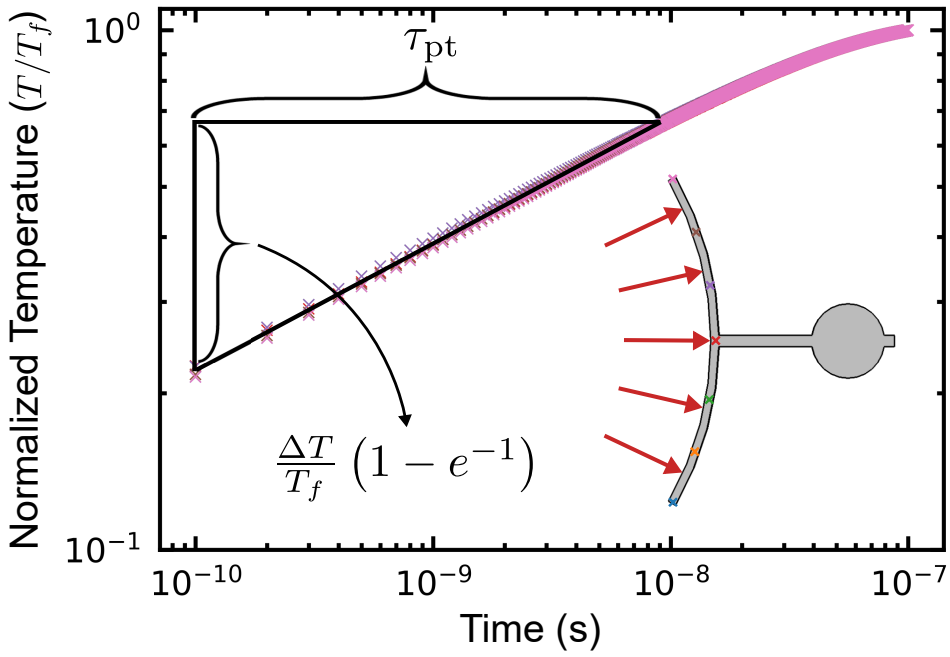

Figure 7.4: Plot of the normalized temperature T/T_f versus time for the FEM heating simulation used to determine the thermal relaxation time of the resonator. Inset is a schematic illustrating the simulation procedure, whereby a uniform heat load of 6 μW is applied to the surface of the resonator indicated by the red arrows, while its temperature profile is probed in time at the positions denoted by the coloured crosses. By normalizing each of these extracted data sets (color-coded to match the corresponding probe point) to its final temperature, a universal heating trend along the curved portion of the resonator is demonstrated. From these normalized profiles, we determine the thermal relaxation time of the device ($\tau_{\rm pt}$ = 9.5 ns) as the time required for the temperature to increase from its initial value by an amount $\Delta T\,(1-e^{-1})$ (see Eq. (7.31)). Figure reproduced from Ref. [295]. © 2019 American Physical Society.

found in Eqs. (2.97) and (2.101), we simulate the heating of the device due to absorption of laser power. To do this, the laser-driven heating is approximated as a uniform heat load applied to the inner surface of the resonator facing the disk (see inset of Fig. 7.4). The magnitude of this heat load is chosen to be $P_{\rm abs} = 6$ μW to approximately match the expected absorbed power for the experimental conditions associated with Fig. 7.7 below (*i.e.* $\kappa = 2.04$ GHz, $\kappa_{\rm e} = 0.38$ GHz, and $P_{\rm in} = 10.1$ μW), while also assuming $\kappa_{\rm a} = \kappa_{\rm i}$ and $\Delta = 0$ (see Eq. (4.49)). The simulated temperature increase of the resonator as a function of time was then monitored at seven equally spaced points along its rounded portion, as shown

in Fig. 7.4. Continuing with the Zener approximation (*i.e.* the majority of this thermal relaxation occurs through the fundamental mode of the beam), we expect the temperature at each of these points to increase according to [376, 389, 390]

$$T(t) = T_0 + \Delta T \left(1 - e^{-t/\tau_{\rm pt}}\right). \tag{7.31}$$

Here $\Delta T = T_f - T_0$ is the difference between the resonator's temperature T_0 at $t = 0$ when the heat load is initially applied and its final equilibrium temperature T_f that is reached for $t \gg \tau_{\rm pt}$. We note that while each point on the resonator heats from an initial temperature of $T_0 = 4.2$ K to varying equilibrium temperatures ranging from $T_f = 43$ K to $T_f = 49$ K, when normalized by these final temperatures, each simulated data set collapses onto a single universal trace (see Fig. 7.4). Therefore, we can use Eq. (7.31) to extract the thermal relaxation time as the average time required for the resonator to heat from T_0 to $T_0 + \Delta T(1 - e^{-1})$. Performing this calculation for each of these data sets, we find $\tau_{\rm pt} = 9.5 \pm 0.2$ ns, where the uncertainty is given by the standard deviation of this distribution.

We can also use this simulated value of $\tau_{\rm pt}$ to evaluate how well our irregular resonator geometry is approximated as a uniform rectangular beam (with width w_3 and thickness t). This is done by rearranging Eq. (7.30) to obtain the an effective thermal length of

$$l_{\rm eff} = \sqrt{\frac{1.12\pi^2 \bar{c} \tau_{\rm pt} \sqrt{w_3 t}}{3}}. \tag{7.32}$$

Using the simulated time constant and the parameters for our device, we find this effective length to be $l_{\rm eff} = 6.24$ μm. Comparing this value to the total length of our device, $l_{\rm tot} = l_1 + l_2 + l_3 + 2R_{\rm d} = 7.06$ μm, as measured from the tip of one end of the rounded portion of the resonator to its anchor point, we find that these two lengths agree very well with each other. Thus, our device is well-approximated as a uniform beam provided we introduce a small reduction in its length by a numerical factor of $l_{\rm eff}/l_{\rm tot} = 0.88$.

7.4 Experimental Results

7.4.1 Optomechanical Measurement Scheme

All measurements of the device studied in this chapter are performed inside a cryostat using the custom-built cryogenic optomechanical coupling apparatus described in Section 5.4, with exchange gas added to the vacuum can to promote thermalization of the device to the helium bath temperature of 4.2 K. Using the optical detection circuit described in Section 5.4.3, laser light is injected directly into, and collected from, the optical cavity via a cryogenic dimpled-tapered fiber [163, 312, 326]. The transmission through the optical cavity is then monitored by observing the laser fluence through the fiber using the single-channel photodetector of the detection circuit, while high-frequency fluctuations in the optical signal are either transduced directly using this photodetector, or by switching out to the homodyne detection system. This allows the advantage of being able to measure the mechanical signal using both direct and homodyne detection, as these two schemes are complimentary in a sense that one's response will be maximized for detunings at which the other is minimized (see Section 4.4), allowing for optimal signal-to-noise in the transduced signal over the entire sweep of the optical resonance.

7.4.2 Low Power Measurements

In Fig. 7.5, we show measurements of the studied optomechanical system from two separate optical resonances with center wavelengths located at 1582 nm (Fig. 7.5a) and 1608 nm (Fig. 7.5b). Here the optical resonance at 1582 nm exhibits the behaviour one would expect for a standard radiation-pressure-driven optomechanical system (see Figs. 7.1a/d), where we observe optomechanical damping on the red side of the optical cavity and amplification on the blue side, with the mechanical spring effect exhibiting the opposite detuning dependence. However, this is not the case for the optical resonance at 1608 nm. Instead, the optomechanical damping behaves quite differently, with amplification on the red side of the optical cavity and damping on the blue side. Furthermore, the spring effect seems to qualitatively follow the same detuning dependence as the optomechanical damping, such that these two dynamical backaction effects appear to violate the Kramers-

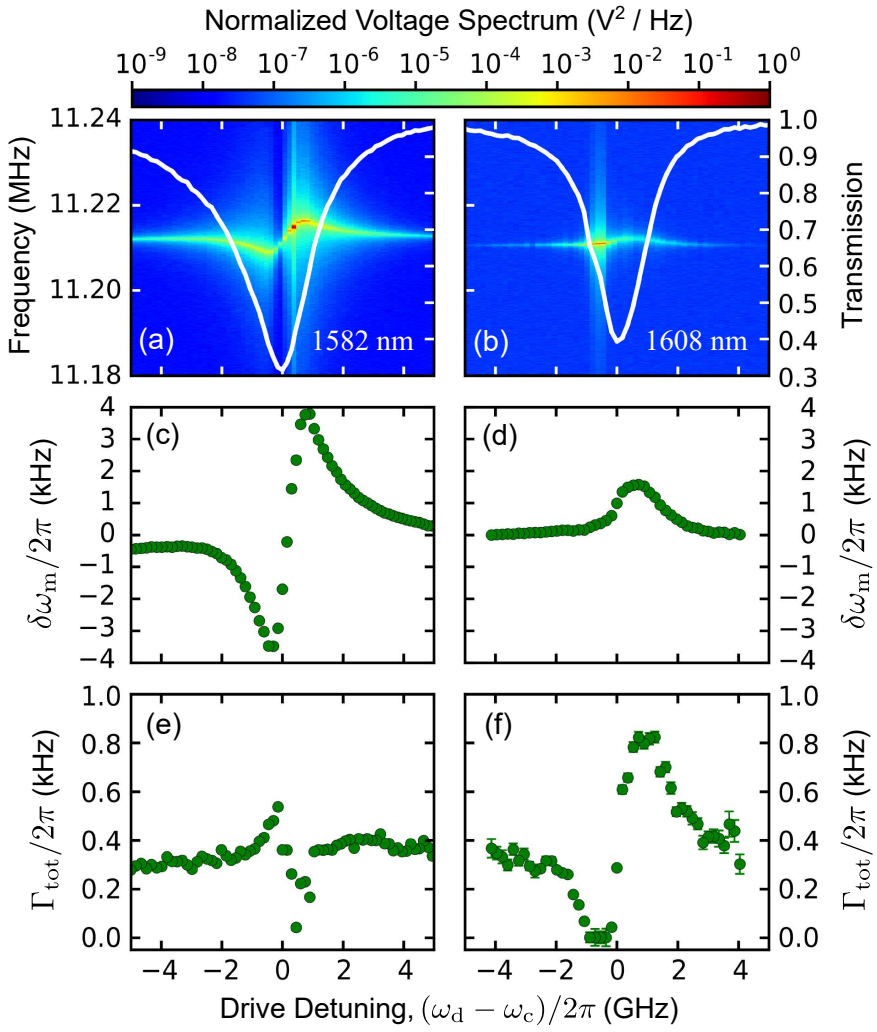

Figure 7.5: Mechanical spectra (normalized to their maximum values) versus detuning for the 11.2 MHz crab mode depicted in Fig. 7.2b for optical resonances at (a) $\lambda_c = 1582$ nm and (b) $\lambda_c = 1608$ nm, with the mechanical frequency on the left axis. Overlaid in white is the transmission through the cavity (right axis) for each optical mode. Note that while in (a) mechanical damping (amplification) occurs on the red (blue) side of the optical resonance, this effect is reversed in (b). Also included are (c)/(d) the optomechanical spring effect $\delta\omega_m$ and (e)/(f) the total mechanical damping rate $\Gamma_{tot} = \Gamma_m + \delta\Gamma_m$, with (c) and (e) corresponding to the mechanical data in (a), while (d) and (f) are extracted from the data in (b). We attribute the lack of spring effect on the red side of the optical resonance in (d) to an optical-heating-induced mechanical frequency shift that offsets the dynamical backaction effects [382]. Measurements are taken at input optical powers to the cavity of (a)/(c)/(e) $P_{in} = 10.9$ μW and (b)/(d)/(f) $P_{in} = 1.9$ μW, chosen such that self-oscillation of the mechanical motion has just begun to onset for each optical mode. Figure reproduced from Ref. [295]. © 2019 American Physical Society.

Kronig relations [292]. We note that this reversal in the detuning dependence of the optomechanical damping is observed over nearly three orders of magnitude in input optical power from approximately 50 nW to 10 μW (see Fig. 7.6), indicating that this seemingly anomalous effect does not onset at a given power threshold within this range. Such a power-dependence is in agreement with an optomechanical damping caused by dueling radiation-pressure and photothermal forces, as both of these effects scale with an identical power-dependence (see Eqs. (7.12) and (7.23)). Therefore, we attribute this behaviour to an additional photothermal force that is present for the 1608 nm optical mode, with β and τ_{pt} satisfying $\beta < 0$ and Eq. (7.17), but not Eq. (7.15), such that this force acts to overwhelm the device's radiation-pressure-driven optomechanical damping, but not its spring effect. We postulate that photothermal effects arise in this optomechanical device for optical modes that heat the inner surface of the mechanical resonator (facing the disk) via optical absorption. This in turn generates a thermal gradient across the width of the curved portion of the resonator, inducing thermoelastic forces that cause it to curl [382, 383], thus actuating the crab mode.

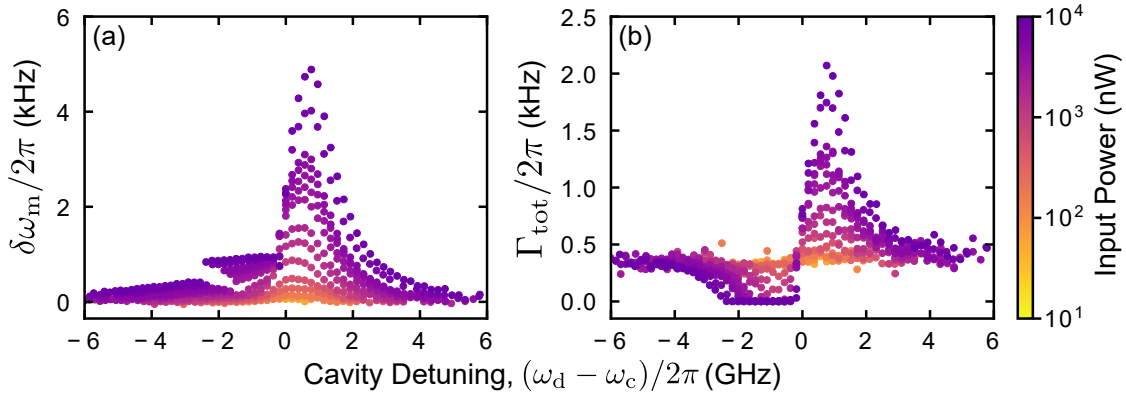

Figure 7.6: Optomechanical (a) spring effect and (b) damping over nearly three orders of magnitude in input optical power, ranging from approximately 50 nW to 10 μW, for the $\lambda_{\mathrm{c}} = 1608$ nm optical mode shown in Fig. 7.5b. Even at very low powers, optomechanical damping occurs for a blue-detuned optical drive, qualitatively matching the detuning dependence of the optomechanical spring effect. Figure reproduced from Ref. [295]. © 2019 American Physical Society.

7.4.3 High Power Measurements

As demonstrated in Fig. 7.7, the inverted detuning dependence associated with this effect becomes more pronounced at higher optical input powers, where we

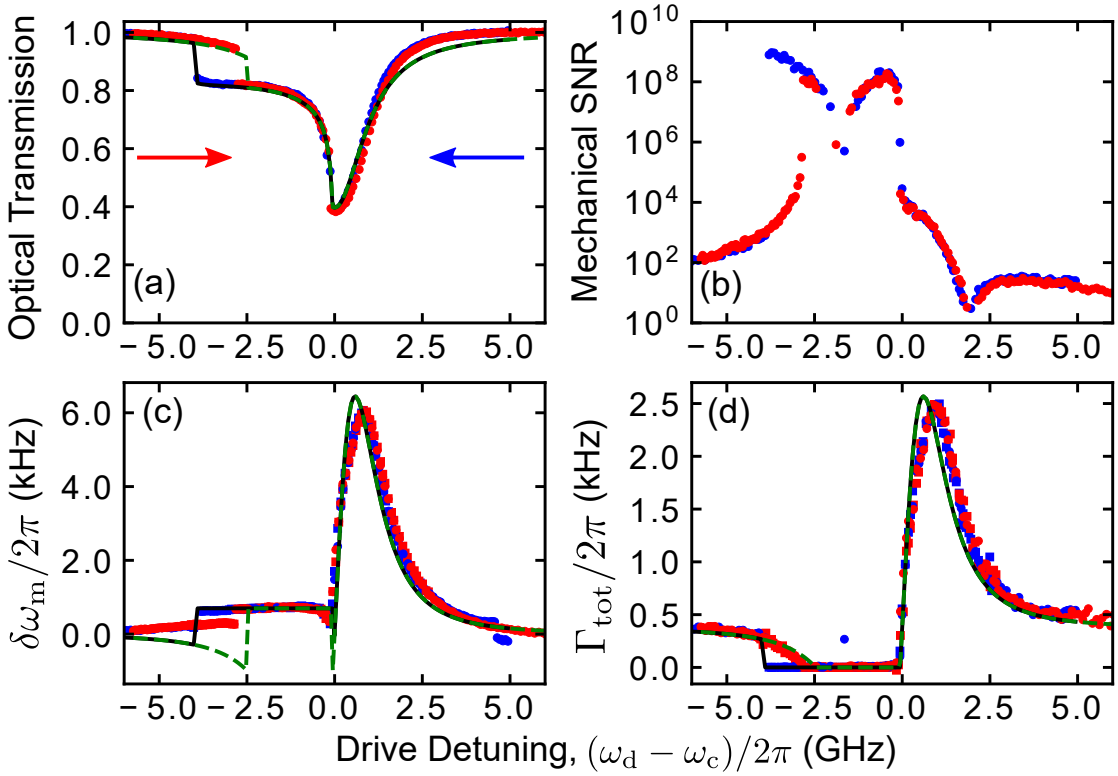

Figure 7.7: At an input power of $P_{\rm in} = 10.1$ μW, we find that the photothermal force drives the mechanical resonator into self-oscillation, causing a drastic increase in its amplitude of motion. This results in a highly nonlinear response for (a) the transmission through the optical cavity and (b) the SNR of the homodyne mechanical spectra, as well as the optomechanical (c) spring effect and (d) damping over the detuning range from $\Delta \sim 0$ to -4 GHz. In each of these plots, red (blue) data points denote an optical drive that was swept starting from the red (blue) side of the optical cavity, *i.e.* from negative to positive (positive to negative) detunings, as indicated by the arrows in (a). The data in (c) and (d) are extracted from mechanical spectra obtained using both direct (squares) and homodyne (circles) detection of the high-frequency portion of the optical signal at each drive detuning, while the SNR in (b) is determined by dividing the maximum value of the homodyne spectra by its off-resonant imprecision noise floor. The data for each detuning takes approximately 5 s to acquire, such that the sweep over the entire ∼160 detunings occurs on the timescale of ∼800 s. The dashed green (solid black) lines in (a), (c), and (d) are fits to the red (blue) data using Eqs. (4.93), (7.22), and (7.23), respectively, allowing for extraction of the optomechanical parameters quoted in the main text. Figure adapted from Ref. [295].

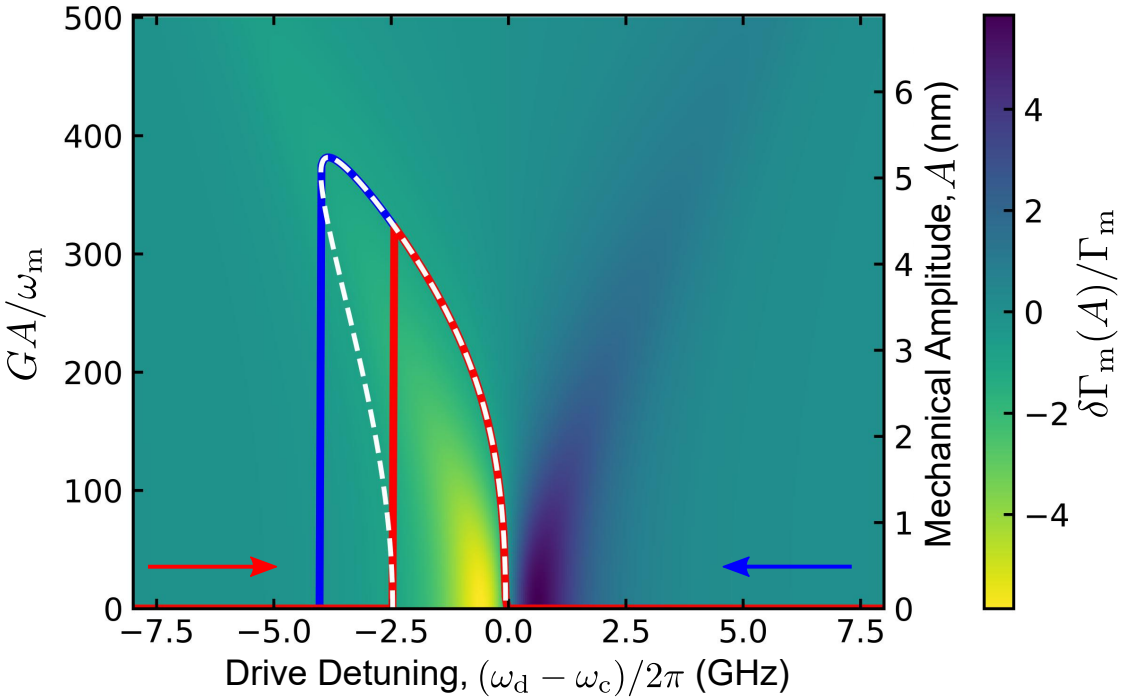

Figure 7.8: The attractor diagram for the data in Fig. 7.7, which is produced by using Eq. (7.23) to calculate $\delta\Gamma_m(A)$ for a number of mechanical amplitudes and optical drive detunings. The white dashed line indicates the condition of $\delta\Gamma_m(A)/\Gamma_m = -1$ (*i.e.* $\Gamma_{tot} = 0$), such that the red (blue) solid line traces out the physical values of the mechanical amplitude for a detuning sweep originating on the red (blue) side of the optical cavity. Coloured arrows indicate the sweep direction of the optical drive frequency as depicted in Fig. 7.7a. Figure adapted from Ref. [295]. © 2019 American Physical Society.

further find that the observed photothermal amplification is strong enough to reduce the total mechanical damping of the system to zero, inducing a parametric instability [301, 302]. This causes the device to self-oscillate for a near-resonant red-detuned optical pump, driving the mechanical resonator's motion to amplitudes as large as $A_{max} = 5.2$ nm ($= 382\ \omega_m/G$ – see Fig. 7.8), nearly three orders of magnitude greater than its thermally-driven amplitude of $A_{th} = \sqrt{2k_BT/m\omega_m^2} = 11.3$ pm at $T = 4.2$ K. Accompanying this increase in mechanical amplitude (and thus the signal-to-noise (SNR) of the mechanical measurements), we observe highly nonlinear behaviour in each of the optomechanical spring effect/damping, along with the transmission through the optical cavity, as well as a hysteresis in each of these quantities with respect to the sweep direction of the optical drive. We

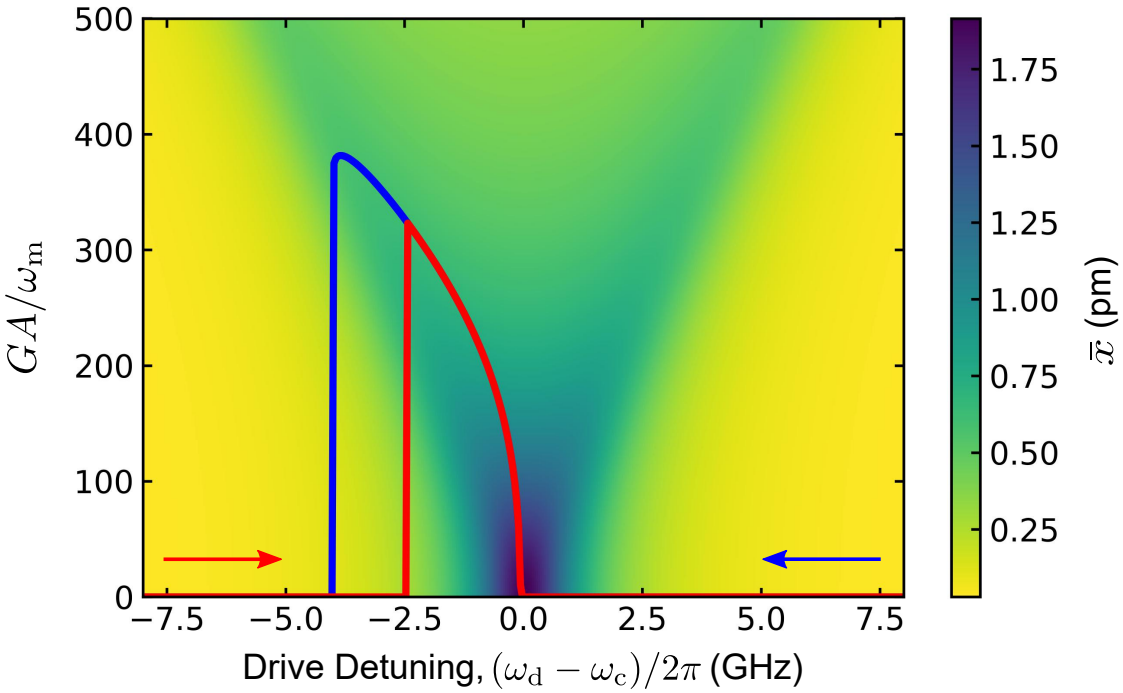

Figure 7.9: A color plot of $\bar{x}$ versus mechanical amplitude and optical drive detuning for the conditions given in Fig. 7.7. The solid lines are the mechanical amplitudes that are traced out for detuning sweeps performed in the direction of the corresponding coloured arrows (see Fig. 7.7). Thus, these contours denote the physical values of $\bar{x}$ that are realized in the experiment. Figure reproduced from Ref. [295]. © 2019 American Physical Society.

note that while the optomechanical interaction causing the device to enter into self-oscillations is nonlinear, the mechanical motion itself still remains within the linear regime, avoiding complications such as Duffing nonlinearities [391].

This peculiar behaviour can be understood by examining the combined photothermal and radiation-pressure attractor diagram of the system displayed in Fig. 7.8, which is generated by evaluating Eq. (7.23) at various mechanical amplitudes A and optical drive detunings $\Delta = \Delta_0 + G\bar{x}$ [301–305]. Note that with this definition of Δ, we include the shift in the cavity resonance due to the static, optomechanically induced displacement of the mechanical resonator as is seen in Fig. 7.9. In principle, this static shift[5] can act to displace the detuning dependence of the attractor diagram [301, 303], however, for the device considered here this

[5]Even at the largest optical power input to the device ($P_{in} = 139$ μW), we find the maximum static displacement of the resonator to be $\bar{x}_{max} = 46$ pm, causing a shift in the detuning that is at most $G\bar{x}_{max} = 38$ MHz $= 0.024\kappa$.

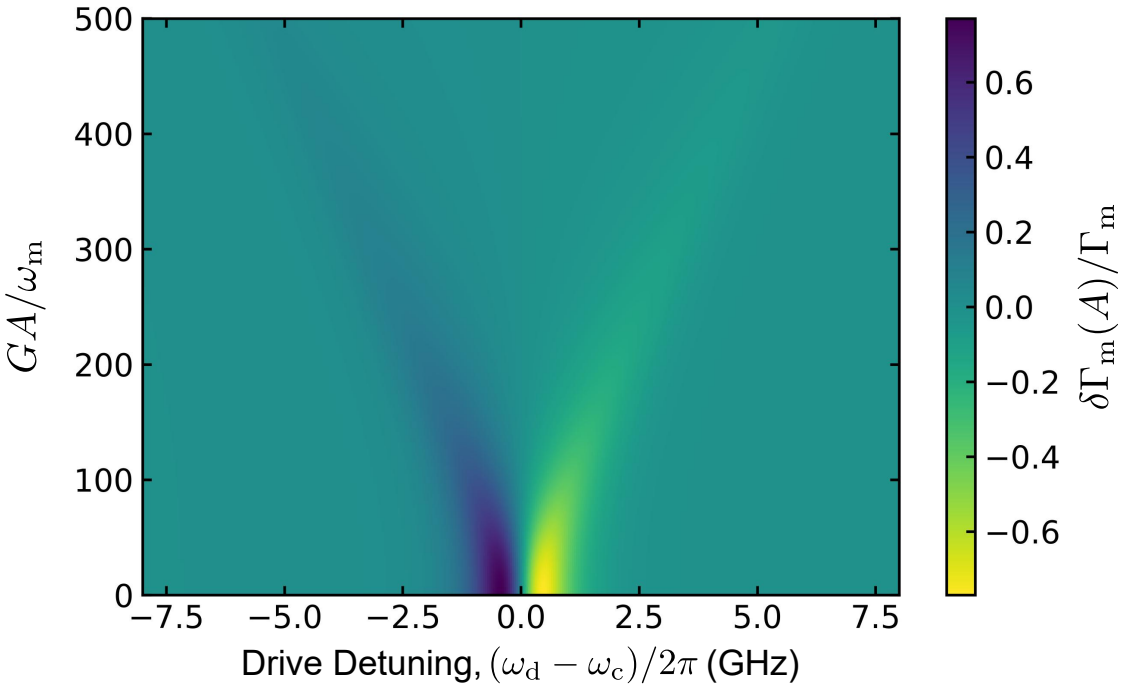

Figure 7.10: Attractor diagram of $\delta\Gamma_{\mathrm{m}}(A)/\Gamma_{\mathrm{m}}$ for the device parameters given in Fig. 7.7, except with $\beta = 0$ such that only radiation-pressure effects are present. We note that not only does the sign of the optomechanical damping reverse, restoring what one would expect for a radiation-pressure-driven system, but the damping force is no longer strong enough to induce mechanical self-oscillations at this power ($P_{\mathrm{in}} = 10.1$ μW), as demonstrated by the fact that $\delta\Gamma_{\mathrm{m}}(A)/\Gamma_{\mathrm{m}} > -1$ for all optical drive detunings. Figure reproduced from Ref. [295]. © 2019 American Physical Society.

shift is negligible, such that $\Delta \approx \Delta_0$.

The physical values for the mechanical amplitude are found to traverse the contours of the attractor diagram that obey the condition $\Gamma_{\mathrm{tot}} = 0 \Rightarrow \delta\Gamma_{\mathrm{m}} = -\Gamma_{\mathrm{m}}$ (see white dashed line in Fig. 7.8), corresponding to an increase in mechanical amplitude in order to dissipate the optical power input to the system [301, 302]. As can be seen in Fig. 7.8, for the non-SBR system considered here, there are two possible mechanical amplitude solutions for optical drive detunings ranging from $\Delta \approx -2.5$ to -4.0 GHz. This leads to dynamical bistability, and therefore, a hysteresis in the mechanical amplitude, as well as the optomechanical properties of the system [303]. We point out that these nonlinear effects, which are photothermal in origin, would not be present for this system if only the radiation-pressure force were considered (*i.e.* by setting $\beta = 0$ – see Fig. 7.10).

Fixing the mechanical resonance frequency and damping rate to their low power values of $\omega_m/2\pi = 11.2$ MHz and $\Gamma_m/2\pi = 374$ Hz, while using $\tau_{pt} = 9.5$ ns determined from the FEM simulations in Section 7.3.2, we fit the data in Fig. 7.7 to Eqs. (4.93), (7.22), and (7.23) by varying G, β, κ, and κ_e. We note that while driven to self-oscillation, the mechanical frequency locks to a position slightly larger than its off-resonant value (see Fig. 7.7c), which we attribute to a small thermal shift in the mechanical resonance due to optically induced heating of the resonator [382], leading to an additional, inconsequential fit parameter. To perform this fitting procedure, we first determine the mechanical amplitude of the resonator as a function of optical drive detuning according to an attractor diagram similar to that seen in Fig. 7.8 for each iteration of trial parameters. These amplitudes are then fed into Eqs. (4.93), (7.22), and (7.23), the results of which are compared to the data in Figs. 7.7a, c, and d, respectively. This process is repeated until the minimization condition of the fitting algorithm is met. Using this procedure, we extract the optomechanical coupling parameters $G/2\pi = 0.817$ GHz/nm ($g_0/2\pi = Gx_{zpf}/2\pi = 52.2$ kHz) and $\beta = -0.316$, as well as a total optical loss rate of $\kappa/2\pi = 2.04$ GHz and an external coupling rate of $\kappa_e/2\pi = 0.38$ GHz, for the studied device. This results in a single-photon cooperativity of $\mathcal{C} = 4g_0^2/\kappa\Gamma_m = 1.4 \times 10^{-2}$ and a maximal cavity-enhanced cooperativity of $\bar{C} = \bar{N}_{max}\mathcal{C} = 68$, where $\bar{N}_{max} = 4\kappa_e P_{in}/\hbar\omega_c\kappa^2 = 4.7 \times 10^3$ is the average number of photons circulating within the cavity for a resonant pump with an input power of $P_{in} = 10.1$ μW. Furthermore, using these extracted parameters, along with $\omega_m\tau_{pt} = 0.67$, we find $1 + \omega_m^2\tau_{pt}^2 = 1.45$ and $|\beta|\kappa\tau_{pt} = 38$. This ensures that Eq. (7.17) is satisfied, while Eq. (7.15) is not, confirming that we are indeed in the dueling regime associated with a radiation-pressure-dominated spring effect, but a photothermal-dominated optomechanical damping.

7.4.4 Power Dependence of Photothermal Properties

We continue to observe nonlinear effects in the optical transmission through the cavity for input powers up to ~140 μW, the data for which can be seen in Fig. 7.11. These measurements were performed under coupling conditions that differed slightly from those used to collect the data in Fig. 7.7, causing a shift in

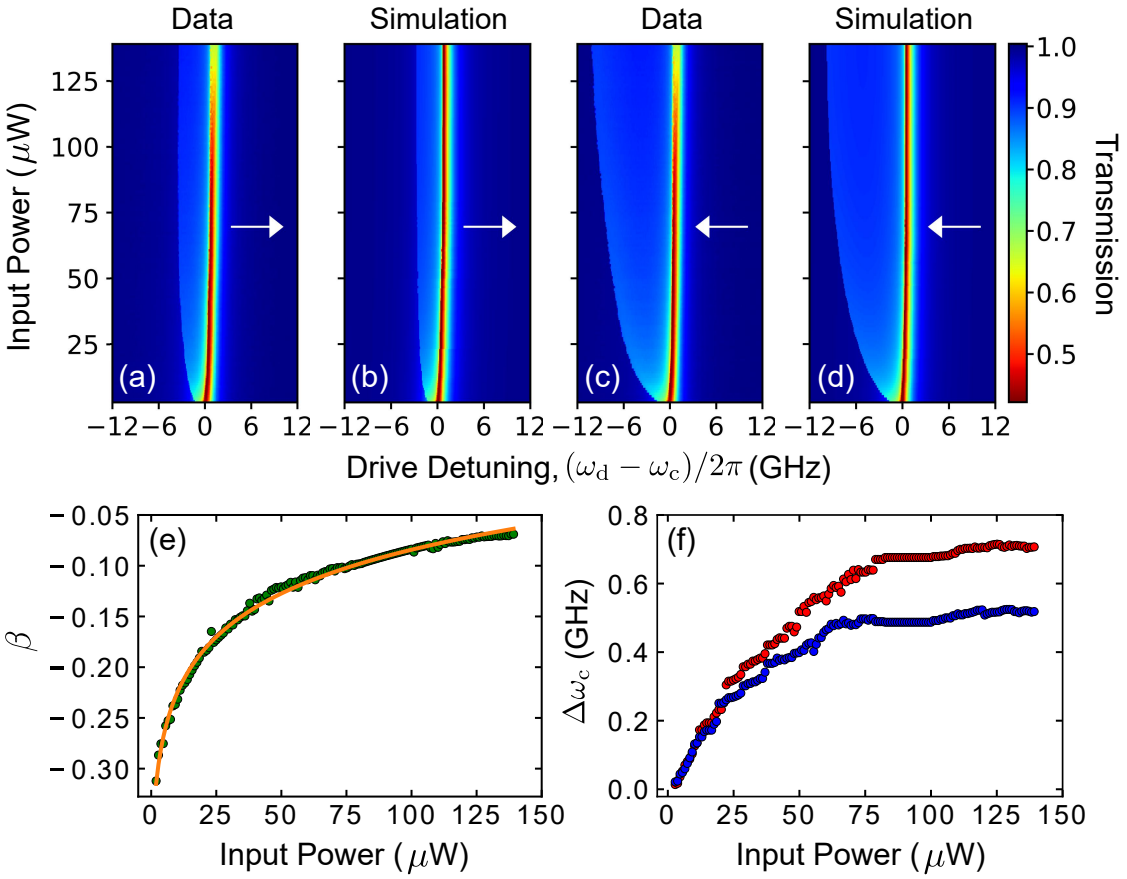

Figure 7.11: (a)–(d) Transmission through the optical cavity as a function of detuning and input power. Here we show (a)/(c) data and (b)/(d) simulation for red and blue detuning sweeps (sweep direction indicated by the white arrow), with each detuning scaled to the cavity's resonance frequency at the lowest measured power of $P_{\text{in}} = 1.9$ μW. Fixing $\kappa/2\pi = 1.59$ GHz and $\kappa_e/2\pi = 0.29$ GHz, we fit the data in (a)/(c) to Eq. (4.93), allowing us to determine β and ω_c versus input optical power to the cavity. In (e), we display these values for β (green circles), which are fit to Eq. (7.33) (orange line) resulting in $\beta_0 = -0.399$, $\beta_* = 0.063$, and $P_* = 0.68$ μW. The simulations in (b)/(d) are calculated by inputting the values of β from this fit, along with ω_c extracted from the fits to (a)/(c) and the aforementioned fixed values of κ and κ_e, into Eq. (4.93). Finally, (f) displays the optical cavity resonance frequency shift $\Delta\omega_c$ (relative to its value at the lowest optical power), with the red/blue data points corresponding to fits of the detuning sweeps originating from the red/blue side of the cavity found in (a)/(c), both of which indicate a blue shift in the cavity resonance with increasing optical power. Figure reproduced from Ref. [295]. © 2019 American Physical Society.

the loss rates of the optical cavity to $\kappa/2\pi = 1.59$ GHz and $\kappa_e/2\pi = 0.29$ GHz. Fixing these values for κ and κ_e, while assuming that the thermal relaxation time remains constant in power/temperature (which should be the case up to roughly

100 K – see Section 7.3.2), we fit the optical scans in Figs. 7.11a/c to Eq. (4.93), extracting β and ω_c versus input optical power to the cavity (see Figs. 7.11e/f). Upon inspection of Fig. 7.11e, we find that β exhibits a logarithmic dependence on input power, which can be fit with the phenomenological equation

$$\beta(P) = \beta_0 + \beta_* \ln\left(1 + \frac{P}{P_*}\right), \tag{7.33}$$

where $\beta_0 = -0.399$ is the value of β at zero input power, while $\beta_* = 0.063$ and $P_* = 0.68$ μW are scaling parameters. Rearranging Eq. (7.33), we can also determine the power at which $\beta = 0$ as $P_0 = P_*(e^{-\beta_0/\beta_*} - 1) = 384$ μW. Inputting β from this fit, along with the extracted values of ω_c versus power, into Eq. (4.93), we show that we are able to reproduce the power-dependent behaviour of the optical transmission data, as can be seen in Figs. 7.11b/d.

The observed power-dependence in β and ω_c is likely a result of the fact that increasing the power input to the optomechanical system causes it to heat up, changing its thermal and optical properties. Due to the complicated nature of optically induced heating, it is difficult to quantitatively ascertain the temperature of the device in this regime, however, we find the qualitative trend that β decreases in magnitude as we move to higher power/temperature. We postulate that it is this decrease in the magnitude of β with increasing temperature that has prevented previous studies of the dueling radiation-pressure and photothermal effects discussed in this chapter, as the majority of optomechanical experiments on nanophotonic silicon devices have been performed at room temperature. Furthermore, in Fig. 7.11f it can be seen that ω_c increases with power/temperature. This observation is consistent with the negative thermal expansion coefficient of silicon between approximately 18 K and 120 K [216–219], as an increase in temperature reduces the diameter of the microdisk cavity, resulting in a blue-shift of its optical resonant frequency [59, 392].

Finally, due to the bistable nature of the attractor diagram shown in Fig. 7.8, amplification of the mechanical resonator's motion results in hysteretic behaviour of the transmission through the cavity depending on whether the pump beam is swept from its red or blue side. As the optical power input to the cavity is increased, optomechanical amplification occurs over a larger range of drive detunings, causing

this hysteresis spacing to expand. In Fig. 7.12, we showcase this effect for the data in Figs. 7.11a/c, where we demonstrate that at high input powers ($P_{\text{in}} \gtrsim 25$ μW), the hysteresis spacing roughly obeys a square-root dependence.

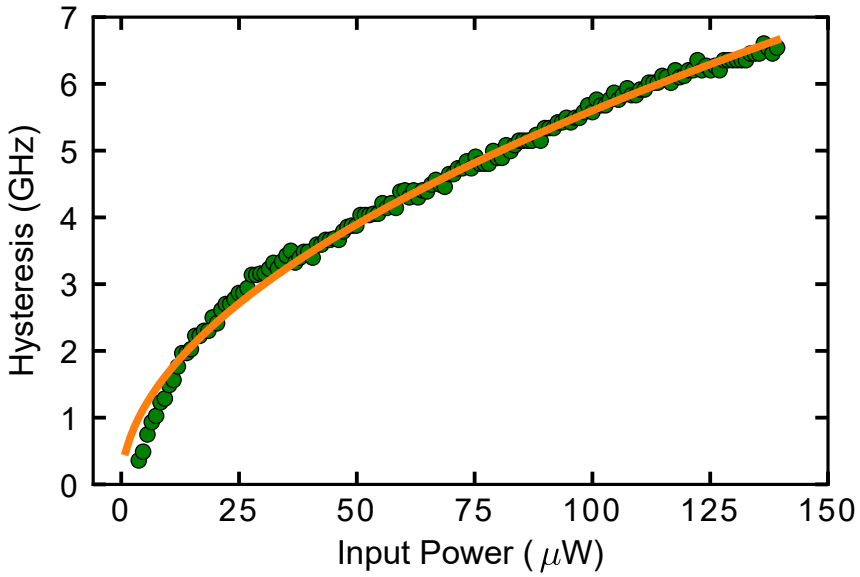

Figure 7.12: Hysteresis spacing of the transmission through the cavity versus optical input power (green circles) extracted from the data in Figs. 7.11a/c. The orange line is a fit to a power law, from which we find an exponent of 0.52, indicating a near square-root dependence of the hysteresis spacing on input optical power. Figure reproduced from Ref. [295]. © 2019 American Physical Society.

We conclude this section by noting that $\beta = -0.232$ at $P_{\text{in}} = 10.2$ μW for the data in Fig. 7.11, which is considerably smaller in magnitude than the value of $\beta = -0.316$ extracted from Fig. 7.7, where $P_{\text{in}} = 10.1$ μW. This discrepancy likely results from the disparity in the optical linewidths between the two measurements due to their differing coupling conditions, which leads to varying amounts of power absorbed by the resonator for identical input powers (see Eq. (4.49)), causing it to heat to a different temperature in each case. For instance, inputting the values of κ and κ_{e} from the two different coupling conditions used to obtain the data found in Figs. 7.7 and 7.11 (while assuming κ_{a} remains the same in each case), we find the power absorbed by the resonator (on cavity resonance) to be approximately 25% larger for the data in Fig. 7.11 compared to Fig. 7.7. It is this effect, coupled with the rapid increase in β at low optical input powers, that we attribute as the cause for the differing value of β between these two data sets for similar input powers.

7.5 Prospects for Photothermal Cooling

Up to this point we have largely focussed on the photothermally driven amplification of mechanical motion that occurs for a pump beam detuned to the red side of the optical resonance. However, photothermal backaction can also be used to perform considerable cooling of the mechanical mode on the opposite (blue) side of the resonance [22, 25, 378, 381–383]. For instance, in Fig. 7.7d we find that the photothermal force increases the total damping rate of the mechanical resonator to as high as $\Gamma_{\rm tot}/2\pi = 2.5$ kHz at $\Delta = 2\pi \times 0.97$ GHz ($= 0.48\ \kappa$), resulting in a factor of 6.7 increase from its intrinsic value of $\Gamma_{\rm m}/2\pi = 374$ Hz. Assuming that the resonator is initially thermalized to the helium bath temperature of $T_{\rm b} = 4.2$ K, this damping effect actively cools the mechanical mode to a temperature of $T_{\rm m} = T_{\rm b}(\Gamma_{\rm m}/\Gamma_{\rm tot}) = 631$ mK (see Eq. (4.44)), equivalent to a reduction in the phonon occupation of the mechanical resonator from $\langle n \rangle \approx 7800$ to $\langle n \rangle \approx 1170$ [150]. This cooling effect is especially intriguing considering that it occurs for a blue-detuned optical pump, such that the photothermal force must overwhelm any radiation-pressure-driven amplification effects.

More interesting, however, is the fundamental limit on minimum reachable phonon number using this cooling method, which is set by the shot noise generated by photons impinging upon the mechanical resonator. For a purely radiation-pressure-driven system, this limit is given by Eq. (4.43), which when minimized with respect to detuning in the non-SBR regime ($\kappa \gg \omega_{\rm m}$) results in $\bar{n}^{\rm rp}_{\rm min} \approx \kappa/4\omega_{\rm m}$ [150, 293]. For the device studied here we find that $\bar{n}^{\rm rp}_{\rm min} \approx 45$, such that it would be impossible to cool it to an average phonon occupation less than one using radiation pressure alone. However, the situation is far more complex when one adds photothermal effects into the picture, as this force interferes with the radiation pressure [290], resulting in the modified expression for the minimum achievable phonon number given by Eq. (7.28). Here we find it useful to define the optical loss rate due to absorption of photons in the mechanical element as a fraction ς of the cavity's total intrinsic loss rate $\kappa_{\rm i}$ according to $\kappa_{\rm a} = \varsigma\kappa_{\rm i}$. For the experimental measurements given in Fig. 7.7, we determine this total intrinsic loss rate to be $\kappa_{\rm i} = \kappa - \kappa_{\rm e} = 2\pi \times 1.66$ GHz. It is difficult to experimentally

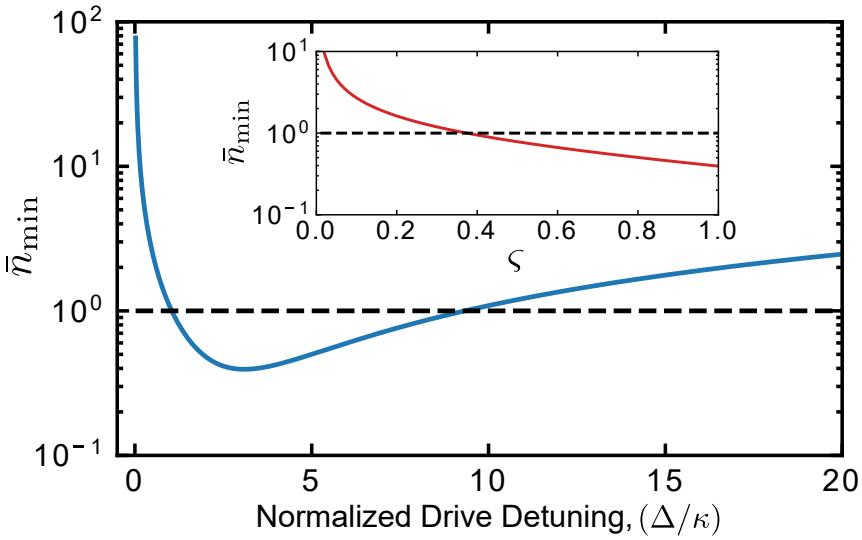

Figure 7.13: Plot of the minimum reachable phonon number according to Eq. (7.28) versus normalized drive detuning using the parameters extracted from the fits in Fig. 7.7, while setting $\kappa_{\mathrm{a}} = \kappa_{\mathrm{i}} = 2\pi \times 1.66$ GHz. The black dashed line corresponds to $\bar{n}_{\mathrm{min}} = 1$, indicating that the resonator can in principle be cooled below single phonon occupancy over a detuning band from $\Delta \sim \kappa$ to 9κ, reaching its minimum value of $\bar{n}_{\mathrm{min}} = 0.39$ at $\Delta_{\mathrm{min}} = 3.1\ \kappa$. Inset is a plot of $\bar{n}_{\mathrm{min}}$ as a function of the ratio $\varsigma = \kappa_{\mathrm{a}}/\kappa_{\mathrm{i}}$, indicating that ground state cooling is still possible for $\varsigma \gtrsim 0.4$. Figure adapted from Ref. [295]. © 2019 American Physical Society.

determine what fraction of this intrinsic loss rate contributes to κ_{a}. However, we initially assume that optical losses are dominated by absorption in the mechanical element (*i.e.* set $\varsigma = 1$), allowing us to set a lower limit on the minimum achievable phonon occupation for the device studied here. Using this condition, along with the extracted experimental values from Fig. 7.7, we plot $\bar{n}_{\mathrm{min}}$ as a function of detuning in Fig. 7.13. As one can see, the minimum achievable phonon number drops below one over a detuning range from $\Delta \sim \kappa$ to 9κ, reaching its optimal value of $\bar{n}_{\mathrm{min}} = 0.39$ at $\Delta_{\mathrm{min}} = 3.1\ \kappa$, which corresponds to a mechanical resonator that is in its ground state 71% of the time. We note that ground state cooling remains possible when relaxing the condition that $\kappa_{\mathrm{a}} = \kappa_{\mathrm{i}}$, with $\bar{n}_{\mathrm{min}} < 1$ for $\varsigma \gtrsim 0.4$ (see inset of Fig. 7.13). While it has long been known theoretically that the photothermal force can be used to cool a non-SBR optomechanical resonator into its motional ground state [289–291, 294, 376], this is the first time that a device has been experimentally demonstrated to exist within the required regime.

To further investigate the parameter space over which ground state photothermal

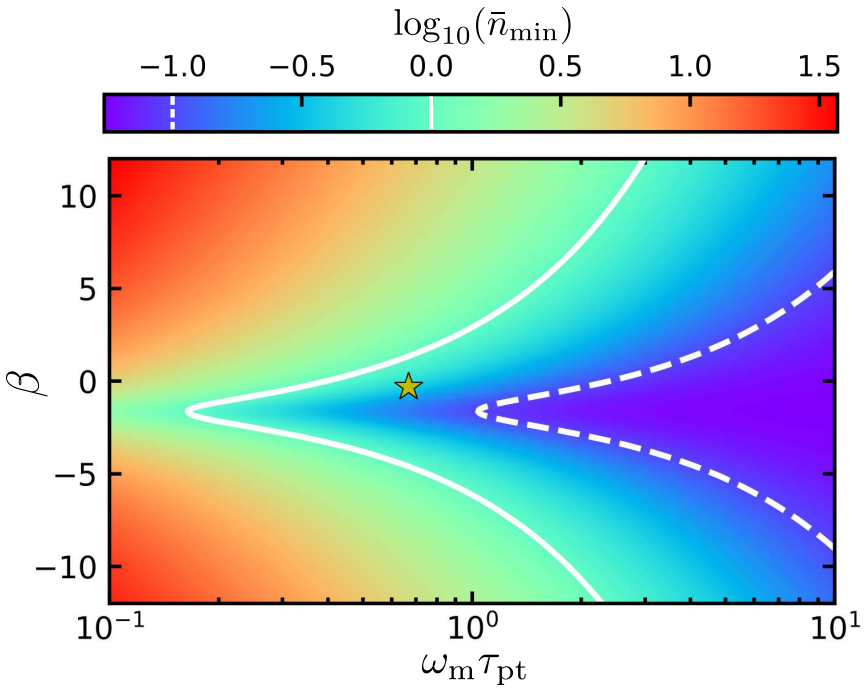

Figure 7.14: A colour plot depicting the base-ten logarithm of $\bar{n}_{\min}$, minimized with respect to detuning, as a function of β and τ_{pt}, with the rest of the parameters the same as in Fig. 7.13. Therefore, while we have expressed the x-axis in terms of the unitless quantity $\omega_{\mathrm{m}}\tau_{\mathrm{pt}}$, the mechanical resonance frequency is fixed to $\omega_{\mathrm{m}} = 2\pi \times 11.2$ MHz such that only τ_{pt} is varied along this axis. Here we have ensured finite (*i.e.* nonzero) β to allow us to focus on photothermal effects, as opposed to the narrow feature that emerges due to the radiation-pressure force for very small β ($\lesssim 0.001$). The solid (dashed) white lines demarcate the contour of $\bar{n}_{\min} = 1$ ($\bar{n}_{\min} = 0.1$), while the yellow star indicates the parameters for the device studied in this chapter. As one can see, there is a region where $\bar{n}_{\min} < 1$ centered near $\beta = 0$, with deviations from a symmetric distribution in β being due to interference between the radiation-pressure and photothermal forces [290]. We further note that while $\bar{n}_{\min}$ decreases for larger values of τ_{pt}, the detuning for which $\bar{n}_{\min}$ is minimized increases with τ_{pt} (see Fig. 7.15), moving away from $\Delta \approx \kappa/2$ where the photothermal force is maximal [289], such that it becomes increasingly difficult to reach $\bar{n}_{\min}$ experimentally. Figure adapted from Ref. [295]. © 2019 American Physical Society.

cooling can occur, we have plotted the logarithm of the minimum achievable phonon number versus β and τ_{pt} in Fig. 7.14. Each point on this plot is obtained by varying β and τ_{pt} in Eq. (7.28) (while again setting all other physical parameters equal to those extracted from the fits to Fig. 7.7) and taking the minimum value of $\bar{n}_{\min}$ with respect to detuning. The result is a large region of photothermal parameter space that allows for cooling below the single phonon level, with a slight asymmetry

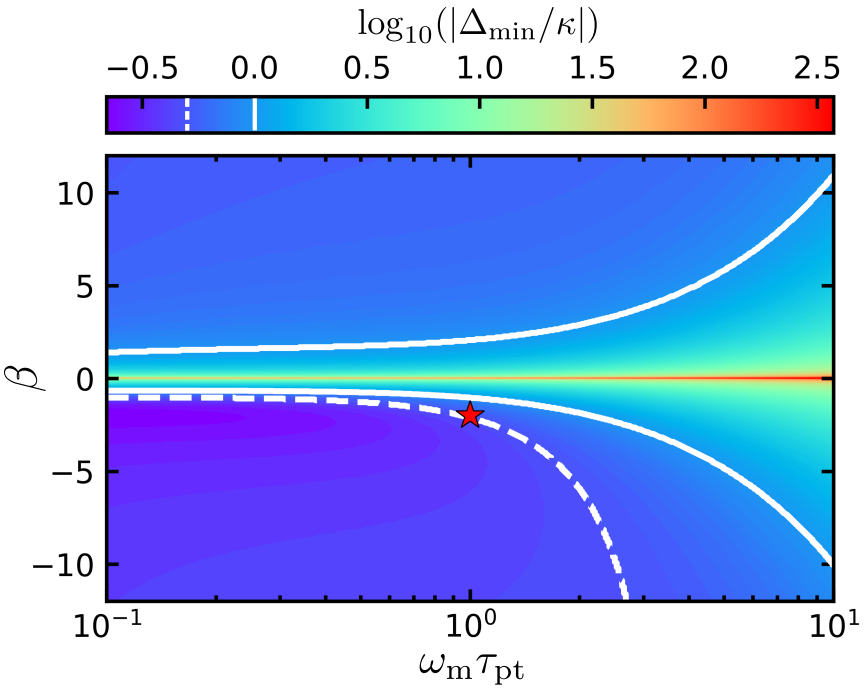

Figure 7.15: Colour plot of $\log_{10}(|\Delta_{\rm min}/\kappa|)$, *i.e.* the base-ten logarithm of the absolute value of the detuning $\Delta_{\rm min}$ for which $\bar{n}_{\rm min}$ is globally minimized (normalized by κ). Here we have used the same optomechanical parameters as those in Fig. 7.14, with the solid (dashed) white line indicating the contour of $|\Delta_{\rm min}| = \kappa$ ($|\Delta_{\rm min}| = \kappa/2$). Note that the sign of $\Delta_{\rm min}$ is opposite of β, such that $\Delta_{\rm min} < 0$ ($\Delta_{\rm min} > 0$) for $\beta > 0$ ($\beta < 0$). As one can see, $|\Delta_{\rm min}|$ is maximized near $\beta = 0$ and increases for larger values of $\tau_{\rm pt}$. We point out, however, that for small β and large $\tau_{\rm pt}$, local minima emerge near $\Delta \approx -\kappa/2$ [not shown here as this figure depicts the global minimum of $\bar{n}_{\rm min}$], corresponding to the region over which radiation-pressure effects begin to dominate. Furthermore, as is seen with $\bar{n}_{\rm min}$ in Fig. 7.14, $|\Delta_{\rm min}|$ is asymmetric with respect to β, which is again due to interference between radiation-pressure and photothermal effects. Finally, we note that the dashed contour of $\Delta_{\rm min} = \kappa/2$ passes very near $\beta = -2.0$ for $\omega_{\rm m}\tau_{\rm pt} = 1$ (see red star), such that these parameters optimize photothermal cooling versus both optical drive detuning and thermal relaxation time (see Fig. 7.16). Figure adapted from Ref. [295]. © 2019 American Physical Society.

between positive and negative β due to interference between the radiation-pressure and photothermal forces [290]. As indicated by the yellow star in Fig. 7.14, the parameters for the device considered in this work lie well within this regime.

One must be careful, however, when interpreting these results, as $\bar{n}_{\rm min}$ describes the fundamental limit on the minimum reachable phonon number using this cooling mechanism. Furthermore, as $\tau_{\rm pt}$ increases, so does the detuning at which $\bar{n}_{\rm min}$

is minimized, reducing the effectiveness of the photothermal cooling. This effect can be seen in Fig. 7.15 for the same parameter space that is mapped out in Fig. 7.14. Here $|\Delta_{\mathrm{min}}|$ grows for decreasing β and increasing τ_{pt}, moving away from the optimal value of $|\Delta_{\mathrm{min}}| \approx \kappa/2$ denoted by the white dashed line, while exhibiting a similar asymmetry about β as was seen for $\bar{n}_{\mathrm{min}}$. Therefore, one generally wishes to maximize the strength of the photothermal damping force, which occurs for $\omega_{\mathrm{m}}\tau_{\mathrm{pt}} \approx 1$ [22, 289, 294, 378] and $\Delta \approx \kappa/2$ (see Fig. 7.7d), in order to decrease the optical power required to reach $\bar{n}_{\mathrm{min}}$. Of particular interest are the photothermal cooling parameters of $\beta = -2.0$ and $\omega_{\mathrm{m}}\tau_{\mathrm{pt}} = 1$ (corresponding to $\tau_{\mathrm{pt}} = 1/\omega_{\mathrm{m}} = 14.2$ ns for the device considered here), which when combined with the other device parameters used in this chapter, results in $\bar{n}_{\mathrm{min}} = 0.11$ at $\Delta_{\mathrm{min}} \approx \kappa/2$ as seen in Fig. 7.16. These conditions therefore maximize photothermal cooling with respect to both thermal relaxation time and optical drive detuning [289], while still allowing for ground state cooling of the mechanical resonator, thus presenting a set of parameters to strive for in future iterations of the device.

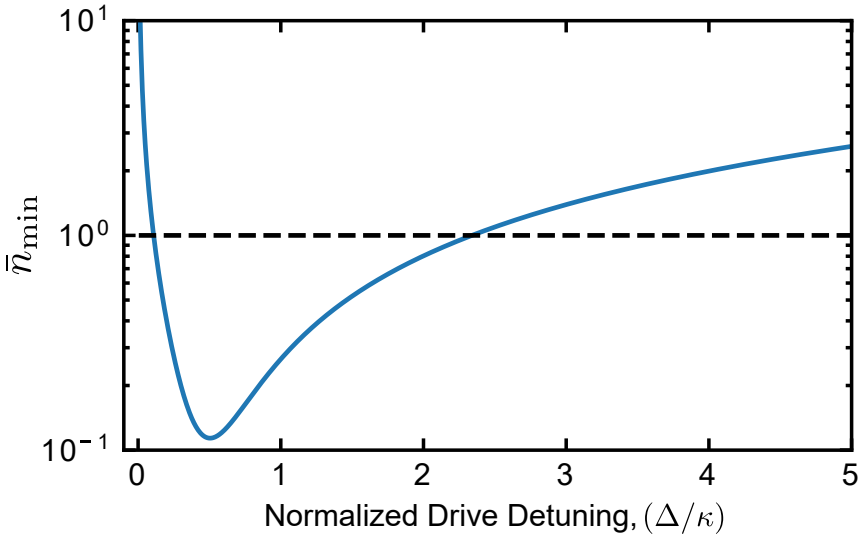

Figure 7.16: Plot of $\bar{n}_{\mathrm{min}}$ versus normalized drive detuning for the photothermal parameters indicated by the red star in Fig. 7.15 ($\beta = -2.0$ and $\omega_{\mathrm{m}}\tau_{\mathrm{pt}} = 1$). Here we see that the lowest achievable phonon number is indeed minimized to $\bar{n}_{\mathrm{min}} = 0.11$ at $\Delta_{\mathrm{min}} \approx \kappa/2$. Figure adapted from Ref. [295].

7.6 Conclusion

In this chapter, we have presented measurements of a silicon WGM optomechanical cavity that exhibits dynamical backaction effects due to competing photothermal and radiation-pressure forces. We find that the radiation-pressure force governs the optomechanical spring effect, while the photothermal force dictates the optomechanical damping. Furthermore, due to the fact that this photothermal force acts to directly oppose its radiation-pressure counterpart, we find that at high enough power we can reduce the mechanical damping to zero on the red side of the cavity resonance, inducing a parametric instability in the mechanical resonator that drives its motion into large-amplitude self-oscillation. At the onset of this self-oscillating behaviour, we observe highly nonlinear effects, as well as a hysteresis depending on the sweep direction of the optical drive, in each of the optomechanical damping, spring effect, and transmission through the optical cavity. Fitting these data with a nonlinear optomechanical model that includes both radiation-pressure and photothermal forces, we extract the optomechanical properties of the system associated with each of these effects. Finally, using these extracted parameters, we infer that this non-SBR optomechanical system can in principle be cooled to an average phonon occupancy less than one. This comprehension of exactly how the radiation-pressure and photothermal forces interact with each other at low temperatures will be crucial as silicon optomechanical cavities continue to be used to perform quantum experiments [135–139, 141–143].

Chapter 8

Phonon Quantum Nondemolition Measurements in Nonlinearly Coupled Optomechanical Cavities

In this chapter, we examine the feasibility of using a quadratically coupled WGM optomechanical cavity to perform quantum nondemolition (QND) measurements of a mechanical resonator's Fock states. This work is based on the publication B. D. Hauer, A. Metelmann, and J. P. Davis, "Phonon quantum nondemolition measurements in nonlinearly coupled optomechanical cavities," *Phys. Rev. A* **98**, 043804 (2018) (Ref. [393]) and draws heavily on the content therein. In order to be consistent with the rest of the thesis, here we have made a number of minor notational changes, along with the following changes in sign convention with respect to the original publication: $G_1 \rightarrow -G_1$ ($g_1 \rightarrow -g_1$), $G_2 \rightarrow -G_2$ ($g_2 \rightarrow -g_2$), $\Delta \rightarrow -\Delta$, and $\chi_c(\omega, \Delta) \rightarrow \chi_c(-\omega, -\Delta)$.

8.1 Introduction

The theory of quantum mechanics has excelled in describing a multitude of phenomena associated with microscopic systems. However, as a system scales to larger sizes, interaction with the surrounding environment causes its quantum mechanical state to decohere into the classical realm [394, 395]. Although there are a number of theories proposing mechanisms by which such decoherence could occur [396–399], this quantum-to-classical transition remains poorly understood, largely due to a lack of experimental systems that can be used to study these processes. To

this end, a number of proposals have been put forward to use cavity optomechanics as an experimental platform to fill this void [128–131].

While experimental progress in quantum cavity optomechanics has been astounding (see Chapter 1 for a brief overview), a crucial experiment still remains: the QND measurement of a mechanical resonator's phonon number [35, 400]. While QND measurements have been demonstrated for single particles [401, 402], photons [403, 404], spins [405], and superconducting qubits [406], as well as for a single quadrature of a micromechanical resonator [114, 115], measurements of the mechanical Fock states of a cavity optomechanical system would provide an engineerable platform to directly probe the decoherence of a mesoscopic quantum state. In this chapter, we theoretically investigate the possibility of performing such a QND measurement using a quadratically coupled WGM optomechanical cavity.

The chapter begins with Section 8.2 where we provide a brief overview of QND measurements, showing that in quadratically coupled optomechanical systems it is possible to monitor the quantized Fock states of a mechanical resonator. In Section 8.3, we then introduce two possible physical realizations of optomechanical quadratic coupling: the traditional membrane-in-the-middle (MIM) system and a WGM geometry similar to that studied in Chapters 6 and 7. Modelling the second-order coupling in each of these optomechanical cavities, we find significant differences in their physical implementations, the most important of which is that the WGM geometry is not subject to the strict single-photon strong-coupling regime imposed for QND measurements using a MIM system. In Section 8.4, we then use a master equation approach to determine the rates at which optomechanically and thermally induced transitions act to contaminate a QND measurement performed using this WGM system. Finally, in Section 8.5 we compare these transition rates to the phonon number measurement rate, allowing us to determine the parameter space for which a QND measurement of thermal jumps in phonon number can be made.

8.2 Optomechanical Quantum Nondemolition Measurements

Quantum nondemolition measurements are a special class of measurements that are specifically designed to probe a quantum mechanical system while leaving the considered quantum state unperturbed. To perform a QND measurement of an observable associated with the operator $\hat{O}$, we require that the Hamiltonian $\hat{H}$ describing the measurement commutes with this operator [202, 407]. Mathematically, this corresponds to

$$[\hat{H}, \hat{O}] = 0. \tag{8.1}$$

Therefore, in order to perform an optomechanical QND measurement of a mechanical resonator's quantized energy, we require a measurement with a Hamiltonian $\hat{H}$ that commutes with the phonon number operator $\hat{n} = \hat{b}^\dagger \hat{b}$, that is

$$[\hat{H}, \hat{n}] = [\hat{H}, \hat{b}^\dagger \hat{b}] = 0. \tag{8.2}$$

Unfortunately, experimentally realizing an optomechanical Hamiltonian of this nature proves to be difficult, largely due to the fact that the majority of optomechanical cavities couple linearly to the mechanical resonator's position [150]. For instance, the Hamiltonian given in Eq. (4.10) corresponds to a standard linear optomechanical system and does not commute with $\hat{b}^\dagger \hat{b}$. Therefore, such a scheme is unsuitable for QND measurements of the resonator's quantized energy, as it is subject to the Heisenberg uncertainty principle [202, 203, 407, 408], which results in a limit on how precisely one can continuously measure the resonator's quantum state (*i.e.* the standard quantum limit discussed in Section 4.4.4).

One must then turn to an optomechanical system where the optical mode is nonlinearly coupled to the resonator's position, providing a method by which QND measurements of its phonon number can be performed [35, 400]. We can arrive at a Hamiltonian that describes such a nonlinear measurement of $\hat{x}$ by expanding the optical cavity frequency to second order in mechanical position (similar to how we introduced first-order dispersive optomechanical coupling in Eq. (4.2)), resulting in

$$\omega_c(\hat{x}) = \omega_c - G_1 \hat{x} - \frac{G_2}{2} \hat{x}^2, \tag{8.3}$$

where again ω_c is the unperturbed cavity frequency, and we have introduced the first- and second-order optomechanical coupling coefficients $G_1 = -d\omega_c/d\hat{x}$ and $G_2 = -d^2\omega_c/d\hat{x}^2$. Note that we have added subscripts to these coupling coefficients with respect to the definition of G in Chapter 2 to allow ourselves to differentiate between their order. Inputting this expanded cavity frequency, as well as the expression for $\hat{x}$ given by Eq. (2.17), into Eq. (4.4), we determine a new, second-order optomechanical interaction Hamiltonian

$$\hat{H} = \hat{H}_0 + \hat{H}', \tag{8.4}$$

$$\hat{H}_0 = \hbar\left[\omega_c - g_2\left(\hat{b}^\dagger\hat{b} + \frac{1}{2}\right)\right]\hat{a}^\dagger\hat{a} + \hbar\omega_m\hat{b}^\dagger\hat{b}, \tag{8.5}$$

$$\hat{H}' = -\hbar g_1\left(\hat{b} + \hat{b}^\dagger\right)\hat{a}^\dagger\hat{a} - \frac{\hbar g_2}{2}\left(\hat{b}\hat{b} + \hat{b}^\dagger\hat{b}^\dagger\right)\hat{a}^\dagger\hat{a}, \tag{8.6}$$

where $g_1 = G_1 x_{zpf}$ ($g_2 = G_2 x_{zpf}^2$) is the single photon, single (two) phonon coupling rate.

In Eq. (8.4), we have chosen to separate $\hat{H}$ into two sub-Hamiltonians, $\hat{H}_0$ and $\hat{H}'$, such that $\hat{H}_0$ commutes with the phonon number operator $\hat{n} = \hat{b}^\dagger\hat{b}$, while $\hat{H}'$ does not. In this way, $\hat{H}_0$ represents a QND measurement of the mechanical resonator's quantized energy [202, 407], collapsing the system into a phononic number state at a rate given by [400]

$$\Gamma_{meas} = \bar{C}_2\Gamma_m, \tag{8.7}$$

where we have introduced the second-order, cavity-enhanced cooperativity of the system $\bar{C}_2 = \bar{N}C_2$, given in terms of the second-order, single-photon cooperativity $C_2 = 4g_2^2/\kappa\Gamma_m$ [150]. The phonon number of the system can then be read out as a per phonon shift of g_2 in the optical cavity's resonant frequency.

On the other hand, $[\hat{H}', \hat{n}] \neq 0$ such that $\hat{H}'$, which contains the interaction terms that evolve rapidly in time[1], acts to contaminate the QND measurement. This is a well-known fact for the first term in $\hat{H}'$, whereby linear coupling simultaneously probes the phase and energy of the mechanical resonator, preventing a QND Fock state measurement [36, 408]. In principle, one could completely eliminate this linear coupling by properly tuning the optical and mechanical symmetries of the system

[1] To first order (*i.e.* for a freely evolving mechanical system) $\hat{b}(t) = \hat{b}e^{-i\omega_m t}$.

(see Appendix C). However, for any realistic quadratically coupled optomechanical cavity, a non-zero amount of linear coupling will always creep into the system due to experimental inaccuracies [35, 63, 409]. We therefore seek to set a limit on the maximum allowable linear coupling that can exist in a quadratically coupled optomechanical device that one wishes to use for a QND measurement of phonon number, as well as determine the regime for which the second term in $\hat{H}'$ can be safely ignored.

8.3 Quadratically Coupled Optomechanical Systems

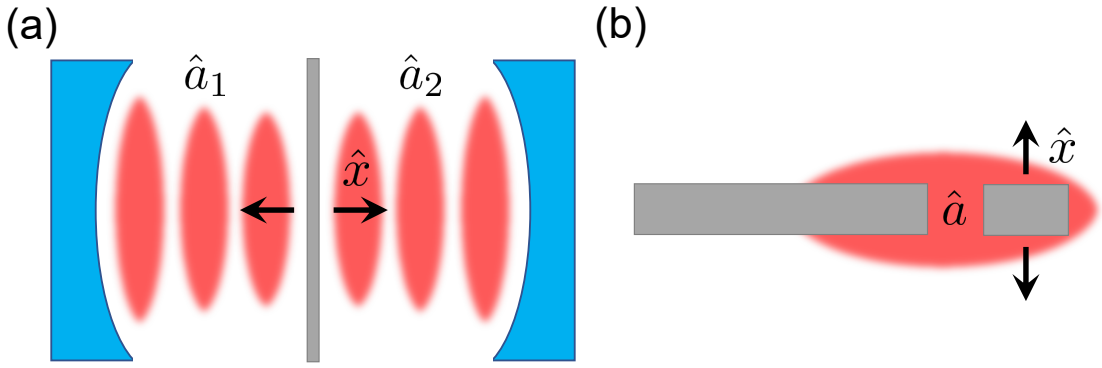

Figure 8.1: Schematic of (a) a membrane-in-the-middle optomechanical system and (b) a mechanical element side-coupled to a whispering gallery mode optical cavity. In (a), quadratic coupling arises due to an avoided crossing between the two optical modes (see Section 8.3.2), labelled by their creation operators $\hat{a}_1$ and $\hat{a}_2$. Meanwhile, in (b), the single optical mode denoted by $\hat{a}$ is coupled to the square of the mechanical motion via shared symmetries between the optics and mechanics (see Appendix C). The direction of the mechanical displacement $\hat{x}$ is indicated by black arrows. Figure reproduced from Ref. [393]. © 2018 American Physical Society.

Before continuing with our analysis, we first briefly compare and contrast two different physical realizations of quadratic optomechanical coupling. The first realization is that of a MIM system (see Fig. 8.1a), whereby a mechanical element – which is typically a thin dielectric membrane [35, 36, 410], but can also be a cloud of cold atoms [48] or a photonic crystal nanobeam [411, 412] – is placed within an optical cavity. Inserting the "membrane" into the cavity causes its degenerate

optical modes to hybridize into two new supermodes that exhibit an avoided level crossing [36, 411]. By moving the membrane to an antinode of the optical mode, linear coupling to the membrane's motion is suppressed and quadratic coupling becomes dominant [35, 36, 411]. However, when optically driving one of these supermodes, parasitic linear coupling to the membrane's position emerges in the opposite mode, leading to an accelerated decoherence of the membrane's Fock state that can only be overcome in the single-photon strong-coupling regime [413–415]. This stringent constraint has proven to be the most difficult obstacle to overcome when performing QND measurements of phonon number in a MIM optomechanical system [411].

The second optomechanical system that we consider in this section is one exhibits second-order coupling due to the shared symmetries between a mechanical resonance and a single optical mode [409]. Such a system could be physically realized as an out-of-plane flexural (or torsional) mode of a mechanical resonator side-coupled to the WGM of a microdisk [63] (see Fig. 8.1b) or the in-plane motion of a paddle located within a photonic crystal nanobeam [409]. As we shall see below, this type of quadratically coupled optomechanical system can be described using a single optical mode, and is therefore not subject to the strict constraints imposed upon MIM optomechanical cavities in the context of performing QND measurements.

8.3.1 Two-Mode Optomechanical Hamiltonian

In order to describe a MIM system, we require an optomechanical model that considers a mechanical resonator simultaneously coupled to two optical modes: one to the left of the membrane and one to its right. It is these two optical modes that hybridize and generate quadratic coupling in such an optomechanical system. We can also use this two-mode model to describe the clockwise and counterclockwise propagating modes in a WGM optomechanical system, however as we shall see below, this treatment is not necessary to generate quadratic coupling in this system.

In this two-mode optomechanical model, each optical resonance is characterized by the annihilation (creation) operators $\hat{a}_1$ ($\hat{a}_1^\dagger$) and $\hat{a}_2$ ($\hat{a}_2^\dagger$), as well as the position-dependent resonant angular frequencies $\omega_1(\hat{x})$ and $\omega_2(\hat{x})$. We also allow these two

optical modes to be coupled to each other at a rate ν. The Hamiltonian for such a two-mode optomechanical system (ignoring the ground state energies, drive terms, and interaction with the environment) will then be given by

$$\hat{H}_{\mathrm{TM}} = \hbar\omega_1(\hat{x})\hat{a}_1^\dagger\hat{a}_1 + \hbar\omega_2(\hat{x})\hat{a}_2^\dagger\hat{a}_2 + \hbar\omega_{\mathrm{m}}\hat{b}^\dagger\hat{b} + \hbar\nu\left(\hat{a}_1^\dagger\hat{a}_2 + \hat{a}_2^\dagger\hat{a}_1\right), \tag{8.8}$$

where the first three terms describe the self energies of the two optical modes and the single mechanical mode, while the last term characterizes the interaction between the two optical modes, with a photon being annihilated in one while simultaneously created in the other. This interaction between the two optical modes physically manifests itself as photons tunneling between the optical modes to the left and right of the membrane in a MIM system [36, 411, 414], or a backscattering of photons between the clockwise and counterclockwise propagating modes of a WGM cavity [416]. As was done in Eq. (8.3), we expand each ith optical frequency to second order in mechanical position as

$$\omega_i(\hat{x}) = \omega_i - G_1^{(a_i)}\hat{x} - \frac{G_2^{(a_i)}}{2}\hat{x}^2. \tag{8.9}$$

Here we again have the unperturbed optical frequency ω_i, as well as the first- and second-order optomechanical coupling coefficients, $G_1^{(a_i)} = -d\omega_i/d\hat{x}$ and $G_2^{(a_i)} = -d^2\omega_i/d\hat{x}^2$, with the superscript (a_i) allowing for one to identify the coupling coefficient associated with each optical mode. Inputting these expressions into Eq. (8.8), we obtain the interaction Hamiltonian for the system

$$\begin{aligned}\hat{H}_{\mathrm{TM}} = {} & \hbar\omega_1\hat{a}_1^\dagger\hat{a}_1 + \hbar\omega_2\hat{a}_2^\dagger\hat{a}_2 + \hbar\omega_{\mathrm{m}}\hat{b}^\dagger\hat{b} + \hbar\nu\left(\hat{a}_1^\dagger\hat{a}_2 + \hat{a}_2^\dagger\hat{a}_1\right) \\ & - \hbar\left(G_1^{(a_1)}\hat{a}_1^\dagger\hat{a}_1 + G_1^{(a_2)}\hat{a}_2^\dagger\hat{a}_2\right)\hat{x} - \frac{\hbar}{2}\left(G_2^{(a_1)}\hat{a}_1^\dagger\hat{a}_1 + G_2^{(a_2)}\hat{a}_2^\dagger\hat{a}_2\right)\hat{x}^2.\end{aligned} \tag{8.10}$$

Choosing the optical modes to be degenerate (in the absence of coupling between them) such that $\omega_1 = \omega_2 = \omega_0$, we introduce the new basis with annihilation operators $\hat{a}_\pm = \left(\hat{a}_1 \pm \hat{a}_2\right)/\sqrt{2}$, which describe the two hybridized supermodes that

emerge. The new Hamiltonian in this supermode basis can then be written as

$$\begin{aligned}\hat{H}_{\mathrm{TM}} &= \hbar\omega_+\hat{a}_+^\dagger\hat{a}_+ + \hbar\omega_-\hat{a}_-^\dagger\hat{a}_- + \hbar\omega_{\mathrm{m}}\hat{b}^\dagger\hat{b} \\ &- \hbar\left(\frac{G_1^{(a_1)}+G_1^{(a_2)}}{2}\right)\left(\hat{a}_+^\dagger\hat{a}_+ + \hat{a}_-^\dagger\hat{a}_-\right)\hat{x} \\ &- \hbar\left(\frac{G_1^{(a_1)}-G_1^{(a_2)}}{2}\right)\left(\hat{a}_+^\dagger\hat{a}_- + \hat{a}_-^\dagger\hat{a}_+\right)\hat{x} \\ &- \hbar\left(\frac{G_2^{(a_1)}+G_2^{(a_2)}}{4}\right)\left(\hat{a}_+^\dagger\hat{a}_+ + \hat{a}_-^\dagger\hat{a}_-\right)\hat{x}^2 \\ &- \hbar\left(\frac{G_2^{(a_1)}-G_2^{(a_2)}}{4}\right)\left(\hat{a}_+^\dagger\hat{a}_- + \hat{a}_-^\dagger\hat{a}_+\right)\hat{x}^2,\end{aligned} \tag{8.11}$$

where we now have the new supermode frequencies $\omega_\pm = \omega_0 \pm \nu$. The splitting between these two new supermodes is $\omega_+ - \omega_- = 2\nu$, such that each can be individually accessed if $\kappa_\pm < 2\nu$, with $\kappa_\pm$ being the linewidth of the mode corresponding to $\hat{a}_\pm$. Up to this point, we have not made any assumptions about the nature of the couplings in this system. In what follows, we will investigate how the Hamiltonian given by Eq. (8.11) can be used to effectively describe an optomechanical MIM system, as well as a mechanical element quadratically coupled to an optical mode via shared symmetries in a WGM optomechanical cavity.

8.3.2 Membrane-in-the-Middle System

As mentioned above, in a conventional MIM optomechanical system, quadratic coupling arises due to the avoided crossing between the two hybridized optical supermodes mentioned above. Therefore, it is unnecessary to expand our optical frequencies to second order and we take $G_2^{(a_i)} = 0$ here. Furthermore, due to the geometry of MIM systems, as the mechanical element is displaced the frequency of one optical mode will increase, while the other mode's frequency will correspondingly decrease, leading to $G_1^{(a_1)} = -G_1^{(a_2)} = G_1$ [36, 411]. As we shall see, this difference in sign between the linear coupling of the two optical modes is crucial for generating quadratic coupling in these systems, as well as enforcing the single-photon strong-coupling condition associated with using them for QND measurements of mechanical Fock states [413–415]. Applying these conditions to the general two-mode optomechanical Hamiltonian in Eq. (8.11), we obtain the

Hamiltonian for a MIM system as [411–415]

$$\hat{H}_{\mathrm{MIM}} = \hbar\omega_+ \hat{a}_+^\dagger \hat{a}_+ + \hbar\omega_- \hat{a}_-^\dagger \hat{a}_- + \hbar\omega_{\mathrm{m}} \hat{b}^\dagger \hat{b} - \hbar G_1 \left(\hat{a}_+^\dagger \hat{a}_- + \hat{a}_-^\dagger \hat{a}_+ \right) \hat{x}. \tag{8.12}$$

Upon inspection of $\hat{H}_{\mathrm{MIM}}$, it is not obvious that quadratic coupling exists. However, by diagonalizing this Hamiltonian we find

$$\hat{H}_{\mathrm{MIM}} = \hbar\omega'_+ \hat{a}'^\dagger_+ \hat{a}'_+ + \hbar\omega'_- \hat{a}'^\dagger_- \hat{a}'_- + \hbar\omega_{\mathrm{m}} \hat{b}^\dagger \hat{b}, \tag{8.13}$$

with corresponding eigenfrequencies

$$\omega'_\pm = \omega_0 \pm \sqrt{\nu^2 + G_1^2 \hat{x}^2}. \tag{8.14}$$

In the limit where $\nu \gg \omega_{\mathrm{m}}$, $\hat{x}$ can be treated as a quasistatic variable [411, 413–415], allowing us to take $G_1 \hat{x} \ll \nu$. In this regime, the lowering operators of the diagonalized modes can be approximated as [414]

$$\hat{a}'_+ \approx a_+ - \frac{G_1 \hat{x}}{2\nu} \hat{a}_-, \tag{8.15}$$

$$\hat{a}'_- \approx -\frac{G_1 \hat{x}}{2\nu} a_+ - a_-, \tag{8.16}$$

with the approximate eigenfrequencies

$$\omega'_\pm \approx \omega_0 \pm \left(\nu + \frac{G_1^2}{2\nu} \hat{x}^2 \right) = \omega_\pm \pm G'_2 \hat{x}^2. \tag{8.17}$$

In this form, it is clear that these diagonalized mode frequencies exhibit a quadratic dependence on the position, with a coupling coefficient $G'_2 = G_1^2/2\nu$. Furthermore, the operators $\hat{a}'_\pm$ are expressed in terms of $\hat{a}_\pm$, where one of these supermode operators is always linearly coupled to the position variable $\hat{x}$. In this situation, even if we solely drive one of the supermodes, photons will tunnel to its counterpart and couple linearly to the mechanical resonator, causing its phononic Fock state to decohere. It is this process that leads to the condition of the single-photon strong-coupling regime ($g_1 \gg \kappa$) required to perform QND measurements of phonon states in MIM optomechanical systems [413–415].

8.3.3 Whispering-Gallery-Mode System

We now consider an optomechanical system where the motion of the mechanical element shifts the frequencies of both optical modes in the same direction. Such a

system could, for example, be realized by sidecoupling the out-of-plane motion of a nanomechanical resonator to an optical WGM cavity [63], with the two degenerate optical modes being the clockwise and counterclockwise propagating modes [416]. In this case, each set of optomechanical coupling coefficients will be equal in both sign and magnitude, leading to $G_1^{(a_1)} = G_1^{(a_2)} = G_1$ and $G_2^{(a_1)} = G_2^{(a_2)} = G_2$. Inserting these coefficients into the interaction Hamiltonian in Eq. (8.11), we find

$$\begin{aligned}\hat{H}_{\mathrm{WGM}} &= \hbar\omega_+\hat{a}_+^\dagger\hat{a}_+ + \hbar\omega_-\hat{a}_-^\dagger\hat{a}_- + \hbar\omega_{\mathrm{m}}\hat{b}^\dagger\hat{b} \\ &- \hbar G_1\left(\hat{a}_+^\dagger\hat{a}_+ + \hat{a}_-^\dagger\hat{a}_-\right)\hat{x} - \frac{\hbar G_2}{2}\left(\hat{a}_+^\dagger\hat{a}_+ + \hat{a}_-^\dagger\hat{a}_-\right)\hat{x}^2.\end{aligned} \tag{8.18}$$

For this system, we are thus left with a Hamiltonian that is already diagonalized, which leads to two very important consequences. First, the quadratic coupling that arose due to the avoided level crossing in the MIM system has vanished. However, there still exists quadratic coupling terms in our Hamiltonian as we have expanded the optical cavity resonance frequency to second order in mechanical position. In contrast to the MIM system, where the quadratic coupling is proportional to the square of the linear coupling, this second-order coupling coefficient can be modified independently of the linear coupling by tuning the relative symmetry of the optical and mechanical modeshapes (see Appendix C). This leads us to the second important consequence of this system: since there is no linear mechanically-mediated coupling between the optical modes resulting from diagonalizing the Hamiltonian, QND measurements using this system are not constrained by the stringent single-photon strong-coupling regime. In place of this condition, we instead find a relaxed limit on the linear coupling strength G_1 with respect to the quadratic coupling G_2, which is determined below in Section 8.5 and given in Eq. (8.56).

8.3.4 Mapping to a Single Optical Mode

We conclude this section by noting that since it is unnecessary to introduce an avoided level crossing to generate quadratic coupling in the WGM optomechanical cavity considered above, a single mode treatment will suffice to evaluate this system for QND measurements of phonons. Mathematically this amounts to setting $G_1^{(a_2)} = G_2^{(a_2)} = 0$, such that $\hat{H}_{\mathrm{WGM}}$ is identical to $\hat{H}$ in Eq. (8.4). This simplification

is justified by the fact that the effect of adding a second, undriven optical mode to the system can be included by noting that the total number of photons in both cavity modes will be given by $\bar{N} = \bar{N}_+ + \bar{N}_- = \bar{N}_1 + \bar{N}_2$, where $\bar{N}_i = \langle \hat{a}_i^\dagger \hat{a}_i \rangle$ is simply the average photon occupancy of the mode corresponding to $\hat{a}_i$. For such a system, if one drives the $\hat{a}_1$ mode (call it the clockwise mode) to a photon occupancy $\hat{N}_1$, then backscattering will cause the $\hat{a}_2$ mode (counterclockwise mode) to be populated to an occupancy [119]

$$\bar{N}_2 = \frac{\nu^2}{\Delta^2 + (\kappa/2)^2} \bar{N}_1. \tag{8.19}$$

For the $\Delta = 0$ condition associated with the phase sensitive measurements discussed in Section 8.5, we then have $\bar{N}_2 = (2\nu/\kappa)^2 \bar{N}_1$. For $2\nu \ll \kappa$, $\bar{N}_2 \ll \bar{N}_1$, such that the counterclockwise mode is essentially unpopulated and we can take $\bar{N} \approx \bar{N}_1$. Therefore, in this regime, we need only consider one mode (in this case the clockwise mode). We note that in this situation a small, but finite leakage of photons into the counterclockwise mode will not lead to the accelerated decoherence associated with the MIM system [413] due to the fact that counterclockwise photons interact with the mechanics in the same way clockwise photons do.

For the case where $2\nu \gg \kappa$, the situation is complicated by the fact that the clockwise and counterclockwise modes hybridize into the two individually accessible symmetric and antisymmetric modes corresponding to $\hat{a}_\pm$. Under these circumstances, the resonant probing condition required for phase sensitive measurements results in $\Delta = \pm\nu$. In either case this leads to $\bar{N}_2 \approx \bar{N}_1$, meaning that even though we are only driving the clockwise mode, strong backscattering ensures that in equilibrium both modes are equally populated. Again, this photon redistribution does nothing to affect the optically induced transition rates of the system. However, as half of the photons now reside in the unmonitored counterclockwise mode, the measurement rate is halved. Therefore, a single mode treatment is still valid in this regime, provided we account for this factor of two decrease in the measurement rate of the mechanical phonon number given by Eq. (8.7).

8.4 Mechanical Fock State Decoherence Rates[2]

For the remainder of this chapter, we determine the conditions imposed upon using a single-mode quadratically coupled optomechanical cavity (*e.g.* the WGM system described in Section 8.3.3) to perform QND measurements of quantized mechanical energy. To do this, we use a master equation approach to calculate the relevant measurement-induced and thermal decoherence rates associated with this system and compare them to the optomechanical QND measurement rate Γ_{meas} given by Eq. (8.7). We begin by assuming the cavity is driven via a strong external drive, such that we can immediately linearize the optical cavity annihilation operator as we did in Section 4.3.3. Furthermore, we switch to a frame that rotates at the optical drive frequency by performing the transformation associated with the unitary operator $\hat{U} = e^{i\omega_{\mathrm{d}}\hat{a}^{\dagger}\hat{a}}$. Applying these two modifications to the quadratic Hamiltonian given in Eq. (8.4), while also including terms associated with the optical drive and the coupling of each mode to their Markovian baths, we construct the full Hamiltonian of the system as

$$\hat{H} = \hat{H}_{\mathrm{c}}^{(\mathrm{lin})} + \hat{H}_{\mathrm{m}} + \hat{H}_{\mathrm{quad}} + \hat{H}_{\mathrm{dr}} + \hat{H}_{\kappa} + \hat{H}_{\Gamma}. \tag{8.20}$$

This Hamiltonian is very similar to the total optomechanical Hamiltonian introduced in Eq. (4.10), save for the fact that we have substituted $\hat{H}_{\mathrm{om}}$ for the linearized quadratic optomechanical interaction Hamiltonian

$$\hat{H}_{\mathrm{quad}} = -\hbar\bar{a}\left[g_1\left(\hat{b}^{\dagger}+\hat{b}\right) + \frac{g_2}{2}\left(2\hat{b}^{\dagger}\hat{b} + \hat{b}^{\dagger}\hat{b}^{\dagger} + \hat{b}\hat{b}\right)\right]\left(\delta\hat{a}^{\dagger} + \delta\hat{a}\right), \tag{8.21}$$

as well as replaced the optical cavity Hamiltonian $\hat{H}_{\mathrm{c}}$ with its linearized counterpart

$$\hat{H}_{\mathrm{c}}^{(\mathrm{lin})} = -\hbar\Delta\delta\hat{a}^{\dagger}\delta\hat{a}. \tag{8.22}$$

Note that $\hat{H}_{\mathrm{quad}}$ is linearized in the sense that we have neglected terms proportional to $\delta\hat{a}^{\dagger}\delta\hat{a}$ and we have taken $\bar{a}$ to be real by choosing the appropriate phase for $\bar{a}_{\mathrm{in}}$. Furthermore, we remind the reader that $\Delta = \omega_{\mathrm{d}} - \omega_{\mathrm{c}}$ is the optical cavity drive detuning, where we have ignored the small shift in the cavity frequency due to the

[2]The master equation calculations used to determine the decoherence rates in this section were performed by Dr. Anja Metelmann from the Freie Universität Berlin and are included here to preserve the continuity of the original publication.

static optomechanical displacement of the mechanical resonator. The rest of the terms in Eq. (8.20), namely $\hat{H}_{\rm m}$, $\hat{H}_{\rm dr}$, $\hat{H}_{\kappa}$, and $\hat{H}_{\Gamma}$, are all defined in Section 4.3.1.

The dynamics of the system is then captured by the master equation, which can be written in superoperator notation as [417]

$$\frac{\partial}{\partial t}\hat{\rho} = \left(\mathcal{L}_{\rm c} + \mathcal{L}_{\rm m} + \mathcal{L}_{\rm om}\right)\hat{\rho}, \tag{8.23}$$

with $\hat{\rho}$ being the total density matrix of the system (including both optical and mechanical components). Here, we have defined the superoperators

$$\mathcal{L}_{\rm c} = -\frac{i}{\hbar}[\hat{H}_{\rm c}^{(\rm lin)}, \bullet] + \frac{\kappa}{2}\mathcal{D}[\delta\hat{a}]\bullet, \tag{8.24}$$

$$\mathcal{L}_{\rm m} = -\frac{i}{\hbar}[\hat{H}_{\rm m}, \bullet] + \frac{\Gamma_{\rm m}}{2}\left\{(\bar{n}_{\rm th}+1)\,\mathcal{D}[\hat{b}] + \bar{n}_{\rm th}\mathcal{D}[\hat{b}^\dagger]\right\}\bullet, \tag{8.25}$$

$$\mathcal{L}_{\rm om} = -\frac{i}{\hbar}[\hat{H}_{\rm quad}, \bullet], \tag{8.26}$$

$$\mathcal{D}[\hat{o}]\bullet = 2\hat{o}\bullet\hat{o}^\dagger - \hat{o}^\dagger\hat{o}\bullet - \bullet\hat{o}^\dagger\hat{o} = [\hat{o}, \bullet\hat{o}^\dagger] + [\hat{o}\bullet, \hat{o}^\dagger], \tag{8.27}$$

where $\hat{o}$ is a generic ladder operator and the $\bullet$ acts as a placeholder for a arbitrary quantum mechanical operator.

We can now move into a new interaction picture with density matrix $\hat{\rho}' = e^{-(\mathcal{L}_{\rm c}+\mathcal{L}_{\rm m})t}\hat{\rho}$ that evolves in time according to

$$\frac{\partial\hat{\rho}'}{\partial t} = e^{-(\mathcal{L}_{\rm c}+\mathcal{L}_{\rm m})t}\mathcal{L}_{\rm om}e^{(\mathcal{L}_{\rm c}+\mathcal{L}_{\rm m})t}\hat{\rho}' \equiv \mathcal{L}'_{\rm om}(t)\hat{\rho}', \tag{8.28}$$

where we have simply used the product rule and Eq. (8.23). This master equation can be formally integrated to obtain the solution

$$\hat{\rho}'(t) = \hat{\rho}'(0) + \int_0^t \mathcal{L}'_{\rm om}(\tau)\hat{\rho}'(\tau)d\tau. \tag{8.29}$$

Substituting this integral back into Eq. (8.28), while performing the trace over the cavity space (denoted by $\mathrm{Tr_c}\{\}$), we then arrive at the new master equation

$$\begin{aligned}\frac{\partial\hat{\rho}'_{\rm m}}{\partial t} &\equiv \frac{\partial}{\partial t}\mathrm{Tr_c}\left\{\hat{\rho}'(t)\right\} \\ &= \mathrm{Tr_c}\left\{\mathcal{L}'_{\rm om}(t)\hat{\rho}'(0)\right\} + \int_0^t \mathrm{Tr_c}\left\{\mathcal{L}'_{\rm om}(t)\mathcal{L}'_{\rm om}(\tau)\hat{\rho}'(\tau)\right\}d\tau,\end{aligned} \tag{8.30}$$

where $\hat{\rho}'_{\rm m}$ is the density matrix of the mechanical resonator in the new interaction frame. Thus we have to calculate

$$\mathcal{L}'_{\rm om} = -i\bar{a}\left[\hat{\mathcal{A}}(t)\hat{\mathcal{B}}(t) - \hat{\mathcal{A}}^\dagger(t)\hat{\mathcal{B}}^\dagger(t)\right], \tag{8.31}$$

with

$$\hat{\mathcal{A}}(t) = e^{-\mathcal{L}_c t}\left(\delta\hat{a}^\dagger + \delta\hat{a}\right) \bullet e^{\mathcal{L}_c t}, \tag{8.32}$$

$$\hat{\mathcal{B}}(t) = e^{-\mathcal{L}_m t}\hat{B} \bullet e^{\mathcal{L}_m t}, \tag{8.33}$$

where we have introduced the new mechanical operator $\hat{B} = -g_1\left(\hat{b}^\dagger + \hat{b}\right) - \frac{g_2}{2}\left(2\hat{b}^\dagger\hat{b} + \hat{b}^\dagger\hat{b}^\dagger + \hat{b}\hat{b}\right)$. Note that while $\hat{B}$ and $\left(\delta\hat{a}^\dagger + \delta\hat{a}\right)$ are Hermitian, we have $(\hat{o}\bullet)^\dagger = \bullet\hat{o}^\dagger$, hence the appearance of $\hat{\mathcal{A}}^\dagger(t)$ and $\hat{\mathcal{B}}^\dagger(t)$ in Eq. (8.31). Finally, to evaluate the superoperator $\mathcal{L}'_{\rm om}$, we also need the dynamics of the cavity operator in this interaction picture:

$$\hat{\mathcal{A}}(t) = \delta\hat{a} \bullet e^{\left(i\Delta - \frac{\kappa}{2}\right)t} + \delta\hat{a}^\dagger \bullet e^{-\left(i\Delta - \frac{\kappa}{2}\right)t} - \bullet\delta\hat{a}^\dagger e^{-i\Delta t}\left(e^{\frac{\kappa}{2}t} - e^{-\frac{\kappa}{2}t}\right). \tag{8.34}$$

So far we have not made any approximations; the above treatment resembles the standard derivation for a master equation. In what follows, we adiabatically eliminate the cavity to obtain a reduced density matrix for the mechanics. This implies the assumption that the cavity photons adiabatically follow the phonon occupation, *i.e.* that $\kappa \gg \Gamma_{\rm th}$ is fulfilled [400], where $\Gamma_{\rm th}$ is the thermal decoherence rate of the phonon state in question (see Eq. (8.49) below). Within this limit, we assume that the optical cavity and mechanical resonator are effectively uncorrelated at all times, so that the density matrix factorizes as $\hat{\rho} \equiv \hat{\rho}_{\rm m} \otimes \hat{\rho}_{\rm c}$ [418], where $\hat{\rho}_{\rm c}$ denotes the density matrix of the cavity mode. We also make a Born approximation and assume that the cavity mode fluctuations $\delta\hat{a}$ and $\delta\hat{a}^\dagger$ are not affected by the dynamics of the mechanics, that is we set $\hat{\rho}_{\rm c}(t) \approx \hat{\rho}_{\rm c}(0)$. This means that the total density matrix remains a product of the initial cavity density matrix and the mechanical density matrix, *i.e.* $\hat{\rho}'(t) \approx \hat{\rho}'_{\rm m}(t) \otimes \hat{\rho}_{\rm c}(0) \equiv \hat{\rho}'_{\rm m}(t) \otimes |0\rangle\langle 0|$ (for the cavity being in the vacuum state in this displaced frame). Under this assumption the first term in Eq. (8.30) vanishes and with

$$\mathrm{Tr}_{\rm c}\left\{\hat{\mathcal{A}}(t)\hat{\mathcal{A}}(\tau)\,|0\rangle\langle 0|\right\} = \mathrm{Tr}_{\rm c}\left\{\hat{\mathcal{A}}^\dagger(t)\hat{\mathcal{A}}(\tau)\,|0\rangle\langle 0|\right\} = e^{\left(i\Delta - \frac{\kappa}{2}\right)(t-\tau)}, \tag{8.35}$$

$$\mathrm{Tr}_{\rm c}\left\{\hat{\mathcal{A}}^\dagger(t)\hat{\mathcal{A}}^\dagger(\tau)\,|0\rangle\langle 0|\right\} = \mathrm{Tr}_{\rm c}\left\{\hat{\mathcal{A}}(t)\hat{\mathcal{A}}^\dagger(\tau)\,|0\rangle\langle 0|\right\} = e^{-\left(i\Delta + \frac{\kappa}{2}\right)(t-\tau)}, \tag{8.36}$$

we can evaluate the second term as

$$\begin{aligned}&\mathrm{Tr}_{\rm c}\left\{\mathcal{L}'_{\rm om}(t)\mathcal{L}'_{\rm om}(\tau)\hat{\rho}'(\tau)\right\} = \\ &-\bar{N}\left[\left\{\hat{\mathcal{B}}(t)\hat{\mathcal{B}}(\tau) - \hat{\mathcal{B}}^\dagger(t)\hat{\mathcal{B}}(\tau)\right\}e^{\left(i\Delta - \frac{\kappa}{2}\right)(t-\tau)} + \mathrm{h.c.}\right]\hat{\rho}'_{\rm m}(\tau).\end{aligned} \tag{8.37}$$

Using the expression in Eq. (8.37), the master equation yields (with change of variables $t' = t - \tau$)

$$\begin{aligned}\frac{\partial \hat{\rho}'_{\mathrm{m}}}{\partial t} = -\bar{N}\int_0^t \hat{\rho}'_{\mathrm{m}}(t-t')\Big[\big\{&\hat{\mathcal{B}}(t)\hat{\mathcal{B}}(t-t') \\ &- \hat{\mathcal{B}}^\dagger(t)\hat{\mathcal{B}}(t-t')\big\}e^{\left(i\Delta-\frac{\kappa}{2}\right)t'} + \mathrm{h.c.}\Big]dt',\end{aligned} \tag{8.38}$$

which we can transform back to the initial frame knowing that $\hat{\rho}_{\mathrm{m}}(t) = e^{\mathcal{L}_{\mathrm{m}}t}\hat{\rho}'_{\mathrm{m}}(t)$ and move into an interaction picture with respect to the free mechanical Hamiltonian. This gives us

$$\begin{aligned}\frac{\partial \hat{\rho}_{\mathrm{m}}}{\partial t} = -\bar{N}\int_0^t \hat{\rho}_{\mathrm{m}}(t-t')\Bigg(&\Bigg\{g_1^2\Big[\left\{\hat{b}\hat{b}^\dagger \bullet - \hat{b}^\dagger \bullet \hat{b}\right\}e^{-i\omega_{\mathrm{m}}t'} \\ &+ \left\{\hat{b}^\dagger\hat{b} \bullet - \hat{b} \bullet \hat{b}^\dagger\right\}e^{+i\omega_{\mathrm{m}}t'}\Big] + g_2^2\left[\hat{b}^\dagger\hat{b}\hat{b}^\dagger\hat{b} \bullet - \hat{b}^\dagger\hat{b} \bullet \hat{b}^\dagger\hat{b}\right] \\ &+ \frac{g_2^2}{4}\Big[\left\{\hat{b}\hat{b}\hat{b}^\dagger\hat{b}^\dagger \bullet - \hat{b}^\dagger\hat{b}^\dagger \bullet \hat{b}\hat{b}\right\}e^{-i2\omega_{\mathrm{m}}t'} \\ &+ \left\{\hat{b}^\dagger\hat{b}^\dagger\hat{b}\hat{b} \bullet - \hat{b}\hat{b} \bullet \hat{b}^\dagger\hat{b}^\dagger\right\}e^{+i2\omega_{\mathrm{m}}t'}\Big]\Bigg\}e^{-\left(i\Delta+\frac{\kappa}{2}\right)t'} + \mathrm{h.c.}\Bigg)dt' \\ &+ \frac{\Gamma_{\mathrm{m}}}{2}\left\{(\bar{n}_{\mathrm{th}}+1)\,\mathcal{D}[\hat{b}] + \bar{n}_{\mathrm{th}}\mathcal{D}[\hat{b}^\dagger]\right\}\hat{\rho}_{\mathrm{m}}(t),\end{aligned} \tag{8.39}$$

where we have also used the rotating wave approximation [150]. In the next step we apply a Markov approximation and solve the integrals for $t \to \infty$, obtaining

$$\begin{aligned}\frac{\partial \hat{\rho}_{\mathrm{m}}}{\partial t} = &-\frac{i\bar{N}}{\hbar}[\hat{H}_{\mathrm{r}}, \hat{\rho}_{\mathrm{m}}(t)] + \bar{N}\Big(g_1^2\mathrm{Re}\left\{\chi_{\mathrm{c}}(-\omega_{\mathrm{m}})\right\}\mathcal{D}[\hat{b}^\dagger] \\ &+ g_1^2\mathrm{Re}\left\{\chi_{\mathrm{c}}(\omega_{\mathrm{m}})\right\}\mathcal{D}[\hat{b}] + g_2^2\mathrm{Re}\left\{\chi_{\mathrm{c}}(0)\right\}\mathcal{D}[\hat{b}^\dagger\hat{b}] \\ &+ \frac{g_2^2}{4}\mathrm{Re}\left\{\chi_{\mathrm{c}}(-2\omega_{\mathrm{m}})\right\}\mathcal{D}[\hat{b}^\dagger\hat{b}^\dagger] + \frac{g_2^2}{4}\mathrm{Re}\left\{\chi_{\mathrm{c}}(2\omega_{\mathrm{m}})\right\}\mathcal{D}[\hat{b}\hat{b}]\Big)\hat{\rho}_{\mathrm{m}}(t) \\ &+ \frac{\Gamma_{\mathrm{m}}}{2}\left\{(\bar{n}_{\mathrm{th}}+1)\,\mathcal{D}[\hat{b}] + \bar{n}_{\mathrm{th}}\mathcal{D}[\hat{b}^\dagger]\right\}\hat{\rho}_{\mathrm{m}}(t),\end{aligned} \tag{8.40}$$

where the coherent dynamics of the system are described by the Hamiltonian

$$\begin{aligned}\hat{H}_{\mathrm{r}} = &\hbar g_1^2\left(\mathrm{Im}\left\{\chi_{\mathrm{c}}(-\omega_{\mathrm{m}})\right\} + \mathrm{Im}\left\{\chi_{\mathrm{c}}(\omega_{\mathrm{m}})\right\}\right)\hat{b}^\dagger\hat{b} \\ &+ \hbar g_2^2\mathrm{Im}\left\{\chi_{\mathrm{c}}(0)\right\}\hat{b}^\dagger\hat{b}\hat{b}^\dagger\hat{b} + \frac{\hbar g_2^2}{4}\Big(\mathrm{Im}\left\{\chi_{\mathrm{c}}(-2\omega_{\mathrm{m}})\right\}\hat{b}\hat{b}\hat{b}^\dagger\hat{b}^\dagger \\ &+ \mathrm{Im}\left\{\chi_{\mathrm{c}}(2\omega_{\mathrm{m}})\right\}\hat{b}^\dagger\hat{b}^\dagger\hat{b}\hat{b}\Big),\end{aligned} \tag{8.41}$$

and we have introduced the real and imaginary parts of the optical cavity's

susceptibility as

$$\mathrm{Re}\left\{\chi_{\mathrm{c}}(\omega)\right\} = \frac{\kappa/2}{(\omega+\Delta)^2+(\kappa/2)^2}, \tag{8.42}$$

$$\mathrm{Im}\left\{\chi_{\mathrm{c}}(\omega)\right\} = \frac{(\omega+\Delta)}{(\omega+\Delta)^2+(\kappa/2)^2}. \tag{8.43}$$

Note that $\mathrm{Re}\left\{\chi_{\mathrm{c}}(\omega)\right\} = S_{NN}(-\omega)/2\bar{N}$, where $S_{NN}(-\omega)$ is the photon number spectral density given in Eq. (4.36). Eq. (8.40) governs the dynamics of the mechanical mode under influence of the QND measurement, as well as its contamination due to the linear coupling, counter-rotating second-order terms, and the influence of the thermal environment. Meanwhile, the first term in $\hat{H}_{\mathrm{r}}$ describes a shift induced by the linear coupling, while the second and third terms are of the Kerr-type (Lamb shifts). Furthermore, for zero detuning ($\Delta = 0$) the above Hamiltonian simplifies to $\hat{H}_{\mathrm{r}} = \hbar g_2^2 \mathrm{Im}\left\{\chi_{\mathrm{c}}(-2\omega_{\mathrm{m}})\right\}\left(\hat{b}^\dagger\hat{b} + \frac{1}{2}\right)$, resulting in a static shift of the mechanical frequency. As expected, the mechanical occupation is not affected by the pure QND measurement (*i.e.* terms associated with the susceptibility on resonance $\chi_{\mathrm{c}}(0)$ in Eq. (8.40)), nor the photon-induced coherent interaction characterized by $\hat{H}_{\mathrm{r}}$ ($[\hat{H}_{\mathrm{r}}, \hat{b}^\dagger\hat{b}] = 0$).

We now use the fact that we can determine the probability p_n of being in the nth Fock state by taking the inner product of the density matrix using the number state basis vectors, that is $p_n(t) = \langle n|\,\hat{\rho}_{\mathrm{m}}(t)\,|n\rangle$. If we assume that the system is initially in the nth mechanical Fock state, such that $p_n(0) = 1$, then the total rate at which this pure state decoheres can be found using Eq. (8.40). This results in

$$\left|\frac{dp_n}{dt}\right| = \left|\langle n|\,\frac{\partial\hat{\rho}_{\mathrm{m}}}{\partial t}\,|n\rangle\right| = \Gamma_{n+1} + \Gamma_{n-1} + \Gamma_{n+2} + \Gamma_{n-2} + \Gamma_{\mathrm{th}}, \tag{8.44}$$

where

$$\Gamma_{n+1} = (n+1)g_1^2 S_{NN}(-\omega_{\mathrm{m}}), \tag{8.45}$$

$$\Gamma_{n-1} = n g_1^2 S_{NN}(\omega_{\mathrm{m}}), \tag{8.46}$$

$$\Gamma_{n+2} = (n+1)(n+2)\frac{g_2^2}{4} S_{NN}(-2\omega_{\mathrm{m}}), \tag{8.47}$$

$$\Gamma_{n-2} = n(n-1)\frac{g_2^2}{4} S_{NN}(2\omega_{\mathrm{m}}), \tag{8.48}$$

are the rates at which the phonon state of the mechanical resonator decoheres due

to measurement-induced jumps from $n \to n \pm 1$ and $n \to n \pm 2$, while

$$\Gamma_{\rm th} = \Gamma_{\rm m} \left[(\bar{n}_{\rm th} + 1)\, n + \bar{n}_{\rm th}\, (n+1) \right], \tag{8.49}$$

is the rate associated the thermal decoherence of the mechanical resonator's nth Fock state due to coupling with its dissipative bath [287, 419]. As can be seen in Fig. 8.2, each of the decoherence rates given by Eqs. (8.45)–(8.49) decrease as we move to lower Fock states, taking on their minimum values for a mechanical resonator in its ground state.

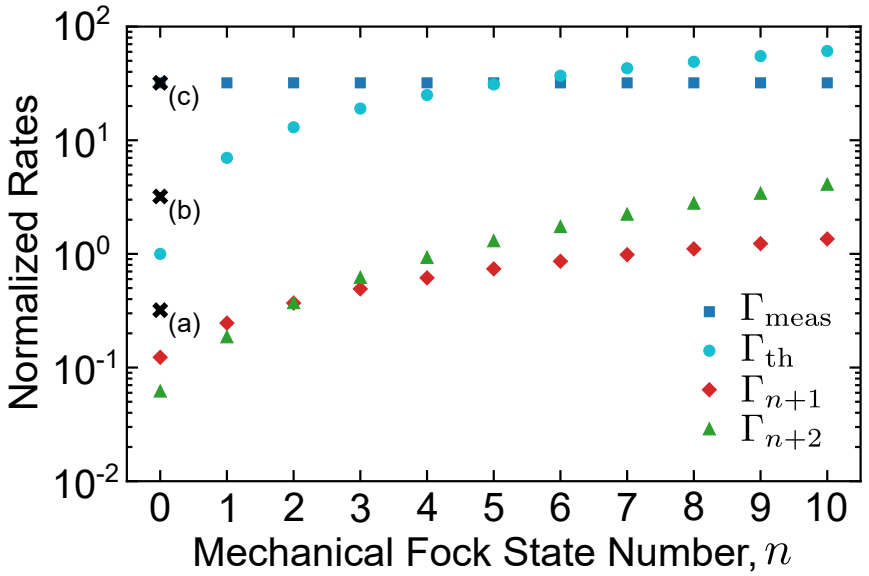

Figure 8.2: Plot of the measurement rate $\Gamma_{\rm meas}$ and thermal decoherence rate $\Gamma_{\rm th}$, as well as the first- and second-order measurement-induced transition rates, Γ_{n+1} and Γ_{n+2}, normalized to the thermal decoherence rate of the ground state $\Gamma^0_{\rm th} = \bar{n}_{\rm th}\Gamma_{\rm m}$, for the first ten Fock states of an optomechanical system. The system parameters are: $\omega_{\rm m}/2\pi = 2$ GHz, $\Gamma_{\rm m}/2\pi = 1$ kHz ($Q_{\rm m} = 2 \times 10^6$), $\bar{n}_{\rm th} = 0.25$ ($T \approx 60$ mK), $\Delta = 0$, $\kappa/2\pi = 500$ MHz, $\bar{N} = 100$, $g_1/2\pi = 50$ kHz, $g_2/2\pi = 100$ kHz, corresponding to the cooperativities $C_1 = 0.02$, $\bar{C}_1 = 2$, $\tilde{C}_1 = 8$ and $C_2 = 0.08$, $\bar{C}_1 = 8$, $\tilde{C}_1 = 32$. Here, $n_{\rm max} \approx 5$ such that the first six mechanical Fock states (including the ground state) can be monitored continuously using the QND measurement discussed in this chapter. The black crosses indicate the measurement rate values used for the trajectory simulations in Fig. 8.3. Figure reproduced from Ref. [393].

8.5 Quantum Nondemolition Measurement Conditions

With the decoherence rates of the system's mechanical Fock states calculated in the previous subsection, we now look to determine the necessary conditions required to use the optomechanical QND measurement of phonon number considered in this chapter to study the thermal decoherence of a mechanical resonator. In order to perform such measurements, one must temporally resolve jumps between the mechanical resonator's phonon number states by measuring the system faster than it decoheres. Comparing the measurement rate given in Eq. (8.7) to the decoherence rates found in Eqs. (8.45)–(8.49) of the previous section, we find that this condition is satisfied for the following hierarchy of rates:

$$\Gamma_{\rm meas} \gg \Gamma_{\rm th} \gg \Gamma_{n\pm1}, \Gamma_{n\pm2}. \tag{8.50}$$

The right-hand side of Eq. (8.50) ensures that thermal transitions dominate over optically induced phonon jumps, leading to the "linear-coupling condition" $\Gamma_{\rm th} \gg \Gamma_{n\pm1}$ and the "quadratic-coupling condition" $\Gamma_{\rm th} \gg \Gamma_{n\pm2}$. In this situation, one would expect a phonon distribution exhibiting Bose-Einstein statistics, with an average phonon occupation of $\langle n \rangle = \bar{n}_{\rm th}$ [400]. However, if one were to enter a regime where $\Gamma_{\rm th} \lesssim \Gamma_{n\pm1}, \Gamma_{n\pm2}$, phonon trajectories would be dominated by optomechanically induced jumps, leading to far more complex phonon statistics.

Also included in Eq. (8.50) is the "fast-measurement condition" $\Gamma_{\rm meas} \gg \Gamma_{\rm th}$ [400], which tells us that one must be able to measure the phonon state of the resonator before it thermally decoheres in order to resolve quantized mechanical energy jumps [35, 36, 415, 418]. To confirm this condition, we have performed Monte Carlo simulations of mechanical phonon trajectories according to the master equation in Eq. (8.40) [420]. As can be seen in Fig. 8.3, one can enter into a regime where the optomechanical measurement rate is fast enough to allow for observation of quantum jumps in mechanical phonon number. We note that the fast-measurement condition can also be used determine the largest Fock state number that can be continuously monitored using this QND scheme as

$$n_{\rm max} = \frac{\bar{C}_2 - \bar{n}_{\rm th}}{2\bar{n}_{\rm th} + 1}. \tag{8.51}$$

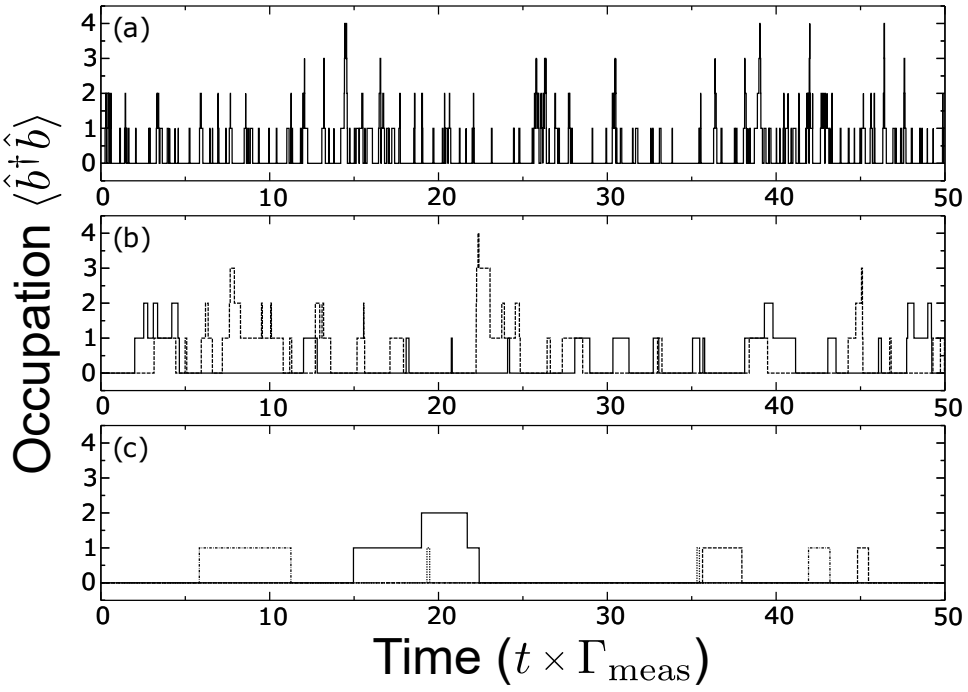

Figure 8.3: Monte Carlo simulations of the mechanical occupation dynamics using the master equation given in Eq. (8.40) for three measurement rates: $\Gamma_{\rm meas}/\Gamma_{\rm th} =$ (a) 0.32, (b) 3.2, and (c) 32. The remaining parameters are those found in the caption of Fig. 8.2. In each plot we have included (a) a single trajectory, (b) two trajectories, and (c) four trajectories. Graph (a) depicts the case where thermally-induced jumps dominate. Here, a QND measurement is not possible and the final detected signal would only give information about the average phonon number. In contrast, if the inverse measurement rate is the smallest time scale in the system, as seen in (c), the QND read-out of the occupation can occur fast enough to resolve quantum jumps in phonon number. We note that in an actual experiment, the phonon trajectory would be inferred from a physical observable, such as the current from a homodyne detector [400]. Figure reproduced from Ref. [393]. © 2018 American Physical Society.

The above analysis is valid for any arbitrary Fock state of the mechanical resonator. However, the minimum requirement necessary to perform a QND measurement of the mechanical oscillator's energy will occur when the system is in its ground state, as $\Gamma_{\rm th}$, $\Gamma_{n\pm1}$, and $\Gamma_{n\pm2}$ are all indeed minimized for $n = 0$ (see Fig. 8.2). In this situation, we are no longer concerned with rates corresponding to a reduction in phonon number (*i.e.* Γ_{n-1} and Γ_{n-2}), as the mechanical ground state is unable to emit phononic energy. Furthermore, in order to experimentally resolve shifts in the optical cavity resonance frequency due to the creation/annihilation of a single phonon, one often turns to a phase sensitive transduction scheme, such as

optical homodyne detection, which has maximal signal at $\Delta = 0$ (see Section 4.4.3). Finally, we wish to operate in the sideband-resolved regime ($\omega_{\mathrm{m}} \gg \kappa$), which as we shall see below is necessary for the QND measurements of the mechanical ground state. Under these circumstances, the rate hierarchy of Eq. (8.50) becomes

$$\Gamma_{\mathrm{meas}} \gg \Gamma_{\mathrm{th}}^{0} \gg \Gamma_1, \Gamma_2, \tag{8.52}$$

where $\Gamma_{\mathrm{th}}^{0} = \bar{n}_{\mathrm{th}}\Gamma_{\mathrm{m}}$ is the rate at which the ground state of the mechanical resonator thermally decoheres (found by setting $n = 0$ in Eq. (8.49)). Furthermore, Γ_1 and Γ_2 are the measurement-induced rates associated with transitions to the first and second excited states from this ground state at $\Delta = 0$ and are given by

$$\Gamma_1 = \frac{\bar{N} g_1^2 \kappa}{\omega_{\mathrm{m}}^2} = \frac{\bar{C}_1 \Gamma_{\mathrm{m}} \kappa^2}{4\omega_{\mathrm{m}}^2}, \tag{8.53}$$

$$\Gamma_2 = \frac{\bar{N} g_2^2 \kappa}{8\omega_{\mathrm{m}}^2} = \frac{\bar{C}_2 \Gamma_{\mathrm{m}} \kappa^2}{32\omega_{\mathrm{m}}^2}, \tag{8.54}$$

where similar to before we have introduced the first-order, cavity-enhanced cooperativity $\bar{C}_1 = \bar{N} C_1$ in terms of the corresponding first-order, single-photon cooperativity $C_1 = 4g_1^2/\kappa\Gamma_{\mathrm{m}}$. Using these two expressions for Γ_1 and Γ_2, the limits in Eq. (8.52) can be recast in terms of the first- and second-order quantum cooperativities, $\tilde{C}_1 = \bar{C}_1/\bar{n}_{\mathrm{th}}$ and $\tilde{C}_2 = \bar{C}_2/\bar{n}_{\mathrm{th}}$ [150], as

$$\tilde{C}_2 \gg 1 \gg \tilde{C}_1 \left(\frac{\kappa^2}{4\omega_{\mathrm{m}}^2}\right), \tilde{C}_2 \left(\frac{\kappa^2}{32\omega_{\mathrm{m}}^2}\right). \tag{8.55}$$

We now look to interpret the fundamental limits associated with this type of QND measurement. First, by ensuring $\Gamma_{\mathrm{meas}} \gg \Gamma_2$ – that is to say we can measure the phononic state of the system before an optically induced transition to the second excited state occurs – we arrive at the condition $32\omega_{\mathrm{m}}^2 \gg \kappa^2$, which will certainly be satisfied for a sideband-resolved optomechanical system. Physically, this limit can be interpreted as the lifetime of the cavity photons being longer than the mechanical period, such that each photon samples the mechanical motion over many cycles. This effectively averages out rapidly oscillating, transition-inducing second-order terms in the Hamiltonian in favour of terms that are constant in time.

Furthermore, the requirement that $\Gamma_{\mathrm{meas}} \gg \Gamma_1$ allows us to set the following limit on the linear coupling rate with respect to the quadratic coupling rate

$$|g_2| \gg |g_1| \frac{\kappa}{2\omega_{\mathrm{m}}}, \tag{8.56}$$

where we have taken the magnitude of both g_1 and g_2, as it is possible that they are different in sign. By satisfying this inequality, quadratic coupling is strong enough to overcome any contamination from linear coupling that would prevent optomechanical QND measurements of phonon number from being performed. Upon further inspection of Eq. (8.56), we see that the sideband resolution condition discussed in the previous paragraph aids in suppressing the detrimental effect of linear coupling. A slightly more subtle observation is that since g_2 is proportional to x_{zpf}^2 while g_1 is linear in x_{zpf}, larger zero-point fluctuation amplitudes (corresponding to smaller effective masses and mechanical resonance frequencies) act to further relax the condition of small linear coupling. We note that in order to satisfy this limit, the relative strengths of g_1 and g_2 (or equivalently G_1 and G_2) must be independently tunable. For the system considered here, this can be done by exploiting the symmetry between the optical and mechanical modes (see Appendix C). However, this is not the case for MIM systems, where quadratic coupling resulting from the hybridization of two nearly degenerate optical modes leads to $g_2 = g_1^2/2\nu$ (see Section 8.3.2). In fact, one can put this relation into Eq. (8.56) to recover the single-photon strong-coupling requirement $g_1 \gg \kappa$, where we have assumed $2\nu \gg \omega_{\mathrm{m}}$ as is often done with MIM systems [411, 413–415]. Therefore, Eq. (8.56) provides a more general, less stringent condition for QND measurements of phonon number using a quadratically coupled optomechanical cavity.

As a final note, we point out that even if the above conditions are met, one must still satisfy the ground state linear- and quadratic-coupling conditions, *i.e.* $\Gamma_{\mathrm{th}}^0 \gg \Gamma_1, \Gamma_2$. Therefore, systems that are more sideband resolved and have stronger linear coupling suppression will exhibit a larger difference between Γ_{meas} and both measurement-induced transition rates, Γ_1 and Γ_2, such that a wider range of ground state thermal decoherence rates that will satisfy Eq. (8.52). Furthermore, we emphasize the importance of low thermal bath occupation. Even if one can cool the mechanical mode to near its ground state using back-action cooling techniques [26, 52, 76, 106, 107, 421], it is not possible to reduce the thermal decoherence rate of a given Fock state below $\Gamma_{\mathrm{th}}^0 = \bar{n}_{\mathrm{th}}\Gamma_{\mathrm{m}}$. Therefore, passive cooling of an optomechanical system using a refrigeration system [55, 58, 59, 422–424] will likely be necessary to facilitate these types of continuous QND measurements.

8.6 Conclusion

In this chapter, we have investigated the limits involved with performing QND measurements of the quantized mechanical Fock states in an optomechanical cavity where quadratic coupling arises due to shared symmetries between a single optical and mechanical mode. By imposing the requirement that the measurement occurs faster than Fock state thermally decoheres or transitions to another state via the optomechanical interaction itself, it was shown that the single-photon strong-coupling condition associated with MIM systems can be circumvented. Instead a new, less stringent limit on the strength of the linear coupling was imposed, along with optomechanical sideband resolution.

Chapter 9

Summary and Outlook

As was the case in during the transistor revolution of the late 1950s and early 1960s, silicon devices have remained at the forefront of the burgeoning quantum technology sector. More specifically, silicon optomechanical cavities have flourished, with implementations in near quantum-limited sensing [98], transduction [140], and storage [137, 139], as well as probing the boundaries of quantum physics [141–143]. In each of these applications there is one very important common denominator: the device must be cold. It is therefore imperative that we develop a thorough understanding of the cryogenic nature of silicon optomechanical cavities in order to continue improving existing silicon technologies, as well as develop new ones.

In this thesis, we have studied the low temperature behaviour of single-crystal-silicon nanomechanical beam resonators sidecoupled to WGM optical microdisks using a custom-built optomechanical coupling apparatus housed on the base plate of a dilution refrigerator. In Chapters 2 and 3, we reviewed the theoretical treatment used to model the isolated mechanical and optical modes of our system, while in Chapter 4 we investigated the optomechanical phenomena that emerge once we allow these two systems to dispersively couple to one another. With this theoretical framework laid out, in Chapter 5 we went on to discuss the optomechanical devices studied in this work, along with the cryogenic optical measurement system used to measure their properties. Using this experimental apparatus, we performed two separate experiments on our silicon devices at low temperatures.

The first experiment was detailed in Chapter 6, where we used a novel optomechanically mediated ringdown technique to ascertain the dissipation in

four individual modes of a single half-ring mechanical resonator, with frequencies between 3 and 19 MHz, for fridge temperatures ranging from 10 mK to 10 K. Here we found that the mechanical dissipation dropped off linearly between approximately 100 mK and 10 K, while plateauing to a constant value at low temperatures. Refurbishing the standard tunneling model to include crystalline nanoresonators, we showed that such a temperature dependence is consistent with mechanical damping associated with parasitic coupling to TLS defects confined to the one-dimensional geometry of our nanobeam. Quantitatively fitting our data with this theory, we extracted a TLS density of states parameter of $\mathcal{P}_0 \sim 1 - 4 \times 10^{44}$ J^{-1} m^{-3} and a deformation potential of $\gamma \sim 1$ - 2 eV, which we attribute to TLS defects existing on the surface of our resonators.

To identify and eliminate these sources of TLS dissipation, one could apply more sophisticated silicon surface treatments, such as the addition and subsequent removal of an oxide layer [250] or surface passivation and reconstruction in a hydrogen atmosphere [425–427], to reduce defects at the device's surface. Higher resistivity silicon could also be used to remove any effects dopants may have [374]. In fact, in a recent publication studying the effects of TLS damping in 1D photonic crystal nanobeams [135], it was shown that the dissipation could be decreased by a factor of roughly 2-3 by moving to high-resistivity silicon. Furthermore, one could determine whether the plateau at low temperatures is a result of phonons tunneling into the substrate by implementing phononic crystal radiation shields [67, 135, 254, 255] or soft-clamping [256, 257] into the system and observing their effects. Finally, the thermally mediated ringdown technique developed here can also be applied to other device geometries and materials, as has already been demonstrated in GHz-frequency GaAs photonic crystal nanobeams [428].

Furthermore, at our lowest fridge temperature of 10 mK, each studied mechanical mode couples to less than a single thermally excited TLS on average. Defect-phonon coupling on this level opens the door to proposed cavity-QED-like experiments between an individual defect and phonons within the resonator, providing a nonlinear quantum interaction which could be used for the storage of quantum information [429], quantum control of a single defect center [430, 431] or nonclassical state preparation of the mechanical element [175]. By tailoring the phononic

structure and mode frequencies of a nanoresonator, it may also be possible to engineer a Purcell-like defect-phonon interaction, leading to enhancement or suppression of TLS radiation into a specific mechanical mode [162]. Conversely, one could imagine using the mechanical resonator as a probe of the dynamics of a single quantum defect, furthering our incomplete knowledge of the microscopic nature of TLS defects, as well as their interactions with each other [358, 432, 433].

In Chapter 7, we investigated the seemingly anomalous backaction effects associated with photothermal forces in our devices originating from photon absorption at low temperatures. Here we observed that the photothermal force acts to directly oppose conventional radiation-pressure backaction effects in our device, resulting in optomechanical amplification for a red-detuned optical cavity drive, while optomechanical damping occurs on the blue side of the cavity. Fitting the nonlinear optical transmission, damping, and spring effects of our device using a photothermal coupling model, we determine the optomechanical properties of the system. Using these extracted parameters, we further showed that this photothermal damping mechanism can, in principle, be used to cool the mechanical resonator into its quantum ground state, a feat which would not be possible for our device if it were purely radiation-pressure driven.

While the ability to photothermally cool a non-SBR optomechanical cavity below single phonon occupancy is promising, reaching this regime in practice presents a significant challenge, largely due to residual heating from inevitable photon absorption processes [290, 294]. However, as this device was not purposefully designed for photothermal coupling, it may be possible to engineer this effect to achieve the photothermal parameters detailed at the end of Section 7.5, perhaps by adding a metallic layer to the resonator to enhance its differential thermal contractions and optical absorption [21–25, 303, 377, 378, 387]. One could also imagine modifying the thermal time constant by changing the dimensions of the resonator, which would also affect the strength of the photothermal damping. Increasing the photothermal coupling in this way may provide a path to cool a photothermally-driven optomechanical device into its motional ground state, as well as allow for future investigation of other photothermally enhanced optomechanical effects, such as entanglement [291, 376] or induced chaos [434, 435] between the

optical and mechanical modes of the system.

To complement these two experimental studies, in Chapter 8 we theoretically investigated using the WGM geometry associated with our device to perform optomechanical QND measurements of the Fock states of our resonator. Here we showed that linear optomechanical coupling can be suppressed in favour of quadratic coupling by tuning symmetries between the optical and mechanical modes inherent to this geometry, which is a prerequisite for this type of measurement. Using a master equation approach, we determine the mechanical decoherence rates associated with each of these couplings, as well as interactions with the thermal bath. Comparing these decoherence rates to the rate at which the quadratic optomechanical measurement collapses the mechanical system into a Fock state, we determined that such a QND measurement is feasible if the second order quantum cooperativity of the system is much greater than one. Furthermore, we imposed a limit on the maximum allowable linear coupling strength relative to its quadratic counterpart, which itself is a more general, less stringent version of the strong coupling regime required to perform Fock state QND measurements using MIM systems.

With these conditions satisfied, such a WGM optomechanical system could be used to perform quantum jump spectroscopy [402] on the thermally-induced transitions between mechanical quanta. One could also consider using this type of QND measurement to freeze the resonator into a given Fock state, prolonging its coherence time via the quantum Zeno effect [436], as has been demonstrated for trapped ions [437] and cold atoms [438, 439]. Such an effect could be useful for a number of optomechanical quantum information protocols [440, 441], where long coherence times are beneficial for applications such as quantum memories [127, 137, 139] and transducers [123–126, 140]. Furthermore, the ability to observe and manipulate the decoherence of these mesoscopic quantum mechanical states would provide a long sought-after experimental platform to aid in the understanding of the elusive quantum-to-classical transition.

References

[1] P. Apian, *Astronicum Caesareum* (1540).

[2] J. Kepler, *De cometis libelli tres* (1619).

[3] J. C. Brandt and R. D. Chapman, *Introduction to Comets*, 2nd edition, Cambridge Planetary Science (Cambridge University Press, Cambridge, 2004).

[4] J. C. Maxwell, *A Treatise on Electricity and Magnetism*, 1st edition, Vol. 2 (Clarendon Press, Oxford, 1873).

[5] P. Lebedew, "Untersuchungen über die druckkräfte des lichtes," *Ann. der Phys.* **311**, 433–458 (1901).

[6] E. F. Nichols and G. F. Hull, "A preliminary communication on the pressure of heat and light radiation," *Phys. Rev.* **13**, 307–320 (1901).

[7] E. F. Nichols and G. F. Hull, "The pressure due to radiation," *Astrophys. J.* **17**, 315–351 (1903).

[8] E. F. Nichols and G. F. Hull, "The pressure due to radiation. (second paper.)," *Phys. Rev.* **17**, 26–50 (1903).

[9] T. H. Maiman, "Stimulated optical radiation in ruby," *Nature* **187**, 493–494 (1960).

[10] M. E. Gertsenshtein, "Wave resonance of light and gravitational waves," *Sov. Phys. JETP* **14**, 84–85 (1962).

[11] M. E. Gertsenshtein and V. I. Pustovoit, "On the detection of low frequency gravitational waves," *Sov. Phys. JETP* **16**, 433–435 (1963).

[12] V. B. Braginsky, "On the limits which determine the possibility of measuring gravitational effects," *Sov. Phys. JETP* **17**, 1050–1053 (1963).

[13] V. B. Braginsky, "Gravitational radiation and the prospect of its experimental discovery," *Sov. Phys. Usp.* **8**, 513–521 (1966).

[14] V. B. Braginsky and A. B. Manukin, "Ponderomotive effects of electromagnetic radiation," *Sov. Phys. JETP* **25**, 653–655 (1967).

[15] V. B. Braginsky, Y. I. Vorontsov, and F. Y. Khalili, "Optimal quantum measurements in detectors of gravitation radiation," *JETP Lett.* **27**, 276–280 (1978).

[16] V. B. Braginsky, A. B. Manukin, and M. Y. Tikhonov, "Investigation of dissipative ponderomotive effects of electromagnetic radiation," *Sov. Phys. JETP* **31**, 829–830 (1970).

[17] A. Dorsel, J. D. McCullen, P. Meystre, E. Vignes, and H. Walther, "Optical bistability and mirror confinement induced by radiation pressure," *Phys. Rev. Lett.* **51**, 1550–1553 (1983).

[18] A. Abramovici, W. E. Althouse, R. W. P. Drever, Y. Gürsel, S. Kawamura, F. J. Raab, D. Shoemaker, L. Sievers, R. E. Spero, K. S. Thorne, R. E. Vogt, R. Weiss, S. E. Whitcomb, and M. E. Zucker, "LIGO: The Laser Interferometer Gravitational-Wave Observatory," *Science* **256**, 325–333 (1992).

[19] B. P. Abbott *et al.* (LIGO Scientific Collaboration and Virgo Collaboration), "Observation of gravitational waves from a binary black hole merger," *Phys. Rev. Lett.* **116**, 061102 (2016).

[20] I. Tittonen, G. Breitenbach, T. Kalkbrenner, T. Müller, R. Conradt, S. Schiller, E. Steinsland, N. Blanc, and N. F. de Rooij, "Interferometric measurements of the position of a macroscopic body: Towards observation of quantum limits," *Phys. Rev. A* **59**, 1038–1044 (1999).

[21] M. Vogel, C. Mooser, K. Karrai, and R. J. Warburton, "Optically tunable mechanics of microlevers," *Appl. Phys. Lett.* **83**, 1337–1339 (2003).

[22] C. Höhberger Metzger and K. Karrai, "Cavity cooling of a microlever," *Nature* **432**, 1002–1005 (2004).

[23] J. G. E. Harris, B. M. Zwickl, and A. M. Jayich, "Stable, mode-matched, medium-finesse optical cavity incorporating a microcantilever mirror: Optical characterization and laser cooling," *Rev. Sci. Instrum.* **78**, 013107 (2007).

[24] I. Favero, C. Metzger, S. Camerer, D. König, H. Lorenz, J. P. Kotthaus, and K. Karrai, "Optical cooling of a micromirror of wavelength size," *Appl. Phys. Lett.* **90**, 104101 (2007).

[25] G. Jourdan, F. Comin, and J. Chevrier, "Mechanical mode dependence of bolometric backaction in an atomic force microscopy microlever," *Phys. Rev. Lett.* **101**, 133904 (2008).

[26] S. Gigan, H. R. Böhm, M. Paternostro, F. Blaser, G. Langer, J. B. Hertzberg, K. C. Schwab, D. Bäuerle, M. Aspelmeyer, and A. Zeilinger, "Self-cooling of a micromirror by radiation pressure," *Nature* **444**, 67–70 (2006).

[27] D. Kleckner, W. Marshall, M. J. A. de Dood, K. N. Dinyari, B.-J. Pors, W. T. M. Irvine, and D. Bouwmeester, "High finesse opto-mechanical cavity with a movable thirty-micron-size mirror," *Phys. Rev. Lett.* **96**, 173901 (2006).

[28] H. R. Böhm, S. Gigan, F. Blaser, A. Zeilinger, M. Aspelmeyer, G. Langer, D. Bäuerle, J. B. Hertzberg, and K. C. Schwab, "High reflectivity high-Q micromechanical bragg mirror," *Appl. Phys. Lett.* **89**, 223101 (2006).

[29] S. Gröblacher, J. B. Hertzberg, M. R. Vanner, G. D. Cole, S. Gigan, K. C. Schwab, and M. Aspelmeyer, "Demonstration of an ultracold micro-optomechanical oscillator in a cryogenic cavity," *Nat. Phys.* **5**, 485–488 (2009).

[30] G. D. Cole, Y. Bai, M. Aspelmeyer, and E. A. Fitzgerald, "Free-standing $Al_xGa_{1-x}As$ heterostructures by gas-phase etching of germanium," *Appl. Phys. Lett.* **96**, 261102 (2010).

[31] D. Kleckner, B. Pepper, E. Jeffrey, P. Sonin, S. M. Thon, and D. Bouwmeester, "Optomechanical trampoline resonators," *Opt. Express* **19**, 19708–19716 (2011).

[32] E. Serra, A. Borrielli, F. S. Cataliotti, F. Marin, F. Marino, A. Pontin, G. A. Prodi, and M. Bonaldi, "Ultralow-dissipation micro-oscillator for quantum optomechanics," *Phys. Rev. A* **86**, 051801 (2012).

[33] A. G. Kuhn, M. Bahriz, O. Ducloux, C. Chartier, O. Le Traon, T. Briant, P.-F. Cohadon, A. Heidmann, C. Michel, L. Pinard, and R. Flaminio, "A micropillar for cavity optomechanics," *Appl. Phys. Lett.* **99**, 121103 (2011).

[34] S. Anguiano, A. E. Bruchhausen, B. Jusserand, I. Favero, F. R. Lamberti, L. Lanco, I. Sagnes, A. Lemaître, N. D. Lanzillotti-Kimura, P. Senellart, and A. Fainstein, "Micropillar resonators for optomechanics in the extremely high 19–95-GHz frequency range," *Phys. Rev. Lett.* **118**, 263901 (2017).

[35] J. D. Thompson, B. M. Zwickl, A. M. Jayich, F. Marquardt, S. M. Girvin, and J. G. E. Harris, "Strong dispersive coupling of a high-finesse cavity to a micromechanical membrane," *Nature* **452**, 72–75 (2008).

[36] A. M. Jayich, J. C. Sankey, B. M. Zwickl, C. Yang, J. D. Thompson, S. M. Girvin, A. A. Clerk, F. Marquardt, and J. G. E. Harris, "Dispersive optomechanics: a membrane inside a cavity," *New J. Phys.* **10**, 095008 (2008).

[37] D. J. Wilson, C. A. Regal, S. B. Papp, and H. J. Kimble, "Cavity optomechanics with stoichiometric SiN films," *Phys. Rev. Lett.* **103**, 207204 (2009).

[38] J. Liu, K. Usami, A. Naesby, T. Bagci, E. S. Polzik, P. Lodahl, and S. Stobbe, "High-Q optomechanical GaAs nanomembranes," *Appl. Phys. Lett.* **99**, 243102 (2011).

[39] U. Kemiktarak, M. Metcalfe, M. Durand, and J. Lawall, "Mechanically compliant grating reflectors for optomechanics," *Appl. Phys. Lett.* **100**, 061124 (2012).

[40] I. Favero, S. Stapfner, D. Hunger, P. Paulitschke, J. Reichel, H. Lorenz, E. M. Weig, and K. Karrai, "Fluctuating nanomechanical system in a high finesse optical microcavity," *Opt. Express* **17**, 12813–12820 (2009).

[41] S. Kuhn, P. Asenbaum, A. Kosloff, M. Sclafani, B. A. Stickler, S. Nimmrichter, K. Hornberger, O. Cheshnovsky, F. Patolsky, and M. Arndt, "Cavity-assisted manipulation of freely rotating silicon nanorods in high vacuum," *Nano Lett.* **15**, 5604–5608 (2015).

[42] F. Fogliano, B. Besga, A. Reigue, P. Heringlake, L. Mercier de Lépinay, C. Vaneph, J. Reichel, B. Pigeau, and O. Arcizet, "Cavity nano-optomechanics in the ultrastrong coupling regime with ultrasensitive force sensors," arXiv:1904.01140 (2019).

[43] J. Gieseler, B. Deutsch, R. Quidant, and L. Novotny, "Subkelvin parametric feedback cooling of a laser-trapped nanoparticle," *Phys. Rev. Lett.* **109**, 103603 (2012).

[44] N. Kiesel, F. Blaser, U. Delić, D. Grass, R. Kaltenbaek, and M. Aspelmeyer, "Cavity cooling of an optically levitated submicron particle," *Proc. Natl. Acad. Sci.* **110**, 14180–14185 (2013).

[45] G. Ranjit, D. P. Atherton, J. H. Stutz, M. Cunningham, and A. A. Geraci, "Attonewton force detection using microspheres in a dual-beam optical trap in high vacuum," *Phys. Rev. A* **91**, 051805 (2015).

[46] K. W. Murch, K. L. Moore, S. Gupta, and D. M. Stamper-Kurn, "Observation of quantum-measurement backaction with an ultracold atomic gas," *Nat. Phys.* **4**, 561–564 (2008).

[47] F. Brennecke, S. Ritter, T. Donner, and T. Esslinger, "Cavity optomechanics with a Bose-Einstein condensate," *Science* **322**, 235–238 (2008).

[48] T. P. Purdy, D. W. C. Brooks, T. Botter, N. Brahms, Z.-Y. Ma, and D. M. Stamper-Kurn, "Tunable cavity optomechanics with ultracold atoms," *Phys. Rev. Lett.* **105**, 133602 (2010).

[49] M. H. Schleier-Smith, I. D. Leroux, H. Zhang, M. A. Van Camp, and V. Vuletić, "Optomechanical cavity cooling of an atomic ensemble," *Phys. Rev. Lett.* **107**, 143005 (2011).

[50] S. Camerer, M. Korppi, A. Jöckel, D. Hunger, T. W. Hänsch, and P. Treutlein, "Realization of an optomechanical interface between ultracold atoms and a membrane," *Phys. Rev. Lett.* **107**, 223001 (2011).

[51] M. Hossein-Zadeh, H. Rokhsari, A. Hajimiri, and K. J. Vahala, "Characterization of a radiation-pressure-driven micromechanical oscillator," *Phys. Rev. A* **74**, 023813 (2006).

[52] A. Schliesser, P. Del'Haye, N. Nooshi, K. J. Vahala, and T. J. Kippenberg, "Radiation pressure cooling of a micromechanical oscillator using dynamical backaction," *Phys. Rev. Lett.* **97**, 243905 (2006).

[53] G. Anetsberger, O. Arcizet, Q. P. Unterreithmeier, R. Rivière, A. Schliesser, E. M. Weig, J. P. Kotthaus, and T. J. Kippenberg, "Near-field cavity optomechanics with nanomechanical oscillators," *Nat. Phys.* **5**, 909–914 (2009).

[54] R. Ma, A. Schliesser, P. Del'Haye, A. Dabirian, G. Anetsberger, and T. J. Kippenberg, "Radiation-pressure-driven vibrational modes in ultrahigh-Q silica microspheres," *Opt. Lett.* **32**, 2200–2202 (2007).

[55] Y.-S. Park and H. Wang, "Resolved-sideband and cryogenic cooling of an optomechanical resonator," *Nat. Phys.* **5**, 489–493 (2009).

[56] M. Tomes and T. Carmon, "Photonic micro-electromechanical systems vibrating at X-band (11-GHz) rates," *Phys. Rev. Lett.* **102**, 113601 (2009).

[57] V. Fiore, Y. Yang, M. C. Kuzyk, R. Barbour, L. Tian, and H. Wang, "Storing optical information as a mechanical excitation in a silica optomechanical resonator," *Phys. Rev. Lett.* **107**, 133601 (2011).

[58] A. J. R. MacDonald, G. G. Popowich, B. D. Hauer, P. H. Kim, A. Fredrick, X. Rojas, P. Doolin, and J. P. Davis, "Optical microscope and tapered fiber coupling apparatus for a dilution refrigerator," *Rev. Sci. Instrum.* **86**, 013107 (2015).

[59] A. J. R. MacDonald, B. D. Hauer, X. Rojas, P. H. Kim, G. G. Popowich, and J. P. Davis, "Optomechanics and thermometry of cryogenic silica microresonators," *Phys. Rev. A* **93**, 013836 (2016).

[60] X. Jiang, Q. Lin, J. Rosenberg, K. Vahala, and O. Painter, "High-Q double-disk microcavities for cavity optomechanics," *Opt. Express* **17**, 20911–20919 (2009).

[61] G. S. Wiederhecker, L. Chen, A. Gondarenko, and M. Lipson, "Controlling photonic structures using optical forces," *Nature* **462**, 633–636 (2009).

[62] L. Ding, C. Baker, P. Senellart, A. Lemaitre, S. Ducci, G. Leo, and I. Favero, "Wavelength-sized GaAs optomechanical resonators with gigahertz frequency," *Appl. Phys. Lett.* **98**, 113108 (2011).

[63] C. Doolin, B. D. Hauer, P. H. Kim, A. J. R. MacDonald, H. Ramp, and J. P. Davis, "Nonlinear optomechanics in the stationary regime," *Phys. Rev. A* **89**, 053838 (2014).

[64] M. Eichenfield, R. Camacho, J. Chan, K. J. Vahala, and O. Painter, "A picogram- and nanometre-scale photonic-crystal optomechanical cavity," *Nature* **459**, 550–555 (2009).

[65] A. H. Safavi-Naeini, T. P. Mayer Alegre, M. Winger, and O. Painter, "Optomechanics in an ultrahigh-Q two-dimensional photonic crystal cavity," *Appl. Phys. Lett.* **97**, 181106 (2010).

[66] Y.-G. Roh, T. Tanabe, A. Shinya, H. Taniyama, E. Kuramochi, S. Matsuo, T. Sato, and M. Notomi, "Strong optomechanical interaction in a bilayer photonic crystal," *Phys. Rev. B* **81**, 121101 (2010).

[67] J. Chan, A. H. Safavi-Naeini, J. T. Hill, S. Meenehan, and O. Painter, "Optimized optomechanical crystal cavity with acoustic radiation shield," *Appl. Phys. Lett.* **101**, 081115 (2012).

[68] E. Gavartin, R. Braive, I. Sagnes, O. Arcizet, A. Beveratos, T. J. Kippenberg, and I. Robert-Philip, "Optomechanical coupling in a two-dimensional photonic crystal defect cavity," *Phys. Rev. Lett.* **106**, 203902 (2011).

[69] T. Antoni, A. G. Kuhn, T. Briant, P.-F. Cohadon, A. Heidmann, R. Braive, A. Beveratos, I. Abram, L. L. Gratiet, I. Sagnes, and I. Robert-Philip, "Deformable two-dimensional photonic crystal slab for cavity optomechanics," *Opt. Lett.* **36**, 3434–3436 (2011).

[70] M. Wu, A. C. Hryciw, C. Healey, D. P. Lake, H. Jayakumar, M. R. Freeman, J. P. Davis, and P. E. Barclay, "Dissipative and dispersive optomechanics in a nanocavity torque sensor," *Phys. Rev. X* **4**, 021052 (2014).

[71] A. H. Safavi-Naeini, J. T. Hill, S. Meenehan, J. Chan, S. Gröblacher, and O. Painter, "Two-dimensional phononic-photonic band gap optomechanical crystal cavity," *Phys. Rev. Lett.* **112**, 153603 (2014).

[72] B. D. Cuthbertson, M. E. Tobar, E. N. Ivanov, and D. G. Blair, "Parametric back-action effects in a high-Q cyrogenic sapphire transducer," *Rev. Sci. Instrum.* **67**, 2435–2442 (1996).

[73] C. A. Regal, J. D. Teufel, and K. W. Lehnert, "Measuring nanomechanical motion with a microwave cavity interferometer," *Nat. Phys.* **4**, 555–560 (2008).

[74] J.-M. Pirkkalainen, S. U. Cho, J. Li, G. S. Paraoanu, P. J. Hakonen, and M. A. Sillanpää, "Hybrid circuit cavity quantum electrodynamics with a micromechanical resonator," *Nature* **494**, 211–215 (2013).

[75] M. A. Sillanpää, J. Sarkar, J. Sulkko, J. Muhonen, and P. J. Hakonen, "Accessing nanomechanical resonators via a fast microwave circuit," *Appl. Phys. Lett.* **95**, 011909 (2009).

[76] T. Rocheleau, T. Ndukum, C. Macklin, J. B. Hertzberg, A. A. Clerk, and K. C. Schwab, "Preparation and detection of a mechanical resonator near the ground state of motion," *Nature* **463**, 72–75 (2010).

[77] F. Massel, T. T. Heikkilä, J.-M. Pirkkalainen, S. U. Cho, H. Saloniemi, P. J. Hakonen, and M. A. Sillanpää, "Microwave amplification with nanomechanical resonators," *Nature* **480**, 351–354 (2011).

[78] L. A. De Lorenzo and K. C. Schwab, "Superfluid optomechanics: Coupling of a superfluid to a superconducting condensate," *New J. Phys.* **16**, 113020 (2014).

[79] X. Rojas and J. P. Davis, "Superfluid nanomechanical resonator for quantum nanofluidics," *Phys. Rev. B* **91**, 024503 (2015).

[80] G. I. Harris, D. L. McAuslan, E. Sheridan, Y. Sachkou, C. Baker, and W. P. Bowen, "Laser cooling and control of excitations in superfluid helium," *Nat. Phys.* **12**, 788–793 (2016).

[81] A. D. Kashkanova, A. B. Shkarin, C. D. Brown, N. E. Flowers-Jacobs, L. Childress, S. W. Hoch, L. Hohmann, K. Ott, J. Reichel, and J. G. E. Harris, "Superfluid Brillouin optomechanics," *Nat. Phys.* **13**, 74–79 (2017).

[82] A. D. Kashkanova, A. B. Shkarin, C. D. Brown, N. E. Flowers-Jacobs, L. Childress, S. W. Hoch, L. Hohmann, K. Ott, J. Reichel, and J. G. E. Harris, "Optomechanics in superfluid helium coupled to a fiber-based cavity," *J. Opt.* **19**, 034001 (2017).

[83] C. Brown, "Optical, Mechanical and Thermal Properties of Superfluid Liquid Helium Drops Magnetically-Levitated in Vacuum," PhD thesis (Yale University, 2019).

[84] A. J. Shook, V. Vadakumbatt, P. Senarath Yapa, C. Doolin, R. Boyack, P. H. Kim, G. G. Popowich, F. Souris, H. Christani, J. Maciejko, and J. P. Davis, "Stabilized pair density wave via nanoscale confinement of superfluid ^{3}He," arXiv:1908.01779 (2019).

[85] M. Wu, N. L.-Y. Wu, T. Firdous, F. Fani Sani, J. E. Losby, M. R. Freeman, and P. E. Barclay, "Nanocavity optomechanical torque magnetometry and radiofrequency susceptometry," *Nat. Nanotechnol.* **12**, 127–131 (2016).

[86] P. H. Kim, F. Fani Sani, M. R. Freeman, and J. P. Davis, "Broadband optomechanical transduction of nanomagnetic spin modes," *Appl. Phys. Lett.* **113**, 083104 (2018).

[87] C. Belacel, Y. Todorov, S. Barbieri, D. Gacemi, I. Favero, and C. Sirtori, "Optomechanical terahertz detection with single meta-atom resonator," *Nat. Commun.* **8**, 1578 (2017).

[88] O. Arcizet, P.-F. Cohadon, T. Briant, M. Pinard, A. Heidmann, J.-M. Mackowski, C. Michel, L. Pinard, O. Français, and L. Rousseau, "High-sensitivity optical monitoring of a micromechanical resonator with a quantum-limited optomechanical sensor," *Phys. Rev. Lett.* **97**, 133601 (2006).

[89] Y. Hadjar, P. F. Cohadon, C. G. Aminoff, M. Pinard, and A. Heidmann, "High-sensitivity optical measurement of mechanical Brownian motion," *Europhys. Lett.* **47**, 545–551 (1999).

[90] A. Schliesser, G. Anetsberger, R. Rivière, O. Arcizet, and T. J. Kippenberg, "High-sensitivity monitoring of micromechanical vibration using optical whispering gallery mode resonators," *New J. Phys.* **10**, 095015 (2008).

[91] A. G. Krause, M. Winger, T. D. Blasius, Q. Lin, and O. Painter, "A high-resolution microchip optomechanical accelerometer," *Nat. Photonics* **6**, 768–772 (2012).

[92] J. D. Teufel, T. Donner, M. A. Castellanos-Beltran, J. W. Harlow, and K. W. Lehnert, "Nanomechanical motion measured with an imprecision below that at the standard quantum limit," *Nat. Nanotechnol.* **4**, 820–823 (2009).

[93] K. Srinivasan, H. Miao, M. T. Rakher, M. Davanço, and V. Aksyuk, "Optomechanical transduction of an integrated silicon cantilever probe using a microdisk resonator," *Nano Lett.* **11**, 791–797 (2011).

[94] E. Gavartin, P. Verlot, and T. J. Kippenberg, "A hybrid on-chip optomechanical transducer for ultrasensitive force measurements," *Nat. Nanotechnol.* **7**, 509–514 (2012).

[95] G. Ranjit, M. Cunningham, K. Casey, and A. A. Geraci, "Zeptonewton force sensing with nanospheres in an optical lattice," *Phys. Rev. A* **93**, 053801 (2016).

[96] D. Mason, J. Chen, M. Rossi, Y. Tsaturyan, and A. Schliesser, "Continuous force and displacement measurement below the standard quantum limit," *Nat. Phys.* **15**, 745–749 (2019).

[97] P. H. Kim, C. Doolin, B. D. Hauer, A. J. R. MacDonald, M. R. Freeman, P. E. Barclay, and J. P. Davis, "Nanoscale torsional optomechanics," *Appl. Phys. Lett.* **102**, 053102 (2013).

[98] P. H. Kim, B. D. Hauer, C. Doolin, F. Souris, and J. P. Davis, "Approaching the standard quantum limit of mechanical torque sensing," *Nat. Commun.* **7**, 13165 (2016).

[99] L. He, H. Li, and M. Li, "Optomechanical measurement of photon spin angular momentum and optical torque in integrated photonic devices," *Sci. Adv.* **2**, e1600485 (2016).

[100] T. S. Biswas, J. Xu, N. Miriyala, C. Doolin, T. Thundat, J. P. Davis, and K. S. D. Beach, "Time-resolved mass sensing of a molecular adsorbate nonuniformly distributed along a nanomechanical string," *Phys. Rev. Appl.* **3**, 064002 (2015).

[101] X. C. Zhang, E. B. Myers, J. E. Sader, and M. L. Roukes, "Nanomechanical torsional resonators for frequency-shift infrared thermal sensing," *Nano Lett.* **13**, 1528–1534 (2013).

[102] D. Rugar, R. Budakian, H. J. Mamin, and B. W. Chui, "Single spin detection by magnetic resonance force microscopy," *Nature* **430**, 329–332 (2004).

[103] S. Forstner, S. Prams, J. Knittel, E. D. van Ooijen, J. D. Swaim, G. I. Harris, A. Szorkovszky, W. P. Bowen, and H. Rubinsztein-Dunlop, "Cavity optomechanical magnetometer," *Phys. Rev. Lett.* **108**, 120801 (2012).

[104] P. H. Kim, B. D. Hauer, T. J. Clark, F. Fani Sani, M. R. Freeman, and J. P. Davis, "Magnetic actuation and feedback cooling of a cavity optomechanical torque sensor," *Nat. Commun.* **8**, 1355 (2017).

[105] W. Yu, W. C. Jiang, Q. Lin, and T. Lu, "Cavity optomechanical spring sensing of single molecules," *Nat. Commun.* **7**, 12311 (2016).

[106] J. D. Teufel, T. Donner, D. Li, J. W. Harlow, M. S. Allman, K. Cicak, A. J. Sirois, J. D. Whittaker, K. W. Lehnert, and R. W. Simmonds, "Sideband cooling of micromechanical motion to the quantum ground state," *Nature* **475**, 359–363 (2011).

[107] J. Chan, T. P. Mayer Alegre, A. H. Safavi-Naeini, J. T. Hill, A. Krause, S. Gröblacher, M. Aspelmeyer, and O. Painter, "Laser cooling of a nanomechanical oscillator into its quantum ground state," *Nature* **478**, 89–92 (2011).

[108] A. H. Safavi-Naeini, J. Chan, J. T. Hill, T. P. Mayer Alegre, A. Krause, and O. Painter, "Observation of quantum motion of a nanomechanical resonator," *Phys. Rev. Lett.* **108**, 033602 (2012).

[109] A. J. Weinstein, C. U. Lei, E. E. Wollman, J. Suh, A. Metelmann, A. A. Clerk, and K. C. Schwab, "Observation and interpretation of motional sideband asymmetry in a quantum electromechanical device," *Phys. Rev. X* **4**, 041003 (2014).

[110] A. H. Safavi-Naeini, S. Gröblacher, J. T. Hill, J. Chan, M. Aspelmeyer, and O. Painter, "Squeezed light from a silicon micromechanical resonator," *Nature* **500**, 185–189 (2013).

[111] E. E. Wollman, C. U. Lei, A. J. Weinstein, J. Suh, A. Kronwald, F. Marquardt, A. A. Clerk, and K. C. Schwab, "Quantum squeezing of motion in a mechanical resonator," *Science* **349**, 952–955 (2015).

[112] J.-M. Pirkkalainen, E. Damskägg, M. Brandt, F. Massel, and M. A. Sillanpää, "Squeezing of quantum noise of motion in a micromechanical resonator," *Phys. Rev. Lett.* **115**, 243601 (2015).

[113] C. F. Ockeloen-Korppi, E. Damskägg, J.-M. Pirkkalainen, M. Asjad, A. A. Clerk, F. Massel, M. J. Woolley, and M. A. Sillanpää, "Stabilized entanglement of massive mechanical oscillators," *Nature* **556**, 478–482 (2018).

[114] F. Lecocq, J. B. Clark, R. W. Simmonds, J. Aumentado, and J. D. Teufel, "Quantum nondemolition measurement of a nonclassical state of a massive object," *Phys. Rev. X* **5**, 041037 (2015).

[115] C. U. Lei, A. J. Weinstein, J. Suh, E. E. Wollman, A. Kronwald, F. Marquardt, A. A. Clerk, and K. C. Schwab, "Quantum nondemolition measurement of a quantum squeezed state beyond the 3 dB limit," *Phys. Rev. Lett.* **117**, 100801 (2016).

[116] J. B. Hertzberg, T. Rocheleau, T. Ndukum, M. Savva, A. A. Clerk, and K. C. Schwab, "Back-action-evading measurements of nanomechanical motion," *Nat. Phys.* **6**, 213–217 (2010).

[117] J. Suh, A. J. Weinstein, C. U. Lei, E. E. Wollman, S. K. Steinke, P. Meystre, A. A. Clerk, and K. C. Schwab, "Mechanically detecting and avoiding the quantum fluctuations of a microwave field," *Science* **344**, 1262–1265 (2014).

[118] I. Shomroni, L. Qiu, D. Malz, A. Nunnenkamp, and T. J. Kippenberg, "Optical backaction-evading measurement of a mechanical oscillator," *Nat. Commun.* **10**, 2086 (2019).

[119] D. J. Wilson, V. Sudhir, N. Piro, R. Schilling, A. Ghadimi, and T. J. Kippenberg, "Measurement-based control of a mechanical oscillator at its thermal decoherence rate," *Nature* **524**, 325–329 (2015).

[120] M. Rossi, D. Mason, J. Chen, Y. Tsaturyan, and A. Schliesser, "Measurement-based quantum control of mechanical motion," *Nature* **563**, 53–58 (2018).

[121] M. Rossi, D. Mason, J. Chen, and A. Schliesser, "Observing and verifying the quantum trajectory of a mechanical resonator," *Phys. Rev. Lett.* **123**, 163601 (2019).

[122] J. Guo, R. A. Norte, and S. Gröblacher, "Feedback cooling of a room temperature mechanical oscillator close to its motional groundstate," arXiv:1911.01586 (2019).

[123] J. Bochmann, A. Vainsencher, D. D. Awschalom, and A. N. Cleland, "Nanomechanical coupling between microwave and optical photons," *Nat. Phys.* **9**, 712–716 (2013).

[124] R. W. Andrews, R. W. Peterson, T. P. Purdy, K. Cicak, R. W. Simmonds, C. A. Regal, and K. W. Lehnert, "Bidirectional and efficient conversion between microwave and optical light," *Nat. Phys.* **10**, 321–326 (2014).

[125] M. Forsch, R. Stockill, A. Wallucks, I. Marinković, C. Gärtner, R. A. Norte, F. van Otten, A. Fiore, K. Srinivasan, and S. Gröblacher, "Microwave-to-optics conversion using a mechanical oscillator in its quantum ground state," *Nat. Phys.* (2019).

[126] T. A. Palomaki, J. W. Harlow, J. D. Teufel, R. W. Simmonds, and K. W. Lehnert, "Coherent state transfer between itinerant microwave fields and a mechanical oscillator," *Nature* **495**, 210–214 (2013).

[127] A. P. Reed, K. H. Mayer, J. D. Teufel, L. D. Burkhart, W. Pfaff, M. Reagor, L. Sletten, X. Ma, R. J. Schoelkopf, E. Knill, and K. W. Lehnert, "Faithful conversion of propagating quantum information to mechanical motion," *Nat. Phys.* **13**, 1163–1167 (2017).

[128] S. Bose, K. Jacobs, and P. L. Knight, "Scheme to probe the decoherence of a macroscopic object," *Phys. Rev. A* **59**, 3204–3210 (1999).

[129] W. Marshall, C. Simon, R. Penrose, and D. Bouwmeester, "Towards quantum superpositions of a mirror," *Phys. Rev. Lett.* **91**, 130401 (2003).

[130] O. Romero-Isart, A. C. Pflanzer, F. Blaser, R. Kaltenbaek, N. Kiesel, M. Aspelmeyer, and J. I. Cirac, "Large quantum superpositions and interference of massive nanometer-sized objects," *Phys. Rev. Lett.* **107**, 020405 (2011).

[131] Y. Chen, "Macroscopic quantum mechanics: theory and experimental concepts of optomechanics," *J. Phys. B* **46**, 104001 (2013).

[132] I. Pikovski, M. R. Vanner, M. Aspelmeyer, M. S. Kim, and Č. Brukner, "Probing Planck-scale physics with quantum optics," *Nat. Phys.* **8**, 393–397 (2012).

[133] C. Pfister, J. Kaniewski, M. Tomamichel, A. Mantri, R. Schmucker, N. McMahon, G. Milburn, and S. Wehner, "A universal test for gravitational decoherence," *Nat. Commun.* **7**, 13022 (2016).

[134] A. Belenchia, D. M. T. Benincasa, S. Liberati, F. Marin, F. Marino, and A. Ortolan, "Testing quantum gravity induced nonlocality via optomechanical quantum oscillators," *Phys. Rev. Lett.* **116**, 161303 (2016).

[135] G. S. MacCabe, H. Ren, J. Luo, J. D. Cohen, H. Zhou, A. Sipahigil, M. Mirhosseini, and O. Painter, "Phononic bandgap nano-acoustic cavity with ultralong phonon lifetime," arXiv:1901.04129 (2019).

[136] J. D. Cohen, S. M. Meenehan, G. S. MacCabe, S. Gröblacher, A. H. Safavi-Naeini, F. Marsili, M. D. Shaw, and O. Painter, "Phonon counting and intensity interferometry of a nanomechanical resonator," *Nature* **520**, 522–525 (2015).

[137] R. Riedinger, S. Hong, R. A. Norte, J. A. Slater, J. Shang, A. G. Krause, V. Anant, M. Aspelmeyer, and S. Gröblacher, "Non-classical correlations between single photons and phonons from a mechanical oscillator," *Nature* **530**, 313–316 (2016).

[138] H. Ren, M. H. Matheny, G. S. MacCabe, J. Luo, H. Pfeifer, M. Mirhosseini, and O. Painter, "Two-dimensional optomechanical crystal cavity with high quantum cooperativity," arXiv:1910.02873 (2019).

[139] A. Wallucks, I. Marinković, B. Hensen, R. Stockill, and S. Gröblacher, "A quantum memory at telecom wavelengths," arXiv:1910.07409 (2019).

[140] J. T. Hill, A. H. Safavi-Naeini, J. Chan, and O. Painter, "Coherent optical wavelength conversion via cavity optomechanics," *Nat. Commun.* **3**, 1196 (2012).

[141] S. Hong, R. Riedinger, I. Marinković, A. Wallucks, S. G. Hofer, R. A. Norte, M. Aspelmeyer, and S. Gröblacher, "Hanbury Brown and Twiss interferometry of single phonons from an optomechanical resonator," *Science* **358**, 203–206 (2017).

[142] R. Riedinger, A. Wallucks, I. Marinković, C. Löschnauer, M. Aspelmeyer, S. Hong, and S. Gröblacher, "Remote quantum entanglement between two micromechanical oscillators," *Nature* **556**, 473–477 (2018).

[143] I. Marinković, A. Wallucks, R. Riedinger, S. Hong, M. Aspelmeyer, and S. Gröblacher, "Optomechanical Bell test," *Phys. Rev. Lett.* **121**, 220404 (2018).

[144] L. D. Landau, E. M. Lifshitz, A. M. Kosevich, and L. P. Pitaevskii, *Theory of Elasticity*, 3rd edition, Vol. 7, Course of Theoretical Physics (Butterworth-Heinemann, Oxford, 1986).

[145] B. D. Hauer, C. Doolin, K. S. D. Beach, and J. P. Davis, "A general procedure for thermomechanical calibration of nano/micro-mechanical resonators," *Ann. Phys.* **339**, 181–207 (2013).

[146] M. Eichenfield, J. Chan, A. H. Safavi-Naeini, K. J. Vahala, and O. Painter, "Modeling dispersive coupling and losses of localized optical and mechanical modes in optomechanical crystals," *Opt. Express* **17**, 20078–20098 (2009).

[147] V. S. Ilchenko, A. A. Savchenkov, A. B. Matsko, and L. Maleki, "Whispering-gallery-mode electro-optic modulator and photonic microwave receiver," *J. Opt. Soc. Am. B* **20**, 333–342 (2003).

[148] M. Pinard, Y. Hadjar, and A. Heidmann, "Effective mass in quantum effects of radiation pressure," *Eur. Phys. J. D* **7**, 107–116 (1999).

[149] A. N. Cleland, *Foundations of Nanomechanics: From Solid-State Theory to Device Applications* (Springer, Berlin, 2003).

[150] M. Aspelmeyer, T. J. Kippenberg, and F. Marquardt, "Cavity optomechanics," *Rev. Mod. Phys.* **86**, 1391–1452 (2014).

[151] B. D. Hauer, J. Maciejko, and J. P. Davis, "Nonlinear power spectral densities for the harmonic oscillator," *Ann. Phys.* **361**, 148–183 (2015).

[152] V. B. Braginsky, V. P. Mitrofanov, and V. I. Panov, *Systems with Small Dissipation*, edited by K. S. Thorne and C. Eller, translated by E. Gliner (University of Chicago Press, Chicago, 1985).

[153] M. Bao, *Analysis and Design Principles of MEMS Devices* (Elsevier Science, Amsterdam, 2005).

[154] C. Kittel, *Quantum Theory of Solids*, 2nd edition (Wiley, New York, 1987).

[155] W. P. Mason, *Physical Acoustics and the Properties of Solids*, Bell Telephone Laboratories Series (Van Nostrand, Princeton, 1958).

[156] S. Timoshenko and J. N. Goodier, *Theory of Elasticity*, 3rd edition, Engineering Societies Monographs (McGraw-Hill, New York, 1970).

[157] A. E. H. Love, *A Treatise on the Mathematical Theory of Elasticity*, 4th edition (Cambridge University Press, Cambridge, 1927).

[158] M. F. Beatty, "Introduction to Nonlinear Elasticity," Chap. 2 in *Nonlinear Effects in Fluids and Solids*, Vol. 45, Mathematical Concepts and Methods in Science and Engineering, edited by M. M. Carroll and M. A. Hayes (Springer, Boston, 1996).

[159] E. H. Dill, *Continuum Mechanics: Elasticity, Plasticity, and Viscoelasticity*, 1st edition (CRC Press, Boca Raton, 2006).

[160] W. M. Lai, D. Rubin, and E. Krempl, *Introduction to Continuum Mechanics*, 4th edition (Butterworth-Heinemann, Woburn, 2009).

[161] Y. I. Dimitrienko, *Nonlinear Continuum Mechanics and Large Inelastic Deformations*, 1st edition, Vol. 174, Solid Mechanics and Its Applications, edited by G. M. L. Gladwell (Springer, Dordrecht, 2011).

[162] R. O. Behunin, F. Intravaia, and P. T. Rakich, "Dimensional transformation of defect-induced noise, dissipation, and nonlinearity," *Phys. Rev. B* **93**, 224110 (2016).

[163] B. D. Hauer, P. H. Kim, C. Doolin, F. Souris, and J. P. Davis, "Two-level system damping in a quasi-one-dimensional optomechanical resonator," *Phys. Rev. B* **98**, 214303 (2018).

[164] J. L. Rose, *Ultrasonic Guided Waves in Solid Media* (Cambridge University Press, Cambridge, 2014).

[165] J. J. Wortman and R. A. Evans, "Young's modulus, shear modulus, and Poisson's ratio in silicon and germanium," *J. Appl. Phys.* **36**, 153–156 (1965).

[166] W. A. Brantley, "Calculated elastic constants for stress problems associated with semiconductor devices," *J. Appl. Phys.* **44**, 534–535 (1973).

[167] M. A. Hopcroft, W. D. Nix, and T. W. Kenny, "What is the young's modulus of silicon?" *J. Microelectromech. Syst.* **19**, 229–238 (2010).

[168] L. Zhang, R. Barrett, P. Cloetens, C. Detlefs, and M. Sanchez del Rio, "Anisotropic elasticity of silicon and its application to the modelling of X-ray optics," *J. Synchrotron Rad.* **21**, 507–517 (2014).

[169] P. M. Morse and H. Feshbach, *Methods of Theoretical Physics*, International Series in Pure and Applied Physics (McGraw-Hill, New York, 1953).

[170] E. B. Christoffel, "Ueber die fortpflanzung von stössen durch elastische feste körper," *Ann. Mat. Pura Appl.* **8**, 193–243 (1877).

[171] G. P. Srivastava, *The Physics of Phonons*, 1st edition (CRC Press, Boca Raton, 1990).

[172] *COMSOL Multiphysics*®, v. 5.4 (2018), `https://www.comsol.com`, COMSOL AB, Stockholm, Sweden.

[173] J. D. Achenbach, *Wave Propagation in Elastic Solids*, Vol. 16, Applied Mathematics and Mechanics, edited by H. A. Lauwerier and W. T. Koiter (Elsevier Science, Amsterdam, 1973).

[174] M. H. Sadd, *Elasticity: Theory, Applications, and Numerics*, 3rd edition (Academic Press, Boston, 2014).

[175] T. Ramos, V. Sudhir, K. Stannigel, P. Zoller, and T. J. Kippenberg, "Nonlinear quantum optomechanics via individual intrinsic two-level defects," *Phys. Rev. Lett.* **110**, 193602 (2013).

[176] R. P. Feynman and F. L. Vernon, "The theory of a general quantum system interacting with a linear dissipative system," *Ann. Phys.* **24**, 118–173 (1963).

[177] A. O. Caldeira and A. J. Leggett, "Influence of dissipation on quantum tunneling in macroscopic systems," *Phys. Rev. Lett.* **46**, 211–214 (1981).

[178] A. O. Caldeira and A. J. Leggett, "Quantum tunnelling in a dissipative system," *Ann. Phys.* **149**, 374–456 (1983).

[179] A. O. Caldeira and A. J. Leggett, "Path integral approach to quantum Brownian motion," *Physica A* **121**, 587–616 (1983).

[180] R. Bowley and M. Sanchez, *Introductory Statistical Mechanics*, 2nd edition (Clarendon Press, Oxford, 1999).

[181] A.-T. Petit and P.-L. Dulong, "Researches on some important points of the Theory of Heat," *Ann. Philos.* **14**, 189–198 (1819).

[182] N. W. Ashcroft and N. D. Mermin, *Solid State Physics*, 1st edition (Brooks Cole, Belmont, 1976).

[183] P. Debye, "Zur theorie der spezifischen wärmen," *Ann. der Phys.* **344**, 789–839 (1912).

[184] A. K. McCurdy, H. J. Maris, and C. Elbaum, "Anisotropic heat conduction in cubic crystals in the boundary scattering regime," *Phys. Rev. B* **2**, 4077–4083 (1970).

[185] H. J. Maris and S. Tamura, "Heat flow in nanostructures in the Casimir regime," *Phys. Rev. B* **85**, 054304 (2012).

[186] J. R. Rumble, editor, *CRC Handbook of Chemistry and Physics*, 100th edition (CRC Press, Boca Raton, 2019).

[187] C. Enss and S. Hunklinger, *Low-Temperature Physics* (Springer, Berlin, 2005).

[188] F. Pobell, *Matter and Methods at Low Temperatures*, 3rd edition (Springer, Berlin, 2007).

[189] C. Kittel, *Introduction to Solid State Physics*, 8th edition (Wiley, Hoboken, 2005).

[190] P. H. Keesom and G. Seidel, "Specific heat of germanium and silicon at low temperatures," *Phys. Rev.* **113**, 33–39 (1959).

[191] P. Flubacher, A. J. Leadbetter, and J. A. Morrison, "The heat capacity of pure silicon and germanium and properties of their vibrational frequency spectra," *Philos. Mag.* **4**, 273–294 (1959).

[192] L. Weber and E. Gmelin, "Transport properties of silicon," *Appl. Phys. A* **53**, 136–140 (1991).

[193] R. Peierls, "Zur kinetischen theorie der wärmeleitung in kristallen," *Ann. der Phys.* **395**, 1055–1101 (1929).

[194] W. J. De Haas and T. Biermasz, "The thermal conductivity of KBr, KCl and SiO_2 at low temperatures," *Physica* **4**, 752–756 (1937).

[195] H. B. G. Casimir, "Note on the conduction of heat in crystals," *Physica* **5**, 495–500 (1938).

[196] J. M. Ziman, *Electrons and Phonons: The Theory of Transport Phenomena in Solids*, Oxford Classic Texts in the Physical Sciences (Oxford University Press, Oxford, 2001).

[197] J. S. Heron, T. Fournier, N. Mingo, and O. Bourgeois, "Mesoscopic size effects on the thermal conductance of silicon nanowire," *Nano Lett.* **9**, 1861–1865 (2009).

[198] J.-S. Heron, C. Bera, T. Fournier, N. Mingo, and O. Bourgeois, "Blocking phonons via nanoscale geometrical design," *Phys. Rev. B* **82**, 155458 (2010).

[199] D. G. Cahill, P. V. Braun, G. Chen, D. R. Clarke, S. Fan, K. E. Goodson, P. Keblinski, W. P. King, G. D. Mahan, A. Majumdar, H. J. Maris, S. R. Phillpot, E. Pop, and L. Shi, "Nanoscale thermal transport. II. 2003–2012," *Appl. Phys. Rev.* **1**, 011305 (2014).

[200] R. Lifshitz and M. L. Roukes, "Thermoelastic damping in micro- and nanomechanical systems," *Phys. Rev. B* **61**, 5600–5609 (2000).

[201] C. Seoánez, F. Guinea, and A. H. Castro Neto, "Surface dissipation in nanoelectromechanical systems: Unified description with the standard tunneling model and effects of metallic electrodes," *Phys. Rev. B* **77**, 125107 (2008).

[202] V. B. Braginsky and F. Y. Khalili, *Quantum Measurement*, edited by K. S. Thorne (Cambridge University Press, Cambridge, 1995).

[203] A. A. Clerk, M. H. Devoret, S. M. Girvin, F. Marquardt, and R. J. Schoelkopf, "Introduction to quantum noise, measurement, and amplification," *Rev. Mod. Phys.* **82**, 1155–1208 (2010).

[204] S. M. Meenehan, J. D. Cohen, G. S. MacCabe, F. Marsili, M. D. Shaw, and O. Painter, "Pulsed excitation dynamics of an optomechanical crystal resonator near its quantum ground state of motion," *Phys. Rev. X* **5**, 041002 (2015).

[205] C. Zener, "Internal friction in solids. I. Theory of internal friction in reeds," *Phys. Rev.* **52**, 230–235 (1937).

[206] C. Zener, "Internal friction in solids II. General theory of thermoelastic internal friction," *Phys. Rev.* **53**, 90–99 (1938).

[207] C. Zener, W. Otis, and R. Nuckolls, "Internal friction in solids III. Experimental demonstration of thermoelastic internal friction," *Phys. Rev.* **53**, 100–101 (1938).

[208] C. Zener, *Elasticity and Anelasticity of Metals* (University of Chicago Press, Chicago, 1948).

[209] A. S. Nowick and B. S. Berry, *Anelastic Relaxation in Crystalline Solids*, Materials Science Series, edited by A. M. Alper, J. L. Margrave, and A. S. Nowick (Academic Press, New York, 1972).

[210] A. Akhiezer, "On the absorption of sound in solids," *J. Phys. (USSR)* **1**, 277–287 (1939).

[211] H. E. Bömmel and K. Dransfeld, "Excitation and attenuation of hypersonic waves in quartz," *Phys. Rev.* **117**, 1245–1252 (1960).

[212] T. O. Woodruff and H. Ehrenreich, "Absorption of sound in insulators," *Phys. Rev.* **123**, 1553–1559 (1961).

[213] L. Landau and G. Rumer, "On the absorption of sound in solids," *Phys. Z. Sowjet.* **11**, 18 (1937).

[214] P. G. Klemens, "Effect of Thermal and Phonon Processes on Ultrasonic Attenuation," Chap. 5 in *Physical Acoustics: Lattice Dynamics*, Vol. 3, edited by W. P. Mason (Academic Press, New York, 1965).

[215] W. P. Mason, "Effect of Impurities and Phonon Processes on the Ultrasonic Attenuation of Germanium, Crystal Quartz, and Silicon," Chap. 6 in *Physical Acoustics: Lattice Dynamics*, Vol. 3, edited by W. P. Mason (Academic Press, New York, 1965).

[216] P. W. Sparks and C. A. Swenson, "Thermal expansions from 2 to 40° K of Ge, Si, and four III-V compounds," *Phys. Rev.* **163**, 779–790 (1967).

[217] R. H. Carr, R. D. McCammon, and G. K. White, "Thermal expansion of germanium and silicon at low temperatures," *Philos. Mag.* **12**, 157–163 (1965).

[218] K. G. Lyon, G. L. Salinger, C. A. Swenson, and G. K. White, "Linear thermal expansion measurements on silicon from 6 to 340 K," *J. Appl. Phys.* **48**, 865–868 (1977).

[219] T. Middelmann, A. Walkov, G. Bartl, and R. Schödel, "Thermal expansion coefficient of single-crystal silicon from 7 K to 293 K," *Phys. Rev. B* **92**, 174113 (2015).

[220] P. W. Anderson, B. I. Halperin, and C. M. Varma, "Anomalous low-temperature thermal properties of glasses and spin glasses," *Philos. Mag.* **25**, 1–9 (1972).

[221] W. A. Phillips, "Tunneling states in amorphous solids," *J. Low Temp. Phys.* **7**, 351–360 (1972).

[222] W. A. Phillips, "Two-level states in glasses," *Rep. Prog. Phys.* **50**, 1657–1708 (1987).

[223] P. Esquinazi, *Tunneling Systems in Amorphous and Crystalline Solids* (Springer, Berlin, 1998).

[224] I. Pomeranchuk, "On the thermal conductivity of dielectrics at temperatures lower than that of Debye," *J. Phys. USSR* **6**, 237 (1942).

[225] P. G. Klemens, "The scattering of low-frequency lattice waves by static imperfections," *Proc. Phys. Soc. A* **68**, 1113–1128 (1955).

[226] P. G. Klemens, "Thermal Conductivity and Lattice Vibrational Modes," Chap. 1 in *Solid State Physics*, Vol. 7, Advances in Research and Applications, edited by F. Seitz and D. Turnbull (Academic Press, New York, 1958).

[227] P. Carruthers, "Theory of thermal conductivity of solids at low temperatures," *Rev. Mod. Phys.* **33**, 92–138 (1961).

[228] S. Tamura, "Isotope scattering of dispersive phonons in Ge," *Phys. Rev. B* **27**, 858–866 (1983).

[229] S. Tamura, J. A. Shields, and J. P. Wolfe, "Lattice dynamics and elastic phonon scattering in silicon," *Phys. Rev. B* **44**, 3001–3011 (1991).

[230] A. V. Inyushkin, A. N. Taldenkov, J. W. Ager, E. E. Haller, H. Riemann, N. V. Abrosimov, H.-J. Pohl, and P. Becker, "Ultrahigh thermal conductivity of isotopically enriched silicon," *J. Appl. Phys.* **123**, 095112 (2018).

[231] N. V. Abrosimov *et al.*, "A new generation of 99.999% enriched ^{28}Si single crystals for the determination of Avogadro's constant," *Metrologia* **54**, 599–609 (2017).

[232] B. Andreas *et al.*, "Determination of the Avogadro constant by counting the atoms in a ^{28}Si crystal," *Phys. Rev. Lett.* **106**, 030801 (2011).

[233] B. Andreas *et al.*, "Counting the atoms in a ^{28}Si crystal for a new kilogram definition," *Metrologia* **48**, S1–S13 (2011).

[234] A. D. McConnell and K. E. Goodson, "Thermal Conduction in Silicon Micro- and Nanostructures," Chap. II.3 in *Annual Review of Heat Transfer*, Vol. 14, edited by V. Prasad, Y. Jaluria, and G. Chen (Begell House, Danbury, 2005).

[235] C. A. Ratsifaritana and P. G. Klemens, "Scattering of phonons by vacancies," *Int. J. Thermophys.* **8**, 737–750 (1987).

[236] G. D. Watkins, "The vacancy in silicon: identical diffusion properties at cryogenic and elevated temperatures," *J. Appl. Phys.* **103**, 106106 (2008).

[237] Y. Shimuzu, M. Uematsu, and K. M. Itoh, "Experimental evidence of the vacancy-mediated silicon self-diffusion in single-crystalline silicon," *Phys. Rev. Lett.* **98**, 095901 (2007).

[238] V. V. Voronkov and R. Falster, "Vacancy and self-interstitial concentration incorporated into growing silicon crystals," *J. Appl. Phys.* **86**, 5975–5982 (1999).

[239] R. B. Bhiladvala and Z. J. Wang, "Effect of fluids on the q factor and resonance frequency of oscillating micrometer and nanometer scale beams," *Phys. Rev. E* **69**, 036307 (2004).

[240] S. Bianco, M. Cocuzza, S. Ferrero, E. Giuri, G. Piacenza, C. F. Pirri, A. Ricci, L. Scaltrito, D. Bich, A. Merialdo, P. Schina, and R. Correale, "Silicon resonant microcantilevers for absolute pressure measurement," *J. Vac. Sci. Technol. B* **24**, 1803–1809 (2006).

[241] A. H. Nayfeh and M. I. Younis, "A new approach to the modeling and simulation of flexible microstructures under the effect of squeeze-film damping," *J. Micromech. Microeng.* **14**, 170–181 (2004).

[242] S. S. Verbridge, R. Ilic, H. G. Craighead, and J. M. Parpia, "Size and frequency dependent gas damping of nanomechanical resonators," *Appl. Phys. Lett.* **93**, 013101 (2008).

[243] T. Veijola, "Compact models for squeezed-film dampers with inertial and rarefied gas effects," *J. Micromech. Microeng.* **14**, 1109–1118 (2004).

[244] S. Matteucci, Y. Yampolskii, B. D. Freeman, and I. Pinnau, "Transport of Gases and Vapors in Glassy and Rubbery Polymers," Chap. 1 in *Materials Science of Membranes for Gas and Vapor Separation*, edited by Y. Yampolskii, B. D. Freeman, and I. Pinnau (Wiley, Chichester, 2006).

[245] F. R. Blom, S. Bouwstra, M. Elwenspoek, and J. H. J. Fluitman, "Dependence of the quality factor of micromachined silicon beam resonators on pressure and geometry," *J. Vac. Sci. Technol. B* **10**, 19–26 (1992).

[246] M. Bao, H. Yang, H. Yin, and Y. Sun, "Energy transfer model for squeeze-film air damping in low vacuum," *J. Micromech. Microeng.* **12**, 341–346 (2002).

[247] R. G. Christian, "The theory of oscillating-vane vacuum gauges," *Vacuum* **16**, 175–178 (1966).

[248] Y. Jimbo and K. Itao, "Energy loss of a cantilever vibrator," *J. Horological Inst. Jpn.* **47**, 1–15 (1968).

[249] M. C. Cross and R. Lifshitz, "Elastic wave transmission at an abrupt junction in a thin plate with application to heat transport and vibrations in mesoscopic systems," *Phys. Rev. B* **64**, 085324 (2001).

[250] Z. Hao, A. Erbil, and F. Ayazi, "An analytical model for support loss in micromachined beam resonators with in-plane flexural vibrations," *Sens. Act. A* **109**, 156–164 (2003).

[251] D. M. Photiadis and J. A. Judge, "Attachment losses of high Q oscillators," *Appl. Phys. Lett.* **85**, 482–484 (2004).

[252] J. A. Judge, D. M. Photiadis, J. F. Vignola, B. H. Houston, and J. Jarzynski, "Attachment loss of micromechanical and nanomechanical resonators in the limits of thick and thin support structures," *J. Appl. Phys.* **101**, 013521 (2007).

[253] I. Wilson-Rae, "Intrinsic dissipation in nanomechanical resonators due to phonon tunneling," *Phys. Rev. B* **77**, 245418 (2008).

[254] T. P. Mayer Alegre, A. Safavi-Naeini, M. Winger, and O. Painter, "Quasi-two-dimensional optomechanical crystals with a complete phononic bandgap," *Opt. Express* **19**, 5658–5669 (2011).

[255] P.-L. Yu, K. Cicak, N. S. Kampel, Y. Tsaturyan, T. P. Purdy, R. W. Simmonds, and C. A. Regal, "A phononic bandgap shield for high-Q membrane microresonators," *Appl. Phys. Lett.* **104**, 023510 (2014).

[256] Y. Tsaturyan, A. Barg, E. S. Polzik, and A. Schliesser, "Ultracoherent nanomechanical resonators via soft clamping and dissipation dilution," *Nat. Nanotechnol.* **12**, 776–783 (2017).

[257] A. H. Ghadimi, S. A. Fedorov, N. J. Engelsen, M. J. Bereyhi, R. Schilling, D. J. Wilson, and T. J. Kippenberg, "Elastic strain engineering for ultralow mechanical dissipation," *Science* **360**, 764–768 (2018).

[258] J. D. Jackson, *Classical Electrodynamics*, 3rd edition (Wiley, New York, 1998).

[259] J. Vučković, C. Santorit, D. Fattal, M. Pelton, G. S. Solomon, and Y. Yamamoto, "Cavity-Enhanced Single Photons from a Quantum Dot," Chap. 4 in *Optical Microcavities*, Vol. 5, Advanced Series in Applied Physics, edited by K. Vahala (World Scientific, Singapore, 2004).

[260] R. Loudon, *The Quantum Theory of Light*, 3rd edition (Oxford University Press, Oxford, 2000).

[261] D. F. Walls and G. J. Milburn, *Quantum Optics*, 2nd edition (Springer, Berlin, 2008).

[262] A. H. Safavi-Naeini, "Quantum Optomechanics with Silicon Nanostructures," PhD thesis (California Institute of Technology, 2013).

[263] B. J. Frey, D. B. Leviton, and T. J. Madison, "Temperature-dependent refractive index of silicon and germanium," in Optomechanical Technologies for Astronomy, Proc. SPIE **6273**, 790–799 (International Society for Optics and Photonics, 2006).

[264] J. Komma, C. Schwarz, G. Hofmann, D. Heinert, and R. Nawrodt, "Thermo-optic coefficient of silicon at 1550 nm and cryogenics temperatures," *Appl. Phys. Lett.* **101**, 041905 (2012).

[265] M. K. Chin, D. Y. Chu, and S. Ho, "Estimation of the spontaneous emission factor for microdisk lasers via the approximation of whispering gallery modes," *J. Appl. Phys.* **75**, 3302–3307 (1994).

[266] M. Borselli, "High-Q Microresonators as Lasing Elements for Silicon Photonics," PhD thesis (California Institute of Technology, 2006).

[267] H. Haus, W. Huang, S. Kawakami, and N. Whitaker, "Coupled-mode theory of optical waveguides," *J. Light. Technol.* **5**, 16–23 (1987).

[268] B. E. Little, S. T. Chu, H. A. Haus, J. Foresi, and J.-P. Laine, "Microring resonator channel dropping filters," *J. Light. Technol.* **15**, 998–1005 (1997).

[269] C. Manolatou, M. J. Khan, S. Fan, P. R. Villeneuve, H. A. Haus, and J. D. Joannopoulos, "Coupling of modes analysis of resonant channel add-drop filters," *J. Quant. Elec.* **35**, 1322–1331 (1999).

[270] M. Cai, O. Painter, and K. J. Vahala, "Observation of critical coupling in a fiber taper to a silica-microsphere whispering-gallery mode system," *Phys. Rev. Lett.* **85**, 74–77 (2000).

[271] R. D. Kekatpure and M. L. Brongersma, "Fundamental photophysics and optical loss processes in Si-nanocrystal-doped microdisk resonators," *Phys. Rev. A* **78**, 023829 (2008).

[272] J. Degallaix, J. Komma, D. Forest, G. Hofmann, M. Granata, D. Heinert, C. Schwarz, R. Nawrodt, L. Pinard, C. Michel, R. Flaminio, and G. Cagnoli, "Measurement of the optical absorption of bulk silicon at cryogenic temperature and the implication for the Einstein Telescope," *Class. Quantum Grav.* **31**, 185010 (2014).

[273] J. Degallaix, R. Flaminio, D. Forest, M. Granata, C. Michel, L. Pinard, T. Bertrand, and G. Cagnoli, "Bulk optical absorption of high resistivity silicon at 1550 nm," *Opt. Lett.* **38**, 2047–2049 (2013).

[274] M. Borselli, T. J. Johnson, and O. Painter, "Measuring the role of surface chemistry in silicon microphotonics," *Appl. Phys. Lett.* **88**, 131114 (2006).

[275] M. Kuznetsov and H. Haus, "Radiation loss in dielectric waveguide structures by the volume current method," *J. Quant. Elec.* **19**, 1505–1514 (1983).

[276] M. Borselli, K. Srinivasan, P. E. Barclay, and O. Painter, "Rayleigh scattering, mode coupling, and optical loss in silicon microdisks," *Appl. Phys. Lett.* **85**, 3693–3695 (2004).

[277] M. Borselli, T. J. Johnson, and O. Painter, "Beyond the Rayleigh scattering limit in high-Q silicon microdisks: Theory and experiment," *Opt. Express* **13**, 1515–1530 (2005).

[278] N. C. Frateschi and A. F. J. Levi, "The spectrum of microdisk lasers," *J. Appl. Phys.* **80**, 644–653 (1996).

[279] S. G. Johnson, M. Ibanescu, M. A. Skorobogatiy, O. Weisberg, J. D. Joannopoulos, and Y. Fink, "Perturbation theory for Maxwell's equations with shifting material boundaries," *Phys. Rev. E* **65**, 066611 (2002).

[280] D. K. Biegelsen, "Photoelastic tensor of silicon and the volume dependence of the average gap," *Phys. Rev. Lett.* **32**, 1196–1199 (1974).

[281] J. Chan, "Laser Cooling of an Optomechanical Crystal Resonator to Its Quantum Ground State of Motion," PhD thesis (California Institute of Technology, 2012).

[282] C. Baker, W. Hease, D.-T. Nguyen, A. Andronico, S. Ducci, G. Leo, and I. Favero, "Photoelastic coupling in gallium arsenide optomechanical disk resonators," *Opt. Express* **22**, 14072–14086 (2014).

[283] F. Elste, S. M. Girvin, and A. A. Clerk, "Quantum noise interference and backaction cooling in cavity nanomechanics," *Phys. Rev. Lett.* **102**, 207209 (2009).

[284] A. Xuereb, R. Schnabel, and K. Hammerer, "Dissipative optomechanics in a Michelson-Sagnac interferometer," *Phys. Rev. Lett.* **107**, 213604 (2011).

[285] T. Weiss and A. Nunnenkamp, "Quantum limit of laser cooling in dispersively and dissipatively coupled optomechanical systems," *Phys. Rev. A* **88**, 023850 (2013).

[286] M. Li, W. H. P. Pernice, and H. X. Tang, "Reactive cavity optical force on microdisk-coupled nanomechanical beam waveguides," *Phys. Rev. Lett.* **103**, 223901 (2009).

[287] C. Gardiner and P. Zoller, *Quantum Noise: A Handbook of Markovian and Non-Markovian Quantum Stochastic Methods with Applications to Quantum Optics*, 3rd edition, Springer Series in Synergetics (Springer, Berlin, 2004).

[288] H. M. Wiseman and G. J. Milburn, *Quantum Measurement and Control* (Cambridge University Press, Cambridge, 2010).

[289] M. Pinard and A. Dantan, "Quantum limits of photothermal and radiation pressure cooling of a movable mirror," *New J. Phys.* **10**, 095012 (2008).

[290] J. Restrepo, J. Gabelli, C. Ciuti, and I. Favero, "Classical and quantum theory of photothermal cavity cooling of a mechanical oscillator," *C. R. Physique* **12**, 860–870 (2011).

[291] M. Abdi and A. R. Bahrampour, "Improving the optomechanical entanglement and cooling by photothermal force," *Phys. Rev. A* **85**, 063839 (2012).

[292] M. Aspelmeyer, T. J. Kippenberg, and F. Marquardt, *Cavity Optomechanics*, 1st edition, Quantum Science and Technology, edited by N. Gisin, R. Laflamme, G. Lenhart, D. Lidar, G. J. Milburn, M. Ohya, A. Rauschenbeutel, R. Renner, M. Schlosshauer, and H. M. Wiseman (Springer, Berlin, 2014).

[293] F. Marquardt, J. P. Chen, A. A. Clerk, and S. M. Girvin, "Quantum theory of cavity-assisted sideband cooling of mechanical motion," *Phys. Rev. Lett.* **99**, 093902 (2007).

[294] S. De Liberato, N. Lambert, and F. Nori, "Quantum noise in photothermal cooling," *Phys. Rev. A* **83**, 033809 (2011).

[295] B. D. Hauer, T. J. Clark, P. H. Kim, C. Doolin, and J. P. Davis, "Dueling dynamical backaction in a cryogenic optomechanical cavity," *Phys. Rev. A* **99**, 053803 (2019).

[296] M. L. Gorodetksy, A. Schliesser, G. Anetsberger, S. Deleglise, and T. J. Kippenberg, "Determination of the vacuum optomechanical coupling rate using frequency noise calibration," *Opt. Express* **18**, 23236–23246 (2010).

[297] A. Schliesser, O. Arcizet, R. Rivière, G. Anetsberger, and T. J. Kippenberg, "Resolved-sideband cooling and position measurement of a micromechanical oscillator close to the Heisenberg uncertainty limit," *Nat. Phys.* **5**, 509–514 (2009).

[298] A. G. Krause, T. D. Blasius, and O. Painter, "Optical read out and feedback cooling of a nanostring optomechanical cavity," arXiv:1506.01249 (2015).

[299] J. D. Teufel, F. Lecocq, and R. W. Simmonds, "Overwhelming thermomechanical motion with microwave radiation pressure shot noise," *Phys. Rev. Lett.* **116**, 013602 (2016).

[300] V. B. Braginsky, S. E. Strigin, and S. P. Vyatchanin, "Parametric oscillatory instability in Fabry–Perot interferometer," *Phys. Lett. A* **287**, 331–338 (2001).

[301] F. Marquardt, J. G. E. Harris, and S. M. Girvin, "Dynamical multistability induced by radiation pressure in high-finesse micromechanical optical cavities," *Phys. Rev. Lett.* **96**, 103901 (2006).

[302] M. Ludwig, B. Kubala, and F. Marquardt, "The optomechanical instability in the quantum regime," *New J. Phys.* **10**, 095013 (2008).

[303] C. Metzger, M. Ludwig, C. Neuenhahn, A. Ortlieb, I. Favero, K. Karrai, and F. Marquardt, "Self-induced oscillations in an optomechanical system driven by bolometric backaction," *Phys. Rev. Lett.* **101**, 133903 (2008).

[304] A. G. Krause, J. T. Hill, M. Ludwig, A. H. Safavi-Naeini, J. Chan, F. Marquardt, and O. Painter, "Nonlinear radiation pressure dynamics in an optomechanical crystal," *Phys. Rev. Lett.* **115**, 233601 (2015).

[305] F. M. Buters, H. J. Eerkens, K. Heeck, M. J. Weaver, B. Pepper, S. de Man, and D. Bouwmeester, "Experimental exploration of the optomechanical attractor diagram and its dynamics," *Phys. Rev. A* **92**, 013811 (2015).

[306] T. Carmon, H. Rokhsari, L. Yang, T. J. Kippenberg, and K. J. Vahala, "Temporal behavior of radiation-pressure-induced vibrations of an optical microcavity phonon mode," *Phys. Rev. Lett.* **94**, 223902 (2005).

[307] T. J. Kippenberg, H. Rokhsari, T. Carmon, A. Scherer, and K. J. Vahala, "Analysis of radiation-pressure induced mechanical oscillation of an optical microcavity," *Phys. Rev. Lett.* **95**, 033901 (2005).

[308] H. Rokhsari, T. J. Kippenberg, T. Carmon, and K. J. Vahala, "Radiation-pressure-driven micro-mechanical oscillator," *Opt. Express* **13**, 5293–5301 (2005).

[309] A. MacDonald, "Cryogenic Optomechanics with Silica Microresonators," Master's thesis (University of Alberta, 2015).

[310] A. Schliesser, R. Rivière, G. Anetsberger, O. Arcizet, and T. J. Kippenberg, "Resolved-sideband cooling of a micromechanical oscillator," *Nat. Phys.* **4**, 415–419 (2008).

[311] M. Ludwig, "Collective Quantum Effects in Optomechanical Systems," PhD thesis (Friedrich-Alexander-Universität Erlangen-Nürnberg, 2013).

[312] B. D. Hauer, P. H. Kim, C. Doolin, A. J. R. MacDonald, H. Ramp, and J. P. Davis, "On-chip cavity optomechanical coupling," *EPJ Tech. Instrum.* **1**, 4 (2014).

[313] P. H.-C. Kim, "Passive and active cooling of cavity optomechanical torque sensors for magnetometry applications," PhD thesis (University of Alberta, 2019).

[314] Y. J. Chabal, G. S. Higashi, K. Raghavachari, and V. A. Burrows, "Infrared spectroscopy of Si(111) and Si(100) surfaces after HF treatment: Hydrogen termination and surface morphology," *J. Vac. Sci. Technol. A* **7**, 2104–2109 (1989).

[315] G. S. Higashi, Y. J. Chabal, G. W. Trucks, and K. Raghavachari, "Ideal hydrogen termination of the Si (111) surface," *Appl. Phys. Lett.* **56**, 656–658 (1990).

[316] D. K. Sparacin, S. J. Spector, and L. C. Kimerling, "Silicon waveguide sidewall smoothing by wet chemical oxidation," *J. Light. Technol.* **23**, 2455–2461 (2005).

[317] Y.-S. Park, A. K. Cook, and H. Wang, "Cavity QED with diamond nanocrystals and silica microspheres," *Nano Lett.* **6**, 2075–2079 (2006).

[318] D. Taillaert, P. Bienstman, and R. Baets, "Compact efficient broadband grating coupler for silicon-on-insulator waveguides," *Opt. Lett.* **29**, 2749–2751 (2004).

[319] M. Li, W. H. P. Pernice, C. Xiong, T. Baehr-Jones, M. Hochberg, and H. X. Tang, "Harnessing optical forces in integrated photonic circuits," *Nature* **456**, 480–484 (2008).

[320] R. Marchetti, C. Lacava, A. Khokhar, X. Chen, I. Cristiani, D. J. Richardson, G. T. Reed, P. Petropoulos, and P. Minzioni, "High-efficiency grating-couplers: Demonstration of a new design strategy," *Sci. Rep.* **7**, 16670 (2017).

[321] V. R. Almeida, R. R. Panepucci, and M. Lipson, "Nanotaper for compact mode conversion," *Opt. Lett.* **28**, 1302–1304 (2003).

[322] S. Gröblacher, J. T. Hill, A. H. Safavi-Naeini, J. Chan, and O. Painter, "Highly efficient coupling from an optical fiber to a nanoscale silicon optomechanical cavity," *Appl. Phys. Lett.* **103**, 181104 (2013).

[323] J. D. Cohen, S. M. Meenehan, and O. Painter, "Optical coupling to nanoscale optomechanical cavities for near quantum-limited motion transduction," *Opt. Express* **21**, 11227–11236 (2013).

[324] J. C. Knight, G. Cheung, F. Jacques, and T. A. Birks, "Phase-matched excitation of whispering-gallery-mode resonances by a fiber taper," *Opt. Lett.* **22**, 1129–1131 (1997).

[325] P. E. Barclay, K. Srinivasan, M. Borselli, and O. Painter, "Efficient input and output fiber coupling to a photonic crystal waveguide," *Opt. Lett.* **29**, 697–699 (2004).

[326] C. P. Michael, M. Borselli, T. J. Johnson, C. Chrystal, and O. Painter, "An optical fiber-taper probe for wafer-scale microphotonic device characterization," *Opt. Express* **15**, 4745–4752 (2007).

[327] J.-P. Laine, B. E. Little, and H. A. Haus, "Etch-eroded fiber coupler for whispering-gallery-mode excitation in high-Q silica microspheres," *IEEE Photon. Technol. Lett.* **11**, 1429–1430 (1999).

[328] E. J. Zhang, W. D. Sacher, and J. K. S. Poon, "Hydrofluoric acid flow etching of low-loss subwavelength-diameter biconical fiber tapers," *Opt. Express* **18**, 22593–22598 (2010).

[329] L. Tong, R. R. Gattass, J. B. Ashcom, S. He, J. Lou, M. Shen, I. Maxwell, and E. Mazur, "Subwavelength-diameter silica wires for low-loss optical wave guiding," *Nature* **426**, 816–819 (2003).

[330] G. Brambilla, V. Finazzi, and D. J. Richardson, "Ultra-low-loss optical fiber nanotapers," *Opt. Express* **12**, 2258–2263 (2004).

[331] T. E. Dimmick, G. Kakarantzas, T. A. Birks, and P. S. J. Russell, "Carbon dioxide laser fabrication of fused-fiber couplers and tapers," *Appl. Opt.* **38**, 6845–6848 (1999).

[332] G. Kakarantzas, T. E. Dimmick, T. A. Birks, R. L. Roux, and P. S. J. Russell, "Miniature all-fiber devices based on CO_2 laser microstructuring of tapered fibers," *Opt. Lett.* **26**, 1137–1139 (2001).

[333] J. M. Ward, D. G. O'Shea, B. J. Shortt, M. J. Morrissey, K. Deasy, and S. G. Nic Chormaic, "Heat-and-pull rig for fiber taper fabrication," *Rev. Sci. Instrum.* **77**, 083105 (2006).

[334] L. Ding, C. Belacel, S. Ducci, G. Leo, and I. Favero, "Ultralow loss single-mode silica tapers manufactured by a microheater," *Appl. Opt.* **49**, 2441–2445 (2010).

[335] T. A. Birks and Y. W. Li, "The shape of fiber tapers," *J. Light. Technol.* **10**, 432–438 (1992).

[336] K. Okamoto, *Fundamentals of Optical Waveguides*, 2nd edition (Academic Press, Burlington, 2006).

[337] I. H. Malitson, "Interspecimen comparison of the refractive index of fused silica," *J. Opt. Soc. Am.* **55**, 1205–1209 (1965).

[338] M. Pöllinger, D. O'Shea, F. Warken, and A. Rauschenbeutel, "Ultrahigh-Q tunable whispering-gallery-mode microresonator," *Phys. Rev. Lett.* **103**, 053901 (2009).

[339] K. Srinivasan, P. E. Barclay, M. Borselli, and O. J. Painter, "An optical-fiber-based probe for photonic crystal microcavities," *IEEE J. Sel. Areas Commun.* **23**, 1321–1329 (2005).

[340] Attocube Systems, *Power dissipation of a piezo*, White Paper.

[341] R. O. Pohl, X. Liu, and E. Thompson, "Low-temperature thermal conductivity and acoustic attenuation in amorphous solids," *Rev. Mod. Phys.* **74**, 991–1013 (2002).

[342] R. N. Kleiman, G. Agnolet, and D. J. Bishop, "Two-level systems observed in the mechanical properties of single-crystal silicon at low temperatures," *Phys. Rev. Lett.* **59**, 2079–2082 (1987).

[343] R. E. Mihailovich and J. M. Parpia, "Anomalous low temperature mechanical properties of single-crystal silicon," *Physica B* **165/166**, 125–126 (1990).

[344] W. A. Phillips, "Comment on Two-level systems observed in the mechanical properties of single-crystal silicon at low temperatures," *Phys. Rev. Lett.* **61**, 2632 (1988).

[345] R. W. Keyes, "Two-level systems in the mechanical properties of silicon at low temperatures," *Phys. Rev. Lett.* **62**, 1324 (1989).

[346] F. Hoehne, Y. A. Pashkin, O. Astafiev, L. Faoro, L. B. Ioffe, Y. Nakamura, and J. S. Tsai, "Damping in high-frequency metallic nanomechanical resonators," *Phys. Rev. B* **81**, 184112 (2010).

[347] G. Zolfagharkhani, A. Gaidarzhy, S.-B. Shim, R. L. Badzey, and P. Mohanty, "Quantum friction in nanomechanical oscillators at millikelvin temperatures," *Phys. Rev. B* **72**, 224101 (2005).

[348] S. B. Shim, J. S. Chun, S. W. Kang, S. W. Cho, S. W. Cho, and Y. D. Park, "Micromechanical resonators fabricated from lattice-matched and etch-selective GaAs/InGaP/GaAs heterostructures," *Appl. Phys. Lett.* **91**, 133505 (2007).

[349] M. Imboden and P. Mohanty, "Evidence of universality in the dynamical response of micromechanical diamond resonators at millikelvin temperatures," *Phys. Rev. B* **79**, 125424 (2009).

[350] A. K. Hüttel, G. A. Steele, B. Witkamp, M. Poot, L. P. Kouwenhoven, and H. S. J. van der Zant, "Carbon nanotubes as ultrahigh quality factor mechanical resonators," *Nano Lett.* **9**, 2547–2552 (2009).

[351] K.-H. Ahn and P. Mohanty, "Quantum friction of micromechanical resonators at low temperatures," *Phys. Rev. Lett.* **90**, 085504 (2003).

[352] H. Jiang, M.-F. Yu, B. Liu, and Y. Huang, "Intrinsic energy loss mechanisms in a cantilevered carbon nanotube beam oscillator," *Phys. Rev. Lett.* **93**, 185501 (2004).

[353] P. Mohanty, D. A. Harrington, K. L. Ekinci, Y. T. Yang, M. J. Murphy, and M. L. Roukes, "Intrinsic dissipation in high-frequency micromechanical resonators," *Phys. Rev. B* **66**, 085416 (2002).

[354] R. C. Zeller and R. O. Pohl, "Thermal conductivity and specific heat of noncrystalline solids," *Phys. Rev. B* **4**, 2029–2041 (1971).

[355] J. Jäckle, "On the ultrasonic attenuation in glasses at low temperatures," *Z. Phys.* **257**, 212–223 (1972).

[356] J. Jäckle, L. Piché, W. Arnold, and S. Hunklinger, "Elastic effects of structural relaxation in glasses at low temperatures," *J. Non-Chryst. Solids* **20**, 365–391 (1976).

[357] W. Heinicke, G. Winterling, and K. Dransfeld, "Low-temperature measurement of the hypersonic absorption in fused quartz by stimulated brillouin scattering," *J. Acoust. Soc. Am.* **49**, 954–958 (1971).

[358] A. J. Leggett, S. Chakravarty, A. T. Dorsey, M. P. A. Fisher, A. Garg, and W. Zwerger, "Dynamics of the dissipative two-state system," *Rev. Mod. Phys.* **59**, 1–85 (1987).

[359] D. V. Anghel, T. Kühn, Y. M. Galperin, and M. Manninen, "Interaction of two-level systems in amorphous materials with arbitrary phonon fields," *Phys. Rev. B* **75**, 064202 (2007).

[360] S. Hunklinger and W. Arnold, "Ultrasonic Properties of Glasses at Low Temperatures," Chap. 3 in *Physical Acoustics: Principles and Methods*, Vol. 12, edited by W. P. Mason and R. N. Thurston (Academic Press, New York, 1976).

[361] C. Doolin, "Integrated optical and mechanical resonators for evanescent field sensing," PhD thesis (University of Alberta, 2019).

[362] E. Lai, *Practical Digital Signal Processing for Engineers and Technicians* (Newnes, Oxford, 2003).

[363] J. Gao, M. Daal, A. Vayonakis, S. Kumar, J. Zmuidzinas, B. Sadoulet, B. A. Mazin, P. K. Day, and H. G. LeDuc, "Experimental evidence for a surface distribution of two-level systems in superconducting lithographed microwave resonators," *Appl. Phys. Lett.* **92**, 152505 (2008).

[364] J. Suh, M. D. Shaw, H. G. LeDuc, A. J. Weinstein, and K. C. Schwab, "Thermally induced parametric instability in a back-action evading measurement of a micromechanical quadrature near the zero-point level," *Nano Lett.* **12**, 6260–6265 (2012).

[365] J. Suh, A. J. Weinstein, and K. C. Schwab, "Optomechanical effects of two-level systems in a back-action evading measurement of micro-mechanical motion," *Appl. Phys. Lett.* **103**, 052604 (2013).

[366] G. K. White, "The thermal conductivity of gold at low temperatures," *Proc. Phys. Soc. A* **66**, 559–564 (1953).

[367] M. G. Holland, "Analysis of lattice thermal conductivity," *Phys. Rev.* **132**, 2461–2471 (1963).

[368] B. Golding, J. E. Graebner, and R. J. Schutz, "Intrinsic decay lengths of quasimonochromatic phonons in a glass below 1 K," *Phys. Rev. B* **14**, 1660–1662 (1976).

[369] B. Golding and J. E. Graebner, "Phonon echoes in glass," *Phys. Rev. Lett.* **37**, 852–855 (1976).

[370] B. Golding, J. E. Graebner, and A. B. Kane, "Phase velocity of high-frequency phonons in glass below 1 K," *Phys. Rev. Lett.* **37**, 1248–1250 (1976).

[371] X. Liu, J. F. Vignola, H. J. Simpson, B. R. Lemon, B. H. Houston, and D. M. Photiadis, "A loss mechanism study of a very high Q silicon micromechanical oscillator," *J. Appl. Phys.* **97**, 023524 (2005).

[372] M. Hamoumi, P. E. Allain, W. Hease, E. Gil-Santos, L. Morgenroth, B. Gérard, A. Lemaître, G. Leo, and I. Favero, "Microscopic nanomechanical dissipation in gallium arsenide resonators," *Phys. Rev. Lett.* **120**, 223601 (2018).

[373] J. E. Graebner and B. Golding, "Phonon echoes in a glass at low temperatures," *Phys. Rev. B* **19**, 964–975 (1979).

[374] R. E. Mihailovich and J. M. Parpia, "Low temperature mechanical properties of boron-doped silicon," *Phys. Rev. Lett.* **68**, 3052–3055 (1992).

[375] T. A. Palomaki, J. D. Teufel, R. W. Simmonds, and K. W. Lehnert, "Entangling mechanical motion with microwave fields," *Science* **342**, 710–713 (2013).

[376] M. Abdi, A. R. Bahrampour, and D. Vitali, "Quantum optomechanics of a multimode system coupled via a photothermal and a radiation pressure force," *Phys. Rev. A* **86**, 043803 (2012).

[377] J. Mertz, O. Marti, and J. Mlynek, "Regulation of a microcantilever response by force feedback," *Appl. Phys. Lett.* **62**, 2344–2346 (1993).

[378] C. Metzger, I. Favero, A. Ortlieb, and K. Karrai, "Optical self cooling of a deformable Fabry-Perot cavity in the classical limit," *Phys. Rev. B* **78**, 035309 (2008).

[379] K. Aubin, M. Zalalutdinov, T. Alan, R. B. Reichenbach, R. Rand, A. Zehnder, J. Parpia, and H. Craighead, "Limit cycle oscillations in CW laser-driven NEMS," *J. Microelectromech. Syst.* **13**, 1018–1026 (2004).

[380] D. Yuvaraj, M. B. Kadam, O. Shtempluck, and E. Buks, "Optomechanical cavity with a buckled mirror," *J. Microelectromech. Syst.* **22**, 430–437 (2012).

[381] M. W. Pruessner, T. H. Stievater, J. B. Khurgin, and W. S. Rabinovich, "Integrated waveguide-DBR microcavity opto-mechanical system," *Opt. Express* **19**, 21904–21918 (2011).

[382] K. Usami, A. Naesby, T. Bagci, B. Melholt Nielsen, J. Liu, S. Stobbe, P. Lodahl, and E. S. Polzik, "Optical cavity cooling of mechanical modes of a semiconductor nanomembrane," *Nat. Phys.* **8**, 168–172 (2012).

[383] A. Xuereb, K. Usami, A. Naesby, E. S. Polzik, and K. Hammerer, "Exciton-mediated photothermal cooling in GaAs membranes," *New J. Phys.* **14**, 085024 (2012).

[384] R. A. Barton, I. R. Storch, V. P. Adiga, R. Sakakibara, B. R. Cipriany, B. Ilic, S. P. Wang, P. Ong, P. L. McEuen, J. M. Parpia, and H. G. Craighead, "Photothermal self-oscillation and laser cooling of graphene optomechanical systems," *Nano Lett.* **12**, 4681–4686 (2012).

[385] S. Zaitsev, A. K. Pandey, O. Shtempluck, and E. Buks, "Forced and self-excited oscillations of an optomechanical cavity," *Phys. Rev. E* **84**, 046605 (2011).

[386] M. Hosseini, G. Guccione, H. J. Slatyer, B. C. Buchler, and P. K. Lam, "Multimode laser cooling and ultra-high sensitivity force sensing with nanowires," *Nat. Commun.* **5**, 4663 (2014).

[387] R. De Alba, T. S. Abhilash, R. H. Rand, H. G. Craighead, and J. M. Parpia, "Low-power photothermal self-oscillation of bimetallic nanowires," *Nano Lett.* **17**, 3995–4002 (2017).

[388] M. J. Rudd, P. H. Kim, C. A. Potts, C. Doolin, H. Ramp, B. D. Hauer, and J. P. Davis, "Coherent magneto-optomechanical signal transduction and long-distance phase-shift keying," *Phys. Rev. Appl.* **12**, 034042 (2019).

[389] M. W. Pruessner, T. H. Stievater, M. S. Ferraro, and W. S. Rabinovich, "Thermo-optic tuning and switching in SOI waveguide fabry-perot microcavities," *Opt. Express* **15**, 7557–7563 (2007).

[390] H. S. Carslaw and J. C. Jaeger, *Conduction of Heat in Solids*, 2nd edition, Oxford Science Publications (Clarendon Press, Oxford, 1959).

[391] R. Lifshitz and M. C. Cross, "Nonlinear Dynamics of Nanomechanical and Micromechanical Resonators," Chap. 1 in *Reviews of Nonlinear Dynamics and Complexity*, Vol. 1, edited by H. G. Schuster (Wiley-VCH, Weinheim, 2008).

[392] T. Carmon, L. Yang, and K. J. Vahala, "Dynamical thermal behavior and thermal self-stability of microcavities," *Opt. Express* **12**, 4742–4750 (2004).

[393] B. D. Hauer, A. Metelmann, and J. P. Davis, "Phonon quantum nondemolition measurements in nonlinearly coupled optomechanical cavities," *Phys. Rev. A* **98**, 043804 (2018).

[394] E. Joos, H. D. Zeh, C. Kiefer, D. J. W. Giulini, J. Kupsch, and I.-O. Stamatescu, *Decoherence and the Appearance of a Classical World in Quantum Theory*, 2nd edition (Springer, Berlin, 2003).

[395] M. A. Schlosshauer, *Decoherence: and the Quantum-To-Classical Transition*, 1st edition, The Frontiers Collection, edited by A. C. Elitzur, M. P. Silverman, J. Tuszynski, R. Vaas, and H. D. Zeh (Springer, Berlin, 2007).

[396] G. C. Ghirardi, A. Rimini, and T. Weber, "Unified dynamics for microscopic and macroscopic systems," *Phys. Rev. D* **34**, 470–491 (1986).

[397] L. Diósi, "Models for universal reduction of macroscopic quantum fluctuations," *Phys. Rev. A* **40**, 1165–1174 (1989).

[398] R. Penrose, "On gravity's role in quantum state reduction," *Gen. Relativ. Gravit.* **28**, 581–600 (1996).

[399] W. H. Zurek, "Decoherence, einselection, and the quantum origins of the classical," *Rev. Mod. Phys.* **75**, 715–775 (2003).

[400] A. A. Gangat, T. M. Stace, and G. J. Milburn, "Phonon number quantum jumps in an optomechanical system," *New J. Phys.* **13**, 043024 (2011).

[401] J. C. Bergquist, R. G. Hulet, W. M. Itano, and D. J. Wineland, "Observation of quantum jumps in a single atom," *Phys. Rev. Lett.* **57**, 1699–1702 (1986).

[402] S. Peil and G. Gabrielse, "Observing the quantum limit of an electron cyclotron: QND measurements of quantum jumps between Fock states," *Phys. Rev. Lett.* **83**, 1287–1290 (1999).

[403] G. Nogues, A. Rauschenbeutel, S. Osnaghi, M. Brune, J. M. Raimond, and S. Haroche, "Seeing a single photon without destroying it," *Nature* **400**, 239–242 (1999).

[404] S. Gleyzes, S. Kuhr, C. Guerlin, J. Bernu, S. Deléglise, U. Busk Hoff, M. Brune, J.-M. Raimond, and S. Haroche, "Quantum jumps of light recording the birth and death of a photon in a cavity," *Nature* **446**, 297–300 (2007).

[405] P. Neumann, J. Beck, M. Steiner, F. Rempp, H. Fedder, P. R. Hemmer, J. Wrachtrup, and F. Jelezko, "Single-shot readout of a single nuclear spin," *Science* **329**, 542–544 (2010).

[406] A. Lupaşcu, S. Saito, T. Picot, P. C. de Groot, C. J. P. M. Harmans, and J. Mooij, "Quantum non-demolition measurement of a superconducting two-level system," *Nat. Phys.* **3**, 119–123 (2007).

[407] V. B. Braginsky, Y. I. Vorontsov, and K. S. Thorne, "Quantum nondemolition measurements," *Science* **209**, 547–557 (1980).

[408] W. G. Unruh, "Analysis of quantum-nondemolition measurement," *Phys. Rev. D* **18**, 1764–1772 (1978).

[409] H. Kaviani, C. Healey, M. Wu, R. Ghobadi, A. Hryciw, and P. E. Barclay, "Nonlinear optomechanical paddle nanocavities," *Optica* **2**, 271–274 (2015).

[410] J. C. Sankey, C. Yang, B. M. Zwickl, A. M. Jayich, and J. G. E. Harris, "Strong and tunable nonlinear optomechanical coupling in a low-loss system," *Nat. Phys.* **6**, 707–712 (2010).

[411] T. K. Paraïso, M. Kalaee, L. Zang, H. Pfeifer, F. Marquardt, and O. Painter, "Position-squared coupling in a tunable photonic crystal optomechanical cavity," *Phys. Rev. X* **5**, 041024 (2015).

[412] M. Kalaee, T. K. Paraïso, H. Pfeifer, and O. Painter, "Design of a quasi-2D photonic crystal optomechanical cavity with tunable, large x^2-coupling," *Opt. Express* **24**, 21308–21328 (2016).

[413] H. Miao, S. Danilishin, T. Corbitt, and Y. Chen, "Standard quantum limit for probing mechanical energy quantization," *Phys. Rev. Lett.* **103**, 100402 (2009).

[414] M. Ludwig, A. H. Safavi-Naeini, O. Painter, and F. Marquardt, "Enhanced quantum nonlinearities in a two-mode optomechanical system," *Phys. Rev. Lett.* **109**, 063601 (2012).

[415] Y. Yanay, J. C. Sankey, and A. A. Clerk, "Quantum backaction and noise interference in asymmetric two-cavity optomechanical systems," *Phys. Rev. A* **93**, 063809 (2016).

[416] T. J. Kippenberg, S. M. Spillane, and K. J. Vahala, "Modal coupling in traveling-wave resonators," *Opt. Lett.* **27**, 1669–1671 (2002).

[417] H. J. Carmichael, *Statistical Methods in Quantum Optics 2: Non-Classical Fields*, 1st edition, Vol. 2, Theoretical and Mathematical Physics, edited by W. Beiglböck, J.-P. Eckmann, H. Grosse, M. Loss, S. Smirnov, L. Takhtajan, and J. Yngvason (Springer, Berlin, 2008).

[418] I. Martin and W. H. Zurek, "Measurement of energy eigenstates by a slow detector," *Phys. Rev. Lett.* **98**, 120401 (2007).

[419] D. H. Santamore, A. C. Doherty, and M. C. Cross, "Quantum nondemolition measurement of Fock states of mesoscopic mechanical oscillators," *Phys. Rev. B* **70**, 144301 (2004).

[420] J. R. Johansson, P. D. Nation, and F. Nori, "QuTiP 2: A Python framework for the dynamics of open quantum systems," *Comput. Phys. Commun.* **184**, 1234–1240 (2013).

[421] R. Rivière, S. Deléglise, S. Weis, E. Gavartin, O. Arcizet, A. Schliesser, and T. J. Kippenberg, "Optomechanical sideband cooling of a micromechanical oscillator close to the quantum ground state," *Phys. Rev. A* **83**, 063835 (2011).

[422] R. Rivière, O. Arcizet, A. Schliesser, and T. J. Kippenberg, "Evanescent straight tapered-fiber coupling of ultra-high Q optomechanical microresonators in a low-vibration helium-4 exchange-gas cryostat," *Rev. Sci. Instrum.* **84**, 043108 (2013).

[423] S. M. Meenehan, J. D. Cohen, S. Gröblacher, J. T. Hill, A. H. Safavi-Naeini, M. Aspelmeyer, and O. Painter, "Silicon optomechanical crystal resonator at millikelvin temperatures," *Phys. Rev. A* **90**, 011803 (2014).

[424] A. G. Kuhn, J. Teissier, L. Neuhaus, S. Zerkani, E. van Brackel, S. Deléglise, T. Briant, P.-F. Cohadon, A. Heidmann, C. Michel, L. Pinard, V. Dolique, R. Flaminio, R. Taïbi, O. Chartier, and O. L. Traon, "Free-space cavity optomechanics in a cryogenic environment," *Appl. Phys. Lett.* **104**, 044102 (2014).

[425] H. Bender, S. Verhaverbeke, M. Caymax, O. Vatel, and M. M. Heyns, "Surface reconstruction of hydrogen annealed (100) silicon," *J. Appl. Phys.* **75**, 1207–1209 (1994).

[426] K. Y. Yasumura, T. D. Stowe, E. M. Chow, T. Pfafman, T. W. Kenny, B. C. Stipe, and D. Rugar, "Quality factors in micron- and submicron-thick cantilevers," *J. Microelectromech. Syst.* **9**, 117–125 (2000).

[427] J. Yang, T. Ono, and M. Esashi, "Energy dissipation in submicrometer thick single-crystal silicon cantilevers," *J. Microelectromech. Syst.* **11**, 775–783 (2002).

[428] H. Ramp, B. D. Hauer, K. C. Balram, T. J. Clark, K. Srinivasan, and J. P. Davis, "Elimination of thermomechanical noise in piezoelectric optomechanical crystals," *Phys. Rev. Lett.* **123**, 093603 (2019).

[429] M. Neeley, M. Ansmann, R. C. Bialczak, M. Hofheinz, N. Katz, E. Lucero, A. O'Connell, H. Wang, A. N. Cleland, and J. M. Martinis, "Process tomography of quantum memory in a Josephson-phase qubit coupled to a two-level state," *Nat. Phys.* **4**, 523–526 (2008).

[430] O. Arcizet, V. Jacques, A. Siria, P. Poncharal, P. Vincent, and S. Seidelin, "A single nitrogen-vacancy defect coupled to a nanomechanical oscillator," *Nat. Phys.* **7**, 879–883 (2011).

[431] D. A. Golter, T. Oo, M. Amezcua, K. A. Stewart, and H. Wang, "Optomechanical quantum control of a nitrogen-vacancy center in diamond," *Phys. Rev. Lett.* **116**, 143602 (2016).

[432] Y. Fu, "Interdefect elastic interaction in glass fiber and the theory of tunneling systems," *Phys. Rev. B* **40**, 10056–10059 (1989).

[433] K. Agarwal, I. Martin, M. D. Lukin, and E. Demler, "Polaronic model of two-level systems in amorphous solids," *Phys. Rev. B* **87**, 144201 (2013).

[434] F. Marino and F. Marin, "Chaotically spiking attractors in suspended-mirror optical cavities," *Phys. Rev. E* **83**, 015202 (2011).

[435] F. Marino and F. Marin, "Coexisting attractors and chaotic canard explosions in a slow-fast optomechanical system," *Phys. Rev. E* **87**, 052906 (2013).

[436] B. Misra and E. C. G. Sudarshan, "The Zeno's paradox in quantum theory," *J. Math. Phys.* **18**, 756–763 (1977).

[437] W. M. Itano, D. J. Heinzen, J. J. Bollinger, and D. J. Wineland, "Quantum zeno effect," *Phys. Rev. A* **41**, 2295–2300 (1990).

[438] M. C. Fischer, B. Gutiérrez-Medina, and M. G. Raizen, "Observation of the quantum Zeno and anti-Zeno effects in an unstable system," *Phys. Rev. Lett.* **87**, 040402 (2001).

[439] Y. S. Patil, S. Chakram, and M. Vengalattore, "Measurement-induced localization of an ultracold lattice gas," *Phys. Rev. Lett.* **115**, 140402 (2015).

[440] Y.-D. Wang and A. A. Clerk, "Using interference for high fidelity quantum state transfer in optomechanics," *Phys. Rev. Lett.* **108**, 153603 (2012).

[441] K. Stannigel, P. Komar, S. J. M. Habraken, S. D. Bennett, M. D. Lukin, P. Zoller, and P. Rabl, "Optomechanical quantum information processing with photons and phonons," *Phys. Rev. Lett.* **109**, 013603 (2012).

[442] I. S. Gradshteyn and I. M. Ryzhik, *Table of Integrals, Series, and Products*, 8th edition, edited by D. Zwillinger and V. Moll (Academic Press, Waltham, 2014).

[443] R. P. Wang and M.-M. Dumitrescu, "Theory of optical modes in semiconductor microdisk lasers," *J. Appl. Phys.* **81**, 3391–3397 (1997).

[444] A. W. Snyder and J. Love, *Optical Waveguide Theory*, 1st edition (Chapman and Hall, London, 1983).

[445] D. Gloge, "Weakly guiding fibers," *Appl. Opt.* **10**, 2252–2258 (1971).

[446] K.-M. C. Fu, P. E. Barclay, C. Santori, A. Faraon, and R. G. Beausoleil, "Low-temperature tapered-fiber probing of diamond nitrogen-vacancy ensembles coupled to GaP microcavities," *New J. Phys.* **13**, 055023 (2011).

[447] V. R. Dantham, S. Holler, V. Kolchenko, Z. Wan, and S. Arnold, "Taking whispering gallery-mode single virus detection and sizing to the limit," *Appl. Phys. Lett.* **101**, 043704 (2012).

[448] G. M. Hale and M. R. Querry, "Optical constants of water in the 200-nm to 200-μm wavelength region," *Appl. Opt.* **12**, 555–563 (1973).

[449] A. W. Rodriguez, A. P. McCauley, P.-C. Hui, D. Woolf, E. Iwase, F. Capasso, M. Loncar, and S. G. Johnson, "Bonding, antibonding and tunable optical forces in asymmetric membranes," *Opt. Express* **19**, 2225–2241 (2011).

[450] I. Nusinsky and A. A. Hardy, "Approximate analysis of two-dimensional photonic crystals with rectangular geometry. I. E polarization," *J. Opt. Soc. Am. B* **25**, 1135–1143 (2008).

[451] M. J. Collett and C. W. Gardiner, "Squeezing of intracavity and traveling-wave light fields produced in parametric amplification," *Phys. Rev. A* **30**, 1386–1391 (1984).

[452] C. W. Gardiner and M. J. Collett, "Input and output in damped quantum systems: Quantum stochastic differential equations and the master equation," *Phys. Rev. A* **31**, 3761–3774 (1985).

Appendix A

Mathematical Definitions and Relations

In this appendix, we provide a number of mathematical definitions and relations that are useful for the calculations performed throughout this thesis.

A.1 Fourier Transform

Throughout this thesis, we choose to use the nonunitary, angular frequency representation of the Fourier transform, which for an arbitrary function $f(t)$[1], is defined as

$$f(\omega) = \int_{-\infty}^{\infty} f(t) e^{i\omega t} dt. \tag{A.1}$$

With this definition, the inverse Fourier transform is then given by

$$f(t) = \int_{-\infty}^{\infty} f(\omega) e^{-i\omega t} d\omega. \tag{A.2}$$

Using these two relations, we can translate any time-domain function into the frequency domain and vice versa.

A.2 Delta Functions

The Dirac delta function $\delta(x)$ is a distribution that is defined as [149]

$$\int_{-\infty}^{\infty} \delta(x - x_0) dx = \begin{cases} 1, & x = x_0 \\ 0, & x \neq x_0 \end{cases}. \tag{A.3}$$

[1]This function acts as an arbitrary placeholder for either a quantum mechanical operator or a classical variable.

Note that if the upper limit only goes to x_0, we have [203]

$$\int_{-\infty}^{x_0} \delta(x - x_0)dx = \frac{1}{2}. \tag{A.4}$$

Alternatively, the Dirac delta function can be defined in integral form as

$$\delta(x - x') = \frac{1}{2\pi} \int_{-\infty}^{\infty} e^{ik(x-x')}dk. \tag{A.5}$$

When integrated with an arbitrary function $f(x)$, the Dirac delta function has the useful property

$$\int_{-\infty}^{\infty} f(x)\delta(x - x_0)dx = f(x_0). \tag{A.6}$$

Finally, we also define the Kronecker delta function as

$$\delta_{ij} = \begin{cases} 1, & i = j \\ 0, & i \neq j \end{cases}. \tag{A.7}$$

This function is the discrete version of the Dirac delta function, and is very useful as it can collapse a sum over an arbitrary quantity a_j as

$$\sum_j a_j \delta_{ij} = a_i. \tag{A.8}$$

A.3 Bessel Functions

The νth-order Bessel functions of the first $J_\nu(z)$ and second $Y_\nu(z)$ kinds are the solutions to the differential equation [442]

$$z^2 \frac{d^2Z}{dz^2} + z\frac{dZ}{dz} + (z^2 - \nu^2)Z = 0. \tag{A.9}$$

Meanwhile, the modified νth-order Bessel functions of the first $K_\nu(z)$ and second $I_\nu(z)$ kinds are the solutions to [442]

$$z^2 \frac{d^2Z}{dz^2} + z\frac{dZ}{dz} - (z^2 + \nu^2)Z = 0. \tag{A.10}$$

Equations (A.9) and (A.10) arise when solving the wave equation in cylindrical coordinates (see Appendix B below).

The Bessel function $J_\nu(z)$ has the useful properties [336, 442]

$$J_{-\nu}(z) = (-1)^\nu J_\nu(z), \tag{A.11}$$
$$\frac{\nu}{z} J_\nu(z) = \frac{1}{2}\left[J_{\nu-1}(z) + J_{\nu+1}(z)\right], \tag{A.12}$$
$$J'_\nu(z) = \frac{1}{2}\left[J_{\nu-1}(z) - J_{\nu+1}(z)\right], \tag{A.13}$$
$$J'_0(z) = -J_1(z), \tag{A.14}$$

while the modified Bessel function $K_\nu(z)$ obeys

$$K_{-\nu}(z) = K_\nu(z), \tag{A.15}$$
$$\frac{\nu}{z} K_\nu(z) = -\frac{1}{2}\left[K_{\nu-1}(z) - K_{\nu+1}(z)\right], \tag{A.16}$$
$$K'_\nu(z) = -\frac{1}{2}\left[K_{\nu-1}(z) - K_{\nu+1}(z)\right], \tag{A.17}$$
$$K'_0(z) = -K_1(z), \tag{A.18}$$

where $J'_\nu(z) = dJ_\nu/dz$ and $K'_\nu(z) = dK_\nu/dz$.

A.4 Power Spectral Densities

The PSD is a frequency-domain function that quantifies the power of a signal over a given interval in frequency space, and thus, provides a useful description for signals that fluctuate in time. For an arbitrary time-dependent quantum fluctuation operator $\delta\hat{y}(t)$, the two-sided[2] PSD is defined as

$$S_{yy}(\omega) = \int_{-\infty}^{\infty} \langle \delta\hat{y}(t)\delta\hat{y}(0)\rangle \, e^{i\omega t} dt. \tag{A.19}$$

That is, the PSD is the Fourier transform of the operator's autocorrelation function (ACF) $\langle \delta\hat{y}(t)\delta\hat{y}(0)\rangle$, which gives a measure of the correlation of the operator $\delta\hat{y}(0)$ with itself at a later time t and for finite temperature T is given by[3]

$$\langle \delta\hat{y}(t)\delta\hat{y}(0)\rangle = \frac{\mathrm{Tr}\left\{e^{-\hat{H}/k_\mathrm{B}T} e^{i\hat{H}t/\hbar}\delta\hat{y}(0)e^{-i\hat{H}t/\hbar}\delta\hat{y}(0)\right\}}{\mathrm{Tr}\left\{e^{-\hat{H}/k_\mathrm{B}T}\right\}}, \tag{A.20}$$

[2] Two-sided refers to the fact that the PSD is defined for both positive and negative frequencies.

[3] In general, the ACF would have the form $\langle \delta\hat{y}(t)\delta\hat{y}(t')\rangle$, however, the ACF depends only on the interval $t - t'$ between these two instances in time. Therefore, we can take $t' = 0$ to simplify our calculations without loss of generality.

where $\hat{H}$ is the Hamiltonian of the considered system. Note that by inverting Eq. (A.19), the ACF for a signal can also be determined from the inverse Fourier transform of its PSD as

$$\langle \delta\hat{y}(t)\delta\hat{y}(0)\rangle = \frac{1}{2\pi}\int_{-\infty}^{\infty} S_{yy}(\omega)e^{-i\omega t}d\omega. \tag{A.21}$$

Furthermore, by setting $t = 0$ in Eq. (A.21), we are able to relate the expectation value of $\delta\hat{y}^2(t)$ to the PSD via the relation

$$\langle \delta\hat{y}^2\rangle = \frac{1}{2\pi}\int_{-\infty}^{\infty} S_{yy}(\omega)d\omega. \tag{A.22}$$

Physically, this relation tells us that the energy of the signal will be given by integrating the power of the signal over all frequencies.

Finally, often one finds that it is much easier to determine the Fourier transform of a signal as opposed to its time-domain representation. It is therefore useful to derive an alternate expression for the PSD in terms of the Fourier transform of the signal. This is done by inputting the definition of the inverse Fourier transform given by Eq. (A.2) into Eq. (A.19), while using the integral definition of the Dirac delta function given in Eq. (A.5) to obtain

$$S_{yy}(\omega) = \frac{1}{2\pi}\int_{-\infty}^{\infty} \langle \delta\hat{y}(\omega)\delta\hat{y}(\omega')\rangle \, d\omega'. \tag{A.23}$$

This relation proves to be very useful for calculating the PSDs used in this thesis.

Appendix B

Electromagnetic Fields in Cylindrical Coordinates

B.1 Maxwell's Equations

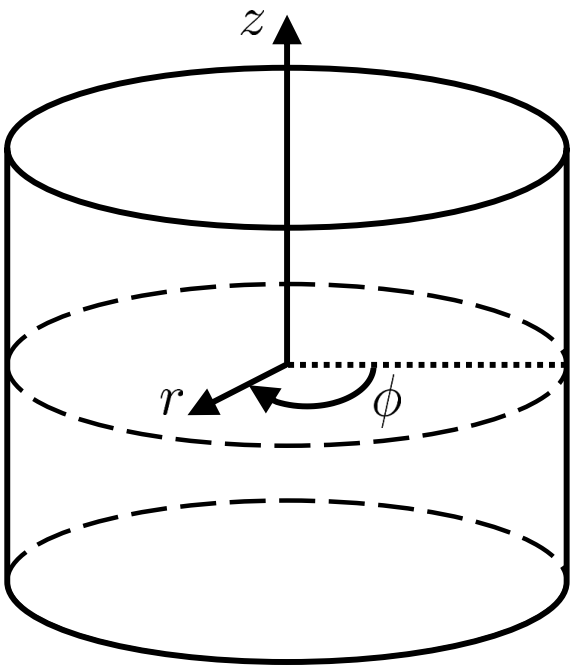

Figure B.1: Schematic illustrating the coordinate system associated with our cylindrical geometry.

As the two most prevalent optical components discussed in this thesis are microdisk cavities and cylindrical optical fibers, it is useful to solve the for the modeshape of the electromagnetic fields using a cylindrical coordinate system. In

this case, the modeshapes of the electric and magnetic fields can be represented as

$$\mathbf{E}(r,\phi,z) = E_r(r,\phi,z)\mathbf{i}_r + E_\phi(r,\phi,z)\mathbf{i}_\phi + E_z(r,\phi,z)\mathbf{i}_z, \tag{B.1}$$

$$\mathbf{B}(r,\phi,z) = B_r(r,\phi,z)\mathbf{i}_r + B_\phi(r,\phi,z)\mathbf{i}_\phi + B_z(r,\phi,z)\mathbf{i}_z, \tag{B.2}$$

where $\mathbf{i}_r$, $\mathbf{i}_\phi$, and $\mathbf{i}_z$ are units vectors along the r, ϕ, and z coordinate directions as defined in Fig. B.1. It was shown by Wang and Dumitrescu [443] that for a non-magnetic source-free dielectric in cylindrical coordinates, the electromagnetic gauge potentials can be used to express these electric field components as

$$E_r = i\omega\left(\frac{1}{\tilde{k}^2(\mathbf{r})}\frac{\partial^2\psi_{\mathrm{TM}}}{\partial r\partial z} + \frac{1}{r}\frac{\partial\psi_{\mathrm{TE}}}{\partial\phi}\right), \tag{B.3}$$

$$E_\phi = i\omega\left(\frac{1}{\tilde{k}^2(\mathbf{r})}\frac{\partial^2\psi_{\mathrm{TM}}}{\partial r\partial\phi} - \frac{\partial\psi_{\mathrm{TE}}}{\partial r}\right), \tag{B.4}$$

$$E_z = i\omega\left(\psi_{\mathrm{TM}} + \frac{1}{\tilde{k}^2(\mathbf{r})}\frac{\partial^2\psi_{\mathrm{TM}}}{\partial z^2}\right), \tag{B.5}$$

while the magnetic fields are given by

$$B_r = \frac{\partial^2\psi_{\mathrm{TE}}}{\partial r\partial z} + \frac{1}{r}\frac{\partial\psi_{\mathrm{TM}}}{\partial\phi}, \tag{B.6}$$

$$B_\phi = \frac{1}{r}\frac{\partial^2\psi_{\mathrm{TE}}}{\partial\phi\partial z} - \frac{\partial\psi_{\mathrm{TM}}}{\partial\phi}, \tag{B.7}$$

$$B_z = \tilde{k}^2(\mathbf{r})\psi_{\mathrm{TE}} + \frac{\partial^2\psi_{\mathrm{TE}}}{\partial z^2}, \tag{B.8}$$

where $\psi_{\mathrm{TE}}(r,\phi,z)$ and $\psi_{\mathrm{TM}}(r,\phi,z)$ are two scalar functions that each obey Helmholtz equations similar to that given in Eq. (3.9). In cylindrical coordinates, this corresponds to

$$\frac{1}{r}\frac{\partial}{\partial r}\left(r\frac{\partial\psi}{\partial r}\right) + \frac{1}{r^2}\frac{\partial^2\psi}{\partial\phi^2} + \frac{\partial^2\psi}{\partial z^2} + \tilde{k}^2(\mathbf{r})\psi = 0, \tag{B.9}$$

where we have used ψ as a placeholder for one of either ψ_{TE} or ψ_{TM}. Note that since both ψ_{TE} and ψ_{TM} satisfy Eq. (B.9), they will have an identical functional form, though with differing proportionality constants. With the fields defined in this way, setting $\psi_{\mathrm{TM}} = 0$ is associated with TE modes, where the electric field has no component along the z-axis of the considered cylinder, while for $\psi_{\mathrm{TE}} = 0$, there is no magnetic field in the z-direction and TM modes emerge. Finally, in the situation where $\psi_{\mathrm{TE}} \neq 0$ and $\psi_{\mathrm{TM}} \neq 0$, both E_z and B_z are non-zero corresponding

to hybrid modes, which are further classified as being either E_z-dominated (EH) or B_z-dominated (HE). With this formalism for treating electromagnetic field in cylindrical coordinates in place, we now look to determine ψ_{TE} and ψ_{TE} (and thus the electromagnetic fields for each mode through Eqs. (B.3)–(B.8)) for the two geometries of an infinite cylinder and a disk of finite height.

B.2 Infinitely Long Cylinders

To begin with, we consider an infinitely long cylinder of radius r_{c} and uniform index of refraction $\tilde{n}_1$. Using a cylindrical coordinate system where the z-axis runs down the center of the cylinder, as shown in Fig. B.1, the refractive index of the structure will then depend only on the radial coordinate r according to the piecewise function

$$\tilde{n}(r) = \begin{cases} \tilde{n}_1, & r \leq r_{\mathrm{c}} \\ \tilde{n}_2, & r > r_{\mathrm{c}} \end{cases}, \tag{B.10}$$

where $\tilde{n}_2$ is the index of refraction of the surrounding medium. With the refractive index defined in this way, the piecewise wavenumber of the system will then be given

$$\tilde{k}(r) = \begin{cases} \tilde{k}_1 = \tilde{n}_1 \tilde{k}_0, & r \leq r_{\mathrm{c}} \\ \tilde{k}_2 = \tilde{n}_2 \tilde{k}_0, & r > r_{\mathrm{c}} \end{cases}, \tag{B.11}$$

where $\tilde{k}_0 = 2\pi/\lambda_0$ is the vacuum wavenumber of the system, expressed in terms of the optical field's vacuum wavelength λ_0. Here we look to determine the modeshapes for the electromagnetic waves travelling down the axis of the cylinder for a given vacuum wavelength λ_0, as these are the modes associated with the fiber optic waveguides we use to couple light into our optical cavity. This is done by solving Eq. (B.9) using a separation of variables approach by writing ψ as a product of three separate functions according to

$$\psi(r, \phi, z) = \mathcal{M} \psi_r(r) \psi_\phi(\phi) \psi_z(z), \tag{B.12}$$

where $\mathcal{M}$ is an appropriately chosen normalization constant, with the relative strengths of $\mathcal{M}_{\mathrm{TE}}$ and $\mathcal{M}_{\mathrm{TM}}$ set by the boundary conditions of the considered system. Inputting this ansatz into Eq. (B.9), we then obtain a separate differential

equation for each variable as

$$\frac{d^2\psi_z}{dz^2} + \tilde{k}_z^2\psi_z = 0, \tag{B.13}$$

$$\frac{d^2\psi_\phi}{d\phi^2} + m^2\psi_\phi = 0, \tag{B.14}$$

$$r^2\frac{d^2\psi_r}{dr^2} + r\frac{d\psi_r}{dr} + \left[r^2\tilde{k}_\mathrm{t}(r) - m^2\right]\psi_r(r) = 0. \tag{B.15}$$

Here $\tilde{k}_z$ and m are two constants corresponding to the z-component of the mode's wavenumber and azimuthal mode label, such that $\psi_z(z)$ and $\psi_\phi(\phi)$ have the trivial harmonic plane wave solutions

$$\psi_z(z) = e^{\pm i\tilde{k}_z z}, \tag{B.16}$$

and

$$\psi_\phi(\phi) = e^{\pm im\phi}. \tag{B.17}$$

Note that due to the cylindrical symmetry of the system, we require $\psi_\phi(\phi) = \psi_\phi(\phi + 2\pi)$, which constrains m to be an integer. For any non-zero m, this functional form of $\psi_\phi(\phi)$ allows for two degenerate solutions, corresponding to the real and imaginary parts of $\psi_\phi(\phi)$, $\mathrm{Re}\{\psi_\phi(\phi)\} = \cos m\phi$ and $\mathrm{Im}\{\psi_\phi(\phi)\} = \sin m\phi$, respectively. Meanwhile, $\tilde{k}_\mathrm{t}(r) = \sqrt{\tilde{k}^2(r) - \tilde{k}_z^2}$ is the wavenumber of the wavevector transverse to the cylinder's z-axis. Therefore, $\tilde{k}_\mathrm{t}^2(r < r_\mathrm{c}) = \tilde{k}_1^2 - \tilde{k}_z^2 \equiv q_1^2 > 0$ inside the cylinder and Eq. (B.15) is the Bessel equation, such that its solutions are the mth-order Bessel functions of the first and second kinds, $J_m(q_1 r)$ and $Y_m(q_1 r)$ (see Appendix A). Outside the cylinder we then have that $\tilde{k}_\mathrm{t}^2(r > r_\mathrm{c}) = \tilde{k}_2^2 - \tilde{k}_z^2 \equiv -q_2^2 < 0$, which transforms Eq. (B.15) into the modified Bessel function with its solutions becoming the mth-order modified Bessel functions of the first and second kind, $I_m(q_2 r)$ and $K_m(q_2 r)$. Since $Y_m(q_1 r)$ diverges as $r \to 0$ and $I_m(q_2 r)$ diverges as $r \to \infty$, we discard these two terms to ensure our fields represent bound, physical solutions to the Helmholtz equation, resulting in the piecewise representation for $\psi_r(r)$ as

$$\psi_r(r) = \begin{cases} J_m(q_1 r), & r \le r_\mathrm{c} \\ K_m(q_2 r), & r > r_\mathrm{c} \end{cases}. \tag{B.18}$$

We can now insert the solutions for $\psi_z(z)$, $\psi_\phi(\phi)$, and $\psi_r(r)$ given by Eqs. (B.16), (B.17), and (B.18) into Eq. (B.12) to determine the functional forms of ψ_TE and ψ_TM.

Assuming a guided plane wave propagating through the cylinder in the positive z-direction by taking the negative sign solution in Eq. (B.16), while choosing the appropriate phase for ϕ, we find

$$\psi_{\mathrm{TE}}(r,\phi,z) = \begin{cases} \mathcal{M}_{\mathrm{TE},1} J_m(q_1 r)\cos(m\phi)e^{-i\tilde{k}_z z}, & r \le r_{\mathrm{c}} \\ \mathcal{M}_{\mathrm{TE},2} K_m(q_2 r)\cos(m\phi)e^{-i\tilde{k}_z z}, & r > r_{\mathrm{c}} \end{cases}, \tag{B.19}$$

$$\psi_{\mathrm{TM}}(r,\phi,z) = \begin{cases} \mathcal{M}_{\mathrm{TM},1} J_m(q_1 r)\sin(m\phi)e^{-i\tilde{k}_z z}, & r \le r_{\mathrm{c}} \\ \mathcal{M}_{\mathrm{TM},2} K_m(q_2 r)\sin(m\phi)e^{-i\tilde{k}_z z}, & r > r_{\mathrm{c}} \end{cases}, \tag{B.20}$$

where

$$\mathcal{M}_{\mathrm{TE},2} = -\frac{q_1^2 J_m(q_1 r_{\mathrm{c}})}{q_2^2 K_m(q_2 r_{\mathrm{c}})}\mathcal{M}_{\mathrm{TE},1}, \tag{B.21}$$

$$\mathcal{M}_{\mathrm{TM},2} = -\frac{q_1^2 J_m(q_1 r_{\mathrm{c}})}{q_2^2 K_m(q_2 r_{\mathrm{c}})}\mathcal{M}_{\mathrm{TM},1}. \tag{B.22}$$

The electromagnetic fields of the mode can then be found by inputting these solutions for ψ_{TE} and ψ_{TM} into Eqs. (B.3)–(B.8) to find the fields inside the cylinder ($r < r_{\mathrm{c}}$) as [336]

$$E_r = -i\mathcal{U}_1 \frac{\tilde{k}_z}{q_1}\left[\frac{1-\Upsilon}{2}J_{m-1}(q_1 r) - \frac{1+\Upsilon}{2}J_{m+1}(q_1 r)\right]\cos(m\phi), \tag{B.23}$$

$$E_\phi = i\mathcal{U}_1 \frac{\tilde{k}_z}{q_1}\left[\frac{(1-\Upsilon)}{2}J_{m-1}(q_1 r) + \frac{(1+\Upsilon)}{2}J_{m+1}(q_1 r)\right]\sin(m\phi), \tag{B.24}$$

$$E_z = \mathcal{U}_1 J_m(q_1 r)\cos(m\phi), \tag{B.25}$$

$$B_r = -i\mathcal{U}_1 \frac{\tilde{k}_1^2}{\omega_{\mathrm{c}} q_1}\left[\frac{(1-\Upsilon_1)}{2}J_{m-1}(q_1 r) + \frac{(1+\Upsilon_1)}{2}J_{m+1}(q_1 r)\right]\sin(m\phi), \tag{B.26}$$

$$B_\phi = -i\mathcal{U}_1 \frac{\tilde{k}_1^2}{\omega_{\mathrm{c}} q_1}\left[\frac{(1-\Upsilon_1)}{2}J_{m-1}(q_1 r) - \frac{(1+\Upsilon_1)}{2}J_{m+1}(q_1 r)\right]\cos(m\phi), \tag{B.27}$$

$$B_z = -\mathcal{U}_1 \frac{\tilde{k}_z}{\omega_{\mathrm{c}}}\Upsilon J_m(q_1 r)\sin(m\phi), \tag{B.28}$$

while the fields outside the cylinder ($r > r_c$) are given by

$$E_r = -i\mathcal{U}_2 \frac{\tilde{k}_z}{q_2}\left[\frac{(1-\Upsilon)}{2}K_{m-1}(q_2 r) + \frac{(1+\Upsilon)}{2}K_{m+1}(q_2 r)\right]\cos(m\phi), \tag{B.29}$$

$$E_\phi = i\mathcal{U}_2 \frac{\tilde{k}_z}{q_2}\left[\frac{(1-\Upsilon)}{2}K_{m-1}(q_2 r) - \frac{(1+\Upsilon)}{2}K_{m+1}(q_2 r)\right]\sin(m\phi), \tag{B.30}$$

$$E_z = \mathcal{U}_2 K_m(q_2 r)\cos(m\phi), \tag{B.31}$$

$$B_r = -i\mathcal{U}_2 \frac{\tilde{k}_2^2}{\omega_c q_2}\left[\frac{(1-\Upsilon_2)}{2}K_{m-1}(q_2 r) + \frac{(1+\Upsilon_2)}{2}K_{m+1}(q_2 r)\right]\sin(m\phi), \tag{B.32}$$

$$B_\phi = -i\mathcal{U}_2 \frac{\tilde{k}_2^2}{\omega_c q_2}\left[\frac{(1-\Upsilon_2)}{2}K_{m-1}(q_2 r) - \frac{(1+\Upsilon_2)}{2}K_{m+1}(q_2 r)\right]\cos(m\phi), \tag{B.33}$$

$$B_z = -\mathcal{U}_2 \frac{\tilde{k}_z}{\omega_c}\Upsilon K_m(q_2 r)\sin(m\phi). \tag{B.34}$$

Here we have introduced the factors

$$\Upsilon = \frac{\dfrac{m}{r_c}\left(\dfrac{1}{q_1^2}+\dfrac{1}{q_2^2}\right)}{\dfrac{J'_m(q_1 r_c)}{q_1 J_m(q_1 r_c)} + \dfrac{K'_m(q_2 r_c)}{q_2 K_m(q_2 r_c)}}, \tag{B.35}$$

$$\Upsilon_1 = \frac{\tilde{k}_z^2}{\tilde{k}_1^2}\Upsilon, \tag{B.36}$$

$$\Upsilon_2 = \frac{\tilde{k}_z^2}{\tilde{k}_2^2}\Upsilon, \tag{B.37}$$

which along with the dispersion relation

$$\begin{aligned}\left[\frac{J'_m(q_1 r_c)}{q_1 J_m(q_1 r_c)} + \frac{K'_m(q_2 r_c)}{q_2 K_m(q_2 r_c)}\right]\left[\frac{\tilde{n}_1 J'_m(q_1 r_c)}{q_1 J_m(q_1 r_c)} + \frac{\tilde{n}_2 K'_m(q_2 r_c)}{q_2 K_m(q_2 r_c)}\right] \\ = \frac{m^2}{r_c^2}\left(\frac{1}{q_1^2}+\frac{1}{q_2^2}\right)\left(\frac{\tilde{n}_1^2}{q_1^2}+\frac{\tilde{n}_2^2}{q_2^2}\right),\end{aligned} \tag{B.38}$$

ensures the appropriate boundary conditions of the fields. Note that in determining the dispersion relation given in Eq. (B.38), we have implicitly used the identity

$$\frac{\tilde{k}_z^2}{\tilde{k}_0^2}\left(\frac{1}{q_1^2}+\frac{1}{q_2^2}\right) = \frac{\tilde{n}_1^2}{q_1^2}+\frac{\tilde{n}_2^2}{q_2^2}, \tag{B.39}$$

as well as introduced the notation $J'_m(x) = dJ_m/dx$ and $K'_m(x) = dK_m/dx$. Finally, we note that in Eqs. (B.23)–(B.34) we have introduced the new appropriately rescaled normalization constants $\mathcal{U}_i$, which satisfy the relation [336]

$$\mathcal{U}_1 = \frac{K_m(q_2 r_c)}{J_m(q_1 r_c)}\mathcal{U}_2. \tag{B.40}$$

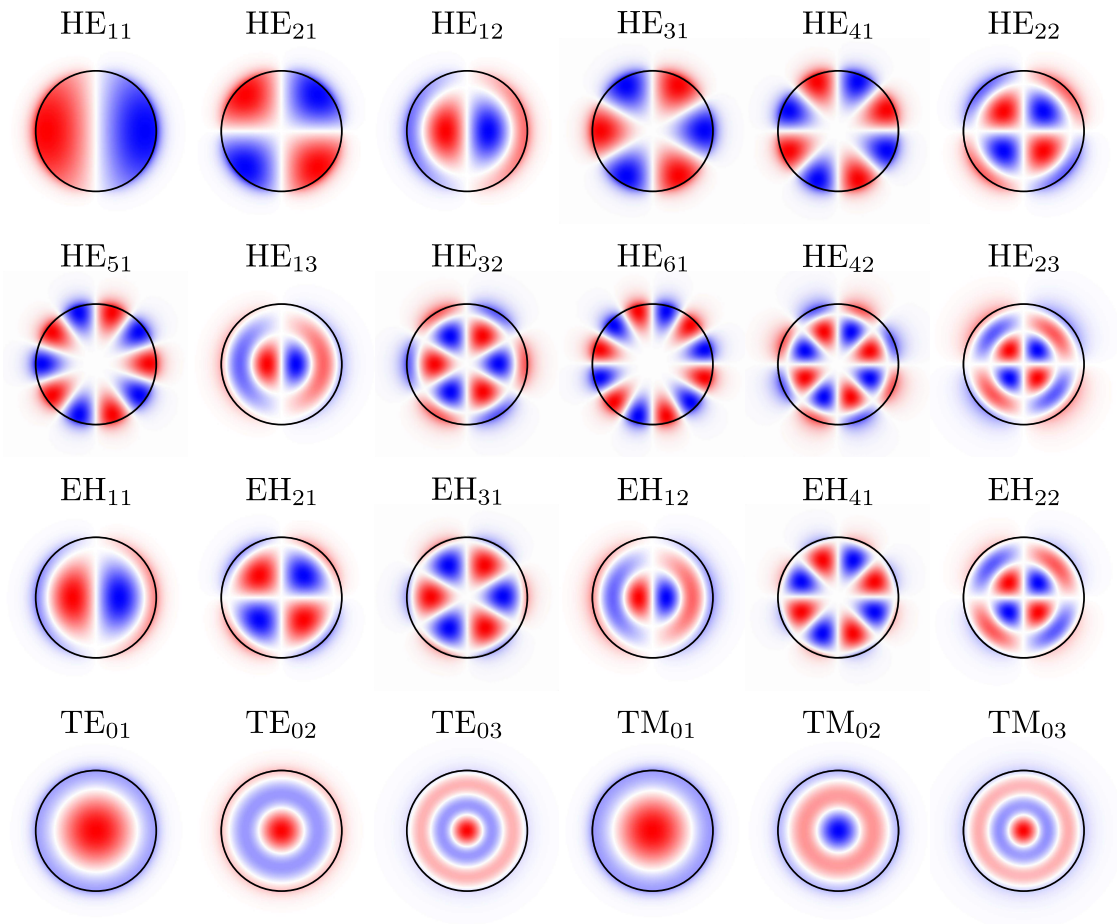

Figure B.2: The first 24 guided modes of an infinite cylinder, increasing in order from left to right. Here we show the in-plane profile of the E_z field for the HE_{mn} (first two rows), EH_{mn} (third row), and TM_{0n} (last row) modes, while for the TE_{0n} modes we plot the B_z field (as the $E_z = 0$ in this case). Each mode is calculated using FEM simulation for a silica cylinder ($\tilde{n}_1 = 1.47$) of radius $r_c = 2.5$ μm surrounded by vacuum/air ($\tilde{n}_2 = 1.00$) at a wavelength of $\lambda = 1550$ nm.

For the hybrid modes of the system, $\tilde{k}_z$, and therefore q_1 and q_2, can be determined for a vacuum wavelength λ_0 and azimuthal mode number $m \geq 1$ from the solutions of Eq. (B.38). For a given family of azimuthal modes, Eq. (B.38) will in general have n solutions, corresponding to the n radial modes supported by the cylinder, which we label HE_{mn} and EH_{mn}. In this notation, $2m$ counts the number of nodes in the azimuthal direction, while n ($n+1$) counts the number of nodes in the radial direction of the E_z and B_z fields for each of the HE_{mn} (EH_{mn}) modes. For example, the E_z field of the HE_{42} mode has 8 nodes in the ϕ-direction and 2 nodes in the r-direction, as seen in Fig. B.2.

With our generalized approach, we can also determine dispersion relations for the TE_{mn} and TM_{mn} modes of the cylinder by taking $m = 0$ in Eq. (B.38). This condition is satisfied for the TE modes by setting the first term in brackets on the left-hand side to zero resulting in

$$\frac{J_0'(q_1 r_\mathrm{c})}{q_1 J_0(q_1 r_\mathrm{c})} + \frac{K_0'(q_2 r_\mathrm{c})}{q_2 K_0(q_2 r_\mathrm{c})} = 0, \tag{B.41}$$

whereas the dispersion relation for TM modes is found by setting the second term in brackets to zero to find

$$\frac{\tilde{n}_1 J_0'(q_1 r_\mathrm{c})}{q_1 J_0(q_1 r_\mathrm{c})} + \frac{\tilde{n}_2 K_0'(q_2 r_\mathrm{c})}{q_2 K_0(q_2 r_\mathrm{c})} = 0. \tag{B.42}$$

According to Eq. (B.35), this $m = 0$ condition sets $\Upsilon = \Upsilon_1 = \Upsilon_2 = 0$ in this situation. The fields associated with the TE (TM) modes can then be found by inputting the solution for ψ_TE (ψ_TM) into Eqs. (B.3)–(B.8), while also taking $\psi_\mathrm{TM} = 0$ ($\psi_\mathrm{TE} = 0$). Note that since $m = 0$ for these modes, they have no nodes in the azimuthal direction, while n counts their nodes in the radial direction, as can be seen in Fig. B.2.

Using Poynting's theorem [258], we can also also determine the time-averaged power carried by these propagating modes in the positive z-direction as

$$P_z = \frac{1}{2\mu_0}\int_0^{2\pi}\int_0^{\infty} (\mathbf{E}\times\mathbf{B}^*)\cdot\mathbf{i}_z r dr d\phi = \frac{1}{2\mu_0}\int_0^{2\pi}\int_0^{\infty} \left(E_r B_\phi^* - E_\phi B_r^*\right) r dr d\phi, \tag{B.43}$$

Inputting the radial and azimuthal components of the electric and magnetic fields of the cylinder into this equation, we find the power propagating within the confines of the cylinder to be

$$P_1 = \frac{\pi}{4}\frac{|\mathcal{U}_1|^2 \tilde{k}_z \tilde{k}_1^2 r_\mathrm{c}^2}{\mu_0 \omega_\mathrm{c} q_1^2}\left\{\begin{array}{l}(1-\Upsilon)(1-\Upsilon_1)\left[J_{m-1}^2(q_1 r_\mathrm{c}) - J_m(q_1 r_\mathrm{c}) J_{m-2}(q_1 r_\mathrm{c})\right] \\ +(1+\Upsilon)(1+\Upsilon_1)\left[J_{m+1}^2(q_1 r_\mathrm{c}) - J_m(q_1 r_\mathrm{c}) J_{m+2}(q_1 r_\mathrm{c})\right]\end{array}\right\}, \tag{B.44}$$

whereas the power contained within the evanescent field of the mode is given by

$$P_2 = \frac{\pi}{4}\frac{|\mathcal{U}_2|^2 \tilde{k}_z \tilde{k}_2^2 r_\mathrm{c}^2}{\mu_0 \omega_\mathrm{c} q_2^2}\left\{\begin{array}{l}(1-\Upsilon)(1-\Upsilon_2)\left[K_{m-1}^2(q_2 r_\mathrm{c}) - K_m(q_2 r_\mathrm{c}) K_{m-2}(q_2 r_\mathrm{c})\right] \\ +(1+\Upsilon)(1+\Upsilon_2)\left[K_{m+1}^2(q_2 r_\mathrm{c}) - K_m(q_2 r_\mathrm{c}) K_{m+2}(q_2 r_\mathrm{c})\right]\end{array}\right\}. \tag{B.45}$$

The total power carried by each guided mode is then simply given by the sum of these two powers as $P_\mathrm{tot} = P_1 + P_2$.

The above results provide exact solutions for the electromagnetic fields of an infinite cylinder, with their propagation constant $\tilde{k}_z$ determined using the dispersion relation of Eq. (B.38). Unfortunately, this dispersion relation is a complicated implicit transcendental function of the waveguide's parameters, such that it gives little intuition into the behaviour of the system. However, the situation is simplified considerably if we implement the weakly-guiding approximation (WGA) [444, 445], for which $\tilde{n}_1 \approx \tilde{n}_2$. Note that for standard fiber optics, $\tilde{n}_1 \approx 1.5$ such that the WGA approximation holds reasonably well even for fiber cores surrounded by air/vacuum where $\tilde{n}_2 \approx 1$. In this case, the dispersion relation given in Eq. (B.38) becomes

$$\frac{J'_m(q_1 r_c)}{q_1 J_m(q_1 r_c)} + \frac{K'_m(q_2 r_c)}{q_2 K_m(q_2 r_c)} = \pm \frac{m}{r_c}\left(\frac{1}{q_1^2} + \frac{1}{q_2^2}\right), \tag{B.46}$$

where the plus (minus) sign corresponds to the EH_{mn} (HE_{mn}) modes. Comparing Eq. (B.46) to Eq. (B.38), we see that this new dispersion relation is equivalent to setting $\Upsilon = \Upsilon_1 = \Upsilon_2 = 1$ for EH_{mn} modes and $\Upsilon = \Upsilon_1 = \Upsilon_2 = -1$ for HE_{mn} modes. Inputting these relations into Eqs. (B.23)–(B.34), as well as Eqs. (B.44) and (B.45), we can determine the electromagnetic fields of, and the power carried by, these simplified EH and HE hybrid modes. Note that in the WGA, the TE_{0n} and TM_{0n} modes become degenerate, with their new shared dispersion relation given by setting $m = 0$ in Eq. (B.46). Using the recursion relations of the Bessel functions found in Appendix A, we can therefore write the WGA dispersion relation in the unified form

$$\frac{q_1 J_{\nu-1}(q_1 r_c)}{J_\nu(q_1 r_c)} = -\frac{q_2 K_{\nu-1}(q_2 r_c)}{K_\nu(q_2 r_c)}, \tag{B.47}$$

where $\nu = m + 1$ for EH_{mn} modes, $\nu = m - 1$ for HE_{mn} modes, and $\nu = 1$ for $\mathrm{TE}_{0n}/\mathrm{TM}_{0n}$ modes. The lowest order mode (corresponding to the smallest value of ν) is given by the HE_{11} mode, which obeys the dispersion relation

$$\frac{q_1 J_1(q_1 r_c)}{J_0(q_1 r_c)} = \frac{q_2 K_1(q_2 r_c)}{K_0(q_2 r_c)}, \tag{B.48}$$

where we have used the identities $J_{-1}(q_1 r_c) = -J_1(q_1 r_c)$ and $K_{-1}(q_2 r_c) = K_1(q_2 r_c)$ (see Appendix A). Note that since $\lim_{q_2 r_c \to 0} q_2 r_c K_1(q_2 r_c)/K_0(q_2 r_c) = 0$, there will always be a choice of $q_1 r_c$ that satisfies this dispersion relation. Therefore, this fundamental HE_{11} mode will always exist regardless of how small r_c becomes.

In general, an infinitely long cylinder will support a multitude of optical TE_{0n}, TM_{0n}, EH_{mn}, and HE_{mn} modes, lending to the description of a multimode fiber. As we reduce the radius of the cylinder, however, the higher order modes of the system will begin to die out, until finally, the penultimate TE_{01} and TM_{01} are cut off. Below this critical radius, known as the single-mode cut-off radius r_*, the fiber becomes single mode, supporting only the single HE_{11}. As this is the mode that exists in the single-mode tapered fiber waveguide we use to couple to the modes of our optical cavities, we spend the rest of this subsection determining this cut-off radius, as well as detailing the properties of the HE_{11} mode.

Continuing with the WGA[1], we determine r_* as the cylinder radius at which $\tilde{k}_z = \tilde{k}_2$ for the TE_{01} and TM_{01} modes, such that they evanescently decay into their surroundings, preventing these modes from being guided down the cylinder. Mathematically, this is equivalent to setting $\nu = 1$ ($m = 0$) and $q_2 = 0$ in Eq. (B.47). Using the fact that $\lim_{q_2 r_c \to 0} q_2 r_c K_0(q_2 r_c)/K_1(q_2 r_c) = 0$, Eq. (B.47) will then have solutions when $q_1 r_c J_0(q_1 r_c) = 0$. Therefore, one solution will always exist for for $q_1 r_c = 0$, which corresponds to the HE_{11} mode (see Eq. (B.48)). The penultimate degenerate TE_{01} and TM_{01} modes then come into existence when $J_0(q_1 r_c) \geq 0$, which occurs for

$$q_1 r_c \geq Z_{0,0} \approx 2.4048, \tag{B.49}$$

where $Z_{m,n}$ is the nth zero of $J_m(z)$ (*i.e.* the mth-order Bessel function of the first kind). Using the fact that $\tilde{k}_z = \tilde{k}_2$ for $r_c = r_*$, we can take equality in Eq. (B.49) and rearrange to solve for the single mode cut-off diameter of the cylinder as

$$d_* = 2r_* = \frac{Z_{0,0}\lambda_0}{\pi\sqrt{\tilde{n}_1^2 - \tilde{n}_2^2}} \approx \frac{2.4048\lambda_0}{\pi\sqrt{\tilde{n}_1^2 - \tilde{n}_2^2}}. \tag{B.50}$$

Table B.1 gives this cut-off diameter for a number of commonly used experimental wavelengths in both vacuum and aqueous environments.

For cylinder radii $r_c < r_*$, all light travelling through the cylinder will reside in the fundamental HE_{11} mode, whose electric fields within the cylinder can be found

[1] One could also determine the exact radius at which the fiber becomes single mode by taking $m = 0$ and solving Eq. (B.38) numerically by iteratively increasing r until a solution emerges. However, this procedure is cumbersome and is ultimately unnecessary for the fiber waveguides considered in Section 5.3.

λ_0 (nm)	$\tilde{n}_1$	$\tilde{n}_1$	d_* (nm)	
			WGA	Numerical
637	1.47	1.00	452.6	452.6
	1.47	1.33	778.8	778.9
780	1.47	1.00	554.1	554.2
	1.47	1.33	953.6	953.7
1310	1.47	1.00	930.7	930.7
	1.47	1.33	1601.6	1601.7
1550	1.47	1.00	1101.2	1101.2
	1.47	1.33	1895.0	1895.1

Table B.1: Single mode cutoff diameter calculated using both the WGA approximation and numerical calculations for green light (637 nm) observed in nitrogen vacancy photoluminescence [446] and near-infrared light (780 nm) used in aqueous biosensing [447], as well as the dispersionless and low attenuation telecom wavelengths of 1310 nm and 1550 nm. All calculations are performed for a standard telecom optical silica fiber ($\tilde{n}_1 = 1.47$) in both vacuum/air ($\tilde{n}_2 = 1.0$) and aqueous ($\tilde{n}_2 = 1.33$) environments. Here we assume the indices of refraction are constant over the considered wavelength range, as is observed for these media [337, 448]. The appropriate number of digits are retained to show the difference in WGA and numerical calculations.

by inputting $m = 1$ and $\Upsilon = -1$ into Eqs. (B.23)–(B.25) to find

$$E_r = -i\mathcal{U}_1 \frac{\tilde{k}_z}{q_1} J_0(q_1 r)\cos(\phi), \tag{B.51}$$

$$E_\phi = i\mathcal{U}_1 \frac{\tilde{k}_z}{q_1} J_0(q_1 r)\sin(\phi), \tag{B.52}$$

$$E_z = \mathcal{U}_1 J_1(q_1 r)\cos(\phi), \tag{B.53}$$

with similar expressions outside the cylinder found by taking $J_0(q_1 r) \to K_0(q_2 r_c)$, $J_0(q_1 r) \to K_0(q_2 r_c)$, and $\mathcal{U}_1 \to \mathcal{U}_2$. Note that since $\tilde{k}_z > q_1$ and $J_0(q_1 r) > J_1(q_1 r)$ for $r < r_*$, $E_r, E_\phi > E_z$ such that the transverse electric fields dominate the mode. Furthermore, by rotating to a Cartesian representation of these transverse fields, we find

$$E_x = E_r\cos\phi - E_\phi \sin\phi = -i\mathcal{U}_1 \frac{\tilde{k}_z}{q_1} J_0(q_1 r), \tag{B.54}$$

$$E_y = E_r \sin\phi + E_\phi \cos\phi = 0. \tag{B.55}$$

Therefore, in the WGA the HE_{11} mode behaves like a TE mode, with its electric field polarized along the x-axis of the fiber. It is this linearly polarized mode, which

is often labelled the LP_{01} mode, that is used to guide light through all standard single-mode optical fibers[2].

Finally, by inputting $m = 1$ and $\Upsilon = \Upsilon_1 = \Upsilon_2 = -1$ into Eqs. (B.44) and (B.45), we determine the power carried both within the cylinder and through its surroundings as

$$P_1 = \frac{\pi |\mathcal{U}_1|^2 \tilde{k}_z \tilde{k}_1^2 r_\mathrm{c}^2 J_0^2(q_1 r_\mathrm{c})}{\mu_0 \omega_\mathrm{c} q_1^2} \left[1 + \frac{q_2^2}{q_1^2} \frac{K_1^2(q_2 r_\mathrm{c})}{K_0^2(q_2 r_\mathrm{c})}\right], \tag{B.56}$$

$$P_2 = \frac{\pi |\mathcal{U}_1|^2 \tilde{k}_z \tilde{k}_2^2 r_\mathrm{c}^2 J_0^2(q_1 r_\mathrm{c})}{\mu_0 \omega_\mathrm{c} q_2^2} \left[\frac{K_1^2(q_2 r_\mathrm{c})}{K_0^2(q_2 r_\mathrm{c})} - 1\right], \tag{B.57}$$

respectively. Here we have used the WGA recursion relation for the HE_{11} mode given by Eq. (B.48), as well as the relation between $\mathcal{U}_1$ and $\mathcal{U}_2$ given by Eq. (B.40). The total power guided by the HE_{11} mode of the cylinder is then found as

$$\begin{aligned} P_\mathrm{tot} &= \frac{\pi |\mathcal{U}_1|^2 \tilde{k}_z \tilde{k}_1^2 r_\mathrm{c}^2 J_0^2(q_1 r_\mathrm{c}) \left(q_1^2 + q_2^2\right)}{\mu_0 \omega_\mathrm{c} q_1^4} \frac{K_1^2(q_2 r_\mathrm{c})}{K_0^2(q_2 r_\mathrm{c})} \\ &= \frac{\pi |\mathcal{U}_1|^2 \tilde{k}_z \tilde{k}_1^2 r_\mathrm{c}^2 J_1^2(q_1 r_\mathrm{c})}{\mu_0 \omega_\mathrm{c}} \frac{q_1^2 + q_2^2}{q_1^2 q_2^2}, \end{aligned} \tag{B.58}$$

where we have again invoked the WGA to make the approximation $\tilde{k}_1 \approx \tilde{k}_2$ and used the dispersion relation in Eq. (B.48) to get from the first line to the second line. Assuming that $\mathcal{U}_1$ is real-valued, we can also invert Eq. (B.58) to determine this field amplitude coefficient in terms of the total power injected into the fundamental mode as

$$\mathcal{U}_1 = \frac{q_1 q_2}{\tilde{k}_1 r_\mathrm{c} J_1(q_1 r_\mathrm{c})} \sqrt{\frac{\mu_0 \omega_0 P_\mathrm{tot}}{\pi \tilde{k}_z \left(q_1^2 + q_2^2\right)}}, \tag{B.59}$$

where $\omega_0 = c\tilde{k}_0$ is the frequency of the guided light. Finally, dividing each of P_1 and P_2 by this total power, we find the ratio of guided power both inside and outside the cylinder

$$\frac{P_1}{P_\mathrm{tot}} = 1 - \frac{q_1^2}{q_1^2 + q_2^2} \left[1 - \frac{K_0^2(q_2 r_\mathrm{c})}{K_1^2(q_2 r_\mathrm{c}}\right], \tag{B.60}$$

$$\frac{P_2}{P_\mathrm{tot}} = \frac{q_1^2}{q_1^2 + q_2^2} \left[1 - \frac{K_0^2(q_2 r_\mathrm{c})}{K_1^2(q_2 r_\mathrm{c})}\right]. \tag{B.61}$$

[2]Note that the choice of orientation along the x-axis was set by the arbitrarily chosen phase for the ϕ-axis. In practice, the polarization direction of the guided light will be set by the polarization of the incoming wave and may also rotate due to strain-induced birefringence.

In Fig. B.3, we plot each of these ratios as a function of the cylinder radius normalized to the single-mode cut-off radius, demonstrating how the power in the guided mode leaks into its surroundings as the cylinder radius is reduced.

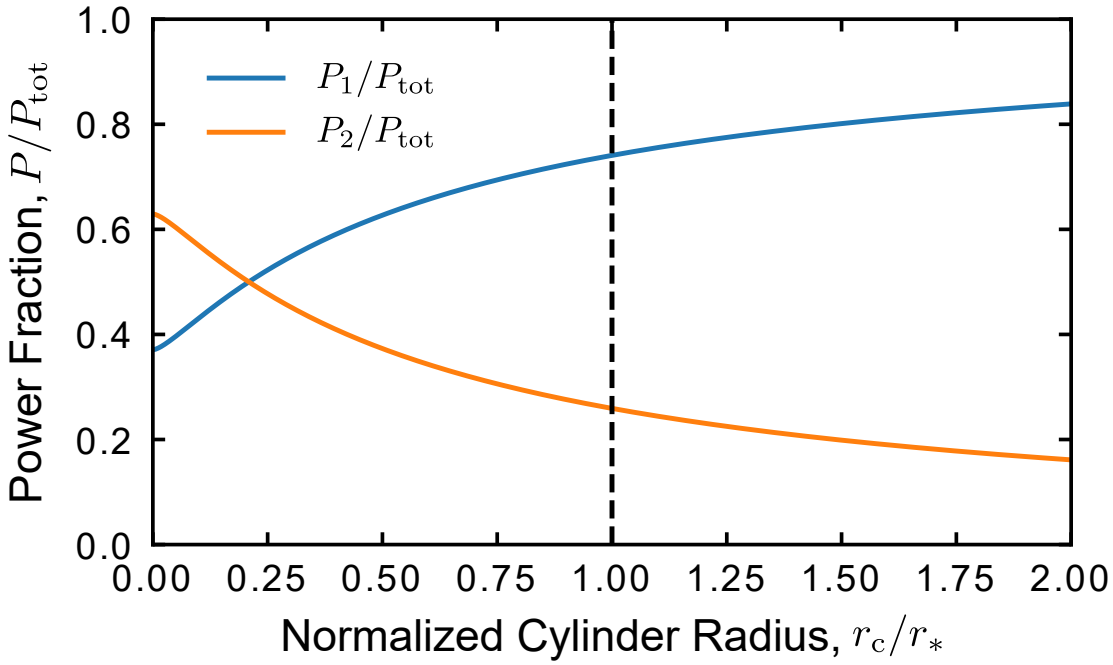

Figure B.3: Fraction of the total power guided both within the cylinder (blue) and in the surrounding medium (orange) versus cylinder radius (normalized to the single-mode cut-off radius r_*) for the HE_{11} mode according to Eqs. (B.60) and (B.61), respectively. Here we have taken the index of refraction of the cylinder to be $\tilde{n}_1 = 1.47$, matching the index for our tapered fiber waveguides discussed in Section 5.3. The black dashed line indicates the single-mode cut-off diameter, at which approximately three-quarters of the guided optical power exists within the cylinder, with the remaining one-quarter found outside its confines. Below this point, we find that the power inside (outside) the cylinder continues to decrease (increase) with decreasing radius, with equal power in both regions at approximately one-quarter the single-mode cut-off radius.

B.3 Optical Microdisks

The general formalism used to calculate the electromagnetic fields in cylindrically symmetric geometries introduced in Section B.1 can also be used to determine the electromagnetic fields in thin microdisk cavities. Here we consider a thin disk of thickness t and radius R with a refractive index of $\tilde{n}_d$, immersed in a surrounding medium with refractive index $\tilde{n}_s$. Placing the origin of the cylindrical coordinate

system at the center of the disk, with the z-axis aligned as seen in Fig. B.1, the refractive index profile of the disk will then be given by

$$\tilde{n}(r,z) = \begin{cases} \tilde{n}_{\mathrm{d}}, & r \leq R;\ -\frac{t}{2} \leq z \leq \frac{t}{2} \\ \tilde{n}_{\mathrm{s}}, & \text{otherwise} \end{cases}. \tag{B.62}$$

Unfortunately, due to the sharp corners of the disk at $r = R$ and $z = \pm t/2$, combined with the diffraction of any light that exits the disk radially [265], it is difficult, if not impossible to determine exact analytical solutions for the optical modes of such a geometry. However, here we introduce a simple effective index method that allows us to very accurately approximate the optical fields within the disk, while also predicting their resonance conditions.

Unlike an infinite cylinder, the thin optical microdisk considered here is unable to support hybrid modes, such that we need only consider the case of TE and TM modes. Here we will focus on the TE modes of the disk, as they are the relevant modes for our experiments (see Section 3.3). As before, to calculate the electromagnetic fields of these modes we first determine the scalar function ψ_{TE}, which we then input into Eqs. (B.3)–(B.8), while setting $\psi_{\mathrm{TM}} = 0$. Fortunately, the geometry of our disk is very similar to the infinite cylinder discussed in the previous subsection, save for the truncation in the z-direction. Therefore, we can recycle the functional form for ψ given by Eq. (B.12), where we use Eqs. (B.17) and (B.18) as the solutions for $\psi_\phi(\phi)$ and $\psi_r(r)$, respectively, while we introduce a new piecewise function for $\psi_z(z)$ as [443]

$$\psi_z(z) = \begin{cases} e^{-q_{\mathrm{t}}(z-t/2)}\cos(\tilde{k}_z t/2), & z > \frac{t}{2} \\ \cos(\tilde{k}_z z), & -\frac{t}{2} \leq z \leq \frac{t}{2} \\ e^{q_{\mathrm{t}}(z+t/2)}\cos(\tilde{k}_z t/2) & z < -\frac{t}{2} \end{cases} \tag{B.63}$$

where q_{d} and q_{s} are defined similar to q_1 and q_2 in the previous section (*i.e.* $q_{\mathrm{d}}^2 = k_{\mathrm{d}}^2 - \tilde{k}_z^2$ and $q_{\mathrm{s}}^2 = \tilde{k}_z^2 - k_{\mathrm{s}}^2$), while $q_{\mathrm{t}}^2 = \tilde{k}_0^2(\tilde{n}_{\mathrm{d}}^2 - \tilde{n}_{\mathrm{s}}^2) - \tilde{k}_z^2$. Note that in this new $\psi_z(z)$ function we have implicitly assumed that the disk is thin enough that it can only support one mode in the z-direction [265]. Furthermore, with this $\psi_z(z)$ function the evanescent fields of the disk will decay exponentially as we move away from its top and bottom, representing a bound optical mode as opposed to the travelling electromagnetic wave of an infinite cylinder described in the previous

subsection. Using this representation for $\psi_z(z)$, the scalar function for the TE modes is then determined as

$$\frac{\psi_{\mathrm{TE}}(\mathbf{r})}{\mathcal{M}_{\mathrm{TE}}} = \begin{cases} J_m(q_{\mathrm{d}}r)e^{-q_{\mathrm{t}}(z-t/2)}\cos(\tilde{k}_z t/2)e^{im\phi}, & r \le R;\ z > \frac{t}{2} \\ \dfrac{J_m(q_{\mathrm{d}}R)}{K_m(q_{\mathrm{s}}R)}K_m(q_{\mathrm{s}}r)e^{-q_{\mathrm{t}}(z-t/2)}\cos(\tilde{k}_z t/2)e^{im\phi}, & r \ge R;\ z > \frac{t}{2} \\ J_m(q_{\mathrm{d}}r)\cos(\tilde{k}_z z)e^{im\phi}, & r \le R;\ -\frac{t}{2} \le z \le \frac{t}{2} \\ -\dfrac{q_{\mathrm{d}}^2 J_m(q_{\mathrm{d}}R)}{q_{\mathrm{s}}^2 K_m(q_{\mathrm{s}}R)}K_m(q_{\mathrm{s}}r)\cos(\tilde{k}_z z)e^{im\phi}, & r \ge R;\ -\frac{t}{2} \le z \le \frac{t}{2} \\ J_m(q_{\mathrm{d}}r)e^{q_{\mathrm{t}}(z+t/2)}\cos(\tilde{k}_z t/2)e^{im\phi}, & r \le R;\ z < -\frac{t}{2} \\ \dfrac{J_m(q_{\mathrm{d}}R)}{K_m(q_{\mathrm{s}}R)}K_m(q_{\mathrm{s}}r)e^{q_{\mathrm{t}}(z+t/2)}\cos(\tilde{k}_z t/2)e^{im\phi}, & r \ge R;\ z < -\frac{t}{2} \end{cases}. \tag{B.64}$$

Here we have chosen to normalize the scalar function in each region to ensure that the B_z field satisfy their corresponding electromagnetic boundary conditions [258]. In this way, we can then simply input these scalar functions into Eqs. (B.3)–(B.8) to determine the electromagnetic fields for the microdisk. For example, B_z will be given by

$$B_z(r,\phi,z) = \left[k^2(r,z) + \tilde{\zeta}^2(z)\right]\psi_{\mathrm{TE}}(r,\phi,z), \tag{B.65}$$

where again $\tilde{k}(r,z) = \tilde{k}_0\tilde{n}(r,z)$ is the position-dependent wavenumber of the cavity mode and $\tilde{\zeta}(z)$ is defined as

$$\tilde{\zeta}(z) = \begin{cases} -q_{\mathrm{t}}, & z > \frac{t}{2} \\ i\tilde{k}_z, & -\frac{t}{2} \le z \le \frac{t}{2} \\ q_{\mathrm{t}}, & z < -\frac{t}{2} \end{cases}. \tag{B.66}$$

Note that as with the infinite cylinder, the modes with $m \neq 0$ are doubly-degenerate, such that there are two solutions for each mode given by the real and imaginary parts of their calculated fields. In Fig. B.4, we plot the normalized spatial distribution of the B_z field given in Eq. (B.65) and compare its to its FEM-simulated counterpart. Here we see that our result provides an excellent approximation to the electromagnetic fields of the disk, with a discrepancy of $\sim$5% between the analytically calculated and simulated fields. Unsurprisingly, this maximal discrepancy occurs at the sharp corners of the disk located at $r = R$ and $z = \pm t/2$, which introduce a singular boundary condition such that the fields are poorly-defined in this region. Using the approximation of B_z given by Eq. (B.65), we

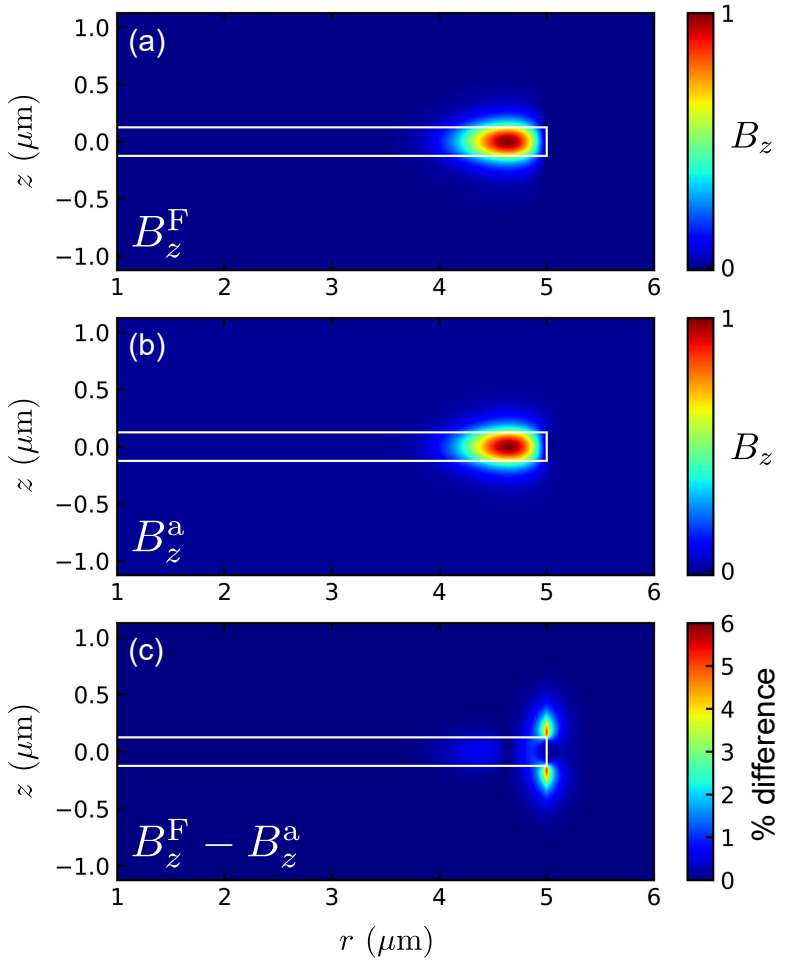

Figure B.4: Comparison of B_z for the $n = 1$, $m = 51$ TE mode simulated at $\lambda_c = 1555.384$ nm for the microdisk cavities studied in this thesis ($R = 5$ μm, $t = 250$ nm, $\tilde{n}_d \approx 3.45$) computed using (a) FEM simulation (B_z^{F}) and (b) the analytical approximation calculated using Eqs. (B.64) and (B.65) (B_z^{a}). Each of these fields are normalized to their maximum values, with the residual between the two ($B_z^{\mathrm{F}} - B_z^{\mathrm{a}}$) given in (c). Here we see that the analytical calculation always undershoots the value of B_z compared to the FEM simulation, with a maximum percent difference between these two methods of $\sim$5% occurring at the corners of the disk.

can analytically calculate a number of properties for the TE modes of our microdisk resonators, such as their effective refractive indices and resonant wavelengths.

With the functional form of the electromagnetic modes of the disks determined, we now look to calculate their dispersion relations. This is done by matching the electromagnetic fields at each interface according to the appropriate boundary condition [258]. Here we have two independent boundaries, with one at $r = R$

and one at $z = \pm t/2$, such that we obtain two dispersion relations for each mode. Matching the fields for the TE modes, we find the two dispersion relations for the mth-order azimuthal mode[3] as

$$\tan\left(\frac{\tilde{k}_0 t}{2}\sqrt{\tilde{n}_{\mathrm{d}}^2 - \tilde{n}_{\mathrm{TE}}^2}\right) = \frac{\sqrt{\tilde{n}_{\mathrm{TE}}^2 - \tilde{n}_{\mathrm{s}}^2}}{\sqrt{\tilde{n}_{\mathrm{d}}^2 - \tilde{n}_{\mathrm{TE}}^2}}, \tag{B.67}$$

$$\frac{J_m'(q_{\mathrm{d}}R)}{q_{\mathrm{d}}J_m(q_{\mathrm{d}}R)} + \frac{K_m'(q_{\mathrm{s}}R)}{q_{\mathrm{s}}J_m(q_{\mathrm{s}}R)} = 0, \tag{B.68}$$

where we have introduced the effective refraction index of the TE mode as $\tilde{n}_{\mathrm{TE}} = q_{\mathrm{d}}/\tilde{k}_0$.

The dispersion relations given by Eqs. (B.67) and (B.68) are complicated transcendental functions that must be solved numerically in order to determine the resonance frequencies of the disk's optical modes. This is done by first inputting an initial guess wavelength λ_1 into Eq. (B.67) and solving this transcendental equation to extract $\tilde{n}_{\mathrm{TE}}$ at λ_1. Once solved for, this value of $\tilde{n}_{\mathrm{TE}}$ is used to determine q_{d}, as well as $\tilde{k}_z$ and q_{s}, at the considered wavelength. All of these wavevectors are then fed into Eq. (B.68), which is solved to determine the resonance wavelength of the disk $\lambda_{mn,1}$ at the considered effective index. Generally, after a single run through of this procedure, $\lambda_{mn,1} \neq \lambda_1$. Therefore, we repeat this recipe by taking our new initial guess wavelength to be $\lambda_2 = \lambda_{mn,1}$, and continue iteratively until $\lambda_{mn,i} = \lambda_i$ to within the desired tolerance[4]. Note that this procedure can be used to determine each of the n radial modes of the disk, which correspond to the nth solution of Eq. (B.68). Using this numerical method, we calculate the resonant wavelengths of the fundamental radial ($n = 1$) TE modes of our microdisks over the wavelength range of 1500 - 1640 nm, as summarized by Table 3.1 in Section 3.3, where we see good agreement between our analytically calculated results and the corresponding FEM-simulated values.

[3]The azimuthal mode number m counts the $2m$ nodes of the WGM in the ϕ-direction.

[4]Alternatively, one could interpolate the effective index over the range of interest (see Fig. 3.2), extracting $\tilde{n}_{\mathrm{TE}}$ as a function of wavelength, which can then be put into Eq. (B.68) to determine λ_{mn} directly.

Appendix C

Determination of the Optomechanical Coupling Coefficients using Non-Degenerate Perturbation Theory

Here we use the perturbative approach developed by Johnson *et al.* [279] to determine the first- and second-order optomechanical coupling coefficients for mechanical systems coupled to non-degenerate optical modes. In doing so, we show that it is possible, in principle, to completely eliminate linear coupling in favour of quadratic coupling by exploiting the symmetry of an optomechanical system.

We begin by considering a high-Q optical mode with resonant angular frequency ω_i and a corresponding electric field profile $\mathbf{E}_i(\mathbf{r},t) = \mathcal{E}_i(t)\mathbf{E}_i(\mathbf{r})$. As is detailed in Section 3.2, we can then use Maxwell's equations for a source-free, non-magnetic dielectric to obtain the Helmholtz equation for the electric field modeshape $\mathbf{E}_i(\mathbf{r})$ (see Eq. (3.9)) as

$$\nabla^2 |\mathcal{E}_i\rangle = -\frac{\omega_i^2 \epsilon_i(\mathbf{r})}{c^2} |\mathcal{E}_i\rangle \,, \tag{C.1}$$

where the cavity's geometry is specified by its spatially-varying relative permittivity profile $\epsilon_i(\mathbf{r}) = \tilde{n}_i^2(\mathbf{r})$. Here we have also chosen to follow the notation of Johnson *et al.* by representing the electric field of the cavity mode using the Dirac braket state vector notation, where $|\mathcal{E}_i\rangle = \mathbf{E}_i(\mathbf{r})$ and $\langle\mathcal{E}_i| = \mathbf{E}_i^*(\mathbf{r})$. The inner product between

two optical modes characterized by the state vectors $|\mathcal{E}_i\rangle$ and $|\mathcal{E}_j\rangle$ is then defined as

$$\langle \mathcal{E}_i | \mathcal{E}_j \rangle \equiv \int_V \mathbf{E}_i^*(\mathbf{r}) \cdot \mathbf{E}_j(\mathbf{r}) dV, \tag{C.2}$$

where the integral is performed over the entire volume of the optomechanical system [279]. With this definition, the optical modes of the cavity are orthogonal in the sense that $\langle \mathcal{E}_i | \, \epsilon_i \, | \mathcal{E}_j \rangle = \langle \mathcal{E}_i | \, \epsilon_i \, | \mathcal{E}_i \rangle \, \delta_{ij}$.

We now imagine introducing a small shift in the cavity's permittivity profile, resulting in $\epsilon_i(\mathbf{r}) \to \epsilon_i(\mathbf{r}) + \delta\epsilon_i(\mathbf{r})$. Treating the problem perturbatively, we determine the new electric field vector $|\mathcal{E}_i'\rangle$, along with the corresponding cavity resonance frequency ω_i', in this shifted geometry by expanding to second order as

$$|\mathcal{E}_i'\rangle = |\mathcal{E}_i^{(0)}\rangle + |\mathcal{E}_i^{(1)}\rangle + |\mathcal{E}_i^{(2)}\rangle \, , \tag{C.3}$$

$$\omega_i' = \omega_i^{(0)} + \omega_i^{(1)} + \omega_i^{(2)}. \tag{C.4}$$

Here the superscript (0) denotes the original unperturbed quantity, while the (1) and (2) indicate the first- and second-order corrections, proportional to $\delta\epsilon_i$ and $(\delta\epsilon_i)^2$, respectively. We note that these higher order corrections to the electric field are chosen to be orthogonal to the unperturbed field in the same sense as before such that $\langle \mathcal{E}_i^{(0)} | \, \epsilon_i \, | \mathcal{E}_i^{(n>0)} \rangle = 0$.

For perturbations that are optomechanical in nature, the shift of the dielectric profile will be induced due to the motion of a mechanical element. In this case, we can also expand the optical mode frequency to second order in a similar fashion to Eq. (8.9) as

$$\omega_i' = \omega_i - G_1 \delta x - \frac{G_2}{2} (\delta x)^2, \tag{C.5}$$

where G_1 and G_2 are defined in Section 8.3.1, while δx is the resonator's displacement from equilibrium. Matching these terms with the ones found in Eq. (C.4), Eq. (C.1) can be solved order-by-order to find [146, 279, 409, 449, 450]

$$\omega_i = \omega_i^{(0)}, \tag{C.6}$$

$$G_1 = \frac{\omega_i^{(1)}}{\delta x} = -\frac{\omega_i}{2} \frac{\langle \mathcal{E}_i^{(0)} | \, \frac{d\epsilon_i}{dx} \, | \mathcal{E}_i^{(0)} \rangle}{\langle \mathcal{E}_i^{(0)} | \, \epsilon_i \, | \mathcal{E}_i^{(0)} \rangle}, \tag{C.7}$$

$$G_2 = \frac{\omega_i^{(2)}}{(\delta x)^2} = \frac{3 G_1^2}{\omega_i} + \sum_{\omega_j \neq \omega_i} \mathcal{G}_{ij}, \tag{C.8}$$

where the sum is performed over all other optical cavity modes and

$$\mathcal{G}_{ij} = \frac{\omega_i^3}{\omega_i^2 - \omega_j^2} \frac{|\langle \mathcal{E}_j^{(0)}| \frac{d\epsilon_i}{dx} |\mathcal{E}_i^{(0)}\rangle|^2}{\langle \mathcal{E}_i^{(0)}| \epsilon_i |\mathcal{E}_i^{(0)}\rangle \langle \mathcal{E}_j^{(0)}| \epsilon_i |\mathcal{E}_j^{(0)}\rangle}. \tag{C.9}$$

Upon inspection of Eq. (C.7), we see that linear coupling is proportional to the self-overlap of the optical mode, mediated by the change in relative permittivity with respect to the mechanical displacement. Meanwhile, in Eq. (C.8) the quadratic coupling exhibits both a self-overlap term, as well as a term depending on the cross-coupling between the original unperturbed modes and the other non-degenerate cavity modes (the case of quadratic coupling in degenerate cavity modes was discussed in Section 8.3). Therefore, linear optomechanical coupling will in principle be zero if the field self-overlap term vanishes, that is $\langle \mathcal{E}_i^{(0)}| \frac{d\epsilon_i}{dx} |\mathcal{E}_i^{(0)}\rangle = 0$ [409]. Furthermore, in this situation the quadratic coupling is given by

$$G_2 = \sum_{\omega_j \neq \omega_i} \mathcal{G}_{ij}, \tag{C.10}$$

with only the cross-coupling terms surviving. Therefore, provided these terms do not sum to zero, a non-zero quadratic coupling can be achieved in the absence of linear coupling [409].

To better understand the physical conditions that lead to vanishing linear optomechanical coupling, we investigate the case where the optomechanical coupling is due to shifting the boundary conditions of the optical mode (as opposed to the photoelastic effect [67, 280–282]), pertinent to the majority of optomechanical systems. For this situation, we find that [146, 279]

$$\langle \mathcal{E}_i| \frac{d\epsilon_i}{dx} |\mathcal{E}_j\rangle = \int_S \mathbf{u}(\mathbf{r}) \cdot \mathbf{n}(\mathbf{r}) \left[\Delta\epsilon \mathbf{E}_i^{\parallel *} \cdot \mathbf{E}_j^{\parallel} - \Delta\epsilon^{-1} \boldsymbol{\mathcal{D}}_i^{\perp *} \cdot \boldsymbol{\mathcal{D}}_j^{\perp}\right] dA, \tag{C.11}$$

where $\mathbf{u}(\mathbf{r})$ is the mechanical modeshape function and $\boldsymbol{\mathcal{D}}_i(\mathbf{r}) = \epsilon_0 \epsilon_i(\mathbf{r}) \mathbf{E}_i(\mathbf{r})$ is the electric displacement field, with ϵ_0 being the permittivity of free space. The integral is performed over the surface of the unperturbed optical resonator as defined by its unit normal vector $\mathbf{n}(\mathbf{r})$. We have also introduced the superscripts $\parallel$ and $\perp$ to denote the components of the associated fields parallel and perpendicular to the cavity surface. Finally, $\Delta\epsilon = \epsilon_\mathrm{d} - \epsilon_\mathrm{s}$ and $\Delta\epsilon^{-1} = \epsilon_\mathrm{d}^{-1} - \epsilon_\mathrm{s}^{-1}$, where ϵ_d and ϵ_s are the relative permittivities of the optomechanical device's material and the surrounding medium, respectively.

The expression in Eq. (C.11) will be zero if the integrand is an odd function with respect to the symmetry axes of the optical cavity. In practice, this can be realized by implementing an optical intensity profile that exhibits even symmetry, along with a mechanical modeshape (after dot product with the unit surface normal) that demonstrates odd symmetry [409]. This amounts to having an optical field that is unable to distinguish the direction of motion of the mechanics, leading to an optical frequency shift that is even with respect to mechanical displacement. Therefore, the first term in the cavity expansion (ignoring the zeroth-order term corresponding to the unperturbed cavity frequency) must be proportional to $(\delta x)^2$, leading to quadratic optomechanical coupling.

Appendix D

Derivation of the Optomechanical Quantum Langevin Equations

D.1 Creation and Annihilation Operator Representation

In this appendix, we use the Heisenberg equation given by Eq. (4.11) to determine the QLEs of a dispersively coupled optomechanical system interacting with its surrounding bath. Starting with the creation and annihilation operators of the system, we begin by inputting the Hamiltonian given by Eq. (4.10) into Eq. (4.11), which results in the equations of motion for $\hat{a}(t)$ and $\hat{b}(t)$ as [150]

$$\dot{\hat{a}} = -i\omega_{\mathrm{c}}\hat{a} + ig_0\left(\hat{b}^\dagger + \hat{b}\right)\hat{a} + f_{\mathrm{dr}}\hat{a}_{\mathrm{dr}} + \sum_p f_p\hat{a}_p, \tag{D.1}$$

$$\dot{\hat{b}} = -i\omega_{\mathrm{m}}\hat{b} + ig_0\hat{a}^\dagger\hat{a} + \sum_q f_q\hat{b}_q, \tag{D.2}$$

along with those corresponding to the drive and bath modes given by

$$\dot{\hat{a}}_{\mathrm{dr}} = -i\omega_{\mathrm{d}}\hat{a}_{\mathrm{dr}} - f^*_{\mathrm{dr}}\hat{a}, \tag{D.3}$$

$$\dot{\hat{a}}_p = -i\omega_p\hat{a}_p - f^*_p\hat{a}, \tag{D.4}$$

$$\dot{\hat{b}}_q = -i\omega_q\hat{b}_q - f^*_q\hat{b}. \tag{D.5}$$

To proceed, we solve Eqs. (D.3)–(D.5) for the annihilation operators of the drive and bath modes and input these solutions into Eqs. (D.1) and (D.2).

Beginning with the drive mode, we formally integrate Eq. (D.3), resulting in

$$\hat{a}_{\mathrm{dr}}(t) = e^{-i\omega_{\mathrm{d}}(t-t_i)}\hat{a}_{\mathrm{dr}}(t_i) - f^*_{\mathrm{dr}}\int_{t_i}^{t} e^{-i\omega_{\mathrm{d}}(t-t')}\hat{a}(t')dt', \tag{D.6}$$

where t_i is a time in the distant past long before the drive field has had an opportunity to interact with the cavity [203]. Using this representation for $\hat{a}_{\mathrm{dr}}(t)$, we can then express the third term on the right-hand side of Eq. (D.1) as

$$f_{\mathrm{dr}}\hat{a}_{\mathrm{dr}}(t) = f_{\mathrm{dr}}e^{-i\omega_{\mathrm{d}}(t-t_i)}\hat{a}_{\mathrm{dr}}(t_i) - |f_{\mathrm{dr}}|^2\int_{t_i}^{t} e^{-i\omega_{\mathrm{d}}(t-t')}\hat{a}(t')dt'. \tag{D.7}$$

We now look to determine the coefficient f_{dr} in terms of the coupling rate κ_{e} between the optical cavity and its external coupler (*i.e.* the rate at which photons are coupled into/out of the cavity). This is done using a Fermi's Golden Rule calculation to find [203]

$$\kappa_{\mathrm{e}} = 2\pi|f_{\mathrm{dr}}|^2\delta(\omega_{\mathrm{d}} - \omega_{\mathrm{c}}), \tag{D.8}$$

where the Dirac delta function $\delta(\omega_{\mathrm{d}} - \omega_{\mathrm{c}})$ accounts for the density of states of the drive mode. Note that here we have implicitly made the first Markov approximation, which assumes that the drive field has a short enough memory that it can be considered uncorrelated in time, allowing us to approximate κ_{e} as constant over the narrow frequency bandwidth of the cavity mode. Furthermore, this approximation allows us to determine a time domain expression for κ_{e} by multiplying each side of Eq. (D.8) by $e^{-\omega_{\mathrm{c}}(t-t')}$ and integrating over all ω_{c} to obtain

$$\kappa_{\mathrm{e}}\delta(t-t') = |f_{\mathrm{dr}}|^2 e^{-\omega_{\mathrm{d}}(t-t')}, \tag{D.9}$$

where we have used the integral definition of the Dirac delta function given by Eq. (A.5) of Appendix A. Inputting this time domain expression for $|f_{\mathrm{dr}}|^2 e^{-\omega_{\mathrm{d}}(t-t')}$ into the second term on the right-hand side of Eq. (D.6), we then find the "past time" representation of $f_{\mathrm{dr}}\hat{a}_{\mathrm{dr}}(t)$ as

$$f_{\mathrm{dr}}\hat{a}_{\mathrm{dr}}(t) = \sqrt{\kappa_{\mathrm{e}}}\hat{a}_{\mathrm{in}}(t) - \frac{\kappa_{\mathrm{e}}}{2}\hat{a}(t), \tag{D.10}$$

where we have used the property of the Dirac delta function given by Eq. (A.4) of Appendix A, as well as defined the optical field input operator as[1]

$$\hat{a}_{\mathrm{in}}(t) = \frac{f_{\mathrm{dr}}}{\sqrt{\kappa_{\mathrm{e}}}}e^{-i\omega_{\mathrm{d}}(t-t_i)}\hat{a}_{\mathrm{dr}}(t_i). \tag{D.11}$$

[1]The justification for this definition comes from the fact that this representation resembles the field travelling in an optical transmission line [203, 262].

We note that the choice of integration limits in Eq. (D.6) running from t_i to t is completely arbitrary. Alternatively, we could have instead chosen to write the drive field as

$$\hat{a}_{\mathrm{dr}}(t) = e^{-i\omega_{\mathrm{d}}(t-t_f)}\hat{a}_{\mathrm{dr}}(t_f) + f^*_{\mathrm{dr}}\int_t^{t_f} e^{-i\omega_{\mathrm{d}}(t-t')}\hat{a}(t')dt', \tag{D.12}$$

where t_f is now a time in the distant future long after the drive field has interacted with the cavity [203]. Note that in Eq. (D.12), the sign in front of the integral has changed relative to that in Eq. (D.6), as the integration limits have been inverted. Again, using the relation for $|f_{\mathrm{dr}}|^2 e^{-\omega_{\mathrm{d}}(t-t')}$ given by Eq. (D.9), we can rewrite a "future time" expression for $f_{\mathrm{dr}}\hat{a}_{\mathrm{dr}}(t)$ as

$$f_{\mathrm{dr}}\hat{a}_{\mathrm{dr}}(t) = \sqrt{\kappa_{\mathrm{e}}}\hat{a}_{\mathrm{out}}(t) + \frac{\kappa_{\mathrm{e}}}{2}\hat{a}(t), \tag{D.13}$$

where we have now defined the optical field output operator as

$$\hat{a}_{\mathrm{out}}(t) = \frac{f_{\mathrm{dr}}}{\sqrt{\kappa_{\mathrm{e}}}}e^{-i\omega_{\mathrm{d}}(t-t_f)}\hat{a}_{\mathrm{dr}}(t_f). \tag{D.14}$$

Equating Eqs. (D.10) and (D.13) allows us to express this output field operator in terms of the input field $\hat{a}_{\mathrm{in}}(t)$ and the intracavity field $\hat{a}(t)$ as

$$\hat{a}_{\mathrm{out}}(t) = \hat{a}_{\mathrm{in}}(t) - \sqrt{\kappa_{\mathrm{e}}}\hat{a}(t). \tag{D.15}$$

This expression, known as the "input-output relation" [150], will prove useful when examining the field exiting the cavity, as well as its subsequent detection.

Using a similar procedure to solve Eqs. (D.4) and (D.5) (see Ref. [203] for details), we find

$$\sum_p f_p\hat{a}_p(t) = \sqrt{\kappa_{\mathrm{i}}}\hat{a}_{\mathrm{i}}(t) - \frac{\kappa_{\mathrm{i}}}{2}\hat{a}(t), \tag{D.16}$$

$$\sum_q f_q\hat{b}_q(t) = \sqrt{\Gamma_{\mathrm{m}}}\hat{b}_{\mathrm{i}}(t) - \frac{\Gamma_{\mathrm{m}}}{2}\hat{b}(t), \tag{D.17}$$

where κ_{i} is the internal loss rate of the optical cavity, with $\hat{a}_{\mathrm{i}}(t)$ and $\hat{b}_{\mathrm{i}}(t)$ being the optical and mechanical vacuum noise input operators, defined similarly to $\hat{a}_{\mathrm{in}}(t)$ as

$$\hat{a}_{\mathrm{i}}(t) = \frac{1}{\sqrt{\kappa_{\mathrm{i}}}}\sum_p f_p e^{-i\omega_p(t-t_i)}\hat{a}_p(t_i), \tag{D.18}$$

$$\hat{b}_{\mathrm{i}}(t) = \frac{1}{\sqrt{\Gamma_{\mathrm{m}}}}\sum_q f_q e^{-i\omega_q(t-t_i)}\hat{b}_q(t_i). \tag{D.19}$$

At this point, we now have everything we need to construct the equations of motion for the field operators of the optomechanical cavity. This is done by inputting Eqs. (D.10) and (D.16) into Eq. (D.1), as well as Eq. (D.17) into Eq. (D.2) to obtain

$$\dot{\hat{a}} = -\frac{\kappa}{2}\hat{a} - i\omega_{\mathrm{c}}\hat{a} + ig_0\left(\hat{b}^\dagger + \hat{b}\right)\hat{a} + \sqrt{\kappa_{\mathrm{e}}}\hat{a}_{\mathrm{in}} + \sqrt{\kappa_{\mathrm{i}}}\hat{a}_{\mathrm{i}}\,, \tag{D.20}$$

$$\dot{\hat{b}} = -\frac{\Gamma_{\mathrm{m}}}{2}\hat{b} - i\omega_{\mathrm{m}}\hat{b} + ig_0\hat{a}^\dagger\hat{a} + \sqrt{\Gamma_{\mathrm{m}}}\hat{b}_{\mathrm{i}}\,. \tag{D.21}$$

Together, these two expressions form the nonlinear QLEs for the photonic and phononic annihilation operators of the optomechanical system.

As our optomechanical cavity operates in the dispersive regime, we find it useful to transform the QLE's given by Eqs. (D.20) and (D.21) into the frame that rotates at the optical drive frequency ω_{d}. This is done by multiplying each of the optical fields by $e^{-i\omega_{\mathrm{d}}t}$ [451], resulting in the following transformations for each operator:[2]

$$\hat{a}(t) \rightarrow \hat{a}(t)e^{-i\omega_{\mathrm{d}}t}, \tag{D.22}$$

$$\hat{a}_{\mathrm{in}}(t) \rightarrow \hat{a}_{\mathrm{in}}(t)e^{-i\omega_{\mathrm{d}}t}, \tag{D.23}$$

$$\hat{a}_{\mathrm{i}}(t) \rightarrow \hat{a}_{\mathrm{i}}(t)e^{-i\omega_{\mathrm{d}}t}. \tag{D.24}$$

Note that since we are working in a frame rotating at the optical drive frequency, the drive terms will now be time-independent (aside from temporal quantum fluctuations). In this new rotating frame, the equation of motion for the cavity field operator then becomes

$$\dot{\hat{a}} = -\frac{\kappa}{2}\hat{a} + i\Delta_0\hat{a} + ig_0\left(\hat{b}^\dagger + \hat{b}\right)\hat{a} + \sqrt{\kappa_{\mathrm{e}}}\hat{a}_{\mathrm{in}} + \sqrt{\kappa_{\mathrm{i}}}\hat{a}_{\mathrm{i}}\,, \tag{D.25}$$

where we have introduced the bare detuning of the optical drive frequency from cavity resonance as $\Delta_0 = \omega_{\mathrm{d}} - \omega_{\mathrm{c}}$. Note that with this definition of cavity drive detuning, negative (positive) values indicate a red-detuned (blue-detuned) cavity drive. We further point out that the equation of motion for $\hat{b}$ given in Eq. (D.21) remains unperturbed by this rotation, as the radiation pressure force exerted on the resonator depends only on the number of photons in the cavity (*i.e.* $\hat{a}^\dagger\hat{a}$), which remains constant under this rotation.

[2] This rotation is equivalent to applying the unitary transformation $\hat{U}\hat{H}\hat{U} - i\hbar\hat{U}\frac{\partial\hat{U}^\dagger}{\partial t}$ to the Hamiltonian in Eq. (4.10), where $\hat{U} = e^{i\omega_{\mathrm{d}}\hat{a}^\dagger\hat{a}}$ [150].

Finally, we note that we can take the adjoint of each of the QLE's given in Eqs. (D.21) and (D.25), which results in the corresponding expressions for each of the photonic and phononic creation operators as[3]

$$\dot{\hat{a}}^\dagger = -\frac{\kappa}{2}\hat{a}^\dagger - i\Delta_0\hat{a}^\dagger - ig_0\left(\hat{b}^\dagger + \hat{b}\right)\hat{a}^\dagger + \sqrt{\kappa_\mathrm{e}}\hat{a}_\mathrm{in}^\dagger + \sqrt{\kappa_\mathrm{i}}\hat{a}_\mathrm{i}^\dagger, \tag{D.26}$$

$$\dot{\hat{b}}^\dagger = -\frac{\Gamma_\mathrm{m}}{2}\hat{b}^\dagger + i\omega_\mathrm{m}\hat{b}^\dagger - ig_0\hat{a}^\dagger\hat{a} + \sqrt{\Gamma_\mathrm{m}}\hat{b}_\mathrm{i}^\dagger, \tag{D.27}$$

where

$$\hat{a}_\mathrm{in}^\dagger(t) = \left[\hat{a}_\mathrm{in}(t)\right]^\dagger = \frac{f_\mathrm{dr}^*}{\sqrt{\kappa_\mathrm{e}}}e^{i\omega_\mathrm{d}(t-t_i)}\hat{a}_\mathrm{d}^\dagger(t_i), \tag{D.28}$$

$$\hat{a}_\mathrm{i}^\dagger(t) = \left[\hat{a}_\mathrm{i}(t)\right]^\dagger = \frac{1}{\sqrt{\kappa_\mathrm{i}}}\sum_p f_p^* e^{i\omega_p(t-t_i)}\hat{a}_p^\dagger(t_i), \tag{D.29}$$

$$\hat{b}_\mathrm{i}^\dagger(t) = \left[\hat{b}_\mathrm{i}(t)\right]^\dagger = \frac{1}{\sqrt{\Gamma_\mathrm{m}}}\sum_q f_q^* e^{i\omega_q(t-t_i)}\hat{b}_q^\dagger(t_i), \tag{D.30}$$

are simply the adjoints of the input operators given in Eqs. (D.11), (D.18), and (D.19), respectively.

D.2 Position and Momentum Operator Representation

In the previous section, the motion of the mechanical resonator was quantified in terms of its phononic creation and annihilation operators. However, as the dispersive optomechanical systems considered in this work couple directly to the displacement of the resonator, a more natural choice would be to describe the mechanical motion in terms of the position and momentum operators defined in Eqs. (2.17) and (2.19), respectively. In this representation, the Hamiltonian describing the free evolution of the mechanical resonator is then given by

$$\hat{H}_\mathrm{m} = \frac{1}{2}m\omega_\mathrm{m}^2\hat{x}^2 + \frac{\hat{p}^2}{2m}. \tag{D.31}$$

In principle, one could insert this Hamiltonian into Eq. (4.10) and then use Eq. (4.11) to determine the equations of motion for both $\hat{x}$ and $\hat{p}$. However, it is much easier

[3]This equations of motion could also have been obtained by inputting $\hat{a}^\dagger$ and $\hat{b}^\dagger$ in the Heisenberg equation given in Eq. (4.11).

to simply take the time derivatives of Eqs. (2.17) and (2.19) while inputting Eqs. (D.20)–(D.27) for the time derivatives of the creation/annihilation operators of photons and phonons in the system to find

$$\dot{\hat{x}} = -\frac{\Gamma_{\rm m}}{2}\hat{x} + \sqrt{\Gamma_{\rm m}}\hat{x}_{\rm i} + \frac{\hat{p}}{m}, \tag{D.32}$$

$$\dot{\hat{p}} = -\frac{\Gamma_{\rm m}}{2}\hat{p} - m\omega_{\rm m}^2\hat{x} + \sqrt{\Gamma_{\rm m}}\hat{p}_{\rm i} + 2g_0 p_{\rm zpf}\hat{a}^\dagger\hat{a}, \tag{D.33}$$

where we have defined the input noise position $\hat{x}_{\rm i}$ and momentum $\hat{p}_{\rm i}$ operators as

$$\hat{x}_{\rm i}(t) = x_{\rm zpf}\left[\hat{b}_{\rm i}^\dagger(t) + \hat{b}_{\rm i}(t)\right], \tag{D.34}$$

$$\hat{p}_{\rm i}(t) = ip_{\rm zpf}\left[\hat{b}_{\rm i}^\dagger(t) - \hat{b}_{\rm i}(t)\right]. \tag{D.35}$$

We now look to combine Eqs. (D.32) and (D.33) in order to eliminate $\hat{p}$, resulting in an equation of motion for the mechanical position operator $\hat{x}$. This is done by first taking another time derivative of Eq. (D.32), and using Eq. (D.33) to obtain

$$\ddot{\hat{x}} = -\frac{\Gamma_{\rm m}}{2}\dot{\hat{x}} + \sqrt{\Gamma_{\rm m}}\dot{\hat{x}}_{\rm i} + \frac{1}{m}\left[-\frac{\Gamma_{\rm m}}{2}\hat{p} - m\omega_{\rm m}^2\hat{x} + \sqrt{\Gamma_{\rm m}}\hat{p}_{\rm i} + 2g_0 p_{\rm zpf}\hat{a}^\dagger\hat{a}\right]. \tag{D.36}$$

Next, we rearrange Eq. (D.32) to solve for $\hat{p}$ and input the result into Eq. (D.36), while using the relations $g_0 = Gx_{\rm zpf}$ and $x_{\rm zpf}p_{\rm zpf} = \hbar/2$ to find

$$\ddot{\hat{x}} = -\Gamma_{\rm m}\dot{\hat{x}} - \omega_{\rm m}^2\hat{x} + \sqrt{\Gamma_{\rm m}}\dot{\hat{x}}_{\rm i} + \frac{\sqrt{\Gamma_{\rm m}}}{m}\hat{p}_{\rm i} + \frac{\hbar G\hat{a}^\dagger\hat{a}}{m} - \frac{\Gamma_{\rm m}^2}{4}\hat{x} + \frac{\Gamma_{\rm m}\sqrt{\Gamma_{\rm m}}}{2}\hat{x}_{\rm i}. \tag{D.37}$$

We then invoke the high-Q approximation ($Q_{\rm m} = \omega_{\rm m}/\Gamma_{\rm m} \gg 1$), allowing us to neglect the last two terms on the right-hand side of Eq. (D.37), resulting in

$$\ddot{\hat{x}} + \Gamma_{\rm m}\dot{\hat{x}} + \omega_{\rm m}^2\hat{x} = \frac{1}{m}\left[\hat{F}_{\rm th} + \hat{F}_{\rm rp}\right], \tag{D.38}$$

where we have interpreted $\hat{F}_{\rm th}$ as a thermal Langevin force acting upon the mechanical resonator given by

$$\hat{F}_{\rm th} = 2\sqrt{\Gamma_{\rm m}}\hat{p}_{\rm i} = i\sqrt{2\hbar\omega_{\rm m}\Gamma_{\rm m}m}\left[\hat{b}_{\rm i}^\dagger(t) - \hat{b}_{\rm i}(t)\right]. \tag{D.39}$$

Note that in this definition we have made use of the relation $\hat{p}_{\rm i} = m\dot{\hat{x}}_{\rm i}$.

Upon inspection of Eq. (D.38), we find that we have arrived at a quantized version of the equation of motion for the classical damped harmonic oscillator given by Eq. (2.7), with the forcing function identified as $\hat{F}(t) = \hat{F}_{\rm th}(t) + \hat{F}_{\rm rp}(t)$. That

is to say, the mechanical motion is driven by an intrinsic thermal force due to its environment, as well as a radiation pressure force exerted by photons in the cavity.

Finally, we wish to express the equation of motion for the cavity photon annihilation operator in terms of the mechanical position. This is done by using Eq. (2.17) to replace the phonon creation and annihilation operators in the third term on the right-hand side of Eq. (D.25) with the position operator $\hat{x}$, resulting in

$$\dot{\hat{a}} = -\frac{\kappa}{2}\hat{a} + i\Delta_0\hat{a} + iG\hat{x}\hat{a} + \sqrt{\kappa_\mathrm{e}}\hat{a}_\mathrm{in} + \sqrt{\kappa_\mathrm{i}}\hat{a}_\mathrm{i}\,. \tag{D.40}$$

Appendix E

Markovian Noise Commutators and Correlators

In order to calculate the PSDs of the optomechanical system discussed in Chapter 4, we need to determine its noise correlators similar to those seen under the integrals in Eqs. (A.19) and (A.23). Here we will show that the first Markov approximation invoked in Appendix D (*i.e.* the loss rates of the system are frequency-independent) leads to Markovian, or delta-correlated noise, which is the quantum equivalent of classical white noise.

We start by looking at the canonical commutation relations of each of the noise operators introduced in the previous sections. As we did in Appendix D, we will focus on the optical input operator $\hat{a}_{\mathrm{in}}(t)$ and apply the results to the other noise operators. Using Eq. (D.11) for $\hat{a}_{\mathrm{in}}(t)$ and Eq. (D.28) for $\hat{a}^{\dagger}_{\mathrm{in}}(t)$, we find the canonical correlator of this input optical field as [203]

$$[\hat{a}_{\mathrm{in}}(t), \hat{a}^{\dagger}_{\mathrm{in}}(t')] = [\delta\hat{a}_{\mathrm{in}}(t), \delta\hat{a}^{\dagger}_{\mathrm{in}}(t')] = \frac{|f_{\mathrm{dr}}|^2}{\kappa_{\mathrm{e}}} e^{-i\omega_{\mathrm{d}}(t-t')} = \delta(t-t'), \tag{E.1}$$

where we have also used Eq. (D.9), as well as the fact that $[\hat{a}_{\mathrm{dr}}(t_i), \hat{a}^{\dagger}_{\mathrm{dr}}(t_i)] = 1$. Performing similar calculations for $\hat{a}_{\mathrm{i}}(t)$ and $\hat{b}_{\mathrm{i}}(t)$, we find [203, 452]

$$[\hat{a}_{\mathrm{i}}(t), \hat{a}^{\dagger}_{\mathrm{i}}(t')] = [\delta\hat{a}_{\mathrm{i}}(t), \delta\hat{a}^{\dagger}_{\mathrm{i}}(t')] = \delta(t-t'), \tag{E.2}$$

$$[\hat{b}_{\mathrm{i}}(t), \hat{b}^{\dagger}_{\mathrm{i}}(t')] = [\delta\hat{b}_{\mathrm{i}}(t), \delta\hat{b}^{\dagger}_{\mathrm{i}}(t')] = \delta(t-t'), \tag{E.3}$$

where $\delta\hat{b}_{\mathrm{i}}(t)$ and $\delta\hat{b}^{\dagger}_{\mathrm{i}}(t')$ for the phonon modes are defined similarly to their optical counterparts. The commutators in Eqs. (E.1)–(E.3) are the first hallmark of Markovian noise [203, 452].

We also look to determine the correlators for each of the fluctuation terms of these noise quantities in the Markovian regime. In a fashion similar to how we calculated the commutator for $\hat{a}_{\rm in}(t)$, we determine the correlators for its fluctuations as

$$\langle \delta\hat{a}_{\rm in}(t)\delta\hat{a}^{\dagger}_{\rm in}(t')\rangle = (\bar{N}_{\rm in}+1)\delta(t-t'), \tag{E.4}$$

$$\langle \delta\hat{a}^{\dagger}_{\rm in}(t)\delta\hat{a}_{\rm in}(t')\rangle = \bar{N}_{\rm in}\delta(t-t'), \tag{E.5}$$

$$\langle \delta\hat{a}_{\rm in}(t)\delta\hat{a}_{\rm in}(t')\rangle = \langle \delta\hat{a}^{\dagger}_{\rm in}(t)\delta\hat{a}^{\dagger}_{\rm in}(t')\rangle = 0, \tag{E.6}$$

where we have used the relations $\langle \hat{a}_{\rm dr}(t_i)\hat{a}^{\dagger}_{\rm dr}(t_i)\rangle = (\bar{N}_{\rm in}+1)$, $\langle \hat{a}^{\dagger}_{\rm dr}(t_i)\hat{a}_{\rm dr}(t_i)\rangle = \bar{N}_{\rm in}$, and $\langle \hat{a}_{\rm dr}(t_i)\hat{a}_{\rm dr}(t_i)\rangle = \langle \hat{a}^{\dagger}_{\rm dr}(t_i)\hat{a}^{\dagger}_{\rm dr}(t_i)\rangle = 0$, with $\bar{N}_{\rm in}$ being the average number of photons due to fluctuations in the optical input channel[1]. Applying this treatment to the other noise quantities of the system, we find [150, 203, 289]

$$\langle \delta\hat{a}_j(t)\delta\hat{a}^{\dagger}_j(t')\rangle = \delta(t-t'), \tag{E.7}$$

$$\langle \delta\hat{a}^{\dagger}_j(t)\delta\hat{a}_j(t')\rangle = \langle \delta\hat{a}_j(t)\delta\hat{a}_j(t')\rangle = \langle \delta\hat{a}^{\dagger}_j(t)\delta\hat{a}^{\dagger}_j(t')\rangle = 0, \tag{E.8}$$

$$\langle \delta\hat{b}_{\rm i}(t)\delta\hat{b}^{\dagger}_{\rm i}(t')\rangle = [\bar{n}_{\rm b}(\omega)+1]\delta(t-t'), \tag{E.9}$$

$$\langle \delta\hat{b}^{\dagger}_{\rm i}(t)\delta\hat{b}_{\rm i}(t')\rangle = \bar{n}_{\rm b}(\omega)\delta(t-t'), \tag{E.10}$$

$$\langle \delta\hat{b}_{\rm i}(t)\delta\hat{b}_{\rm i}(t')\rangle = \langle \delta\hat{b}^{\dagger}_{\rm i}(t)\delta\hat{b}^{\dagger}_{\rm i}(t')\rangle = 0, \tag{E.11}$$

where $\bar{n}_{\rm b}(\omega)$ is the thermal occupation of the phonon bath given by Eq. (2.73). In Eqs. (E.7) and (E.8) we have used $\delta\hat{a}_j$ as a placeholder for either of the optical fluctuation amplitudes $\delta\hat{a}_{\rm in}$ and $\delta\hat{a}_{\rm i}$, as well as assumed a zero temperature bath for each optical mode due to the fact that $\hbar\omega_j \gg k_{\rm B}T$ for the optical frequencies ($\omega_j/2\pi \sim 200$ THz) and temperatures ($T < 100$ K) considered in this thesis. We can also input the correlators for the mechanical bath operators given in Eqs. (E.9) and (E.10) into Eq. (D.39) to find a correlator for $\delta\hat{F}_{\rm th}(t)$ as

$$\langle \delta\hat{F}_{\rm th}(t)\delta\hat{F}_{\rm th}(t')\rangle = \hbar\omega m\Gamma_{\rm m}\coth\left(\frac{\hbar\omega}{2k_{\rm B}T}\right)\delta(t-t'), \tag{E.12}$$

where we have used the relation $2\bar{n}_{\rm b}(\omega)+1 = \coth(\hbar\omega/2k_{\rm B}T)$. Note that any cross-correlations between the noise terms given in Eqs. (E.4)–(E.12) will equate to zero.

[1]Because we are considering the fluctuations in the input field here, $\bar{N}_{\rm in}$ includes contributions due to both vacuum and thermal noise, however, it does not include the coherent input proportional to $|\bar{a}_{\rm in}|^2$.

We also find it useful to calculate the correlators for each of these noise operators in the frequency domain. This can be done using the definition of the Fourier transform (see Appendix A), which results in the non-zero correlators

$$\langle \hat{a}_j(\omega)\hat{a}_j^\dagger(\omega')\rangle = 2\pi\delta(\omega+\omega'), \tag{E.13}$$

$$\langle \delta\hat{b}_{\mathrm{i}}(\omega)\delta\hat{b}_{\mathrm{i}}^\dagger(\omega')\rangle = 2\pi[\bar{n}_{\mathrm{b}}(\omega)+1]\delta(\omega+\omega'), \tag{E.14}$$

$$\langle \delta\hat{b}_{\mathrm{i}}^\dagger(\omega)\delta\hat{b}_{\mathrm{i}}(\omega')\rangle = 2\pi\bar{n}_{\mathrm{b}}(\omega)\delta(\omega+\omega'), \tag{E.15}$$

$$\langle \delta\hat{F}_{\mathrm{th}}(\omega)\delta\hat{F}_{\mathrm{th}}(\omega')\rangle = 2\pi\hbar\omega m\Gamma_{\mathrm{m}}\coth\left(\frac{\hbar\omega}{2k_{\mathrm{B}}T}\right)\delta(\omega+\omega'). \tag{E.16}$$

In Chapter 4, we use these correlators to calculate the PSDs for the various properties of our system using Eq. (A.23) from Appendix A.

In the form given by Eqs. (E.7)–(E.16), it is not intuitive how exactly these delta-correlated quantum correlators are equivalent to classical white noise. The situation becomes much clearer, however, when we consider the PSDs associated with these noise quantities. For example, the PSD of the fluctuating thermal force acting on the resonator is given by [151, 203, 289, 296]

$$S_{FF}^{\mathrm{th}}(\omega) = \frac{1}{2\pi}\int_{-\infty}^{\infty}\langle \delta\hat{F}_{\mathrm{th}}(\omega)\delta\hat{F}_{\mathrm{th}}(\omega')\rangle\, d\omega' = \hbar\omega m\Gamma_{\mathrm{m}}\coth\left(\frac{\hbar\omega}{2k_{\mathrm{B}}T}\right). \tag{E.17}$$

In the classical regime, $k_{\mathrm{B}}T \gg \hbar\omega$, such that[2] [145]

$$S_{FF}^{\mathrm{th}}(\omega) \approx 2m\Gamma_{\mathrm{m}}k_{\mathrm{B}}T, \tag{E.18}$$

which is simply the classical fluctuation-dissipation theorem [149, 203]. Here we see that the spectrum in Eq. (E.18) is indeed flat, such that the thermal force noise in our system constitutes a white noise bath in the classical regime, provided Γ_{m} is frequency-independent, as is guaranteed by our initial Markov approximation.

[2]Here we consider the two-sided thermal force spectral density, though often the one-sided spectral density is considered, which is larger by a factor of two to account for the reduction of the defined integration space by one-half.

Appendix F

Mechanical Resonator Heating Model

As was the case for the silicon optomechanical devices studied in Refs. [135, 204, 423], we attribute the heating in our mechanical resonators as being due to the excitation of sub-bandgap electronic defect states found at the surfaces of silicon devices [274], which undergo nonradiative phonon-assisted decay, generating a local bath of hot phonons that heat up our mechanical resonator. We model this thermalization process for a given mode of our mechanical resonator as a harmonic oscillator at frequency ω_{m}, coupled at its intrinsic damping rate Γ_{m} to the device's cold environmental bath at temperature T_{b} as well as at a rate Γ_{p} to this hot phonon bath[1] at temperature T_{p}, as depicted schematically in Fig. F.1a. Due to the high quality factors of the mechanical modes considered in this paper, we can treat both of these environmental and photon-induced baths as harmonic oscillators at the mechanical frequency, each with an average occupancy of $\bar{n}_{\mathrm{th}}$ and $\bar{n}_{\mathrm{p}}$, respectively. In this situation, the rate equation for the average occupation of the mechanical mode will be given by [204]

$$\dot{\langle n \rangle} = -\Gamma_{\mathrm{h}} \langle n \rangle + \Gamma_{\mathrm{m}} \bar{n}_{\mathrm{th}} + \Gamma_{\mathrm{p}} \bar{n}_{\mathrm{p}}, \tag{F.1}$$

with $\Gamma_{\mathrm{h}} = \Gamma_{\mathrm{m}} + \Gamma_{\mathrm{p}}$ being the total rate at which the mode equilibrates to the two baths. We note that our treatment of the mechanical mode occupation dynamics differs from that of Ref. [204], in that we have not included a time-dependent term proportional to $\bar{n}_{\mathrm{p}}$, which accounts for the finite equilibration time of the

[1] Its also possible that this hot phonon bath could be partially due to the quantum radiation backaction process described in Section 4.4.4.

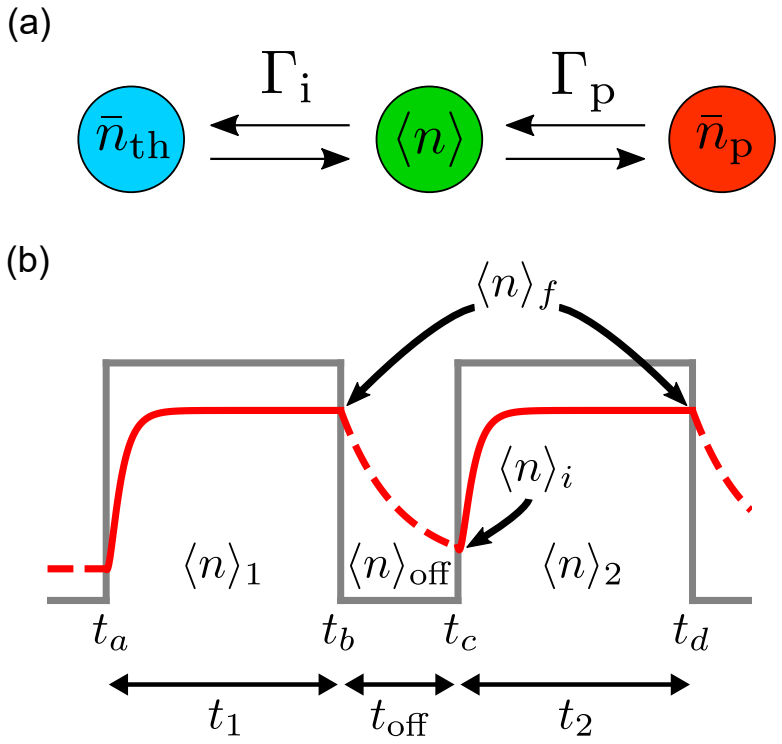

Figure F.1: (a) Block diagram of the heating model for the experimentally relevant case where the mechanical mode is coupled to a cold environmental bath at its intrinsic damping rate Γ_m and a hot photon-induced bath at a rate Γ_p, each with phonon occupancies of $\bar{n}_\mathrm{th}$ and $\bar{n}_\mathrm{p}$, respectively. (b) Diagram of the double pulse measurement scheme used in this work. The solid grey line indicates the duty cycle of the laser, while the solid (dashed) red line expresses the phonon occupation of the mechanical mode with the laser on (off). Figure reproduced from Ref. [163]. © 2018 American Physical Society.

hot photon-induced bath. This is justified by the fact that the thermal relaxation time for our device (see Section 7.3.2), found by approximating each half of our resonator as a simple rectangular beam [200, 208, 389] 10 μm in length with a cross-section-limited thermal conductivity [184, 185, 197–199], is at most 20 ns. Therefore, our measurement scheme, with a temporal resolution on the order of 1 μs, is unable to resolve this thermalization process.

Solving the rate equation given in Eq. (F.1), we find the time-dependent mechanical mode occupancy to be

$$\langle n \rangle (t) = \langle n \rangle (t_0) e^{-\Gamma_\mathrm{h}(t-t_0)} + \bar{n}_\mathrm{eq} \left(1 - e^{-\Gamma_\mathrm{h}(t-t_0)}\right), \tag{F.2}$$

where $\langle n \rangle (t_0)$ is the phonon occupancy at the initial time t_0 and $\bar{n}_\mathrm{eq} = (\Gamma_\mathrm{m}\bar{n}_\mathrm{th} + \Gamma_\mathrm{p}\bar{n}_\mathrm{p})/\Gamma_\mathrm{h}$ is the occupancy of the mechanical mode at times $t \gg \Gamma_\mathrm{h}^{-1}$, long enough

that the mode is able to equilibrate to an average of the bath occupations, weighted by their coupling rates. Furthermore, if the connection to the hot photon-induced bath is severed (*i.e.* by turning the laser off), we take $\Gamma_{\rm p} = 0$ such that the mechanical mode occupation will tend towards equilibrium with the environmental bath at its intrinsic damping rate according to (see Section 2.4.5)

$$\langle n \rangle (t) = \langle n \rangle (t_0) e^{-\Gamma_{\rm m}(t-t_0)} + \bar{n}_{\rm th} \left(1 - e^{-\Gamma_{\rm m}(t-t_0)}\right). \tag{F.3}$$

For the experiment considered in Chapter 6, we measure the low temperature damping rate of our mechanical device, using the pump/probe measurement outlined in Section 6.4.5. This procedure can be described by the general two pulse scheme depicted in Fig. F.1b, where a pump pulse that turns on at $t = t_a$ and off at $t = t_b$ (pulse length $t_1 = t_b - t_a$), is followed by a probe pulse that turns on at $t = t_c$ and off at $t = t_d$ (pulse length $t_2 = t_d - t_c$), with a delay between the two pulses of $t_{\rm off} = t_c - t_b$. For this situation, the occupation of the mechanical mode during the pump pulse will evolve in time according to Eq. (F.2) as

$$\langle n \rangle_1 (t) = \langle n \rangle (t_a) e^{-\Gamma_{\rm h}(t-t_a)} + \bar{n}_{\rm eq} \left(1 - e^{-\Gamma_{\rm h}(t-t_a)}\right). \tag{F.4}$$

Once the pump pulse has been turned off, the resonator's occupancy will cool towards that of the environmental bath, as governed by Eq. (F.3), giving

$$\langle n \rangle_{\rm off} (t) = \langle n \rangle (t_b) e^{-\Gamma_{\rm m}(t-t_b)} + \bar{n}_{\rm th} \left(1 - e^{-\Gamma_{\rm m}(t-t_b)}\right). \tag{F.5}$$

Finally, the occupation of the mechanical mode during the probe pulse will obey

$$\langle n \rangle_2 (t) = \langle n \rangle (t_c) e^{-\Gamma_{\rm h}(t-t_c)} + \bar{n}_{\rm eq} \left(1 - e^{-\Gamma_{\rm h}(t-t_c)}\right). \tag{F.6}$$

Assuming the experimentally relevant case of $t_1 = t_2 \gg \Gamma_{\rm h}^{-1}$, the final occupancy at the end of either the pump or probe pulse will be given by $\langle n \rangle (t_b) = \langle n \rangle (t_d) = \bar{n}_{\rm eq}$, while the initial occupancy of the mode at the beginning of the probe pulse can be found to be $\langle n \rangle (t_c) = \bar{n}_{\rm eq} e^{-\Gamma_{\rm m} t_{\rm off}} + \bar{n}_{\rm th} \left(1 - e^{-\Gamma_{\rm m} t_{\rm off}}\right)$. Using these two expressions, we can determine the ratio of the *measured* occupancy at the beginning of the probe pulse $\langle n \rangle_i$ to the final *measured* occupancy of either the probe or the pump pulse

$\langle n \rangle_f$ as

$$\begin{aligned} \frac{\langle n \rangle_i}{\langle n \rangle_f} &= \frac{\langle n \rangle (t_c) + \bar{n}_{\mathrm{imp}}}{\langle n \rangle (t_b) + \bar{n}_{\mathrm{imp}}} = \frac{\langle n \rangle (t_c) + \bar{n}_{\mathrm{imp}}}{\langle n \rangle (t_d) + \bar{n}_{\mathrm{imp}}} \\ &= \frac{(\bar{n}_{\mathrm{eq}} - \bar{n}_{\mathrm{th}})\, e^{-\Gamma_{\mathrm{m}} t_{\mathrm{off}}} + \bar{n}_{\mathrm{th}} + \bar{n}_{\mathrm{imp}}}{\bar{n}_{\mathrm{eq}} + \bar{n}_{\mathrm{imp}}}, \end{aligned} \tag{F.7}$$

where we have included the noise due to the imprecision of the measurement as an apparent phonon occupancy $\bar{n}_{\mathrm{imp}}$ (see Section 4.4.4). Using this equation, thermal ringdown data for the mechanical mode can be fit to extract its intrinsic damping rate, as is done in Fig. 6.10.

We conclude on the note that it is often the case that $\bar{n}_{\mathrm{eq}} \approx \bar{n}_{\mathrm{p}} \gg \bar{n}_{\mathrm{th}}, \bar{n}_{\mathrm{imp}}$, such that Eq. (F.7) simplifies to

$$\frac{\langle n \rangle_i}{\langle n \rangle_f} \approx e^{-\Gamma_{\mathrm{m}} t_{\mathrm{off}}} + \frac{\bar{n}_{\mathrm{th}} + \bar{n}_{\mathrm{imp}}}{\bar{n}_{\mathrm{eq}}}, \tag{F.8}$$

as can be seen by the fact that $\langle n \rangle_i / \langle n \rangle_f \approx 1$ for $t_{\mathrm{off}} \ll \Gamma_{\mathrm{m}}^{-1}$ in Fig. 6.10.

Appendix G

Coupling to Ensembles of Crystalline TLS Defects

In this appendix, we calculate the relaxation damping rate of a mechanical resonator coupled to a crystalline ensemble of TLS defects, and compare it to the results for the amorphous TLS distributions studied in Chapter 6.

G.1 Mechanical Damping Rate

For TLS ensembles that exhibit crystalline behaviour, a narrow distribution in TLS energies exists. To account for this, Phillips [344] suggested a density of states function of the form

$$\mathcal{P}(\Delta, \Delta_0) = D_0 \sqrt{\frac{2}{\pi}} \frac{1}{\delta E_\Delta} e^{-\frac{1}{2}\left(\frac{E_\Delta}{\delta E_\Delta}\right)^2} \delta(E_0 - \bar{E}_0), \tag{G.1}$$

that is, the crystalline nature of the TLS ensemble results in a well-defined tunneling energy of $\bar{E}_0$ and a Gaussian spread in the asymmetry energy, with a standard deviation of δE_Δ centered around $E_\Delta = 0$, with a density specified by D_0. We note that with this choice of distribution function, we need only consider the relevant case of $\omega_\mathrm{m}\tau_\mathrm{TLS} \gg 1$, due to the fact that the experimentally measured dissipation increases monotonically with temperature for each of the mechanical modes studied in this paper (see Fig. 6.11) [344]. This allows us to approximate the mechanical damping rate in Eq. (6.41) as

$$\Gamma_\mathrm{c} = \frac{\gamma^2 D_0}{\rho c_q^2 k_\mathrm{B} T \delta E_\Delta} \sqrt{\frac{2}{\pi}} \int_0^\infty \left(\frac{E_\Delta}{\bar{E}}\right)^2 \mathrm{sech}^2\left(\frac{\bar{E}}{2k_\mathrm{B}T}\right) e^{-\frac{1}{2}\left(\frac{E_\Delta}{\delta E_\Delta}\right)^2} \tau_\mathrm{TLS}^{-1}(E_\Delta, \bar{E}_0) dE_\Delta, \tag{G.2}$$

where $\bar{E}^2 = E_\Delta^2 + \bar{E}_0^2$ and we have expressed τ_{TLS} as an explicit function of E_Δ and E_0. To examine the low temperature limit of the damping due to this crystalline TLS distribution, we take $T \ll (E_\Delta^2 + \bar{E}_0^2)^{1/2}/k_{\mathrm{B}}$, allowing for the approximations $\mathrm{sech}^2\left(\bar{E}/2k_{\mathrm{B}}T\right) \approx 4e^{-\bar{E}/k_{\mathrm{B}}T}$ and $\coth\left(\bar{E}/2k_{\mathrm{B}}T\right) \approx 1$ over the regions of integration in Eq. (G.2) that provide the majority of the contribution to Γ_{c}, resulting in a low-temperature dependence according to

$$\Gamma_{\mathrm{c}} \approx \frac{4\gamma^4 D_0 \bar{E}_0^2}{A\rho^2\hbar^2 c_q^2 c_{\mathrm{e}}^3 k_{\mathrm{B}} T \delta E_\Delta}\sqrt{\frac{2}{\pi}}\int_0^\infty \frac{E_\Delta^2}{\bar{E}^3} e^{-\frac{\bar{E}}{k_{\mathrm{B}}T}} e^{-\frac{1}{2}\left(\frac{E_\Delta}{\delta E_\Delta}\right)^2} dE_\Delta. \tag{G.3}$$

In the opposite limit of $T \gg (\delta E_\Delta^2 + \bar{E}_0^2)^{1/2}/k_{\mathrm{B}}$, we have $\mathrm{sech}^2\left(\bar{E}/2k_{\mathrm{B}}T\right) \approx 1$ and $\coth\left(\bar{E}/2k_{\mathrm{B}}T\right) \approx 2k_{\mathrm{B}}T/\bar{E}$, such that the high temperature limit for Γ_{c} is given by

$$\Gamma_{\mathrm{c}} \approx \frac{2\gamma^4 D_0 \bar{E}_0^2}{A\rho^2\hbar^2 c_q^2 c_{\mathrm{e}}^3 \delta E_\Delta}\sqrt{\frac{2}{\pi}}\int_0^\infty \frac{E_\Delta^2}{\bar{E}^4} e^{-\frac{1}{2}\left(\frac{E_\Delta}{\delta E_\Delta}\right)^2} dE_\Delta. \tag{G.4}$$

Here, the factor of $k_{\mathrm{B}}T$ from the approximation of $\coth\left(\bar{E}/2k_{\mathrm{B}}T\right)$ cancels that in the denominator of Eq. (G.2), such that at high temperatures, Γ_{c} is temperature independent, similar to the high-temperature limit of the damping rate due to the amorphous TLS distribution, albeit at a different value.

G.2 Fits to Amorphous and Crystalline TLS Damping Models

Here, we present fits of the one-dimensional TLS dissipation models, with both amorphous and crystalline distributions, to the mechanical damping rate data for the four mechanical modes studied in Chapter 6. These fits are displayed in Fig. G.1, with the parameters extracted from the crystalline fits displayed in Table G.1. As one can see in Fig. G.1, the crystalline model exhibits a rapid decline in dissipation versus temperature as compared to the amorphous model, far undershooting the measured damping rates for $T \lesssim 500$ mK. Furthermore, this crystalline model plateaus to a constant value at high temperature that is slightly smaller than the amorphous model predicts. The amorphous TLS damping model is therefore a better fit to our data, implying that the low-temperature dissipation in our mechanical modes is caused by coupling to a glassy distribution of defects.

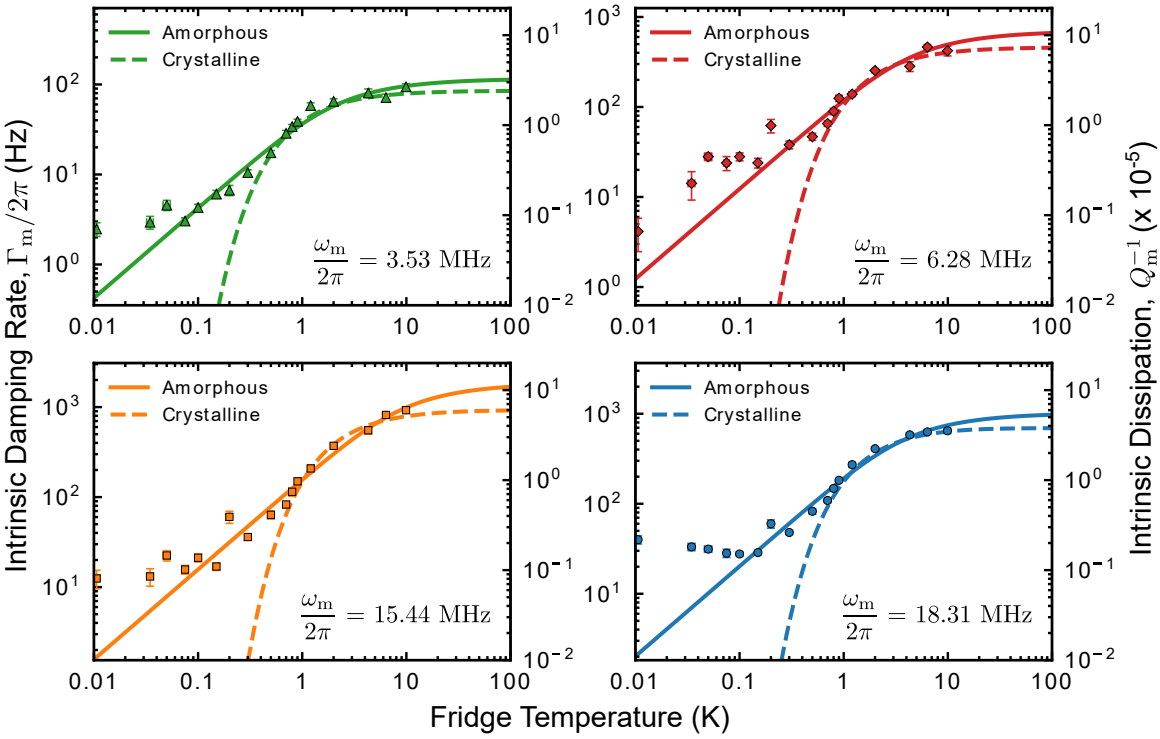

Figure G.1: The intrinsic damping rate Γ_m for each of the four mechanical modes studied in Chapter 6 versus temperature, with the right axis displaying their intrinsic dissipation $Q_m^{-1} = \Gamma_m/\omega_m$. Each mode is fit to both the amorphous (solid line) and crystalline (dashed line) TLS damping models given by Eqs. (6.43) and (G.2), respectively. From the fits to the crystalline TLS damping model we extract $\bar{E}_0$, δE_Δ, and $\gamma^4 D_0$ for each mechanical mode. The parameters from this fit are displayed in Table G.1. Figure reproduced from Ref. [163]. © 2018 American Physical Society.

$\omega_m/2\pi$ (MHz)	$\bar{E}_0$ (μeV)	δE_Δ (meV)	$\gamma^4 D_0$ (eV^4 m^{-3})
3.53	74 ± 6	24.6 ± 0.7	(3.6 ± 0.1) ×10^{24}
6.28	133 ± 19	37.3 ± 1.1	(1.7 ± 0.2) ×10^{25}
15.44	165 ± 12	19.3 ± 397	(2 ± 30) ×10^{25}
18.31	129 ± 8	3.5 ± 2.0	(3.0 ± 1.7) ×10^{24}

Table G.1: Summary of the tunneling energy $\bar{E}_0$ and spread in asymmetry energy δE_Δ, as well as $\gamma^4 D_0$, for the fits to the mechanical damping rate using the crystalline TLS damping model (*i.e.* Eq. (G.2)) in Fig. G.1 (dashed line). The uncertainty in each parameter is given by their standard deviations from the fit.

Appendix H

Integral Approximations of Nonlinear Photothermal Optomechanical Properties

Though Eqs. (7.21)–(7.23) in Section 7.2.4 provide an exact representation for the optomechanically induced shift in mechanical equilibrium position, spring effect, and damping for a photothermally driven cavity, computing these quantities numerically can be cumbersome. This is due to the fact that in order to accurately model the nonlinear behaviour of the system, the number of terms that one must keep for each of the sums found in Eqs. (7.21)–(7.25) is on the order of ξ, which can be as large as 1500 for the conditions studied in Chapter 7. Fortunately, it was shown by Metzger *et al.* [303] that in the non-SBR regime, the integral in Eq. (7.20) can be performed directly by assuming the optical intensity inside the cavity adiabatically follows the quasistatic motion of the mechanical resonator. This allows for a simpler, more computationally efficient treatment of the nonlinear optomechanical system considered in this work, with minimal error introduced into the final results when compared to those given in Eqs. (7.21)–(7.23) (see Fig. H.1 below). Here we provide a brief overview of this method, resulting in approximate expressions for each of the nonlinear optomechanical properties given in the previous section.

As mentioned above, for this integral approach we immediately assume the non-SBR regime, such that the optical field in the cavity reacts nearly instantaneously to the resonator's mechanical motion [303]. In this case, we treat $x(t)$ as a quasistatic

variable, inserting the ansatz given by Eq. (4.84) into Eq. (4.19) (*i.e.* by taking $\Delta = \Delta_0 + G\bar{x} + GA\cos(\omega_\mathrm{m} t)$), allowing us to directly solve for the quasistatic cavity field amplitude as

$$a(t) = \frac{\sqrt{\kappa_\mathrm{e}}\bar{a}_\mathrm{in}}{\kappa/2 - i\left[\Delta_0 + G\bar{x} + GA\cos(\omega_\mathrm{m} t)\right]}. \tag{H.1}$$

Using this approximate expression for the cavity field amplitude, we can again take the time average of Eq. (7.2) to find an integral form for $\bar{x}$ as

$$\bar{x}(A) = \frac{\hbar G \kappa_\mathrm{e} |\bar{a}_\mathrm{in}|^2 (1+\beta)}{2\pi m \omega_\mathrm{m}^2} \int_0^{2\pi} \frac{d\vartheta}{(\kappa/2)^2 + (\Delta_0 + G\bar{x} + GA\cos\vartheta)^2}. \tag{H.2}$$

In comparing this expression with what was found for $\bar{x}$ in Section 7.2.4, we find that this approximation is equivalent to replacing the sum in Eq. (7.21) with an integral according to

$$\sum_{l=-\infty}^{\infty} |\tilde{a}_l|^2 \approx \frac{1}{2\pi} \int_0^{2\pi} \frac{d\vartheta}{(\kappa/2)^2 + (\Delta_0 + G\bar{x} + GA\cos\vartheta)^2}. \tag{H.3}$$

Furthermore, this integral can be solved analytically, resulting in

$$\int_0^{2\pi} \frac{d\vartheta}{(\kappa/2)^2 + (\Delta_0 + G\bar{x} + GA\cos\vartheta)^2} = \frac{2\pi\sqrt{2}}{\kappa\sqrt{\mathcal{X}}} \sqrt{\sqrt{\mathcal{X}} + \mathcal{Y}}, \tag{H.4}$$

where $\mathcal{X} = \mathcal{Y}^2 + \kappa^2(\Delta_0 + G\bar{x})^2$ and $\mathcal{Y} = G^2A^2 + \kappa^2/4 - (\Delta_0 + G\bar{x})^2$. Therefore, we can write $\bar{x}$ in the purely analytical form

$$\bar{x}(A) = \frac{\sqrt{2}\hbar G \kappa_\mathrm{e} |\bar{a}_\mathrm{in}|^2 (1+\beta)}{m\omega_\mathrm{m}^2 \kappa} \frac{\sqrt{\sqrt{\mathcal{X}} + \mathcal{Y}}}{\sqrt{\mathcal{X}}}. \tag{H.5}$$

Performing a similar analysis to determine the integral form for $\delta\Gamma_\mathrm{m}(A)$, we multiply Eq. (7.2) by $\dot{x}(t)$ and take the time average, while using the approximation for $a(t)$ given by Eq. (H.1) to obtain

$$\delta\Gamma_\mathrm{m}(A) = \frac{\hbar G \kappa_\mathrm{e} |\bar{a}_\mathrm{in}|^2 \beta}{\pi A m \omega_\mathrm{m}} \frac{\omega_\mathrm{m}\tau_\mathrm{pt}}{1 + \omega_\mathrm{m}^2 \tau_\mathrm{pt}^2} \int_0^{2\pi} \frac{\cos\vartheta d\vartheta}{(\kappa/2)^2 + (\Delta_0 + G\bar{x} + GA\cos\vartheta)^2}. \tag{H.6}$$

We note that this integral expression is only valid in the regime where photothermal forces dominate the optomechanical damping (see Eq. (7.14)), as $\delta\Gamma_\mathrm{m}(A) = 0$ for $\beta = 0$ here. Similar to the integral expression for $\bar{x}$, we find that Eq. (H.6) approximates Eq. (7.23) by replacing its sum with the integral

$$\begin{aligned} &\sum_{l=-\infty}^{\infty} \mathrm{Im}\left\{\tilde{a}_l \tilde{a}_{l+1}^* \left(1 + \frac{\beta}{1 - i\omega_\mathrm{m}\tau}\right)\right\} \\ &\approx \frac{\beta}{2\pi} \frac{\omega_\mathrm{m}\tau}{1 + \omega_\mathrm{m}^2\tau^2} \int_0^{2\pi} \frac{\cos\vartheta d\vartheta}{(\kappa/2)^2 + (\Delta_0 + G\bar{x} + GA\cos\vartheta)^2}. \end{aligned} \tag{H.7}$$

This integral also has an analytical expression given by

$$\begin{aligned}&\int_0^{2\pi} \frac{\cos\vartheta d\vartheta}{(\kappa/2)^2+(\Delta_0+G\bar{x}+GA\cos\vartheta)^2}\\&=-\mathrm{sgn}(\Delta_0+G\bar{x})\frac{2\pi\sqrt{2}}{GA\kappa\sqrt{\mathcal{X}}}\left(|\Delta_0+G\bar{x}|\sqrt{\sqrt{\mathcal{X}}-\mathcal{Y}}-\frac{\kappa}{2}\sqrt{\sqrt{\mathcal{X}}-\mathcal{Y}}\right),\end{aligned} \tag{H.8}$$

where $\mathrm{sgn}(z)$ is the signum function. Using this relation, we can then express $\delta\Gamma_\mathrm{m}(A)$ in the analytical form

$$\begin{aligned}\delta\Gamma_\mathrm{m}(A)=&\frac{-2\sqrt{2}\hbar\kappa_\mathrm{e}|\bar{a}_\mathrm{in}|^2\beta}{A^2m\omega_\mathrm{m}\kappa}\frac{\omega_\mathrm{m}\tau_\mathrm{pt}}{1+\omega_\mathrm{m}^2\tau_\mathrm{pt}^2}\frac{\mathrm{sgn}(\Delta_0+G\bar{x})}{\sqrt{\mathcal{X}}}\\&\times\left(|\Delta_0+G\bar{x}|\sqrt{\sqrt{\mathcal{X}}-\mathcal{Y}}-\frac{\kappa}{2}\sqrt{\sqrt{\mathcal{X}}-\mathcal{Y}}\right).\end{aligned} \tag{H.9}$$

It is also possible to arrive at an integral expression for $\delta\omega_\mathrm{m}$, which looks similar to Eq. (H.6) except the factor of $\cos(\vartheta)$ in the numerator of the integrand is replaced with $\sin(\vartheta)$. This, however, results in an integral that evaluates to zero, as one would expect in the self-oscillating regime (see Section 4.5), and therefore offers no new insight into Eq. (7.22).

In Fig. H.1, we compare the attractor diagrams of $\delta\Gamma_\mathrm{m}(A)$ for the optomechanical device studied in this work generated using both the exact sums given in Eqs. (7.21) and (7.23), as well as the integral approximations of Eqs. (H.2) and (H.6). As the device studied in Chapter 7 exists deeply in the non-SBR regime ($\kappa/\omega_\mathrm{m}\approx 180$), the integral approximations presented in this section accurately model its nonlinear optomechanical behaviour. This is demonstrated by the fact the percent difference in $\delta\Gamma_\mathrm{m}(A)$ between these two methods is at most 13.4% for the conditions given in Fig. 7.7 (see Fig. H.1c). Furthermore, we note that while the integral approach slightly overshoots the value of $\delta\Gamma_\mathrm{m}(A)$, it still provides an excellent approximation of the mechanical amplitude, as can be seen by the nearly matching contour lines in Figs. H.1a/b.

We conclude this section by noting that while we have used Eqs. (H.2)–(H.9) for preliminary assessment of our optomechanical device, as well as the computationally intensive calculations associated with the varying power measurements shown in Fig. 7.11, the fits and attractor diagram in Figs. 7.7 and 7.8 were determined using the exact expressions given by Eqs. (7.21)–(7.23).

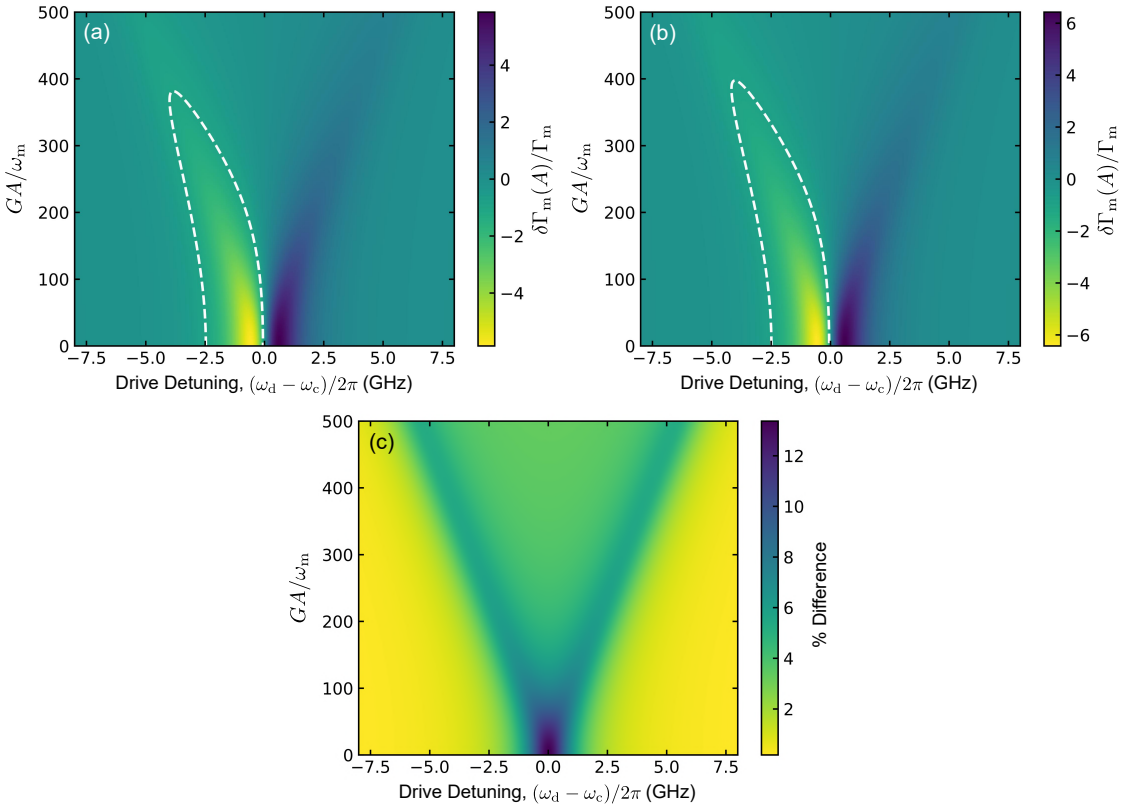

Figure H.1: Attractor diagrams of $\delta\Gamma_{\rm m}(A)/\Gamma_{\rm m}$ (color scale) for the device parameters given in Fig. 7.7 using (a) the exact sum formalism of Eqs. (7.21) and (7.23), and (b) the integral approximations given by Eqs. (H.2) and (H.6). The white dashed line indicates the contour of $\delta\Gamma_{\rm m}(A)/\Gamma_{\rm m} = -1$, demarcating the region of self-oscillations. For the sums in (a), terms up to $l = \pm 1000$ were used, while the integrals in (b) were performed using a numerical solver (trapezoidal method). In (c), we show the percent difference between the attractor diagrams given in (a) and (b). Here, we highlight the fact that over the displayed detuning and amplitude range, there is at most a 13.4% difference between the sum and integral methods for calculating $\delta\Gamma_{\rm m}(A)$, which is located near zero detuning for small mechanical amplitudes. Figure adapted from Ref. [295]. © 2019 American Physical Society.